

TURBINE AERODYNAMICS

**AXIAL-FLOW AND RADIAL-INFLOW TURBINE DESIGN
AND ANALYSIS**

Ronald H. Aungier

NEW YORK

ASME PRESS

2005

To my wife Anne, with love
My companion and partner in everything worthwhile

TABLE OF CONTENTS

PREFACE	xiii
<hr/>	
1. INTRODUCTION	1
1.1 Basic Turbine Configurations	2
1.2 Radial-Inflow and Axial-Flow Turbine Features	5
1.3 Velocity Diagrams for a Stage	7
1.4 Similitude and Performance Characteristics	10
1.5 Units and Conventions	16
<hr/>	
2. THERMODYNAMICS	17
2.1 First and Second Laws of Thermodynamics	18
2.2 Efficiency	20
2.3 Fluid Equation-of-State Fundamentals	22
2.4 The Caloric Equation of State	24
2.5 Entropy and the Speed of Sound	25
2.6 The Thermal Equation of State for Real Gases	26
2.7 Thermodynamic Properties of Real Gases	31
2.8 Thermally and Calorically Perfect Gases	32
2.9 The Pseudoperfect Gas Model	33
2.10 Liquid-Phase Properties	34
2.11 Gas Viscosity	36

2.12	Component Performance Parameters	36
2.13	A Computerized Equation of State Package	40

3.	FLUID MECHANICS	43
-----------	------------------------	-----------

3.1	Flow in a Rotating Coordinate System	45
3.2	Adiabatic Inviscid Compressible Flow	48
3.3	Adiabatic Inviscid Compressible Flow Applications	50
3.4	Boundary Layer Analysis	52
3.5	Two-Dimensional Boundary Layer Analysis	54
3.6	Axisymmetric Three-Dimensional Boundary Layer Analysis	57
3.7	Vector Operators in Natural Coordinates	59

4.	EMPIRICAL PERFORMANCE MODELS FOR AXIAL-FLOW TURBINE BLADE ROWS	61
-----------	---	-----------

4.1	Blade Row Geometry	63
4.2	Fluid Deviation Angle	65
4.3	Overview of the Loss System	68
4.4	Profile Loss Coefficient	69
4.5	Secondary Flow Loss Coefficient	79
4.6	Trailing-Edge Loss Coefficient	81
4.7	Shock Loss Coefficient	81
4.8	Supersonic Expansion Loss Coefficient	82
4.9	Blade Clearance Loss Coefficient	83
4.10	Lashing Wire Loss Coefficient	83
4.11	Leakage Bypass Loss	83
4.12	Partial Admission Loss	87
4.13	Disk Friction Loss	88

4.14	Clearance Gap Windage Loss	90
4.15	Moisture Loss	91

5. AERODYNAMIC PERFORMANCE ANALYSIS OF AXIAL-FLOW TURBINES 93

5.1	The Meridional Coordinate System	95
5.2	The Approximate Normal Equilibrium Model	97
5.3	Inviscid Adiabatic Flow on A Quasi-Normal	101
5.4	Linking Quasi-Normals	104
5.5	The Flow Profiles on a Quasi-Normal	106
5.6	Turbine Performance Analysis	111
5.7	Typical Performance Analysis Results	121
5.8	Diaphragm-Disk Rotor Leakage Flows	125
5.9	Blade Forces and Rotor Thrust	127
5.10	Concluding Remarks	130

6. PRELIMINARY AERODYNAMIC DESIGN OF AXIAL-FLOW TURBINE STAGES 133

6.1	Preliminary Aerodynamic Design Strategy	135
6.2	Velocity Triangles at the Design Radius	136
6.3	The Vortex Type and Swirl Velocity Distributions	138
6.4	Stage Efficiency	139
6.5	The Optimum Pitch-to-Chord Ratio	143
6.6	Initializing the Total Thermodynamic Conditions	145
6.7	The Stage Inlet Flow Profiles	146
6.8	Sizing the Annulus	147
6.9	Selecting the Blade Row Geometry	149
6.10	A Computerized Preliminary Design System	150

6.11	Selection of the Dimensionless Performance Parameters.....	153
6.12	Selection of the Swirl Velocity Vortex Type	157
6.13	Concluding Remarks	165
7.	DETAILED AIRFOIL DESIGN FOR AXIAL-FLOW TURBINES	167
7.1	Definition of the Airfoil Geometry	168
7.2	The Airfoil Profile Model	171
7.3	Determining the Polynomial Coefficients.....	173
7.4	Leading and Trailing Edge Profiles	175
7.5	The Passage Throat Calculation.....	176
7.6	Adjusting the Uncovered Turning	178
7.7	Design of a Complete Blade.....	179
7.8	The Optional Defining Points.....	180
7.9	Evaluation of the Airfoil Design	180
7.10	A Computerized Airfoil Design System.....	182
8.	INDUSTRIAL AXIAL-FLOW TURBINE APPLICATION PROCEDURES	185
8.1	Stage Performance Rating Curves.....	187
8.2	Reynolds Number Effects.....	191
8.3	Reaction Rating Curves.....	193
8.4	Application Procedures Based on Rating Curves	194
9.	AERODYNAMIC PERFORMANCE ANALYSIS OF RADIAL-INFLOW TURBINES	197
9.1	Radial-Inflow Turbine Stage Geometry.....	200
9.2	Boundary Layer Analysis	201

9.3	The Boundary Layer Loss Coefficient	203
9.4	Inlet Volute Analysis.....	205
9.5	Nozzle Row Analysis.....	207
9.6	Rotor Analysis	211
9.7	Vaneless Annular Passage Analysis.....	218
9.8	Exhaust Diffuser Analysis.....	219
9.9	Imposed Total Pressure Loss	222
9.10	Inlet Station Analysis	222
9.11	The Performance Analysis Strategy.....	222
9.12	Mass Balance Procedures	223
9.13	Subcritical Performance Analysis.....	224
9.14	Supercritical Performance Analysis	227
9.15	Typical Performance Analysis Results	229
<hr/>		
10.	PRELIMINARY AERODYNAMIC DESIGN OF RADIAL-INFLOW TURBINE STAGES	233
10.1	Preliminary Aerodynamic Design Strategy.....	235
10.2	Rotor Tip Sizing	238
10.3	Rotor Design Specifications	239
10.4	Rotor Sizing	241
10.5	Evaluating the Rotor Design	243
10.6	Rotor End-Wall Contours	244
10.7	Straight-Line Element Rotor Blade Camberlines	247
10.8	Radial Element Rotor Blade Camberlines	249
10.9	Nozzle Blade Geometry	250
10.10	Nozzle Row Sizing	254
10.11	Evaluating the Nozzle Design	255
10.12	Initial Estimates of the Nozzle Design Specifications	256
10.13	Volute Preliminary Design	257

10.14	Exhaust Diffuser Sizing	259
10.15	A Typical Preliminary Design Example	260
10.16	A Computerized Preliminary Design System	262
<hr/>		
11.	DETAILED AERODYNAMIC DESIGN OF RADIAL-INFLOW TURBINE COMPONENTS	265
11.1	Nozzle Blade Detailed Design	267
11.2	A General Approach to Gaspath Detailed Design	270
11.3	Useful Curve Forms	273
11.4	Constructing the Annulus and Quasi-Normals	280
11.5	Constructing the Blade Camberline	282
11.6	Constructing the Blade Surfaces	283
11.7	The Blade Passage Throat Geometry	286
11.8	An Effective Gaspath Design System	287
11.9	Application to Impeller Design	290
<hr/>		
12.	AERODYNAMIC DESIGN AND PERFORMANCE ANALYSIS OF EXHAUST DIFFUSERS	295
12.1	Basic Diffuser Technology	297
12.2	An Approximate Performance Analysis	298
12.3	Sizing the Exhaust Diffuser	299
12.4	A Detailed Aerodynamic Performance Analysis	302
<hr/>		
13.	TWO-DIMENSIONAL ANALYSIS OF THE FLOW IN THE BLADE-TO-BLADE PLANE	309
13.1	The Blade-to-Blade Flow Problem	311
13.2	Coordinate System and Velocity Components	314
13.3	The Potential Flow Solution Procedure	315

13.4	A Linearized Potential Flow Procedure	325
13.5	The Time-Marching Solution Procedure	329
13.6	Blade Surface Boundary Layer Analysis	340
13.7	Summary	346
14.	QUASI-THREE-DIMENSIONAL BLADE PASSAGE FLOW FIELD ANALYSIS	349
14.1	Quasi-Three-Dimensional Flow	351
14.2	The Quasi-Normal Coordinate System	353
14.3	Numerical Integration of the Governing Equations	357
14.4	Repositioning the Stream Surfaces	360
14.5	The Hub-to-Shroud Flow Analysis	360
14.6	Coupling the Two Basic Flow Analyses	362
14.7	Boundary Layer Analysis	364
REFERENCES		377
ABOUT THE AUTHOR		387
INDEX		389

PREFACE

This book addresses the subject of turbine aerodynamic design and analysis following the same basic approach used in my previous books on compressor aerodynamics [1, 2]. All three books are written specifically for the aerodynamicist seeking detailed information and practical guidance on the effective application of modern technology to turbomachinery aerodynamic design and analysis. When I started working in this field thirty-five years ago, there were several excellent books of that type available, but their modern equivalents simply don't exist. The expanded roles of the computer and of proprietary industrial research and development have become so pervasive that books offering a comprehensive description of modern turbomachinery aerodynamic design and analysis technology have become rather impractical. Musing over this unfortunate lack of modern information on this subject led me to consider a different type of book to meet this need. Since a general description is no longer practical, a detailed description of a specific aerodynamic design and analysis system might be a viable alternative. So I decided to write a book of that type on centrifugal compressor aerodynamics and managed to find a publisher willing to take a chance on this unconventional approach [1]. Feedback from its readers confirmed that there is a definite interest in this type of book as well as a significant audience. That encouraged me to apply the same approach to axial-flow compressor aerodynamics [2]. This book applies the same approach to the remaining types of turbomachinery for which I have developed comprehensive aerodynamic design and analysis systems.

This approach does involve some inherent limitations. A thorough description of methods I have found to be effective does not provide equal coverage to alternative approaches. While I do cite references to the significant alternatives of which I am aware, that obviously does not provide the same detailed treatment to those alternatives. Readers should recognize that many of the basic functions accomplished by the methods described here have been approached in different ways by other investigators. Nor is the effectiveness of an approach totally independent of the applications for which it is intended. My experience is with industrial turbomachinery, which has undoubtedly influenced my choices of the design and analysis procedures used.

I decided to treat both axial-flow and radial-inflow turbines in a single book primarily because it is practical to do so. But it is also considered beneficial for other reasons. Unlike compressors, it is often far from obvious whether an axial-flow or radial-inflow turbine is the better choice for a specific application. Both types are capable of comparable efficiency levels, except as impacted by

manufacturing limitations. Consideration of cost, mechanical integrity, manufacturing issues and suitability to the specific application should be the basis of selecting the type of turbine to be used. But it is far more common to choose the turbine type based on an organization's expertise, experience and confidence, which almost always strongly favors one of the two types. My initial involvement with developing radial-inflow turbine design and analysis procedures was prompted by a former employer's somewhat arbitrary perception that this type was almost mandatory for certain geothermal energy applications. By the time viable procedures had been developed, validated and applied, commercial interest in those applications had dramatically diminished. The organization promptly returned to its axial-flow turbine comfort zone. Periodic special needs for the new radial-inflow turbine technology consistently confirmed that it was exceptionally effective and reliable. During the same period, evidence mounted to cast doubt on the axial-flow turbine aerodynamic technology then in use. But the paradigm shift needed to seriously consider the radial-inflow turbine as an alternative to the axial-flow turbine proved to be too great an obstacle. An important objective of this book is to demonstrate that either turbine type can be designed and analyzed with confidence and to provide viable technology to do it. I hope this may lead to better choices and fewer missed opportunities.

Development of an aerodynamic design and analysis system is an evolutionary process, which establishes what capabilities should be included, how to use them effectively and how they can interact efficiently to support the overall process. Organizing and applying basic technology in a working design and analysis system is a very complex process involving many decisions and false starts. All developers expend time and effort formulating virtually identical models for phenomena that are fundamental to the process. These critical details are quite important to aerodynamicists who seek to develop, maintain or improve an aerodynamic design and analysis system. Like my previous books on compressor aerodynamics, this book presents comprehensive aerodynamic design and analysis systems for both turbine types in sufficient detail that readers can implement all or part of these systems.

Considerable care is taken to provide complete and detailed descriptions of these aerodynamic design and analysis systems. The basic principles of thermodynamics and fluid mechanics required are presented in a form particularly well suited to turbomachinery applications. Well-defined empirical models are used to augment these basic principles to address the essential problem areas of performance analysis, stage preliminary design, detailed component design and internal flow analysis. Descriptions of numerical methods used are included as well as other critical considerations important to readers who choose to apply these methods in their own design and analysis system. In a few cases where methods common to both my compressor and turbine design and analysis systems are used, I refer to my previous books rather than repeat some rather lengthy and detailed descriptions intended only as supplemental guidance for readers who choose to implement those specific methods.

All of the design and analysis methods described in this book have been implemented and applied on personal computers. Indeed, a personal computer of rather modest capability by today's standards is quite adequate for this purpose. For example, my own aerodynamic design and analysis system was developed

on a seven-year-old Pentium II PC and is regularly applied on the same computer. The methodology used is sufficiently efficient to make this quite acceptable even when dealing with the complex multiple choked blade-row cases and nonideal working fluids often encountered in multistage industrial turbines.

Three-dimensional viscous flow computational fluid dynamics (CFD) is an important technology in modern turbomachinery fluid dynamics that is not specifically covered in this book, although it is cited often as a means to effectively compensate for the impact of approximations inherent in the conventional fluid dynamics analyses. There are several excellent commercially available CFD codes in use today. Most turbomachinery development groups now use one or more of them in the design process. Although viscous CFD technology has not yet attained the illusive status of an exact solution, it can add a substantial level of refinement to the methods described in this book when applied wisely. I had the good fortune to benefit from collaboration with some excellent CFD analysts in recent years. They were aware of the capabilities and limitations of the codes they used and they carefully assessed the impact of necessary approximations imposed by computer limitations. But I also encountered several significant turbomachinery development failures directly traceable to the misuse of CFD. One common cause is application of viscous CFD to configurations poorly suited to the application. A sophisticated CFD analysis can not compensate for solving the wrong problem. In one case, a conventional performance analysis showed that a stage development program would be a dismal failure and clearly identified why it would have to fail. But the fundamentals were ignored so this expensive and unnecessary failure occurred anyway. Two other major development programs were severely compromised by the failure to recognize the impact of inherent limitations of current CFD technology and of subtle but important differences between the CFD models formulated and the actual turbomachinery components developed. In both cases, conventional turbomachinery fluid dynamics technology could have and should have warned the investigators that viscous CFD was not being properly applied. Indeed, the sophistication of many CFD codes in use today is sufficient that the expertise of the analyst often becomes their most critical limitation. Nevertheless, it is now well established that evaluation and refinement of well-designed turbomachinery components by a skilled viscous CFD analyst can substantially reduce uncertainties and identify valuable performance enhancement opportunities not recognized by the conventional design and analysis techniques described in this book. As with all emerging technologies, the engineer's major task is to contain the early exuberance and establish the engineering discipline needed to use it effectively. Fortunately, the industry seems to be maturing in its approach to the use of this important technology.

**Ronald H. Aungier
Greensburg, PA
June 2005**

Chapter 1

INTRODUCTION

Axial-flow turbines and radial-inflow turbines are the two most common types of dynamic turbines. The flow streamlines through the blade rows of an axial-flow turbine have essentially a constant radius, whereas there is a substantial reduction in radius through the radial-inflow turbine. A less common type of dynamic turbine is the radial-outflow turbine, where there is a substantial increase in radius through the blade rows. Since the work done on the fluid depends directly on the change in fluid angular momentum across the rotor, the radial-outflow turbine has a substantial disadvantage relative to the radial-inflow turbine due to its lower rotor inlet radius. Indeed, radial-outflow turbine's higher rotor discharge radius places it at a substantial disadvantage relative to both the axial-flow turbine and the radial-inflow turbine. This writer's experience with the radial-outflow turbine is limited to a single case. A combination of the methods described in this book appeared to be reasonably effective in estimating its performance, but the questionable accuracy of the experimental performance data available introduced too much uncertainty to recommend a design and analysis procedure for that type. Hence, this book will address only the axial-flow and radial-inflow turbine types, where sufficient experimental data has been available to validate the procedures recommended.

NOMENCLATURE

- A* = characteristic passage area
a = sound speed
C = absolute velocity
c_p = specific heat at constant pressure
c_v = specific heat at constant volume
C₀ = spouting velocity
D = characteristic diameter
H = total enthalpy
h = enthalpy
k = ratio of specific heats = c_p/c_v
M = Mach number
m = meridional coordinate
m̄ = mass flow rate
N = rotation speed, rpm
P = pressure

2 • TURBINE AERODYNAMICS

P_R = pressure ratio
 Q = volume flow
 r = radius
 U = blade speed = $r\omega$
 W = relative velocity
 z = axial coordinate
 α = absolute flow angle
 α' = relative flow angle
 η = efficiency
 θ = tangential coordinate
 v = velocity ratio = U/C_0
 ρ = fluid density
 ω = rotation speed (radians/sec)

Subscripts

1 = parameter at the nozzle inlet
2 = parameter at the nozzle exit and rotor inlet
3 = parameter at the rotor exit
 id = an ideal, isentropic condition
 m = meridional component
 r = radial component
 p = prototype test condition
 t = total thermodynamic condition
 z = axial component
 θ = tangential component
* = condition corresponding to sonic flow

1.1 Basic Turbine Configurations

Figures 1-1 and 1-2 illustrate the basic configuration of a radial-inflow turbine stage. The flow enters the stage through an inlet volute or scroll, whose cross-sectional area is progressively reduced circumferentially as the fluid exits the volute in the radial direction. In some cases, a constant cross-section inlet passage is used rather than a volute. In either case, the fluid enters the inlet in the circumferential direction to provide substantial angular momentum relative to the rotor. Usually the flow next passes through a nozzle row, which accelerates the flow to add additional fluid angular momentum. Sometimes the nozzle row may be omitted or it may act primarily to guide the fluid rather than substantially increase the fluid angular momentum. Then the fluid passes through the rotor, which removes some or all of the fluid angular momentum to produce the turbine output power. The fluid then passes through an exhaust diffuser, which converts some of the fluid kinetic energy to static pressure to improve the stage efficiency.

Figure 1-3 shows an axial-flow turbine stage viewed on a cylindrical surface (commonly called the blade-to-blade view). The flow accelerates through a

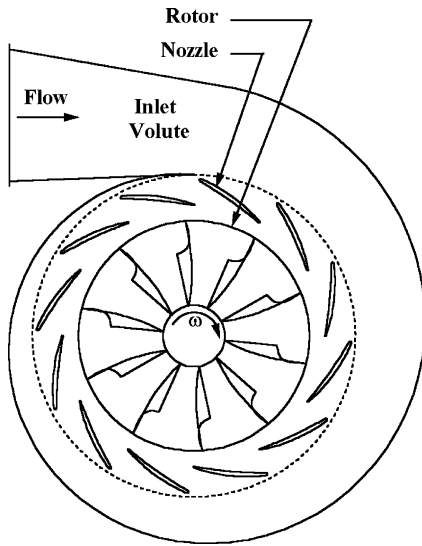


FIGURE 1-1. Radial-Inflow Turbine Front View

nozzle row, which adds angular momentum to the fluid. Then the fluid passes through the rotor, which removes some or all of the fluid angular momentum to produce the turbine output power. Often, several stages will be used in series, each contributing to the overall power. After the last stage, the fluid

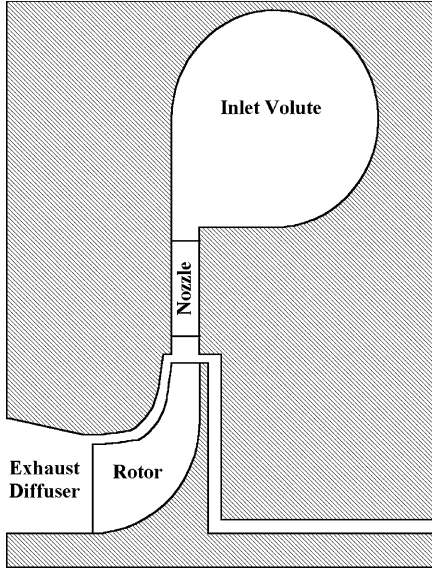
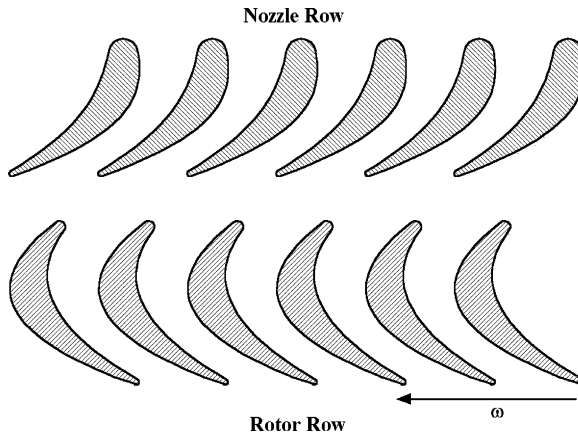


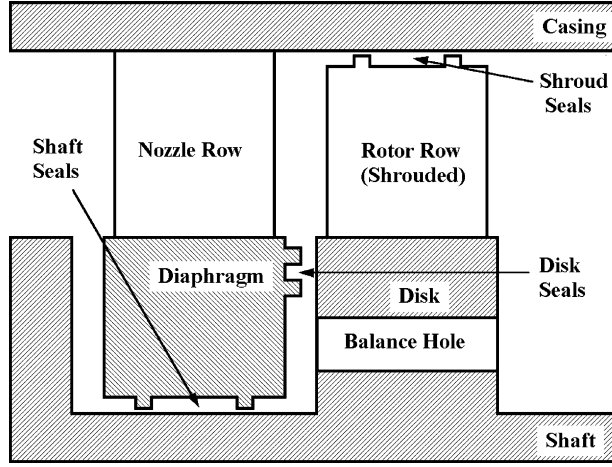
FIGURE 1-2. Radial-Inflow Turbine Side View

**FIGURE 1-3. AXIAL-FLOW TURBINE BLADE-TO-BLADE VIEW**

typically passes through an exhaust diffuser, which converts some of the fluid kinetic energy to static pressure to improve the turbine efficiency.

Figure 1-4 shows a side view of the diaphragm-disk arrangement commonly used for industrial axial-flow turbines. The rotor blades are mounted on a disk attached to the shaft. The nozzles are attached to the casing and include the diaphragm extension between disks. Seals along the shaft and the disk are often used to minimize leakage flows in the clearance gaps. Figure 1-5 shows an alternate style commonly called a drum-rotor or solid-rotor. Here, the rotor blades are attached directly to the shaft and the nozzle blades do not require the diaphragm extension.

Blade rows may include a shroud band connecting the blades on the clearance end, or may be unshrouded. Both configurations are shown in figure 1-5.

**FIGURE 1-4. DIAPHRAGM-DISK AXIAL-FLOW TURBINE**

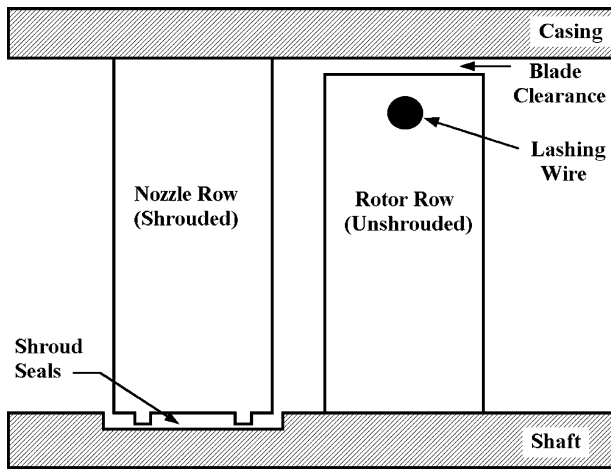
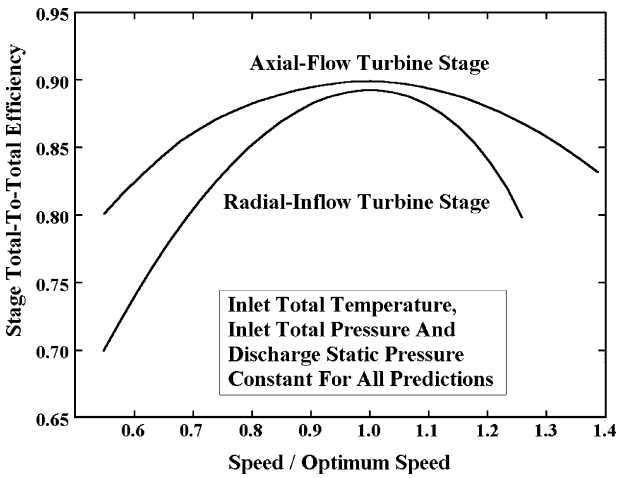


FIGURE 1-5. Drum-Rotor Style Axial-Flow Turbine

Shrouds are often used for reasons of mechanical integrity and to control clearance gap leakage losses when it is impractical to maintain very small clearances. Often the shroud band will include seal fins to reduce leakage losses. These seal fins are thin enough to avoid serious damage to the rotor, casing and blades if a rotor excursion causes them to contact the shaft or casing. Basically the seal fins will be sacrificed if this occurs, but other damage will be minimal. If mechanical stress levels do not permit a shroud band on the rotor row, industrial turbines sometimes use lashing wire to tie the blades together to avoid resonance problems, as illustrated in figure 1-5. Sometimes balance holes through the rotor disk may be used to reduce axial thrust forces, as illustrated in figure 1-4.

1.2 Radial-Inflow and Axial-Flow Turbine Features

The basic radial-inflow turbine configuration is not well suited to multistage applications unless the downstream stages are axial-flow stages. Unlike the centrifugal compressor, there is no well-established design procedure for components to transition the flow between two radial stages. Overhung shaft arrangements, such as integral-gear units, can use simple piping connections between stages if the arrangement permits without unacceptable losses. There are a few multistage radial-inflow turbines commercially available, but single-stage applications are far more common. By contrast, the axial-flow turbine is easily applied in multistage arrangements. That added flexibility is a significant advantage enjoyed by the axial-flow turbine over the radial-inflow turbine. Radial-inflow turbines are particularly attractive for small units such as turbochargers and micro-turbines, where maintaining the blade profile accuracy level required for high-efficiency axial-flow turbines may be impractical or prohibitively expensive. The radial-inflow turbine is less sensitive to blade profile tolerance issues and it requires far fewer blades

**FIGURE 1-6. Stage Efficiency Comparison**

per blade row, which can offer a significant cost advantage, particularly in the smaller sized units.

Figure 1-6 shows a comparison of predicted efficiencies for the two types of turbine. The stages selected are both tested designs reported by the National Aeronautics and Space Administration (NASA), which are predicted very accurately by the performance analysis methods presented in this book. Since the two stages were designed for different applications, some caution is needed when drawing conclusions from this comparison. Hence, the efficiency based on inlet and discharge total thermodynamic conditions is shown as a function of the ratio of the rotor speed to the optimum speed. The same turbine inlet total thermodynamic conditions and discharge static pressure are used for the two predictions. It is seen that the peak efficiency levels for the two stages are nearly identical with the axial-flow turbine showing a slight advantage. The rotor tip diameter of the axial-flow stage is 30 inches versus 6 inches for the radial-inflow stage. This size difference accounts for the most of difference seen in the peak efficiencies. The need to turn the flow 90° through the radial-inflow rotor will have some adverse effect, but it is relatively insignificant in a well-designed stage. Note that the axial-flow stage's efficiency is much less sensitive to changes in speed for these constant pressure-ratio cases. This is a significant difference in the performance characteristics of the two-stage types.

Figure 1-7 shows the same efficiency data plotted as a function of the ratio of rotor inlet blade speed to the spouting velocity. That ratio is a commonly used dimensionless parameter that will be discussed later in this book. For the present discussion, it is sufficient to recognize that the spouting velocity is identical for the two stages. This shows that the optimum efficiency for the radial-inflow stage corresponds to a higher blade speed than for the axial-flow stage. This can be a disadvantage if mechanical integrity is an issue. It can also be an advantage in terms of the work-per-stage capability. Stages optimized to single-stage duty normally attempt to minimize the rotor exit fluid kinetic energy. In these cases, axial-flow and radial-inflow stages typically achieve about

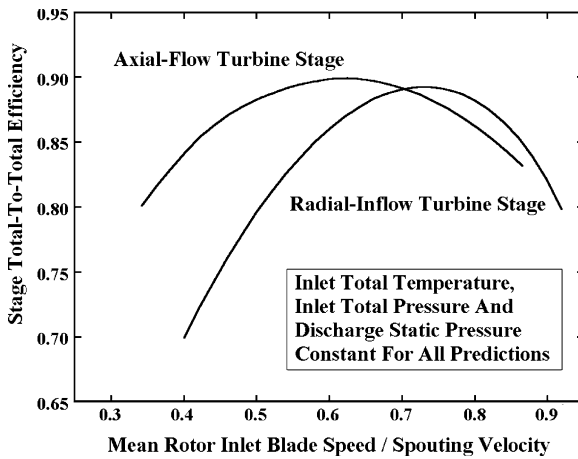


FIGURE 1-7. Efficiency as a Function of Blade Speed

the same work coefficient. The work coefficient is the ratio of stage work to the square of the blade speed. Hence, the radial-inflow stage has the potential for greater work per stage at optimum efficiency. That is a well-known advantage of the centrifugal compressor stage over the axial-flow compressor stage. But the absence of diffusion limits in accelerating flow make it much less significant for turbine stages, particularly since the axial-flow stage can readily be used in a multistage arrangement if needed.

Figure 1-8 compares the mass flow per unit frontal area for the two stages. The rotor tip diameter is used to define the axial-flow stage's frontal area, while the nozzle outer diameter is used for the radial-inflow stage. Similar to compressors, flow capacity per unit frontal area of the axial-flow stage is significantly greater than for the radial-inflow stage.

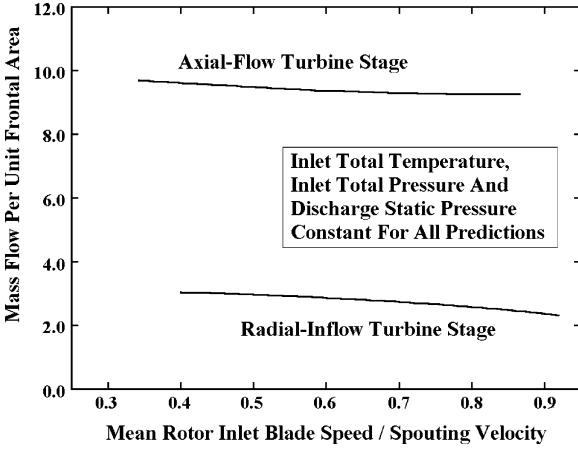


FIGURE 1-8. Flow Capacity per Unit Frontal Area

It can be concluded that the two stage types offer comparable efficiency potential. Hence, this will not normally be the deciding factor in choosing one type over the other. If flow capacity per unit frontal area is important, the axial-flow stage is clearly superior. The axial-flow stage is also much better suited to multistage applications. In other cases, production cost, mechanical integrity, manufacturing constraints and suitability to the specific application are more likely to determine which type will be the better choice.

1.3 Velocity Diagrams for a Stage

The construction of velocity diagrams or velocity triangles is a fundamental tool for all turbomachinery aerodynamic design and analysis. Since successive blade rows alternate between stationary and rotating, it is necessary to be able to view the velocity vectors in both stationary and rotating coordinate systems at any location. For generality to either axial-flow or radial-inflow turbines, the velocity triangles will be constructed in stream surfaces passing through the machine. By definition, a stream surface has no mass flow crossing it and no fluid velocity component normal to it. An orthogonal coordinate system (m, θ) is used where θ is the polar angle of a cylindrical coordinate system. For an ideal axial-flow stage, the meridional coordinate, m , is identical to the axial coordinate, z . The same is true at the rotor exit of an ideal radial-inflow stage. Upstream of the rotor in an ideal radial-inflow stage, m is identical to the radial coordinate, r . In the more general case, m has both a radial and an axial component, i.e.,

$$(dm)^2 = (dz)^2 + (dr)^2 \quad (1-1)$$

Figure 1-9 shows the velocity diagrams on a stream surface for the nozzle inlet and discharge locations. Subscript 1 refers to the nozzle inlet station, subscript 2 to the nozzle exit or rotor inlet station and subscript 3 to the rotor exit station. The

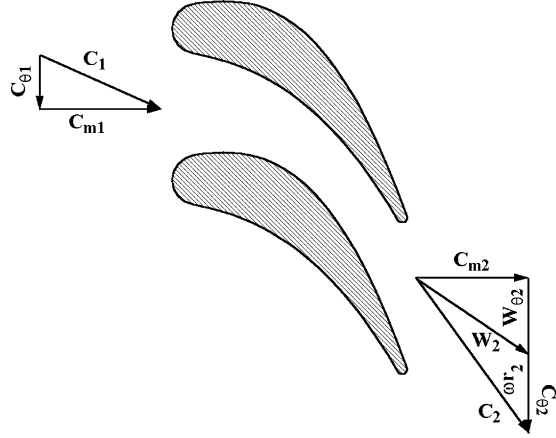


FIGURE 1-9. Nozzle Velocity Diagrams

velocity in the stationary coordinate system (the absolute velocity) is designated as C . The velocity in the rotating coordinate system (the relative velocity) is designated as W . The meridional velocity component combines the axial and radial velocity components, which are identical in either coordinate system, i.e.,

$$W_m = C_m = \sqrt{C_z^2 + C_r^2} \quad (1-2)$$

If ω is the angular velocity of the rotating coordinate system, the local blade speed is $r\omega$. Then the absolute and relative tangential velocity components are related by

$$W_\theta = C_\theta - \omega r \quad (1-3)$$

The overall velocities are given by

$$C = \sqrt{C_m^2 + C_\theta^2} \quad (1-4)$$

$$W = \sqrt{C_m^2 + W_\theta^2} \quad (1-5)$$

The flow angle with respect to the tangential direction in the stationary frame of reference, α , is given by

$$\tan \alpha = C_m / C_\theta \quad (1-6)$$

Similarly, the flow angle with respect to the tangential direction in the rotating coordinate system, α' , is given by

$$\tan \alpha' = C_m / W_\theta \quad (1-7)$$

Given the inlet velocity diagram, the nozzle's performance determines the absolute velocity diagram at the nozzle exit. Then Eqs. (1-3), (1-5) and (1-7) complete the velocity diagram to include the velocity components and flow angle in a rotating coordinate system, i.e., the relative velocity data at the rotor inlet. Figure 1-10 uses this velocity diagram as rotor inlet conditions. The inlet relative velocity diagram and the rotor's performance determine the relative velocity diagram at the rotor exit. Then Eqs. (1-3), (1-4) and (1-6) complete this velocity diagram to include the velocity components and flow angle in the stationary coordinate system, i.e., the absolute velocity data at the next nozzle inlet. This simple velocity diagram construction process is a fundamental technique used by the turbomachinery aerodynamicist to convert between absolute and relative flow conditions. Indeed, in the early days of the science, it was the key step in the design process, requiring designers to construct dozens of velocity diagrams to design a turbomachine. Now that computerized design and analysis is the norm, manual construction is relatively rare. But knowledge of the process remains essential to an effective understanding of what those computerized methods are actually doing.

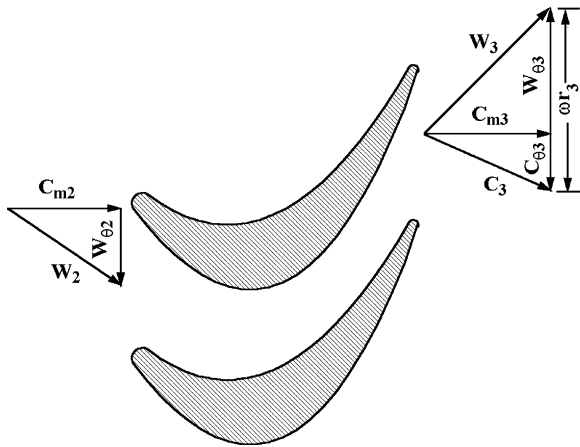


FIGURE 1-10. Rotor Velocity Diagrams

1.4 Similitude and Performance Characteristics

Similitude or similarity is another concept fundamental to turbomachinery aerodynamics. Two turbomachines are completely similar if the ratios of corresponding dimensions, velocity components and forces are all equal [3]. By properly defining equivalent performance parameters, it is possible to develop a general performance map for a specific turbomachine that will apply to all similar turbomachines. This greatly expands the number of applications that can be achieved from a development program for a single turbomachine or for a component of a turbomachine such as a stage. It permits the designer to scale the design to different sizes or even apply it to different working fluids without repeating the development process. Similitude is an essential concept, but it is also a very dangerous concept. In truth, complete similarity is really never achieved. If the deviations from perfect similarity are not recognized, serious application errors can result. Applying equivalent performance parameters from one field of turbomachinery to another is another fairly common error that can lead to serious mistakes. Misuse of similitude is probably more common in industrial turbines than any other type of turbomachine. The industrial turbine is often applied with a working fluid quite different from that used on the baseline development program. Also, working fluids often exhibit substantial nonideal gas behavior. In these cases, different operating conditions can compromise similarity almost as much as using different working fluids. It is essential that the turbine aerodynamicist recognize unacceptable deviations from similarity and either avoid them or apply suitable corrections to compensate for them.

An obvious requirement for similarity is that the two turbomachines have similar velocity diagrams. But to achieve similar velocity diagrams while satisfying conservation of mass, the two turbomachines must achieve a similar variation in gas density through the machine. The most common way to achieve that is to require that the Mach number distribution be the same in both machines. This is commonly referred to as Mach number

similarity. This can be shown to be a reasonable criterion if the two machines use the same working fluid and that fluid satisfies the perfect gas equation of state. There may still be deviations due to Reynolds number effects, but these can often be neglected or accounted for with a suitable correction procedure. Mach number similarity is sufficient for some industrial turbines. For example, turbocharger turbines often operate on air with minor concentrations of fuel components. To a very good approximation, they use the same working fluid and the fluid follows the perfect gas equation of state. But industrial turbines applied to steam or hydrocarbon mixtures often fail to meet those requirements due to different working fluids or to nonideal gas behavior. Even here, similarity can often be used to advantage with appropriate care. Mach number similarity can usually provide a reasonable approximation for a turbine stage, even when it isn't sufficient for the multistage turbine. This allows known stage performance characteristics to be used to estimate the performance in a different application so long as it is applied to individual stages and combined into an overall performance estimate. It also allows correction of performance data from a development program accomplished on one working fluid to applications with a different working fluid.

To develop suitable Mach number equivalence performance parameters for turbines, several thermodynamic and fluid dynamic parameters are required. They will be familiar to most readers and will be used here without rigorous development, recognizing that they are covered in detail in chapters 2 and 3. First, consider the meridional Mach number. It can be represented in the form

$$M_m = C_m / a \propto \dot{m} / (\rho a A) \quad (1-8)$$

where A is the passage area, a is an appropriate sound speed and ρ is an appropriate gas density. The blade rotational Mach number can be represented by

$$M_U = \omega r / a \propto ND / a \quad (1-9)$$

where N is the rotation speed and D is an appropriate diameter. The tangential Mach number equivalence also needs to be represented. The rotor work provides a means to accomplish this. The well-known Euler turbine equation defines the enthalpy change across the rotor in the form

$$\Delta H = \omega(r_3 C_{\theta 3} - r_2 C_{\theta 2}) \quad (1-10)$$

Since M_U will be used to establish Mach number equivalence on $r\omega$, equivalence on tangential Mach number can be established by a parameter designated as M_H

$$M_H = \Delta H / a^2 \quad (1-11)$$

Hence, Mach number equivalence exists for two turbomachines having equal values of M_m , M_U and M_H . It remains to establish what values of density and sound speed should be used in these equivalence parameters. Usual practice is to use the inlet total conditions for this purpose. That is a suitable choice so long as the working fluids involved are not too different and the Mach numbers involved are well below unity. Turbines often involve cases where this is not a good choice. It is quite common for turbines to operate with one or more blade rows choked, where Mach numbers exceed unity. It is often convenient to test a turbine stage in one working fluid (e.g., air) but apply it to a much different working fluid (e.g., steam). The weakness of using total sound speed can be illustrated for two working fluids that obey the perfect gas equation of state, i.e.,

$$P = \rho RT \quad (1-12)$$

and whose ratio of specific heats, k , are both constant. Assume k and the gas constant, R , are both different for the two applications. Also assume the two turbines are geometrically identical. Designating the known conditions from a prototype test with a subscript, p , and total thermodynamic conditions with a subscript, t , the mass flow for the new application can be computed using similarity on M_m .

$$\dot{m} = \dot{m}_p a_t \rho_t / (a_{tp} \rho_{tp}) \quad (1-13)$$

Consider the special case where the prototype mass flow corresponds to the onset of choke. Using a subscript, $*$, to designate parameters corresponding to sonic flow conditions and neglecting losses, this requires

$$\dot{m}_p = \rho_* a_* A_{cr} \quad (1-14)$$

where A_{cr} is the critical passage area where choke first occurs (e.g., the nozzle throat area). But for a perfect gas, it can be shown that

$$\frac{\rho_* a_*}{\rho_t a_t} = \left[\frac{2}{k+1} \right]^{\frac{k+1}{2(k-1)}} \quad (1-15)$$

Eqs. (1-13) through (1-15) yield

$$\dot{m} = \rho_t a_t A_{cr} \left[\frac{2}{k_p + 1} \right]^{\frac{k_p + 1}{2(k_p - 1)}} \quad (1-16)$$

But Eqs. (1-14) and (1-15) must also apply for the new application, i.e.,

$$\dot{m} = \rho_t a_t A_{cr} \left[\frac{2}{k+1} \right]^{\frac{k+1}{2(k-1)}} \quad (1-17)$$

Clearly, the only way the similarity condition of Eq. (1-13) can correctly estimate the choke flow for the new application is if $k_p = k$. Hence, use of total density and total sound speed in the equivalence relations is not a good choice. The sonic density and sound speed are a much better choice. This choice results in exact similarity in mass flow at both zero mass flow and the choke mass flow. Although exact similarity for other mass flows is not guaranteed when the working fluids are significantly different, this will certainly yield more accurate similarity than the choice of total conditions. The validity of this choice has been demonstrated by Kofskey and Holeski [4]. They report experimental results for a turbine tested in both air and argon. Although these fluids have quite different values of k and R , similarity of the performance maps is demonstrated. They chose to include an additional correction parameter to reference performance to the inlet total pressure, which can be expressed in analytical form so long as the perfect gas equation of state applies to both fluids. An analytical investigation by Whitney and Stewart [5] has shown that k has no significant influence on equivalent performance over a range of values from 1.2 to 1.67. But many working fluids used in turbines are not perfect gases. For the general case, the fundamental equivalent performance parameters are

$$\frac{\dot{m}}{A\rho_* a_*}, \frac{ND}{a_*}, \frac{\Delta H}{a_*^2} \quad (1-18)$$

Other equivalent performance parameters can be calculated from these basic parameters by assuming that the efficiency is unchanged between equivalent operating conditions. In effect, efficiency is also considered to be an equivalent performance parameter. The ideal or isentropic enthalpy change across the turbine is defined as

$$\Delta H_{id} = \Delta H / \eta \quad (1-19)$$

Hence, equivalence on ΔH_{id} follows the same equivalence relation as ΔH . The ratio of the rotor blade speed to the spouting velocity shown in figure 1-7 is a commonly used performance parameter. The spouting velocity is a fictitious velocity corresponding to ΔH_{id} , i.e.,

$$C_0 = \sqrt{2\Delta H_{id}} \quad (1-20)$$

The local blade speed, $U = r\omega$, is defined at an appropriate radius, such as the rotor inlet mean radius. Then the velocity ratio is defined by

$$v = U / C_0 \quad (1-21)$$

This can be expressed as an equivalent performance parameter using Eqs. (1-9), (1-11), (1-19) and (1-20). This shows that the sonic velocity should be used to normalize both U and C_0 , which cancel in Eq. (1-21). Hence v is also a basic equivalent performance parameter that does not require correction to be used on an equivalent performance map. Pressure ratio is a commonly used parameter

for performance maps. But pressure ratio is a direct equivalent performance parameter only if the working fluid is perfect gas and is the same for all cases. Otherwise, an equivalent pressure ratio must be calculated from the map reference inlet conditions, efficiency and the equivalent ΔH to be graphed on an equivalent performance map.

Hence, the fundamental equivalent performance parameters that can be used directly on an equivalent performance map are

$$\frac{\dot{m}}{A\rho_* a_*}, \frac{ND}{a_*}, \frac{\Delta H}{a_*^2}, \frac{\Delta H_{id}}{a_*^2}, \frac{C_0}{a_*}, v, \eta \quad (1-22)$$

To use other performance parameters, they need to be calculated from these basic equivalent performance parameters and the reference inlet thermodynamic conditions assigned to the map. Although reference inlet thermodynamic conditions corresponding to sonic flow are the most direct, it is often more useful to use alternate values, such as inlet total conditions. If that is done, additional corrections will be needed such that the basic equivalence parameters of Eq. (1-22) are preserved.

Figures 1-11 and 1-12 show basic formats that might be used for general equivalent performance maps. Except for the equivalent pressure ratio, all parameters are direct results from the turbine test data or the performance predictions used to generate the maps. In the general case, the equivalent pressure ratio is a calculated parameter. This is easily illustrated for working fluids that follow the perfect gas equation of state. In chapter 2, it will be shown that any isentropic process (no losses) of a perfect gas with constant specific heats satisfies the following equation.

$$P_R = (T_R)^{\frac{k}{k-1}} \quad (1-23)$$

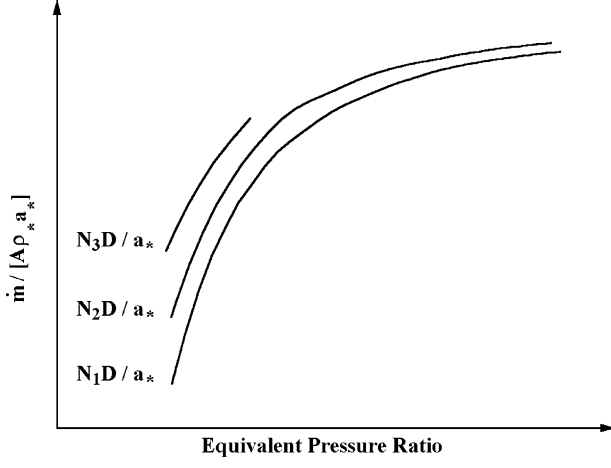


FIGURE 1-11. An Equivalent Mass Flow Map

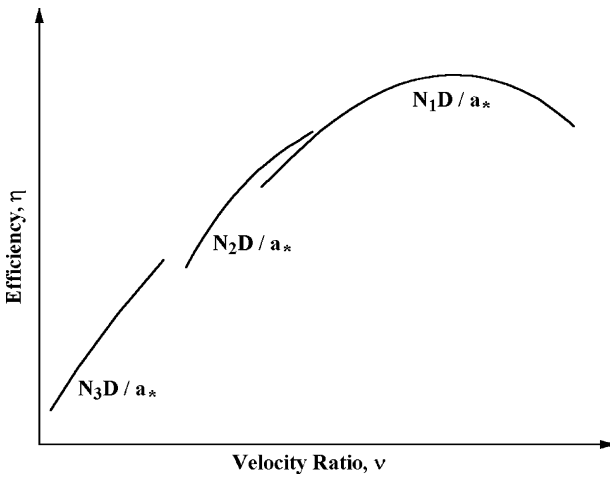


FIGURE 1-12. An Equivalent Efficiency Map

P_R and T_R are the ratios of total pressure and total temperature, respectively. This can be shown to yield

$$P_R = \left[1 + \frac{2(k-1)}{k+1} \frac{\Delta H}{a_*^2} \right]^{\frac{k}{k-1}} \quad (1-24)$$

where the sonic velocity is defined at the inlet. Hence, if k is constant, pressure ratio can be regarded as a direct equivalent performance parameter. However, if the value of k for the source of the performance data differs from the value of k assigned to the map, pressure ratio must be calculated from the equivalent ideal enthalpy change using Eq. (1-24). The same conclusion applies to nonideal working fluids, but the correction from one working fluid to another is a numerical process rather than the analytical expression in Eq. (1-24). Hence, if turbine test performance data are used to generate an equivalent performance map for a different working fluid, the equivalent pressure ratio for the map must be calculated. Note that it is not necessary to assign a specific working fluid to the equivalent performance maps if fundamental equivalent performance parameters are used. In that case, the maps will apply to any working fluid. But the use of pressure ratio in figure 1-11 inherently restricts the map to a specific working fluid. Given the inlet total thermodynamic conditions, discharge total pressure, N , D , A and the appropriate equation of state, we can calculate P_R , ΔH_{id} , a_* , ρ_* and v to apply the equivalent performance maps to other working fluids. However, the pressure ratio calculated is not compatible with values plotted in figure 1-11. It is necessary to employ equivalence on ΔH_{id} or C_o to calculate the equivalent pressure ratio appropriate to the working fluid assumed for the map. Hence, complications encountered with equivalent performance maps are often unnecessary problems that are created by the desire to use parameters that are not fundamental equivalence parameters, to reference the maps to a

specific working fluid or to use reference thermodynamic conditions other than the sonic flow conditions. That is certainly acceptable practice if care is taken to properly conform to the fundamental similarity parameters. But failure to use extreme care can easily result in invalid application of the similarity concept with the possibility of serious errors in performance estimates.

So far, the development of similarity concepts has dealt with performance based on inlet and discharge total thermodynamic conditions. This is usually referred to as total-to-total performance. It is often more appropriate to consider performance based on inlet total thermodynamic conditions and discharge static pressure, i.e., total-to-static performance. If the isentropic change in enthalpy between these end conditions is designated as Δh_{id} , all of the above similarity parameters apply if Δh_{id} is substituted for ΔH_{id} and pressure ratio is defined as the ratio of inlet total pressure to discharge static pressure.

Chapter 8 provides additional background on similitude and its limitations by applying it to the development of axial-flow turbine stage performance rating curves. Rating curves provide a means of using predetermined stage performance to configure multistage industrial turbomachines for a wide range of applications. In this way, accurate performance data obtained from prototype testing or from the best available prediction methods can be used for any operating conditions required by a specific application. Multistage industrial turbomachines are often one-of-a-kind units configured to a specific customer's application. With no duplicate units to share in absorbing development costs, it is essential that application procedures be both accurate and cost-effective. Rating curves based on similitude provide a practical approach that is consistent with those requirements.

1.5 Units and Conventions

This book assumes consistent units throughout, such that the reader may use any set of consistent units preferred. For historical reasons, many turbomachinery organizations do not use consistent units, often using different units for different disciplines such as aerodynamics and thermodynamics. For example, it is not uncommon to find energy terms, fluid velocity and equation-of-state parameters expressed in inconsistent units, necessitating conversion factors in expressions such as Eq. (1-11). It will be left to the reader to recognize the need for those conversion factors. Following steam turbine practice, flow angles and blade angles will be measured from the tangential direction. The swirl velocity components C_θ and W_θ , are considered to be positive in the direction of rotation. While the nomenclature is reasonably consistent throughout, the wide range of topics covered does not permit unique symbols for every parameter. Consequently, each chapter will include its own list of nomenclature to avoid confusion.

Chapter 2

THERMODYNAMICS

This chapter reviews fundamental concepts from thermodynamics that are essential to the aerodynamic design and analysis of turbines. Thermodynamics provides the basis for defining and evaluating the energy transfer processes. It also contributes the equation of state for the working fluid, which is one of the governing equations of fluid flow through turbomachinery. The requirements for the equation of state are particularly demanding for turbines. The commonly used ideal gas equation of state does have applications, such as some turbocharger and gas turbine applications. But many industrial turbines are applied to nonideal working fluids such as steam and various hydrocarbons. This writer's general ideal/nonideal equation of state model is suitable for this purpose [1, 2, 6, 7]. The previous descriptions of this model addressed compressor aerodynamics applications. Unlike compressors, two-phase flow is not at all uncommon in turbines. Some extensions to that model are needed to treat cases where liquid is present.

NOMENCLATURE

A = Helmholtz energy, $dA = -PdV$

a = sound speed and gas constant defined in Eq. (2-32)

b = gas constant defined in Eq. (2-33)

C = velocity

c = gas constant defined in Eq. (2-34)

c_p = specific heat at constant pressure and pressure recovery coefficient

c_v = specific heat at constant volume

H = total enthalpy

h = enthalpy

k = ratio of specific heats = c_p/c_v

M = molecular weight

\dot{m} = mass flow rate

n = exponent in Eq. (2-35)

P = pressure

Q = quality

q = specific heat transfer

\dot{q} = heat transfer rate

R = gas constant
 R_U = universal gas constant
 s = specific entropy
 T = temperature
 u = specific internal energy
 V = specific volume
 \dot{w} = specific work input
 \dot{w} = power input rate
 z = compressibility factor
 ΔHv = heat of vaporization
 η = efficiency
 μ = gas viscosity
 ρ = gas density
 ω = acentric factor
 ξ = parameter defined in Eq. (2-76)
 $\bar{\omega}$ = loss coefficient

Subscripts

ad = adiabatic-reversible (isentropic) process
 c = critical point parameter
 d = discharge condition
 i = inlet condition
 p = polytropic process
 r = reduced parameter (normalized by its critical point value)
 ref = reference condition
 t = total condition
 1 = condition ahead of a nozzle blade row
 2 = condition ahead of a rotor blade row
 3 = condition following a rotor blade row

Superscript

0 = condition where the ideal gas model applies

2.1 First and Second Laws of Thermodynamics

The first law of thermodynamics is the basic principle of conservation of energy. For an open system such as a turbine, the first law can be applied, but only if the flow is steady. If \dot{w} is the power output from the turbine and \dot{q} is the heat transfer between the turbine and its surroundings, the first law of thermodynamics requires

$$\dot{q} - \dot{w} = \dot{m}\Delta\left[u + \frac{1}{2}C^2 + P/\rho\right] \quad (2-1)$$

where \dot{m} is the mass flow rate, u is the specific internal energy, C is velocity, P is pressure, ρ is density and the effect of gravitational force is neglected. The term *specific* indicates the value of a parameter per unit mass. The terms in brackets include the internal energy, kinetic energy and the flow work, P/ρ . Flow work is the work necessary to move the fluid across the boundaries of the system. When steady flow crosses the system's boundaries, P/ρ provides a direct measure of the flow work, which restricts Eq. (2-1) to the steady flow case. The normal practice in fluid dynamics is to combine the internal energy and flow work terms into a single parameter called the enthalpy, h .

$$h = u + P/\rho \quad (2-2)$$

The above thermodynamic conditions are simple state variables or static conditions. It is useful to introduce a special class of thermodynamic conditions referred to as total or stagnation conditions. A total thermodynamic condition is defined as the value of a parameter that will exist if the fluid is brought to rest with no transfer of heat or external work, i.e., all kinetic energy is completely recovered. Total conditions will generally be designated with a subscript, t . Total enthalpy occurs so often that an exception will be made and H will be used instead of h_t . Total enthalpy is given by

$$H = h + \frac{1}{2} C^2 \quad (2-3)$$

If heat transfer is neglected, the flow is called adiabatic and Eqs. (2-1) through (2-3) combine to yield

$$\dot{w} = \dot{m}(H_i - H_d) \quad (2-4)$$

where the subscripts i and d refer to the turbine's inlet and discharge conditions, respectively. Eq. (2-4) is the basic energy equation for steady, adiabatic flow through a turbine.

The second law of thermodynamics introduces the concept of a reversible process. A process is reversible if the system and its surroundings can be returned to their original states after the process has occurred. If that is not the case, the process is called irreversible. Processes influenced by heat transfer or friction effects are common examples of irreversible processes. The specific entropy, s , is defined as

$$ds = \frac{dq_{rev}}{T} \quad (2-5)$$

where T is the temperature, q is the specific heat transfer and the subscript, rev , designates a reversible process. The second law of thermodynamics can be expressed as

$$\Delta s \geq 0 \quad (2-6)$$

Hence, an adiabatic, reversible process is also a constant entropy or isentropic process. Indeed, it is fairly common practice in turbomachinery to use the terms adiabatic and isentropic interchangeably, although the latter is clearly the more precise term. Entropy provides a fundamental measure of the irreversibility of a process, i.e., the inefficiency or losses associated with the process. If the first law of thermodynamics is applied to a fluid element in a closed system,

$$(dq)_{rev} = Tds = du + dw = du + PdV \quad (2-7)$$

where w is the specific work and $V = 1/\rho$ is the specific volume. Eqs. (2-2) and (2-7) provide a fundamental thermodynamic equation for entropy that is valid for any process, i.e.,

$$Tds = dh - VdP \quad (2-8)$$

2.2 Efficiency

The aerodynamic quality of a turbine or a turbine component is evaluated by its efficiency, which is a measure of actual performance relative to an ideal performance that would be achieved by some reversible process. Figure 2-1 illustrates a typical enthalpy-entropy diagram for a turbine or a portion of a turbine that includes at least one rotor row, such that work has been extracted from the fluid. The inlet conditions are designated as P_{ti} , T_{ti} , s_i and H_i . The turbine extracts work from the fluid to produce discharge conditions P_{td} , T_{td} , s_d and H_d . Since static

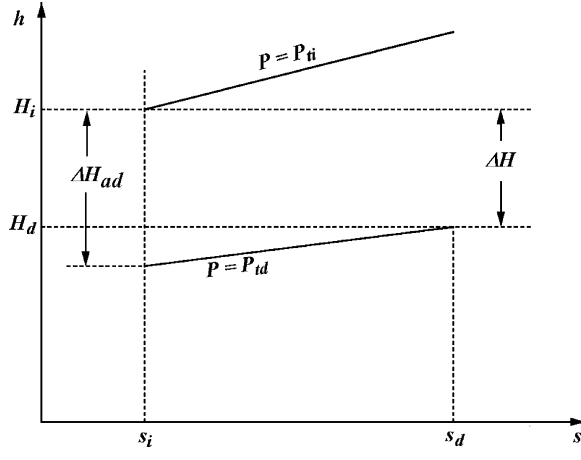


FIGURE 2-1. An Enthalpy-Entropy Diagram

and total conditions are, by definition, related by a reversible process, there is no difference between total and static entropy so the subscript, t , can be omitted for s . One measure of efficiency is to compare the actual process to an ideal adiabatic (isentropic) process. As seen in figure 2-1, an isentropic process could produce an enthalpy drop ΔH_{ad} from the change in total pressure. The actual process produces an enthalpy drop of $\Delta H = H_i - H_d$. Since lines of constant pressure always diverge on an $h-s$ diagram, ΔH is always less than ΔH_{ad} for a nonisentropic process. Hence, the turbine adiabatic or isentropic efficiency, η_{ad} , is defined as

$$\eta_{ad} = \frac{\Delta H}{\Delta H_{ad}} \quad (2-9)$$

From Eq. (2-8), ΔH_{ad} is given by

$$\Delta H_{ad} = - \int_{P_i}^{P_d} \frac{dP}{\rho}; \quad (s = s_i) \quad (2-10)$$

This development of efficiency has considered a turbine operating between inlet and discharge total conditions. Hence it is often called the total-to-total adiabatic efficiency. It is often the case that the fluid kinetic energy at the turbine discharge serves no useful purpose to a specific application. In that case, P_{td} may be replaced by the static pressure, P_d , in Eq. (2-10) to yield the total-to-static adiabatic efficiency. The additional substitution of P_i for P_{ti} yields the static-to-static adiabatic efficiency. Some care is required to understand which basic definition is being used when interpreting efficiency data. It is not uncommon for the term *adiabatic efficiency* to be used for any of the above three types without qualification.

Adiabatic efficiency is the most common definition used for turbines. But it has a definite weakness as a means of evaluating the aerodynamic quality of a design. As illustrated in figure 2-1, constant pressure lines diverge on an $h-s$ diagram. This means that two turbines having the same basic aerodynamic design quality, but operating at different pressure ratios, will have different adiabatic efficiencies. Hence, adiabatic efficiency is not particularly useful to an aerodynamic designer seeking to evaluate the true aerodynamic quality of a turbine or a stage design. Polytropic efficiency is a more useful definition, which eliminates this undesirable thermodynamic effect. It is often used to evaluate compressors but is seldom used for turbines even though it offers the same advantage to all types of turbomachines. Polytropic efficiency is sometimes referred to as the "small-stage" or "true aerodynamic" efficiency. Instead of using a path of constant entropy as the reversible path, polytropic efficiency uses a path of constant efficiency defined by

$$\eta_p = \frac{1}{\rho} \frac{dP}{dh} \quad (2-11)$$

where η_p is defined such that the path passes through the two end points of the process, e.g., (P_{ti}, H_i) and (P_{td}, H_d) . This is straightforward in principle, but less so in practice. For many years, common practice was to approximate a

polytrope by a path defined by $P/\rho^e = \text{constant}$. This approximation is appropriate for ideal gases, but can introduce large errors for nonideal gases. Shultz [8] and Mallen and Saville [9] have reported models for polytropic efficiency using nonideal gases. Huntington [10] studied the problem in detail and showed that the Mallen-Saville model yields excellent accuracy. Huntington proposed a slightly better model by including an intermediate point on the path, but this had the disadvantage of requiring a numerical method to use it conveniently. Hence, this writer employs the Mallen-Saville model in all cases. This model uses an empirical path defined by

$$T \frac{ds}{dT} = \text{constant} \quad (2-12)$$

Eqs. (2-8) and (2-12) can be combined to yield the polytropic head, ΔH_p , as

$$\Delta H_p = \Delta H + (s_d - s_i)(T_{td} - T_{ti}) / \ln(T_{td}/T_{ti}) \quad (2-13)$$

Then the total-to-total polytropic efficiency, η_p , is defined as

$$\eta_p = \frac{\Delta H}{\Delta H_p} \quad (2-14)$$

Extension of Eq. (2-13) to total-to-static and static-to-static efficiency is analogous to adiabatic efficiency as previously discussed. Basically, it is now possible to employ polytropic efficiency with no more difficulty than adiabatic efficiency. It is only necessary to have an appropriate equation of state to use either model.

2.3 Fluid Equation-of-State Fundamentals

Thermodynamics also contributes the equation of state, which is one of the fundamental governing equations for turbine aerodynamic design and analysis. There are actually two equations of state required. The first is the thermal equation of state, which supplies a relationship among the fundamental state variables, typically in the functional form $P=P(\rho, T)$. The second is the caloric equation of state, which relates the energy content of the fluid to state variables, typically in the functional form $h=h(T, P)$ or $u=u(T, P)$. These equations of state may be derived from kinetic theory or statistical mechanics, or they may be developed empirically from experimental data.

A fluid is considered to be an ideal or thermally perfect gas if P , T and ρ can be related by the simple linear thermal equation of state

$$P = \rho RT \quad (2-15)$$

where R is the gas constant for the fluid. R is computed from the universal gas constant, R_u , and the fluid's molecular weight, M

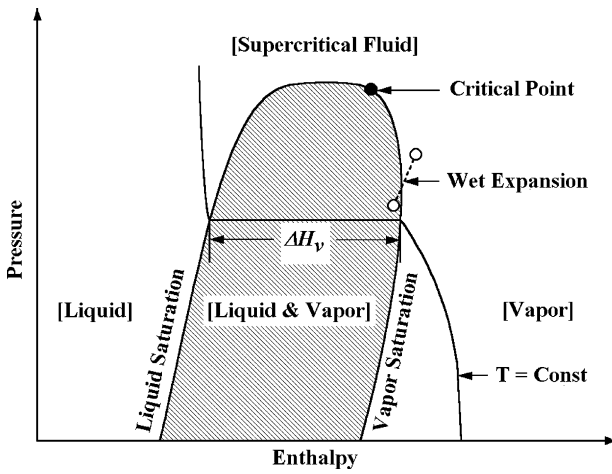


FIGURE 2-2. A Pressure-Enthalpy Diagram

$$R = R_U / M \quad (2-16)$$

where $R_U = 8314 \text{ Pa-m}^3/(\text{kmole-}^\circ\text{K})$ in metric units. All working fluids exhibit nonideal behavior under some conditions. Figure 2-2 is a schematic of a pressure-enthalpy diagram for any working fluid. It is seen that the fluid may be liquid, vapor or both at various state points. Clearly, a thermally perfect gas equation of state cannot model all possible state points. This is true even when the equation is restricted to the vapor phase. The highest temperature at which liquid and vapor can coexist defines the fluid's critical point as illustrated in figure 2-2. Experimental measurements of critical-point properties (T_c , P_c , ρ_c) for many fluids are available in the literature and almost never conform to Eq. (2-15). The thermally perfect gas equation of state can be expected to provide a reasonable approximation if T is much greater than T_c and P is much less than P_c . At pressures well above P_c , the fluid is said to be in the supercritical regime. Again, experimental data show that supercritical fluids almost always show nonideal gas behavior.

Yet the role of the thermally perfect gas equation of state is far more significant than just providing a useful approximation. Indeed, at sufficiently low values of density, all fluids follow the thermally perfect gas law. Under conditions where the gas is thermally perfect, it can be shown that the energy content of a fluid is independent of pressure, i.e., $h^0 = h^0(T)$ and $u^0 = u^0(T)$, where the superscript 0 designates conditions where the fluid is thermally perfect. This means that the caloric equation of state can always be specified as a function of only one state variable. This provides a dramatic simplification to the process of modeling nonideal gases and greatly reduces the gas property data that must be supplied for the fluid. The equation of state requirements for turbines are often much more demanding than for compressors. Since compressors are rarely intentionally applied to two-phase flows, this writer's previous coverage of this topic [1, 2] has largely ignored that aspect of the problem. But

excursions into the wet region are not at all uncommon for industrial turbines. For example, the wet expansion line in figure 2-2 illustrates an expansion process across a turbine or a turbine stage that results in two-phase flow at the discharge. The liquid and vapor saturation lines are boundaries to the fluid's wet region as shown in figure 2-2. Between those two limits, the fluid undergoes a phase change with a corresponding enthalpy change at constant temperature, ΔH_V , equal to the fluid's heat of vaporization. Hence, an equation of state suitable for general turbine aerodynamics applications must specifically address the two-phase flow problem.

2.4 The Caloric Equation of State

Since all fluids follow the thermally perfect gas law at sufficiently low values of density, the caloric equation of state can be specified in a general form for use in either an ideal or nonideal gas model. When the fluid is thermally perfect, the specific heats at constant pressure and at constant volume are defined as

$$c_p^0(T) = \left(\frac{\partial h^0}{\partial T} \right)_p \quad (2-17)$$

$$c_v^0(T) = \left(\frac{\partial u^0}{\partial T} \right)_V \quad (2-18)$$

For a thermally perfect gas, it can be shown that

$$c_p^0(T) - c_v^0(T) = R \quad (2-19)$$

The caloric equation of state can be specified by supplying either $c_p^0(T)$ or $c_v^0(T)$ and using Eqs. (2-17) through (2-19), i.e.,

$$h^0(T) = h^0(T_{ref}) = \int_{T_{ref}}^T c_p^0(T) dT \quad (2-20)$$

$$u^0(T) = u^0(T_{ref}) = \int_{T_{ref}}^T c_v^0(T) dT \quad (2-21)$$

where h^0 and u^0 can be assigned any desired values at a reference state point (T_{ref} , P_{ref}). Specific heat correlations as a function of temperature are readily available for most fluids of interest, e.g., Ried et al. [11, 12] and Yaws [13]. For the special case where the specific heats are constant, the gas is referred to as a calorically perfect gas. In that case, Eqs. (2-20) and (2-21) can be directly integrated to yield analytical equations, i.e.,

$$h^0(T) = h^0(T_{ref}) + c_p^0(T - T_{ref}) \quad (2-22)$$

$$u^0(T) = u^0(T_{ref}) + c_v^0(T - T_{ref}) \quad (2-23)$$

Most books on turbomachinery aerodynamics limit attention to thermally and calorically perfect gases. This conveniently reduces some concepts to simple analytical forms. This writer avoids that practice because it can result in some unfortunate and unintended consequences. Even experienced turbomachinery engineers have occasionally applied these simplified concepts beyond their limits of validity, resulting in some invalid conclusions. It has also encouraged developers of computerized aerodynamic analyses to incorporate special thermodynamic relations that are limited to this special class of fluids. That provides no real benefit to the numerical analysis but makes it very difficult to generalize the analysis later, should that become necessary. It is quite possible to have hundreds of such relations scattered throughout an analysis, all of which must be generalized.

2.5 Entropy and the Speed of Sound

An entropy equation is fundamental to turbomachinery aerodynamic design and analysis. The efficiency definitions introduced previously in this chapter all require an entropy equation. Even the simplest aerodynamic analyses require an entropy equation to convert between total and static thermodynamic conditions. This conversion is an isentropic process, accomplished by imposing a change in enthalpy (the kinetic energy) at constant entropy. An entropy equation is also required to impose a nonisentropic loss mechanism such as a total pressure loss. It is useful to develop the entropy equation consistent with the caloric equation of state defined for a thermally perfect gas. This will be needed for the nonideal gas model described later in this chapter. For any pressure where the gas is thermally perfect, the specific entropy is given by Eq. (2-8), i.e.,

$$s^0(T, P) = s^0(T_{ref}, P_{ref}) + \int_{T_{ref}}^T \frac{c_p^0(T)}{T} dT - R \ln(P/P_{ref}) \quad (2-24)$$

where s^0 can be assigned any desired value at any reference state point (T_{ref}, P_{ref}). For a calorically perfect gas, this simplifies to

$$s^0(T, P) = s^0(T_{ref}, P_{ref}) + c_p^0 \ln(T/T_{ref}) - R \ln(P/P_{ref}) \quad (2-25)$$

The speed of sound is also an essential parameter governing the performance of any turbomachine. From fundamental thermodynamics, the speed of sound, a , for any gas is given by

$$a^2 = \left(\frac{\partial P}{\partial \rho} \right)_s = k \left(\frac{\partial P}{\partial \rho} \right)_T \quad (2-26)$$

where k is the ratio of specific heats.

$$k = c_p / c_v \quad (2-27)$$

For a thermally perfect gas, this yields

$$a^0 = \sqrt{kRT} \quad (2-28)$$

2.6 The Thermal Equation of State for Real Gases

The general thermal equation of state for any fluid is

$$P / (\rho RT) = z(T, P) \quad (2-29)$$

where z is the compressibility factor. The thermally perfect gas is a special case, where $z=1$. For many years the compressibility factor was obtained from generalized tabular data, e.g., Nelson and Obert [14] and Pitzer et al. [15]. But modern practice is to employ one of the many excellent real gas equations of state that are available. Real gas equations of state can provide the many other thermodynamic parameters required and normally yield better accuracy and superior computational speed when used in numerical analyses. One of the simple two-parameter equations of state is a good choice for general aerodynamic design and analysis. These models offer good accuracy, excellent computational speed and easy access to the required gas property data for almost any working fluid or fluid mixture. The Redlich-Kwong equation [16] and various modifications to it (Aungier [7], Barnes [17], Soave [18] and Wilson [19]) are among the most accurate of the two-parameter equations. Aungier [5] evaluated these five equations of state in considerable detail for twelve different compounds over a wide range of temperatures and pressures. Specific emphasis was placed on covering a wide range of acentric factors, ω , since that parameter is used by the various modified Redlich-Kwong equations to improve the prediction accuracy. Acentric factor is defined by Pitzer et al. [15] as

$$\omega = -\log_{10}(P_v / P_c) - 1; \quad T / T_c = 0.7 \quad (2-30)$$

where P_v is pressure on the vapor saturation line and the subscript c designates a critical point property (figure 2-2). The compounds investigated and their acentric factors are listed in Table 2-1. It was concluded that only the original Redlich-Kwong equation and Aungier's modified Redlich-Kwong equation are suitable for general turbomachinery aerodynamic design and analysis. The modified equations of Barnes, Soave and Wilson all showed improved accuracy over the original equation for the types of compounds and thermodynamic property ranges for which they were developed. But they were found to have serious deficiencies for $\omega < 0$, and they exhibited reduced accuracy for supercritical fluids (i.e., $P > P_c$, figure 2-2). Consequently, only the original

Table 2-1. List of Compounds

Compound	ω
Ammonia	0.2550
Carbon dioxide	0.2250
Ethylene	0.0868
Helium	-0.464
Hydrogen	-0.220
I-Butane	0.1848
Methane	0.0080
N-Pentane	0.2539
Nitrogen	0.0400
Propane	0.1520
Refrigerant R134a	0.3254
Steam	0.3440

Redlich-Kwong equation and Aungier's modified form will be described here. The original Redlich-Kwong equation [16] is

$$P = \frac{RT}{V - b} - \frac{a}{V(V + b)\sqrt{T_r}} \quad (2-31)$$

where $T_r = T / T_c$ is referred to as the reduced temperature, and

$$a = 0.42747R^2T_c^2 / P_c \quad (2-32)$$

$$b = 0.08664RT_c / P_c \quad (2-33)$$

Eqs. (2-32) and (2-33) are derived from the thermodynamic stability condition, which requires that the first and second partial derivatives of P with respect to V must both equal zero at the critical point. This equation requires only the critical temperature and critical pressure for the fluid and the caloric equation of state data for its application. It offers very good accuracy over a wide range of thermodynamic conditions. It has one well-known deficiency near the critical point for the fluid. For any fluid, this equation yields $z = 1/3$ at the critical point, which is not typical of most fluids. Hence, this equation should never be used for points close to the critical point.

Aungier's modified Redlich-Kwong equation of state [7] is

$$P = \frac{RT}{V - b + c} - \frac{a}{V(V + b)T_r^n} \quad (2-34)$$

where a and b are given by Eqs. (2-32) and (2-33), respectively, n is given by

$$n = 0.4986 + 1.1735\omega + 0.4754\omega^2 \quad (2-35)$$

The constant, c , is calculated directly by applying Eq. (2-34) at the critical point with all critical point properties specified. It is included to remove the deficiency in the original equation for points near the critical point. This equation of state requires two more specified parameters than the original equation, i.e., ω and either V_c or z_c . Note that if $c = 0$ and $n=0.5$, Aungier's equation reduces to the original equation. If $a=b=c=0$, the thermally perfect gas equation of state is obtained. This makes it very easy to develop a computerized equation of state package for use in any aerodynamic analysis, which can offer all three equations of state.

Figure 2-3 shows a comparison of the prediction accuracy of Aungier's modified Redlich-Kwong equation with the original form. About 25% of the data points considered in [7] are included on this figure. Tabular P - V - T data from the literature were used for this comparison. The two equations of state were used to predict P from the tabular values of T and V . The results were compared to the tabular value of P to compute the error for each model. It is seen that Aungier's model provides significantly better prediction accuracy for a vast majority of the points considered. Aungier [7] notes that this model resulted in about a 50% reduction in the root-mean-square error for the complete set of data considered. This writer uses Aungier's model for all nonideal gas problems, while maintaining the original model as a viable alternative. No equation of state is infallible, so it is good practice to have an alternative available. Either of the above equations of state can be used if the acentric factor and the critical point properties are known. This is a major advantage since those data

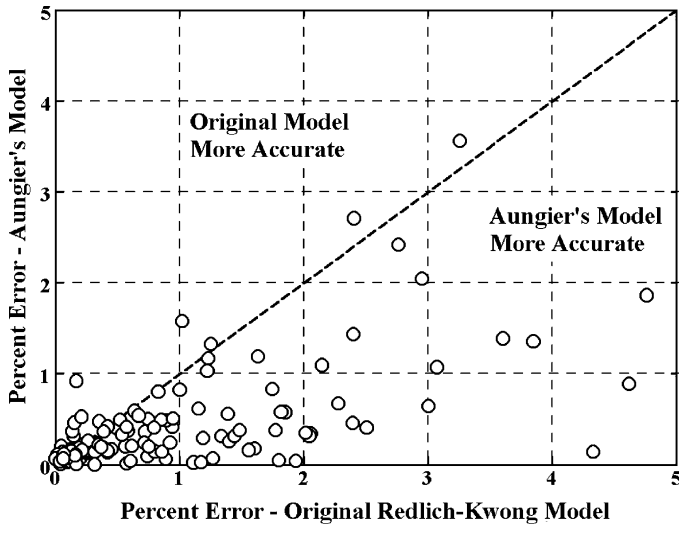


FIGURE 2-3. STATE-POINT PREDICTION ACCURACY

are readily available for virtually any compound likely to be encountered in turbomachinery applications. Reid et al. [11, 12] and Yaws [13] are good sources for the required gas property data.

Eqs. (2-31) and (2-34) can also be applied to gas mixtures. If the subscript, i , designates the i th compound in a mixture of N compounds and x_i is its mole fraction, the constants for the mixture are given by

$$\sqrt{a} = \sum_{i=1}^N x_i \sqrt{a_i} \quad (2-36)$$

$$b = \sum_{i=1}^N x_i b_i \quad (2-37)$$

$$z_c = \sum_{i=1}^N x_i z_{ci} \quad (2-38)$$

$$\omega = \sum_{i=1}^N x_i \omega_i \quad (2-39)$$

$$M = \sum_{i=1}^N x_i M_i \quad (2-40)$$

$$c_p = \sum_{i=1}^N x_i c_{pi} \quad (2-41)$$

The gas constant for the mixture is given by $R = R_U/M$. The effective values of T_c and P_c for the mixture can be computed from a , b and R , using the definitions in Eqs. (2-32) and (2-33). Then c can be computed from Eq. (2-34). Note that Eq. (2-41) requires that c_p be the specific heat per mole rather than per unit mass. For the original Redlich-Kwong equation, $c = 0$, and Eqs. (2-38) and (2-39) are not used.

After some manipulation, Eq. (2-34) can be reduced to the form

$$z^3 + (PC - 1)z^2 + (P^2CB - P^2B^2 - PB + PA)z + PA(PC - PB) = 0 \quad (2-42)$$

$$A = a/[R^2 T^{(2+n)}] \quad (2-43)$$

$$B = b/(RT) \quad (2-44)$$

$$C = c/(RT) \quad (2-45)$$

These equations are also valid for Eq. (2-31) when $n = 0.5$ and $c = 0$. They provide a means to calculate z as a function of T and P . The standard solution for the roots of a cubic equation is given in standard mathematics handbooks and similar references. When two phases of the fluid exist, the equation will have three roots. The smallest root will be the liquid-phase value and the largest root will be the vapor-phase value. Otherwise, the single, positive real root is the vapor-phase value. Hence, in principle, the above nonideal gas models can be applied to the general two-phase flow problem. In practice, the accuracy of the models becomes somewhat suspect for conditions near or to the left of the vapor saturation line. This writer prefers to restrict the equation of state to the vapor phase and address the effect of any liquid phase contribution with generalized empirical models described subsequently in this chapter. Indeed, a mixture equation of state formed as described above must be limited to the vapor phase. This follows from the fact that the composition of the two phases may be different and may vary with state-point conditions. This is rarely a problem for industrial turbines, since most two-phase flow applications involve a single component fluid such as steam or a pure hydrocarbon. But, if a mixture involving two-phase flow must be treated for some reason, it should be recognized that the phase-change modeling described in this book is not rigorous for those cases. It is worth noting a special case of two-phase flow that is often encountered in centrifugal compressors. When intercoolers are located between stages, some mixture components may liquefy and drop out of the mixture. This is commonly referred to as liquid-knockout, and can be modeled by an equilibrium flash calculation. That calculation is not discussed in this book, since it is unlikely to be needed for turbines. Aungier [1] describes the equilibrium-flash calculation using the equations of state presented here, should the reader have need of that capability.

Hence, the real-gas equations of state will only be used for vapor phase calculations. This requires definition of the vapor saturation line illustrated on figure 2-2. Ried and Sherwood [20] note that the vapor saturation pressure, P_v , varies proportional to $1/T$. The gas property specifications required for Aungier's model include two points on the vapor saturation line shown in figure 2-2. One point is the critical point, while the other follows from the definition of the acentric factor in Eq. (2-30). Thus, the vapor saturation pressure can be approximated by

$$\log_{10}(P_v / P_c) = 7(1 + \omega)(1 - T_c / T) / 3 \quad (2-46)$$

This equation can easily be inverted to predict the vapor saturation temperature as a function of pressure. These relations can be used to limit the relevant independent thermodynamic conditions in all calculations intended only for the vapor phase. Eq. (2-46) has been used effectively for compressor applications [1, 2], but has since been modified to provide better estimates for turbines operating at very low pressures. The modified form imposes a correction to Eq. (2-46) based on Ried et al. [12] but specifically adjusted to match low-pressure steam vapor pressure data.

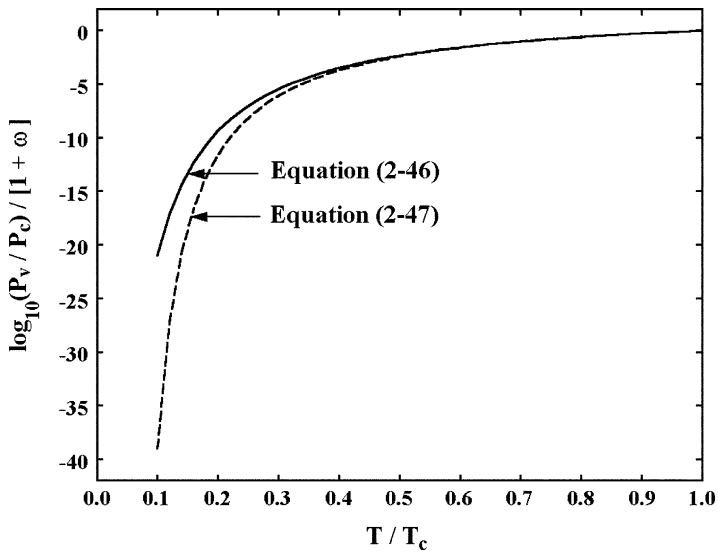


FIGURE 2-4. Vapor Pressure Correlation

$$\log_{10}(P_v / P_c) = \frac{6.5(1+\omega)}{3} \left[1 - \frac{0.95}{(T/T_c - 0.05)} \right] \quad (2-47)$$

This equation is also easily inverted to predict the vapor saturation temperature as a function of pressure. But it is necessary to limit $T / T_c \geq 0.06$ to avoid the singularity in Eq. (2-47). That is not significant, since vapor pressures will be close to zero at values less than this limit. Figure 2-4 shows a comparison of results from the two empirical equations. Clearly, they yield virtually identical results except at extremely low pressures and temperatures. Indeed, it was necessary to plot the logarithmic form shown for the difference to be visible in figure 2-4.

2.7 Thermodynamic Properties of Real Gases

The caloric equation of state (h^0 or u^0) has been specified as a function of temperature for state points where the fluid is thermally perfect. For nonideal fluids, h and u are also functions of pressure. Ried et al. [11] introduce the concept of departure functions for the calculation of the thermodynamic properties of a nonideal fluid. Departure functions are defined as the difference between the actual value of a parameter and its value under conditions where the fluid is thermally perfect, e.g., the quantity $h - h^0$ is the enthalpy departure function. This requires specification of the pressure at which the fluid can be considered to be thermally perfect, P^0 . This is somewhat arbitrary so long as it is a low (but nonzero) value where the thermally perfect gas approximation can be considered to be valid. From Eq. (2-15), the corresponding specific volume is

$V^0 = RT / P^0$. If A is the Helmholtz energy, Ried et al. [11] show that the relevant departure functions are

$$A - A^0 = - \int_{\infty}^V (P - RT/V) dV - RT \ln(V/V^0) \quad (2-48)$$

$$s - s^0 = - \left(\frac{\partial(A - A^0)}{\partial T} \right)_V \quad (2-49)$$

$$h - h^0 = (A - A^0) + T(s - s^0) + RT(z - 1) \quad (2-50)$$

$$u - u^0 = (A - A^0) + T(s - s^0) \quad (2-51)$$

For the Aungier's modified Redlich-Kwong equation of state, the departure functions are

$$h - h^0 = PV - RT - \frac{a}{b}(n+1)T_r^{-n} \ln \left[\frac{V+b}{V} \right] \quad (2-52)$$

$$s - s^0 = R \ln \left[\frac{V}{V^0} \frac{V-b+c}{V} \right] - \frac{na}{bT} T_r^{-n} \ln \left[\frac{V+b}{V} \right] \quad (2-53)$$

These also apply to the original Redlich-Kwong equation of state if $c=0$ and $n=0.5$. Basic thermodynamics provides the other parameters commonly required for an aerodynamic analysis, i.e.,

$$c_p = \left(\frac{\partial h}{\partial T} \right)_p \quad (2-54)$$

$$c_v = \left(\frac{\partial u}{\partial T} \right)_V = c_p - R \left[z + T \left(\frac{\partial z}{\partial T} \right)_p \right]^2 / \left[z - P \left(\frac{\partial z}{\partial P} \right)_T \right] \quad (2-55)$$

$$a^2 = k \left(\frac{\partial P}{\partial \rho} \right)_T = \frac{k z RT}{1 - \frac{P}{z} \left(\frac{\partial z}{\partial P} \right)_T} \quad (2-56)$$

2.8 Thermally and Calorically Perfect Gases

A fluid is thermally and calorically perfect if c_p , c_v and k are constants and $z=1$. Equation of state calculations are greatly simplified for this class of fluids. Designating an arbitrary reference state point (T_{ref} , P_{ref}), the corresponding

enthalpy and entropy, h_{ref} and s_{ref} , can be assigned arbitrary values. Then Eqs. (2-22) and (2-25) can be written

$$h = h_{ref} + c_p(T - T_{ref}) \quad (2-57)$$

$$s = s_{ref} + c_p \ln(T/T_{ref}) - R \ln(P/P_{ref}) \quad (2-58)$$

Combining Eqs. (2-3) and (2-53) the total and static temperatures are related by

$$c_p(T_t - T) = \frac{1}{2} C^2 \quad (2-59)$$

For an isentropic or adiabatic-reversible process Eq. (2-58) requires

$$T/T_{ref} = (P/P_{ref})^{\frac{k-1}{k}} = (\rho/\rho_{ref})^{k-1} \quad (2-60)$$

Eqs. (2-59) and (2-60) provide simple analytical expressions to relate total and static conditions. Similarly, the efficiency calculations in Eqs. (2-9) and (2-14) simplify to

$$\eta_{ad} = \frac{(P_{td}/P_{ti})^{\frac{k-1}{k}} - 1}{T_{td}/T_{ti} - 1} \quad (2-61)$$

$$\eta_p = \frac{k-1}{k} \frac{\ln(P_{td}/P_{ti})}{\ln(T_{td}/T_{ti})} \quad (2-62)$$

Reduction of these thermodynamic relations to simple analytical form can yield substantial reductions in computation time for computerized aerodynamic analyses. If the fluid is calorically imperfect, numerical integration of Eqs. (2-20) and (2-21) will be necessary. For thermally imperfect fluids, the departure functions of Eqs. (2-52) and (2-53) must also be applied. In either case, numerical iteration will be required for isentropic processes to satisfy the constant entropy condition. This is the primary source of increased computation time. An aerodynamic analysis can be expected to perform a massive number of isentropic calculations to relate total and static conditions and to relate conditions in rotating and stationary coordinate systems. A calorically imperfect, thermally perfect fluid requires nearly as much computation time as a general nonideal gas. Hence, the thermally and calorically perfect gas model offers significant advantages when it can be employed.

2.9 The Pseudoperfect Gas Model

Aungier [1, 2, 6] introduce the concept of a pseudoperfect gas model. This is a very useful concept that often provides all of the benefits of the thermally and

calorically perfect gas model for cases where that model is not adequate. Use of this model requires that the aerodynamic analysis be formulated to avoid use of any state relations that assume the relationships between c_p , c_v , R and k expressed in Eqs. (2-19) and (2-27). This really does not complicate the analysis but is required to take advantage of the pseudoperfect gas model. The concept is to use fictitious values of c_p , c_v , R , and k in an otherwise standard thermally and calorically perfect gas model. Using an overbar to designate the fictitious constants, they can be calculated from any two state points, designated by subscripts 1 and 2.

$$\bar{R} = R\sqrt{z_1 z_2} \quad (2-63)$$

$$\bar{c}_p = (h_2 - h_1)/(T_2 - T_1) \quad (2-64)$$

$$\bar{c}_v = (u_2 - u_1)/(T_2 - T_1) \quad (2-65)$$

$$\bar{k} = \ln(P_2/P_1)/\ln(\rho_2/\rho_1) \quad (2-66)$$

When using the pseudoperfect gas model, this writer selects the inlet total conditions and the conditions corresponding to sonic flow as the two state points to define the fictitious constants. The full nonideal gas model is used to compute the constants. Then the pseudoperfect gas model is used in the actual analysis.

Eq. (2-66) yields the fluid's isentropic exponent, which can be quite different from the ratio of specific heats for a nonideal gas. The pseudoperfect gas model is generally adequate as long as the values of z_1 and z_2 are not too different. This is almost always true for compressor components operating on a nonideal fluid. Indeed, it can usually be applied to multistage compressor performance analysis, simply by recomputing the fictitious constants between stages or between blade rows. This writer has used it extensively for industrial compressor performance analysis. No compressor analysis problem has been encountered to date where the pseudoperfect gas model yields results significantly different from a full nonideal gas model for compressors.

Unfortunately, the same cannot be said for turbine performance analysis. There it is quite common to find that the values of z_1 and z_2 are too different to achieve sufficient accuracy. This writer's practice is to limit use of the pseudoperfect gas model for turbines to detailed internal flow field analysis in support of component design applications. While it can sometimes be used in a broader context, it usually requires more time and effort to confirm its validity than to simply use a more general equation of state.

2.10 Liquid-Phase Properties

A turbine aerodynamic performance analysis must be capable of addressing two-phase flow problems such as the wet expansion illustrated in figure 2-2. The

phase change corresponds to a change in enthalpy and density from the saturated vapor values that occurs at constant temperature and pressure as illustrated in figure 2-2. Eq. (2-47) defines the saturation pressure, P_v , as a function of temperature. It is easily inverted to define the saturation temperature, T_v , as a function of pressure. The saturation vapor enthalpy, h_v , is given by the basic nonideal gas equation of state as a function of the saturation temperature and pressure. As illustrated in figure 2-2, the saturated liquid enthalpy, h_l , is given by $h_l = h_v - \Delta H_v$, where ΔH_v is the heat of vaporization. Chen [21] has published a generalized correlation for the heat of vaporization.

$$\Delta H_v = T[7.9T_r - 7.82 - 7.11\log_{10}(P_r)]/[M(1.07 - T_r)] \quad (2-67)$$

The subscript, r , designates reduced values (i.e., normalized by the critical point value). Eq. (2-67) departs from this book's normal practice of avoiding specific units. Here, the units of ΔH_v are cal/gm or, equivalently, btu/lbm. Ried and Sherwood [20] suggest that Eq. (2-63) can be expected to be accurate within about 2.5%. Ried et al. [11], p. 60, recommend a correlation for the saturated liquid specific volume, V_l , attributed to Gunn and Yamada [22]

$$V_l = V_{sc} V_{r0} (1 - \omega \Gamma) \quad (2-68)$$

where

$$V_{sc} = RT_c(0.292 - 0.0967\omega)/P_c \quad (2-69)$$

$$\Gamma = 0.29607 - 0.09045T_r - 0.04842T_r^2 \quad (2-70)$$

$$V_{r0} = 0.33593(1 - T_r) + 1.51941T_r^2 - 2.02512T_r^3 + 1.11422T_r^4; \quad T_r < 0.8 \quad (2-71)$$

$$V_{r0} = 1 + 1.3\sqrt{1 - T_r} \log_{10}(1 - T_r) - 0.50879(1 - T_r) - 0.91534(1 - T_r)^2; \quad T_r \geq 0.8 \quad (2-72)$$

Defining the flow quality, Q , as

$$Q = (h - h_l)/\Delta H_v \quad (2-73)$$

For turbine aerodynamic analysis the fully condensed fluid case is the limit of our interest, so the limits $0 \leq Q \leq 1$ are imposed on Eq. (2-73). Note that $Q = 0$ corresponds to 100% liquid while $Q = 1$ corresponds to 100% vapor. Hence, when $Q < 1$,

$$V = V_l + (V_v - V_l)Q \quad (2-74)$$

Since the phase change occurs at constant pressure and temperature, Eq. (2-8) yields

$$s = s_v + (Q - 1)\Delta H_v / T_v \quad (2-75)$$

2.11 Gas Viscosity

Gas viscosity is often required for aerodynamic analysis. A generalized estimation method compatible with the previous equation of state models is provided by Dean and Stiel [23], and is reviewed by Ried and Sherwood [20]. It is necessary to depart from this book's practice of maintaining independence from specific units in this case. The Dean and Stiel model predicts viscosity in centipoises and employs a dimensional parameter defined by

$$\xi = T_c^{1/6} / (\sqrt{M} P_c^{2/3}) \quad (2-76)$$

where T_c is in degrees Kelvin and P_c is in atmospheres. The low-pressure fluid viscosity is given by

$$\mu^0 \xi = (3.4 \cdot 10^{-4}) T_r^{5/9}; \quad T_r \leq 1.5 \quad (2-77)$$

$$\mu^0 \xi = 0.001668(0.1338T_r - 0.0932)^{5/9}; \quad T_r > 1.5 \quad (2-78)$$

Then, the viscosity at any pressure is defined by a departure function

$$(\mu - \mu^0) \xi = (1.08 \cdot 10^{-4}) [\exp(1.439\rho_r) - \exp(-1.111\rho_r^{1.858})] \quad (2-79)$$

Ried and Sherwood [20] indicate that accuracy within 5% can be expected for nonpolar molecules, with somewhat larger errors possible for polar molecules. This viscosity estimation method is quite compatible with the equation of state models previously recommended in this chapter as long as the fluid is in the vapor phase. In principle, the real gas equations of state apply to the liquid or two-phase fluid also, but this viscosity model does not. The critical point data needed for Aungier's modified Redlich-Kwong equation of state are sufficient for this gas viscosity model also, but appropriate care is required to adjust the units of T_c and P_c in Eq. (2-76) and of the predicted viscosity.

2.12 Component Performance Parameters

The adiabatic and polytropic efficiencies introduced previously in this chapter can be used to evaluate the performance of a turbine, a turbine stage or even a

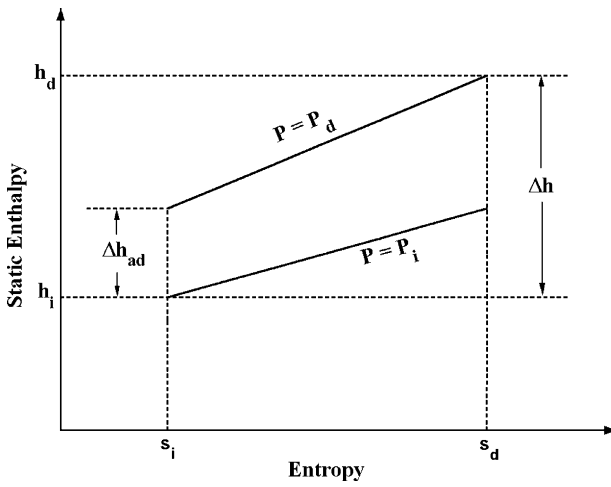


FIGURE 2-5. A Diffuser h-s Diagram

single rotor blade row. But they have no meaning for stationary turbine components, since total enthalpy is constant for those components. Yet, it is useful to be able to evaluate a stationary component's performance against some ideal, reversible process. Most components in a turbine serve to accelerate the flow. But there is usually an exhaust diffuser that seeks to diffuse the flow to convert kinetic energy into static pressure. One method of evaluating a diffusing component is known as the diffuser efficiency. Its definition is really quite similar to the adiabatic efficiency introduced previously, except that static enthalpy is used as its basis. Figure 2-5 presents a schematic of an *h-s* diagram for a diffuser. Flow enters the diffuser with a velocity, C_i , and exits the diffuser with a lower velocity, C_d . Since the total enthalpy, H , is constant, Eq. (2-3) can be used to compute the static enthalpy at the inlet, h_i , and at the discharge, h_d . It is seen from figure 2-5 that this process results in an increase in static enthalpy of Δh . Since irreversible losses such as friction occur, the entropy increases from s_i to s_d . Now, trace the line of constant pressure for the discharge pressure back to the inlet entropy. This shows that the static enthalpy increase required for an adiabatic, reversible process to produce the same pressure increase is Δh_{ad} . Therefore, a diffuser efficiency can be defined as

$$\eta_{diff} = \frac{\Delta h_{ad}}{\Delta h} \quad (2-80)$$

A more common parameter used to evaluate the performance of a diffuser is the static pressure recovery coefficient, c_p . This expresses the ratio of the static pressure rise to the available kinetic energy at the inlet. Usually, the available kinetic energy is expressed as a "velocity pressure," which is the difference between the total and static pressure.

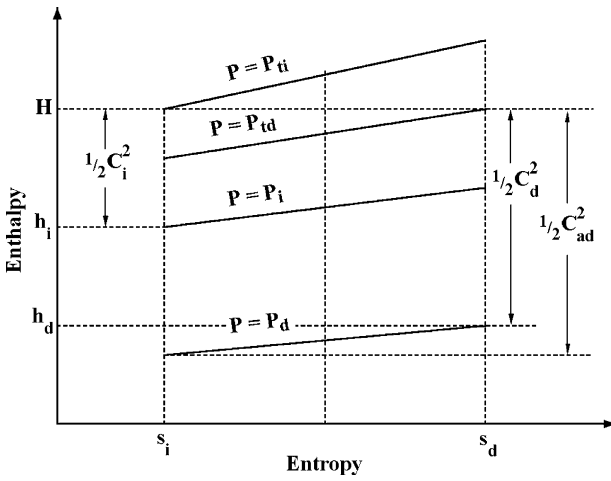


FIGURE 2-6. A Nozzle h-s Diagram

$$c_p = \frac{P_d - P_i}{P_{ti} - P_i} \quad (2-81)$$

Hence, c_p is the fraction of the available kinetic energy that has been recovered as static pressure by the diffuser.

Turbines are basically expanding machines that accelerate the flow. Expanding components can be evaluated using the nozzle efficiency. Figure 2-6 illustrates the parameters used to define it. The flow accelerates from the inlet velocity, C_i , to a higher discharge velocity, C_d . Due to irreversible processes such as wall friction, the entropy increases from s_i to s_d and the total pressure decreases from P_{ti} to P_{td} . If the flow is adiabatic (no heat transfer), the total enthalpy, H , is constant for this process. Eq. (2-3) relates H , h and C at the inlet and the discharge. This is illustrated in figure 2-6, along with the ideal discharge velocity, C_{ad} , which would be produced by an isentropic process between the actual inlet pressure, P_i and discharge pressure, P_d . A nozzle efficiency can be defined as the ratio of the actual increase in kinetic energy to the increase in kinetic energy corresponding to the isentropic process, i.e.,

$$\eta_{noz} = \frac{C_d^2 - C_i^2}{C_{ad}^2 - C_i^2} \quad (2-82)$$

Occasionally, a simpler definition is used: It employs the velocity pressure, $P_t - P$, in place of C^2 as the measure of the kinetic energy and uses $P_{ti} - P_d$ as the ideal (no loss in total pressure) discharge kinetic energy. Simple substitution of these alternate kinetic energy terms into Eq. (2-82) yields

$$\eta_{noz} = 1 - \frac{P_{ti} - P_{td}}{P_i - P_d} \quad (2-83)$$

The most fundamental measure of irreversibility is the increase in entropy. But an entropy increase is difficult to interpret, so total pressure loss is more commonly used. If Eq. (2-8) is applied to total conditions, with total enthalpy constant,

$$\frac{\Delta P_t}{\rho} = \frac{P_{ti} - P_{td}}{\rho} = T \Delta s \quad (2-84)$$

It is known from observation that total pressure loss is usually proportional to kinetic energy, so a logical definition of loss coefficient can be obtained by dividing by $\frac{1}{2} C^2$, i.e., the loss coefficient can be defined as

$$\bar{\omega} = \frac{\Delta P_t}{\frac{1}{2} \rho C^2} \quad (2-85)$$

Experience has shown that use of velocity pressure as a measure of kinetic energy provides a better definition, i.e.,

$$\bar{\omega} = \frac{\Delta P_t}{P_t - P} \quad (2-86)$$

It is found that the second definition is much less sensitive to changes in the Mach number. This is very important in any turbomachinery performance analysis. Typically, blade row performance is predicted with empirical loss coefficient models derived from low-speed cascade tests, but applied to blade rows with relatively high inlet Mach numbers. The flow is essentially incompressible (Mach number essentially zero) in the low-speed cascade tests, so the two definitions of loss coefficient are basically identical. But when empirical loss coefficient models are applied to predict losses in higher Mach number blade rows, Eq. (2-86) is found to yield substantially better results.

Eqs. (2-85) and (2-86) are ambiguous with regard to what kinetic energy is to be used in the denominator. The usual practice is use of the largest kinetic energy relevant to the component. For diffusing components, such as diffusers and compressor blade rows, the inlet kinetic energy is usually employed. For accelerating components, such as turbine blade rows, the discharge kinetic energy is usually employed. The formulation for loss coefficient assumed constant total enthalpy, which is far from true for rotor blade rows. But chapter 3 will show that total enthalpy viewed in a frame of reference rotating with the blades (the relative total enthalpy) is constant for axial flow. So, the above definitions can be used for rotors in that context. There is a subtle thermodynamic effect present when applying empirical loss coefficient models to rotating blade rows. In fact, the flow is not usually precisely axial, i.e., there is usually some

change in radius as a streamline passes through a rotor. Consequently, even the relative total enthalpy is not usually constant through the blade row. For axial-flow turbomachines, this effect is so small that it can be neglected in virtually all cases. The situation is quite different in radial-flow and mixed-flow turbomachines, where consideration of this thermodynamic effect may be essential. Aungier [1] develops a correction procedure to apply empirical loss coefficients to rotating blade rows with a significant change in radius from inlet to discharge. The difficulty arises when a total pressure loss is calculated at one location (e.g., at the impeller inlet) but is applied at a different location (e.g., at the impeller discharge). In that case, Eq. (2-8) must be employed to account for the relative total enthalpy change such that the correct entropy increase is applied. Since most turbine losses are calculated and applied at the blade row exit, this effect is less important for radial-inflow turbines than for centrifugal compressors. But it will be seen that the impeller performance analysis for radial-inflow turbine will require this type of correction for a few loss models.

2.13 A Computerized Equation of State Package

One of the most useful tools for the developer of turbomachinery design and analysis software is a computerized equation of state package that can be used as a module in any other analysis to handle all equation-of-state input, output and thermodynamic calculations. Some useful features to include are the following.

- Provide the nonideal gas, ideal gas (with variable specific heats) and pseudoperfect gas as options always available to the user. Provision should be made to automatically select the pseudoperfect gas for analyses that require it, or to prohibit it for analyses that shouldn't use it. For a basic ideal gas, the pseudoperfect gas model functions directly as a thermally and calorically perfect gas model. Include the capability to specify pseudoperfect gas data directly, or to have these data computed from the equation of state and the specified gas mixture.
- Maintain a database of gas property data for compounds needed. Establish the capability to set up any of the equation of state models from these data simply by selecting compounds in the mixture and supplying their mole fractions. For the models described in this chapter, the data needed are M , P_c , T_c , V_c (or z_c), ω and $c_p(T)$. This writer uses a third-order polynomial fit of c_p as a function of T , consistent with Ried et al. [11] which is a good source of all the data required for a very wide range of compounds. Note that setup of the pseudoperfect gas model from the equation of state must be requested by the main analysis when appropriate thermodynamic conditions are known, as described previously in this chapter. Include a routine to accomplish this on demand.
- Include logic to save and recover gas property data so that input files of other programs maintain a common format for all aerodynamic software. It is a good idea to include the logic for basic checks on data validity to be sure the equation of state is complete. Reserve a special code for the

equation of state model to signal to the program using this module that data are lacking or invalid.

- It is useful to include a standard output routine that can be used to insert a description of the mixture and the equation of state in use in output files for other programs.
- Include routines for the basic thermodynamic calculations needed in aerodynamic analysis. Standard functions likely to be needed include $V(T, P)$, $P(T, V)$, $T(V, P)$, $a(T, P)$, $h(T, P)$, $s(T, P)$, $\eta_{ad}(T_b, P_i, T_d, P_d)$ and $\eta_p(T_b, P_i, T_d, P_d)$. A routine to compute the isentropic change in P and T for a specified change in h is essential to for conversion between static and total thermodynamic conditions and between rotating and stationary coordinate systems. A routine to compute the speed of sound at sonic flow conditions for known total conditions is often useful.
- Include the capability to edit the thermodynamic model to modify the compounds in the mixture, their mole fractions and the equation of state model to be used.
- The Dean and Stiel [23] viscosity estimation model can be included to treat all gases and gas mixtures formed from the gas property database. If pseudopercfect gas data are specified rather than calculated from the equation of state, viscosity data will also need to be specified.

Using this approach, development of aerodynamic design and analysis software will involve minimal logic related to the equation of state. In general, the equation of state calculations should be limited to the vapor phase using the constraint expressed in Eq. (2-47), supplemented where necessary by the empirical liquid phase models described in this chapter.

Chapter 3

FLUID MECHANICS

Fluid mechanics and thermodynamics are the fundamental sciences used for turbine aerodynamic design and analysis. This chapter highlights some fundamental concepts from fluid mechanics to complement the concepts from thermodynamics covered in chapter 2. The governing equations will be developed in forms suitable for the various aerodynamic analyses commonly employed for turbines. Detailed solution procedures will be covered in subsequent chapters. The content of this chapter is quite similar to this writer's previous coverage of this topic for compressor aerodynamics [1, 2], but is specifically adapted to be more relevant to turbine aerodynamics.

Several types of fluid dynamic analysis are useful for this purpose. The through-flow analysis is widely used in axial-flow turbine performance analysis. This involves solving the governing equations for inviscid flow in the hub-to-shroud plane at stations located between blade rows. The flow is normally considered to be axisymmetric at these locations, but still three-dimensional because of the existence of a tangential velocity component. Empirical models are employed to account for the fluid turning and losses that occur when the flow passes through the blade rows. By contrast, hub-to-shroud through-flow analysis is not very useful for the performance analysis of radial-flow turbomachines such as radial-inflow turbines and centrifugal compressors. The inviscid flow governing equations do not adequately model the flow in the curved passages of radial turbomachines to be used as a basis for performance analysis. Instead, a simplified "pitch-line" or "mean-line" one-dimensional flow model is used, which ignores the hub-to-shroud variations. These also continue to be used for axial-flow turbine performance analysis, but are no longer particularly relevant to the problem. Computers are sufficiently powerful today that there is really no longer a need to simplify the problem that much for axial-flow turbomachinery. More fundamental internal flow analyses are often useful for the aerodynamic design of specific components, particularly blade rows. These include two-dimensional flow analyses in either the blade-to-blade or hub-to-shroud direction, and quasi-three-dimensional flow analyses developed by combining those two-dimensional analyses. Wall boundary layer analysis is often used to supplement these analyses with an evaluation of viscous effects.

Viscous computational fluid dynamics (CFD) solutions are also in use for turbines. These are typically three-dimensional flow analyses, which consider the effects of viscosity, thermal conductivity and turbulence. In most cases, commercial viscous CFD codes are used although some in-house codes are in use within the larger companies. Most design organizations cannot

commit the dedicated effort required to develop these highly sophisticated codes, particularly since viscous CFD technology is changing so rapidly that any code developed will soon be obsolete unless its development continues as an ongoing activity. Consequently, viscous CFD is not covered in this book beyond recognizing it as an essential technology and pointing out some applications for which it can be effectively used to supplement conventional aerodynamic analysis techniques.

NOMENCLATURE

- a = sound speed
- b = stream sheet thickness
- C = absolute velocity
- E = entrainment function
- \vec{e} = unit vector
- f = body force
- H = total enthalpy
- h = static enthalpy
- I = rothalpy
- m = meridional coordinate
- \dot{m} = mass flow rate
- n = normal coordinate
- P = pressure
- r = radius
- \vec{r} = position vector in space
- s = entropy
- T = temperature
- u = velocity in x direction
- \vec{V} = a general vector
- v = velocity in y direction
- W = relative velocity
- \dot{w} = power
- x = coordinate along a wall
- y = coordinate normal to a wall
- z = axial coordinate
- δ = boundary layer thickness
- δ^* = displacement thickness
- θ = tangential coordinate and momentum thickness
- κ = curvature
- ν = force defect thickness
- ρ = gas density
- τ = torque and shear stress
- ϕ = streamline slope with axis and a general function
- ω = rotation speed

Subscripts

- e = boundary layer edge condition
- m = meridional component

n = normal component

r = radial component

t = total thermodynamic condition

w = parameter at a wall

1 = blade inlet parameter and meridional defect parameter

11 = meridional defect parameter

12 = tangential flux defect parameter

2 = blade exit parameter and tangential defect parameter

22 = tangential defect parameter

θ = tangential component

Superscript

' = a relative value in the rotating coordinate system

3.1 Flow in a Rotating Coordinate System

It is convenient to analyze the flow in rotating blade rows in a coordinate system that rotates with the blade. The flow conditions in a rotating coordinate system are referred to as the relative conditions. If a blade row is rotating with an angular velocity, ω , the relative tangential velocity in a coordinate system rotating with the blade, W_θ , is related to the absolute tangential velocity, C_θ , by

$$W_\theta = C_\theta - \omega r \quad (3-1)$$

The axial and radial velocity components are independent of the rotation, i.e.,

$$W_z = C_z \quad (3-2)$$

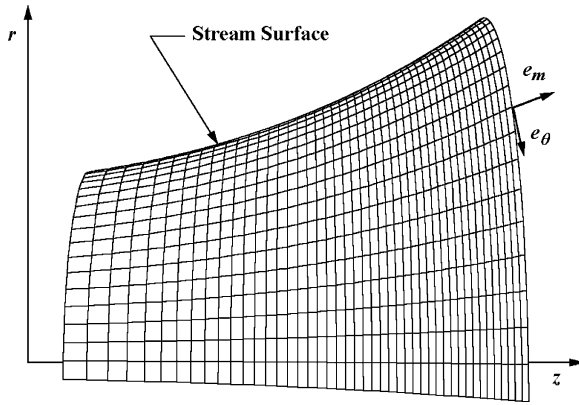
$$W_r = C_r \quad (3-3)$$

But it is more convenient to work with the meridional velocity component, W_m , defined as

$$W_m = \sqrt{W_z^2 + W_r^2} = C_m \quad (3-4)$$

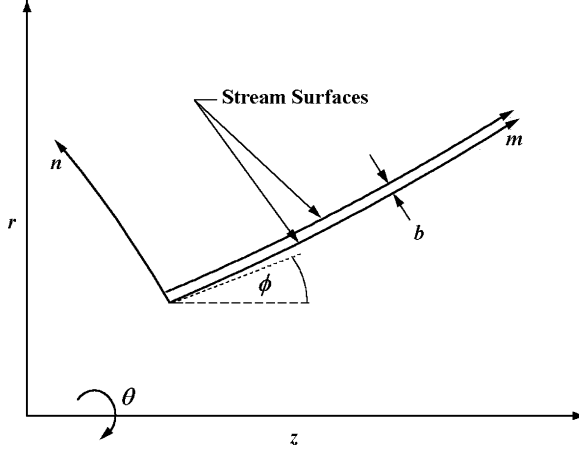
W_m is the velocity component lying in the meridional (constant θ) plane and in a stream surface. A stream surface is defined as a surface having no fluid velocity component normal to it and, therefore, no mass flow across it. Thus, a defining characteristic of a stream surface is that the mass flow rate between it and the hub contour surface is constant everywhere. The meridional coordinate, m , is measured along the stream surface and in a meridional plane, i.e.,

$$(dm)^2 = (dr)^2 + (dz)^2 \quad (3-5)$$

**FIGURE 3-1 Schematic of a Stream Surface**

It is almost always reasonable to assume stream surfaces in turbines are axisymmetric. That assumption will be used throughout this book. Figure 3-1 illustrates a schematic of a stream surface and unit vectors for the meridional and polar coordinates. Normal to these unit vectors, and to the stream surface, is the third coordinate of interest, the normal coordinate, n , as shown in figure 3-2. It is convenient to develop the governing equations of fluid mechanics in this “natural” coordinate system (θ, m, n) , where by definition

$$W_n = C_n = 0 \quad (3-6)$$

**FIGURE 3-2 Natural Coordinate System**

Now consider the flow through a thin stream sheet, i.e., a thin annular passage bounded by two stream surfaces. The torque, τ , acting on the fluid between meridional stations 1 and 2 is given by conservation of angular momentum.

$$\tau = \dot{m}(r_2 C_{\theta 2} - r_1 C_{\theta 1}) \quad (3-7)$$

This torque must balance the power input, i.e.,

$$\dot{W} = \omega \tau = \omega \dot{m}(r_2 C_{\theta 2} - r_1 C_{\theta 1}) \quad (3-8)$$

Combining Eq. (3-8) with Eq. (2-4) yields the well-known Euler turbine equation

$$H_2 - H_1 = \omega(r_2 C_{\theta 2} - r_1 C_{\theta 1}) \quad (3-9)$$

This is the general energy equation relating the total enthalpy change produced by a transfer of mechanical energy between the fluid and a rotating blade row. It is convenient to introduce the rothalpy, I , defined by

$$I = H - \omega r C_\theta \quad (3-10)$$

Introducing Eq. (3-10) into Eq. (3-9), it can be seen that rothalpy is constant on a stream surface. Hence, rothalpy is the basic parameter expressing energy conservation for a rotating blade row. It is also valid for a stationary blade row, since $I = H$ in that case and Eq. (3-9) requires that H be constant in the absence of energy transfer with a rotating blade row.

Turbine aerodynamic analysis involves alternately solving the governing equations in stationary coordinates (nozzles) and rotating coordinates (rotors). Hence, we need to relate the relative total enthalpy, H' , in a rotating coordinate system to the absolute total enthalpy, H , in a stationary coordinate system. Noting that static thermodynamic conditions are identical for either coordinate system,

$$h = H' - \frac{1}{2} W^2 = H - \frac{1}{2} C^2 \quad (3-11)$$

The relative velocity, W , follows from Eqs. (3-1), (3-4) and (3-6)

$$W = \sqrt{W_m^2 + W_\theta^2} \quad (3-12)$$

Eqs. (3-1), (3-10), (3-11) and (3-12) combine to yield

$$H' = H - \omega r C_\theta + \frac{1}{2}(\omega r)^2 = I + \frac{1}{2}(\omega r)^2 \quad (3-13)$$

Noting that entropy is identical for total and static conditions, and therefore identical for rotating and stationary coordinate systems, Eq. (3-13) can be used to relate thermodynamic parameters in the two coordinate systems. For example, the change in all other relative total thermodynamic conditions between the

two coordinate systems can be calculated from an appropriate equation of state as a function of (H, H', s) . This requires calculation of the isentropic change in the parameter of interest for a specified change in enthalpy. Hence, Eq. (3-13) is an important relation that allows us to relate all thermodynamic parameters between the stationary and the rotating coordinate systems. Also, since rothalpy is constant on a stream surface, Eq. (3-13) allows calculation of H' at all points on a stream surface when one value is known, e.g., at the inlet.

3.2 Adiabatic Inviscid Compressible Flow

Adiabatic compressible inviscid flow analysis is commonly used in turbomachinery. This flow model assumes that the effects of fluid viscosity and thermal conductivity can be neglected. Basic conservation of mass, momentum and energy, supported by a suitable equation of state, govern the flow. It is useful to derive the governing equations in a rotating coordinate system, noting that these equations will also be valid for a stationary coordinate system if ω is set to zero. The vector form of the momentum equation can be written (Novak [24], Vavra [25], and Wu [26])

$$\frac{d\vec{C}}{dt} = -\frac{1}{\rho} \vec{\nabla} P = \frac{d\vec{W}}{dt} + 2(\vec{\omega} \times \vec{W}) + \vec{\omega} \times (\vec{\omega} \times \vec{r}) \quad (3-14)$$

The last two terms in Eq. (3-14) are the Coriolis and centrifugal accelerations imposed by the rotating coordinate system, and the time derivative is the substantial derivative, i.e.,

$$\frac{d\vec{W}}{dt} = \frac{\partial \vec{W}}{\partial t} + (\vec{W} \cdot \vec{\nabla}) \vec{W} \quad (3-15)$$

Hence, the momentum equation in rotating coordinates is

$$\frac{\partial \vec{W}}{\partial t} + (\vec{W} \cdot \vec{\nabla}) \vec{W} + 2(\vec{\omega} \times \vec{W}) + \vec{\omega} \times (\vec{\omega} \times \vec{r}) = -\frac{\vec{\nabla} P}{\rho} \quad (3-16)$$

Using standard vector identities, this equation can also be written as

$$\frac{\partial \vec{W}}{\partial t} - \vec{W} \times (\vec{\nabla} \times \vec{W} + 2\vec{\omega}) - r\omega^2 \vec{e}_r + \frac{1}{2} \vec{\nabla} W^2 = -\frac{\vec{\nabla} P}{\rho} \quad (3-17)$$

where \vec{e}_r is a unit vector in the radial direction. On introducing Eqs. (2-3), (2-8), (3-10) and (3-11) an alternate form of Eq. (3-17) is obtained.

$$\frac{\partial \vec{W}}{\partial t} - \vec{W} \times (\vec{\nabla} \times \vec{W} + 2\vec{\omega}) = T \vec{\nabla} s - \vec{\nabla} I \quad (3-18)$$

The continuity and energy equations in vector form are

$$\frac{\partial \rho}{\partial t} + \vec{\nabla} \cdot (\rho \vec{W}) = 0 \quad (3-19)$$

$$\frac{\partial I}{\partial t} - \frac{1}{\rho} \frac{\partial P}{\partial t} + (\vec{W} \cdot \vec{\nabla}) I = 0 \quad (3-20)$$

Eqs. (3-16) through (3-20) are vector equations, which are valid in any coordinate system. To express the equations in the natural coordinates (θ, m, n), standard curvilinear coordinate transformations are used. These can be found in most advanced calculus books, which cover vector field theory. Appendix A of Vavra [25] provides specific and detailed derivations of the vector operators and governing equations in natural coordinates. For general reference, the important vector operators are provided without derivation at the end of this chapter. The resulting governing equations are

$$\frac{\partial \rho}{\partial t} + \frac{1}{r} \left[\frac{\partial r \rho W_m}{\partial m} + \frac{\partial \rho W_\theta}{\partial \theta} \right] + \kappa_n \rho W_m = 0 \quad (3-21)$$

$$\frac{\partial W_m}{\partial t} + W_m \frac{\partial W_m}{\partial m} + \frac{W_\theta}{r} \frac{\partial W_m}{\partial \theta} - \frac{\sin \phi}{r} [W_\theta + \omega r]^2 = -\frac{1}{\rho} \frac{\partial P}{\partial m} \quad (3-22)$$

$$\frac{\partial W_\theta}{\partial t} + W_m \frac{\partial W_\theta}{\partial m} + \frac{W_\theta}{r} \frac{\partial W_\theta}{\partial \theta} + \frac{W_m \sin \phi}{r} [W_\theta + 2\omega r] = -\frac{1}{r \rho} \frac{\partial P}{\partial \theta} \quad (3-23)$$

$$\kappa_m W_m^2 + \frac{\cos \phi}{r} [W_\theta + \omega r]^2 = \frac{1}{\rho} \frac{\partial P}{\partial n} \quad (3-24)$$

$$\frac{\partial I}{\partial t} - \frac{1}{\rho} \frac{\partial P}{\partial t} + W_m \frac{\partial I}{\partial m} + \frac{W_\theta}{r} \frac{\partial I}{\partial \theta} = 0 \quad (3-25)$$

The curvature of the stream sheet, κ_m , and of the normal surface, κ_n , are related to the angle ϕ shown in figure 3-2.

$$\kappa_m = -\frac{\partial \phi}{\partial m} \quad (3-26)$$

$$\kappa_n = \frac{\partial \phi}{\partial n} = \frac{1}{b} \frac{\partial b}{\partial m} \quad (3-27)$$

Parameter b in Eq. (3-27) is the thickness of a stream sheet bounded by two stream surfaces, as shown in figure 3-2. Hence, the curvature κ_n is related to the meridional divergence or convergence of the stream surfaces. That form

is useful in some applications of these governing equations, particularly when analyzing the two-dimensional flow in a blade-to-blade stream surface. Eqs. (3-22) through (3-24) can be expressed in an alternate form using Eq. (3-18).

$$\frac{\partial W_m}{\partial t} + \frac{W_\theta}{r} \left[\frac{\partial W_m}{\partial \theta} - \frac{\partial(rW_\theta + \omega r^2)}{\partial m} \right] = T \frac{\partial s}{\partial m} - \frac{\partial I}{\partial m} \quad (3-28)$$

$$\frac{\partial W_\theta}{\partial t} - \frac{W_m}{r} \left[\frac{\partial W_m}{\partial \theta} - \frac{\partial(rW_\theta + \omega r^2)}{\partial m} \right] = T \frac{\partial s}{\partial \theta} - \frac{\partial I}{\partial \theta} \quad (3-29)$$

$$\kappa_m W_m^2 + \frac{W_\theta}{r} \frac{\partial(rW_\theta + \omega r^2)}{\partial n} + W_m \frac{\partial W_m}{\partial n} = \frac{\partial I}{\partial n} - T \frac{\partial s}{\partial n} \quad (3-30)$$

Since there are only two velocity components (i.e., $W_n = 0$), one of the three momentum equations is redundant. The redundant equation has been replaced by the assumption that the stream surfaces are known or can somehow be determined as part of the solution. If the meridional surfaces are not stream surfaces, the governing equations must be modified to include a normal velocity component, W_n . This will not be required for analyses described in this book, although there is no reason why a flow analysis could not be accomplished in an arbitrary (θ, m, n) coordinate system. Aungier [1] includes the more general form of the governing equations appropriate for that type of analysis.

3.3 Adiabatic Inviscid Compressible Flow Applications

The governing equations are applied in a variety of analyses in the aerodynamic design and analysis of turbines. Most analyses employ the time-steady form of the governing equations, although the unsteady form does find application when the fluid velocity exceeds the sonic flow velocity. One of the most common applications is to determine the flow in the meridional plane. This application normally restricts the solution to stations outside of the blade rows, using empirical models to impose the influence of blade rows between stations in terms of fluid turning and total pressure loss correlations. These analyses treat the flow as axisymmetric while requiring conservation of mass, normal momentum and energy. Various simplifications may be employed in these analyses. If stream surface curvature is neglected ($\kappa_m = 0$) and the gradient of entropy across the passage is assumed to be zero, the analysis is referred to as a "simple normal equilibrium" solution. If the gradient of entropy is included, the analysis is referred to as a "simple nonisentropic normal equilibrium" solution. When curvature and entropy are both included, the term *full normal equilibrium* is often used. Advances in computer technology and numerical analysis techniques have reduced the role of simple normal equilibrium solutions to cases where the entropy gradient cannot be properly defined, such as for a general-purpose stage design for arbitrary inlet conditions. Simple nonisentropic normal equilibrium is useful in basic blade row or

stage design, where the streamline curvatures to be encountered in the actual application are not known. Indeed, simple nonisentropic normal equilibrium analysis is often quite sufficient for actual axial-flow turbines, where stream surface curvatures may be negligible. When the stream surface curvature can be ignored, a dramatic reduction in computation time is realized, since the analysis becomes a simple marching solution. This follows from the fact that the flow at any axial station is not dependent on the flow at downstream stations. A simple variant used by this writer [2] is to approximate stream surface curvatures from end-wall contours by simple linear interpolation. This allows the advantages of a simple nonisentropic normal equilibrium analysis, yet can approximate curvatures imposed by end-wall contour design.

Solutions for the two-dimensional flow in the meridional plane within blade passages are also fairly common. These usually seek to predict the average flow in the passage from the hub to the shroud as a two-dimensional flow problem. In the more general case, these hub-to-shroud analyses may solve for the two-dimensional flow on specific stream surfaces from hub to shroud. In both cases, either the flow angle or W_θ distributions throughout the blade passage must be supplied to replace solution of the tangential momentum equation.

Analysis of the flow passing through a blade row and lying on a stream surface is also common in turbine design and analysis. These two-dimensional flow analyses are commonly called blade-to-blade flow analyses. Typically, the stream surface geometry is specified along with the distribution of the stream sheet thickness, b . Then, conservation of mass, energy, tangential momentum and meridional momentum can describe the flow. If the flow is assumed to be isentropic, it is seen from Eqs. (3-28) and (3-29) that one of the momentum equations is redundant, resulting in a simpler problem. This is fairly common practice for subsonic flow problems and is referred to as potential flow or irrotational flow. This results in a classical boundary value problem of an elliptic equation. Indeed, the governing equations for inviscid flow are elliptic in form as long as $W < a$ throughout the flow field. When supersonic flow is encountered ($W > a$), the governing equations become hyperbolic in mathematical form, which requires a marching type solution—such as the method of characteristics—rather than a boundary value problem solution. Cases where the flow is supersonic throughout are rare. Usually mixed subsonic-supersonic flow is involved. Then the time-steady governing equations are elliptic in some regions and hyperbolic in others, requiring two different solution techniques that must be matched together in some fashion. It is now fairly common practice to employ the time-unsteady equations for these cases. The advantage of that approach is that the unsteady equations of motion are hyperbolic in form for both subsonic and supersonic flow. This allows a single numerical method to be used for the mixed subsonic-supersonic flow case. This approach is commonly called the “time-dependent” or “time-marching” method of solution.

Hub-to-shroud and blade-to-blade flow analyses may also be combined to form a “quasi-three-dimensional” flow analysis within blade passages. A hub-to-shroud analysis can supply the stream surface geometry and stream

sheet thickness distribution required for a blade-to-blade flow analysis. Similarly, a blade-to-blade flow analysis can supply the distribution of flow angle or tangential velocity required for a hub-to-shroud flow analysis. Thus an iterative solution solving these two two-dimensional flow problems with interaction between them can provide an approximate three-dimensional flow analysis. This approach was originally suggested by Wu [26] and is a commonly used analysis technique for compressors. It is somewhat less useful for turbines due to its inability to handle the wide range of Mach number levels involved. Its main use in turbines is to evaluate impeller designs for radial-inflow turbines, where the quality of the impeller design can be evaluated at more moderate Mach numbers. In principle, it can be used the same way to evaluate an axial-flow turbine blade row design. But in practice, it provides little more benefit than a simpler two-dimensional blade-to-blade flow analysis for that case.

Analysis of the complete three-dimensional inviscid flow problem is seldom used today. The additional information supplied relative to the simpler and faster quasi-three-dimensional flow analysis is relatively minor. Also, the evolution of three-dimensional viscous CFD analysis techniques has discouraged use of a three-dimensional inviscid flow analysis. As discussed at the beginning of this chapter, most turbomachinery design groups use one of the many excellent commercially available viscous CFD codes when a more detailed and fundamental analysis is needed.

3.4 Boundary Layer Analysis

Adiabatic inviscid flow analyses, such as those described in the previous sections, are commonly augmented by boundary layer analysis techniques to evaluate viscous effects that are not considered by those analyses. The basic premise of boundary layer theory is that viscous effects are confined to a thin layer close to the physical surfaces bounding the flow passages [27, 28]. This is by no means always the case in turbomachinery, but selective use of boundary layer analysis has been found to be very effective in many applications. As with the discussion of three-dimensional inviscid flow analysis in the previous section, practical trade-off with fully viscous flow analyses must be considered. Boundary layers in turbomachinery always involve significant three-dimensional character. Yet, there is little merit to a fully three-dimensional boundary layer analysis today, when commercially available viscous CFD codes can treat the problem much more accurately. Rather, it is the simplified boundary layer analysis techniques that are most effective in augmenting the inviscid flow analyses discussed in the previous section. Indeed, it is little short of remarkable that boundary layer analysis has been used so effectively in turbomachinery design and analysis, considering the fact that the fundamental boundary layer approximations are almost always violated to some degree and very often to a substantial degree. There are two important types of boundary layer analysis commonly used in turbomachinery aerodynamics. These involve boundary layers on the blade surfaces and those on the end-wall contours.

Two-dimensional boundary layer analysis is a useful approximation for blade surface boundary layers, particularly in blade design. The primary goals of blade design are really governed by viscous effects, namely minimizing viscous losses and avoiding or delaying flow separation. Two-dimensional boundary layer analysis provides at least a qualitative assessment of these effects, yet adds very little complexity or computational time to the overall analysis. Indeed, conventional practice for blade design is to design blade sections in the context of simple two-dimensional cascades, where two-dimensional boundary layer analysis is directly applicable. These blade sections are then “stacked” to create the actual three-dimensional blade. When applied to the actual blade surface boundary layers, two-dimensional boundary layer analysis provides only qualitative results, since three-dimensional effects not considered by the analysis often become significant.

By contrast, end-wall boundary layers are necessarily three-dimensional, due to the presence of the swirl velocity component and tangential blade forces. Axisymmetric, three-dimensional boundary layer approximations have been used effectively to model a variety of end-wall boundary layer problems. This model is quite rigorous when applied for an internal flow and aerodynamic performance analysis of swirling flows in annular passages with no blades or vanes present, such as inlets and diffusers, e.g., Aungier [29], Davis [30] and Senoo [31]. It has also been used effectively to predict end-wall boundary layers in axial-flow compressors as an essential part of an aerodynamic performance analysis, e.g., Balsa and Mellor [32] and Aungier [2]. In this context, it is applied at stations between blade rows where the axisymmetric flow assumption is a reasonable approximation. When a blade row lies between successive computing stations, the axisymmetric assumption is violated within the blade passage. That requires use of supplemental empirical models to address the influence of the blade rows. Horlock [33] and Aungier [1, 2] have used this model to treat end-wall boundary layers within blade passages. While these boundary layers are far from axisymmetric, this model is used to provide an evaluation of the average or mean boundary layer behavior between the blades along the end-wall contours.

Boundary layer analysis offers substantial benefits for compressor aerodynamic design and analysis. The diffusing flow in compressors requires close attention to boundary layer separation or stall characteristics in most components. This can strongly influence the compressor's limit of stable operation or surge. Similarly, end-wall boundary layer analysis is essential to obtaining an accurate prediction of the performance of axial-flow compressors. The benefits offered by boundary layer analysis are far more modest when applied to the accelerating flow in turbines. Indeed, effective turbine component designs can and have been developed without support from boundary layer analysis. Viscous effects are certainly important to turbine performance. But, in contrast to compressors, the boundary layers in turbines are relatively thin, well behaved and less likely to result in a catastrophic break down in performance.

The basic boundary layer equations relevant to these two types of boundary layers will be developed in the remainder of this chapter. Specific applications of these governing equations will be discussed as required in subsequent chapters to support the various inviscid flow analyses.

3.5 Two-Dimensional Boundary Layer Analysis

Basic conservation of mass and momentum provide the governing equations for two-dimensional boundary layer flow over an adiabatic wall.

$$\frac{\partial \rho b u}{\partial x} + \frac{\partial \rho b v}{\partial y} = 0 \quad (3-31)$$

$$u \frac{\partial u}{\partial x} + v \frac{\partial u}{\partial y} + \frac{1}{\rho} \frac{\partial P}{\partial x} = \frac{1}{\rho} \frac{\partial \tau}{\partial y} \quad (3-32)$$

where τ is the shear stress. The coordinates (x, y) and velocity components (u, v) are illustrated in figure 3-3, along with a typical boundary layer velocity profile. The stream sheet thickness, b , has been included in Eq. (3-31) since it is often a function of x in turbomachinery applications, i.e., streamlines often converge or diverge. This directly affects conservation of mass. The basic assumption of boundary layer theory is that the pressure is constant across the boundary layer, i.e., P is a function of x only. Boundary layer analysis in turbomachinery is most conveniently accomplished by applying the governing equations in integral form. Eq. (3-31) can be integrated across the boundary layer, using the Liebnitz rule to interchange the order of integration and differentiation, to yield

$$\frac{\partial}{\partial x} \int_0^\delta b \rho u dy = b \rho_e u_e \frac{\partial \delta}{\partial x} - b \rho_e v_e = \frac{\partial}{\partial x} [b \rho_e u_e (\delta - \delta^*)] \quad (3-33)$$

The subscript e denotes inviscid flow conditions at the boundary layer edge, δ is the boundary layer thickness and δ^* is called the displacement thickness or mass defect thickness, defined as

$$\rho_e u_e \delta^* = \int_0^\delta [\rho_e u_e - \rho u] dy \quad (3-34)$$

Eq. (3-34) can be rewritten as

$$\int_0^\delta \rho u dy = \rho_e u_e [\delta - \delta^*] \quad (3-35)$$

The displacement thickness is a fictitious thickness that can be used to correct the mass balance relative to the inviscid flow solution. As seen from Eq.(3-35), if the inviscid boundary layer edge or “free stream” conditions are applied within the boundary layer and the thickness δ^* is assumed to have zero mass flow, mass conservation will be corrected for viscous effects. Eqs. (3-31) and (3-32) can be combined to express the momentum equation in conservation form. This yields

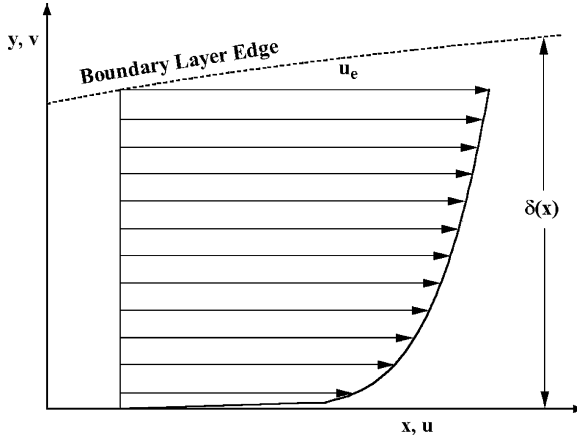


FIGURE 3-3 Boundary Layer Nomenclature

$$\frac{1}{b} \frac{\partial b \rho u^2}{\partial x} + \frac{\partial \rho u v}{\partial y} + \frac{\partial P}{\partial x} = \frac{\partial \tau}{\partial y} \quad (3-36)$$

Analogous to the displacement thickness, the momentum thickness or momentum defect thickness, θ , is defined as

$$\rho_e u_e^2 \theta = \int_0^\delta \rho u [u_e - u] dy \quad (3-37)$$

Eqs. (3-35) and (3-37) combine to yield

$$\int_0^\delta \rho u^2 dy = \rho_e u_e^2 [\delta - \delta^* - \theta] \quad (3-38)$$

If the free stream conditions are applied within the boundary layer with no flow in the thickness δ^* and, in addition, no momentum in the thickness θ , momentum conservation will be corrected for viscous effects. Hence, if δ^* and θ can be predicted, we have a simple method to correct the known inviscid free stream mass and momentum flux for viscous effects. This is really the basis of integral boundary layer analysis methods. Integrating Eq. (3-36) across the boundary layer, again using the Liebnitz rule, and noting that $P = P_e$ is constant across the boundary layer yields

$$\frac{\partial}{\partial x} \int_0^\delta b \rho u^2 dy - \rho_e u_e^2 \frac{\partial \delta}{\partial x} + \rho_e u_e v_e + \delta \frac{\partial P_e}{\partial x} = -\tau_w \quad (3-39)$$

Combining Eqs. (3-33), (3-38) and (3-39) yields

$$\frac{1}{b} \frac{\partial}{\partial x} [b\rho_e u_e^2 (\delta - \delta^* - \theta)] - \frac{u_e}{b} \frac{\partial}{\partial x} [b\rho_e u_e (\delta - \delta^*)] + \delta \frac{\partial P_e}{\partial x} = -\tau_w \quad (3-40)$$

Eq. (3-40) can be rearranged to yield

$$\frac{1}{b} \frac{\partial b\rho_e u_e^2 \theta}{\partial x} + \delta^* \rho_e u_e \frac{\partial u_e}{\partial x} - \tau_w = \delta \left[\frac{\partial P_e}{\partial x} + \rho_e u_e \frac{\partial u_e}{\partial x} \right] \quad (3-41)$$

By applying Eq. (3-32) at the boundary layer edge, where the gradients of u and τ in the y direction are zero, it is easily seen that the right-hand side of Eq. (3-41) is identically zero. Hence, Eq. (3-41) reduces to the well-known momentum integral equation.

$$\frac{1}{b} \frac{\partial b\rho_e u_e^2 \theta}{\partial x} + \delta^* \rho_e u_e \frac{\partial u_e}{\partial x} = \tau_w \quad (3-42)$$

In the special case of two-dimensional, axisymmetric flow, it can be noted that b is proportional to radius, r , and the momentum integral equation becomes

$$\frac{1}{r} \frac{\partial r \rho_e u_e^2 \theta}{\partial x} + \delta^* \rho_e u_e \frac{\partial u_e}{\partial x} = \tau_w \quad (3-43)$$

The momentum integral equation is valid for both laminar and turbulent boundary layers. Laminar boundary layer analysis usually employs specific boundary layer flow profile assumptions to permit direct integration of the momentum integral equation. Turbulent boundary layer analysis usually employs several empirical models for solution, which may include specific boundary layer flow profile assumptions. Usually, turbulent boundary layer analysis employs a second conservation equation, such as conservation of mass, energy or moment of momentum. Rotta [34] provides a very concise summary of a number of alternate choices for this purpose. This writer prefers conservation of mass as the second equation, commonly called the entrainment equation. This is the well-known and widely used entrainment method of turbulent boundary layer analysis suggested by Head [35, 36]. In this case, Eq. (3-33) is written in the form

$$\frac{\partial}{\partial x} [b\rho_e u_e (\delta - \delta^*)] = b\rho_e u_e E \quad (3-44)$$

The parameter E is called the entrainment function, which specifies the rate at which free stream fluid is entrained into the boundary layer at the boundary layer edge. To employ this model, an empirical correlation for E is required, which must be derived from experiment. Combining Eqs. (3-33) and (3-44), it is seen that the entrainment function is given by

$$E = \frac{\partial \delta}{\partial x} - \frac{v_e}{u_e} \quad (3-45)$$

Indeed, entrainment is governed by the gradient of the shear stress at the boundary layer edge. Hence, entrainment should depend on the shape of the boundary layer profiles, which is the usual basis for empirical models.

3.6 Axisymmetric Three-Dimensional Boundary Layer Analysis

Eq. (3-43) describes axisymmetric boundary layers where the flow field is two dimensional, i.e., there is no tangential velocity component. When a tangential velocity component is present in an otherwise axisymmetric flow field, the meridional and tangential components of the boundary layer profiles develop differently, resulting in a three-dimensional flow problem. The analysis of these problems is referred to as axisymmetric three-dimensional boundary layer analysis.

The governing equations for axisymmetric three-dimensional boundary layer flow in a rotating coordinate system in natural coordinates (θ, m, y) are

$$\frac{1}{r} \frac{\partial \rho W_m}{\partial m} + \frac{\partial \rho W_y}{\partial y} = 0 \quad (3-46)$$

$$W_m \frac{\partial W_m}{\partial m} + W_y \frac{\partial W_m}{\partial y} - \frac{\sin \phi}{r} (W_\theta + \omega r)^2 = \frac{1}{\rho} \left[f_m - \frac{\partial P_e}{\partial m} - \frac{\partial \tau_m}{\partial y} \right] \quad (3-47)$$

$$W_m \frac{\partial W_\theta}{\partial m} + W_y \frac{\partial W_\theta}{\partial y} + \frac{\sin \phi}{r} W_m (W_\theta + 2\omega r) = \frac{1}{\rho} \left[f_\theta - \frac{\partial \tau_\theta}{\partial y} \right] \quad (3-48)$$

A rotating coordinate system is needed for turbomachinery applications, since end-walls may be either rotating or stationary. The coordinate system should rotate with the end-wall to simplify imposing the boundary condition that all velocity components are identically zero at the wall. The terms, f_m and f_θ , in Eqs. (3-47) and (3-48) are body force terms used to account for blade forces acting on the flow. The blade forces at the boundary layer edge can be evaluated directly by applying Eqs. (3-47) and (3-48) to the inviscid flow at the boundary layer edge, where all inviscid free stream conditions are known and where W_n and the shear stress terms are identically zero. Hence,

$$f_{me} = \rho_e W_{me} \frac{\partial W_{me}}{\partial m} + \frac{\partial P_e}{\partial m} - \frac{\sin \phi}{r} \rho_e (W_{\theta e} + \omega r)^2 \quad (3-49)$$

$$f_{\theta e} = \rho_e W_{me} \frac{\partial W_{\theta e}}{\partial m} + \frac{\sin \phi}{r} \rho_e W_{me} (W_{\theta e} + 2\omega r) = \frac{\rho_e W_{me}}{r} \frac{\partial r C_{\theta e}}{\partial m} \quad (3-50)$$

The boundary layer equations are converted to integral form in the same fashion as described earlier. The algebra is more tedious and several additional defect thicknesses are required. The resulting integral equations are

$$\frac{\partial}{\partial m} [r \rho_e W_{me} (\delta - \delta_1^*)] = r \rho_e W_e E \quad (3-51)$$

$$\frac{\partial}{\partial m} [r \rho_e W_{me}^2 \theta_{11}] + \delta_1^* r \rho_e W_{me} \frac{\partial W_{me}}{\partial m} - \rho_e W_{\theta e} \sin \phi [W_{\theta e} (\delta_2^* + \theta_{22}) + 2 \omega r \delta_2^*] = r [\tau_{mw} + f_{me} v_m] \quad (3-52)$$

$$\frac{\partial}{\partial m} [r^2 \rho_e W_{me} W_{\theta e} \theta_{12}] + r \delta_1^* \rho_e W_{me} \left[r \frac{\partial W_{\theta e}}{\partial m} + \sin \phi (W_{\theta e} + 2r\omega) \right] = r^2 [\tau_{\theta e} + f_{\theta e} v_{\theta}] \quad (3-53)$$

The various mass, momentum and force defects used in these equations are defined as follows.

$$\rho_e W_{me} \delta_1^* = \int_0^\delta (\rho_e W_{me} - \rho W_m) dy \quad (3-54)$$

$$\rho_e W_{me}^2 \theta_{11} = \int_0^\delta \rho W_m (W_{me} - W_m) dy \quad (3-55)$$

$$\rho_e W_{me} W_{\theta e} \theta_{12} = \int_0^\delta \rho W_m (W_{\theta e} - W_{\theta}) dy \quad (3-56)$$

$$\rho_e W_{\theta e} \delta_2^* = \int_0^\delta (\rho_e W_{\theta e} - \rho W_{\theta}) dy \quad (3-57)$$

$$\rho_e W_{\theta e}^2 \theta_{22} = \int_0^\delta \rho W_{\theta} (W_{\theta e} - W_{\theta}) dy \quad (3-58)$$

$$v_m f_{me} = \int_0^\delta (f_{me} - f_m) dy \quad (3-59)$$

$$v_{\theta} f_{\theta e} = \int_0^\delta (f_{\theta e} - f_{\theta}) dy \quad (3-60)$$

The momentum integral equations can be simplified by assuming that the blade forces are constant through the boundary layer. This would certainly be consistent with the usual boundary layer approximations, but it is now known that this is often not true for end-wall boundary layers within blade passages. Mellor and Wood [37] advanced compelling arguments for the existence of blade force defects. Smith [38], Koch and Smith [39] and Hunter and Cumpsty [40] report experimental measurements of blade force defects. For vaneless annular passages, these body force terms will normally vanish, but Aungier [29] uses them to advantage to treat cases where the boundary layers merge to form fully developed viscous flow profiles.

3.7 Vector Operators in Natural Coordinates

The development of the governing equations in an axisymmetric natural coordinate system presented in this chapter requires use of several standard vector operators. Appendix A of Vavra [25] provides detailed derivations of these operators. Here, the various operators are presented for reference purposes, without derivation. The gradient of any function ϕ is given by

$$\vec{\nabla}\phi = \frac{\partial\phi}{\partial m}\vec{e}_m + \frac{\partial\phi}{\partial n}\vec{e}_n + \frac{1}{r}\frac{\partial\phi}{\partial\theta}\vec{e}_\theta \quad (3-61)$$

where \vec{e} is a unit vector. The divergence of any vector \vec{V} is given by

$$\nabla \cdot \vec{V} = \frac{1}{r} \left[\frac{\partial r V_m}{\partial m} + \frac{\partial r V_n}{\partial n} + \frac{\partial V_\theta}{\partial\theta} \right] + \kappa_n V_m + \kappa_m V_n \quad (3-62)$$

The curl of any vector \vec{V} is given by

$$\vec{\nabla} \times \vec{V} = \left[\frac{\partial V_n}{\partial m} - \frac{\partial V_m}{\partial n} + \kappa_n V_n - \kappa_m V_m \right] \vec{e}_\theta + \frac{1}{r} \left[\frac{\partial r V_\theta}{\partial n} - \frac{\partial V_n}{\partial\theta} \right] \vec{e}_m + \frac{1}{r} \left[\frac{\partial V_m}{\partial\theta} - \frac{\partial r V_\theta}{\partial m} \right] \vec{e}_n \quad (3-63)$$

The Laplacian of any function ϕ is given by

$$\nabla^2\phi = \frac{1}{r^2} \frac{\partial^2\phi}{\partial\theta^2} + \frac{\partial^2\phi}{\partial m^2} + \frac{\partial^2\phi}{\partial n^2} + \left[\frac{1}{r} \frac{\partial r}{\partial m} + \kappa_n \right] \frac{\partial\phi}{\partial m} + \left[\frac{1}{r} \frac{\partial r}{\partial n} + \kappa_m \right] \frac{\partial\phi}{\partial n} \quad (3-64)$$

In evaluating the convective derivative in Eq. (3-15), the following vector identity is useful.

$$(\vec{V} \cdot \vec{\nabla})\vec{V} = \frac{1}{2} \vec{\nabla}(\vec{V} \cdot \vec{V}) - \vec{V} \times (\vec{\nabla} \times \vec{V}) \quad (3-65)$$

Eq. (3-65) is usually written as

$$(\vec{V} \cdot \vec{\nabla})\vec{V} = \frac{1}{2} \vec{\nabla}V^2 - \vec{V} \times (\vec{\nabla} \times \vec{V}) \quad (3-66)$$

where V^2 is the square of the magnitude of the vector \vec{V} as given by the dot product.

Chapter 4

EMPIRICAL PERFORMANCE MODELS FOR AXIAL-FLOW TURBINE BLADE ROWS

This chapter presents empirical models used by this writer for predicting the fluid turning and the total pressure losses in axial-flow turbine blade rows. This is the logical starting point for the discussion of this class of turbines, since all aerodynamic design and analysis procedures are governed by these basic performance characteristics. Ainley and Mathieson [41] published a design and off-design performance system for axial-flow turbines in 1951. Dunham and Came [42] published a series of improvements to the Ainley-Mathieson system in 1970. This modified system is commonly referred to as the AMDC performance system. Kacker and Okapuu [43] suggested further refinements to the AMDC system in 1981. The performance system described in this chapter is derived from these three references, but with several modifications.

The original performance systems were all developed for use in one-dimensional or mean-line performance analyses. The present performance system is intended for use in the more general hub-to-shroud or multiple-streamline performance analysis of chapter 5. A hub-to-shroud performance analysis provides the benefit of more detailed fluid dynamic data that mean-line methods must seek to estimate from the mean-line flow data. But it also requires addressing the more severe off-design operating conditions that are often encountered near the end-walls. A number of practical modifications were necessary to generalize the original methods to the intended application and to achieve a performance system that is reliable under severe off-design operating conditions. Several extensions to the original methods were found necessary to treat modern high-pressure steam turbines. The methods for including Reynolds number effects required extension to consider the effects of surface finish, which has become essential for the high-Reynolds-number applications encountered today. It was also necessary to consider cases where the flow is diffusing through the blade row. This condition can be encountered near the hub stream surface under off-design operating conditions. It can result in a total breakdown of some of the original mean-line models. Many of the original performance models are provided in graphical form. In keeping with the objective of this book to provide complete descriptions, the empirical equations developed to apply the graphical models are provided and compared with the original graphical models.

While derivatives of the AMDC performance system are probably the most widely used methods, a number of alternative methods have been published. Among the best-documented alternatives are those of Craig and Cox [44], Traupel [45] and Stewart [46]. The method of Craig and Cox is particularly significant and unique in regard to its thorough treatment of Reynolds number effects, including the effect of surface finish. In that context, it influenced the development of the present performance system by providing independent confirmation of the approach used.

NOMENCLATURE

- a = sound speed
- b = stream sheet thickness
- b_z = axial chord length
- C = absolute velocity
- C_D = drag coefficient
- C_L = lift coefficient
- C_M = disk torque coefficient
- c = chord
- c_f = skin friction coefficient
- D = diameter
- e = peak-to-valley surface roughness
- e_{rms} = rms surface roughness
- F_{AR} = aspect ratio correction factor
- H = total enthalpy
- h = static enthalpy; also, blade height or span
- I = rothalpy
- i = incidence angle
- K = various correction factors defined in section 4.4
- M = Mach number
- m = meridional coordinate
- m = mass flow rate
- N = number of blades, lashing wires or balance holes
- o = throat width
- P = pressure
- p = seal pitch
- Q = quality
- R_c = suction surface radius of curvature at the blade trailing edge
- Re = Reynolds number
- r = radius
- S_θ = flow angle sign correction factor
- s = pitch
- T = temperature
- t = seal fin thickness
- t_{\max} = maximum blade thickness
- t_2 = trailing edge blade thickness
- W = relative velocity

Y = total pressure loss coefficient
 Y_{CL} = blade clearance loss coefficient
 Y_{EX} = supersonic expansion loss coefficient
 Y_{LW} = lashing wire loss coefficient
 Y_p = profile loss coefficient
 Y_{p1} = nozzle profile loss coefficient
 Y_{p2} = impulse blade profile loss coefficient
 Y_s = secondary flow loss coefficient
 Y_{SH} = shock loss coefficient
 Y_{TE} = trailing edge loss coefficient
 Z = Ainley loading parameter
 z = axial coordinate
 α = flow angle with respect to tangent
 β = blade angle with respect to tangent
 β_g = gauging angle = $\text{arc sin}(o/s)$
 Δ = clearance gap width
 ΔH = various parasitic losses defined in section 4.3
 δ = deviation angle; also, blade tip or seal clearance
 ε = arc of admission
 θ = polar angle
 μ = viscosity
 ρ = gas density
 τ = torque or shear stress
 $\xi = (90^\circ - \beta_1)/(90^\circ - \alpha_2)$
 ω = blade row rotation speed
 ζ = rotor shielding arc

Subscripts

m = meridional component or mean value
 t = total thermodynamic condition
 1 = blade row inlet parameter
 2 = blade row exit parameter
 θ = tangential component
 $*$ = value of a parameter at sonic flow conditions

Superscript

' = a relative value in the rotating coordinate system

4.1 Blade Row Geometry

Figure 4-1 shows the basic nomenclature used to specify the geometry of a blade row in a form suitable for the AMDC performance system. These parameters are supplied at a series of radii for use in the hub-to-shroud performance analysis described in chapter 5. Hence, the number of blades, N , is specified and used to compute the blade pitch, s , at any radius by

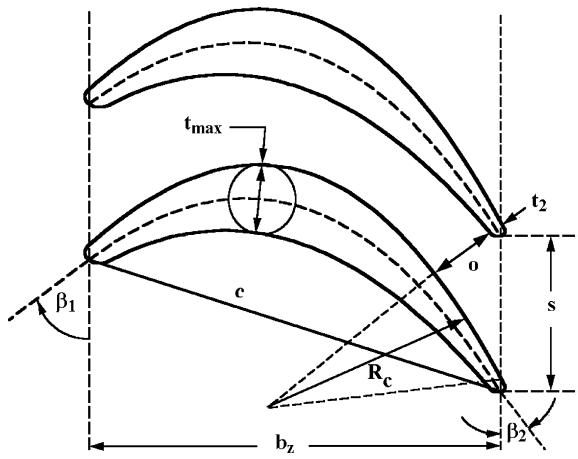


FIGURE 4-1. Blade Row Geometry

$$s = 2\pi r / N \quad (4-1)$$

The throat opening, o , and the pitch define the well-known gauging angle, β_g .

$$\sin \beta_g = o / s \quad (4-2)$$

Hence, either o or β_g can be supplied. The AMDC system requires both the blade maximum thickness, t_{\max} , and trailing edge thickness, t_2 . Also required are the blade chord, c , axial chord, b_z , and the parameter R_c , which is the average suction surface radius of curvature between the throat and the trailing edge. Although not shown, the root-mean-square surface finish, e_{rms} , is also required. The actual (peak-to-valley) surface roughness, e , is estimated by assuming a sin-wave form.

$$e = e_{rms} / 0.3535 \quad (4-3)$$

Similarly the blade must be specified as either shrouded or unshrouded and the corresponding blade clearance or seal geometry must be supplied. Following traditional steam turbine practice, the inlet and discharge blade angles, β_1 and β_2 , are defined with respect to the tangential direction.

When calculating the blade row performance with the models presented in this chapter, it is necessary to use velocity components relative to the blade, which may be rotating or stationary. This requires some care in converting between the flow field velocity triangles and the flow angles, α_1 and α_2 , to be consistent with the blade angle convention. As previously noted in chapter 3, the relative tangential velocity, W_θ , is related to the absolute tangential velocity, C_θ , by

$$W_\theta = C_\theta - \omega r \quad (4-4)$$

where C_θ and W_θ are positive in the direction of the turbine's rotation and ω is the rotation speed of the blade row under consideration. To convert between the flow field and the blade angle conventions, define $S_\theta = 1$ for stationary blades and $S_\theta = -1$ for rotor blades. The inlet flow angle consistent with the blade angle convention is

$$\cot \alpha'_1 = -S_\theta W_\theta / C_m \quad (4-5)$$

The blade row performance system provides the discharge flow angle in the blade angle convention. To convert back to the flow field convention, $W_{\theta 2}$ is given by

$$W_{\theta 2} = S_\theta C_{m2} \cot \alpha'_2 \quad (4-6)$$

4.2 Fluid Deviation Angle

The primary function of any turbine blade row is to impart fluid turning to change the angular momentum of the fluid passing through it. Nozzle rows accelerate the fluid to increase the angular momentum. Rotor rows then reduce the fluid angular momentum to extract work from the fluid. Hence, the fluid discharge angle prediction is an essential step in performance analysis. A useful reference value is provided for the case where the discharge relative Mach number, M'_2 , is one. In this case, the blade row must be choked, so the throat Mach number is also one. It is reasonable to assume that losses between the throat and the discharge have negligible effect on the gas density. Designating the value of a parameter at sonic flow conditions by a subscript, $*$, conservation of mass requires

$$\rho_* W_* o = \rho_* C_{m2} s \quad (4-7)$$

$$\sin \alpha'_2 = C_{m2} / W_* = o / s \quad (4-8)$$

Combining with Eq. (4-2) this states that $\alpha'_2 = \beta_g$ when $M'_2 = 1$. Hence, the gauging angle is a fundamental reference discharge angle. It is common practice to reference the discharge flow angle to the gauging angle by defining the deviation angle, δ , as

$$\delta = \alpha'_2 - \beta_g \quad (4-9)$$

Hence, $\delta = 0$ when $M'_2 = 1$.

Subsonic deviation angle correlations typically indicate essentially constant values for $M'_2 < 0.5$, e.g., Ainley and Mathieson [41] and Lee [47]. These correlations are in general agreement with regard to trends. Low subsonic deviation angle increases with β_g , starting with $\delta = 0^\circ$ at $\beta_g \approx 10$ to 20° and reaching values of $\delta \approx 5$ to 6° at $\beta_g \approx 50^\circ$. Variation of deviation angle for M'_2

between 0.5 and 1.0 seems to be more or less a matter of convenience, ranging from simple linear variation to more complex variations with an inflection point. This writer developed the correlation illustrated in figure 4-2, following similar trends and guided by comparison of stage performance predictions with experimental data. In this case, the variation of deviation angle with M'_2 for M'_2 between 0.5 and 1.0 is definitely a matter of convenience. Convergence of the numerical analysis is substantially improved when the slope of the deviation angle versus Mach number curves approaches zero at $M'_2 = 1$. Defining the deviation angle at $M'_2 = 0$ as

$$\delta_0 = \arcsin[(o/s)[1 + (1 - o/s)(\beta_g / 90)^2]] - \beta_g \quad (4-10)$$

The subsonic deviation is given by

$$\delta = \delta_0; \quad M'_2 \leq 0.5 \quad (4-11)$$

$$\delta = \delta_0[1 - 10X^3 + 15X^4 - 6X^5]; \quad M'_2 > 0.5 \quad (4-12)$$

$$X = 2M'_2 - 1 \quad (4-13)$$

These equations were used to generate the curves shown in figure 4-2.

When $M'_2 > 1$, the local stream sheet in the hub-to-shroud analysis is choked. Hence, supersonic deviation angles are calculated directly from conservation of mass based on sonic flow conditions at the throat.

$$\delta = \arcsin[(o/s)\rho_* W_*/(\rho_2 W_2)] - \beta_g \quad (4-14)$$

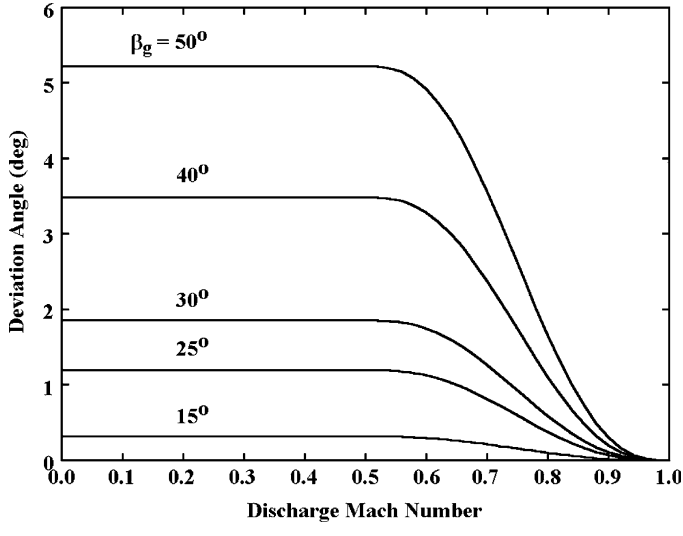


FIGURE 4-2. Subsonic Deviation Correlation

Some care is required in specifying the sonic flow conditions used in Eq. (4-14). The overall numerical analysis for the flow field at the blade row exit can experience severe convergence problems unless the subsonic and supersonic deviation angle models yield inconsistent results when $M'_2 \approx 1$. In this case, the analysis may alternate between these two models on successive iterations. Hence, it is important that Eq. (4-14) yield results consistent with $\delta = 0$ when $M'_2 = 1$. This can be accomplished if the sonic flow conditions are calculated based on the discharge total pressure and total enthalpy, but with any supersonic expansion loss removed. As will be seen subsequently in this chapter, the supersonic expansion loss is specifically associated with $M'_2 > 1$. That loss occurs downstream of the throat, so it is not relevant to the local stream sheet choke limit. When this process is followed the subsonic and supersonic deviation angle models yield consistent results when the discharge Mach number approaches unity from either direction.

It can be noted that the ratio o/s is a key parameter in the deviation angle prediction. The specified blade geometry data provides a value, $(o/s)_{id}$, for an ideal, two-dimensional flow case. This requires some adjustment to be appropriate for the real flow case being considered. The adjusted value of this ratio that is used to predict the deviation angle is given by

$$o/s = (o/s)_{id} F_{AR} F_{TE} \quad (4-15)$$

F_{AR} is a correction for any variation in stream sheet area across the blade row. It is assumed that the throat lies at about 80% of the blade passage meridional length. Computing the stream sheet area ratio from conservation of mass yields.

$$F_{AR} = 0.8 + 0.2(\rho_2 C_{m2})/(\rho_1 C_{m1}) \quad (4-16)$$

F_{TE} is a rather minor correction to account for the effect of the trailing edge loss. This loss occurs downstream of the trailing edge, so it is not relevant to a mass balance between the throat and the trailing edge. Since this loss occurs at all values of M'_2 , it can not be handled in the same fashion as the supersonic expansion loss without compromising the desired consistency between the subsonic and supersonic deviation angle models. If Y_{TE} is the trailing edge loss coefficient, F_{TE} is estimated by

$$F_{TE} = 1 + Y_{TE}(P'_{t2} - P_2)/P'_{t2} \quad (4-17)$$

4.3 Overview of the Loss System

The loss system for predicting the performance of a turbine blade row must consider the total pressure loss, parasitic loss and leakage mass flow. The total pressure loss accounts for the direct loss in total pressure due to

irreversible processes as the flow passes through the blade row. The parasitic loss accounts for wasted work due to disk friction, shear forces and partial admission. It also accounts for the reduced work due to moisture losses and leakage flow that bypasses the blade row. These are reflected in an increase in total enthalpy of the discharge flow relative to the value produced when the flow passes through the blade row. This results in a reduction in efficiency but does not affect the total pressure. Although leakage flows are not really losses, they affect the power produced by the turbine and the discharge swirl relative to the value produced when the flow passes through the blade row.

The total pressure loss coefficient, Y , is defined in terms of the discharge velocity pressure in the form

$$Y = (P'_{t1} - P'_{t2}) / (P'_{t2} - P_2) \quad (4-18)$$

The total pressure loss system used can be represented as

$$Y = Y_p + Y_s + Y_{CL} + Y_{TE} + Y_{EX} + Y_{SH} + Y_{LW} \quad (4-19)$$

The component loss coefficients are

Y_p = the profile loss coefficient

Y_s = the secondary flow loss coefficient

Y_{CL} = the blade clearance loss coefficient

Y_{TE} = the trailing edge loss coefficient

Y_{EX} = the supersonic expansion loss coefficient

Y_{SH} = the shock loss coefficient

Y_{LW} = the lashing wire loss coefficient (rotors)

The parasitic loss is defined in terms of a discharge total enthalpy increase, ΔH_{par}

$$\Delta H_{par} = \Delta H_{adm} + \Delta H_{DF} + \Delta H_{seal} + \Delta H_{gap} + \Delta H_Q \quad (4-20)$$

The component parasitic losses are

ΔH_{adm} = partial admission work (rotors)

ΔH_{DF} = disk friction work (diaphragm-disk rotors)

ΔH_{lea} = leakage bypass loss (shrouded rotors and rotor balance holes)

ΔH_{gap} = clearance gap windage loss (shrouded blades and nozzle of diaphragm-disk rotors)

ΔH_Q = moisture work loss (rotors)

The remainder of this chapter provides detailed descriptions of the various component loss models.

4.4 Profile Loss Coefficient

The profile loss coefficient is a modified form of the Ainley-Mathieson [41] model. It can be represented as

$$Y_p = K_{\text{mod}} K_{\text{inc}} K_M K_p K_{\text{RE}} [(Y_{p1} + \xi^2 (Y_{p2} - Y_{p1})) (5t_{\max}/c)^\xi - \Delta Y_{TE}] \quad (4-21)$$

K_{mod} is an experience factor suggested by Kacker and Okapuu [43] to adjust the Ainley-Mathieson model to account for the superior performance of modern designs due to improved design technology. They suggest a value of 1.0 for older designs and 0.67 for modern, highly optimized designs. The Ainley-Mathieson model includes the trailing edge loss specifically assuming that $t_2 = 0.02s$. Since the trailing edge loss is treated separately in the present model, ΔY_{TE} subtracts the trailing edge loss coefficient computed by the present trailing edge loss model for $t_2 = 0.02s$. The term involving t_{\max} corrects the loss from the Ainley-Mathieson source data, which had $t_{\max}/c = 0.2$. The other terms in Eq. (4-21) are

K_{inc} = correction for off-design incidence effects

K_M = correction for Mach number effects

K_p = correction for compressibility effects

K_{RE} = correction for Reynolds number effects

Y_{p1} = profile loss coefficients for nozzle blades ($\beta_1 = 90^\circ$)

Y_{p2} = profile loss coefficients for impulse blades ($\alpha'_2 = \beta_1$)

$\xi = (90^\circ - \beta_1)/(90^\circ - \alpha'_2)$

Figure 4-3 shows the nozzle blade profile loss coefficient, Y_{p1} , as a function of the pitch-to-chord ratio, including the Ainley-Mathieson graphical correlation and an empirical model that accurately approximates that correlation in analytical form. Note that the empirical model extrapolates beyond the limits of the graphical correlation so that it is usable over a wider range of applications. The location of the minimums of the curves is approximated by

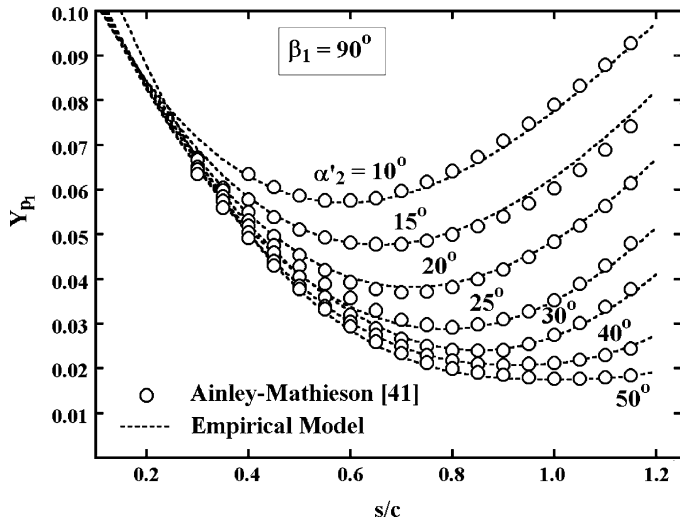
$$(s/c)_{\min} = 0.46 + \alpha'_2 / 77; \quad \alpha'_2 \leq 30^\circ \quad (4-22)$$

$$(s/c)_{\min} = 0.614 + \alpha'_2 / 130; \quad \alpha'_2 > 30^\circ \quad (4-23)$$

The loss coefficient is approximated by

$$Y_{p1} = A + BX^2 + CX^3; \quad \alpha'_2 \leq 30^\circ \quad (4-24)$$

$$Y_{p1} = A + B|X|^n; \quad \alpha'_2 > 30^\circ \quad (4-25)$$

**FIGURE 4-3. Nozzle Blade Profile Loss Model**

The parameters used in this empirical model are defined as follows

$$X = s/c - (s/c)_{\min} \quad (4-26)$$

$$n = 1 + \alpha'_2 / 30 \quad (4-27)$$

$$A = 0.025 + (27 - \alpha'_2) / 530; \quad \alpha'_2 \leq 27^\circ \quad (4-28)$$

$$A = 0.025 + (27 - \alpha'_2) / 3085; \quad \alpha'_2 > 27^\circ \quad (4-29)$$

$$B = 0.1583 - \alpha'_2 / 1640; \quad \alpha'_2 \leq 30^\circ \quad (4-30)$$

$$C = 0.08[(\alpha'_2 / 30)^2 - 1] \quad (4-31)$$

Figure 4-4 shows the impulse blade profile loss coefficient, Y_{p2} , as a function of the pitch-to-chord ratio, including the Ainley-Mathieson graphical correlation and an empirical model that accurately approximates that correlation in analytical form. Again, the empirical model extrapolates beyond the limits of the graphical correlation so that it is usable over a wider range of applications. The location of the minimums of the curves is approximated by

$$(s/c)_{\min} = 0.224 + 1.575(\alpha'_2 / 90) - (\alpha'_2 / 90)^2 \quad (4-32)$$

The loss coefficient is approximated by

$$Y_{p2} = A + BX^2 - CX^3 \quad (4-33)$$

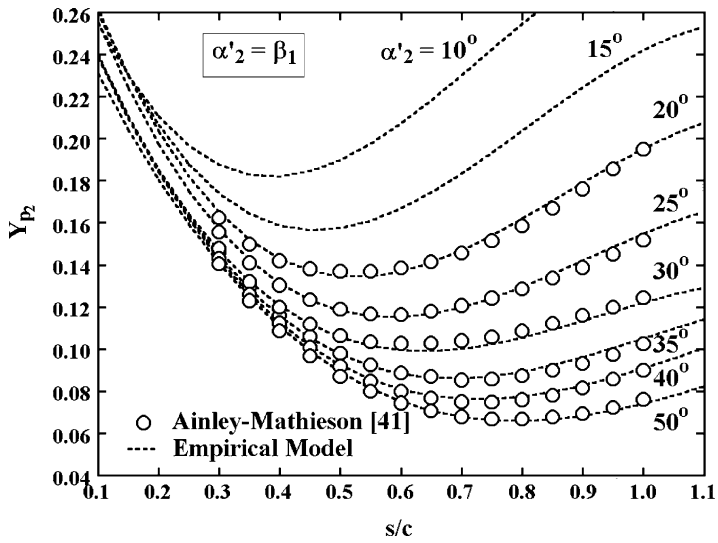


FIGURE 4-4. Impulse Blade Profile Loss Model

The parameters used in this empirical model are

$$X = s/c - (s/c)_{\min} \quad (4-34)$$

$$A = 0.242 - \alpha'_2 / 151 + (\alpha'_2 / 127)^2 \quad (4-35)$$

$$B = 0.3 + (30 - \alpha'_2) / 50; \quad \alpha'_2 \leq 30^\circ \quad (4-36)$$

$$B = 0.3 + (30 - \alpha'_2) / 275; \quad \alpha'_2 > 30^\circ \quad (4-37)$$

$$C = 0.88 - \alpha'_2 / 42.4 + (\alpha'_2 / 72.8)^2 \quad (4-38)$$

Figure 4-5 shows the off-design incidence correction factor, K_{inc} , as a function of the ratio of the incidence angle, i , to the stalling incidence angle i_s , including the Ainley-Mathieson graphical data and an empirical model that accurately approximates that data in analytical form. Note that the empirical model extrapolates beyond the limits of the graphical correlation so that it is usable over a wider range of applications. The empirical equations are

$$i = \beta_1 - \alpha'_1 \quad (4-39)$$

$$K_{inc} = -1.39214 - 1.90738(i/i_s); \quad i/i_s < -3 \quad (4-40)$$

$$K_{inc} = 1 + 0.52 |i/i_s|^{1.7}; \quad -3^\circ \leq i/i_s < 0^\circ \quad (4-41)$$

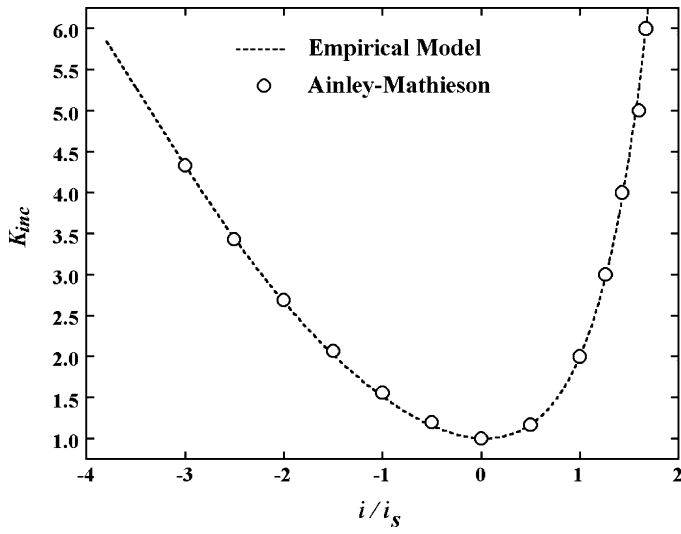


FIGURE 4-5. Off-Design Incidence Correction Factor

$$K_{inc} = 1 + (i/i_s)^{(2.3+0.5i/i_s)}, \quad 0^\circ \leq i/i_s < 1.7^\circ \quad (4-42)$$

$$K_{inc} = 6.23 - 9.8577(i/i_s - 1.7); \quad i/i_s \geq 1.7^\circ \quad (4-43)$$

An upper limit of $K_{inc} \leq 20$ is required. The stalling incidence angle is a function of α'_2 , ξ and s/c , where

$$\xi = (90 - \beta_1)/(90 - \alpha'_2) \quad (4-44)$$

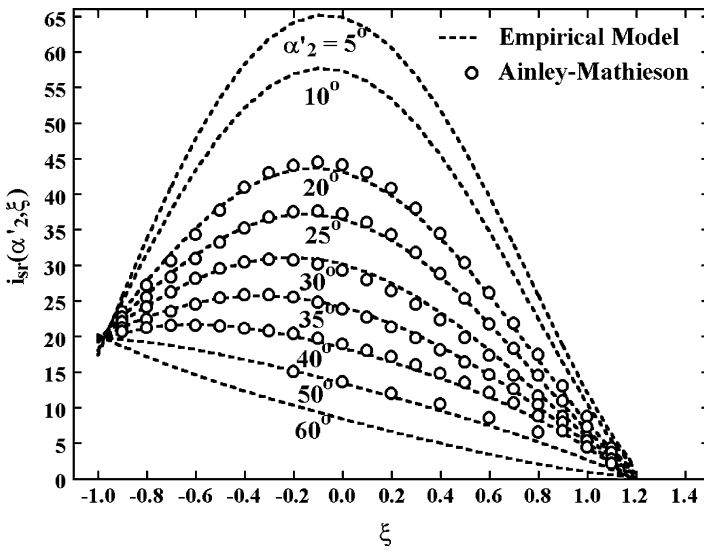
It is computed from a reference value, $i_{sr}(\alpha'_2, \xi)$, corresponding to $s/c = 0.75$ and a correction term, $\Delta i_s(\alpha'_2, s/c)$, to adjust it to other values of s/c , i.e.,

$$i_s = i_{sr}(\alpha'_2, \xi) + \Delta i_s(\alpha'_2, s/c) \quad (4-45)$$

Figure 4-6 shows the stalling incidence for $s/c = 0.75$ as a function of the ratio of α'_2 and ξ including the Ainley-Mathieson graphical data and an empirical model that accurately approximates that data in analytical form. Note that the empirical model extrapolates beyond the limits of the graphical correlation so that it is usable over a wider range of applications. The empirical equations for $\alpha'_2 \leq 40^\circ$ are

$$i_{sr}(\alpha'_2, \xi) = i_{s0} + A - B\xi^2 + C\xi^3 + D\xi^4; \quad \alpha'_2 \leq 40^\circ \quad (4-46)$$

$$i_{s0} = 20 - (\xi + 1)/0.11 \quad (4-47)$$

FIGURE 4-6. Stalling Incidence for $s/c = 0.75$

$$A = 61.8 - (1.6 - \alpha'_2 / 165) \alpha'_2 \quad (4-48)$$

$$B = 71.9 - 1.69 \alpha'_2 \quad (4-49)$$

$$C = 7.8 - (0.28 - \alpha'_2 / 320) \alpha'_2 \quad (4-50)$$

$$D = 14.2 - (0.16 + \alpha'_2 / 160) \alpha'_2 \quad (4-51)$$

The empirical model includes an extrapolation of the Ainley-Mathieson graphical data for $\alpha'_2 > 40^\circ$, which can be encountered on occasion. This case is approximated by

$$i_{sr}(\alpha'_2, \xi) = i_{s0} + |i_{sr}(40, \xi) - i_{s0}| |55 - \alpha'_2| / 15; \quad \alpha'_2 > 40^\circ \quad (4-52)$$

Figure 4-7 shows the correction term, $\Delta i_s(\alpha'_2, s/c)$, including the Ainley-Mathieson graphical data and an empirical model that accurately approximates that data in analytical form. The empirical equations are

$$X = s/c - 0.75 \quad (4-53)$$

$$\Delta i_s = -38X - 53.5X^2 - 29X^3; \quad s/c \leq 0.8 \quad (4-54)$$

$$\Delta i_s = 2.0374 - (s/c - 0.8)[69.58 - (\alpha'_2 / 14.48)^{3.1}]; \quad s/c > 0.8 \quad (4-55)$$

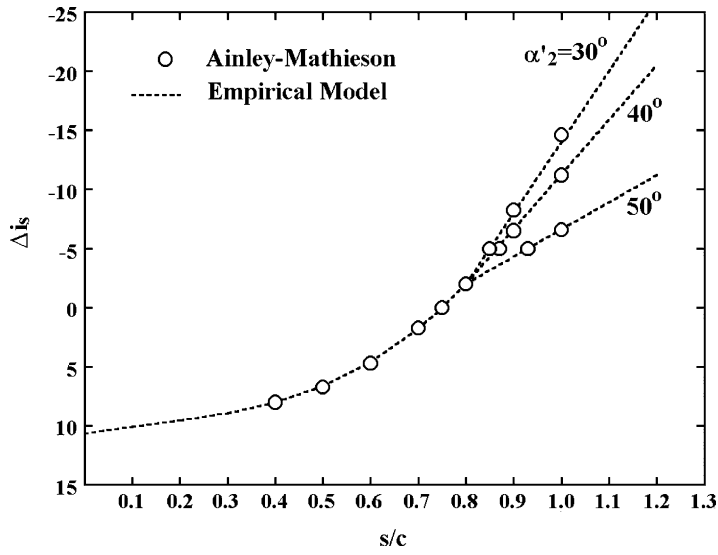
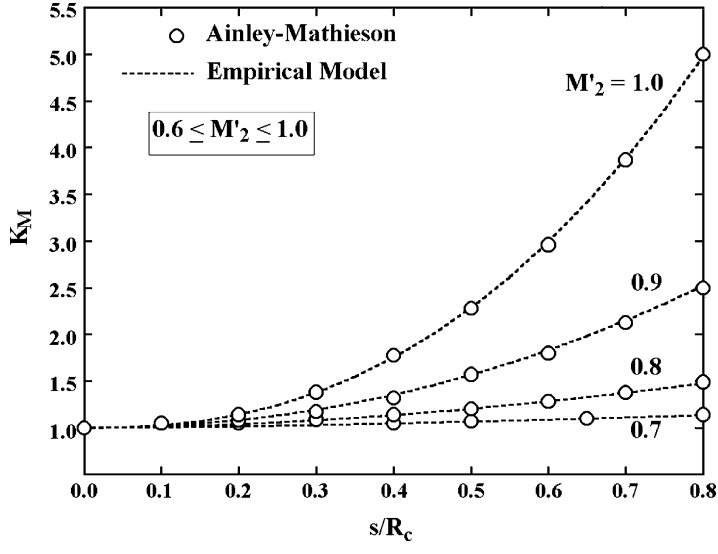
**FIGURE 4-7. Stalling Incidence Correction Factor**

Figure 4-8 shows the Mach number correction to the profile loss coefficient, K_M , as a function of the discharge relative Mach number, M'_2 , and the ratio of the pitch to the suction surface radius of curvature, s/R_c . Both the Ainley-Mathieson graphical data and an empirical model that accurately approximates that data in analytical form are included. There is no correction

**FIGURE 4-8. The Mach Number Correction**

when $M'_2 \leq 0.6$, i.e., $K_M = 1$. Also, the loss associated with $M'_2 > 1$ is handled separately in the supersonic expansion loss. The empirical equation used is

$$K_M = 1 + [1.65(M'_2 - 0.6) + 240(M'_2 - 0.06)^2](s/R_c)^{(3M'_2 - 0.6)} \quad (4-56)$$

The Mach number range is limited to $0.6 \leq M'_2 \leq 1$ when applying Eq. (4-56).

Kacker and Okapuu [43] suggest including the compressibility correction term, K_p , in Eq. (4-21) to account for the beneficial effects of Mach number levels in excess of those present in low speed cascade tests. The effect of compressibility in accelerating flow is to thin the boundary layers and suppress flow separations. Since the Ainley-Mathieson profile loss model is based on low speed cascade tests, it can be expected to be pessimistic when applied to typical turbine stage applications. Kacker and Okapuu suggest the following form.

$$K_1 = 1 - 0.625[M'_2 - 0.2 + |M'_2 - 0.2|] \quad (4-57)$$

$$K_p = 1 - (1 - K_1)(M'_1/M'_2)^2 \quad (4-58)$$

Note that $K_p = 1$ when $M'_2 \leq 0.2$. For normal turbine operating conditions, this model works fairly well. But under unusual, yet feasible, conditions, this can result in profile loss coefficients essentially zero, or even negative. Kacker and Okapuu were less likely to experience such conditions in their mean-line analysis than is the case for the hub-to-shroud analysis of chapter 5. Under off-design operation, and near the end-wall contours, it is quite possible for the passage to be diffusing rather than accelerating, which can yield particularly absurd results. Hence, the Kacker and Okapuu model has been revised as follows:

$$\tilde{M}'_1 = [M'_1 + 0.566 - |0.566 - M'_1|]/2 \quad (4-59)$$

$$\tilde{M}'_2 = [M'_2 + 1 - |M'_2 - 1|]/2 \quad (4-60)$$

$$X = 2\tilde{M}'_1/[\tilde{M}'_1 + \tilde{M}'_2 + |\tilde{M}'_2 - \tilde{M}'_1|] \quad (4-61)$$

$$K_1 = 1 - 0.625[\tilde{M}'_2 - 0.2 + |\tilde{M}'_2 - 0.2|] \quad (4-62)$$

$$K_p = 1 - (1 - K_1)X^2 \quad (4-63)$$

Basically, this procedure limits $M'_2 \leq 1$, $M'_1 \leq 0.566$ and $X \leq 1$. As a result, K_p is limited to values greater than about 0.5. For most typical turbine operating conditions, the revised model will yield results quite similar to that of Kacker and Okapuu. But it avoids the potential for absurd results in severe off-design operating conditions.

The correction term, K_{RE} , in Eq. (4-21) adjusts the profile loss coefficient for Reynolds numbers different from cascade tests upon which the model is based. Reynolds number correction schemes in axial-flow turbines are generally based on boundary layer skin friction models that relate to the total drag force on a flat plate. These models are provided in most books on boundary layer or viscous flow theory, e.g., Pai [48, 49]. The skin friction coefficients are functions of the Reynolds number, Re_L . If L is the length of the plate and μ is the viscosity,

$$Re_L = \rho CL / \mu \quad (4-64)$$

The skin friction coefficient, c_f , for laminar flow is given by

$$c_f = 1.328 / \sqrt{Re_L} \quad (4-65)$$

For turbulent flow, the best available model is

$$c_f = 0.455 / [\log_{10} Re_L]^{2.58} \quad (4-66)$$

Eq. (4-66) assumes that the flow is turbulent over the entire length of the plate. In practice, a portion of the flow will be laminar until the local Reynolds number exceeds the transition value, Re_{tr} . Typically, $Re_{tr} = 5 \times 10^5$ is used, but that is really an approximate value. Boundary layer transition depends on many factors, such as surface roughness, free-stream turbulence, pressure gradient, etc. When Re_L is greater than Re_{tr} , the effective overall skin friction coefficient must be computed as a weighted average of the laminar and turbulent contributions. The skin friction coefficient attributed to the laminar portion is given by

$$c_{flr} = 1.328 / \sqrt{Re_{tr}} \quad (4-67)$$

The turbulent skin friction coefficient, c_{ft} , is given by (Eq. 4-66). For this simple flat-plate case, the ratio Re_{tr}/Re_L defines the fractional length of the laminar portion. Hence, the effective skin friction coefficient is given by

$$c_f = c_{flr} + [c_{ft} - c_{flr}] [1 - Re_{tr}/Re_L] \quad (4-68)$$

Figure 4-9 shows the overall skin friction coefficients obtained from Eqs. (4-65), (4-66) and (4-68). The skin friction can also be influenced by surface roughness. If e is the true (peak-to-valley) roughness height, a roughness Reynolds number, Re_e , can be defined as

$$Re_e = \rho Ce / \mu \quad (4-69)$$

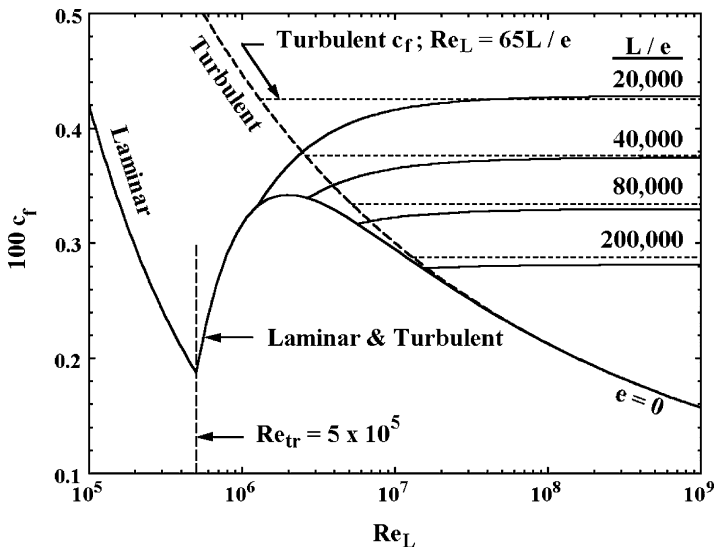


FIGURE 4-9. Boundary Layer Skin Friction Coefficient

The skin friction coefficient for a fully rough turbulent boundary layer is also well known.

$$c_{fe} = [1.89 + 1.62 \log_{10}(L/e)]^{-2.5} \quad (4-70)$$

Since, roughness has no effect on c_f in the laminar portion of the boundary layer, this value must be corrected to account for the laminar portion of the boundary layer also. Hence,

$$c_f = c_{fir} + [c_{fe} - c_{fir}] [1 - Re_{tr}/Re_L] \quad (4-71)$$

Then the effective value of the turbulent skin friction coefficient is the larger of the two values given by Eqs. (4-68) and (4-71). Skin friction coefficients for several roughness levels are shown in figure 4-9. Aungier [2] notes that the fully rough skin friction coefficient can also be evaluated from Eq. (4-66) using a value of Re_L that yields a critical value of Re_e in the range of 60 to 100. Figure 4-9 shows the result of this approach when $Re_e = 65$ is used.

These models are adapted to the turbine blade row application. Reynolds number corrections are normally based on the blade chord Reynolds number, Re_c , evaluated at the discharge flow conditions.

$$Re_c = \rho_2 W_2 c / \mu_2 \quad (4-72)$$

It is generally assumed that cascade empirical loss models apply to a Reynolds number of about 200,000. This lies in transition region where the skin friction models are too approximate to provide a good basis for a Reynolds number correction. Similar to Kacker and Okapuu [43], $K_{RE} = 1$ is assumed in the transition region. The present method uses a transition region defined by $1 \times 10^5 < Re_c < 5 \times 10^5$. When $Re_c < 1 \times 10^5$, K_{RE} is based on the laminar skin friction model, i.e.,

$$K_{RE} = \sqrt{(1 \times 10^5) / Re_c} \quad (4-73)$$

Similarly, when $Re_c > 5 \times 10^5$, K_{RE} is based on the turbulent skin friction model, i.e.,

$$K_{RE} = [\log_{10}(5 \times 10^5) / \log_{10}(Re_c)]^{2.58} \quad (4-74)$$

This model is extended to include surface roughness effects following Aungier [1, 2]. Pai [49] notes that roughness effects become significant when $Re_e \geq 100$, where

$$Re_e = \rho_2 W_2 e / \mu_2$$

Now define a critical blade chord Reynolds number, Re_r , above which roughness effects become significant by

$$Re_r = 100c/e \quad (4-75)$$

If Re_r is used in Eq. (4-74), the resulting value of K_{RE} is used when $Re_c > Re_r$. But surface roughness has no effect for laminar flow, so a correction similar to Eq. (4-71) is needed when $Re_r < Re_{tr}$, i.e.,

$$K_{RE} = 1 + \{[\log_{10}(5 \times 10^5) / \log_{10}(Re_r)]^{2.58} - 1\}[1 - (5 \times 10^5) / Re_c] \quad (4-76)$$

Figure 4-10 shows basic results from this Reynolds number correction. This model is similar to the method suggested by Kacker and Okapuu [43]. An important difference is that Kacker and Okapuu do not consider surface roughness effects. The AMDC [42] Reynolds number correction is proportional to $Re^{-0.2}$ and referenced to $Re = 2 \times 10^5$. This is based on Ainley and Mathieson [41], although that reference suggests a more severe correction for $Re < 1 \times 10^5$. The AMDC model also ignores the effects of surface roughness. One of the few published Reynolds number corrections to consider surface roughness effects is the method of Craig and Cox [44]. They note that turbine blades with standard surface finish have values of c/e in the range of 10,000

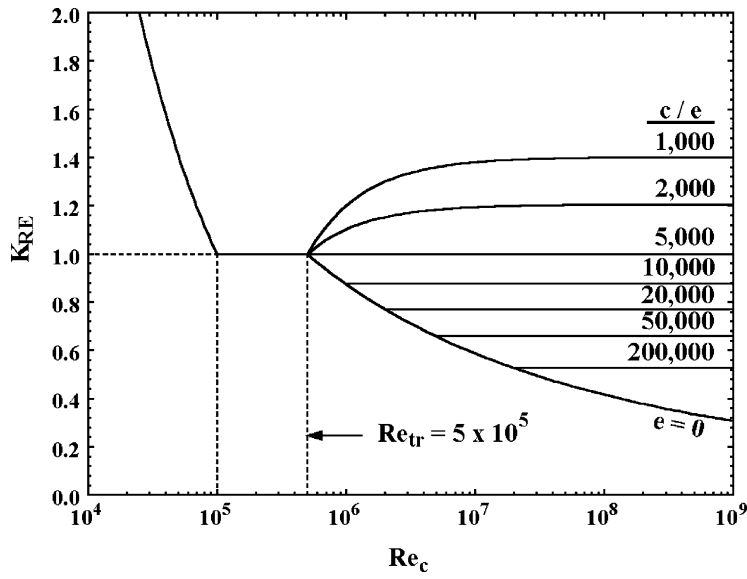


FIGURE 4-10. The Reynolds Number Correction

to 20,000, which is consistent with this writer's experience. As seen in figure 4-10, the present method will show much less Reynolds number influence for very high Reynolds numbers than methods that ignore surface roughness. It is encouraging to note that figure 4-10 shows values of K_{RE} comparable to the Craig and Cox method when surface roughness effects are significant. Indeed, any correction for Reynolds number that does not account for surface roughness should be used with extreme caution. Some rather serious high-pressure steam turbine performance deficiencies have been traced to that oversight.

4.5 Secondary Flow Loss Coefficient

The secondary flow loss coefficient is quite similar to the AMDC model reported by Dunham and Came [42] as revised by Kacker and Okapuu [43]. The lift coefficient is defined as

$$C_L = 2(\cot \alpha'_1 + \cot \alpha'_2)s/c \quad (4-77)$$

Eq. (4-77) may appear incorrect to some readers unless it is recalled that the flow angles conform to the blade angle convention rather than the flow field convention as discussed at the start of this chapter. The Ainley loading parameter, Z , is defined as

$$Z = (C_L c / s)^2 \sin^2 \alpha'_2 / \sin^3 \alpha'_m \quad (4-78)$$

The mean flow angle, α'_m , is given by

$$\alpha'_m = 90^\circ - \arctan[(\cot(\alpha'_1) - \cot(\alpha'_2)) / 2] \quad (4-79)$$

A preliminary estimate of the secondary flow loss coefficient is calculated as

$$\tilde{Y}_s = 0.0334 F_{AR} Z \sin \alpha'_2 / \sin \beta_1 \quad (4-80)$$

F_{AR} is an aspect ratio correction, based on the blade height or span, h , and the chord.

$$\begin{aligned} F_{AR} &= c/h; \quad h/c \geq 2 \\ F_{AR} &= 0.5(2c/h)^{0.7}; \quad h/c < 2 \end{aligned} \quad (4-81)$$

Figure 4-11 shows a comparison of F_{AR} for $h/c < 2$, with the original Dunham and Came [42] form and a modified form suggested by Kacker and Okapuu [43]. Kacker and Okapuu developed their modification to improve predictions at low aspect ratios. Some predictions based on their form with aspect ratios even lower than those they considered were again found to be slightly pessimistic. Hence the modified form in Eq. (4-81) is currently used.

Use of this mean-line model in a hub-to shroud analysis can result in excessive values of this loss coefficient at extreme off-design conditions near the end-wall contours. Although this rarely occurs, it was found necessary to impose an asymptotic upper limit on the preliminary estimate of about 0.365

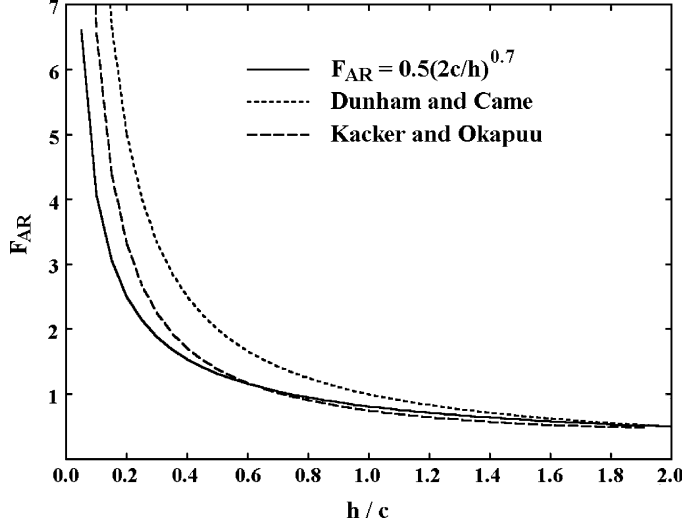


FIGURE 4-11. Aspect Ratio Effect on Secondary Loss

to permit an analysis under those extreme conditions. Hence, the secondary flow loss coefficient is given by

$$Y_s = K_{RE} K_s \sqrt{\tilde{Y}_s^2 / (1 + 7.5 \tilde{Y}_s^2)} \quad (4-82)$$

K_{RE} is the same Reynolds number correction as used for Y_p and K_s is a modified form of the compressibility correction suggested by Kacker and Okapuu [43].

$$K_s = 1 - (1 - K_p)(b_z/h)^2 / [1 + (b_m/h)^2] \quad (4-83)$$

The parameter b_z is the axial projection of the chord length. K_s differs from the original formulation in two respects. First, K_p is a modification as discussed previously in this chapter. Second, the term in the denominator of Eq. (4-83) is not present in the original model. It was added to prevent excessive values of K_s for extreme cases where b_z/h is very large. For the vast majority of cases, this model will yield values of K_s comparable to the original Kacker and Okapuu model.

4.6 Trailing-Edge Loss Coefficient

The trailing-edge loss coefficient is computed as a classical expansion loss due to an abrupt area enlargement, e.g., see Benedict et al. [50]. If W_2 is the velocity after mixing and the flow angle is approximately equal to the gauging angle, the effective passage width after mixing is $(s \sin \beta_g)$. The effective passage width before mixing is reduced by the trailing edge thickness to yield $(s \sin \beta_g - t_2)$. If density is approximately constant, the total pressure expansion loss can be approximated by

$$\Delta P_t = \frac{1}{2} \rho W_2^2 [s \sin \beta_g / (s \sin \beta_g - t_2) - 1]^2 \quad (4-84)$$

Hence, the trailing-edge loss coefficient is

$$Y_{TE} = 2\Delta P_t / (\rho W_2^2) = [t_2 / (s \sin \beta_g - t_2)]^2 \quad (4-85)$$

4.7 Shock Loss Coefficient

Kacker and Okapuu [43] introduced the concept of a shock loss associated with shock waves that form near the hub stream surface. Their model seeks to estimate this hub stream surface behavior from mean-line flow data. Since the present loss system is intended for use in a hub-to-shroud

performance analysis, their model required considerable modification for this application. Overall flow diffusion across the blade row is a significant loss source that has been ignored by all published loss systems. That is not too surprising since overall diffusion is rarely encountered in a performance analysis conducted along the mean stream surface. But it does occur in a more complete hub-to-shroud performance analysis, particularly near the hub stream surface at far off-design operating conditions. Both of these loss sources are modeled in the shock loss coefficient in the present loss system. The shock loss contribution is based on the parameter X_1 , defined by

$$\begin{aligned} X_1 &= 0; \quad M'_1 \leq 0.4 \\ X_1 &= M'_1 - 0.4; \quad M'_1 > 0.4 \end{aligned} \quad (4-86)$$

The diffusion loss contribution is based on the parameter X_2 , defined by

$$\begin{aligned} X_2 &= 0; \quad M'_1 \leq M'_2 \\ X_2 &= M'_1 / M'_2 - 1; \quad M'_1 > M'_2 \end{aligned} \quad (4-87)$$

A preliminary estimate of the shock loss coefficient is computed by

$$\tilde{Y}_{SH} = 0.8X_1^2 + X_2^2 \quad (4-88)$$

The actual shock loss coefficient is computed by imposing an asymptotic upper limit of 1.0, i.e.,

$$Y_{SH} = \sqrt{\tilde{Y}_{SH}^2 / (1 + \tilde{Y}_{SH}^2)} \quad (4-89)$$

4.8 Supersonic Expansion Loss Coefficient

When the flow at the discharge of a blade row is over-expanded to supersonic discharge Mach numbers, shock waves form to produce additional losses, commonly referred to as supersonic expansion losses or supersonic drag losses. Dunham and Came [42] suggested a model for this loss contribution, imposed as a multiplier on the AMDC profile loss coefficient. They note that their model is a rather arbitrary correction factor based on very limited information. Indeed, this writer has had little success using that approach. Kacker and Okapuu [43] also comment on the weakness of this AMDC model, but do not offer an alternative. The present loss system imposes a supersonic expansion loss that is independent of the profile loss. Indeed, there appears to be little reason to expect that the supersonic expansion loss should depend on the profile loss. When $M'_2 > 1$, the supersonic expansion loss is calculated as

$$Y_{EX} = [(M'_2 - 1) / M'_2]^2 \quad (4-90)$$

Of course, $Y_{EX} = 0$ when $M'_2 \leq 1$.

4.9 Blade Clearance Loss Coefficient

The blade clearance loss coefficient for unshrouded blade rows is computed directly from the method of Dunham and Came [42]. If δ is the clearance between the blade tip and the end-wall and Z is the Ainley loading parameter of Eq. (4-78), the clearance loss coefficient is given by

$$Y_{CL} = 0.47Z(c/h)(\delta/c)^{0.78} \quad (4-91)$$

Dunham and Came estimate leakage losses in shrouded blade rows using a modified form of Eq. (4-91). The present loss system uses a more fundamental seal leakage calculation that is discussed in section 4.11. The overall total-pressure loss across the blade row due to the shroud seal leakage is simply the seal pressure drop times the ratio of leakage mass flow to the total mass flow. The shear work due to the rotating wall in the seal is considered in section 4.14. Seal leakage affects rotor rows much different from stationary rows, since no useful work is extracted from the leakage flow through rotors. This is also considered in section 4.11.

4.10 Lashing Wire Loss Coefficient

Occasionally, lashing wire is used to bind steam turbine blades together for reasons of mechanical integrity. The loss introduced by the presence of these lashing wires can be calculated from well-known drag coefficients, C_D , for the flow over circular cylinders. These can be found in many references, e.g., Kreith [51]. It is assumed that the fluid velocity at the position of the wires is approximately equal to C_{m2} . If the lashing wire diameter is denoted as D , the governing Reynolds number is computed from

$$Re = \rho_2 C_{m2} D / \mu_2 \quad (4-92)$$

$C_D \approx 1.0$ if $Re \leq 5 \times 10^5$ and $C_D \approx 0.35$ if $Re > 5 \times 10^5$. If N is the number of wires, the lashing wire loss coefficient is

$$Y_{LW} = NC_D DC_{m2}^2 / (hW_2^2) \quad (4-93)$$

4.11 Leakage Bypass Loss

Figure 4-12 illustrates the basic geometry of a labyrinth seal. These seals are used in many locations in a typical industrial turbine. In terms of blade row performance, the labyrinth seals on blade shrouds and the nozzle shaft seals in a diaphragm-disk arrangement require consideration. The leakage flow through these seals bypasses the blade row and mixes with the blade row through-flow to directly influence the overall discharge flow. In the case of a

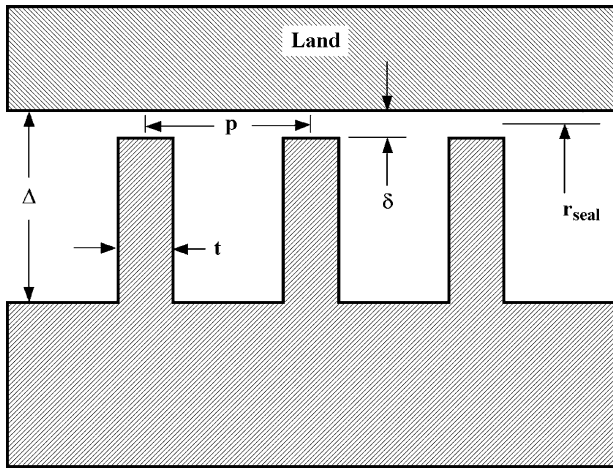


FIGURE 4-12. Labyrinth Seal Geometry

rotor row, no useful work is extracted from the leakage flow, which directly affects the turbine's power output. Typically seal fins are attached to the shroud band or nozzle diaphragm to reduce the clearance gap leakage flow, yet protect the turbine from serious damage in the event that a rotor excursion should cause the shaft or casing to come in contact with the shroud or nozzle diaphragm. The seal allows use of larger base clearances between the shroud band or nozzle diaphragm and the end-wall without causing excessive leakage flows. If contact occurs, the seal strips will be sacrificed, but the more expensive components should be undamaged.

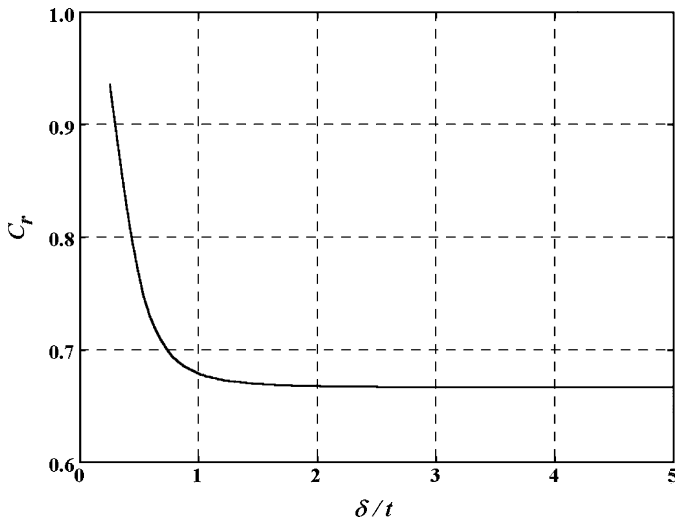
The leakage mass flow through the labyrinth seal can be computed by the method of Egli [52], who expresses the seal leakage mass flow in the form

$$\dot{m}_{seal} = 2\pi r_{seal} \delta C_c C_t C_r \rho \sqrt{RT} \quad (4-94)$$

The density and temperature in Eq. (4-94) are evaluated on the high-pressure side of the seal, r_{seal} is the seal radius and δ is the seal clearance. Aungier [1] provides general empirical equations to approximate the coefficients in Eq. (4-94), developed from Egli's graphical data. The contraction ratio, C_r , is a function of δ and the fin width, t . Figure 4-13 shows the contraction ratio as approximated by

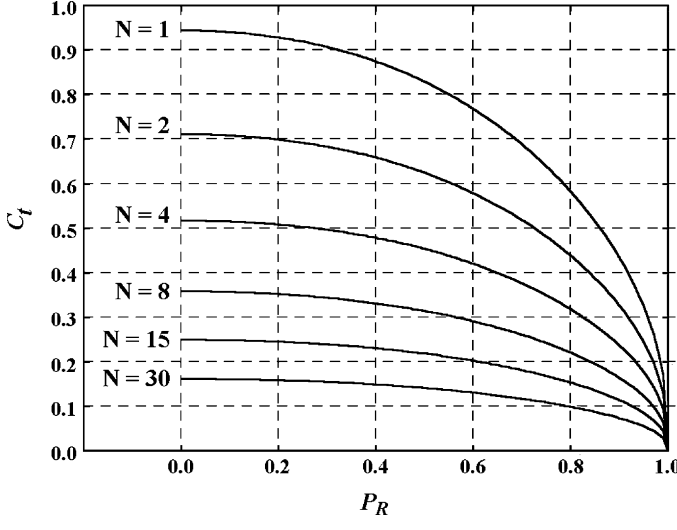
$$C_r = 1 - \frac{1}{3 + \left[\frac{54.3}{1+100\delta/t} \right]^{3.45}} \quad (4-95)$$

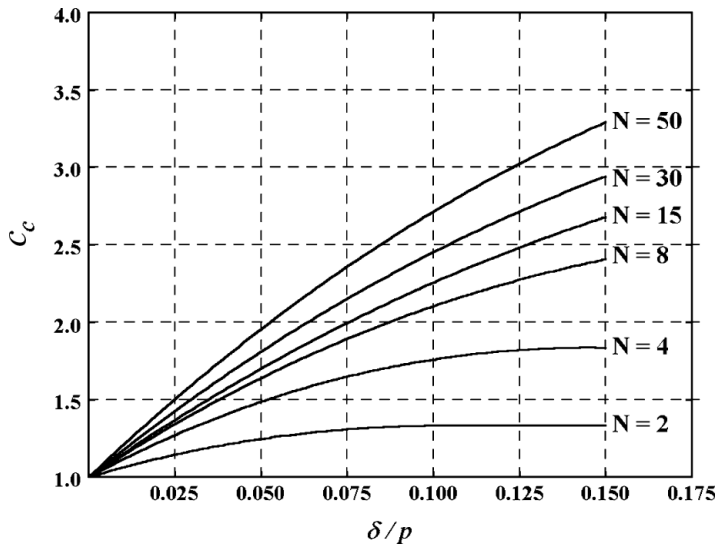
Egli shows a direct dependence of C_r on t as well as on δ/t . It seems highly questionable that a dimensional parameter can be used to compute a dimensionless parameter. Indeed, other sources available to this writer suggest

**FIGURE 4-13. The Seal Contraction Ratio**

that the lower of Egli's two curves should be used for all values of t , which is the basis for Eq. (4-95). The throttling coefficient, C_t , is a function of the ratio of the lower pressure to the higher pressure across the seal, P_R , and the number of seal fins, N . Figure 4-14 shows the throttling coefficient approximated by

$$C_t = \frac{2.143 \ln(N) - 1.464}{N - 4.322} [1 - P_R]^{(0.375P_R)} \quad (4-96)$$

**FIGURE 4-14. The Seal Throttling Coefficient**

**FIGURE 4-15. The Seal Carryover Coefficient**

The carryover coefficient, C_c , is a function of the seal clearance and the seal pitch, p . Figure 4-15 shows the carryover coefficient as approximated by

$$C_c = 1 + \frac{X_1[\delta_c/p - X_2 \ln(1 + \delta_c/p)]}{1 - X_2} \quad (4-97)$$

If $N \leq 12$,

$$X_1 = 15.1 - 0.05255 \exp[0.507(12 - N)] \quad (4-98)$$

$$X_2 = 1.058 + 0.0218N \quad (4-99)$$

If $N > 12$,

$$X_1 = 13.15 + 0.1625N \quad (4-100)$$

$$X_2 = 1.32 \quad (4-101)$$

Eq. (4-97) yields a maximum when $\delta/p = X_2 - 1$. This represents a poor seal design, which exceeds the range of Egli's model. It is rarely encountered, but it is wise to require $\delta/p \leq X_2 - 1$ when applying Eq. (4-97). In some cases labyrinth seals in turbines are stepped, i.e., the seal radius is different for

successive seal fins. In that case, there is no carryover influence, so $C_c = 1$ should be used.

Another source of rotor bypass leakage is the use of balance holes as illustrated in figure 1-4. Balance holes are used to reduce the axial thrust force on the rotor. Balance hole leakage can be estimated from a simple orifice flow model. If N is the number of balance holes and D is the diameter of the balance holes, the approximation used is

$$\dot{m}_{BH} = \frac{1}{8} N \pi D^2 \sqrt{2(P_1 - P_2) / \rho} \quad (4-102)$$

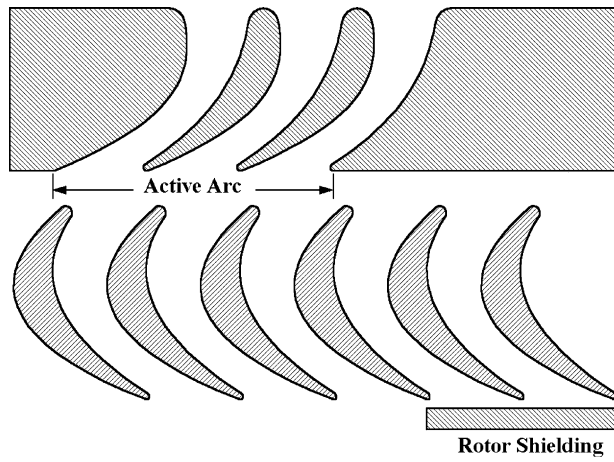
Leakage flow always results in a difference between the blade row through-flow and its final discharge flow. In the case of rotors, it also reduces the overall work done by the rotor. It is useful to include this in the parasitic losses, although it is not really wasted energy. This is just a convenient way to correct the total enthalpy at the blade row discharge to account for the bypass effect. Hence, the leakage bypass loss is given by

$$\Delta H_{leak} = (\dot{m}_{seal} + \dot{m}_{BH})(H_1 - H_2) / \dot{m} \quad (4-103)$$

Note that $\Delta H_{leak} = 0$ for stationary blades since $H_2 = H_1$. Occasionally the rotor leakage flow will be reversed to flow from discharge to inlet. Considering that case greatly complicates the rotor performance analysis. Since leakage flows will be rather small in those cases, ΔH_{leak} is simply set to zero.

4.12 Partial Admission Loss

Partial admission refers to operation with a portion of the total arc of the annulus blocked off as illustrated in figure 4-16. The flow through the nozzle row is restricted to a fraction, ε , of the total arc, referred to as the active arc. This results in wasted energy in the downstream rotor row as some of the flow through the active blade passages in the rotor reenters inactive passages to produce windage losses. In addition, rotor passages crossing the ends of the active arc may be only partially filled to operate at reduced mass flow, resulting in more wasted energy often referred to as the end of sector loss. Sometimes rotor shielding is used to reduce the windage losses. This involves blocking a fraction of the annulus, ζ , at the rotor exit and within the inactive arc to reduce the recirculation into the inactive blade passages. The effect of partial admission losses is to produce an increase in total enthalpy, ΔH_{adm} , which consumes some of the useful work accomplished by the rotor blades. About the best available model for this loss is that of Suter and Traupel [53] which has been adapted from the description in Horlock [54]. Designating parameters evaluated at the average rotor exit radius with a subscript m , the windage loss, ΔH_w , is given by

**FIGURE 4-16. Partial Admission Arrangement**

$$\Delta H_w = 0.05\pi\rho_2 D_m U_m^3 h(1 - \varepsilon - \zeta/2) / \dot{m} \quad (4-104)$$

The end of sector loss, ΔH_{sec} , is given by

$$\Delta H_{sec} = 0.15Nb_z U_m C_1 \psi_{noz} / (D_m \varepsilon) \quad (4-105)$$

N is the number of active sectors comprising the overall active arc and ψ_{noz} is the nozzle velocity coefficient defined by

$$\psi_{noz} = C_1 / \sqrt{2(H_1 - h_{1,is})} = C_1 / C_{1,is} \quad (4-106)$$

The subscript, is , designates nozzle exit (or rotor inlet) data assuming isentropic flow through the nozzle to the actual static pressure, P_1 . The overall partial admission loss is

$$\Delta H_{adm} = \Delta H_w + \Delta H_{sec} \quad (4-107)$$

4.13 Disk Friction Loss

The diaphragm-disk type rotor of figure 1-4 requires consideration of the disk friction loss to account for the power consumed by an enclosed rotating disk. If τ is the torque, r is the disk radius and ρ is assumed constant, the disk torque coefficient, C_M , is defined as

$$C_M = \tau / (\rho \omega^2 r^5) \quad (4-108)$$

The power consumed by the disk is $\omega\tau$. Hence, the disk friction loss, ΔH_{DF} , is

$$\Delta H_{DF} = C_M \rho \omega^3 r^5 / \dot{m} \quad (4-109)$$

Daily and Nece [55, 56] provide an excellent model for the torque coefficient that is well qualified against experiment. Aungier [1] developed empirical equations to implement their model. Daily and Nece identify four flow regimes that may occur in the enclosed rotating disk.

1. Laminar, merged boundary layers
2. Laminar, separate boundary layers
3. Turbulent, merged boundary layers
4. Turbulent, separate boundary layers

The torque coefficient for smooth disks is a function of the disk-housing clearance, Δ , and the Reynolds number

$$Re = \rho \omega r^2 / \mu \quad (4-110)$$

The torque coefficients for the four flow regimes are

$$C_{M1} = \frac{2\pi}{(\Delta/r)Re} \quad (4-111)$$

$$C_{M2} = \frac{3.7(\Delta/r)^{0.1}}{\sqrt{Re}} \quad (4-112)$$

$$C_{M3} = \frac{0.08}{(\Delta/r)^{1/6} Re^{1/4}} \quad (4-113)$$

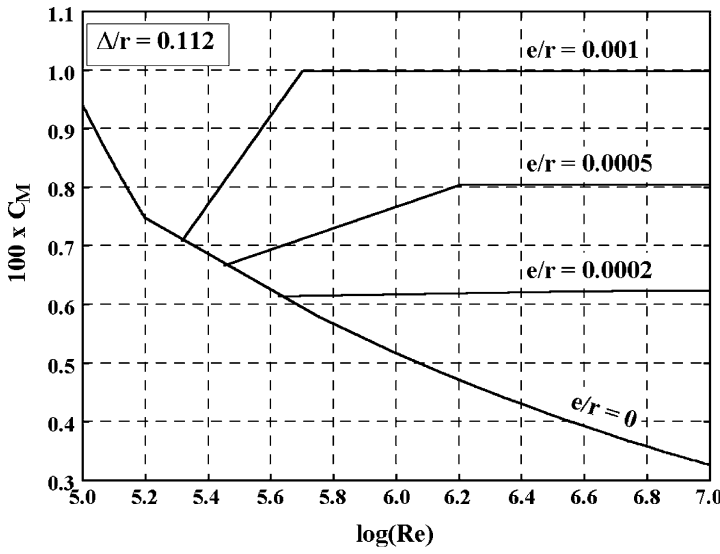
$$C_{M4} = \frac{0.102(\Delta/r)^{0.1}}{Re^{0.2}} \quad (4-114)$$

These four torque coefficients are all calculated for the specific values of Δ and Re . The relevant flow regime is identified by the torque coefficient equation that yields the largest value. Similar to the previous discussion of boundary layer skin friction, at sufficiently high values of Re , surface roughness may become significant. If e is the peak-to-valley roughness height, the fully rough torque coefficient is given by

$$1/\sqrt{C_{Mr}} = 3.8 \log_{10}(r/e) - 2.4(\Delta/r)^{0.25} \quad (4-115)$$

Daily and Nece provide equations to define the Reynolds numbers bounding the transition zone from smooth to fully rough torque coefficients. The Reynolds number where roughness first becomes significant is given by

$$Re_s \sqrt{C_M} = 1,100(e/r)^{-0.4} \quad (4-116)$$

**FIGURE 4-17. Rotating Disk Torque Coefficient**

Since roughness is significant only for turbulent flow, Eq. (4-116) is combined with Eq. (4-113) or (4-114) as appropriate to solve for Re_s . The Daily and Nece equation for the fully rough limit appears questionable based on the experimental data presented. Aungier [1] replaced their equation with the following.

$$Re_r = 1,100(r/e) - 6 \times 10^6 \quad (4-117)$$

Between the limits of Re_s and Re_r , the torque coefficient is estimated from

$$C_M = C_{Ms} + (C_{Mr} - C_{Ms}) \log(Re/Re_s) / \log(Re_r/Re_s) \quad (4-118)$$

Figure 4-17 shows torque coefficient curves generated with these empirical equations for a specific value of Δ/r .

4.14 Clearance Gap Windage Loss

Shear forces on the rotating wall associated with the clearance gap over a shrouded blade are another source of wasted energy. This also occurs for the nozzle diaphragm of the diaphragm disk type rotor of figure 1-4. Fluid in the clearance gap between a rotating and a stationary wall produces viscous shear forces on both walls. In the case of the rotating wall, work is done, which consumes some of the useful work done by the turbine. Figure 4-12 shows the basic geometry involved if the labyrinth seal is ignored. The two walls are separated by the base clearance, Δ . The mean rotation speed of the

fluid in the gap is assumed to be half of the turbine rotation speed. Well-known pipe friction factor models provide a reasonable approximation to the wall skin friction coefficient if the pipe diameter is replaced by Δ . If r is the radius of the rotating wall, the governing Reynolds number is

$$Re = \rho r \omega \Delta / (2\mu) \quad (4-119)$$

If $Re \leq 2,000$, the flow is laminar and the skin friction coefficient is given by

$$c_f = 16 / Re \quad (4-120)$$

If $Re > 2,000$, the flow is turbulent and the skin friction coefficient can be approximated by the well-known Blasius formula

$$c_f = 0.0791 / Re^{1/4} \quad (4-121)$$

If Δm is the meridional length of the clearance gap, the shear force applied to the rotating wall is

$$f = \frac{1}{2} c_f \rho \left(\frac{1}{2} r \omega \right)^2 (2\pi r \Delta m) \quad (4-122)$$

From Eq. (3-8), the power consumed is given by ω times the torque on the rotating wall, so the parasitic work is

$$\Delta H_{gap} = \pi \rho c_f r^4 \omega^3 \Delta m / (4\dot{m}) \quad (4-123)$$

4.15 Moisture Loss

Moisture loss is associated with the reduction in stage efficiency when some of the working fluid condenses to the liquid phase. Although the mechanism is not completely clear, it seems likely that it is associated with reduced rotor work rather than a total pressure loss. Like the seal leakage bypass loss, this is probably reduced work rather than wasted energy. Nevertheless, it is convenient to include it as a parasitic loss. The most likely mechanism is that liquid particles are generally unable to follow the streamline pattern of the gas phase. Hence, the fluid turning calculated for the nozzle and rotor rows is simply not fully realized for the liquid phase. It is assumed that, the actual rotor work is approximately equal to the calculated work times the rotor's average flow quality. Expressed as a parasitic loss to be added to the calculated work, the rotor row moisture loss is

$$\Delta H_Q = \frac{1}{2} (2 - Q_1 - Q_2)(H_1 - H_2) \quad (4-124)$$

This writer formulated this fairly simple model many years ago in response to an unexpected need to consider moisture losses in radial-inflow turbines. Lacking familiarity with the subject and time to research it, this was just an educated guess at a moisture loss model. Subsequently, it was a pleasant surprise to find a close similarity to other moisture loss models that are based on performance observations. For example, the model by Baumann [57] is commonly cited. Baumann proposes a one-percent loss in stage efficiency for each 1 percent of moisture. The present moisture loss model is essentially equivalent to Baumann's approximation and it is much easier to apply in a performance analysis. Hence, this writer continues to use it for lack of anything better.

Chapter 5

AERODYNAMIC PERFORMANCE ANALYSIS OF AXIAL-FLOW TURBINES

An aerodynamic performance analysis is essential for nearly all aspects of axial-flow turbine aerodynamic design and application. The most common approach is the one-dimensional or mean-line method, which analyzes the performance along a mean stream surface. As noted in chapter 4, most published blade row performance systems [41–44] were specifically developed for use in a mean-line method. If applied to well-designed stages, the mean-line performance may be considered to be representative of the overall performance, at least near the turbine's design operating conditions. This approach is more questionable for off-design performance prediction. In those cases, blade incidence angle matching, blade loading levels, Mach number levels, etc. may vary dramatically at different locations along the blade span, such that the mean-line performance is no longer representative of the overall performance. In off-design operation, the extremes in incidence angle, Mach number and reaction will almost always occur on the hub or the shroud contours. Some one-dimensional methods include approximate calculations at the hub-and-shroud contours to provide additional guidance to the user and to better evaluate tip clearance losses and shroud seal leakage effects.

A more general approach is to conduct the performance analysis for a series of stream surfaces from hub to shroud. These methods are referred to by various names, such as streamline methods, through-flow methods, streamline-curvature methods or three-dimensional methods. Hub-to-shroud performance analysis is a more accurate term, which is used in this book. Most hub-to-shroud performance analyses for axial-flow turbomachines rely on the full normal equilibrium equation given in Eq. (3-30). This approach is much less reliable than the mean-line method and requires substantially longer computer times. These issues are significant problem areas for axial-flow compressor performance analysis. They are far more serious for axial-flow turbine performance analysis. The need to analyze turbines operating with one or more blade rows choked requires highly sophisticated numerical methods. The diffusing flow in compressors normally dictates use of smooth end-wall contours. By contrast, it is not uncommon to see discontinuous step-changes along turbine end-wall contours. In those cases the stream surface curvature term is undefined, requiring some rather arbitrary stream-surface smoothing

approximations. Many turbine performance analyses require a much more complex equation-of-state model than a typical axial-flow compressor analysis. As noted in chapter 2, section 2.9, simplified nonideal fluid equations of state that are quite effective for compressors have been found to be rather unreliable for turbines. Turbines often involve two-phase flow when the working fluid condenses, which is rarely encountered in a compressor. Indeed, turbine performance analysis is a very formidable problem involving many complications not encountered in compressor performance analysis.

Aungier [2] introduced an approximate normal-equilibrium model for axial-flow compressor performance analysis, which yields performance predictions that are virtually identical to the full normal equilibrium model. This approximate model offers excellent reliability and very modest computation times as compared to the more exact formulation. Its recent application to the more formidable problem of axial-flow turbine performance analysis provided even more dramatic benefits. The hub-to-shroud performance analysis described in this chapter is based on this approximate normal equilibrium model.

NOMENCLATURE

- A = stream sheet area
- a = sound speed
- b = stream sheet thickness
- C = absolute velocity
- F = general function; also total blade force
- f = general function; also blade force per unit length
- H = total enthalpy
- h = static enthalpy; also, blade height or span
- I = rothalpy
- M = Mach number; also blade bending moment
- m = meridional coordinate
- \dot{m} = mass flow rate
- N = number of blades and rotation speed (rpm)
- N_{QN} = number of quasi-normals
- n = normal coordinate
- P = pressure
- r = radius
- s = entropy
- T = temperature; also rotor thrust force
- W = relative velocity
- Y = loss coefficient
- y = coordinate along a quasi-normal
- z = axial coordinate
- α = flow angle with respect to tangent
- β = blade angle with respect to tangent
- ε = $\phi - \lambda$; deviation of quasi-normal from a true normal
- κ_m = stream surface curvature

λ = quasi-normal angle

ϕ = stream surface angle with axial direction

θ = polar angle

ρ = gas density

ω = rotation speed (radians/sec)

Subscripts

c = value of a parameter on the reference stream surface

eq = Mach number equivalence parameter

h = hub parameter

m = meridional component or mean value

s = shroud parameter

t = total thermodynamic condition

z = axial component

1 = blade row inlet parameter

2 = blade row exit parameter

θ = tangential component

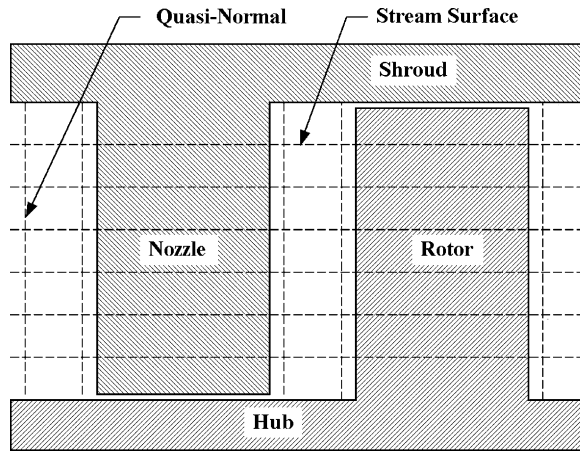
Superscript

' = a relative value in the rotating coordinate system

5.1 The Meridional Coordinate System

Figure 5-1 illustrates the meridional coordinate system used in the through-flow analysis. The annular passage is divided into a series of stream sheets bounded by stream surfaces. By definition, a stream surface has no velocity component normal to it and no mass flow across it. Hence, the mass flow in any stream sheet is constant. The annulus end-wall contours are always stream surfaces. But the location of other stream surfaces requires knowledge of the flow field. Hence, the stream surface construction is part of the solution procedure. A series of fixed, linear quasi-normals are located before and after the blade rows. Construction of the quasi-normals is fairly arbitrary, but they should be selected to be approximately normal to the stream surfaces. The distance along a quasi-normal measured from the hub is designated as y . The distance along a stream surface measured from the first quasi-normal is the meridional coordinate, m . The third coordinate is the usual polar angle of a cylindrical coordinate system, θ . Hence, this (θ, m, y) coordinate system is axisymmetric.

Figure 5-1 illustrates this coordinate system for a very simple axial-flow turbine stage. But the coordinate system is applicable to far more complex passage geometry, including rather general hub and shroud contour slopes

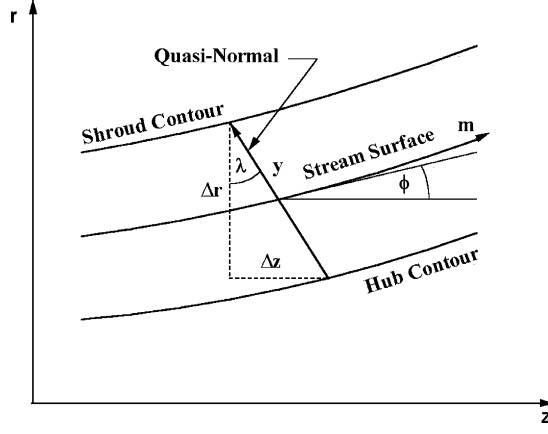
**FIGURE 5-1. Meridional Coordinate System**

and curvatures. Figure 5-2 illustrates the quasi-normal construction for more general end-wall contour shapes. The quasi-normal is defined by the (z, r) coordinates on the two end-wall contours. The quasi-normal angle, λ , is given by

$$\tan \lambda = \frac{\Delta z}{\Delta r} = \frac{z_h - z_s}{r_s - r_h} \quad (5-1)$$

The stream surface slope angle, ϕ , is defined as

$$\sin \phi = \frac{\partial r}{\partial m} \quad (5-2)$$

**FIGURE 5-2. Quasi-Normal Construction**

From figure 5-2 it is easily seen that a normal to the quasi-normal makes an vangle λ with the axial direction. Hence, the local angle between a quasi-normal and a true stream surface normal is

$$\varepsilon = \phi - \lambda \quad (5-3)$$

Although the construction of quasi-normals is fairly arbitrary, it is good practice to maintain fairly small values of ε to minimize numerical inaccuracies in the solution process. This suggests that ε should be about equal in magnitude but opposite in sign on the two end-wall contours. For the vast majority of cases in axial-flow turbines, simple radial quasi-normals such as shown in figure 5-1 will be quite adequate.

Katsanis [58] suggested the use of quasi-normals as a means of simplifying the through-flow analysis in turbomachines. This basic coordinate system is particularly well suited to the governing equations developed in chapter 3 for the (θ, m, n) natural coordinate system. It is easily shown that the derivatives with respect to the normal coordinate, n , can be replaced by

$$\frac{\partial}{\partial n} = \frac{1}{\cos \varepsilon} \left[\frac{\partial}{\partial y} + \sin \varepsilon \frac{\partial}{\partial m} \right] \quad (5-4)$$

The numerical analysis is greatly simplified by use of the fixed coordinate y to avoid the need to compute n as part of the solution procedure.

5.2 The Approximate Normal Equilibrium Model

The flow profiles along quasi-normals are modeled as an adiabatic, inviscid flow problem. The general form of the governing equations in the natural coordinate system are developed in chapter 3 as Eqs. (3-21), (3-25), (3-29) and (3-30). A performance analysis is clearly a steady flow problem, so these equations can be simplified to their time-steady form. If the flow is also assumed to be locally axisymmetric, a solution in the meridional (constant θ) plane can completely characterize the flow field. Clearly, the flow is far from axisymmetric within the blade passages. But it is usually considered to be a reasonable approximation along quasi-normals, since they always lie outside of the blade passages. This is the basis of the well-known meridional through-flow analysis that is commonly used in the performance analysis of axial-flow turbomachines. It is more convenient to express conservation of mass in integral form rather than using Eq. (3-21). This can be expressed as

$$\dot{m} = 2\pi \int_0^{y_s} r \rho C_m \cos \varepsilon dy \quad (5-5)$$

The tangential and normal momentum equations are given by Eqs. (3-29) and (3-30), reduced to their time-steady, axisymmetric form.

$$\frac{\partial(rW_\theta + r^2\omega)}{\partial m} = \frac{\partial rC_\theta}{\partial m} = 0 \quad (5-6)$$

$$\kappa_m C_m^2 + \frac{W_\theta}{r} \frac{\partial(rW_\theta + r^2\omega)}{\partial n} + C_m \frac{\partial C_m}{\partial n} = \frac{\partial I}{\partial n} - T \frac{\partial s}{\partial n} \quad (5-7)$$

κ_m is the stream surface curvature given by Eq. (3-26), i.e.,

$$\kappa_m = -\frac{\partial \phi}{\partial m} \quad (5-8)$$

Conservation of energy follows directly from Eq. (3-26), reduced to its time-steady, axisymmetric form.

$$\frac{\partial I}{\partial m} = 0 \quad (5-9)$$

Substitution of Eqs. (5-6) and (5-9) into Eq. (3-25) yields

$$\frac{\partial s}{\partial m} = 0 \quad (5-10)$$

Eqs. (5-6) and (5-10) may seem inappropriate, since it is clear that angular momentum and entropy do vary along stream surfaces through an axial-flow turbine. But these equations only state that the meridional gradients of these parameters are locally zero on quasi-normals. They do not preclude changes in these parameters between quasi-normals, which certainly do occur when a blade row lies between them. Substituting Eq. (5-4) into Eq. (5-7) and simplifying the result using Eqs. (5-6), (5-9) and (5-10) yields the normal equilibrium equation in the (θ, m, y) coordinate system.

$$C_m \frac{\partial C_m}{\partial y} + \kappa_m C_m^2 \cos \varepsilon - C_m \sin \varepsilon \frac{\partial C_m}{\partial m} + \frac{W_\theta}{r} \frac{\partial rC_\theta}{\partial y} = \frac{\partial I}{\partial y} - T \frac{\partial s}{\partial y} \quad (5-11)$$

It is often useful to express this equation in terms of the relative flow angle, α' , rather than W_θ . Noting that $W_\theta = C_m \cot \alpha'$, yields

$$C_m \frac{\partial C_m}{\partial y} + \kappa_m C_m^2 \cos \varepsilon - C_m \sin \varepsilon \frac{\partial C_m}{\partial m} + \frac{C_m \cot \alpha'}{r} \frac{\partial(rC_m \cot \alpha' - r^2\omega)}{\partial y} = \frac{\partial I}{\partial y} - T \frac{\partial s}{\partial y} \quad (5-12)$$

After some tedious algebra and trigonometric substitutions, Eq. (5-12) can be simplified to

$$\begin{aligned} \frac{C_m}{\sin^2 \alpha'} \frac{\partial C_m}{\partial y} + \kappa_m C_m^2 \cos \varepsilon - C_m \sin \varepsilon \frac{\partial C_m}{\partial m} + \frac{C_m^2 \cot \alpha'}{r} \frac{\partial(r \cot \alpha')}{\partial y} \\ + 2C_m \omega \cot \alpha' \cos \lambda = \frac{\partial I}{\partial y} - T \frac{\partial s}{\partial y} \end{aligned} \quad (5-13)$$

The third term in Eqs. (5-11) through (5-13) is not well suited to a numerical solution. When blade rows lie between quasi-normals, a numerical estimate of the meridional gradient of C_m is of questionable validity. Novak [24, 59] removed this uncertainty using the differential form of the continuity equation as given in Eq. (3-21). For axisymmetric, time-steady flow, this equation reduces to

$$\frac{\partial(r \rho C_m)}{\partial m} + \kappa_n r \rho C_m = 0 \quad (5-14)$$

Combining Eqs. (3-27) and (5-14) and expanding the result yields

$$\frac{1}{C_m} \frac{\partial C_m}{\partial m} + \frac{1}{\rho} \frac{\partial \rho}{\partial m} + \frac{\sin \phi}{r} + \frac{\partial \phi}{\partial n} = 0 \quad (5-15)$$

Eq. (5-10) shows that entropy is locally conserved along stream surfaces. Hence Eq. (2-26) can be used to expand the meridional gradient of density to yield

$$\frac{1}{\rho} \frac{\partial \rho}{\partial m} = \frac{1}{\rho} \frac{\partial P}{\partial m} \left(\frac{\partial \rho}{\partial P} \right)_s = \frac{1}{\rho a^2} \frac{\partial P}{\partial m} \quad (5-16)$$

Combining Eq. (5-16) with the time-steady, axisymmetric form of Eq. (3-22) yields

$$\frac{1}{\rho} \frac{\partial \rho}{\partial m} = \frac{1}{a^2} \left[\frac{C_\theta^2 \sin \phi}{r} - C_m \frac{\partial C_m}{\partial m} \right] \quad (5-17)$$

Combining Eqs. (5-15) and (5-17) yields

$$\frac{1}{C_m} \frac{\partial C_m}{\partial m} (1 - M_m^2) = -(1 + M_\theta^2) \frac{\sin \phi}{r} - \frac{\partial \phi}{\partial n} \quad (5-18)$$

where

$$M_m = C_m / a \quad (5-19)$$

$$M_\theta = C_\theta / a \quad (5-20)$$

Substituting Eqs. (5-4) and (5-8) into Eq. (5-18) yields

$$\frac{1}{C_m} \frac{\partial C_m}{\partial m} (1 - M_m^2) = -(1 + M_\theta^2) \frac{\sin \phi}{r} - \frac{1}{\cos \varepsilon} \frac{\partial \phi}{\partial y} - \kappa_m \tan \varepsilon \quad (5-21)$$

Eq. (5-21) provides an expression for the meridional gradient of C_m in Eqs. (5-11) through (5-13) that is independent of the solution on other quasi-normals. Some precaution is necessary to avoid a singularity for $M_m = 1$. This writer imposes the following constraint when solving Eq. (5-21).

$$1 - M_m^2 \geq 0.1 \quad (5-22)$$

The approximate normal equilibrium model achieves its advantage over the full normal equilibrium model by decoupling the solution on a quasi-normal from the flow field on all downstream quasi-normals. This permits a simple marching numerical solution such that the solution is completed on each quasi-normal before starting solution of the next one. That eliminates the major iteration loop that is the primary source of convergence problems and consumes most of the computer time required for the full normal equilibrium model. Review of Eqs. (5-11) and (5-13), supplemented by Eq. (5-21) shows that ϕ and κ_m are the only terms that can depend on the downstream flow field. Both of these parameters can be calculated for the hub and shroud end-wall contours, since they do not depend on the flow field analysis. The approximate normal equilibrium model assumes that ϕ and κ_m vary linearly along the quasi-normal between the known values at the end-walls. Aungier [2] demonstrated that this approximation results in no significant loss of accuracy for typical axial-flow compressor performance analyses.

Axial-flow turbine performance analysis requires a little more care to allow for the possibility of discontinuous changes in the end-wall contour coordinates and slopes along the end-wall contours. This is not uncommon for industrial turbines and can lead to very inaccurate numerical estimates of ϕ and κ_m . Figure 5-3 shows a simple example, where both the hub and shroud end-wall contours are discontinuous between the third and fourth quasi-normals. At least two quasi-normals should be used between blade rows as illustrated in

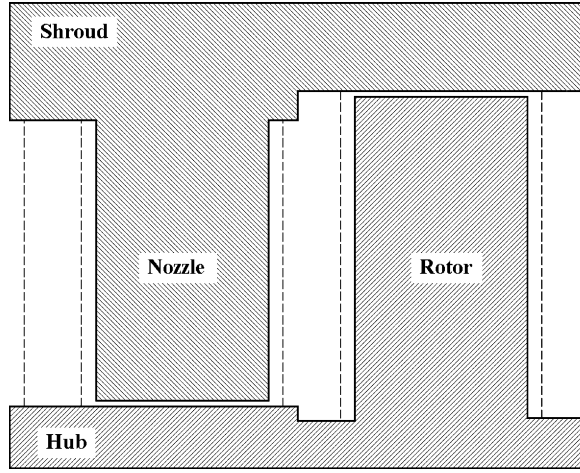


FIGURE 5-3. End-Wall Contour Discontinuities

figure 5-3 to better define the geometry for the critical stations at the inlet and discharge of the blade rows. Provision should be made to permit the user of the analysis to flag points either just before or just after a contour or contour slope discontinuity. Then the numerical approximations for the derivatives in Eqs. (5-2) and (5-8) can be restricted to be based on points on only one side of the discontinuity. In this simple example, the derivatives at the third quasi-normal would be based on upstream points only. Similarly, only downstream points would be used to calculate the derivatives at the fourth quasi-normal.

5.3 Inviscid Adiabatic Flow on a Quasi-Normal

Eqs. (5-11) and (5-13) are the two forms of the normal equilibrium equation to be solved along a quasi-normal. Eq. (5-13) is the appropriate form for the quasi-normals immediately downstream of a blade row where the relative flow angle is known from the empirical models described in chapter 4. For other quasi-normals, C_θ and W_θ are known from conservation of angular momentum. Either form may be used at the first quasi-normal, depending on the type of inlet flow profile specification provided. The normal equilibrium equation can be expressed as

$$\frac{\partial C_m}{\partial y} = f_1(y)C_m + f_2(y) + \frac{f_3(y)}{C_m} \quad (5-23)$$

When C_θ and W_θ are known, the functions in Eq. (5-23) are

$$f_1(y) = -\kappa_m \cos \varepsilon + \frac{\sin \varepsilon}{C_m} \frac{\partial C_m}{\partial m} \quad (5-24)$$

$$f_2(y) = 0 \quad (5-25)$$

$$f_3(y) = \frac{\partial I}{\partial y} - T \frac{\partial s}{\partial y} - \frac{W_\theta}{r} \frac{\partial(rC_\theta)}{\partial y} \quad (5-26)$$

When α' is known, the functions are

$$f_1(y) = \sin^2 \alpha' \left[-\kappa_m \cos \varepsilon - \frac{\cot \alpha'}{r} \frac{\partial(r \cot \alpha')}{\partial y} + \frac{\sin \varepsilon}{C_m} \frac{\partial C_m}{\partial m} \right] \quad (5-27)$$

$$f_2(y) = -2\omega \cos \alpha' \sin \alpha \cos \lambda \quad (5-28)$$

$$f_3(y) = \sin^2 \alpha' \left[\frac{\partial I}{\partial y} - T \frac{\partial s}{\partial y} \right] \quad (5-29)$$

Numerical integration of Eq. (5-23) is straightforward since f_1, f_2 and f_3 are functions of y only. However, this equation will become singular if $C_m = 0$. Aungier [1, 2] avoids that problem by using conservation of mass in a stream tube in the form

$$\Delta\dot{m} = \rho C_m \Delta A \quad (5-30)$$

The stream tube area term is given by

$$\Delta A = 2\pi r \cos \varepsilon \Delta y \quad (5-31)$$

Typically, all stream tubes are assumed to contain equal mass flows, although alternate definitions can certainly be used. Now introduce the function, f_4 , given by

$$f_4(y) = f_2(y) + f_3(y) \frac{\rho \Delta A}{\Delta \dot{m}} \quad (5-32)$$

Then, Eq. (5-23) can be written as

$$\frac{\partial C_m}{\partial y} = f_1(y)C_m + f_4(y) \quad (5-33)$$

The solution of this linear differential equation can be found in almost any textbook on differential equations as

$$C_m(y) = C_m(0)F(y) + F(y) \int_0^y \frac{f_4(y)}{F(y)} dy \quad (5-34)$$

where the function $F(y)$ is given by

$$F(y) = \exp \left[\int_0^y f_1(y) dy \right] \quad (5-35)$$

The meridional velocity on the hub contour, $C_m(0)$, is the constant of integration for Eq. (5-33). The constant of integration does not have to be specified on the hub contour. Indeed, that is not a particularly good choice, since the most extreme variation in operating conditions almost always occurs at that location. A more reliable numerical analysis is obtained by choosing a different reference stream surface for specifying the constant of integration, e.g., the mean stream surface. Designating conditions on the reference stream surface by the subscript, c , $C_m(0)$ can be directly related to the alternate constant of integration, $C_{mc} = C_m(y_c)$, through Eq. (5-34).

$$C_m(0) = C_{mc} / F(y_c) - \int_0^{y_c} \frac{f_4(y)}{F(y)} dy \quad (5-36)$$

In most cases C_{mc} can be determined from conservation of mass through Eq. (5-5). Eqs. (5-33) and (5-5) are solved in an iterative numerical scheme, successively improving the estimate of C_{mc} until mass is conserved and the normal momentum equation is satisfied. This requires calculation of thermodynamic properties such as ρ and a , using an appropriate equation of state from chapter 2. At any point, the relative total enthalpy is given by Eq. (3-13), i.e.,

$$H' = I + \frac{1}{2}(r\omega)^2 \quad (5-37)$$

The local static enthalpy is given by

$$h = H' - \frac{1}{2}W^2 \quad (5-38)$$

Then static thermodynamic conditions are computed from relative total thermodynamic conditions for the change in enthalpy, ($h - H'$), while holding entropy constant.

Figure 5-4 shows the mass flow predicted by Eq. (5-5) as a function of C_{mc} from an analysis of a typical nozzle blade row. Mass flow increases with C_{mc} , passes through a maximum and then starts to decrease. The maximum mass flow that can pass through the annulus for the specified inlet total thermodynamic conditions and swirl velocity or flow angle is referred to as the choked

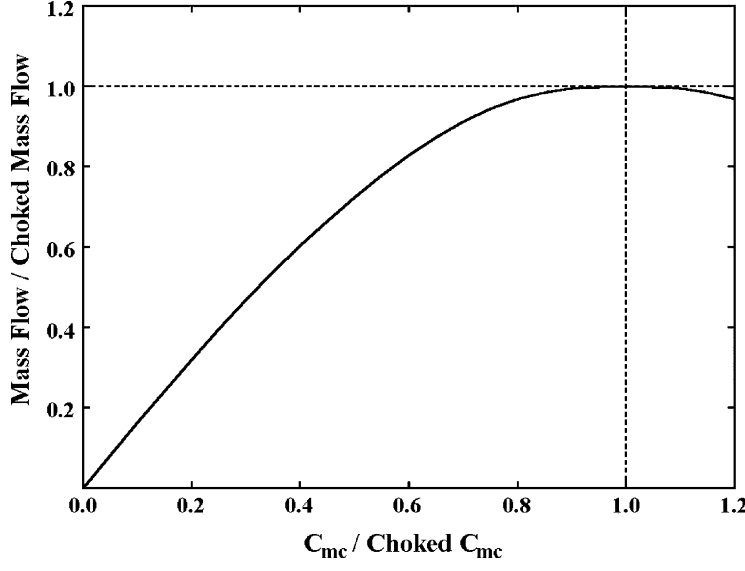


FIGURE 5-4. Mass Flow Variation with C_{mc}

flow. For a mean-line analysis, this can be directly associated to the sonic flow condition at the blade row throat or with the sonic value of C_m in the case of flow in an annular passage with no blades. In the context of the present hub-to-shroud analysis, a more general choked flow condition is required. It is necessary to identify the maximum mass flow predicted by Eq. (5-5) as a function of C_{mc} , i.e.,

$$\frac{\partial \dot{m}}{\partial C_{mc}} = 0 \quad (5-39)$$

It is essential that numerical analysis be able to recognize choked flow in the general context of Eq. (5-39). One way to identify choke is to compare mass flow rates calculated from Eq. (5-5) for two different values of C_{mc} . If the calculated mass flow and C_{mc} vary in opposite directions, the higher value of C_{mc} is beyond the choke limit. An iteration scheme can be used to converge on the actual choking value of C_{mc} . Once the choke limit is reached, Eq. (5-5) ceases to be usable to compute the constant of integration. For a compressor performance analysis such as Aungier [2], that is not a problem since the choke limit is also the limit of the compressor's useful operation. But turbines must often operate with one or more blade rows choked to achieve the discharge static pressure imposed on the turbine. When the flow is choked at a quasi-normal, it is more convenient to seek convergence on static pressure, P_c , rather than C_{mc} . The selection of the appropriate value of P_c is discussed later in this chapter. With an appropriate equation of state from chapter 2, the local entropy, s_c , and P_c , can be used to calculate the static enthalpy, h_c . From Eqs. (5-37) and (5-38) the corresponding constant of integration is given by

$$C_{mc} = \sqrt{2[H'_c - h_c]} \sin \alpha'_c \quad (5-40)$$

This permits an iterative solution to converge on the desired value of P_c . The solution must also yield the mass flow equal to the choked flow. In principle, the supersonic deviation-angle correlation of chapter 4 attempts to accomplish that. But in practice a solution for P_c less than the choked value will also result in different blade row loss coefficients. It may also yield subsonic relative Mach numbers over a significant portion of the annulus height. Hence, a minor adjustment to all relative flow angles is usually required to obtain the correct mass flow.

5.4 Linking Quasi-Normals

Prediction of the flow profiles with the normal equilibrium equations requires known total thermodynamic conditions and tangential velocity or flow angle profiles on the quasi-normal. It also requires known stream surface coordinates, slopes and curvatures. None of these are actually known in advance, since they all depend on the flow profiles to be predicted. Hence, an iterative solution technique is necessary to progressively improve the estimates of the unknowns until a self-consistent solution is achieved. This section describes techniques needed

to link successive quasi-normals together so that this iterative flow analysis can be conducted on all quasi-normals.

To start the process, boundary conditions are needed for the first quasi-normal. The usual process is to supply specifications of the distributions of the inlet flow angle or absolute tangential velocity and inlet total thermodynamic conditions (e.g., P_t and T_t) along the first quasi-normal. Values of these parameters on the stream surfaces of the first quasi-normal are determined by interpolation from these profile specifications. Then the procedures of the previous section can be used to compute the inlet flow profiles.

For all quasi-normals after the first one, the process required is to link the quasi-normal being analyzed to the upstream quasi-normal, where all flow data are known. Subscript 1 will be used to designate known data on the upstream quasi-normal, and subscript 2 will be used to designate conditions on the quasi-normal being analyzed, where both apply to the same stream surface. The simplest case is successive quasi-normals in a simple annular passage with no blade row between them. In this case, Eqs. (5-6), (5-9) and (5-10) provide the linking relations, i.e.,

$$(rC_\theta)_2 = (rC_\theta)_1 \quad (5-41)$$

$$I_2 = H_2 - \omega(rC_\theta)_2 = I_1 = H_1 - \omega(rC_\theta)_1 \quad (5-42)$$

$$s_2 = s_1 \quad (5-43)$$

From Eqs. (5-41) and (5-42), it is seen that $H_2 = H_1$ is the true linking condition implied by Eq. (5-42). Hence, all data needed are known for the quasi-normal flow analysis using the current stream surface pattern.

When a blade row lies between the two quasi-normals, the empirical models of chapter 4 are used to estimate the influence of the blade row. The process will be described in the rotating frame of reference, recognizing that it is applied to a stationary blade by simply setting $\omega = 0$. The empirical models of chapter 4 supply the blade row total pressure loss coefficient and discharge relative flow angle. But the empirical models require knowledge of the discharge meridional velocity, which is not yet known. Hence, blade row performance estimates must be continually improved as part of the iterative solution procedure. Typically the process is started by assuming that $C_{m2} = C_{m1}$ on all stream surfaces. The inlet relative conditions are computed from the known upstream absolute flow conditions.

$$I_1 = H_1 - \omega(rC_\theta)_1 \quad (5-44)$$

$$W_{\theta 1} = C_{\theta 1} - r_1 \omega \quad (5-45)$$

$$W_1 = \sqrt{C_{m1}^2 + W_{\theta 1}^2} \quad (5-46)$$

$$H'_1 = h_1 + \frac{1}{2} W_1^2 \quad (5-47)$$

Other relative total conditions (e.g., P'_{t1} and T'_{t1}) can be computed from the equation of state and the known values of entropy and relative total enthalpy. At the discharge station, conservation of rothalpy requires

$$I_2 = I_1 \quad (5-48)$$

$$H'_2 = I_2 + \frac{1}{2} (r_2 \omega)^2 \quad (5-49)$$

Discharge velocity and static enthalpy are computed from the predicted discharge relative flow angle and the current estimate of C_{m2} .

$$W_2 = C_{m2} / \sin \alpha'_2 \quad (5-50)$$

$$h_2 = H'_2 - \frac{1}{2} W_2^2 \quad (5-51)$$

The ideal (no loss) discharge relative total pressure, P'_{t2id} , is computed from the equation of state, using the known discharge relative total enthalpy and the inlet entropy. Other discharge static thermodynamic conditions are obtained from the equation of state and the current estimate of the discharge entropy. Then the actual discharge relative total pressure is computed from the total pressure loss coefficient.

$$P'_{t2} = [P'_{t2id} + Y P_2] / [1 + Y] \quad (5-52)$$

The empirical models of chapter 4 for Y and α_2 are dependent on the discharge flow conditions. Hence, the presence of an upstream blade row requires use of an iterative procedure to achieve convergence on the blade row performance data and discharge flow conditions.

5.5 The Flow Profiles on a Quasi-Normal

After linking the solution to the upstream quasi-normal, the normal equilibrium equation can be solved to update the C_m distribution on the quasi-normal. Eqs. (5-50) and (5-51), the current entropy distribution and the equation of state can be used to update the discharge static conditions. Then Eq. (5-5) is solved to calculate the current mass flow on the quasi-normal. Use of the approximate normal equilibrium model allows the stream sheet pattern to be updated as part of the iterative solution on a quasi-normal. The new flow profile will generally not be consistent with the stream surface geometry used to predict it. The variation of mass flow along any quasi-normal can be easily determined in functional form using a modified form of Eq. (5-5).

$$\dot{m}(y) = 2\pi \int_0^y r\rho C_m \cos \epsilon dy \quad (5-53)$$

The interior stream surfaces must be repositioned to yield the correct fraction of the mass flow calculated for the shroud stream surface using Eq. (5-53). The actual mass flow is not used so as to avoid any influence from numerical errors in conservation of mass. This numerical calculation is governed by a specified convergence tolerance but will not yield an exact result. The correct locations of the interior stream surfaces for the computed flow field can be obtained by interpolation from this function to yield the values of y that correspond to the correct fraction of the mass flow function at y_s . These computed values of y yield the stream surface coordinates (z , r) for all stream surfaces on all quasi-normals.

$$z(y) = z_h + (z_s - z_h)(y - y_h)/(y_s - y_h) \quad (5-54)$$

$$r(y) = r_h + (r_s - r_h)(y - y_h)/(y_s - y_h) \quad (5-55)$$

Then the estimated values of ϕ and κ_m are updated by interpolation. This is a major simplification provided by the approximate normal equilibrium model. If the full normal equilibrium equation were used, the flow field throughout the turbine must be determined before stream surface slopes and curvatures are updated. This adds a major outer iteration loop that requires very sophisticated numerical damping procedures, substantially increases the computer time required and is the most common source of convergence failures. Aungier [2] shows that this more complicated approach provides virtually no benefit in terms of performance prediction accuracy.

Next C_{mc} is updated to converge on the assigned mass flow or the assigned P_c . The entire quasi-normal profile analysis is repeated until converged. In the assigned mass flow case this iteration process may also terminate with the conclusion that the flow is choked at the quasi-normal and provide the choked mass flow. When this iteration is completed, the absolute discharge flow parameters along the quasi-normal can be computed from

$$C_{\theta 2} = W_{\theta 2} + r_2 \omega = C_{m2} \cot \alpha'_2 + r_2 \omega \quad (5-56)$$

$$H_2 = I_2 + \omega(rC_\theta)_2 \quad (5-57)$$

$$C_2 = \sqrt{C_{m2}^2 + C_{\theta 2}^2} \quad (5-58)$$

The assigned mass flow case is by far the more complicated numerical problem. The objective is to converge on the assigned mass flow or to establish the choking mass flow. In the absence of an upstream blade row, this flow profile iteration procedure is quite straightforward. But the solution at a blade row

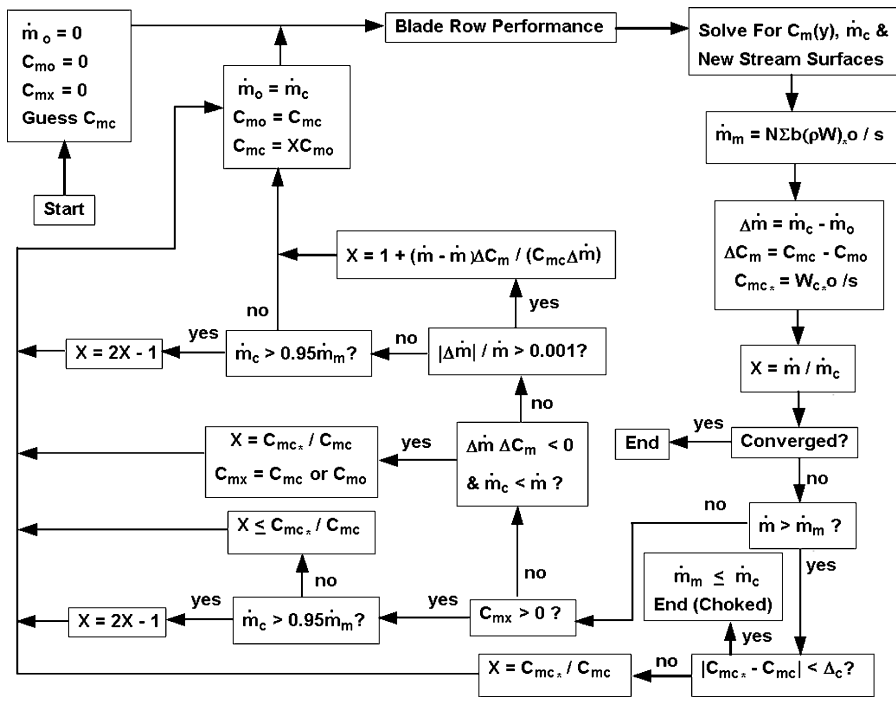


FIGURE 5-5. Assigned Mass Flow Quasi-Normal Iteration Flow Chart

discharge presents a rather complex numerical problem. This solution is always required and usually must be performed many times at each blade row exit station. Convergence on the choked flow condition is a particularly challenging convergence problem. Figure 5-5 shows a basic flow chart for an iteration procedure that has been found to be effective for this purpose. The basic problem is to find a value of C_{mc} on the mean stream surface that yields the specified mass flow rate or to establish the mass flow at which the quasi-normal is choked. In principle, Eq. (5-39) provides the choke criterion. In practice, that criterion can result in severe numerical instability problems. The basic problem is that there are a number of imbedded solution procedures that are very nonlinear and are governed by convergence criteria rather than being exact. These include the blade row performance calculations as well as the normal equilibrium and mass balance calculations. Under these conditions, estimates of the derivative in Eq. (5-39) can be quite erratic in the vicinity of choke. Results on successive iterations may contradict each other due to numerical errors, making it almost impossible to establish a reliable numerical method to converge on the fundamental choke criterion. This situation is really somewhat academic but very troublesome relative to convergence on the choke condition. If the flow is not choked, the solution procedure converges to the specified mass flow quite rapidly. What is needed is a more stable choke criterion to be used when a possible

choke is indicated. An effective criterion has been found to be local blade passage choke at the mean stream surface. From the performance models of chapter 4, the corresponding value of C_{mc} is

$$C_{mc*} = W_{c*} o / s \quad (5-59)$$

For any predicted discharge flow profile, mass flow that can pass through the blade row cannot exceed the sum of the individual stream sheet choked mass flows. If b is the stream sheet thickness and N is the number of blades in the blade row, the performance models of chapter 4 yield a maximum possible mass flow of

$$\dot{m}_m = N \sum (\rho W)_* b o / s \quad (5-60)$$

It can be seen from figure 5-5 that the criterion of Eq. (5-59) is employed when the specified mass flow exceeds this maximum. Although this criterion is not rigorous, it can be seen from figure 5-4 that the variation of mass flow with C_{mc} in the vicinity of choke is very small, so the error in the estimate of the choked mass flow should be negligible. That is the only useful output from this iteration procedure in the case of a choked blade row. A few comments may be helpful in understanding the flow chart of figure 5-5.

- The parameter C_{mx} is initialized to zero. If successive estimates show mass flow and C_{mc} varying in opposite directions, C_{mx} is set to the higher of the two values of C_{mc} . That value is known to be beyond the choke limit per Eq. (5-39). When $C_{mx} > 0$, choke is probable and the alternate choke criterion of Eq. (5-59) is used.
- Values of mass flow and C_{mc} from the previous iteration (initialized to zero) are saved. If there is no danger of a singularity, they are used to generate the next estimate of C_{mc} by linear extrapolation. Otherwise, the C_{mc} correction is a simple ratio of the specified-to-calculated mass flow.
- When the calculated mass flow is within 5% of the maximum mass flow of Eq. (5-60), the simple ratio corrections to C_{mc} result in extremely slow convergence, as can be anticipated from figure 5-4. Hence, the correction is doubled in those cases.

In the case where there is no blade row immediately upstream of the quasi-normal, the flow chart of figure 5-5 can also be applied with a few simplifications. In that case, the blade row performance calculation is not required. The maximum possible mass flow at the quasi-normal can be estimated from the annular passage choke condition that C_m is equal to the local speed of sound, i.e.,

$$\dot{m}_m = 2\pi r \sum (\rho ba) \quad (5-61)$$

Although annular passage choke is rare, it is necessary to consider that possibility. The only choke logic required for this case is to require the mass flow not exceed this maximum value. Hence, the logic to update C_{mc} is greatly simplified.

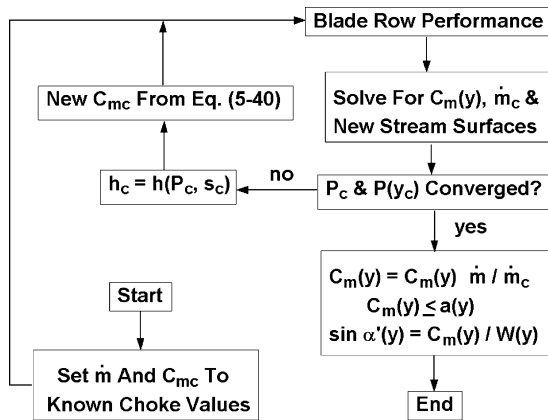
**FIGURE 5-6. Assigned P_c Iteration Flow Chart**

Figure 5-6 shows a flow chart for the simpler case where convergence on an assigned P_c is the objective. This case occurs only when the flow is choked at the quasi-normal. A previous solution with the assigned mass flow logic will have determined the mass flow and the value of C_{mc} that produced it. That value of C_{mc} is used for the first iteration. The calculated static pressure at y_c is compared to the assigned P_c and C_{mc} is updated using Eq. (5-40) until the process converges. When convergence is achieved, a final update of the relative flow angles is required to match the known choked mass flow. The supersonic deviation angle correlation of chapter 4 attempts to accomplish this, but a small additional correction is usually required. It is also prudent to impose the annular passage choke limit in the final correction. This is unlikely to ever be encountered, but it certainly is not impossible.

When a blade row lies upstream of the quasi-normal, a final update to the discharge flow profile is generally required. At this point, the discharge flow analysis has accounted for the blade row fluid turning and total pressure loss, but it has not accounted for the leakage flows or parasitic loss contributions outlined in chapter 4. Parasitic losses contribute an increase in total enthalpy, ΔH . Seal leakage and balance hole leakage may contribute an increase in mass flow relative to the blade row discharge solution. The leakage flows also will contribute a change in angular momentum. Leakage flow can be expected to have an absolute tangential velocity equal to about half of the rotation speed, $r\omega$, of the rotating wall at the seal radius for seal leakage or at the hub contour radius for balance hole leakage. Note that any change in total enthalpy due to rotor bypass leakage was included in ΔH as outlined in chapter 4. The blade row discharge flow is corrected for any seal leakage by

$$\dot{m} = \dot{m}_2 + \dot{m}_{seal} + \dot{m}_{BH} \quad (5-62)$$

The total enthalpy and angular momentum are corrected on all stream surfaces by

$$H = H_2 + \Delta H \quad (5-63)$$

$$C_\theta = [\dot{m}_2 r_2 C_{\theta 2} + (\dot{m}_{seal} r_{seal} + \dot{m}_{BH} r_{hub}) \omega / 2] / (r_2 \dot{m}) \quad (5-64)$$

Then the final discharge flow profile is computed from conservation of mass and the normal equilibrium equation, with C_θ and H treated as the known parameters in Eq. (5-23). This final update also requires an iterative solution similar to the blade row discharge solution, but it converges rapidly and presents no numerical difficulties. There is a remote possibility of an annular passage choke that needs to be considered in the iteration procedure, but this writer has never actually encountered one in this final flow profile update. Eq. (5-39) provides a criterion to check for choked flow that is valid for an annular passage choke also.

5.6 Turbine Performance Analysis

The numerical procedures described for the quasi-normal flow profile analysis may be applied in a variety of ways when analyzing the performance of an axial-flow turbine. A performance analysis for an assigned turbine mass flow has a limited range of application. Basically it is limited to turbine discharge pressures greater or equal to the value that results in choke at one quasi-normal. Since the turbine may be operated with discharge pressures lower than this value, the analysis must also be capable of operating with an assigned discharge static pressure or assigned total-to-static pressure ratio. As the turbine discharge pressure is reduced, the turbine will reach its choke limit where the flow is choked at some blade row in the turbine. With further reduction of the discharge pressure, the turbine may also choke at other blade rows. Hence, an effective turbine performance analysis must be capable of analyzing the flow through a turbine with several blade rows operating in choke.

This is undoubtedly the most formidable numerical analysis problem encountered in turbomachinery performance analysis. Indeed, that is the main reason why most multistage turbine performance analyses are one-dimensional or mean-line methods. More general hub-to-shroud through-flow methods have been formulated and used effectively. One approach is to employ a Newton-Raphson iteration technique to progressively improve estimates of P_c on all quasi-normals while matching the assigned discharge pressure and requiring that the mass flows match on all quasi-normals throughout the turbine. This results in a large number of correction equations that are solved by a matrix method. Numerical stability is a major issue, particularly for a large number of stages or when attempting to handle the various leakage flows that are commonly encountered in axial-flow turbines. Perera [60, 61] succeeded in

establishing an effective performance analysis using this approach. His analysis has been used extensively for many years with considerable success. Its substantial computer running time and reduced reliability for a large number of stages tend to limit its use on multistage turbine problems. But its major limitation is the occasional numerical failures encountered. Like most matrix methods, the cause of the numerical failure is usually unknown and the average user has no hope of resolving the problem. Indeed, even a user highly skilled in the specific numerical analysis and computer code may be unable to resolve the problem without a substantial software upgrade effort.

The approximate normal equilibrium model used here allows a more pragmatic approach that virtually eliminates the weaknesses of the more elegant matrix methods. Indeed, this model offers most of the simplifications enjoyed by mean-line methods while still providing the improved accuracy of a hub-to-shroud method. Since the flow analysis on a quasi-normal is basically independent of downstream profiles, a simple marching type solution is possible. To be sure, an iterative process will be needed to match an assigned discharge pressure, but that is a fairly trivial numerical problem.

Figure 5-7 shows a flow chart of an analysis using the approximate normal equilibrium model. The purpose is to complete an analysis for quasi-normal numbers I_1 through I_2 . This allows for the case where all quasi-normals upstream of I_1 have already been analyzed and the analysis is to stop at quasi-normal I_2 . The approximate normal equilibrium model allows this segmented analysis so long as all upstream quasi-normals have been analyzed. This allows an efficient modularized analysis structure where the module of figure 5-7 can be invoked whenever needed. The module proceeds through the quasi-normals in sequence using the flow profile analysis methods previously described in this chapter. The analysis can be accomplished for either assigned mass flow or assigned P_c . The latter option will be used only if the specific quasi-normal is choked. At each quasi-normal, a check is made to see if the flow exceeds the

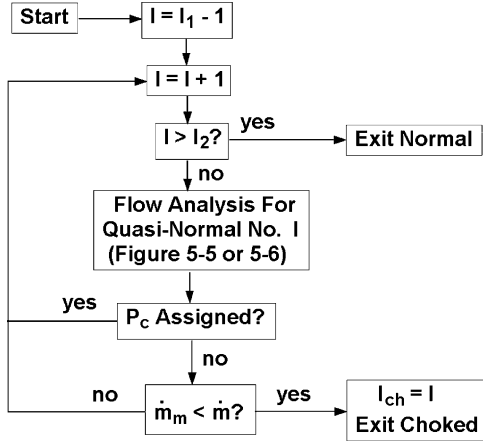


FIGURE 5-7. Flow Chart of the Basic Analysis

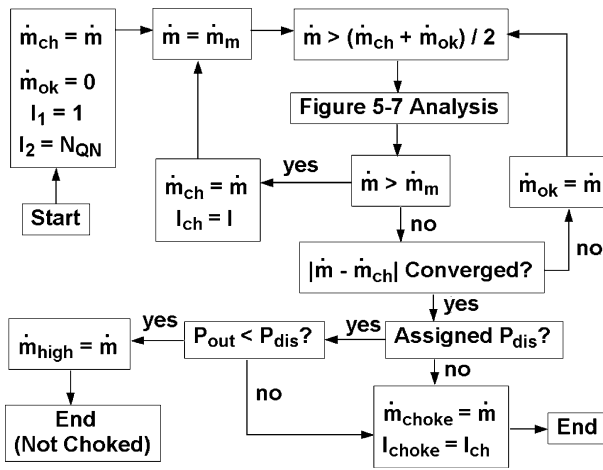


FIGURE 5-8. Flow Chart of the Choked Flow Iteration

maximum mass flow (i.e., the estimated choked mass flow). This check is omitted for the assigned P_c option, since the flow is already choked for that case and the choked mass flow is being used. Choked flow causes an exit from the module after defining which quasi-normal choked and its estimated maximum (choked) mass flow. Otherwise, a normal exit is made after all desired quasi-normals have been successfully analyzed.

When the flow chart of figure 5-7 exits due to choked flow, the choked mass flow for the turbine must be determined. Figure 5-8 shows a flow chart for that iteration process. I_1 and I_2 are set to treat all N_{QN} quasi-normals for the turbine. The mass flow that failed is known to be greater than choked mass flow and is saved. A mass flow known to be less than the choked value is initialized to zero. The iteration procedure systematically reduces the range between those limits until a successful mass flow is achieved that is within an acceptable tolerance of a choked value. That successful mass flow is the desired choked flow limit. The estimated maximum mass flow of figures 5-5 and 5-7 is also used to accelerate convergence. If the performance analysis is being conducted for an assigned mass flow, the final result from figure 5-8 completes the problem with this choked solution. But if the analysis is conducted for an assigned discharge pressure, P_{dis} , it is compared to the calculated discharge pressure, P_{out} , to determine whether the turbine is actually choked for the specified pressure. If it is not choked, the calculated choked mass flow is saved so it can be used as an upper limit on mass flow for additional iterations to converge on P_{dis} . In either case, there is never any reason to repeat this choked flow iteration procedure.

The analysis for an assigned discharge pressure requires identifying the mass flow that yields the specified discharge pressure. This requires an initial guess for the mass flow followed by an iterative process to improve that estimate until convergence is achieved. A safe initial guess is far more important than an accurate initial guess. A poor initial guess can result in immediate numerical failure before the process even gets started. A good starting point is to estimate the flow

coefficient at the exit of the first blade row, which is normally just upstream of the first rotor row. Typical values of flow coefficients for the first rotor are about 0.4 for operation near optimum efficiency. Hence, the following estimate for C_m at this location is used.

$$C_m = 0.4r_h\omega \quad (5-65)$$

The flow coefficient is evaluated at the hub radius to be conservative. It is also wise to limit this estimate by

$$0.1 \leq C_m / a_t \leq 0.5 \quad (5-66)$$

where a_t is the inlet total sound speed. The initial guess for the mass flow is calculated using this estimated C_m , the inlet total density and the local annulus area. For generality, the lower limit in Eq. (5-66) is used if the rotation speed is zero or if no blade row is present. This is an unlikely case, but it could occur if the analysis is used for evaluating an inlet passage or the first nozzle row only.

Figure 5-9 shows a flow chart of the module this writer uses when the discharge pressure is specified. It provides a complete analysis when the assigned discharge pressure is not less than the value that chokes the turbine. For

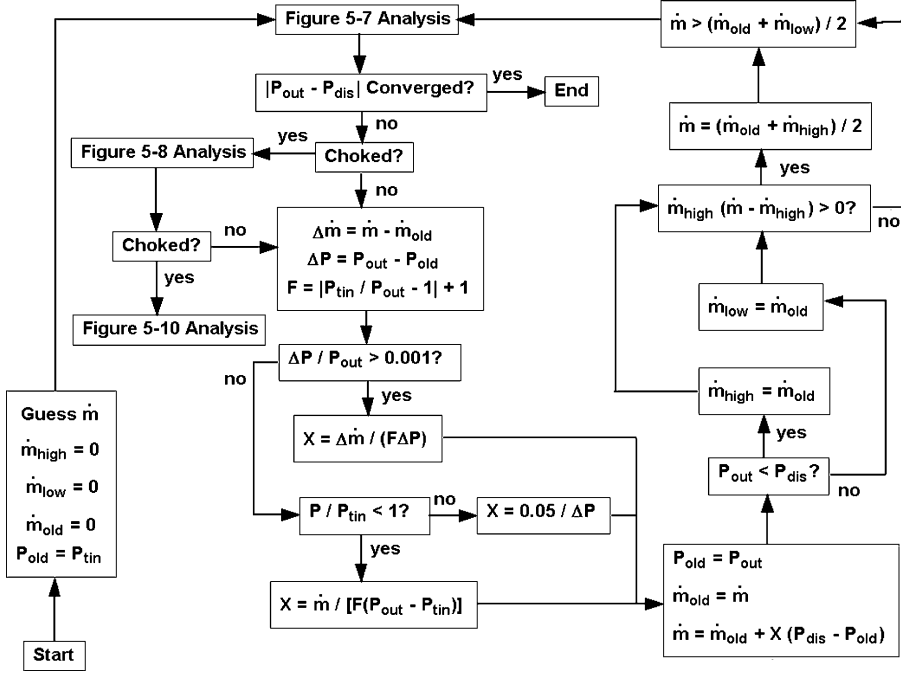
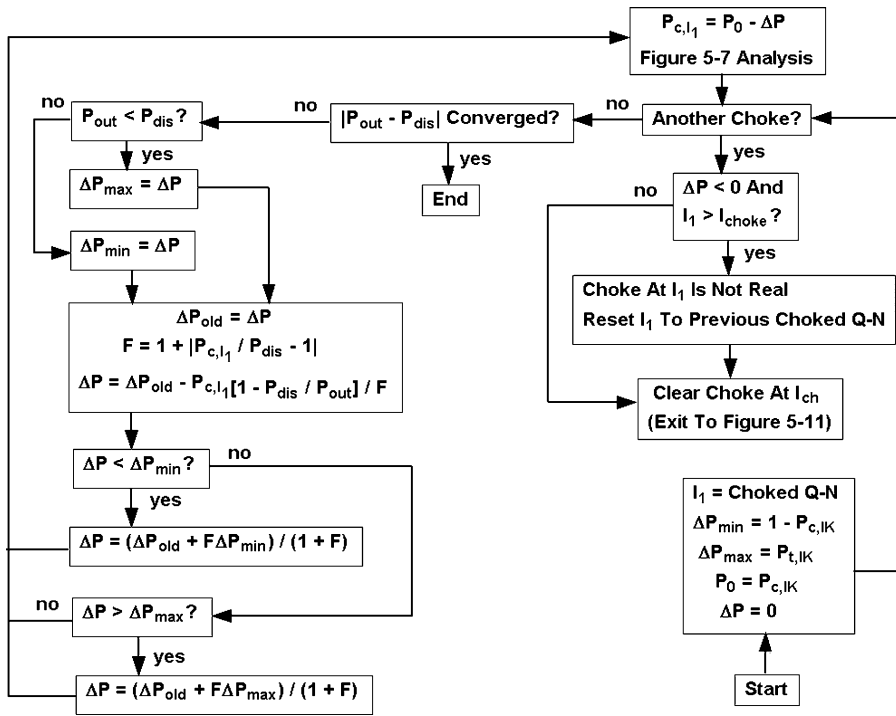


FIGURE 5-9. Flow Chart of the Assigned Discharge Pressure Iteration

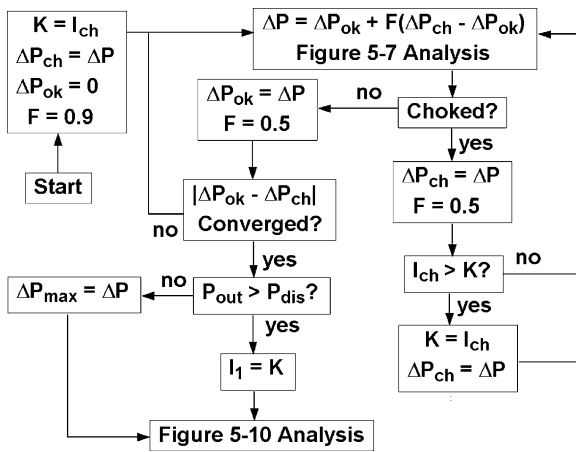
lower discharge pressures, this module starts the process until it is clear that the assigned discharge pressure is lower than the choked value. In that case, this flow chart just shows an exit to another module to be discussed subsequently in this chapter. The iterative process is based on using results for two successive mass flow estimates. It starts with the known result that a discharge pressure equal to the inlet total pressure will have a mass flow of zero. The analysis uses a minimum mass flow that is known to produce a pressure higher than the specified value, which is initialized to the same known result. The analysis also uses a maximum mass flow that yields a pressure less than the specified value is used. This is initialized to zero and is not used until some iteration produces an appropriate value. The general procedure for improving the estimate for mass flow is a simple two-point extrapolation modified by a damping factor, F . This reduces the magnitude of the correction based on the overall turbine pressure ratio. This is necessary for reliable convergence, particularly on multistage turbines where the pressure ratio can be quite large. There are two alternate correction procedures to avoid singularities or to handle situations that can not produce a valid update with the basic correction procedure. If the iteration procedure produces an indicated choke condition, control passes to the module of figure 5-8 to determine the choked mass flow. If this indicates that the turbine is not choked, it sets the maximum mass flow for the module of figure 5-9, so that the choked flow calculation will not occur more than once. If the turbine is choked, control exits from this module with the choked mass flow solution to continue using logic discussed subsequently in this chapter.

The flow charts of figures 5-7 through 5-9 are sufficient to handle all cases where mass flow is assigned and all cases where the assigned discharge pressure does not choke the turbine. When the turbine is choked, the turbine mass flow no longer changes with discharge pressure. To achieve the assigned discharge pressure, a supersonic expansion at the exit to the choked blade row is required. It is possible that this will force one or more downstream blade rows into choke also, which may require several supersonic expansions before the desired discharge pressure is produced. Use of the approximate normal equilibrium model provides an immediate simplification. The choked flow solution of figure 5-8 provides a complete solution for all quasi-normals upstream of the choked quasi-normal. Hence, I_1 of figure 5-7 can be set to the choked quasi-normal number as the starting point for subsequent iterations. The solution at the choked quasi-normal will employ the assigned P_c logic of figure 5-6. Downstream quasi-normals will use the assigned mass flow logic of figure 5-5. The mass flow will be constant except as modified by leakage flows or mass flows specifically inserted or extracted from the turbine. Hence, the solution can be continued using the modules that are flowcharted in figures 5-6 and 5-7.

Figure 5-10 shows a flow chart of a module to treat this supersonic expansion calculation. This is a generalized procedure capable of handling any choked blade row, in case more than one blade row is choked. The logic of figure 5-8 defines the turbine's primary choke location precisely. If the logic of figure 5-7 indicates another choke, it is not certain that it is a real choke. Further analysis may show that the secondary choke indication is simply due to a poor estimate of the expansion pressure for the choked blade row being treated. It may also show that the secondary choke occurs in a blade row further downstream

**FIGURE 5-10. Flow Chart of the Supersonic Expansion Iteration**

than the one first indicated. The latter issue means that it is possible that the choked quasi-normal being treated by the logic of figure 5-10 may not actually be choked. The approach taken is to impose a pressure drop, ΔP , on the reference stream-surface pressure, P_0 , which precisely causes the blade row to choke. Since it is not certain that the blade row is choked, the procedure must allow for negative values of ΔP . I_1 is set to the choked quasi-normal as the starting point for the logic of figure 5-7. The pressure is extracted from the choked solution, which will be available when starting this procedure. Initial values are supplied to maximum and minimum limits for ΔP . These are extreme values that clearly can not be exceeded, including the possibility of negative values. Initially, ΔP is set to zero, which corresponds to the resident solution when this module is entered. Hence, the first iteration can bypass the logic of figure 5-7. On subsequent iterations, station I_1 is treated with the assigned P_c logic. Other downstream quasi-normals are treated with the assigned mass flow option, using the known choked mass flow. The maximum and minimum limits for ΔP can be updated based on a comparison of the calculated and specified values of the turbine discharge pressure. A new estimate is made for ΔP for the next iteration, using a damped correction procedure that has been found to be quite effective for this purpose. If no downstream choke is encountered, the

**FIGURE 5-11. Choke Clearing Operation Flow Chart**

logic of figure 5-10 completes the performance analysis by converging on the specified turbine discharge pressure.

However, the logic of figure 5-7 may return an indication of a downstream choke at quasi-normal number I_{ch} . If that occurs, it is necessary to check for a false choke indication on station I_1 . If this is not the primary choke and ΔP is negative, this station is not actually choked. In other words, choke occurs at a downstream blade row before it occurs in this one. In that case, I_1 is reset to the upstream quasi-normal were choke was previously located. The procedure then exits to determine if the downstream quasi-normal is actually choked. That process will be referred to as a choke clearing operation. Figure 5-11 shows a flow chart of that process. The purpose is to determine the value of ΔP at quasi-normal I_1 that results in choke at the downstream quasi-normal. The downstream quasi-normal number is saved as K . On entry, the resident value of ΔP choked quasi-normal K , which provides an initial value for the upper limit, ΔP_{ch} . It is also known that $\Delta P = 0$ did not choke quasi-normal K , which is an initial value for the lower limit, ΔP_{ok} . If quasi-normal K is actually choked, the value of ΔP that at the onset of choke is between these limits. A very simple iteration procedure is used to systematically reduce the range between these limits to converge on this value of ΔP . If the analysis of figure 5-7 results in choke, ΔP_{ch} is reset to the current ΔP . If the choke occurred at quasi-normal K , the iteration procedure continues. If the choke occurred downstream of K , that station chokes before quasi-normal K , so K is reset before continuing the iteration procedure. If no choke is encountered, ΔP_{ok} is reset to ΔP and the iteration procedure continues. When convergence is achieved, the current value of ΔP is essentially the value at the onset of choke in quasi-normal K , but a complete solution for the turbine has been generated. If the resulting value of the discharge pressure exceeds the specified value, then quasi-normal K is choked and the solution for all quasi-normals upstream of it is complete. I_1 is reset to K and control returns to

the module of figure 5-10 to continue the iteration for the specified discharge pressure. Otherwise, quasi-normal K is not choked and a new upper limit, ΔP_{\max} , is defined before returning to the discharge pressure iteration procedure of figure 5-10. The logic of figures 5-10 and 5-11 provides the capability to converge on the specified discharge pressure even when several blade rows are choked.

The flow charts in figures 5-5 through 5-11 provide a very systematic procedure for the performance analysis of axial-flow turbines. In principle, the various alternatives that may occur have been considered to provide rapid and reliable convergence. In practice, there are some subtle reliability issues that need to be considered. There are a very large number of iterative procedures involved in this process. These procedures all are subject to convergence tolerances such that none of them provide exact results. The cumulative effect of the many approximate solutions involved can produce unexpected and unpredictable numerical problems. These will vary depending on how the various iterative procedures are nested, what convergence tolerances are imposed and how those tolerances interact. The development of a performance analysis following the process described in this chapter is likely to require addressing some additional numerical reliability issues that will be very dependent on the precise way the process is implemented. Most of these issues are related to the process of identifying choke conditions. The blade row analysis seeks to determine the value of C_{mc} that corresponds to choke. Otherwise acceptable numerical errors can cause a false indication of a negative slope on the mass flow curve of figure 5-4. This is not very significant in an absolute sense, since figure 5-4 shows that mass flow is very insensitive to variations in C_{mc} around the choke condition. If the analysis is configured to recognize these situations, some very annoying convergence failures can be avoided. Some of the reliability issues to be expected are listed below, along with general approaches that can be used in resolving them.

- Under appropriate conditions, annulus choking may preclude carrying out the choked blade row logic outlined in this chapter. An obvious example can be cited for the last blade row in the turbine. For a sufficiently low specified turbine discharge pressure, an annulus choke after the last blade row will preclude matching that pressure. This can also occur for other blade rows, although that is less common. Annulus choking should always be recognized as a possibility. It is much better to terminate the solution with an annulus choke message than to encounter unexplained convergence failures.
- Many of the iterative procedures outlined in this chapter rely on calculating specific limits to an acceptable range of values. It is always possible to have interaction of numerical errors in the various nested iteration procedures that produce false values of these limits. When this happens, the range of acceptable values will approach zero. This will require working off of one of the limits in small steps (e.g., the local convergence tolerance) while ignoring the other limit. It is usually obvious which limit should be used and which one should be ignored. For example, when iterating on a choke condition, maintain the choke limit to the range and back off from it in small steps until an unchoked solution is obtained.

- The logic for imposing an expansion pressure shown in figure 5-10 should always allow for the possibility of a negative ΔP . This is an effective way to address the minor uncertainties with regard to the choke estimates. Since the choked mass flow estimate will be quite accurate, simply allowing ΔP to be negative will provide an acceptable approximation in those cases.
- When the discharge pressure is assigned and the choke logic of figure 5-8 indicates the flow is not choked, the upper mass flow limit is reset to prevent encountering a second indication of choke. Again, numerical errors can compromise this step when the turbine is operating very close to its choke limit. This situation can be recognized by a repeat of the figure 5-8 logic and a second conclusion that the turbine is not choked. In this case, define the last quasi-normal of the turbine as choked and complete the solution. Since ΔP is allowed to be negative in the logic of figure 5-10, this will properly complete the analysis.
- Under appropriate conditions, shroud seal or diaphragm shaft seal leakage across a blade row may be reversed to flow from the discharge to the inlet. That produces a very unstable influence on the blade row performance calculations. Leakage flows in the reverse direction have much less influence on performance than the normal leakage flows. Indeed, the numerical instability problems are associated with the leakage flow changing direction on successive iterations. This writer simply ignores the leakage effect on the blade row performance if the leakage flow is directed upstream. It is not considered worthwhile to accept the strong tendency toward instability considering the limited impact on performance.
- When the obvious reliability issues have been addressed, convergence failures will be very rare, but the possibility of numerical errors causing a convergence failure cannot be totally eliminated. Often the problem can be resolved by simply changing the solution's path to convergence. Sometimes this is as simple as just immediately repeating the same problem. Similarly, a very slight and insignificant change to the operating conditions analyzed will often produce a stable solution.

The effectiveness of the performance analysis can be greatly enhanced by including the following features and options.

- The iterative solutions outlined in figures 5-8 through 5-11 should supply a one-line summary on the monitor screen giving the iteration number, type of iteration and convergence status. It is also useful to provide a one-line summary of the number of iterations, numerical errors and key performance data from the most recent performance solution obtained at each blade-row exit. These can be provided in separate windows such that either is available to the user. These are extremely valuable while optimizing the analysis and addressing the numerical reliability issues discussed previously. They also clarify any problems encountered if a converged solution is not obtained.
- Specify a limit for the number of iterations for the analyses of figures 5-8 through 5-11. When one of these limits is exceeded, pause the solution so the user can review the convergence history to decide whether to continue

or terminate the performance analysis. The user should have the option of modifying these limits and the convergence tolerances to be used. The most recent entries should be stored by the computer to be used for future runs. User specification of these data should be optional. It is also useful to provide the user with the option to pause any of the various iterative solutions after convergence to view the convergence history.

- Provision for output files to be viewed on the monitor screen or printed are major enhancements. Absolute and relative data for all quasi-normals, blade row performance data, stage performance data, blade force data and overall turbine performance data are the typical output blocks that will be needed. It is often preferred to generate these output files during the analysis rather than store all the data in memory until the overall solution is completed. Use of the approximate normal equilibrium model makes this approach quite practical. A review of the procedures used shows that it is always clear when the solution at a quasi-normal is complete. For example, once it is known that a quasi-normal is choked, the solution at all upstream quasi-normals is complete. It is only necessary to repeat the solution of those quasi-normals, specifying that output is to be supplied. That is simpler than might be expected. The result from the primary iteration is already known (C_{mc} and possibly P_c), so the solution process at a quasi-normal becomes rather trivial. Also, output blocks will include data not needed for the basic analysis, such as efficiencies, blade forces, etc. Avoiding the need to generate those data during the basic analysis is likely to more than compensate for the simplified repetition. Another benefit is that results from all completed quasi-normals will be available for viewing in the event that the overall analysis does not converge.
- A general performance map utility is a very valuable enhancement. The user should have the option to save results from any performance analysis conducted for use by the performance map utility. This should include a caption to identify separate performance characteristics to be mapped. Provision for the various desired alternative map styles should be included. The user should also be able to input specific test data points when available. The user will also need the option to delete or edit any points in the map data. Map data can be saved in a separate map file or in the basic input file for the case being considered. The user should be able to view the maps on the monitor screen or print them. Development of the basic map utility does require some effort, but the benefits easily justify that effort. It can also be developed as a general module to be used for several applications. This writer uses the same map utility module for centrifugal compressors, axial-flow compressors, radial-inflow turbines and axial-flow turbines.
- It is useful to provide for alternate specifications of the operating conditions. Necessary alternatives include mass flow rate and discharge static pressure or total-to-static pressure ratio. It is useful to specify a conversion for an equivalent mass flow also. Providing the ratio of equivalent mass flow-to-actual mass flow is recommended since many different definitions of equivalent mass flow are encountered. When discharge pressure is supplied, the option to enter the mean total-to-static velocity ratio,

v , is a useful alternative to specifying the rotation speed. It is useful to specify a conversion for an equivalent speed, which can be handled similar to the mass flow conversion. This writer's performance analysis accepts the equivalence ratios to be entered as zero to default to the true sonic flow equivalence parameters discussed in chapter 1.

- The number of stream surfaces to be considered should be arbitrary. It is a good idea to restrict this specification to an odd number so that the mean stream surface corresponds to 50% of the total mass flow. This provides the best definitions for C_{mc} and P_c . Options to use the approximate normal equilibrium model or to simply ignore stream surface curvature effects should be included.
- Provision to include labyrinth seals at the high and low-pressure ends of the turbine is often useful. This must include the exterior seal pressures and temperatures for computing the seal leakage flows. Provision to impose an inlet control valve pressure drop and an exhaust-end total pressure loss coefficient are useful features that permit including the effects of components not directly modeled by the performance analysis.

5.7 Typical Performance Analysis Results

The available non-proprietary axial-flow turbine experimental performance data is extremely limited, but a few examples have appeared in the open literature. Figures 5-12 and 5-13 show a comparison of predictions and experimental performance for a turbine stage designed and tested at the Technical University

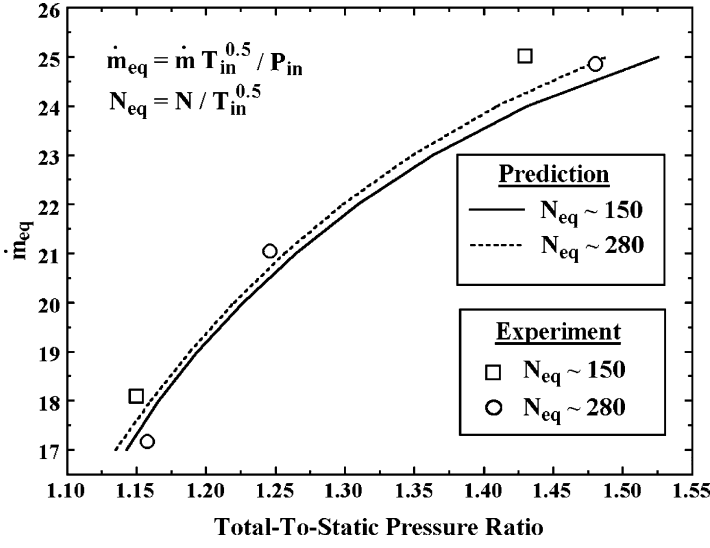


FIGURE 5-12. Hannover Stage Mass Flow Data

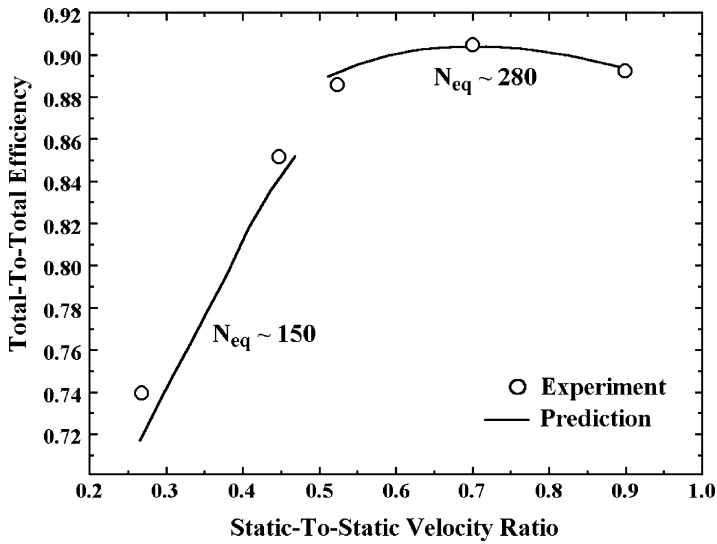
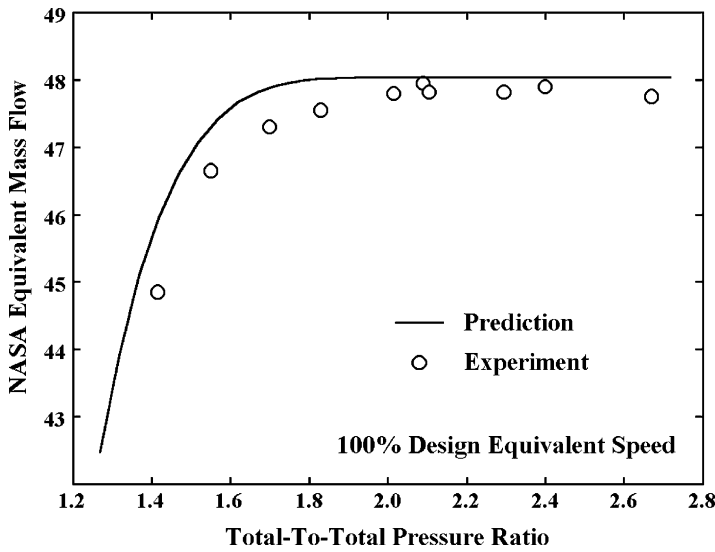


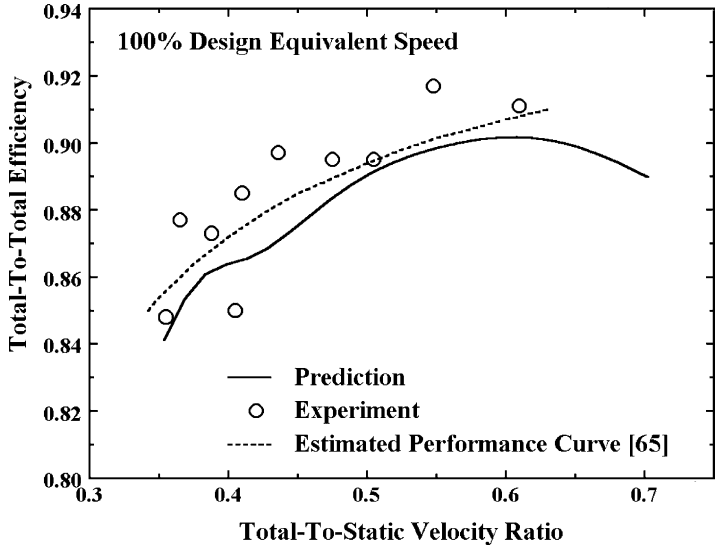
FIGURE 5-13. Hannover Stage Efficiency Data

of Hannover. The design and experimental data were obtained from Hirsch and Denton [62], but originate from a doctoral dissertation by Groschup [63]. The stage is basically a free-vortex design for a pitch line reaction of 50%, which results in a highly twisted rotor blade. The stage was tested using low-pressure air as the working fluid. Test data are reported for nominally two different equivalent speeds. The equivalence definitions used are summarized in figure 5-12. The Mach number levels for all operating points are quite modest for this stage. Hence, it would be expected that the equivalent mass flow versus pressure ratio characteristics for the two equivalent speeds would be nearly identical, which is consistent with the predictions. Agreement with experiment is reasonably good, although the experimental trend with equivalent speed appears to be opposite to the predictions and greater in magnitude. The predicted and experimental efficiencies show excellent agreement at the higher equivalent speed, where the stage operates reasonably close to its optimum conditions. The predicted efficiencies at the lower equivalent speed show a larger deviation from experiment, particularly at the far off-design point. Overall, the accuracy of the present performance analysis is considered to be quite satisfactory for this turbine stage.

Figures 5-14 and 5-15 show comparisons of predicted and experimental performance for a turbine stage reported by Lueders [64, 65]. This stage was designed and tested by the Allison Division of General Motors for the NASA Lewis Research Center. The intended purpose of this stage was for use as a base line for subsequent experimental investigations of advanced concepts to increase rotor blade loading (vortex generators, etc.). To this end, the stage design features very high suction surface diffusion and negative reaction. Performance data are presented using NASA equivalence format referenced to standard sea level air conditions. Several equivalent speeds were tested, but the limited

**FIGURE 5-14. NASA Stage Mass Flow Data**

number of data points and the large data scatter makes it very difficult to identify meaningful trends with variations in equivalent speed. Hence, comparison is made for the design equivalent speed only. The mass flow comparison in figure 5-14 was complicated by the need to rework the nozzle blades during the test phase. This was accomplished after an experimental calibration of

**FIGURE 5-15. NASA Stage Efficiency Data**

the nozzle flow capacity but before the performance tests were accomplished. This resulted in a 4.2% increase in flow capacity that was attributed to nozzle blade distortion [65]. To compensate for this, the design nozzle throat openings were artificially increased by 4.2% for the predictions. Although an increase in throat area of this magnitude undoubtedly occurred, it seems unlikely that the increase was uniform along the entire blade span. Considering this uncertainty, agreement between the predicted and experimental mass flow characteristics is considered to be quite satisfactory. The comparison of efficiency data in figure 5-15 is obscured by the test uncertainty as evidenced by the substantial scatter in the experimental data. An estimated test curve that is provided in Lueders [65] is included in the figure. The predictions appear to consistently underestimate the efficiency, but they do agree with the estimated test curve within about one percentage point over the velocity ratio range it covers. The abrupt reduction in predicted efficiency near the low end of the velocity ratio range is associated with a second choke in the rotor row, such that both blade rows are choked.

Figures 5-16 and 5-17 show a comparison of predicted and experimental performance for a two-stage turbine reported by Welna and Dahlberg [66]. The experimental performance curves are curve fits of experimental data points. These curve fits are provided in figures 75 and 83 of reference [66]. This turbine development program was a demonstration of a high-work, low-pressure fan-drive turbine, featuring controlled-vortex designs with high aspect ratio, shrouded rotor blades. This turbine successfully achieved about 50% higher work as well as higher efficiencies than would be expected from a similar free-vortex design. At design speed ($N_{eq} = 245$), the predicted primary turbine choke initially occurs in the first stage nozzle but then switches to the second stage rotor as pressure ratio increases. As seen in figure 5-16, the agreement between the predicted and

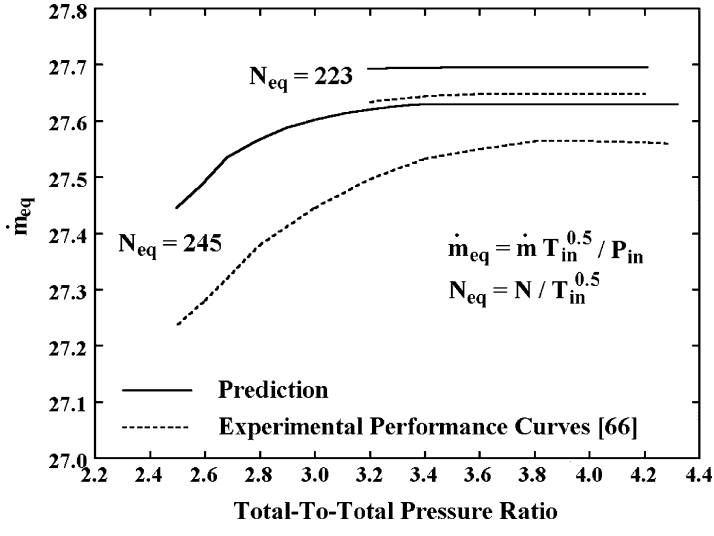


FIGURE 5-16. Two-Stage Turbine Mass Flow Data

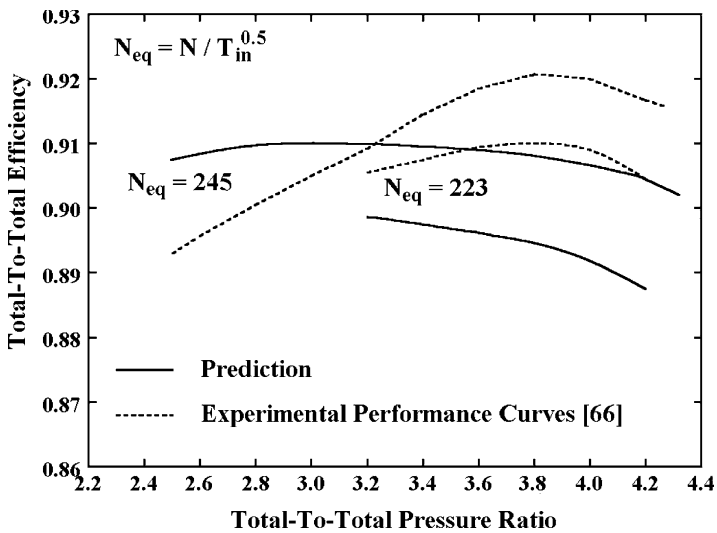


FIGURE 5-17. Two-Stage Turbine Efficiency Data

experimental mass flow characteristics is well within 1% over the entire pressure-ratio range. The overall agreement between the predicted and experimental efficiency levels shown in figure 5-17 is reasonably good, considering that the test data point scatter shown in the reference is on the order of 0.008. However, the predicted and experimental efficiency characteristics differ with regard to their trends with pressure ratio.

The prediction accuracy seen for these three turbines is typical of results that have been observed on other comparisons of predicted and experimental performance involving proprietary turbine stage designs. It is also worthy of note that these three turbines emphasize design features quite different from the cascade data and turbine data used as a basis for the development and validation of the empirical performance models presented in chapter 4. Indeed, these three turbines were developed with the intention of extending design technology beyond the existing state of the art. This resulted in stage designs that deviated significantly from design practices that were well established by past experience.

5.8 Diaphragm-Disk Rotor Leakage Flows

The diaphragm-disk style rotor construction requires special treatment with regard to leakage flows. As shown in figure 5-18, there are potentially three leakage paths that communicate with the diaphragm-disk clearance gap. Each of the three leakage flows can be calculated using methods presented in chapter 4 if the clearance gap pressure, P_g , is known. When leakage flows are directed out of the gap, the clearance gap total enthalpy, H_g , is also required, since it affects the gas stream that receives the leakage flow. The convention used for positive

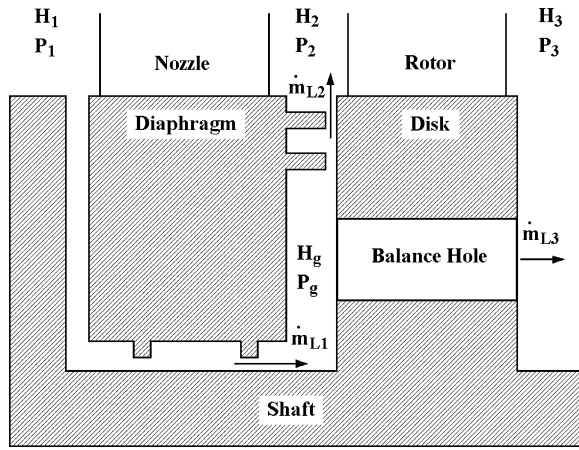


FIGURE 5-18. Diaphragm-Disk Leakage

leakage for the three potential leakage flows is shown in figure 5-18. Since the gap thermodynamic conditions depend on the combined effects of all leakage flows, an iterative procedure is required to compute them. The net leakage flow is given by

$$\dot{m}_g = \dot{m}_{L1} - \dot{m}_{L2} - \dot{m}_{L3} \quad (5-67)$$

An iterative procedure is required to calculate the gap thermodynamic conditions that reduce this net leakage flow to zero (within an acceptable tolerance) to conserve mass. The leakage flow models in chapter 4 all express leakage as proportional to the relevant pressure difference. Hence

$$\dot{m}_{L1} = K_1(P_1 - P_g) \quad (5-68)$$

$$\dot{m}_{L2} = K_2(P_g - P_2) \quad (5-69)$$

$$\dot{m}_{L3} = K_3(P_g - P_3) \quad (5-70)$$

When leakage flows have been calculated from a resident value of P_g , the constants K_1 , K_2 , and K_3 can be calculated from Eqs. (5-68) through (5-70). Differentiating Eq. (5-67) and simplifying with Eqs. (5-68) through (5-70) yields

$$\frac{\partial \dot{m}_g}{\partial P_g} = -K_1 + K_2 + K_3 \quad (5-71)$$

This provides an estimate of the corrected gap pressure required by conservation of mass for use on the next iteration.

$$P_g \rightarrow P_g - \dot{m}_g / (K_2 + K_3 - K_1) \quad (5-72)$$

The gap total enthalpy is given by a mass average of all leakage total enthalpies for which leakage flows enter the clearance gap. Cases where there are no balance holes or no disk rim seals simplify the iteration procedure. So, some care is required in formulating the iterative procedure to include provision for the various simplifications that may exist.

A rigorous treatment of the influence of diaphragm-disk clearance gap leakage effects on all blade rows would substantially complicate the performance analysis to a point that it would become almost unmanageable. Fortunately, that is not necessary if proper use is made of the flow profile update procedure discussed in section 5.5 of this chapter using Eqs. (5-62) through (5-64). The major effect of gap leakage on turbine performance is to impose corrections on conservation of mass and energy at key quasi-normals. It is possible to account for these corrections by conducting the clearance gap iteration procedure along with the basic performance analysis for quasi-normals at rotor row exits. The basic approach is to ignore the shaft leakage while conducting nozzle row exit quasi-normal analyses. For each rotor exit quasi-normal, the following steps are required:

- Perform a preliminary analysis ignoring gap leakage effects.
- Conduct the gap leakage iteration procedure including calculation of all leakage flows. Balance hole leakage and total enthalpy from the upstream rotor (if any) must be saved in memory and used to correct the shaft leakage total enthalpy.
- Next perform a flow profile update at the rotor inlet quasi-normal. Except for the first stage, shaft leakage comes from the nozzle inlet, so remove it from the rotor inlet mass flow before applying this update (which will add it back in, along with the corresponding total enthalpy correction).
- Now repeat the analysis at the rotor exit with balance hole leakage included.

Special handling of the first-stage analysis is required to account for the shaft seal leakage. The turbine inlet seal leakage may not originate from the nozzle inlet. Hence the shaft leakage flow and its total enthalpy may require special treatment. Note that this approach involves a special use of the flow profile update procedure discussed in section 5.5. That update procedure is always applied to quasi-normals at all blade row exits, but here it is needed for a blade row inlet quasi-normal. Hence, this update procedure should be programmed as a separate routine rather than combined with the quasi-normal analysis.

5.9 Blade Forces and Rotor Thrust

A hub-to-shroud performance analysis is well suited for calculating aerodynamic forces for use in evaluating the mechanical integrity of the blades and for sizing thrust bearings. Forces and bending moments acting on blades are often needed as well as the thrust force imposed on the rotor. The distribution of the blade forces per unit length can be calculated from conservation of momentum by noting that the blade force must balance the change in momentum. If N_{ss}

is the number of stream surfaces from hub to shroud, the stream sheet mass flow is

$$\Delta\dot{m} = \dot{m}/(N_{ss} - 1) \quad (5-73)$$

If r is the stream sheet radius and ε is the arc of admission, the local frontal area, A , and radial height, b , of the stream sheet are given by

$$A = \Delta\dot{m}/(\rho C_z) \quad (5-74)$$

$$b = A/(2\pi r\varepsilon)$$

If N is the number of blades in the blade row, the axial and tangential forces per unit length on each blade in the arc of admission are given by

$$f_z = 2[\Delta\dot{m}(C_{z1} - C_{z2}) - P_2 A_2 + P_1 A_1 + (P_2 + P_1)(A_2 - A_1)]/[\varepsilon N(b_1 + b_2)] \quad (5-75)$$

$$f_\theta = 2\Delta\dot{m}[C_{\theta 2} - C_{\theta 1}]/[\varepsilon N(b_1 + b_2)] \quad (5-76)$$

If r_0 is the location where the bending moments are zero (e.g., the free end of a cantilevered blade) and an overbar denotes an average of blade row inlet and discharge values, the bending moments are given by

$$M_z(\bar{r}) = \int_{\bar{r}_h}^{\bar{r}} f_z(\bar{r})[\bar{r}_0 - \bar{r}] d\bar{r} \quad (5-77)$$

$$M_\theta(\bar{r}) = \int_{\bar{r}_h}^{\bar{r}} f_\theta(\bar{r})[\bar{r}_0 - \bar{r}] d\bar{r} \quad (5-78)$$

The contribution of rotor blade axial forces to the rotor thrust force is given by

$$F_z = N\varepsilon \int_{\bar{r}_h}^{\bar{r}_s} f_z(\bar{r}) d\bar{r} \quad (5-79)$$

For diaphragm-disk style rotors, the thrust force contributions on the disk faces must also be calculated. The active disk face area is given by

$$A = \pi(r_h^2 - r_{shaft}^2) \quad (5-80)$$

Assuming that the tangential velocity in the disk clearance gap region is equal to one-half the local rotation speed, the pressure distribution along a disk face

can be estimated from a simple forced vortex relation, i.e.,

$$\frac{\partial P}{\partial r} = \frac{1}{4} \rho \omega^2 r \quad (5-81)$$

Hence, the average pressure on the disk face is given by

$$\bar{P} = P_h + \frac{1}{16} \rho \omega^2 (r_{shaft}^2 - r_h^2) \quad (5-82)$$

If a disk rim seal is present, P_h must be modified by the seal pressure ratio. When dealing with a simple full-admission rotor without balance holes, the disk force contribution to the rotor thrust is given by

$$\Delta F_z = \bar{P}_1 A_1 - \bar{P}_2 A_2 \quad (5-83)$$

The effect of balance holes is to ingest swirling fluid from the main stream on the high-pressure side of the disk. The additional angular momentum and the radial inflow will modify the pressure gradient in Eq. (5-81) to reduce the average pressure on the high-pressure disk face. This is similar to the covered impeller leakage flow problem in centrifugal compressors. Aungier [1] developed a model for that problem, where the clearance gap flow is axisymmetric. However, this writer is unaware of any empirical model to account for this basic mechanism for the nonaxisymmetric balance hole problem. One approach used is to impose an empirical multiplying factor on the disk force contribution when balance holes are used. Clearly, this empirical factor will depend on the organization's specific design practice relative to balance holes. This writer is not aware of a method to estimate this empirical factor that has sufficient validation to be recommended for general use.

Partial admission operation is another area of major uncertainty. Clearly, the pressure difference across a blade row passage having no mass flow must be essentially zero. It is by no means obvious how this alters the circumferential pressure distribution in the clearance gap. The clearance gap pressure clearly must match the hub pressure at the rim of the disk, so about the best that can be done is to assume the pressure difference across the disk is zero over some fraction of the inactive arc. An important exception to this approximation is the case of rotor shielding as illustrated in figure 4-16. When rotor shielding is present the assumption that there is no pressure difference across the rim of the disk is no longer relevant, since a physical barrier is present to sustain a pressure difference. In this case, the most logical assumption is that the pressure in the upstream and downstream gaps will be circumferentially uniform. Hence, if ζ is the rotor shielding arc, the disk contribution to the rotor thrust force can be expressed as

$$\Delta F_z = K_{BH} [\bar{P}_1 A_1 - \bar{P}_2 A_2] [1 - K_{adm} (\varepsilon - \zeta)] \quad (5-84)$$

This writer uses $K_{adm} = 1$ for lack of a better assumption, which is consistent with the blade force model above. K_{BH} is an empirical factor to account for balance hole effects. $K_{BH} = 1$ if balance holes are not used and $K_{BH} < 1$ when balance holes are present. In the absence of better guidance, the empirical model for the centrifugal compressor covered impeller problem is about the only available guidance. Considering the large with-rotation swirl typical of nozzle exit flows, K_{BH} in the range of 0.5 to 0.7 might be reasonable choices when balance holes are present. The total thrust force on the rotor is obtained by summing the thrust forces on all rotor rows, i.e.,

$$T = \sum (F_z + \Delta F_z) \quad (5-85)$$

Modern viscous flow computational fluid dynamics (CFD) codes are commonly used today to address uncertainties of the type encountered here. A CFD investigation into partial admission would require a massive number of computational nodes. It would be necessary to model all blade passages and both disk cavities. Considering the large number of blades in a typical axial-flow turbine blade row, very few organizations have sufficient computer power to handle a problem of that magnitude. This writer did authorize one serious CFD investigation into the balance hole issue. After repeated attempts failed to produce a converged solution, that investigation was finally abandoned. This writer also participated in an effort to establish the empirical constants in Eq. (5-84) using thrust measurements from multistage turbines. This was unsuccessful due to a lack of sufficient good-quality data to arrive at values with any reasonable degree of confidence. Both of these issues require experimental investigation to arrive at a more suitable model. It is likely that proprietary experimental investigations of that type have been conducted. But this writer has not had access to any results of that type nor been able to locate anything relevant in the open literature.

5.10 Concluding Remarks

This chapter provides a very efficient hub-to-shroud aerodynamic performance analysis for axial-flow turbines. The approximate normal equilibrium model has been used to decouple the local flow profile analysis at any axial computing station from the downstream flow solution. This results in a hub-to-shroud performance analysis offering computer running times and reliability comparable to a mean-line performance analysis. It also retains the capability to consider significant stream surface curvature effects imposed by the shape of the end-wall contours. This approach permits the use of a very pragmatic numerical approach that marches the solution through the turbine while systematically addressing choked flow at any number of blade rows. The overall numerical approach has been presented along with specific suggestions for optimizing a specific computer code to deal with convergence issues that will depend on the precise method of implementation.

This approach greatly simplifies maintenance of a computer code when unanticipated situations produce convergence problems. If properly implemented, users can track progress to convergence to immediately identify where the problem occurs and usually why it occurred. When maintenance is required, the user's corrective action centers on a very small portion of the overall analysis, which follows a systematic procedure that is focused on the specific problem area. Hence, effective maintenance activity can be accomplished without an in-depth knowledge of the complete numerical analysis and computer code. Although the vast majority of convergence issues can be resolved during the optimization process, experienced analysts know that the unanticipated problem always occurs at the worst possible time. A significant advantage of this approach is that the casual user can take effective corrective action when necessary. Experience with more elegant and complex numerical approaches to this problem has shown this to be a significant weakness. Too often they leave the user with a failed solution on a critical problem with no practical means for timely resolution.

Comparison of predicted performance with experimental data has shown very good prediction accuracy on some rather challenging problems. It has been applied to many proprietary turbine stages and multistage turbines with similar success. This writer's performance analysis is implemented for interactive use on personal computers. The efficiency of a code optimized to the procedures presented in this chapter is quite sufficient to support that implementation strategy on almost any personal computer in use today.

Chapter 6

PRELIMINARY AERODYNAMIC DESIGN OF AXIAL-FLOW TURBINE STAGES

The aerodynamic design of an axial-flow turbine stage can be conveniently accomplished in a series of well-defined steps. First a preliminary design is accomplished to define the basic stage characteristics such as the stage flow coefficient, work coefficient, reaction and nozzle exit swirl vortex type. In this phase, standard efficiency chart estimates are used to approximate the stage performance. Flow profiles are computed using the simple normal equilibrium model to identify the fluid turning required in the nozzle and rotor to achieve the desired performance. When a preliminary design is configured, its geometry is exported to an input file for the performance analysis of chapter 5 for a more thorough evaluation of its performance characteristics. Some iteration will normally be necessary to obtain a preliminary design that yields satisfactory performance. Then the basic blade characteristics matching the fluid turning requirements are exported from the preliminary design system to the detailed airfoil design system of chapter 7 to design a series of constant-radius airfoil sections and stack them to define the nozzle and rotor blades. The detailed geometry of these blades is exported from the airfoil design system to update the input file for the performance analysis to accomplish a more precise performance analysis.

NOMENCLATURE

- A = annulus area
- a = sound speed
- b_z = blade axial chord
- C = absolute velocity
- C_o = spouting velocity
- c = chord
- H = total enthalpy
- h = static enthalpy and blade height
- I = rothalpy
- M = Mach Number
- m = mass flow rate

N = number of blades and rotation speed (rpm)
 n = normal coordinate
 o = blade passage throat width
 P = pressure
 R_c = stage reaction
 r = radius
 r_c = design radius
 s = blade pitch and specific entropy
 T = temperature; also rotor thrust force
 t_{\max} = blade maximum thickness
 t_2 = blade trailing edge thickness
 U = blade speed = $r\omega$
 W = relative velocity
 y = coordinate along a quasi-normal
 z = axial coordinate
 α = flow angle with respect to tangent
 β = blade angle with respect to tangent
 β_g = blade gauging angle with respect to tangent
 δ = deviation angle; also blade tip or seal clearance
 ε = angle between a quasi-normal and a true normal
 γ = blade setting angle
 η = stage total-to-total efficiency
 η_s = stage total-to-static efficiency
 θ = polar angle
 λ = blade tangential force coefficient
 v = velocity ratio = U/C_0
 ξ = $(90^\circ - \beta_1)/(90^\circ - \alpha_2)$
 ρ = gas density
 ϕ_c = stage flow coefficient
 ψ_c = stage work coefficient
 ω = rotation speed

Subscripts

c = value of a parameter at the design radius
 h = hub parameter
 m = meridional component or a mean value
 n = nozzle row parameter
 r = rotor row parameter
 s = shroud parameter
 t = total thermodynamic condition
 z = axial component
 1 = nozzle row or blade row inlet parameter
 2 = nozzle row or blade row exit parameter
 3 = rotor row inlet parameter
 4 = rotor row exit parameter
 θ = tangential component

Superscript

' = relative value in a coordinate system rotating with the blade

6.1 Preliminary Aerodynamic Design Strategy

An effective preliminary design system will configure a basic stage to match the desired performance characteristics specified by the user. This permits the user to rapidly explore design alternatives before committing the time and effort required for a detailed aerodynamic design. The preliminary design system must yield sufficient definition to permit an evaluation of the design using the performance analysis of chapter 5.

Figure 6-1 illustrates the basic stage configuration used for this purpose. The stage performance will be specified in dimensionless form on a design radius, r_c , which is chosen to be the nozzle inlet mean radius. Some dimensional data are required to accomplish the preliminary design. The design radius and the nozzle inlet blade height must be supplied to start the process. The axial chord of the nozzle, b_{zn} , and of the rotor, b_{zr} , must be supplied along with the axial gap, Δz , between them. The stage inlet total temperature and total pressure, the rotation speed and the equation of state for the working fluid are also required. The preliminary design system must determine the annulus heights at stations 2 through 4, generate flow profiles at the stations 1 through 4, and select blades capable of producing those flow profiles.

Figure 6-2 illustrates the basic blade geometry to be generated by the preliminary design system. This is consistent with the blade geometry required for the AMDC blade row performance models of chapter 4, but some simplifications will be used for the preliminary design. It will be assumed that the suction surface is linear between the throat and the trailing edge, i.e., that there is no

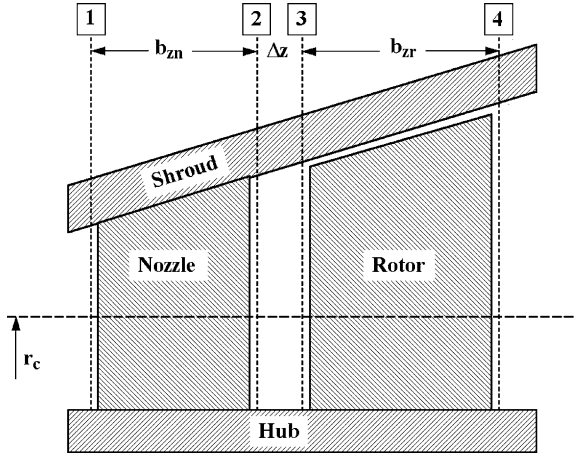
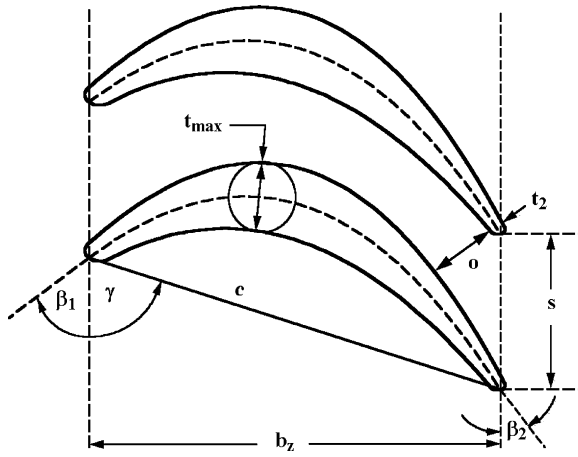


FIGURE 6-1. Basic Stage Configuration

**FIGURE 6-2. Basic Blade Geometry**

uncovered turning. Other required parameters can be approximated based on the design organization's normal design practice. Blade thicknesses are approximated from standard values of t_{\max}/c and t_2/s . Similarly, blade tip and seal clearances, δ , are approximated from standard values of $\delta/(r_c + h/2)$. Standard values are used for surface finish and other seal geometry such as the number of fins, fin thickness and pitch. This writer's preliminary design system supplies default values for these standard values and allows the user to edit them for use on all subsequent preliminary designs. This is normally quite sufficient for preliminary design activity and substantially reduces the input specifications required.

6.2 Velocity Triangles at the Design Radius

It is convenient to express the stage performance in terms of dimensionless parameters at the design radius. Defining the design blade speed as $U_c = r_c \omega$, the stage flow coefficient is defined as

$$\phi_c = C_{m1c} / U_c \quad (6-1)$$

The stage work coefficient is defined in terms of the stage total enthalpy drop at the design radius using Eq. (3-9), i.e.,

$$\psi_c = \Delta H / U_c^2 = (C_{\theta 3c} - C_{\theta 4c}) / U_c \quad (6-2)$$

The stage degree of reaction is defined as the ratio of the static enthalpy drop to the total enthalpy drop that occurs across the rotor blade at the design radius [67], i.e.,

$$R_c = (h_{3c} - h_{4c}) / \Delta H \quad (6-3)$$

If C_{mc} is constant through the stage, Eqs. (2-3), (3-9) and (6-3) yield

$$R_c = 1 - (C_{\theta 3c} + C_{\theta 4c}) / U_c \quad (6-4)$$

From Eqs. (6-3) and (6-4) it is easily shown that

$$C_{\theta 3c} = 1 - R_c + \psi_c / 2 \quad (6-5)$$

$$C_{\theta 4c} = 1 - R_c - \psi_c / 2 \quad (6-6)$$

Since there is no change in total enthalpy between stations 2 and 3, Eq. (3-9) requires that $C_{\theta 2c} = C_{\theta 3c}$. Since C_{mc} is constant through the stage, the specification of ϕ_c , ψ_c and R_c defines all velocity components on the design radius for stations 2 through 4. A useful alternative to specifying R_c is to specify the discharge flow angle, α_{4c} , and use it to calculate R_c . Then,

$$C_{\theta 4c} / U_c = \phi_c \cot \alpha_{4c} \quad (6-7)$$

$$C_{\theta 3c} / U_c = C_{\theta 4c} / U_c + \psi_c \quad (6-8)$$

When control of the discharge swirl velocity is important, this specification avoids the need to guess a value of R_c to produce the desired exit swirl. A typical example is a single stage or a last-stage design where the designer may want to design for no exit swirl to minimize losses in the exhaust diffuser and exhaust end. It remains to define the swirl velocity at station 1. If the design is intended as a general interior stage it is convenient to assume a repeating stage, i.e., the velocity components at station 1 and 4 are identical. For a single-stage or a first-stage design, it is useful to specify the inlet flow angle, α_{1c} .

The velocity triangles at all stations on the design radius can also be expressed in terms of the design performance parameters. Here they will be computed assuming angles are positive in the direction of rotation. Note that these angles will require adjustment to express them in the blade-oriented coordinates of figure 6-2, where angles are measured as positive from the concave side of the blade. The absolute flow angles are

$$\cot \alpha_{1c} = C_{\theta 1c} / \phi_c \quad (6-9)$$

$$\cot \alpha_{2c} = \cot \alpha_{3c} = [1 - R_c + \psi_c / 2] / \phi_c \quad (6-10)$$

$$\cot \alpha_{4c} = [1 - R_c - \psi_c / 2] / \phi_c \quad (6-11)$$

The relative tangential velocity is given by

$$W_{\theta c} = C_{\theta c} - U_c \quad (6-12)$$

Hence the relative flow angles at the rotor inlet and exit are

$$\cot \alpha'_{3c} = [1 - R_c + \psi_c / 2 - U_c] / \phi_c \quad (6-13)$$

$$\cot \alpha'_{4c} = [1 - R_c - \psi_c / 2 - U_c] / \phi_c \quad (6-14)$$

6.3 The Vortex Type and Swirl Velocity Distributions

This defines the velocity triangles at the design radius but does not define the hub-to-shroud profiles. If the hub-to-shroud distributions of C_θ are specified, a simplified form of the normal equilibrium equation given in Eq. (3-30) can be used to solve for the C_m distributions. The swirl velocity distribution at the nozzle exit can be specified by the general vortex equation suggested by Aungier [2].

$$C_{\theta 2} / U_c = (1 - R_c)(r_c / r)^n + (\psi_c / 2)(r_c / r)^m \quad (6-15)$$

The vortex exponents, n and m , are to be supplied by the designer. When α_{4c} is specified, R_c is easily calculated for use in Eq. (6-15). Note that Eq. (6-15) is consistent with Eq. (6-5) at the design radius. It will be shown subsequently in this chapter that this vortex equation offers considerable flexibility and includes the vortex types most commonly used in axial turbine stages. The swirl velocity distribution at station 3 is given by conservation of angular momentum. Hence, Eq. (6-15) applies to station 3 also.

$$C_{\theta 3} / U_c = (1 - R_c)(r_c / r)^n + (\psi_c / 2)(r_c / r)^m \quad (6-16)$$

Requiring constant work from hub to shroud provides the swirl velocity distribution at station 4, i.e.,

$$U(C_{\theta 3} - C_{\theta 4}) = \Delta H = U_c^2 \psi_c \quad (6-17)$$

Eqs. (6-15) and (6-17) yield

$$C_{\theta 4} / U_c = (1 - R_c)(r_c / r)^n + (\psi_c / 2)(r_c / r)^m - \psi_c r_c / r \quad (6-18)$$

If a repeating stage is being designed, Eq. (6-18) also supplies the swirl distribution for station 1. When the stage inlet flow angle is specified, the flow angle is assumed to be constant from hub to shroud.

The meridional velocity distribution at any station can be calculated from the normal equilibrium equation.

$$C_m \frac{\partial C_m}{\partial r} + \frac{C_\theta}{r} \frac{\partial r C_\theta}{\partial r} = 0 \quad (6-19)$$

This is just a simplified form of Eq. (5-11), neglecting stream surface curvature effects and assuming total enthalpy and entropy are constant from hub to shroud. If the absolute flow angle distribution is specified, similar simplifications applied to Eq. (5-13) yield

$$C_m \frac{\partial C_m}{\partial r} + \frac{C_m^2 \sin^2 \alpha}{2r^2} \frac{\partial (r \cot \alpha)^2}{\partial r} = 0 \quad (6-20)$$

6.4 Stage Efficiency

An effective preliminary design system must produce candidate designs likely to be confirmed by the performance analysis of chapter 5. If the performance analysis shows that the candidate design does not achieve the desired performance to within an acceptable approximation, it will be of limited value and will be almost useless as means to investigate design alternatives. Hence, the preliminary design system must include consideration of the stage efficiency. The process could be started with a simple guess for stage efficiency, which could be improved as feedback is obtained from the performance analysis. A better approach is to provide a basis the initial guess in terms of a standardized stage efficiency chart. This type of chart also provides the designer with a logical basis for selecting and adjusting the dimensionless performance parameters during the design process.

There are a number of candidate stage efficiency charts available. Balje [68] presents stage efficiency in terms of specific speed and specific diameter. Smith [70] presents a stage efficiency chart in terms of ϕ and ψ . This is basically a correlation of experimental data corrected to zero tip clearance. This Smith chart is widely accepted as a viable basis for axial-turbine design guidance. Fielding [69] presents a series of stage efficiency charts based on basic Ainley-Mathieson performance predictions. He considers representative 50% reaction interior stages, last stages with zero exit swirl and single stages with zero inlet and exit swirl. Kacker and Okapuu [43] provide a predicted efficiency chart that is quite similar to the Smith chart. Indeed, the performance analysis of Kacker and Okapuu is strongly influenced by their perceived need to achieve compatibility with the Smith chart. This is considered to be the most applicable efficiency chart for the present application. It shows good agreement with experimental performance data. Hence, an empirical correlation of the Kacker and Okapuu efficiency chart was developed. The stage total-to-total efficiency for zero blade tip leakage is approximated by

$$\eta_0 = \eta_{opt} - K(\phi_c - \phi_{opt})^2 \quad (6-21)$$

$$\phi_{opt} = 0.375 + 0.25\psi_c \quad (6-22)$$

$$\eta_{opt} = 0.913 + 0.103\psi_c - 0.0854\psi_c^2 + 0.0154\psi_c^3; \quad \psi_c \leq 2.8 \quad (6-23)$$

$$\eta_{opt} = 1.01 - 0.05\psi_c; \quad \psi_c > 2.8 \quad (6-24)$$

$$K = 0.375 - 0.125\psi_c; \quad \psi_c \leq 2.2 \quad (6-25)$$

$$K = 0.22/\psi_c; \quad \psi_c > 2.2 \quad (6-26)$$

For any value of ψ_c , η_{opt} is the maximum efficiency and ϕ_{opt} is the optimum flow coefficient that yields the maximum efficiency. Figure 6-3 shows an efficiency chart predicted with this empirical model. While this is not precisely the Kacker and Okapuu efficiency chart, it is in very close agreement with it. For reference, contours of constant total-to-total velocity ratio, v , are included. Note that the efficiency chart does not show any dependence on the degree of reaction. This is a significant limitation that follows from the fact that the chart is primarily based on 50% reaction stages. Another significant limitation is that the chart is based on moderate to high aspect ratio stages. Based on performance analysis results for a range of preliminary stage designs, it has

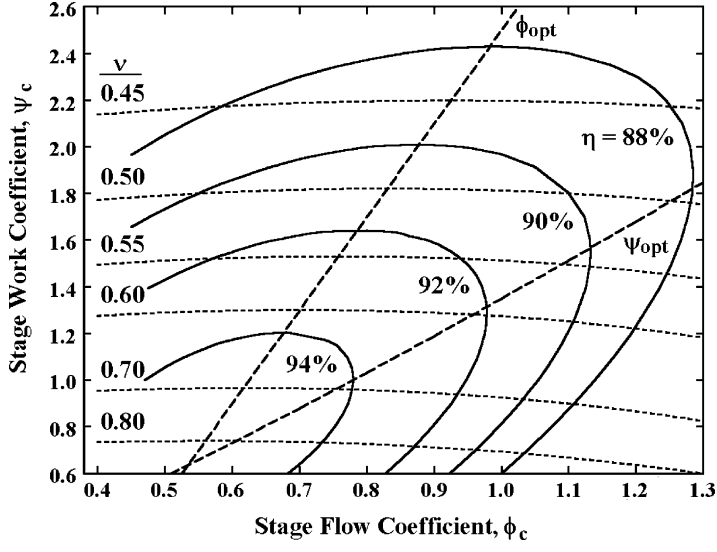


FIGURE 6-3. Interior-Stage Total Efficiency Chart

been found beneficial to include an aspect ratio correction when $b_z/h > 0.4 + 0.5R_c$. Aspect ratio effects were found to be mildly dependent on stage reaction. This is to be expected since low reaction is likely to result in negative reaction near the hub contour at lower values of b_z/h than for higher reaction designs. The efficiency is also corrected for typical rotor clearance losses, based on an empirical correlation by Kacker and Okapuu [43]. Let $K = \delta/(r_c + h_1/2)$ designate the standard tip clearance approximation described previously in this chapter. If $X = h(0.4 + 0.5R_c)/b_z$ and the constraint that $X \leq 1$ is imposed, the corrected efficiency is given by

$$\eta = \eta_0 [1 - 0.93K(r_c/h)(1 + 0.5h/r_c)^2] X^{(0.05+0.04R_c)} \quad (6-27)$$

In many cases, the designer is more concerned with the total-to-static stage efficiency. The estimated total-to-total efficiency can be converted to the total-to-static efficiency using the discharge velocity head at the stage exit.

$$(C_{4c}/U_c)^2 = \phi_c^2 + (1 - R_c - \psi_c/2)^2 \quad (6-28)$$

$$\eta_s = \psi_c / [\psi_c + 0.5(C_{4c}/U_c)^2] \quad (6-29)$$

A turbine stage intended for use as the last stage in an industrial turbine is often designed with zero stage exit swirl ($C_{\theta 4} = 0$) to minimize losses in the diffuser and exhaust end. Figure 6-4 shows a total-to-static efficiency chart developed from figure 6-3 and Eq. (6-29) for $C_{\theta 4} = 0$, i.e., $C_{4c} = \phi_c U_c$. For

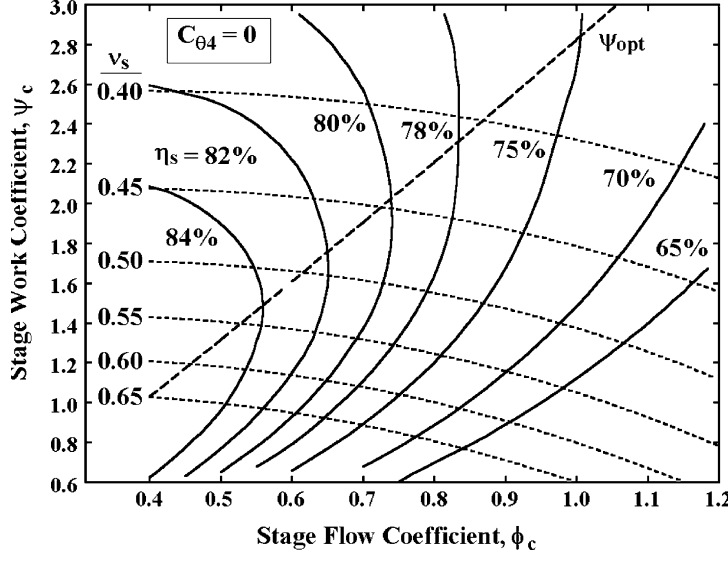


FIGURE 6-4. Last-Stage Static Efficiency Chart

reference, contours of constant total-to-static velocity ratio, v_s , are included. Clearly achieving high static efficiency requires relatively low stage flow coefficients. This efficiency chart provides more useful guidance for stages intended for the last-stage position in a turbine and for many standardized industrial turbine stages. Practical application of standardized industrial turbine stages usually dictates that the design exit swirl velocity be low so they can match to other standardized stages and function well in a last-stage position. Also, the matching of the end-wall contours for these stages often must be compromised significantly based on available standard diameters and blade heights. Hence, recovery of the stage discharge velocity head between stages is often compromised. This will often prompt the industrial turbine stage designer to emphasize stage total-to-static efficiency. American practice for industrial steam turbines commonly emphasizes impulse stages ($R_c = 0$) to minimize rotor axial thrust forces. This also allows somewhat higher work coefficients to reduce the number of stages required. Figure 6-5 shows a total-to-static efficiency chart developed from figure 6-3 and Eq. (6-29) for impulse stages. Again, relatively low stage flow coefficients are required to achieve high static efficiency for impulse stages. Also, it can be seen that optimum efficiency corresponds to higher work coefficients than indicated by either figure 6-4 or figure 6-5. It is common practice to design industrial impulse stages with $\phi_c \approx 0.5$ and $v_c \approx 0.5$. Figure 6-5 is consistent with experience, since it indicates this is a near-optimum choice. The only generalized total efficiency plot for industrial impulse stages known to this writer is a predicted chart by Craig and Cox [44]. This is presented without supporting experimental evidence and includes a significant and poorly defined Reynolds number influence. Although this writer does not use their chart

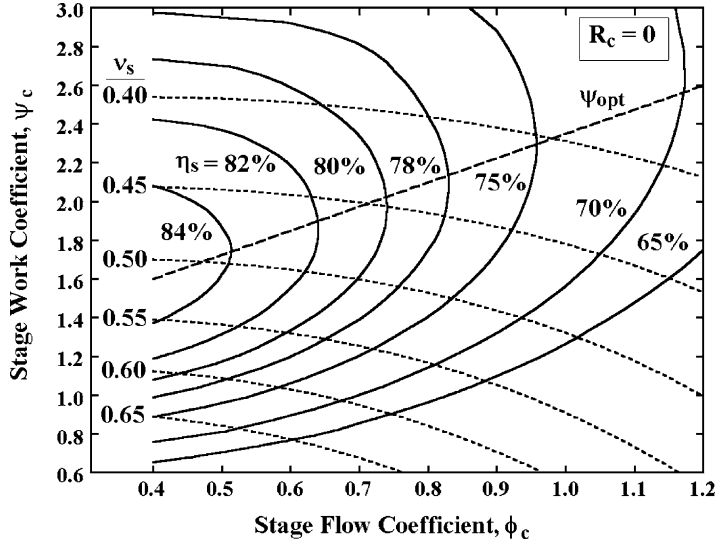


FIGURE 6-5. IMPULSE-STAGE STATIC EFFICIENCY CHART

specifically, it is worth noting that it also indicates impulse stage designs should emphasize relatively low flow coefficients on the order of 0.5.

Figures 6-3, 6-4 and 6-5 also show the optimum work coefficient, ψ_{opt} . This is simply the locus of best efficiency points for a specified flow coefficient. For reference, empirical equations for these curves, given in the order of the figure numbers, are

$$\psi_{opt} = 1.35 \phi_c^{1.2} \quad (6-30)$$

$$\psi_{opt} = 2.825 \phi_c^{1.1} \quad (6-31)$$

$$\psi_{opt} = 1.1 + 1.25 \phi_c \quad (6-32)$$

The static efficiency charts do not show the equivalent of ϕ_{opt} from figure 6-3. Static efficiency improves with reduced flow coefficient over the range shown. There may be an optimum flow coefficient for a specified work coefficient, but it is not well defined by the charts.

When stage performance specifications are being entered, this writer's preliminary design system displays ϕ_{opt} , ψ_{opt} , η and η_s values whenever valid values of ϕ_c and ψ_c have been supplied. That provides guidance for refining the specifications for ϕ_c and ψ_c and for specifying the stage efficiency estimate. The efficiency charts showed in figures 6-3, 6-4 and 6-5 are also displayed on demand for additional guidance.

6.5 The Optimum Pitch-to-Chord Ratio

The number of blades to be used in each blade row can be estimated from empirical models for the optimum pitch-to-chord ratio. One popular estimate is based on matching the Ainley-Mathieson [41] minimum profile loss coefficients shown in figures 4-3 and 4-4. The optimum pitch-to-chord ratio for simple nozzle blades ($\beta_1 = 90^\circ$) can be approximated by

$$(s/c)_0 = 0.427 + \alpha_2 / 58 - (\alpha_2 / 93)^2 \quad (6-33)$$

Similarly, for impulse blades,

$$(s/c)_1 = 0.224 + (1.575 - \alpha_2 / 90) \alpha_2 / 90 \quad (6-34)$$

Defining

$$\xi = (90 - \beta_1) / (90 - \alpha_2) \quad (6-35)$$

Then the optimum pitch-to-chord for the actual blade row is interpolated in the same manner as used for the profile loss coefficient.

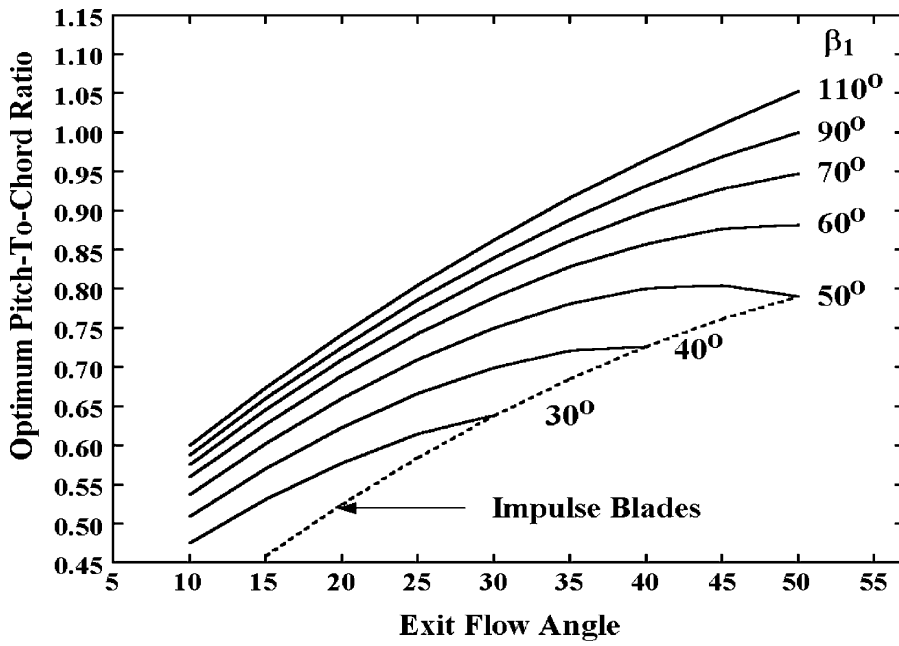


FIGURE 6-6. The Ainley-Mathieson Optimum s/c

$$(s/c)_{opt} = (s/c)_0 + [(s/c)_1 - (s/c)_0] |\xi| \xi \quad (6-36)$$

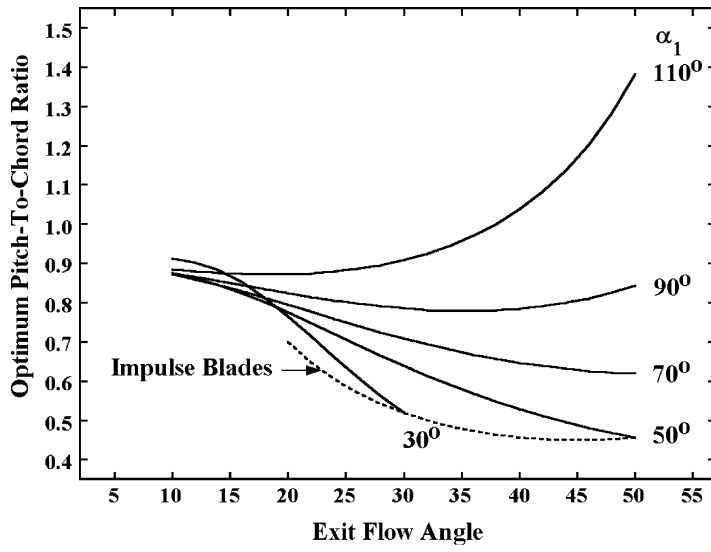
The absolute value in Eq. (6-36) is used to include values of $\beta_1 > 90^\circ$. For the preliminary design, the blades will be selected to yield an incidence angle of zero, i.e., $\beta_1 = \alpha_1$. Figure 6-6 illustrates the optimum pitch-to-chord ratio predicted by Eqs. (6-33) through (6-36).

Zweifel [71] developed an empirical model for the optimum pitch-to-chord ratio based on the observation that minimum losses are approximately associated with a particular value of the tangential force coefficient, λ . This coefficient is the ratio of the blade actual-to-ideal tangential force. The original reference is not easily located today, but Fielding [69] has provided a rather detailed derivation of Zweifel's tangential force coefficient. When expressed in the blade-oriented angle convention of figure 6-2, the tangential force coefficient can be expressed as

$$\lambda = 2 \sin^2 \alpha_2 [\cot \alpha_1 + \cot \alpha_2] (s/c) / \sin \alpha_m \quad (6-37)$$

The usual estimate for the blade mean flow angle, α_m , in the present angle convention is

$$\cot \alpha_m = [\cot \alpha_2 - \cot \beta_1] / 2 \quad (6-38)$$

FIGURE 6-7. The Zweifel Optimum s/c for $\lambda = 0.9$

Hence, from basic trigonometry,

$$\sin \alpha_m = 1 / \sqrt{1 + \cot^2 \alpha_m} \quad (6-39)$$

Zweifel observed that $\lambda \approx 0.8$ for cascades with optimum spacing, although more modern practice appears to be to use $\lambda \approx 0.9$ as an optimum value. Figure 6-7 illustrates the optimum pitch-to-chord ratios predicted by Eqs. (6-37), (6-38) and (6-39) for $\lambda \approx 0.9$. Comparison of figures 6-6 and 6-7 clearly shows that the two empirical models can produce quite different results, particularly at the low and high ends of the inlet and exit flow-angle ranges. Indeed, the optimum pitch-to-chord ratio from Eq. (6-37) is undefined when the exit flow angle approaches zero. As a general rule, this writer has found the Ainley-Mathieson model to be more consistent and reliable. Fielding [69] also expresses a preference for the Ainley-Mathieson model. The optimum pitch-to-chord ratio and chord at the mean radius can be used to estimate the optimum number of blades.

$$N = 2\pi r / [c(s/c)_{opt}] \quad (6-40)$$

Of course, the result from Eq. (6-40) must be converted to an integer. This writer's preliminary design system displays the optimum number of blades computed from these two models when blade data is being entered. The user has the option to use either of these estimates or to specify the number of blades to be used for each blade row.

6.6 Initializing the Total Thermodynamic Conditions

The preliminary design calculations are accomplished assuming that all total thermodynamic conditions, including entropy, are constant from hub to shroud at all of the computing stations identified in figure 6-1. At station 1 the stage inlet total temperature and total pressure specified by the user and the equation of state define H_1 and s_1 . From conservation of energy and the definition of the work coefficient,

$$H_2 = H_3 = H_1 \quad (6-41)$$

$$H_4 = H_1 - \psi_c U_c^2 \quad (6-42)$$

The stage total efficiency is provided from the empirical model illustrated in figure 6-3 or the user may specify it directly. This defines the ideal (isentropic) stage discharge total enthalpy, $H_{4,is}$ as

$$H_{4,is} = H_1 + (H_4 - H_1)/\eta \quad (6-43)$$

The equation of state is used to compute the actual discharge total pressure, P_{t4} , as a function of $H_{4,is}$ and s_1 , the actual discharge entropy, s_4 , as a function of P_{t4} , and H_4 and the ideal (no loss) discharge total pressure, $P_{t4,id}$, as a function of H_4 and s_1 . It is assumed that half of the total pressure loss occurs across the nozzle row. Hence,

$$P_{t3} = P_{t2} = P_{t1} - (P_{t4,id} - P_{t4})/2 \quad (6-44)$$

Since H , P_t and s are known at all stations, the equation of state provides the total temperature, T_t , at all stations.

6.7 The Stage Inlet Flow Profiles

The stage inlet flow profiles can be immediately calculated from the basic design specifications. The hub and shroud radii can be calculated directly from the specified mean radius and nozzle height.

$$r_{h1} = r_c - h_1/2 \quad (6-45)$$

$$r_{s1} = r_c + h_1/2 \quad (6-46)$$

A series of radii are distributed from hub to shroud. The number of radii to be used is specified by the user, subject to the constraints that at least three radii are required and an odd number must be used. Hence, one of the radii will always be r_c . If a repeating stage is being designed, the inlet swirl velocity distribution, $C_{\theta 1}(r)$, is computed by applying Eq. (6-18) at the inlet station. The

meridional velocity distribution, $C_{m1}(r)$, is computed by numerical integration of Eq. (6-19), while matching the known value at the design radius. If the inlet flow angle is being specified, the specified inlet flow angle is assumed constant from hub to shroud. Numerical integration of Eq. (6-20) supplies the $C_{m1}(r)$ distribution and the swirl velocity distribution is

$$C_{\theta1}(r) = C_{m1}(r) \cot \alpha_1 \quad (6-47)$$

The specified stage inlet total temperature, T_{t1} , inlet total pressure, P_{t1} , and the equation of state for the working fluid supply the inlet total enthalpy, H_1 , and the inlet entropy, s_1 . Hence, the static enthalpy distribution is given by

$$h = H_1 - \frac{1}{2} [C_{m1}^2 + C_{\theta1}^2] \quad (6-48)$$

Then the density distribution $\rho_1(r)$ can be calculated from $h_1(r)$ and $s_1(r)$ using the equation of state. The stage mass flow rate is given by numerical integration of

$$\dot{m} = 2\pi \int_{r_h}^{r_s} r \rho C_m \cos \varepsilon dr \quad (6-49)$$

The angle ε is the angle between a true stream-surface normal and a quasi-normal. For the present radial quasi-normals, this is the angle between a tangent to the stream surface and the axial direction. It is used to correct for the fact that C_m is usually not normal to the radial quasi-normals. As with the performance analysis of chapter 5, ε is assumed to vary linearly between the known hub and shroud contour values. Initially it is assumed that $\varepsilon = 0$ on all stream surfaces. This is corrected in an iterative fashion as annulus sizing at subsequent stations provides data to calculate ε on the hub and shroud contours.

6.8 Sizing the Annulus

The next step in the preliminary design process is to size the annulus at stations 2 and 4, i.e., the nozzle and rotor exit stations. This involves calculating hub and shroud radii that will pass the stage mass flow while imposing the design radius velocity triangles and the appropriate vortex equation for the swirl velocity distribution. To accomplish this process, it is necessary to impose an additional constraint sufficient to specify one radius at these stations. For generality, it is useful to let the designer specify one radius that will be held constant through the stage. The obvious alternate choices are the hub, mean or shroud radius.

Annulus sizing requires a fairly simple iterative solution. To start the process, all radii at the station being sized are set equal to the known radii at station 1. The swirl velocity distribution is computed from Eq. (6-15) for the nozzle exit or Eq. (6-18) for the rotor exit. Eq. (6-19) is numerically integrated to compute the radial distribution of C_m , while matching the known value at the design radius. Then numerical integration of Eq. (6-49) provides the calculated mass flow rate, \dot{m}_{cal} , for the resident annulus area. The annulus area is then corrected for any

deviation between the calculated and actual mass flow rate. For the constant hub radius option, this requires

$$r_s^2 \rightarrow (r_s^2 - r_h^2) \dot{m} / \dot{m}_{cal} + r_h^2 \quad (6-50)$$

Similar correction equations are easily developed for the constant mean or shroud radius options. This process is repeated until adequate convergence on the actual mass flow rate is achieved. If annulus sizing at either station fails to produce a hub radius greater than zero, the process terminates with an error message.

When the annulus has been sized at both stations 2 and 4, it is usually appropriate to impose some constraints on the results. The precise constraints (if any) will depend on the designer's preferred design practice. This writer's preliminary design system includes user specifications of the maximum end-wall flare angle ($\varepsilon_s - \varepsilon_h$) for both the nozzle and the rotor and it requires

$$r_{s2} \leq r_{s4} \quad (6-51)$$

$$r_{h2} \geq r_{h4} \quad (6-52)$$

If these constraints require modifying the radii resulting from the annulus sizing at stations 2 or 4, the flow field at those stations must be recalculated to conserve mass. The swirl velocity distribution is recalculated from Eq. (6-15) for the new set of station radii. Then an iterative mass balance procedure is used to calculate a new value of C_{mc} that conserves mass. Since the swirl velocity distribution conforms to the design specifications, energy conservation is not compromised, but the meridional velocity and velocity triangle distributions will deviate somewhat from the design specifications. The iterative process is quite similar to the annulus sizing, except that the geometry is now fixed and C_{mc} is the parameter being adjusted. Eq. (6-19) is numerically integrated to compute the radial distribution of C_m , while matching the resident value of C_{mc} . Then numerical integration of Eq. (6-49) provides the calculated mass flow rate, \dot{m}_{cal} , for the resident value of C_{mc} . Then C_{mc} is then corrected for any deviation between the calculated and actual mass flow rate.

$$C_{mc} \rightarrow C_{mc} \dot{m} / \dot{m}_{cal} \quad (6-53)$$

The process is repeated until adequate convergence on the actual mass flow is achieved.

The annulus geometry to be used at station 3 is also dependent on the designer's preferred practice. This writer's preliminary design system imposes linear interpolation of the end-wall contours between stations 2 and 4. Since the axial chords for nozzle and rotor and the axial gap between them are design specifications, the axial coordinates of all stations are known. This permits calculation of the hub and shroud radii at station 3. Then the mass balance procedure described in the previous paragraph is used to compute the flow profiles at this station. Note that the swirl velocity distribution must be calculated from Eq. (6-16) to satisfy conservation of energy consistent with the design specification.

An iterative procedure is required to define the stage mass flow rate and annulus geometry including the effect of the angle ϵ . This is a fairly simple prediction-correction iteration scheme since both end-wall contours consist of linear segments. Hence, the values of ϵ on the hub and shroud contours are identical for stations 1 and 2. Similarly, they are identical for stations 3 and 4. The only precaution required is to recognize that any change in the station 2 end-wall contours will also change the mass flow rate since the ϵ distribution at station 1 is also changed.

It is often useful to specify reaction at the rotor mean radius rather than at the design radius. That option can easily be incorporated into the preliminary design process. It is only necessary to include an iteration loop on the annulus sizing process that updates the reaction at the design radius until the desired reaction at the rotor mean radius is obtained. Assume R_c equal to the rotor mean reaction to start the iteration. Then add the deviation between the calculated rotor mean reaction and the desire value to R_c and repeat the process until convergence is achieved.

6.9 Selecting the Blade Row Geometry

The nozzle and rotor blade geometry is selected to match the calculated velocity triangles before and after the blade row. For this purpose, the flow angles must be expressed consistent with the blade angle convention shown in figure 6-2. This is accomplished with the following equations.

$$\beta_1 = \alpha_1 = 90^\circ + \arctan[C_{\theta 1} / C_{m1}] \quad (6-54)$$

$$\alpha_2 = 90^\circ - \arctan[C_{\theta 2} / C_{m2}] \quad (6-55)$$

$$\beta_3 = \alpha'_3 = 90^\circ - \arctan[(C_{\theta 3} - U_3) / C_{m3}] \quad (6-56)$$

$$\alpha'_4 = 90^\circ + \arctan[(C_{\theta 4} - U_4) / C_{m4}] \quad (6-57)$$

Note that the blade inlet angles are set equal to the blade row inlet flow angles for operation with an incidence angle of zero. The gauging angles of the blade rows are selected from the discharge flow angle, consistent with the fluid deviation angle model described in chapter 4. Since all flow profile data are available at this point in the process, the deviation angle can be computed for both blades. When the blade exit flow is subsonic, this requires a simple iterative process, since deviation angle is a function of the gauging angle. The gauging angle is initialized to equal the exit flow angle and repeatedly updated using the deviation angle model until converged. The throat-to-pitch ratio distributions for the two blade rows are given by

$$(o/s)_n = F_{AR} \sin(\alpha_2 - \delta_n) \quad (6-58)$$

$$(o/s)_r = F_{AR} \sin(\alpha'_4 - \delta_r) \quad (6-59)$$

The parameter F_{AR} is the stream sheet correction term given in Eq. (4-16). The gauging angles are given by

$$\beta_{gn} = \arcsin[(o/s)_n] \quad (6-60)$$

$$\beta_{gr} = \arcsin[(o/s)_r] \quad (6-61)$$

The blade stagger angles and chords for the nozzle and rotor blades are estimated from these blade angles and the specified axial chords by

$$\gamma_n = [180^\circ - \beta_1 + 1.5\beta_{gn}] / 2.5 \quad (6-62)$$

$$c_n = b_{zn} / \sin \gamma_n \quad (6-63)$$

$$\gamma_r = [180^\circ - \beta_3 + 1.5\beta_{gr}] / 2.5 \quad (6-64)$$

$$c_r = b_{zr} / \sin \gamma_r \quad (6-65)$$

The number of nozzle and rotor blades may be selected from the Ainley-Mathieson or Zweifel empirical models using Eq. (6-40) or the user can specify them directly. As noted previously, it is assumed that $t_{max} = 0.2c$ and $t_2 = 0.02s$ and that there is no uncovered turning. Blade tip clearances and any required seal geometry can be approximated following the design organization's normal design practice. In the case of a diaphragm-disk type rotor, the user must also specify the shaft radius. Hence, all blade row geometry data required for the aerodynamic performance analysis of chapter 5 have been defined.

6.10 A Computerized Preliminary Design System

This preliminary design procedure can easily be implemented in a very efficient computerized preliminary design system. It is useful to constrain the order in which the user provides the design specifications and to automatically carry out the preliminary design calculations to the extent possible with the current specifications. Most situations that preclude completing the process can be specifically identified to the user for guidance in correcting the design specifications. Modern programming languages also permit error trapping so that the preliminary design process can be stopped before it can terminate with a fatal error. In that case, it is not possible to identify the problem to the user explicitly. But if output files containing summaries of the preliminary design progress are generated during the design process, the user will be able to identify where the process failed. That is usually sufficient to suggest what design specifications are likely to be inappropriate. It is simply necessary

to provide the user with the capability to view any available output files on the monitor screen. With appropriate care in implementing the process, it is safe to let the computerized system automatically carry out the design process as far as possible whenever the user enters or modifies the design specifications. That greatly simplifies the process and substantially reduces the time required to accomplish a preliminary aerodynamic design.

The preliminary aerodynamic design system should be interfaced to the aerodynamic performance analysis of chapter 5. This provides a direct evaluation of the preliminary design. This interfacing does not have to be highly sophisticated. Simply providing the capability to export an input file for the performance analysis is quite adequate. Normally the designer will alternate between the preliminary design system and the performance analysis to refine the stage efficiency estimate and the basic design specifications until a preliminary design appropriate for the stage design objectives has been defined. This evaluation is somewhat qualitative, since the detailed design process will further optimize the preliminary design. The goal is to develop a preliminary design with sufficient potential for achieving the design objectives before committing the effort required for a detailed design. A key step in the detailed design process is the detailed design of airfoils for the nozzle and rotor blades. Detailed airfoil design procedures are described in chapter 7. That step can be simplified by providing the capability to export an input file for the airfoil designs system to provide the initial estimates for the airfoil sections based on the preliminary design.

The first data set required for the preliminary design system is the equation of state for the working fluid. All subsequent input specifications will require support from equation-of-state calculations. The computerized equation of state package discussed in chapter 2 can handle this requirement with no additional programming activity. Once the equation of state is defined, the basic stage sizing data set can be supplied. It is useful to provide the user with several options for supplying this data set. Useful options include:

- Design a repeating stage or specify the stage inlet flow angle.
- Specify stage reaction at the design radius, stage reaction at the rotor mean radius or the stage exit flow angle at the design radius.
- Specify the radius to be held constant through the stage (hub, mean or shroud).
- Specify the vortex exponents or design a nozzle with constant exit flow angle from hub to shroud.
- Use the stage efficiency from figure 6-3 (with corrections) or specify it as input data.

Once the appropriate options have been selected, the actual stage sizing data can be entered and the automatic preliminary design process can be activated. The basic sizing data set includes:

- Rotation speed, inlet total temperature and inlet total pressure.
- The design radius, nozzle inlet height, nozzle and rotor axial chords and the axial gap between them.

- The stage flow coefficient, work coefficient and reaction or the exit flow angle at the design radius.
- The swirl velocity vortex exponents (if required).
- The stage inlet flow angle (if required).
- The stage total efficiency (if required).
- The number of constant-radius blade sections to be designed from hub to shroud (also used as the number of radial points from hub to shroud where flow profile data are calculated).
- The maximum nozzle and rotor end-wall flare angles to be allowed.

These design specifications are sufficient to conduct the preliminary design process through Eq. (6-65). When the automatic preliminary sizing process is active, the following conditions should be checked to see if the process should be stopped with an appropriate warning message.

- Stage efficiency is too low, say less than 10%.
- Any calculated flow angles are too shallow, say less than 10° or greater than 170° .
- A flow reversal is encountered, i.e., $C_m \leq 0$.
- Annulus sizing failed to produce a hub radius greater than zero.

Once the preliminary design process has proceeded through the calculation of the nozzle and rotor chords, the blade design data set can be provided. It is useful to provide the user with some alternate options here also, including:

- Nozzle type: shrouded, unshrouded, diaphragm-disk type or no blade clearance.
- Rotor type: shrouded or unshrouded.
- Number of blades per row specification: Ainley-Mathieson, Zweifel or user specified.

If the option to specify the number of blades is selected, then values for the nozzle and rotor rows are entered. If a diaphragm-disk type nozzle is selected, a shaft radius also must be entered. These data are sufficient to complete the preliminary design and export the input files for the performance analysis and the airfoil detailed design system.

Each time the user enters or modifies any design specifications, the automatic preliminary design process is repeated as far as possible. An output summary of the stage sizing process is created, as the data becomes available to guide the user in the event that an unknown error terminates the design process. Data that should be included are:

- Stage work, power, mass flow, discharge total pressure and discharge static pressure.
- Velocity components and flow angles at the design radius.
- Enthalpy and pressure reaction.
- Overall stage performance data (total-to-total and total-to-static).

When data are available, output files of the absolute flow profiles and flow profiles relative to each blade row should be supplied. If blade design was completed, an output file with the blade geometry for both blade rows should be supplied. The user should have the option of viewing any existing output files on the monitor screen. It is also useful to provide a cross-section plot of the gas path, similar to figure 6-1, for the user to view when available.

6.11 Selection of the Dimensionless Performance Parameters

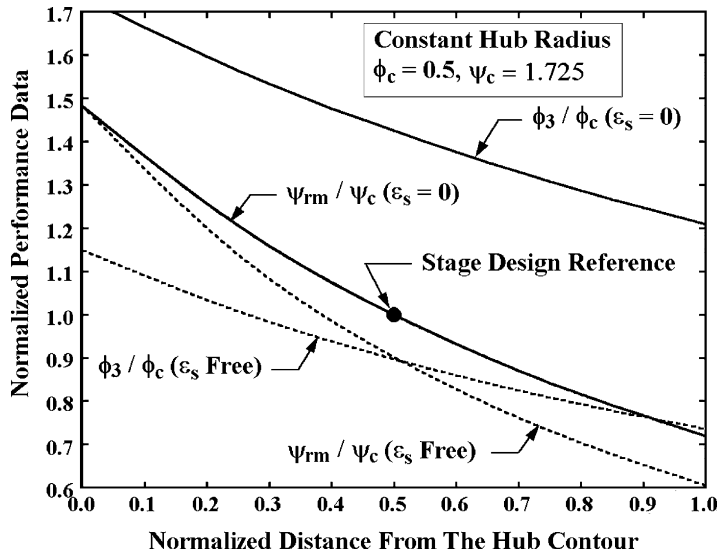
The selection of the dimensionless performance parameters, ϕ_c , ψ_c and R_c , establishes the performance characteristics and the efficiency potential for the stage. Figures 6-3, 6-4 and 6-5 provide some guidance in selecting an appropriate combination of ϕ_c and ψ_c to favor high efficiency, but they do not directly indicate the influence of reaction. It is well known that reaction has a definite influence on the efficiency potential of the stage. Negative reaction is associated with flow diffusion in the rotor, which has a pronounced adverse effect on efficiency. It is generally accepted that reaction of about 50% ($R_c = 0.5$) offers the best efficiency potential. This is intuitively reasonable since it results in balancing the overall flow expansion process equally between the nozzle and the rotor. Indeed, experience has shown that 50% reaction is a near-optimum choice if high efficiency is the primary design objective. As previously noted, the generalized efficiency chart of figure 6-3 probably best represents 50% reaction stages. Yet zero-reaction or impulse stages ($R_c = 0$) are commonly employed for industrial steam turbines. Impulse stages have no change in static pressure across the rotor at the design radius. Reaction normally varies with radius, so static pressure will vary across the rotor at other radii. But average reaction near zero can dramatically reduce the axial thrust force on the rotor to simplify the mechanical design. It also reduces rotor tip leakage losses, possibly eliminating the need for tip seals. Impulse stages also tend to achieve their optimum efficiency at higher values of ψ_c , which results in fewer stages with a significant cost advantage. To some degree, practical application procedures impact the optimum choice for industrial turbines. These are usually one-of-a-kind turbines configured specifically to a customer's requirements. With no duplicate machines to share in absorbing development costs, cost-effective turbine development becomes a major imperative. Common practice is to configure the turbine using a series of standard turbine stage designs with pre-established performance and mechanical integrity. This places particular constraints on the design practice used for the standard industrial turbine stages. Since ideal stage matching is unlikely to occur, the industrial turbine stage design will tend to emphasize total-to-static efficiency over total-to-total efficiency. This also favors designing for low values of the stage exit swirl velocity such that the various standard stages will be better matched to each other and will function well in the last stage position. Consider the case of a design for zero exit swirl velocity. From Eq. (6-6), this requires

$$\psi_c = 2(1 - R_c) \quad (6-66)$$

It can be seen that an impulse stage will perform twice the work of a 50% reaction stage under this condition if both stages operate at the same speed. This will result in requiring about half as many stages when impulse designs are used. This illustrates an important cost-advantage of industrial impulse stage designs. True impulse designs are less likely to be used in modern industrial turbine stages. The designer may use some positive reaction to improve efficiency, primarily to limit the adverse effects of high negative reaction near the hub radius. When the influence of the disk pressure forces is considered, a pure impulse design may not be the best choice for minimum rotor axial thrust forces. Nor is a design for zero exit swirl velocity likely to be considered mandatory, although low levels are likely to be strongly preferred. Indeed, figure 6-5 suggests that the optimum total-to-static efficiency for an impulse design does not occur precisely at the no-exit-swirl condition. Basically, the choice of the degree of reaction will depend primarily on the intended application and the relative priority given to the trade-off between cost and efficiency.

The choice of the work and flow coefficients is also very dependent on the application. If designing one of several unique and well-matched interior stages, total-to-total efficiency will be a priority, which favors a design using the optimum flow coefficient of figure 6-3. If total-to-static efficiency is the more important consideration, low values of flow coefficient will be imperative. In that case, figure 6-4 or figure 6-5 will be a better guide to selecting a good combination of ϕ_c and ψ_c . But the limitations of the generalized efficiency charts do need to be considered when using them for guidance. Not only are they most applicable to 50% reaction stages, but they also assume an ideal stage with constant mean meridional velocity through the stage. That is rarely realized in a practical preliminary stage design. About the only case for which C_m at the mean radius can be constant through the stage is a design with constant mean radius with no limits on the nozzle and rotor end-wall flare angles. An obvious consequence of this is that the static efficiency from the charts may differ significantly from the achievable static efficiency. Once the stage preliminary design is accomplished, the preliminary design system can supply a better estimate of the static efficiency using the actual stage discharge mean C_m in Eq. (6-29). There is also considerable ambiguity with regard to the basic dimensionless performance parameters. The values supplied to the preliminary design system are all referenced to the stage inlet mean radius. The rotor inlet mean flow coefficient may differ significantly from ϕ_c . Similarly, if a mean work coefficient is computed based on an average of the rotor inlet and exit blade speeds, it may differ significantly from ψ_c . It is by no means obvious which reference condition is most appropriate for use with the efficiency charts. Finally, the efficiency charts are primarily applicable to the mean line performance. In many cases, the more general hub-to-shroud performance analysis of chapter 5 will yield significant differences in performance on various stream surfaces, such that the overall stage performance differs from the mean stream surface performance.

A couple of design examples will be used to provide some perspective on the issues involved. These design parameters used were selected to expose the more obvious limitations of the generalized efficiency charts. Both designs are moderate aspect-ratio free-vortex stages with a constant hub radius and

**FIGURE 6-8. Typical Design Ambiguities**

based on $R_c = 0$, $\phi_c = 0.5$ and $\psi_c = 1.725$. One design imposed no limits on the end-wall flare angle (ϵ_s free), while the other required no flare angle for both the nozzle and rotor ($\epsilon_s = 0$). Figure 6-8 shows distributions of normalized rotor inlet flow coefficient, ϕ_3 and work coefficient based on an average of the rotor inlet and exit blade speeds, ψ_{rm} . Figure 6-9 shows the end-wall contours for the two designs. It is seen that only the mean value of ψ_{rm} for the no end-wall

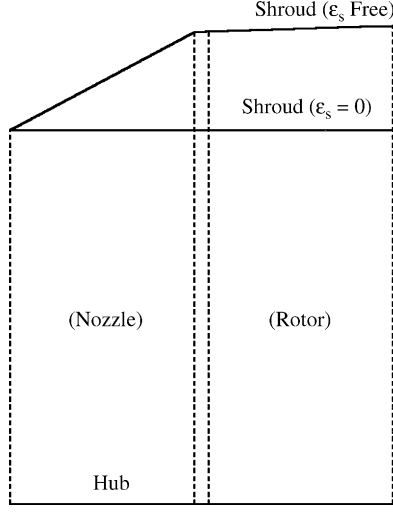
**FIGURE 6-9. End-Wall Contours**

Table 6-1. Summary of Efficiency Estimates

Source	ε_s Free		$\varepsilon_s = 0$	
	η	η_s	η	η_s
Chart	0.901	0.842	0.901	0.842
Before sizing	0.886	0.829	0.886	0.829
After sizing	0.886	0.827	0.886	0.772
Prediction	0.883	0.828	0.862	0.754

flare case corresponds to the stage design value. The mean values of the other parameters shown differ significantly from the corresponding stage design values. To provide some perspective on these ambiguities, the performance analysis of chapter 5 was applied to both preliminary designs. Table 6-1 shows a summary of the various efficiency estimates obtained from this process. The chart efficiency values are from figures 6-3 and 6-5. Before sizing the annulus, the chart values are corrected for aspect ratio and rotor tip clearance, assuming that C_m at the mean radius is constant through the stage. The static efficiency estimate after sizing reflects the actual value of the stage discharge mean C_m . The predicted values result from applying the performance analysis of chapter 5 to the preliminary designs. From the unrestricted flare angle case, it is seen that use of the standard efficiency charts for this impulse stage design provides reasonable estimates of the efficiencies. The no-flare angle case results show that both the total and static efficiencies are overestimated by the charts. The higher rotor inlet flow coefficient for this case does not appear to explain this difference. Indeed, if figure 6-3 is applied with the mean values of ϕ_3 and ψ_{rm} , the estimated total efficiency is actually higher than the estimate based on ϕ_c and ψ_c . A detailed review of the performance predictions for the two cases showed that the reduced total efficiency for the no-flare case is primarily due to the higher blade discharge velocities and a modest increase in the secondary flow loss coefficients due to the lower rotor aspect ratio. Note that the static efficiency estimates for the no-flare case from the charts and from the preliminary design system prior to sizing the annulus would be quite misleading if used for design guidance. Once the annulus sizing is accomplished, the preliminary design system provides a more realistic estimate.

In general, the total efficiency chart with the corrections outlined previously provides a reasonable first estimate, such that the annulus sizing and blade selection is satisfactory. Indeed, a rather large error in total efficiency can be tolerated without significantly affecting the preliminary design process. But the estimates of efficiency based on the design charts often do not reliably indicate the efficiency that will actually be achieved. This writer's practice is to export an input file for the performance analysis and use it to obtain better total and static efficiency estimates. The improved total efficiency estimate can also be used to update the value used to generate the preliminary design if necessary. A single iteration is virtually always sufficient and usually doesn't change the preliminary design significantly.

6.12 Selection of the Swirl Velocity Vortex Type

The swirl velocity vortex equation given in Eq. (6-15) includes a variety of vortex types commonly used in the design of axial-flow turbomachinery. Some of the more popular vortex types include

- Free vortex ($n = m = 1$): This vortex type yields constant angular momentum (rC_θ) and constant C_m from hub to shroud. It has been widely used for axial-flow compressors and is probably the most common choice for axial-flow turbines.
- Constant-swirl vortex ($n = m = 0$): This vortex type yields constant rotor inlet C_θ from hub to shroud. It is often a good choice for axial-flow compressors, since it may allow use of constant-camber, untwisted stator blades to reduce manufacturing cost. It is also occasionally recommended for axial-flow turbine design [68].
- Exponential vortex ($n = 0, m = 1$): This vortex type is popular for axial-flow compressors, since it also may allow use of constant-camber, untwisted stator blades.
- Constant-reaction vortex ($n = -1, m = 1$): The title of this vortex type is misleading, since it does not yield constant reaction except for the special case of $R_c = 1$. If C_m is constant across the rotor, reaction is given by Eq. (6-4) and this vortex appears to yield constant reaction. But the normal equilibrium equation precludes obtaining C_m constant across the rotor from hub to shroud for this vortex type unless $R_c = 1$.
- Constant nozzle-angle vortex ($n = m = \cos^2 \alpha_{2c}$): This vortex type is often recommended for axial-flow turbine design to obtain a low-cost, constant-section nozzle blade [67–69]. It yields constant flow angle from hub to shroud at the nozzle exit. This is easily seen by comparing Eq. (6-15) and the result from integrating Eq. (6-20) with constant α , i.e.,

$$C_{\theta 2} = C_{\theta 2c} (r_c / r)^{\cos^2 \alpha_{2c}} \quad (6-67)$$

$$C_{m2} = C_{m2c} (r_c / r)^{\cos^2 \alpha_{2c}} \quad (6-68)$$

With the exception of the constant nozzle-angle vortex, application of all of these vortex types to axial-flow compressors is reviewed in detail by Aungier [2]. However, the constraints important to compressor and turbine design are too different to generalize those results to axial-flow turbines.

The most important consideration guiding the turbine designer is the hub-to-shroud distribution of reaction. It is generally accepted that $0 \leq R \leq 1$ should be obtained if possible. Extremes in reaction produce highly distorted flow profiles with high relative Mach numbers as well as adversely affecting efficiency due to diffusing flow. Hence, the designer will prefer to avoid negative hub reaction and shroud reaction greater than unity. The reaction at any radial location is given by

$$R = (h_3 - h_4) / \Delta H \quad (6-69)$$

Substituting Eqs. (2-3) and (6-2) into Eq. (6-69) yields

$$R = 1 - \frac{C_{m3}^2 + C_{\theta3}^2 - C_{m4}^2 - C_{\theta4}^2}{2U_c^2\psi_c} \quad (6-70)$$

Differentiating with respect to r yields

$$\frac{\partial R}{\partial r} = \frac{1}{U_c^2\psi_c} \left[C_{m4} \frac{\partial C_{m4}}{\partial r} + C_{\theta4} \frac{\partial C_{\theta4}}{\partial r} - C_{m3} \frac{\partial C_{m3}}{\partial r} - C_{\theta3} \frac{\partial C_{\theta3}}{\partial r} \right] \quad (6-71)$$

Substituting Eq. (6-19) into Eq. (6-71) yields

$$r_c \frac{\partial R}{\partial r} = \frac{1}{\psi_c} \frac{r_c}{r} \left[\frac{C_{\theta3}^2}{U_c^2} - \frac{C_{\theta4}^2}{U_c^2} \right] \quad (6-72)$$

Substituting Eqs. (6-16), (6-17) and (6-18) into Eq. (6-72) yields

$$r_c \frac{\partial R}{\partial r} = 2(1 - R_c)(r_c/r)^{(2+n)} + \psi_c [(r_c/r)^{(2+m)} - (r_c/r)^3] \quad (6-73)$$

Note that if $m = 1$, reaction is independent of ψ_c , which makes those vortex types easier to apply. Equation (6-73) can be integrated directly if it is required that $n = -1$ and $m \neq -1$. This yields

$$R = R_c - \frac{2(1 - R_c)}{n+1} \left[\left(\frac{r_c}{r} \right)^{n+1} - 1 \right] - \frac{\psi_c}{m+1} \left[\left(\frac{r_c}{r} \right)^{m+1} - 1 \right] + \frac{\psi_c}{2} \left[\left(\frac{r_c}{r} \right)^2 - 1 \right] \quad (6-74)$$

For free vortex flow, this yields

$$R = 1 - (1 - R_c)(r_c/r)^2 \quad (6-75)$$

For constant-swirl vortex flows,

$$R = R_c - [2(1 - R_c) - \psi_c(r_c/r - 1)/2](r_c/r - 1) \quad (6-76)$$

For exponential vortex flows,

$$R = R_c - 2(1 - R_c)(r_c/r - 1) \quad (6-77)$$

For constant-reaction vortex flows Eq. (6-73) must be integrated directly after setting $n = -1$, to yield

$$R = R_c - 2(1 - R_c) \ln(r_c/r) \quad (6-78)$$

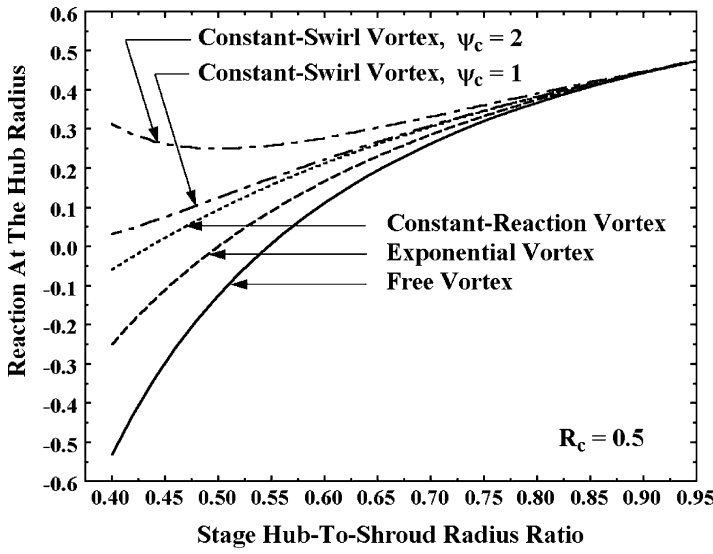
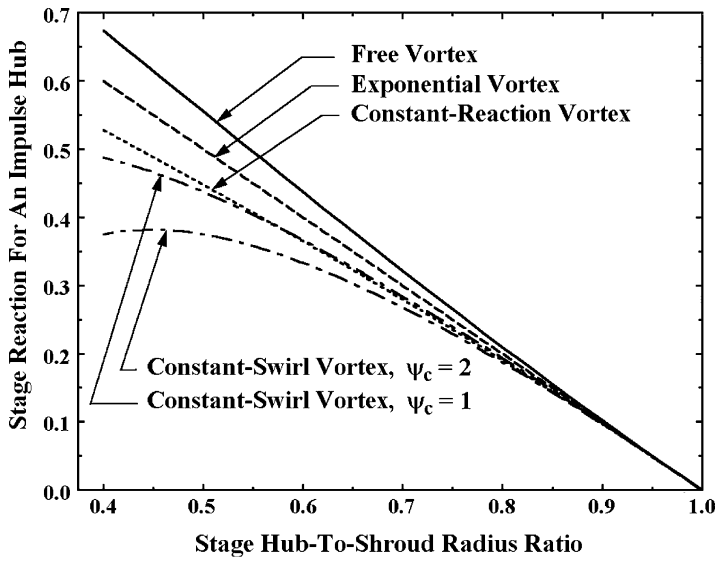


FIGURE 6-10. Effect of Vortex Type on Hub Reaction

Equation (6-74) can also be applied to constant nozzle-angle vortex flows with $n = m = \cos^2 \alpha_{2c}$, but the reaction distribution is a more complicated function of R_c , α_{2c} , ψ_c and radius ratio. It should be noted that the practical constraints imposed on the annulus sizing process usually result in values of reaction somewhat different than predicted by these equations. This is due to the fact that the meridional velocity at the design radius is normally not constant through the stage. Hence, the true reaction at the design radius will differ from R_c .

Eqs. (6-75) through (6-78) can be used to evaluate the influence of vortex type on the reaction distribution. One useful evaluation is to view the hub reaction produced by each vortex type for a range of stage hub-to-shroud radius ratios. Figure 6-10 shows this type of comparison for $R_c = 0.5$. For the constant-swirl vortex, the reaction distribution also depends on ψ_c , so curves are shown for two values of ψ_c . One use for these curves is to determine the lowest value of stage hub-to-shroud radius ratio that can be employed while avoiding negative reaction at the hub. It is seen that the free vortex is the most severely restrictive vortex type, requiring a radius ratio of at least 0.55 to avoid negative reaction. The radius-ratio limit is 0.5 for the exponential vortex and 0.435 for the constant-reaction vortex. Due to the dependence on ψ_c , no general limit can be assigned to the constant-swirl vortex, although for the two cases considered, reaction remains positive down to a radius ratio of 0.4. Figure 6-11 evaluates the influence of vortex type from a different perspective. This figure shows the minimum stage reaction that avoids negative reaction at the hub as a function of stage hub-to-shroud radius ratio. It is also desirable to limit the shroud reaction to not exceed unity. It can be shown that all cases shown on figure 6-11 yield shroud reactions comfortably below this limit. Hence the impulse hub limit is

**FIGURE 6-11. Stage Reaction for an Impulse Hub**

the more restrictive constraint for all of these vortex types. Indeed, it can easily be shown that for all of the vortex types with $m = 1$ considered, shroud reaction will always be less than unity if $R_c > 1$. Only the constant swirl vortex can exceed the shroud reaction limit with $R_c < 1$ and then only for sufficiently large values of ψ_c .

These results show that the free vortex is the least effective type with regard to maintaining a favorable hub reaction level. The constant-swirl vortex is the most effective type, at least for $\psi_c \geq 1$. But hub-to-shroud meridional velocity profile distortion is also a critical consideration. Figure 6-12 illustrates that issue by applying the various vortex types to a typical stage design problem. The stage hub-to-shroud radius ratio was set to 0.4. All cases used a common set of dimensionless performance parameters as shown on the figure, except that a second value of ψ_c was used for the constant-swirl vortex. It is apparent that both of the constant-swirl vortex cases and the constant-reaction vortex case can not be used for this stage due to flow reversal near the shroud at the nozzle exit. Indeed, well before the reverse flow condition is encountered, flow angles will be too low for practical manufacture of the blades. The designer could alleviate this problem by using a higher hub-to-shroud radius ratio or a higher value of ϕ_c . This type of flow-reversal limit is often encountered in axial-flow turbine design due to the highly swirling flows typically required at the nozzle exit. It also is encountered in axial-flow compressors but to a lesser degree due to the lower work coefficients commonly used. Hence, the constant-swirl and constant-reaction vortex types are generally of limited use in axial-flow turbine design. Typically, they are applicable only to rather high-stage hub-to-shroud radius ratios. Note that the constant-swirl vortex cases in figure 6-12 show that use of higher work coefficients substantially increases the meridional profile

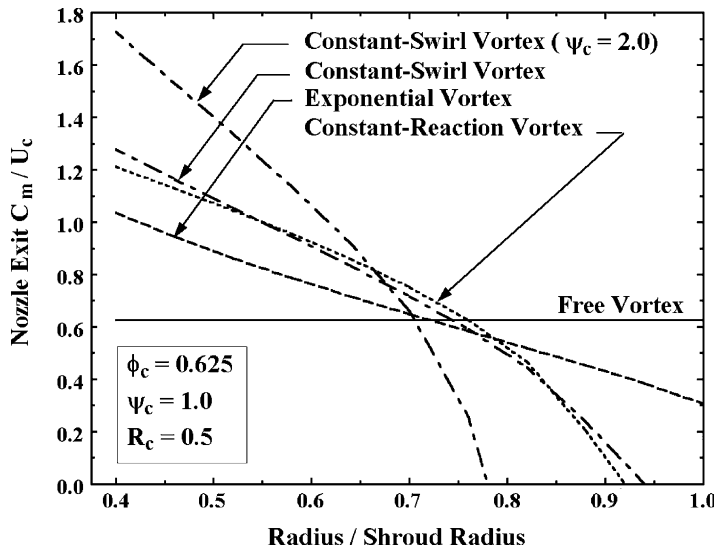
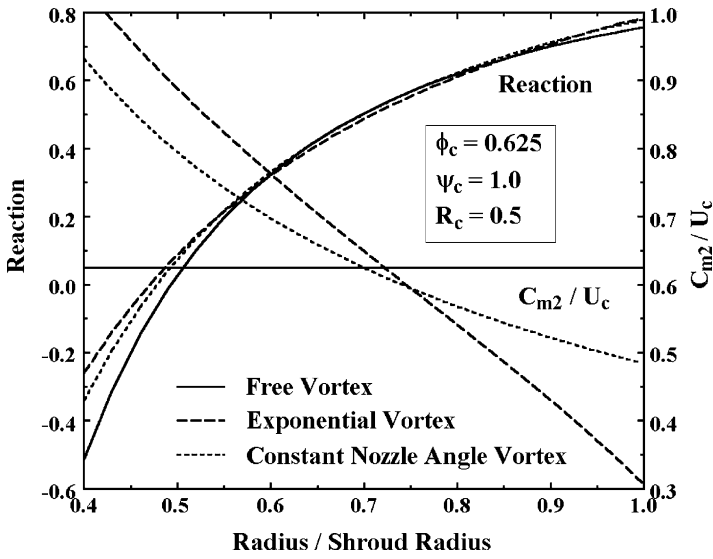


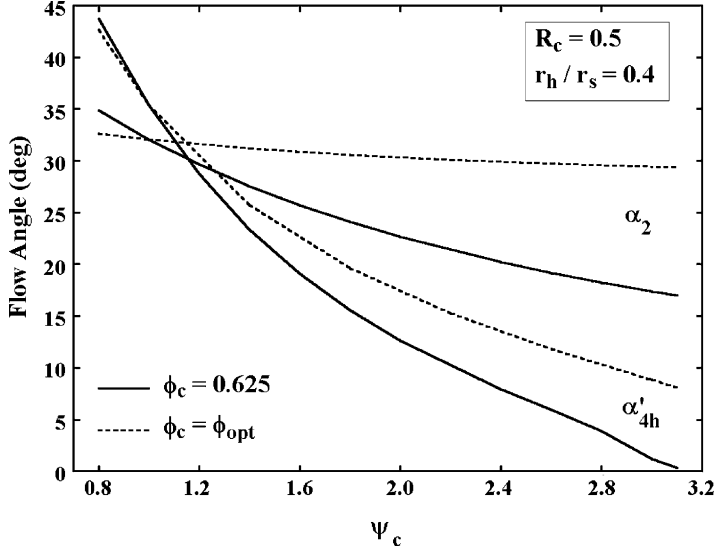
FIGURE 6-12. Meridional Velocity Profile Distortion

distortion. Indeed, further analysis on that design problem showed that flow reversal imposes similar limitations on the exponential vortex type when $\psi_c > 1.7$ is used.

Clearly, the free vortex type has a definite advantage in this regard, since reverse flow cannot occur at either the nozzle or rotor exits. No doubt this is a major reason for its popularity for axial-flow turbine design. The constant nozzle-angle vortex type also cannot experience a flow reversal at the nozzle exit for any practical flow angle as can be seen from Eq. (6-68). However, a flow reversal at the rotor exit is possible for that vortex type also. Figure 6-13 illustrates this vortex type along with the free vortex and exponential vortex types for the same stage design case considered previously. It can be seen that the constant nozzle-angle vortex yields higher hub reaction than the free vortex, almost equaling the exponential vortex in that regard. A hub-to-shroud radius ratio greater than 0.4 would be required to avoid negative reaction, but a value lower than the free vortex case could be used. The constant nozzle-angle vortex also yields less meridional velocity profile distortion than the exponential vortex. Indeed, this vortex type shows quite favorable profile characteristics as well as possibly offering reduced manufacturing cost if a constant section nozzle blade can be used. But there are definite application limits for the constant nozzle-angle vortex. This is illustrated in figure 6-14 by repeating the same basic stage design but covering a range of stage work coefficient values. The nozzle exit flow angle and the rotor exit relative flow angle at the hub are shown to evaluate the effect of profile distortion. One set of curves uses the same stage flow coefficient as the previous cases, which is the optimum flow coefficient for $\psi_c = 1$. It is unlikely that flow angles much less than about 15° would be considered practical in terms of blade manufacturing. Although this presents no serious

**FIGURE 6-13. The Constant Nozzle-Angle Vortex**

problem at the nozzle exit, the rotor exit relative flow angles would significantly limit the application range. Indeed, this flow angle eventually approaches zero, which indicates reverse flow has occurred. If this were an interior stage design, it would be more appropriate to use the optimum stage flow coefficient given by

**FIGURE 6-14. Constant Nozzle-Angle Vortex Limits**

Eq. (6-22). Figure 6-14 shows that use of the optimum flow coefficient significantly increases the practical application range. It is interesting to note that the optimum flow coefficient derived from the generalized total efficiency map of figure 6-3 corresponds to a nearly constant nozzle exit flow angle of approximately 30 to 32° over the range of work coefficients considered.

The vortex type used typically has a less dramatic effect on axial-flow turbine design than on axial-flow compressor design. In part, this is due to the fact that vortex type is effective in addressing many constraints critical to compressor design that are not relevant to turbine design. But vortex type does provide flexibility that sometimes can be used to advantage in turbine design also. The demonstration stage design used previously can be used to illustrate this. The low hub-to-shroud radius ratio clearly is not well suited to most of the standard vortex types. But the general vortex equation given in Eq. (6-15) is not limited to the standard types. A series of preliminary designs were generated for a range of vortex exponent values and processed through the performance analysis of chapter 5 to predict the hub reaction and the stage efficiency achieved by each design. Figure 6-15 shows the hub reaction as a function of the vortex exponent, m , for a several values of the vortex exponent, n . It can be seen that reducing either n or m yields improved hub reaction levels. The lowest value of m considered for each value of n is close to the limit imposed by a flow reversal. Figure 6-16 shows the corresponding predicted stage efficiencies. In comparison to the free vortex design, it is seen that all other combinations of n and m considered yield improved hub reaction and stage efficiency. But it is also clear that the most favorable hub reaction does not necessarily result in the best stage efficiency. The most favorable hub reaction achieved is the near-impulse case

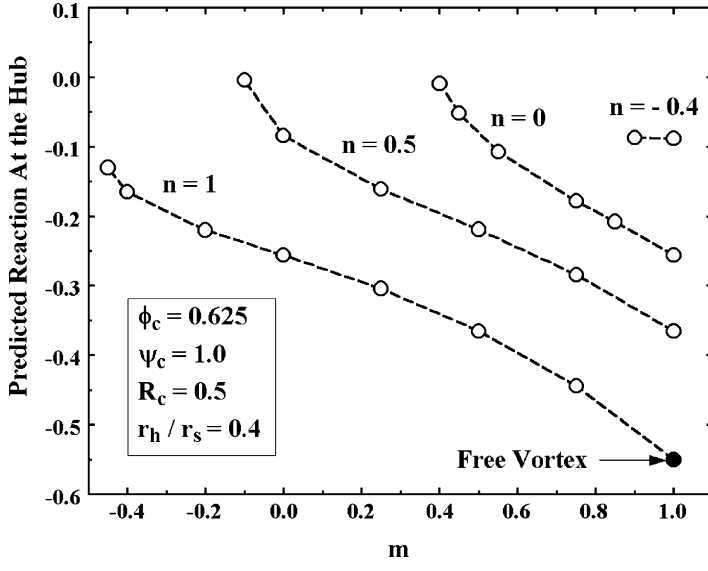


FIGURE 6-15. Effect of Vortex Type on Hub Reaction

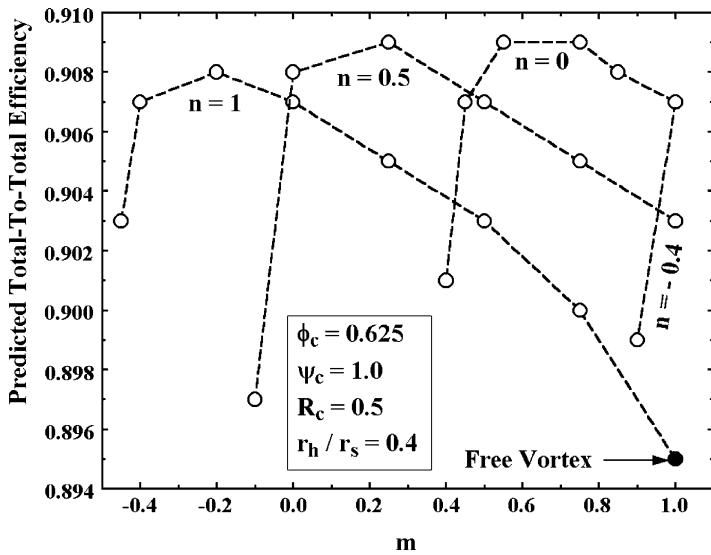


FIGURE 6-16. Effect of Vortex Type on Stage Efficiency

with $n = 0.5$ and $m = -0.1$, yet its efficiency is not significantly better than the free vortex case with its high negative hub reaction. Clearly, highly distorted flow profiles can be as detrimental to stage efficiency as high negative hub reaction. But there are several alternative vortex types that can improve the design point performance of this stage relative to a simple free vortex design. The designer would need to investigate the off-design performance characteristics to decide which vortex type is the best choice.

Somewhat greater flexibility in vortex type is expected when higher hub-to-shroud radius ratios are used. That is typical true for industrial impulse stages. Indeed, it is really necessary if extreme negative hub reaction is to be avoided. But impulse stages are usually designed with emphasis on static efficiency rather than total efficiency. As shown in figure 6-5, that favors relatively high values of ψ_c and relatively low values of ϕ_c , both of which adversely affect the flow reversal limit. Figure 6-17 shows results predicted by the performance analysis of chapter 5 for a series of typical impulse stage preliminary designs. Clearly, reduced values of n and m have minimal effect on hub reaction, and virtually no effect on efficiency. Despite the higher hub-to-shroud radius ratio, flow reversal continues to limit the choices available. Indeed, had the hub and shroud radii not been constrained to be constant through the stage, the range of usable values would have been substantially reduced. Numerous other combinations of n and m were also tried. They are not included in figure 6-17 since they produced no improvement and would simply make the figure confusing. In general, vortex type variation is ineffective as a means of improving the performance of industrial impulse stages. The simpler free vortex or constant nozzle-angle vortex designs are equally effective and much easier to work with. Both of those vortex types permit reasonable end-wall flare angles to be used for

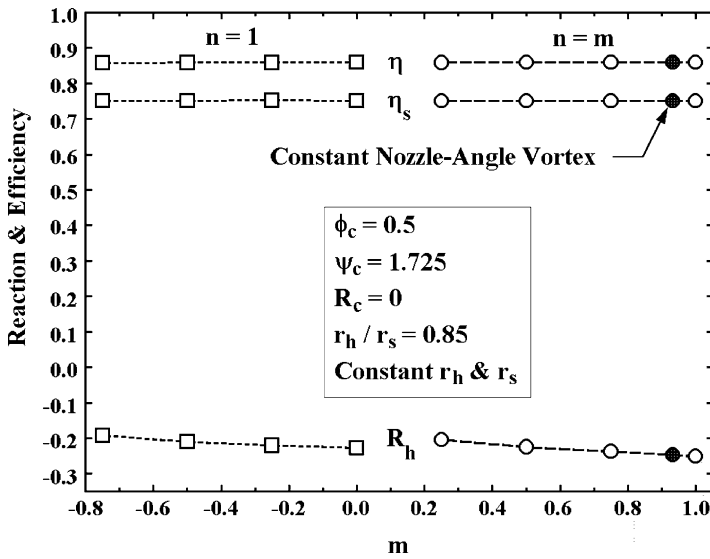


FIGURE 6-17. Effect of Vortex Type for Impulse Stages

this design, which increased the static efficiency by more than five points. That is a far more effective means of improving the stage static efficiency than use of a more complex vortex type. Similarly, a modest increase in stage reaction to $R_c = 0.1$ produced a one-point static efficiency gain. Hence, the dimensionless stage performance parameters selected and use of reasonable end-wall flare angles, where possible, are the primary considerations with regard to the static efficiency of industrial impulse stages.

6.13 Concluding Remarks

The preliminary design system described in this chapter can substantially improve the designer's productivity and effectiveness. A computerized interactive design system is the preferred form, including provision to interface with the performance analysis of chapter 5 and the detailed airfoil design system of chapter 7. The investigation of vortex type for figures 6-15 and 6-16 is a good example. Twenty-one different designs were processed through the preliminary design system and the performance analysis in about ten minutes. Most of that time was spent recording the results for the figures rather than conducting the analyses. It is doubtful that a designer could even consider conducting this type of investigation with a less automated approach. Indeed, its major benefit is to allow the designer to explore a wide range of alternatives to arrive at an optimized basic configuration before expending the effort required for detailed aerodynamic design. Certainly the added productivity is an important benefit, but the improved quality of design is by far its most important contribution. With the detailed description provided in this chapter, the development of a similar

preliminary design system is a relatively simple process. If considered necessary, the approach outlined here can easily be extended to include other enhancements such as radial variations in work, stage exit flow angle, axial chords, etc. But generally those refinements can be left to the detailed design phase without significant compromise.

Chapter 7

DETAILED AIRFOIL DESIGN FOR AXIAL-FLOW TURBINES

The basic airfoil geometry is established by the preliminary design procedure of chapter 6 to match the desired inlet and exit velocity triangles selected for the blade row. Some refinement may be appropriate, based on the more precise flow profile prediction capability of the performance analysis of chapter 5. The selection of some airfoil characteristics will be strongly influenced by the need to achieve adequate mechanical integrity for the intended application. Leading and trailing edge radii, blade thickness distributions, blade taper in the radial direction, etc. are all strongly influenced and possibly dictated by mechanical integrity issues. Many of those issues cannot be fully qualified until the airfoil is designed. Hence, detailed airfoil design is really a collaborative effort between the aerodynamic and mechanical designers. This chapter describes techniques to define airfoils that provide the desired blade characteristics. But it should be recognized that adjustment of some of those characteristics is to be expected as the detailed airfoil design progresses.

Detailed design of axial-flow turbine airfoils involves defining a smooth profile shape that satisfies the basic constraints imposed by the velocity triangles, namely the blade camberline inlet angle, β_1 , and the throat-to-pitch ratio, o/s . Assumed leading and trailing edge geometry reduces the problem to connecting a series of defining points while matching slopes at those points. Airfoil shapes may be defined by simple circular-arc segments, e.g., Fielding [69], spline-connected polynomial segments, e.g., Ye [72], or a combination of both, e.g., Pritchard [73]. The method described in this chapter is quite similar to Ye's method but with several modifications and extensions to make it more general and much easier to use.

NOMENCLATURE

- [A] = matrix containing all polynomial coefficients
 - a = polynomial coefficients
- [B] = matrix containing curve end-point matching conditions
 - b_z = axial chord (figure 7-2)
- [C] = matrix of coefficients used to solve for [A]
 - c = chord
- H = inlet height dimension (figure 7-2)
- N = number of blades; also matrix size

N_c = number of polynomial curve segments defining an airfoil surface
 o = throat width
 R = leading or trailing edge radius
 r = radius
 s = pitch
 t_{max} = blade maximum thickness
 $[Y]$ = matrix containing y coordinates of surface defining points
 y = transverse coordinate (normal to z)
 $[Z]$ = matrix containing z coordinates of surface defining points
 z = axial coordinate
 β = camberline angle with respect to tangent
 β_g = blade gauging angle with respect to tangent
 $\Delta\beta$ = leading or trailing edge wedge angle
 Γ = uncovered turning
 γ = setting angle
 κ = suction surface curvature downstream of the throat

Subscripts

act = actual value
 j = curve number
 k = coefficient number
 P_n = parameter at point P_n ($n = 1$ to 4)
 p = pressure surface parameter
 S_n = parameter at point S_n ($n = 1$ to 5)
 s = suction surface parameter
 1 = airfoil inlet parameter
 2 = airfoil exit parameter

Superscripts

$'$ = first derivative with respect to z
 $''$ = second derivative with respect to z

7.1 Definition of the Airfoil Geometry

Figures 7-1 and 7-2 show the basic parameters used to define the airfoil. The nose radius, R , airfoil camberline angle, β , and wedge angle, $\Delta\beta$, are specified at the airfoil leading and trailing edges. The chord, c , setting angle, γ , the number of blades, N , and the airfoil section radius, r , are also supplied. Based on the discharge velocity triangle and the fluid deviation angle model of chapter 4, the gauging angle, β_g , and the discharge throat-to-pitch ratio, o/s , are also known.

$$\sin \beta_g = o/s \quad (7-1)$$

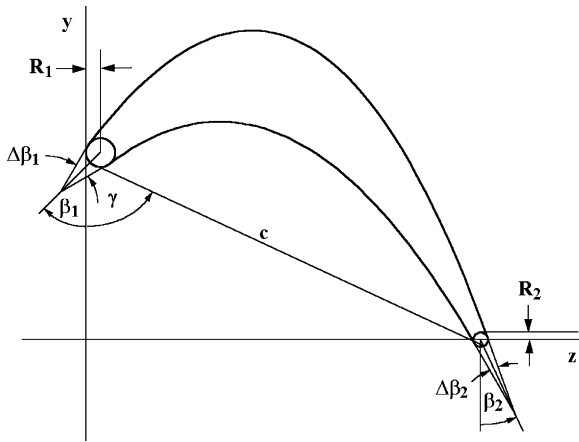


FIGURE 7-1. Basic Airfoil Geometry

The pitch, s , is given by

$$s = 2\pi r / N \quad (7-2)$$

Hence, the throat width, o , is also known. Finally, the uncovered turning, Γ , is used for the airfoil definition. It will be seen subsequently that this may be specified or calculated to match the desired throat width. The basic specifications define the axial chord, b_z , and the inlet height, H , shown in figure 7-2.

$$b_z = c \sin \gamma + R_1(1 - \sin \beta_1) + R_2(1 - \sin \beta_2) \quad (7-3)$$

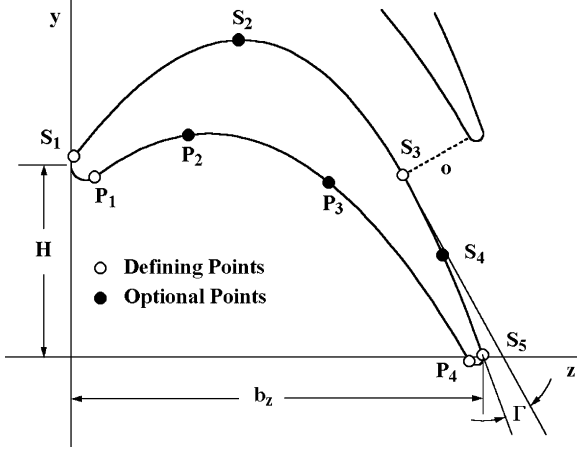


FIGURE 7-2. Airfoil Profile Definition

$$H = c \cos \gamma + R_1 \cos \beta_1 - R_2 \cos \beta_2 \quad (7-4)$$

The coordinates of the leading and trailing edge points or end points of the chord are given by

$$z_l = R_1(1 - \sin \beta_1) \quad (7-5)$$

$$y_l = H - R_1 \cos \beta_1 \quad (7-6)$$

$$z_2 = b_z - R_2(1 - \sin \beta_2) \quad (7-7)$$

$$y_2 = -R_2 \cos \beta_2 \quad (7-8)$$

The airfoil profile is defined by a series of polynomial curves connecting specific points on each surface as shown in figure 7-2. Points S1, S3 and S5 are basic defining points for the suction surface and points S2 and S4 are optional points that can be specified to better control the shape of the surface. Similarly, points P1 and P4 are basic defining points for the pressure surface and points P2 and P3 are optional points. Conditions to be satisfied at the basic defining points follow directly from the airfoil geometry specifications.

$$z_{P1} = R_1[1 + \cos(\beta_1 + \Delta\beta_1 / 2)] \quad (7-9)$$

$$y_{P1} = H - R_1 \sin(\beta_1 + \Delta\beta_1 / 2) \quad (7-10)$$

$$y'_{P1} = \tan(\pi/2 - \beta_1 - \Delta\beta_1 / 2) \quad (7-11)$$

$$z_{P4} = b_z - R_2[1 + \cos(\beta_2 + \Delta\beta_2 / 2)] \quad (7-12)$$

$$y_{P4} = -R_2 \sin(\beta_2 + \Delta\beta_2 / 2) \quad (7-13)$$

$$y'_{P4} = \tan(\beta_2 + \Delta\beta_2 / 2 - \pi/2) \quad (7-14)$$

$$z_{S1} = R_1[1 - \cos(\beta_1 - \Delta\beta_1 / 2)] \quad (7-15)$$

$$y_{S1} = H + R_1 \sin(\beta_1 - \Delta\beta_1 / 2) \quad (7-16)$$

$$y'_{S1} = \tan(\pi/2 - \beta_1 + \Delta\beta_1 / 2) \quad (7-17)$$

$$z_{S3} = z_{P4} - o \cos(\Gamma + \beta_2 - \Delta\beta_2 / 2) \quad (7-18)$$

$$y_{S3} = y_{P4} + s - o \sin(\Gamma + \beta_2 - \Delta\beta_2 / 2) \quad (7-19)$$

$$y'_{S3} = \tan(\Gamma + \beta_2 - \Delta\beta_2 / 2 - \pi/2) \quad (7-20)$$

$$z_{S5} = b_z - R_2[1 - \cos(\beta_2 - \Delta\beta_2 / 2)] \quad (7-21)$$

$$y_{S5} = R_2 \sin(\beta_2 - \Delta\beta_2 / 2) \quad (7-22)$$

$$y'_{S5} = \tan(\beta_2 - \Delta\beta_2 / 2 - \pi/2) \quad (7-23)$$

If any optional points are used, their (z, y) coordinates are specified directly.

7.2 The Airfoil Profile Model

Polynomial segments connecting adjacent points on each surface are used to define the airfoil surfaces. In order to obtain continuous surface curvatures, first and second derivatives should be matched at all interior points where two polynomial segments match. Ye [2] uses a combination of third- and fourth-order polynomials on the suction surface to permit matching all parameters in Eqs. (7-15) through (7-23) while maintaining continuous derivatives. Third-order polynomials are sufficient to match all parameters in Eqs. (7-9) through (7-14) while maintaining continuous derivatives for the pressure surface. The use of fourth-order polynomials has been found to greatly complicate the application of this design method. The resulting suction surface profile is often subject to very unstable oscillations. Identifying airfoil geometry specifications that yield a reasonable airfoil profile can be a very tedious process when this occurs and can force the designer to accept undesirable compromises. This writer employs third-order polynomials for all segments on both surfaces to avoid those problems. This means that not all coordinates, slopes and continuous derivative conditions can be matched at interior points on the suction surface. That is not a fundamental compromise, since the design data can be adjusted to correct these problems. The best practice is to include the following alternate options for addressing this issue.

- Option 1: Use the coordinates of point S3 while requiring continuous first and second derivatives at that point. The slope at the point S3 given by Eq. (7-20) is ignored in this case. This usually results in the throat not being located at point S3 and a throat width different from the desired value. That can be corrected by adjusting the uncovered turning and/or the exit blade angle until the correct throat width and location are obtained.
- Option 2: Match the coordinates and slope at point S3 and ignore point S4. In this case, the second derivative is normally not continuous at point S3. This usually yields the desired throat width, but may result in a second throat or an unacceptable blade shape. Manual adjustments similar to option 1 can be used to correct the problem.
- Option 3: Similar to option 1, but the airfoil design system computes the uncovered turning needed to achieve the desired throat location and throat width. Basically, this just automates a manual correction process that could be used with option 1. With this option, the specified uncovered turning and slope at the point S3 given by Eq. (7-20) are ignored.

Usually option 3 is the most convenient choice to quickly arrive at an acceptable airfoil profile. But it is best to switch to option 1 at the end of the design process to define consistent airfoil specifications and to assure continuous derivatives. At that point, the uncovered turning needed to accomplish this is known from the option 3 result.

The airfoil surfaces are defined by third-order polynomials for each curve connecting adjacent defining points on the two surfaces along with circular-arc segments for the end radii. Designating the curve number by a subscript j and the polynomial coefficient number by a subscript k , the surface values of y and its derivatives for any curve are

$$y_j = \sum_{k=1}^4 a_{j,k} z^{(k-1)} = a_{j,1} + a_{j,2}z + a_{j,3}z^2 + a_{j,4}z^3 \quad (7-24)$$

$$y'_j = \sum_{k=2}^4 (k-1)a_{j,k} z^{(k-2)} = a_{j,2} + 2a_{j,3}z + 3a_{j,4}z^2 \quad (7-25)$$

$$y''_j = \sum_{k=3}^4 (k-1)(k-2)a_{j,k} z^{(k-3)} = 2a_{j,3} + 6a_{j,4}z \quad (7-26)$$

To facilitate a matrix solution for the polynomial coefficients, the curve segments will be numbered in order for each surface. Hence, the suction surface will have two to four curves, depending on whether the optional defining points are used. Similarly, the pressure surface will have one to three curves, depending on whether the optional defining points are used. A simultaneous solution of four equations will be needed to determine the polynomial coefficients for each curve. But the conditions requiring continuous derivatives at the defining points means the coefficients for adjacent curves are not independent, so a systematic matrix solution is the proper solution procedure. It is convenient to follow a very systematic order in imposing the defining equations for the various curves. This will greatly simplify the logic required for a numerical solution. Table 7-1 shows a convenient arrangement of the defining equations applicable to the suction surface for options 1 and 3, which is the most complex case. Note that the sequence of defining equations used for all curves is identical except for the third defining equation for the first curve and the fourth defining equation for the last curve. Hence, this table is easily modified for cases where one or both optional points are omitted, since only the first and last curves used require special treatment. It is only

Table 7-1. Suction Surface Model for Options 1 and 3

Curve	End Points	Defining Equations
1	S1 and S2	1) Match y at S1 2) Match y at S2 3) Match y' at S1 4) Continuous y' at S2
2	S2 and S3	1) Match y at S2 2) Match y at S3 3) Continuous y'' at S2 4) Continuous y' at S3
3	S3 and S4	1) Match y at S3 2) Match y at S4 3) Continuous y'' at S3 4) Continuous y' at S4
4	S4 and S5	1) Match y at S4 2) Match y at S5 3) Continuous y'' at S4 4) Match y' at S5

Table 7-2. Suction Surface Model for Option 2

Curve	End Points	Defining Equations
1	S1 and S2	1) Match y at S1 2) Match y at S2 3) Match y' at S1 4) Continuous y' at S2
2	S2 and S3	1) Match y at S2 2) Match y at S3 3) Continuous y'' at S2 4) Match y' at S3
3	S3 and S5	1) Match y at S3 2) Match y at S4 3) Match y' at S3 4) Match y' at S5

necessary to omit the unused curves from the table, renumber the curves and modify the end point numbers. The same approach can be followed for the pressure surface defining equations. This approach is well suited to a systematic numerical solution. It is only necessary to determine how many curves are used and identify their end points to follow this systematic process of imposing the defining conditions. Use of option 2 for the suction surface definition requires special treatment. In this case, point S4 is ignored and the slope at point S3 is imposed. Table 7-2 shows the defining equations for this case. Note that the same practice as outlined above can be used, followed by imposing a special fourth defining equation for the second to the last curve and a special third defining equation for the last curve. If point S2 is omitted, the same systematic process is followed after renumbering the curves and redefining the curve end-point numbers. Also note that it is no longer possible to require a continuous second derivative at the point S3.

7.3 Determining the Polynomial Coefficients

The polynomial coefficients are determined by solving the following matrix equation.

$$[C][A] = [B] \quad (7-27)$$

If N_c is the number of curves approximating the surface being considered, $[C]$ is an $N \times N$ matrix, where $N = 4N_c$. The matrix $[A]$ is a $1 \times N$ matrix containing the N polynomial coefficients to be determined and $[B]$ is a $1 \times N$ matrix containing the N match point conditions derived from the defining equations. To assign values to $[B]$ and $[C]$, it is convenient to employ two $1 \times (N_c + 1)$ matrices, $[Z]$ and $[Y]$, containing the z and y coordinates of all defining points ordered from

leading edge to trailing edge. First, initialize all elements in [B] and [C] to zero. Then set the standard matching conditions by the following steps for values of j from 1 to N_c .

$$\begin{aligned} n = 4(j-1) + 1: B_n &= Y_j, C_{n,n} = 1, C_{n,n+1} = Z_j, C_{n,n+2} + Z_j^2, C_{n,n+3} = Z_j^3, \\ B_{n+1} &= Y_{j+1}, C_{n+1,n} = 1, C_{n+1,n+1} = Z_{j+1}, C_{n+1,n+2} = Z_{j+1}^2, \\ C_{n,n+3} &= Z_{j+1}^3 \end{aligned}$$

Next, set defining equation 3 for the first curve using y' and z for the first reference point:

$$B_3 = y', C_{3,2} = 1, C_{3,3} = 2z, C_{3,4} = 3z^2,$$

Next, set defining equation 4 for the last curve using y' and z for the last reference point:

$$n = N: B_n = y', C_{n,n-2} = 1, C_{n,n-1} = 2z, C_{n,n} = 3z^2,$$

Next set the continuous y' condition by the following steps for values of j from 1 to $N_c - 1$ unless this is the suction surface using option 2. In that case, use values of j from 1 to $N_c - 2$.

$$\begin{aligned} n = 4j: C_{n,n-2} &= 1, C_{n,n-1} = 2Z_{j+1}, C_{n,n} = 3Z_{j+1}^2, C_{n,n+2} = -1 \\ C_{n,n+3} &= -2Z_{j+1}, C_{n,n+4} = -3Z_{j+1}^2 \end{aligned}$$

Next set the continuous y' condition by the following steps for values of j from 2 to N_c unless this is the suction surface using option 2. In that case, use values of j from 2 to $N_c - 1$.

$$n = 4(j-1) + 3: C_{n,n-4} = 2, C_{n,n-3} = 6Z_j, C_{n,n} = -2, C_{n,n+1} = -6Z_j$$

If treating the suction surface using option 2, impose the special throat slope matching conditions, using y' and z at defining point S3.

$$\begin{aligned} n = N-4: B_n &= y', C_{n,n-6} = 1, C_{n,n-5} = 2z, C_{n,n-4} = 3z^2 \\ n = N-1: B_n &= y', C_{n,n-1} = 1, C_{n,n} = 2z, C_{n,n+1} = 3z^2 \end{aligned}$$

The resulting matrices for the two surfaces can be solved by Gaussian elimination to obtain the array of polynomial coefficients. The individual coefficients can be recovered from the matrix [A] elements by

$$n = 4(j-1) + k: a_{j,k} = A_n$$

The surface profile coordinates for all curve segments between the defining points are given by Eq. (7-24) using the appropriate polynomial coefficients over the range of z between the curve segment end points.

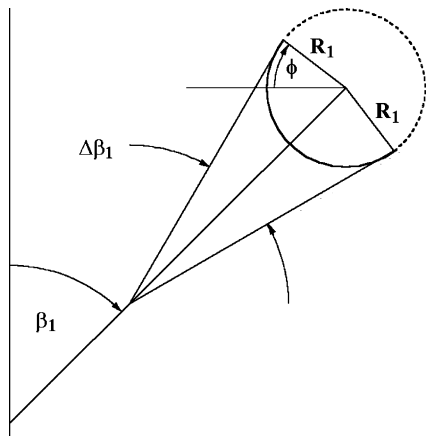


FIGURE 7-3. The Leading Edge Profile

7.4 Leading and Trailing Edge Profiles

The surface profiles for the leading and trailing edges are constructed by imposing the appropriate circular-arc segment. Figure 7-3 illustrates the relevant geometry for the leading edge profile construction. It is easily shown that the surface coordinates can be expressed as a function of the angle ϕ , i.e.,

$$z = R_1(1 - \cos \phi) \quad (7-28)$$

$$y = H + R_1 \sin \phi \quad (7-29)$$

$$\beta_1 + \Delta\beta_1 / 2 - \pi \leq \phi \leq \beta_1 - \Delta\beta_1 / 2 \quad (7-30)$$

The trailing edge construction is quite similar. It is easily shown that the trailing edge coordinates are

$$z = b_z - R_2(1 - \cos \phi) \quad (7-31)$$

$$y = R_2 \sin \phi \quad (7-32)$$

$$\beta_2 + \Delta\beta_2 / 2 - \pi \leq \phi \leq \beta_2 - \Delta\beta_2 / 2 \quad (7-33)$$

7.5 The Passage Throat Calculation

Once the airfoil profile is known, it is necessary to calculate the passage throat width. As previously noted, the throat may not be located at the intended

point S_3 . Also, the actual throat width may not equal the intended value specified by the user. It is also possible to encounter an ambiguous throat, when the throat width does not initiate from the point P_4 on the other side of the passage. Although that might be appropriate for a blade row intended to always operate with a supersonic discharge, the present airfoil design method is not an effective design method for an overexpanded, convergent-divergent passage. This method is intended for more conventional designs where the passage width is intended to decrease smoothly from the passage inlet to the throat width defined between points S_3 and P_4 on adjacent airfoils. Since the gauging angle, or the ratio o/s , is an essential design parameter, the actual throat width obtained provides a critical evaluation of the suitability of the airfoil design for the intended application. Figure 7-4 illustrates a simple method to determine the actual throat. The second airfoil bounding the passage is identical to the base design, but with all y coordinates increased by the pitch. The intended throat location between S_3 and P_4 on adjacent blades, o_c , is used as the initial estimate. Then the passage widths o_- and o_+ are defined to obtain locations on the suction surface well before and after the actual throat. The initial estimates of the axial coordinates for these three widths are

$$z_- = (z_{S_1} + z_{S_3})/2 \quad (7-34)$$

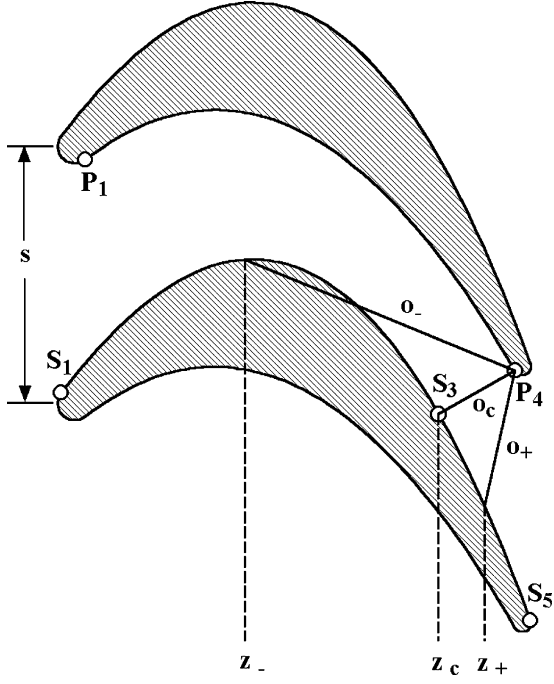


FIGURE 7-4. The Passage Throat Calculation

$$z_c = z_{S3} \quad (7-35)$$

$$z_+ = (z_{S3} + z_{S5})/2 \quad (7-36)$$

The corresponding values of y are computed from the appropriate polynomial curve segments. Then, an iterative numerical process is conducted to systematically reduce the distance between z_- and z_+ to converge within an acceptable tolerance such that the true throat lies between them. The procedure is as follows:

1. Calculate a passage width, o at a value of z midway between z_- and z_c . If $o > o_c$ then set $z_- = z$ and $o_- = o$. Otherwise, set $z_+ = z_c$, $o_+ = o_c$, $z_c = z$ and $o_c = o$.
2. Calculate a passage width, o at a value of z midway between z_+ and z_c . If $o > o_c$ then set $z_+ = z$ and $o_+ = o$. Otherwise, set $z_- = z_c$, $o_- = o_c$, $z_c = z$ and $o_c = o$.
3. Return to step 1 and repeat the process until $(z_+ - z_-)/b_z$ is reduced to a value less than an acceptable tolerance.

When this process is converged, z_c , y_c and o_c define the actual throat width and its location on the suction surface. The appropriate polynomial curve segment also provides the suction surface slope, y'_c , at the throat, which defines the actual uncovered turning. This provides the actual values for the completed design, i.e.,

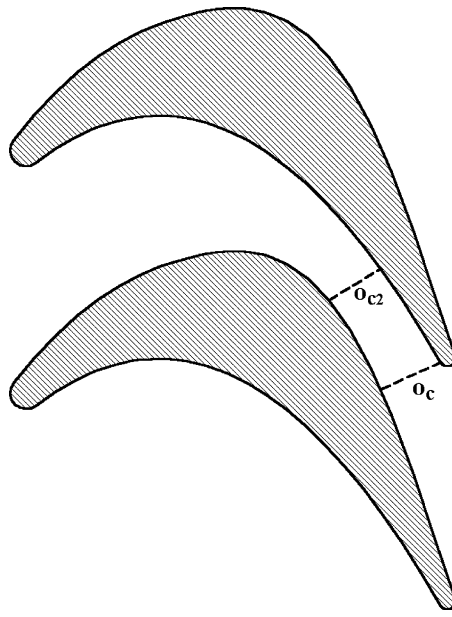
$$\beta_{g,act} = \arcsin(o_c/s) \quad (7-37)$$

$$\Gamma_{act} = \arctan(y'_c) + \pi/2 - \beta_2 + \Delta\beta_2/2 \quad (7-38)$$

Depending on which of the previously mentioned options for modeling the throat is used and the status of the design, these values may not be the same as the specified values. The suction surface curvature downstream of the throat is also an important parameter as described in chapter 4. This can be estimated by

$$\kappa_{act} = \frac{2 \sin(\Gamma_{act}/2)}{\sqrt{(x_c - x_{S5})^2 + (y_c - y_{S5})^2}} \quad (7-39)$$

As a final check, the (x, y) coordinates at a series of points between points between S_1 and S_5 on lower blade and P_1 and P_4 on the upper blade are generated and distances between all combinations of the points on the two surfaces are calculated. If any of those distances is less than the calculated throat width, an ambiguous throat definition exists. Figure 7-5 illustrates an ambiguous throat case. Clearly the passage width o_{c2} is less than the throat width, o_c , at the blade row discharge.

**FIGURE 7-5. An Ambiguous Throat Case**

7.6 Adjusting the Uncovered Turning

It is often convenient to have the airfoil design system determine the uncovered turning required to obtain the desired throat location and throat width or gauging angle. This is the third option to model the throat noted previously in this chapter. It requires accomplishing the airfoil design in an iterative procedure to obtain the required value of Γ . A conservative estimate is used to initiate the process.

$$\Gamma = \arccos[0.9(z_{p4} - z_{s1})/o] - \beta_2 + \Delta\beta_2 / 2 \quad (7-40)$$

After the airfoil has been designed, the estimated value of Γ can be improved as follows:

$$\Gamma = \Gamma_{act}; \quad \Gamma_{act} \geq 0 \quad (7-41) \text{ AQ: Au. please check the numbering of the equations}$$

$$\Gamma \rightarrow \Gamma/2; \quad \Gamma_{act} < 0 \quad (7-43)$$

$$\Gamma \leq 0.475\pi - \beta_2 + \Delta\beta_2 / 2 \quad (7-44)$$

This iterative process is repeated until the specified Γ agrees with the resulting Γ_{act} within an acceptable tolerance. This iterative process converges rapidly,

assuming reasonable airfoil design specifications were entered. Indeed, the limit imposed in Eq. (7-44) is simply a precaution against the possibility that unreasonable specifications might inadvertently be used. When the appropriate value of Γ has been determined, it can be used with the first option to model the throat. This yields the desired throat width and continuous first and second derivatives without the need of the iteration procedure. Indeed, the iterative procedure simply automates a process that could be done manually with the first option. But it greatly expedites the design process while the designer is investigating alternate design specifications.

7.7 Design of a Complete Blade

The design of a complete blade is accomplished by designing a series of airfoil sections for a range of section radii and stacking them to form the complete blade. This requires selecting a stacking axis for the blade and defining stacking coordinates (z_k, y_k) on each airfoil section. Common choices for (z_k, y_k) are the center of gravity, the leading edge or the trailing edge. Usually the stacking axis is a simple radial line, although other choices may be preferred to enhance mechanical integrity. A simple translation of coordinates to relocate the stacking point (z_k, y_k) on the stacking axis for all sections yields the complete stacked blade.

A special case is the constant-section blade where the airfoil geometry is identical on all constant radius sections. Since the pitch varies with radius, a modification of the basic airfoil defining data is necessary to produce the same airfoil at a different radius. This is necessary to obtain the same defining point, S_3 . The parameters that must be modified are r, s, o and Γ . Using an overbar to designate these modified parameters for the new blade section, Eqs. (7-18) and (7-19) require

$$\bar{s} = 2\pi\bar{r} / N \quad (7-45)$$

$$\bar{o} \cos(\bar{\Gamma} + \beta_2 - \Delta\beta_2 / 2) = o \cos(\Gamma + \beta_2 - \Delta\beta_2 / 2) \quad (7-46)$$

$$\bar{s} - \bar{o} \sin(\bar{\Gamma} + \beta_2 - \Delta\beta_2 / 2) = s - o \sin(\Gamma + \beta_2 - \Delta\beta_2 / 2) \quad (7-47)$$

Once the basic airfoil section has been designed, it can be copied to other constant radius section using Eqs. (7-45) through (7-47). The reason for doing that is to obtain the actual values of o, β_g, Γ and κ for the new blade sections to permit a performance analysis of the complete blade row. Note that the actual values of these parameters will be different from those derived from Eqs. (7-45) through (7-47) to define the new airfoil sections. This process requires that all airfoil sections, including the basic section to be copied, must be designed using the first option to model the throat described previously in this chapter.

7.8 The Optional Defining Points

The optional defining points S_2, S_4, P_2 and P_3 , provide the designer with additional control over the airfoil shape. The most effective way to exploit them is through an interactive graphical interface. Once a basic airfoil design is accomplished

using the five basic defining points, the designer should be able to add, modify or delete optional points. The current airfoil profile should be displayed graphically on the monitor screen. If the user chooses to add an optional point, it can be initialized to lie on the existing profile at a convenient location between relevant basic defining points. This will leave the current airfoil profile unchanged but adds the control offered by the optional point. The user should be able to move the optional points with a drag-and-drop interactive capability. Each change to an optional point should cause the airfoil profile to be regenerated on the monitor screen. This is a very efficient way to make use of these optional points to shape the airfoil. Any approach less effective than this is likely to discourage the designer from making full use of this added control due to the difficulty of achieving the desired effect.

7.9 Evaluation of the Airfoil Design

Detailed airfoil design should normally follow the preliminary stage design process described in chapter 6. This should include an aerodynamic performance analysis as described in chapter 5. This provides the designer with a high degree of confidence that the basic stage configuration and velocity triangles selected can achieve the expected performance. In principle, the detailed airfoil design process should not significantly alter the results from an aerodynamic performance analysis. Indeed, the detailed design process contributes design details not directly recognized by the performance analysis of chapter 5. In effect, the performance analysis assumes that "well-designed" components are used. The detailed design process seeks to supply that assumed design quality. In practice, achieving that design quality normally imposes some deviations in the preliminary blade geometry that may alter the performance prediction results. One obvious case where significant changes may result is a blade row with constant airfoil geometry from hub to shroud. When all blade sections are constructed and stacked, it is almost certain to result in values of throat width or gauging angle that are significantly different from those assumed in the preliminary design. In almost any case, suction surface curvatures and maximum blade thicknesses will differ from those assumed for the preliminary design. Hence, a final performance analysis using the relevant geometry from the detailed design process is always wise and sometimes essential.

But the evaluation of the detailed airfoil design must include consideration of the internal flow characteristics not evaluated by the performance analysis. One significant feature is the passage width distribution from inlet to discharge. Passage width should always show continuous reduction from the inlet to the throat. The passage width distribution is easily established using the (x, y) coordinates at a series of points between points between S_1 and S_5 on the blade suction surface and P_1 and P_4 on the pressure surface of an adjacent blade. For each point on the adjacent blade pressure surface, the distance to all points on the blade suction surface is easily calculated. The local passage width is the minimum distance, which can be determined by interpolation. Figure 7-6 shows passage width distributions for the root and tip airfoil sections of a constant-section nozzle blade design. Both airfoil sections achieve the desired

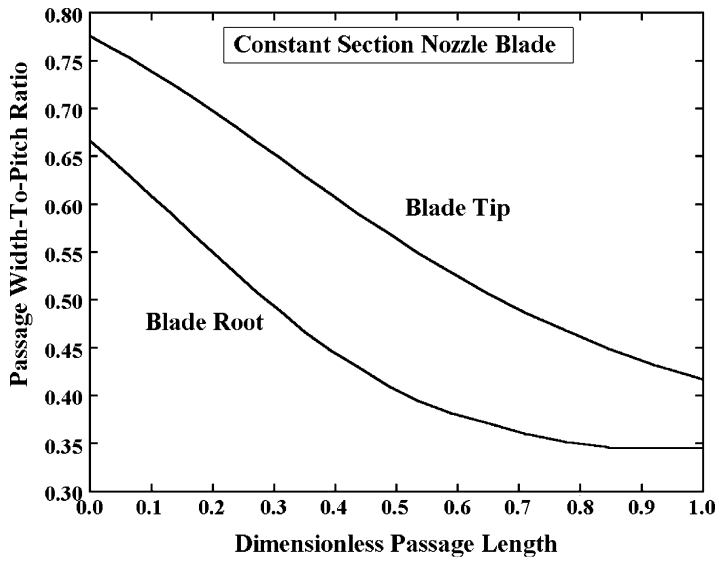


FIGURE 7-6. The Passage Width Distributions

reduction in passage width, although the root section is somewhat marginal. This writer's detailed airfoil design system displays the passage width distribution on demand for the airfoil section being designed. Hence, the designer is guided by this consideration throughout the airfoil profile design process.

A more fundamental evaluation of the airfoil design is concerned with the airfoil surface velocity distributions or blade-loading diagram. This requires conducting a blade-to-blade flow analysis for the various airfoil sections. Blade-to-blade flow analysis techniques suitable for both axial-flow and radial-inflow turbines are described in chapter 13. The suction surface velocity distribution is the most critical consideration for all types of turbomachines, since it normally exhibits the highest velocities. It is generally accepted that for axial-flow turbine blades the suction surface velocity should increase smoothly from the inlet to a maximum value and then remain essentially constant over the aft portion of the blade. Flow diffusion should be avoided as much as possible, particularly on the suction surface. Figure 7-7 shows an experimental blade-loading diagram for a turbine nozzle from Whitney et al. [74], which approximates the desired blade-loading characteristics. It will be seen subsequently in this book that it is relatively easy to include a two-dimensional boundary layer analysis with the blade-to-blade flow analysis to provide some assessment of viscous-flow effects. This provides a better estimate of the potential for boundary layer separation and even gives an estimate of the profile loss coefficient. However, it provides largely a qualitative assessment, since it does not consider secondary flow effects that are often significant. A more fundamental evaluation is supplied by viscous-flow computational fluid dynamics (CFD) codes applied to the entire blade row or even to the entire stage. Most modern turbomachinery design groups employ one or more commercially available CFD codes capable of this type of analysis.

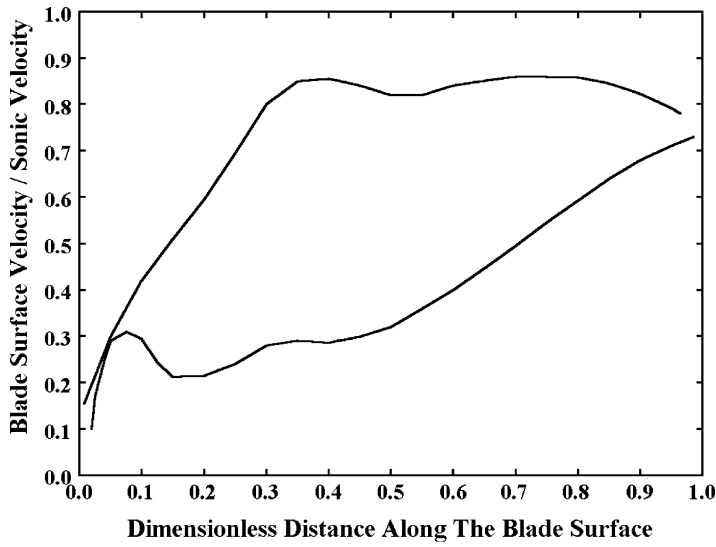


FIGURE 7-7. An Experimental Blade-Loading Diagram

7.10 A Computerized Airfoil Design System

It is relatively easy to implement the procedures described in this chapter in an efficient interactive design system. The following features have been found to be particularly effective.

- The initial estimates for the airfoil section designs can be supplied by the preliminary design system of chapter 6. The simplest approach is to provide the preliminary design system with the capability to export an input file for the detailed airfoil design system.
- The airfoil design system should also be capable of exporting an input file for one of the blade-to-blade flow analyses described subsequently in chapter 13. That greatly simplifies the blade loading diagram evaluation described previously in this chapter.
- The design system should automatically carry out the airfoil design process as far as possible with available design specifications. With error trapping allowed by most modern programming software, this can be accomplished without significant risk of a fatal error terminating the process.
- A few well-chosen monitor screen messages indicating missing specifications, options in use and the status of key design steps are very helpful to the designer.
- The interactive procedure for employing the optional profile definition points is an extremely valuable enhancement that is almost essential to use those optional points effectively.

- Monitor screen graphical displays of the airfoil in a design view (similar to figure 7-1), a profile view (using the chord as the abscissa) and a cascade view (two adjacent blades as they will be applied) are very useful in evaluating the design.
- Design view and profile view profile surface coordinates are also useful output blocks. Blade thickness and passage width distribution can also be included.
- A monitor screen passage area distribution graphical display similar to figure 7-6 is very useful.
- When all airfoil sections have successfully been designed, the design system should save the blade data needed for the performance analysis of chapter 5 in its input file. That permits import of that blade data by the performance analysis for a final prediction. That approach is much simpler than for the airfoil design system to revise the more complicated input file for the performance analysis.
- The three options for modeling the blade throat described previously in this chapter greatly improve the effectiveness of the design system.
- The blade stacking procedures can also be easily incorporated to save time for drafting and manufacturing activity. This just adjusts the blade section coordinates to a common, stacked-blade origin.
- It is useful to include the capability to export data to a text file for subsequent importing by spreadsheet or graphics software. Most of the figures in this chapter were created in that way. This also often permits electronic transfer of data to mechanical designers, CFD analysts, drafting, numerical controlled machining, etc.

With proper planning, the suggested monitor screen output blocks can also be used for creating a printer output file to reduce the development time for the interactive system.

Chapter 8

INDUSTRIAL AXIAL-FLOW TURBINE APPLICATION PROCEDURES

Industrial axial-flow turbines are often one-of-a-kind turbines configured to a specific customer's requirements. With no duplicate machines to share in absorbing development costs, cost-effective turbine development becomes a major imperative. Common practice is to configure the turbine using a series of standard turbine stage designs with preestablished aerodynamic performance and mechanical integrity. This dramatically reduces the engineering time and cost associated with the design and development of these turbines. But efficient and accurate application procedures are essential to the success of this approach. The preestablished aerodynamic performance is often referred to as the rated performance. The stage rated performance is obtained from prototype testing or the best available performance prediction methods. Application procedures apply this rated performance to predict the stage performance for the specific operating conditions required for the application. This will usually involve operating conditions quite different from those used to establish the rated performance. In some cases, even the working fluid will be different from that used to establish the rated performance. To further complicate the problem, the application engineer will usually have to consider a variety of combinations of the standard industrial stages before arriving at an optimum configuration for the application. Hence, efficiency and reliability are mandatory characteristics of an industrial turbine application procedure. For many years, accuracy was a secondary consideration. Most applications were mechanical-drive units, often using condensing turbines. The actual performance of these turbines was extremely difficult to quantify. Sufficient accuracy to ensure that the turbine could accomplish its mechanical-drive function was necessary, but neither the manufacturer nor the customer could accurately establish the actual performance of the turbine. The advent of the special-purpose industrial turbine-generator dramatically changed this situation by providing a direct and meaningful power assessment. Quite abruptly, the accuracy of application procedures became another imperative. This requirement has also expanded into the mechanical-drive turbine market as well. Today, sophisticated customers are far more likely to pursue the difficult assessment of the mechanical-drive turbine's performance through field testing, particularly if there is reason

to suspect a performance deficiency. In this writer's experience, inadequate application procedures are by far the most common source of industrial turbine performance deficiencies. This has resulted in some very expensive warranty problems for manufacturers as well as substantial adverse economic impact for the users. This chapter seeks to point out some common deficiencies in application procedures and to suggest some viable alternatives.

NOMENCLATURE

- A = characteristic passage area
- a = sound speed
- c_p = specific heat at constant pressure
- c_v = specific heat at constant volume
- C_0 = spouting velocity
- D = characteristic diameter
- H = total enthalpy
- h = enthalpy
- K_{RE} = Reynolds number correction factor
- k = ratio of specific heats = c_p/c_v
- M = Mach number
- \dot{m} = mass flow rate
- N = rotation speed, rpm
- P = pressure
- P_R = pressure ratio
- Q = volume flow
- Re_c = blade chord Reynolds number
- Re_{tip} = Reynolds number based on tip radius and speed
- r = radius
- U = blade speed = $r\omega$
- W = relative velocity
- z = compressibility factor
- η = efficiency
- v = velocity ratio = U/C_0
- ρ = fluid density
- ω = rotation speed (radians/sec)

Subscripts

- h = hub parameter
- id = an ideal, isentropic condition
- m = parameter at midpassage height
- s = total-to-static condition or shroud parameter
- t = total thermodynamic condition
- $*$ = a condition corresponding to sonic flow
- 1 = nozzle row inlet parameter
- 2 = nozzle row exit parameter

3 = rotor row inlet parameter

4 = rotor row exit parameter

8.1 Stage Performance Rating Curves

An industrial turbine stage's rated performance is conveniently presented in the form of rating curves. This is a practical application of the principle of similitude discussed in chapter 1. Stage performance data obtained from prototype testing or the best available performance prediction methods are reduced to equivalent performance data. These general rating curves can be used to estimate the stage performance under any operating conditions required for the actual application. This provides a method to apply experimental performance data to virtually any application. In the case of predicted rating curves, it allows performance estimates to be based on prediction methods too sophisticated to provide the efficiency and reliability required for application work. For purpose of illustration, the axial-flow turbine performance prediction method described in chapter 5 is used to generate performance data for a turbine stage using air as the working fluid to simulate results that might be obtained from prototype stage testing. These data are reduced to equivalent form to be used to apply the stage to a steam turbine application. Under the conditions considered, air is basically a thermally perfect gas. Hence, the thermally perfect gas equation of state is applicable, i.e.,

$$P = \rho RT \quad (8-1)$$

However, the specific heats, c_p and c_v , are functions of temperature, so their ratio, k , is not constant. Under the same conditions, steam is a nonideal gas governed by

$$P = z\rho RT \quad (8-2)$$

The compressibility factor, z , as well as k , c_p and c_v , are functions of temperature and pressure, and the values of R and k are quite different from those of air. This fairly severe test of the similarity concept will illustrate its limitations as well as its proper application. It also provides an opportunity to validate some of the conclusions that were stated previously in chapter 1 without supporting evidence. The equivalent rating curves derived from air performance data will be based on fundamental equivalence parameters so they can be applied directly to steam or any other working fluid. These are given in Eq. (1-22), repeated here as Eq. (8-3) for convenient reference.

$$\frac{\dot{m}}{A\rho_* a_*}, \frac{ND}{a_*}, \frac{\Delta H}{a_*^2}, \frac{\Delta H_{id}}{a_*^2}, \frac{C_0}{a_*}, v, \eta \quad (8-3)$$

Note that pressure ratio is not one of the fundamental equivalent performance parameters and should not be used directly. The equivalence parameters were introduced in chapter 1 as total-to-total conditions. It was

simply stated that they apply for total-to-static performance without supporting evidence. Total-to-static performance data will be used here to confirm that statement. Hence, the spouting velocity and velocity ratio used are given by

$$C_{0s} = \sqrt{2(H_1 - h_{4id})} \quad (8-4)$$

$$v_s = U_m / C_{0s} \quad (8-5)$$

The blade speed used, U_m , is the rotor exit blade speed at mid passage height.

$$U_m = \omega(r_{4h} + r_{4s})/2 \quad (8-6)$$

It should be recognized that rating curves could also be based on total-to-total conditions and alternate blade speed definitions if that is more convenient. Evaluation of the accuracy of performance estimates obtained from similitude is accomplished by generating predictions using steam as the working fluid for comparison with the equivalent rating curves derived from air performance.

Figure 8-1 shows an equivalent efficiency map with two rating curves for specific values of C_{0s}/a_* . The values of total-to-static pressure ratio for air as the working fluid are noted on the figure for reference. The equivalent pressure ratios for steam were 1.94 and 3.68, confirming that pressure ratio is not a true equivalent performance parameter. A few points using pressure ratio as an equivalence parameter have been included in figure 8-1 to further emphasize this important point. Different values of pressure ratio will apply to different working fluids and must be calculated consistent similitude on

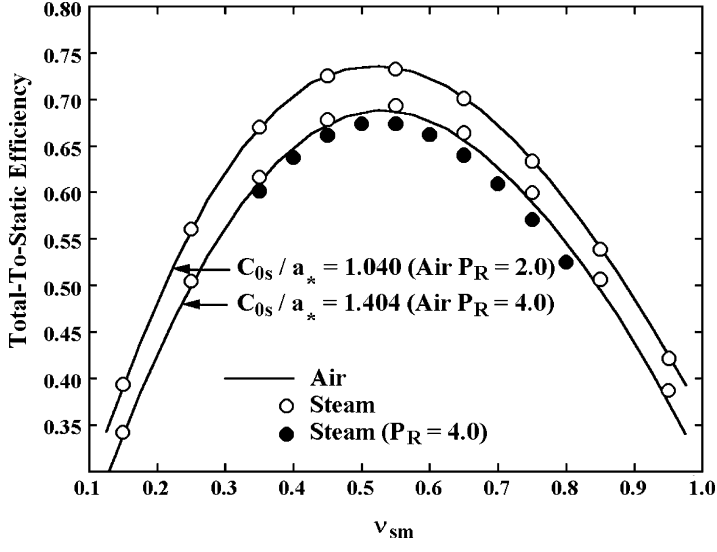


FIGURE 8-1. Efficiency Rating Curves

C_{0s} . Several additional rating curves would normally be employed to cover the range of expected C_{0s}/a_* values. Efficiency for the specific application would be obtained by interpolation. The total-to-static velocity ratio is a convenient choice for the abscissa. Turbine stages perform over a fairly predictable velocity-ratio range, which is well suited to the interpolation process. The corresponding steam performance predictions show the efficiency estimates based on similitude are quite accurate.

Some minor deviations are seen for the larger C_{0s}/a_* rating curve. This results from the fact that complete Mach number equivalence between air and steam cannot be achieved through the entire stage at extreme pressure ratios. The differences in fluid properties as well as nonideal gas behavior for steam result in differences in the gas density distribution through the stage. This is often referred to as a volume-ratio effect. Since conservation of mass is required for both cases, complete Mach number similarity can not be achieved unless volume-ratio similarity is also achieved. It is evident that inlet Mach number similarity does not assure volume-ratio similarity through the stage under all conditions. This is a basic limitation of similitude based on Mach number similarity. It is likely that the slight inaccuracy of performance estimates at extreme pressure ratios will not be a significant concern, since performance guarantees are not normally expected or required in those cases. If necessary, the rating curves could be corrected for volume-ratio effects by adjusting the air-test data based on performance analysis results for the two working fluids.

Figure 8-2 shows an evaluation of mass flow similarity as a function C_{0s}/a_* . For convenience, the mass flow equivalence is expressed as the ratio of mass flow to the ideal (no loss) nozzle choking mass flow, i.e., the reference

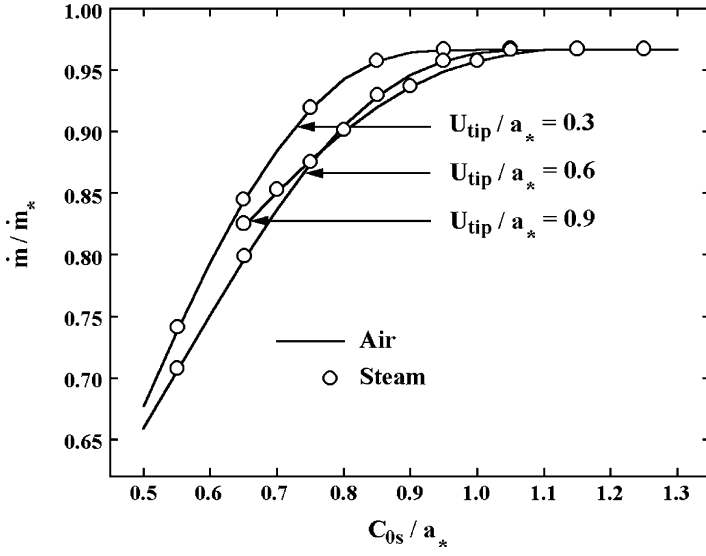


FIGURE 8-2. Mass Flow Equivalence

area used in Eq. (8-3) is the nozzle throat area, A_{th} , such that

$$\dot{m}/\dot{m}_* = \dot{m}/(\rho_* a_* A_{th}) \quad (8-7)$$

Note that this is just a convenient reference, which does not require that choke actually occur in the nozzle. Even when the nozzle does control choke, the actual stage choking mass flow will be less than the ideal nozzle choking mass flow due to losses in the nozzle. Three curves are shown for various equivalent speeds expressed as the ratio of the rotor tip speed to the inlet sonic velocity. It is seen that excellent mass flow estimates for steam will result from similitude with air. However, the equivalent speed parameter used is not well suited for interpolation to obtain performance estimates from a family of rating curves. The highest speed rating curve had to be truncated since the stage reached its runaway condition (i.e., $\Delta H = 0$) at a relatively large value of C_{0s}/a_* . In addition, the various rating curves cross each other to further complicate the process of interpolation. Hence, the rating curve format shown in figure 8-2 is usually not a very good choice for mass flow rating curves.

Figure 8-3 shows an alternate rating curve format using velocity ratio as the parameter. The range of practical values of velocity ratio is fairly predictable and leads to a more uniform operating range for C_{0s}/a_* for the various rating curves. This format is well suited for interpolation. Performance rating curves similar to figures 8-1 and 8-3 provide an effective method to apply the preestablished industrial turbine stage performance for general application work. But misuse of similitude in establishing and applying the rating curves is far too common. In nearly all cases this is due to the failure to employ the fundamental equivalent performance parameters. This

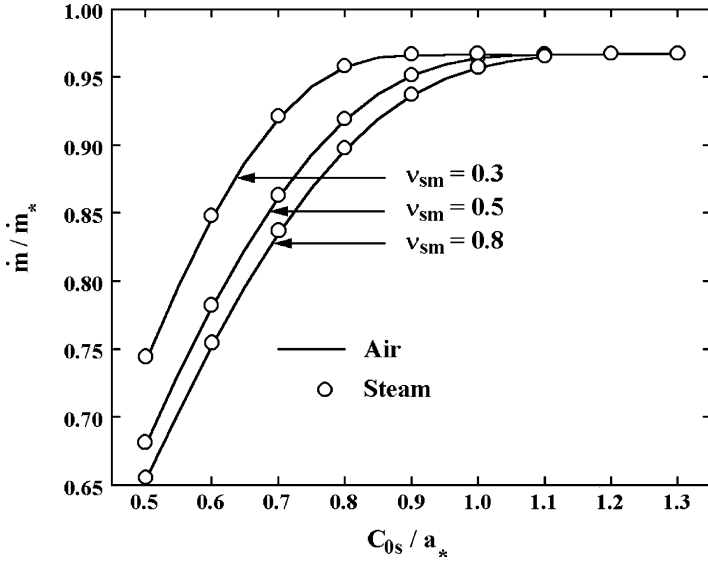


FIGURE 8-3. Mass Flow Rating Curves

usually results from the lack of a proper understanding of similitude. But the desire to use alternate parameters for reasons of convenience and the temptation to customize the rating curves for the expected working fluid are also common causes. Such personal preferences can be accommodated if done correctly. In the present illustrative example, the air rating curves could be converted specifically to steam turbines using pressure ratio as a parameter rather than C_{0s}/a_* . But that approach is not recommended, since it will yield erroneous results when those rating curves are subsequently used to select a turbine to operate with a different working fluid. If use of pressure ratio as the independent parameter is considered important enough, it can be done. In that case the rating curves are specific to a single working fluid. Hence, additional logic is required to calculate an equivalent pressure ratio from C_{0s}/a_* equivalence to translate the rating curves to the actual working fluid.

8.2 Reynolds Number Effects

A significant limitation of equivalent performance maps is associated with Reynolds number effects. That issue was avoided in the previous comparisons by suppressing all Reynolds number corrections in the performance analysis. But air and steam exhibit significantly different Reynolds number values for the cases considered. Had the Reynolds number corrections not been suppressed, figure 8-1 would have shown significant differences in efficiency between air and steam as compared to the estimates based on similitude. Those differences are real, but they cannot be addressed by rating curves based on similitude. When rating curves are used for application work, the Reynolds number to which they apply must always be specified such that Reynolds number corrections can be applied separately. Unfortunately, the literature offers virtually no well-established Reynolds number correction procedure for axial-flow turbines. Balje [68] does provide a calculated Reynolds number correction chart using specific speed as a parameter. His discussion of the assumptions used to develop that chart does not offer much reason for confidence. Attempts to qualify that chart using the performance analysis of chapter 5 resulted in little correlation between the chart and the performance prediction results.

Unable to locate a suitable published method, this writer formulated an axial-flow turbine stage Reynolds number correction based on the parameter, K_{RE} , given by Eqs. (4-73) through (4-76) and shown in figure 4-10. This parameter is used in chapter 4 to correct the profile and secondary flow losses for Reynolds number effects, including laminar and turbulent flow and the effects of surface finish. One immediate problem arises from the fact that K_{RE} is based on the blade chord Reynolds number, Re_c , which is not readily available in a general turbine application procedure. If the rating curve format of figure 8-1 is used, this actually poses no problem. A more convenient Reynolds number definition for a general application procedure is the tip Reynolds number, Re_{tip} , given by

$$Re_{tip} = \rho U_s r_s / \mu \quad (8-8)$$

All parameters are evaluated at the stage exit and the subscript s refers to parameters evaluated at the shroud. Note that the individual efficiency rating curves are effectively curves of constant spouting velocity, C_{0s} . It is well known that the fluid velocities within the stage are proportional to C_{0s} . Hence, the individual rating curves are expected to also be curves of approximately constant Re_c . This has been confirmed through a number of stage performance predictions for constant C_{0s} . Hence, a rating curve Reynolds number reference can be established by specifying Re_{tip} and the ratio Re_c/Re_{tip} . Both of these parameters will vary with velocity ratio, but their ratio will remain essentially constant. Typically these values are specified at the peak efficiency condition, although that is relatively unimportant since essentially the same Re_c will result regardless of where they are specified. It is expected that K_{RE} can be used as a correction on the stage inefficiency, $(1 - \eta)$, i.e.,

$$(1 - \eta) = (1 - \eta_{ref})[1 + f(K_{RE} - 1)] \quad (8-9)$$

The parameter f is the fraction of the overall stage loss that is Reynolds number dependent. Unfortunately, f cannot be regarded as constant on a rating curve. It can be noted that as the velocity ratio increases, the stage work coefficient decreases. Typically, the losses that are not dependent on Reynolds number are reduced as the work coefficient is reduced (e.g., the clearance loss). Hence, it can be expected that f will approach unity at large velocity ratios. Based on performance prediction results, a reasonable approximation is often given by

$$f = V_s^{0.65} \quad (8-10)$$

However, this is the weakest aspect of the present Reynolds number correction. Indeed, f can be quite dependent on the stage type and Mach number level as well as special issues such as moisture loss, seal leakage, partial admission, etc. Hence, Eq. (8-10) should not be considered to be a general result that will be sufficient for all stage rating curves.

Application of this Reynolds number correction is straightforward. Using the reference Re_c for the rating curve, compute K_{RE} and use Eq. (8-9) to compute η_{ref} . Then calculate K_{RE} for the actual Re_c and use Eq. (8-9) to compute η . Figure 8-4 illustrates typical results from this model. Performance curves were generated for a series of Reynolds numbers using the performance analysis of chapter 5. One of these curves is used as a base reference, and estimated efficiencies for the other curves were generated with the present Reynolds number correction method with f given by Eq. (8-10). For purpose of illustration, these results assumed a perfectly smooth surface to avoid suppressing the corrections at the highest Reynolds number due to surface roughness effects. That often occurs in axial-flow turbines w typical surface finishes. Indeed, Fielding [69] suggests that the improvement in efficiency due to Reynolds number greater than the transition value is usually negligible. Results from the present method are often consistent with that conclusion, suggesting that surface finish should always

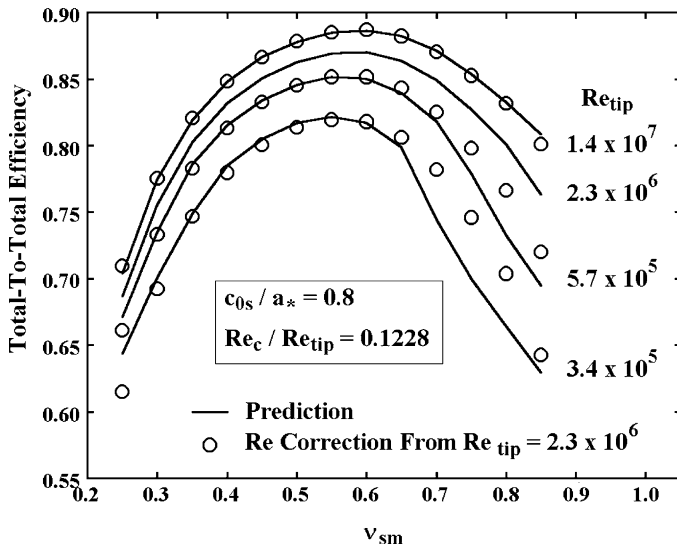
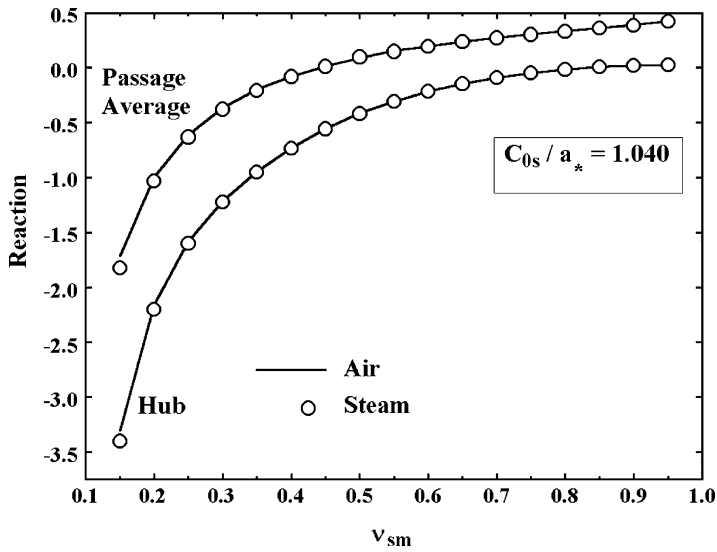


FIGURE 8-4. Typical Reynolds Number Corrections

be considered when correcting for Reynolds number effects. This writer has traced some very expensive turbine performance deficiency problems directly to the omission of surface finish effects in Reynolds number corrections. This has become a serious issue in recent years due to the higher inlet pressures required for modern industrial steam turbine applications. It is evident that the present Reynolds number correction is in rather good agreement with the basic performance analysis. Some deviations can be seen at extreme velocity ratios, particularly at the lowest Reynolds number considered. In part, this results from weaknesses in the model for f given by Eq. (8-10). But it also results from the fact that efficiency is not the only aspect of turbine performance affected by Reynolds number. Nevertheless, this Reynolds number correction should be sufficient for most industrial turbine applications work. The model to estimate f may require refinement based on the specific stage type. It is not possible to define a general form that is certain to be applicable to all stage types and operating conditions.

8.3 Reaction Rating Curves

The efficiency and flow rating curves and the Reynolds number correction are sufficient to estimate the stage performance. But the application engineer may also need to estimate the rotor axial thrust to confirm that the turbine configuration is achievable with practical thrust bearings. This requires knowledge of the average passage reaction to estimate the blade passage thrust forces. In the case of a diaphragm-disk stage arrangement, hub reaction may also be required to estimate the disk thrust force. Figure 8-5 shows predicted reaction rating curves for air and steam using the same

**FIGURE 8-5. Reaction Rating Curves**

similarity parameters as figure 8-1. It is evident that similitude is applicable to the average reaction and hub reaction and can be used to provide rating curves suitable for rotor axial thrust evaluation.

8.4 Application Procedures Based on Rating Curves

Properly defined rating curves permit accurate estimates of stage performance with a relatively simple analysis and minimal stage geometry data. Rating curves cannot be used to model all phenomena encountered in turbine stages. The need for a correction procedure to address Reynolds number effects has already been discussed. Moisture loss is another example where a separate correction procedure is required. Usually this is also true of partial admission losses, unless restricted to a specific set of admission arcs such that individual rating curves can be supplied. Other corrections may be required depending on the type of variations allowed to the standard stages to be used. The appropriate loss models from chapter 4 must be adapted to develop corrections to the performance derived from the rating curves for those variations. The precise procedure will also depend on the type of rating curves (e.g., total-to-total or total-to-static), but the basic process will be similar for any type.

Typically, a stage is selected based on a known rotation speed, mass flow and stage inlet conditions. Given the nozzle throat area, the mass flow rating curve can be used to select appropriate values of C_0/a_* and v to conserve mass. Typically one parameter is selected and the other calculated to balance mass. The stage efficiency is determined from the efficiency rating curves and used to calculate the average stage discharge conditions, assuming a simple one-dimensional flow model. Given the stage discharge area and mean

flow angle, conversion between total and static discharge conditions can be computed from a mass balance. This normally requires the rotor mean gauging angle and a deviation angle model similar to the model described in chapter 4. The Reynolds-number correction and any other corrections required are imposed to obtain the overall stage performance. Alternate values of C_0/a_s and v can be considered to select the best combination. If required, the reaction rating curves can be used to estimate the rotor thrust. This process can be applied to a series of stages to develop a multistage turbine configuration that achieves the required performance. There are many possible variations on this process. An iterative process can be used to work from stage discharge conditions rather than inlet conditions. Some automated optimization is normally used based on preferred constraints.

The most significant compromise relative to the accuracy of the estimated performance is that stage matching is not addressed by the rating curves. This can involve both abrupt changes in end-wall contours and off-design nozzle incidence angles. As mentioned in chapter 6, standard industrial stages are usually designed to optimize static efficiency using low flow coefficients and low inlet swirl velocities to minimize this effect. Also, application procedures usually restrict the range of conditions that can be employed for performance guarantee conditions. But some adjustment to account for stage matching compromises is normally appropriate. This may be as simple as assigning the fraction of the dynamic head or tangential dynamic head that is recovered in the next stage. A nozzle incidence loss and an abrupt area expansion or contraction loss model may also be used to impose corrections on the performance.

This description has reduced the problem to its simplest form to illustrate the role of rating curves. A turbine application procedure must also address a number of issues not directly associated with stage performance. Typical examples include inlet and discharge seal leakage, extraction flows, diffuser and exhaust-end performance and control-valve losses. Often it will also include preliminary evaluation of mechanical integrity issues.

Chapter 9

AERODYNAMIC PERFORMANCE ANALYSIS OF RADIAL-INFLOW TURBINES

An aerodynamic performance analysis is essential for nearly all aspects of radial-inflow turbine aerodynamic design and application. The highly complex three-dimensional flow fields in these machines are strongly influenced by viscous effects and passage curvature. In contrast to the axial-flow turbine, the most effective approach to the performance analysis of radial-inflow turbine is the one-dimensional or mean-line method. Indeed, there is a close parallel with compressor performance analysis where the one-dimensional method is the most effective technique for the centrifugal compressor [1] but the more general hub-to-shroud flow method is the better choice for the axial-flow compressor [2].

One-dimensional performance analysis relies on analysis of the flow along a mean stream surface through various stage components. This approach is quite effective, but also has definite limitations. There are really an infinite number of ways a component can be designed to produce the specific geometrical parameters used by a one-dimensional performance analysis. The best a one-dimensional analysis can do is to predict the expected performance assuming the detailed geometry is based on “good design practice.” Obviously, good design practice is a relative term. In the case of the diffusing flows in compressors, this can result in significant uncertainty, particularly when analyzing older designs. It is a much less serious issue for turbines, where the accelerating flow results in less sensitivity to local flow behavior.

The literature includes a number of investigations into the performance analysis of radial-inflow turbines [67, 68, 75–83]. But unlike other popular turbomachinery types, the literature really doesn’t provide any comprehensive and well-validated performance prediction systems for these machines. The axial-flow turbine performance analysis of chapters 4 and 5 is based on several well-developed and competing systems for modeling the loss and fluid turning. This writer’s performance analyses for centrifugal and axial-flow compressors [1, 2] are based on similar well-developed technology from the open literature. In contrast, the empirical models presented in this chapter are largely unique. Some axial-flow turbine and centrifugal compressor models were adaptable to the radial-inflow turbine application, but most models were formulated

specifically for this aerodynamic performance analysis. Although the open literature is quite limited, there are a number of proprietary performance analyses for radial-inflow turbines that appear to be well developed and effective. Indeed, some of these are implemented in commercially available software systems.

An early version of the present performance analysis was formulated over twenty-five years ago to address a perceived application in the geothermal energy market. After a number of successful applications, that performance analysis became largely inactive, since the perceived application simply did not materialize as a viable market. Subsequently it has been used occasionally for turbocharger repair and upgrade activity and for several other special applications. Recently the radial-inflow turbine performance analysis was essentially redeveloped in the more modern programming systems available today. Investigators involved in engineering software development twenty-five years ago are well aware of the substantial constraints imposed by the mainframe computer environment and relatively crude programming systems available at that time. Others will probably find it difficult to imagine carrying out this task using punched card input while relying entirely on crude line printer output from one or two computer runs per day. The flexibility of the modern programming environment allowed substantial improvement of the accuracy and reliability of the performance analysis to be achieved as well as its conversion to a user-friendly personal computer application. But it does need to be mentioned that the specific formulation described in this chapter has not been used to support any commercial design or analysis activity. Comparison of predictions with experiment has clearly demonstrated that its prediction accuracy is superior to the original formulation, which has provided effective results on many practical applications. But the true test of any software system is provided by direct experience gained through a range of practical design and analysis applications. As of this writing, there has been no opportunity to qualify this software system on that type of practical application.

NOMENCLATURE

- A = passage area
- a = sound speed
- b = passage width
- C = absolute velocity
- C_0 = spouting velocity
- c_f = skin friction coefficient
- d = pipe diameter
- H = total enthalpy; also, boundary layer shape factor
- h = static enthalpy; also, blade height or span
- I = rothalpy
- L = flow path length
- M = Mach number
- m = meridional coordinate
- \dot{m} = mass flow rate

N = number of blades; also, rotation speed (rpm)
 n = the number of components in the turbine
 o = blade passage throat width
 P = pressure
 Re = Reynolds number
 r = radius
 s = blade pitch = $2\pi r/N$; also entropy
 T = temperature
 U = local blade speed = $r\omega$
 u = boundary layer velocity
 W = relative velocity
 Y = loss coefficient
 z = axial coordinate
 α = flow angle with respect to tangent
 β = blade angle with respect to tangent
 Δ = normalized mass defect thickness
 δ = boundary layer thickness
 δ^* = boundary layer displacement thickness
 δ_c = impeller-casing clearance
 δ_d = disk-housing clearance
 ε = impeller radius ratio
 ϕ = mean surface angle with axial direction
 η = efficiency
 Θ = normalized momentum defect thickness
 θ = polar angle; also, boundary layer momentum thickness
 $2\theta_c$ = diffuser divergence angle
 μ = viscosity
 v = velocity ratio = U_{tip}/C_0
 ρ = gas density
 σ = slip factor
 ω = rotation speed

Subscripts

b = blade surface parameter
 $choke$ = value of a parameter at the onset of choke
 dis = turbine discharge condition
 e = boundary layer edge condition
 h = hub parameter
 id = ideal (no loss) parameter
 m = meridional component; also, a mean value
 p = blade pressure surface parameter
 s = shroud or blade suction surface parameter
 t = total thermodynamic condition
 tip = rotor tip parameter
 w = end-wall parameter
 1 = component inlet parameter

- 2 = component mid-passage parameter
- 3 = component exit parameter
- θ = tangential component
- * = a sonic flow condition

Superscripts

- ' = a relative value in the rotating coordinate system
- * = an optimum (minimum loss) blade inlet condition

9.1 Radial-Inflow Turbine Stage Geometry

Figure 9-1 illustrates the geometry of a typical radial-inflow turbine stage. Typically the flow enters the stage through an inlet volute. Sometimes an inlet plenum is used, such that the flow area is constant in the circumferential direction. It then passes through a vaneless annular passage into a nozzle blade row. If the angular momentum imparted to the flow in the inlet volute or plenum is considered adequate, the nozzle row may be omitted. The flow next passes through another vaneless annular passage to enter the rotor row. An exhaust diffuser often follows the rotor row to convert some of the rotor exit velocity to static pressure. Hence, the basic stage components to be analyzed are the inlet volute, nozzle, rotor, vaneless annular passages

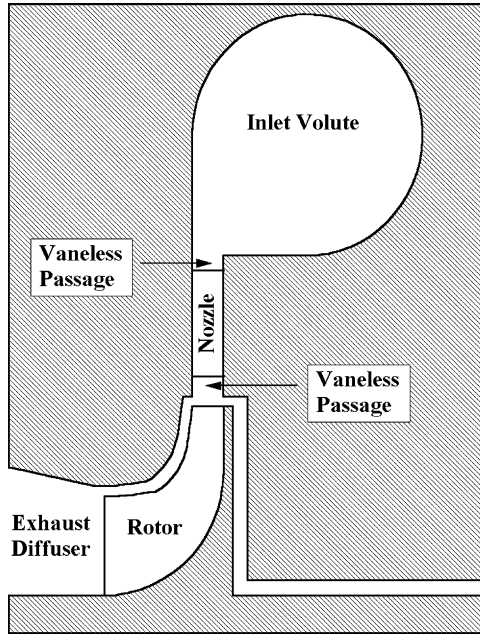


FIGURE 9-1. Radial-Inflow Turbine Stage Geometry

and exhaust diffuser. Most radial-inflow turbines are single-stage units, but some multistage units are also used. Hence, provision to handle interstage piping losses may also be required. There is no widely accepted interstage piping arrangement, so this writer simply includes provision for a fictitious stage component that provides the capability to introduce a total pressure loss that is consistent with the specific piping arrangement used.

9.2 Boundary Layer Analysis

The present performance analysis makes extensive use of a simplified boundary layer analysis to predict the profile loss and viscous blockage in the various stage components. Boundary layer analysis has been found to be particularly effective for estimating losses in radial-inflow turbine components. Except for the diffuser, the flow in turbine components involves favorable pressure gradients. Hence boundary layers remain relatively thin and flow separation is not a serious issue. The boundary layer analysis used is a simplified form of the two-dimensional integral method described in chapter 3, section 3.5. Pai [48, 49] reviews simplified models to predict the boundary layer momentum thickness, θ , in the form

$$\theta = \frac{c_f}{2u_e^n} \int_0^L u_e^n dx \quad (9-1)$$

The momentum thickness is defined in Eq. (3-37), u_e is the boundary layer edge velocity, L is the flow path length through the component and c_f is the skin friction coefficient. Pai references the well-known laminar boundary layer solution by Thwaites [84] and the turbulent boundary layer solution by Buri [85] as methods that conform to Eq. (9-1). The Thwaites solution uses $n = 5$ whereas Buri recommends values of 4.75 for accelerating flow and 5.15 for diffusing flows. Pai suggests that it is sufficient to use $n = 5$ for both cases in the Buri method. Hence, Eq. (9-1) with $n = 5$ provides a general solution when the skin friction coefficient is defined. This writer's practice is to define the flow parameters at the inlet, midpassage and discharge stations of each component in the stage. Designating these stations in order by subscripts 1 through 3, the boundary layer momentum thickness at component discharge is approximated by

$$\theta = c_f \rho_{ave} [(u_1/u_3)^5 + 2(u_2/u_3)^5 + 1] L / (8\rho_3) \quad (9-2)$$

$$\rho_{ave} = [\rho_1 + 2\rho_2 + \rho_3]/4 \quad (9-3)$$

The density ratio included in Eq. (9-2) is an approximate adjustment of the incompressible flow result of Eq. (9-1) for the boundary layer edge density variation. The velocity relative to the wall being analyzed is used in Eq. (9-2). Hence, if the wall is stationary, $u = C$, whereas if it is rotating, $u = W$. Simple one-dimensional flow results are used for the end-wall boundary layer edge conditions. For blade surface boundary layers, the velocity at midpassage is corrected for blade loading effects. That correction will be described subsequently in this chapter. To evaluate the total pressure loss from boundary layer

data, the displacement thickness at the component exit is also required. It is assumed that the boundary layer shape factor for the 1/7th power-law velocity profile applies, which yields $H = 1.2857$. This assumes the boundary layer is turbulent at the discharge, which is usually the case. A shape factor appropriate to laminar boundary layers could be used for the rare exceptions. But that is not recommended since it introduces the potential for numerical instability with H alternating between laminar and turbulent values on successive iterations. From the definition of the shape factor, displacement thickness is given by $\delta^* = H\theta$. It can be shown that for power-law velocity profiles, the boundary layer thickness, δ , is given by

$$\delta = \theta H(H+1)/(H-1) \quad (9-4)$$

The skin friction coefficient could be approximated by boundary layer skin friction coefficient correlations such as those illustrated in Figure 4-9. However, end-wall boundary layers extend through several components. Since boundary layer skin friction coefficient correlations are functions of the Reynolds number based on total path length, they are not well defined for this application. A better choice is the generalized pipe skin friction coefficient correlation. Pipe skin friction coefficients can be used for boundary layers by substituting 2δ for the pipe diameter, d . Except for the inlet volute, boundary layers in turbine components occur on the annular end walls and opposite sides of the blades. Since these boundary layers always occur in pairs on opposite walls, it is reasonable to use the relevant passage width, b , in place of d for those cases, i.e.,

$$Re_d \rightarrow \rho_3 u_3 b_3 / \mu \quad (9-5)$$

That basically assumes the boundary layers have merged into fully developed viscous flow profiles. This will normally not be the case, so the Reynolds number is likely to be overestimated and the skin friction coefficient to be underestimated. However, the skin friction coefficient is a rather weak function of Reynolds number, so this approximation is not unreasonable for the present purpose.

Aungier [1] provides an empirical model for the pipe skin friction coefficient that is in close agreement with the classical experimental results of Nikuradse [86]. The description of that empirical model is repeated here to provide a complete description of the present boundary layer analysis. If Re_d is less than 2000, the skin friction coefficient is independent of surface roughness and is given directly by the laminar skin friction coefficient, c_{fl} .

$$c_f = c_{fl} = 16/Re_d \quad (9-6)$$

When $Re_d > 2,000$, the well-known log-law profile yields the turbulent skin friction coefficient for smooth walls, c_{fs} .

$$\frac{1}{\sqrt{4c_{fs}}} = -2 \log_{10} \left[\frac{2.51}{Re_d \sqrt{4c_{fs}}} \right] \quad (9-7)$$

In the limit where the flow is turbulent and the peak-to-valley surface roughness, e , is sufficient to yield the fully rough-wall skin friction coefficient, c_{fr} ,

$$\frac{1}{\sqrt{4c_{fr}}} = -2 \log_{10} \left[\frac{e}{3.71d} \right] \quad (9-8)$$

Eq. (4-3) can be used to convert the known rms surface roughness to the peak-to-valley surface roughness, e . The experimental results of Nikuradse [86] show that surface roughness becomes significant when

$$Re_e = (Re_d - 2,000)e/d > 60 \quad (9-9)$$

Hence, if $Re_e < 60$, the wall is hydraulically smooth and Eq. (9-7) supplies the turbulent skin friction coefficient. Otherwise, a weighted average of c_{fs} and c_{fr} is used to estimate it, i.e.,

$$c_{fl} = c_{fs}; \quad Re_e \leq 60 \quad (9-10)$$

$$c_{fl} = c_{fs} + (c_{fr} - c_{fs})(1 - 60/Re_e); \quad Re_e > 60 \quad (9-11)$$

If $Re_d \geq 4,000$, the boundary layer is fully turbulent and Eq. (9-10) or Eq. (9-11) yields the appropriate value of the skin friction coefficient. But if $2,000 < Re_d < 4,000$, the boundary layer is in transition from laminar to turbulent flow. The skin friction coefficient in this transition zone is well approximated by a weighted average of the laminar and turbulent values, i.e.,

$$c_f = c_{fl} + (c_{fr} - c_{fl})(Re_d / 2,000 - 1) \quad (9-12)$$

Figure 9-2 shows a map of skin friction coefficient as a function of Reynolds number and surface roughness that was generated with this empirical model.

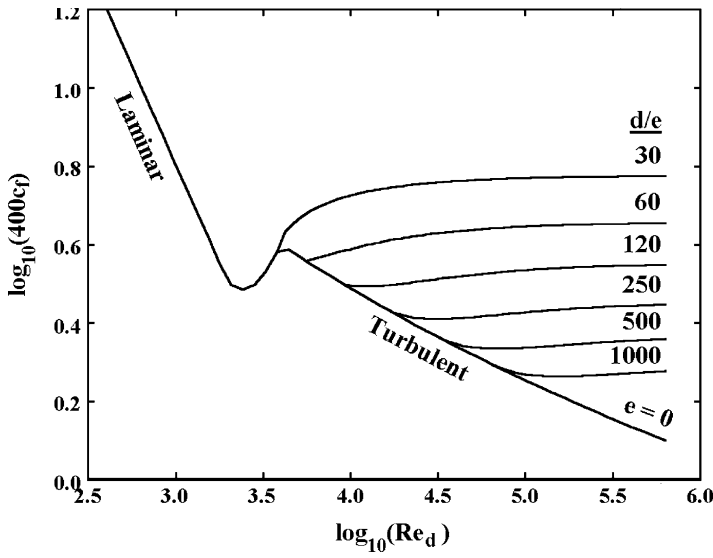
9.3 The Boundary Layer Loss Coefficient

Lieblein and Roudebush [87] derived an approximation for the total pressure loss coefficient due to surface boundary layers in compressor cascades. Their result is also applicable to turbine components if expressed in terms of the ideal (no loss) component discharge dynamic head rather than the inlet dynamic head. The profile loss coefficient, Y_p , due to the two boundary layers on opposing walls separated by an effective passage width b can be expressed as

$$Y_p = \frac{\Delta P_t}{P_{t3,id} - P_3} = \frac{2\Theta + \Delta^2}{(1 - \Delta)^2} + \sum \Delta Y \quad (9-13)$$

$$\Theta = \sum \theta/b \quad (9-14)$$

$$\Delta = \sum \delta^*/b \quad (9-15)$$

**FIGURE 9-2. The Skin Friction Coefficient**

The last term in Eq. (9-13) is a correction term to be described subsequently in this chapter. The derivation of this approximation for the total pressure loss assumes instant mixing of the boundary layer and mainstream fluid while conserving mass and momentum. This approximation is also derived as the solution to exercise 3.6 in Aungier [2]. It is directly applicable to the vaneless components in radial-inflow turbines. Nozzles and rotors have both end-wall and blade surface boundary layers, which overlap in the passage corners. Designating the end-wall and blade boundary layers by the subscripts w and b , respectively, the normalized defect thicknesses for these components to be used in Eq. (9-13) should be calculated from

$$\Theta = 1 - [1 - \sum \theta_w / b_w][1 - \sum \theta_b / b_b] \quad (9-16)$$

$$\Delta = 1 - [1 - \sum \delta_w^* / b_w][1 - \sum \delta_b^* / b_b] \quad (9-17)$$

The effective blade-to-blade passage width is estimated from the blade pitch and camberline angle at the blade discharge, i.e.,

$$b_b = s_3 \sin \beta_3 \quad (9-18)$$

This simple boundary layer analysis does not account for the influence of viscous boundary layer blockage on the mainstream flow. Hence, it is possible for the combined boundary layer thicknesses for the two boundary layers on opposing

walls from Eq. (9-4) to be greater than the passage width. Although this merged boundary layer case rarely occurs, the possibility should always be checked. When it does occur, the mass defect for each set of boundary layers on opposing walls should be corrected by

$$\Delta \rightarrow \Delta(b / \sum \delta) \quad (9-19)$$

Under extreme off-design operating conditions, cases where $\Theta > 1$ may also be encountered. This is certainly physically possible, but it can become very inaccurate under extreme operating conditions. Based on experience it is best to impose limits on this case also. The procedure used by this writer is to set $\Delta = \Theta - 1$ and reset $\Theta = 1$. This is done for each set of boundary layers on opposing walls and all ΔY s are summed as indicated in Eq. (9-13).

9.4 Inlet Volute Analysis

Figure 9-3 illustrates the geometry of a typical inlet volute. The passage area and mean radius are specified at station 1, where the flow is inside the volute, but has not yet started to exit the volute. These parameters are also specified at station 2, where half of the flow has exited from the volute passage. Hence the analysis is not restricted to a classical volute configuration. For example, a constant area plenum where the passage mean radius and area at stations 1 and 2 are identical can be accommodated. Station 3 is the annular passage at the volute exit, where the radius and the hub-to-shroud passage width, b_3 , are

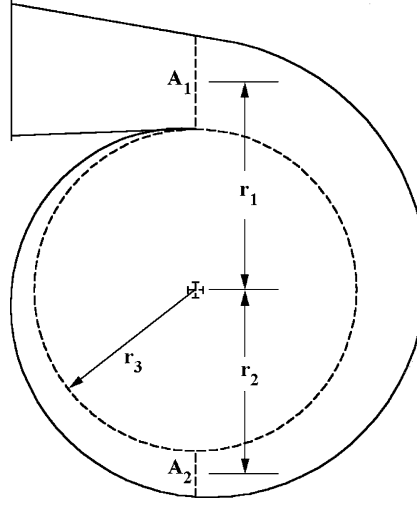


FIGURE 9-3. Inlet Volute Geometry

specified. The exit area is given by

$$A_3 = 2\pi r_3 b_3 \quad (9-20)$$

Since this is the first component in the stage, the inlet total thermodynamic conditions are also specified, or known from a preceding stage analysis. All flow conditions at station 1 are computed by performing a mass balance using the stage inlet mass flow. The same process assuming no losses and using half of the inlet mass flow supplies the flow conditions at station 2. The effective, one-dimensional angular momentum at the volute exit is estimated from conservation of angular momentum based on the flow data at station 2.

$$C_{\theta 3} = r_2 C_2 / r_3 \quad (9-21)$$

A mass balance using the inlet mass flow and this assigned tangential velocity component supplies the other flow conditions at station 3. However, the losses and the corresponding total thermodynamic conditions at station 3 must also be determined, so an iterative process is required. The total pressure losses considered include the profile loss and a circumferential distortion loss. The profile loss is calculated with the simple boundary layer analysis described previously in this chapter. The circumferential distortion loss coefficient accounts for mixing losses associated with circumferentially nonuniform angular momentum imposed at the volute exit. It is given by

$$Y_\theta = [(r_1 C_1 / r_3 - C_{\theta 3}) / C_3]^2 \quad (9-22)$$

If the volute is designed to maintain uniform angular moment in the circumferential direction, this loss will be identically equal to zero. By contrast, a constant area plenum will yield a value of C_2 approximately equal to half of C_1 . From Eqs. (9-21) and (9-22) it is easily seen that the circumferential distortion loss will be significant for that case. The volute exit total pressure is given by

$$Y = Y_p + Y_\theta = (P_{t1} - P_{t3}) / (P_{t3} - P_3) \quad (9-23)$$

$$P_{t3} = (P_{t1} + Y P_3) / (1 + Y) \quad (9-24)$$

For this stationary component, the total enthalpy is constant throughout the volute. Hence, $H_3 = H_1$ and an equation of state from chapter 2 provides all total thermodynamic conditions as a function of P_{t3} and H_3 . The end-wall boundary layer blockage from Eq. (9-15) is also applied to the passage area at the volute exit. Hence, the mass balance at the volute exit with $C_{\theta 3}$ given by Eq. (9-21) can be expressed as

$$\dot{m} = (1 - \Delta) A_3 \rho_3 C_{m3} \quad (9-25)$$

The discharge exit static enthalpy is given by

$$h_3 = H_3 - \frac{1}{2}(C_{m3}^2 + C_{\theta3}^2) \quad (9-26)$$

Since the static entropy and total entropy are equal, the equation of state provides all other static conditions as a function of h_3 and s_3 . It is easily seen that the boundary layer analysis and the losses are functions of the volute exit flow conditions, necessitating an iterative solution at station 3 to converge on Y .

9.5 Nozzle Row Analysis

The nozzle row in radial-inflow turbines is usually a simple radial passage of constant width. But that is not a necessary restriction, so a more general specification of the nozzle geometry is used. The geometry is specified at the inlet, midpassage and exit stations, which are designated by subscripts 1 through 3, respectively. At each of these stations, the axial coordinate, z , radius, r , passage width, b , blade camberline angle, β , and blade thickness, t_b , are specified. In addition, the number of blades, N , the throat blade-to-blade width, o , and passage width at the throat, b_{th} , are supplied. Figure 9-4 illustrates some of the key geometrical parameters supplied.

The nozzle exit flow may be either subsonic or supersonic, depending on the stage discharge pressure. It will be subsequently shown that the supersonic discharge case is treated as an adjustment to the choked nozzle case with $M_3 = 1$. Hence, a subsonic solution is always required and will be considered first. Similar to axial-flow turbines, the nozzle discharge flow angle for $M_3 \leq 1$ is estimated from the well-known sin rule, but with adjustments for variations in passage width and radius between the throat and the nozzle exit. The adjustment for radius variation is particularly significant. Angular momentum must be

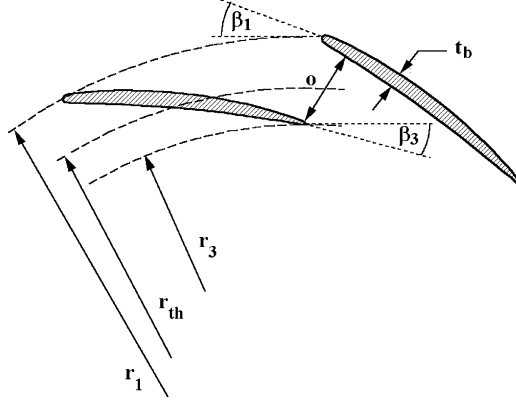


FIGURE 9-4. Nozzle Row Geometry

conserved in the unguided region downstream of the throat. This has a significant influence on the exit flow angle for radial-inflow turbine nozzles that is negligible for axial-flow turbines. The subsonic discharge flow angle is estimated by

$$\sin \alpha_{os} = b_{th} o / (s_3 b_3) \quad (9-27)$$

$$\tan \alpha_3 = (r_3 / r_{th}) \tan \alpha_{os} \quad (9-28)$$

The geometry specifications at stations 1 through 3 provide meridional distances from the leading edge, m_2 and m_3 are computed by numerical integration.

$$m^2 = \int [(dr)^2 + (dz)^2] \quad (9-29)$$

The values of the blade pitch at stations 1 through 3 are given by

$$s = 2\pi r / N \quad (9-30)$$

The gradient of r with respect to m at the trailing edge is estimated from a three-point finite-difference approximation.

$$\left[\frac{\partial r}{\partial m} \right]_3 = \frac{m_3(r_3 - r_2)}{m_2(m_3 - m_2)} - \frac{(m_3 - m_2)(r_3 - r_1)}{m_2 m_3} \quad (9-31)$$

Eq. (9-31) is easily developed from truncated Taylor series approximations for r_3 from data at the other two stations. Then, the mean throat radius is estimated from

$$r_{th} = r_3 - \left[\frac{\partial r}{\partial m} \right]_3 \frac{o^2}{2s_3} \quad (9-32)$$

The flow path length is required to determine the profile loss from the boundary layer analysis described previously in this chapter. This is obtained from numerical integration using data at stations 1 through 3.

$$L = \int_0^m \frac{dm}{\sin \beta} \quad (9-33)$$

The passage areas at stations 1 through 3 are estimated from

$$A = b[2\pi r \sin \beta - t_b N] \quad (9-34)$$

The mean flow data at station 1 can be immediately calculated to balance the known mass flow rate while maintaining the inlet tangential velocity imposed

by the upstream component. Similarly, the mean flow data at station 2 is calculated from a mass balance, assuming that $\alpha_2 = \beta_2$. The mean flow data at station 3 is also calculated from a mass balance with α_3 given by Eq. (9-28). However, this station requires an iterative solution to include the effect of the nozzle loss, which influences the mean flow but is also dependent on it.

The optimum (minimum loss) nozzle incidence angle, i^* , is estimated from an empirical correlation of optimum angle of attack data by Herrig et al. [88] for axial-flow compressor cascades. This model is adapted to radial cascades by approximate conformal mapping and is corrected for the sign of the change in blade angle across the blade row. The optimum incidence angle and inlet flow angle, α^* , are given by

$$i^* = [3.6\sqrt{10t_2/L} + |\beta_3 - \beta_1|/3.4]\sqrt{L/s_3} - |\beta_3 - \beta_1|/2 \quad (9-35)$$

$$\alpha^* = \beta_1 - i^* \operatorname{sign}(\beta_3 - \beta_1) \quad (9-36)$$

The incidence loss is proportional to the inlet velocity pressure. Following the usual practice of expressing turbine loss coefficients as a fraction of the discharge velocity pressure, the incidence loss coefficient used is

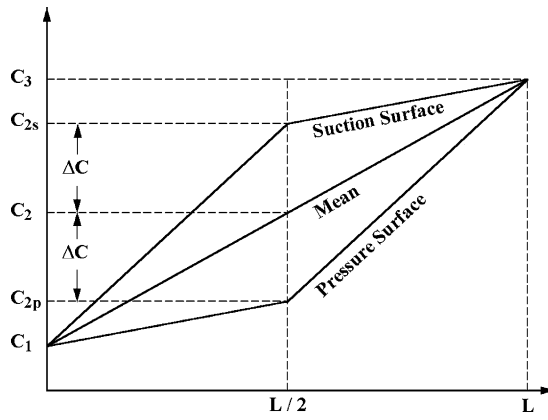
$$Y_{inc} = \sin^2(\alpha_1 - \alpha^*) \frac{P_{t1} - P_1}{P_{t3} - P_3} \quad (9-37)$$

Boundary layers on the two end-walls are assumed to be identical and are calculated using the mean passage flow data at the three stations. The blade surface boundary layer calculation must include the influence of the blade loading effect. The average difference in velocity on the two blade surfaces is given by Stokes's theorem for irrotational flow. This requires that integration about any closed path of the velocity component tangent to the path is identically equal to zero. Hence, the average difference in velocity on the two blade surfaces is

$$\Delta C = 2\pi(r_3 C_{\theta 3} - r_1 C_{\theta 1})/(LN) \quad (9-38)$$

The simple loading diagram shown in figure 9-5 is used to define the blade surface velocity distributions on the blade surfaces for the blade surface boundary layer analysis. Eqs. (9-16) and (9-17) combine the results of the four boundary layer analyses to yield the profile loss through Eq. (9-13). Since the boundary layers develop inside the blade passage, it is good practice to adjust C_3 for the discharge boundary layer blockage. Using values of Δ from the previous iteration, $C_3 \rightarrow C_3/(1 - \Delta)$ for the purpose of the boundary layer analysis only. This is a subtle point that is usually insignificant, but is found to yield better results and avoid convergence problems at extreme off-design conditions. Similar to the volute analysis, the nozzle exit total pressure is given by

$$Y = Y_p + Y_{inc} = (P_{t1} - P_{t3})/(P_{t3} - P_3) \quad (9-39)$$

**FIGURE 9-5. Simple Blade Loading Diagram**

$$P_{t3} = (P_{t1} + Y P_3) / (1 + Y) \quad (9-40)$$

For this stationary component, the total enthalpy is constant throughout the nozzle row. Hence, $H_3 = H_1$ and an equation of state from chapter 2 provides all total thermodynamic conditions as a function of P_{t3} and H_3 . The end-wall boundary layer blockage from Eq. (9-15) is also applied to the passage area at the nozzle exit. Blockage associated with the blade surface boundary layers is not used for this purpose, since those boundary layers will form a wake, which can be expected to quickly decay by mixing with the main flow. Hence, the mass balance at the nozzle exit with α_3 given by Eq. (9-28) can be expressed as

$$\dot{m} = (1 - \Delta) 2\pi r_3 b_3 \rho_3 C_3 \sin \alpha_3 \quad (9-41)$$

The discharge exit static enthalpy is given by

$$h_3 = H_3 - \frac{1}{2} C_3^2 \quad (9-42)$$

Since the static entropy and total entropy are equal, the equation of state provides all other static conditions as a function of h_3 and s_3 . Hence, Eq. (9-41) can be solved to balance mass in an iterative manner. It is easily seen that the boundary layer analysis and the losses are functions of the nozzle exit flow conditions, necessitating an iterative solution at station 3 to converge on Y .

The subsonic nozzle analysis must also check for choked flow. Given the nozzle discharge total thermodynamic conditions, an iterative solution is performed to determine the sonic velocity and density. Designating sonic flow conditions by a subscript *, the mass flow must be limited to not exceed the choking mass flow given by

$$\dot{m}_* = Nb_{th}o(1 - \Delta)\rho_*C_* \quad (9-43)$$

For cases where the nozzle is choked, the above procedure yields the choking mass flow and the choked performance. As will be seen subsequently in this chapter, a choked component requires supplemental calculations to converge on an assigned discharge static pressure that is less than the choked nozzle value. This is accomplished by imposing an isentropic expansion from the choked nozzle solution. This yields all static thermodynamic conditions at the nozzle exit. Then the discharge velocity and flow angle are given by

$$C_3 = \sqrt{2(H_3 - h_3)} \quad (9-44)$$

$$\sin \alpha_3 = \dot{m} / [(1 - \Delta)2\pi r_3 b_3 \rho_3 C_3] \quad (9-45)$$

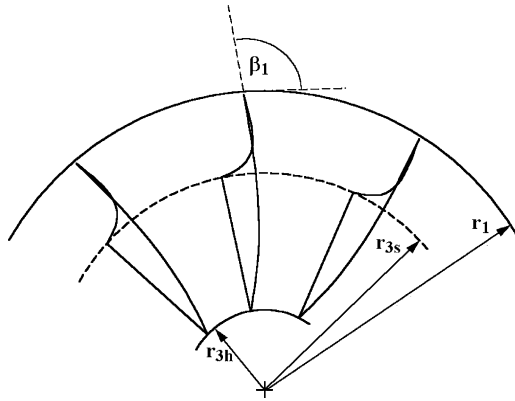
When imposing the isentropic expansion at the nozzle discharge, it is important to check for certain physical limits in case the overall stage performance iteration procedure seeks a choked nozzle discharge pressure that is not achievable. An isentropic expansion may be limited by an annulus choke downstream of the nozzle row. This limit can be identified by the condition that the meridional velocity component is equal to the local sound speed. The minimum pressure that yields an annular passage choke can be determined from an iterative solution to determine the value of C_3 that matches the known total thermodynamic conditions, satisfies the equation of state and Eq. (9-42) and yields

$$C_{m3} = \dot{m} / [(1 - \Delta)2\pi r_3 b_3 \rho_3] = a_3 \quad (9-46)$$

The corresponding value of P_3 is the minimum nozzle exit static pressure that can be matched by an isentropic expansion and also balance mass. When this limit precludes matching the specified exit pressure, the limiting value is used. When this limit restricts the isentropic expansion, corrective action is needed by the overall stage performance iteration. That process will be described subsequently in this chapter.

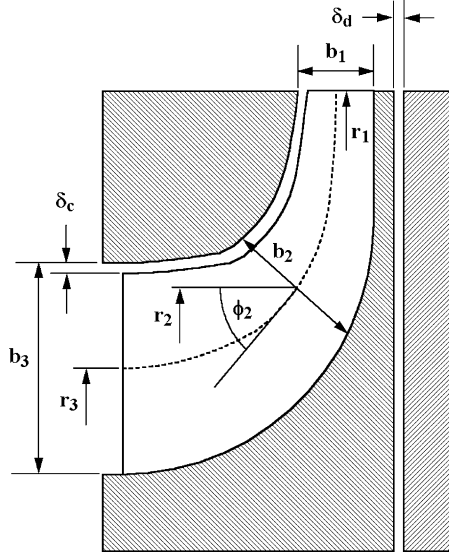
9.6 Rotor Analysis

The flow passage geometry of the rotor is far more complex than the other radial-inflow turbine components. Typically, the flow is turned by 90° from radial to axial in the impeller, producing strong hub-to-shroud flow profile gradients due to passage curvature effects. There are several sources of internal losses in the impeller, including the passage curvature, blade clearance, incidence, blade loading and profile losses. It is also necessary to account for the energy consumed by the rotating disk in the housing. This disk friction loss is commonly referred to as a parasitic loss. It represents wasted energy rather than an aerodynamic loss in total pressure. In the case of condensing working fluids, the potential for

**FIGURE 9-6. Impeller Frontal View**

moisture losses similar to those described for axial-flow turbines may also impact the rotor performance. Often partial-length splitter blades are used to provide additional work capability without reducing the choke capacity of the impeller.

The specification of the rotor geometry requires particular attention to permit consideration of the many loss sources, yet maintain a set of defining parameters that the user can supply without undo hardship. Figures 9-6 and 9-7 show frontal and side views of the rotor to illustrate the geometry required. Similar to other components, the passage geometry is defined at

**FIGURE 9-7. Rotor Side View**

the inlet, midpassage and exit stations numbered 1 through 3, respectively. These data are specifically referenced to a mean surface midway between the hub and shroud surfaces. Like the nozzle row, the axial coordinate, z , radius, r , passage width, b , blade camberline angle, β , and blade thickness, t_b , are specified at these stations. To properly address the passage curvature, the angle, ϕ , formed by a tangent to the mean surface and the axial direction is also specified. This angle is illustrated for station 2 in figure 9-7. This angle is measured in the flow direction. Hence in the case illustrated in figure 9-7, ϕ varies from -90° at the inlet to 0° at the exit. In addition, the number of full blades, N , the throat blade-to-blade width, o , on the mean surface, the passage width at the throat, b_{th} , and the clearances, δ_c and δ_d , are supplied. One or more sets of splitter blades can also be specified, along with the fraction of the mean path length from the inlet occupied by the splitter blades. The analysis assumes splitter blades are identical to the full blades except for length and are equally spaced between the full blades.

Since z , r and ϕ are specified at each station, the flow path length between stations can be accurately calculated by approximating the mean surface with a third-order polynomial that matches the end-point coordinates and slopes. To avoid singular results, a simple rotation of coordinates is accomplished before calculating the path length of each segment. The sum of the two segment lengths yields the total meridional path length, m_3 , from which the average mean surface curvature is given by

$$\kappa_m = |\phi_3 - \phi_1| / m_3 \quad (9-47)$$

Similar to the nozzle row, the subsonic relative discharge flow angle is estimated by the well-known sin rule, but with adjustments for variations in passage width and radius between the throat and the impeller exit.

$$\sin \alpha'_{os} = b_{th} o / (s_3 b_3) \quad (9-48)$$

$$\tan \alpha'_3 = (r_3 / r_{th}) \tan \alpha'_{os} \quad (9-49)$$

$$r_{th} = r_3 - o^2 \sin \phi_3 / (2s_3) \quad (9-50)$$

Note that the blade pitch at the impeller exit, s_3 , is based on the full-length blades only.

The impeller internal performance is calculated in essentially the same manner as for the nozzle row except for the loss models. Since this is a rotating component, the boundary layer analysis is based on relative velocity and relative total thermodynamic parameters. The simple blade-loading diagram shown in figure 9-5 can also be applied to the rotating impeller by replacing C with W and adjusting the result for the possible presence of splitter blades. Hence, Stokes's theorem yields

$$\Delta W = 2\pi |r_3 C_{\theta 3} - r_1 C_{\theta 1}| / [L(N + N_{SB} F_{SB})] \quad (9-51)$$

L is given by Eq. (9-33), N_{SB} is the number of splitter blades (zero or an integer multiple of N) and F_{SB} is the fractional length of the splitter blades. To include the splitter blade influence on the profile loss, Eq. (9-16) is modified by

$$\theta_b \rightarrow \theta_b [1 + N_{SB} F_{SB} / N] \quad (9-52)$$

In other respects, the impeller profile loss coefficient calculation follows the same procedure as used for the nozzle row. Carmichael [67] suggests that the optimum incidence angle for a radial-inflow turbine impeller can be approximated by the natural discharge angle for a similar centrifugal compressor impeller. If U_1 is the inlet blade speed, the optimum (minimum loss) inlet swirl velocity and absolute flow angle can be calculated based on the centrifugal compressor slip factor, σ .

$$C_{\theta 1}^* = \sigma [U_1 - C_{m1} \cot \beta_1] \quad (9-53)$$

$$\cot \alpha_1^* = C_{m1} / C_{\theta 1}^* \quad (9-54)$$

$$Y_{inc} = \sin^2(\alpha_1 - \alpha_1^*) [P'_{t1} - P_1] / [P'_{t3} - P_3] \quad (9-55)$$

The centrifugal compressor slip factor model from Aungier [1] is used for this purpose. That is a modification of the well-known empirical model for slip factor by Wiesner [89]. The basic slip factor is given by

$$\sigma = |\sin \phi_1| \sqrt{\sin \beta_1} / (N + N_{SB})^{0.7} \quad (9-56)$$

Eq. (9-56) yields the slip factor for most practical cases, but requires adjustment if the blade solidity is too low. This is evaluated using σ from Eq. (9-56), β_1 and the impeller radius ratio, $\varepsilon = r_3/r_1$. Eq. (9-56) applies unless ε exceeds a limiting value given by

$$\varepsilon_{lim} = (\sigma - \sigma_0) / (1 - \sigma_0) \quad (9-57)$$

$$\sigma_0 = \sin(19^\circ + \beta_1 / 5) \quad (9-58)$$

When $\varepsilon > \varepsilon_{lim}$, a corrected slip factor is calculated from

$$\sigma_{cor} = \sigma(1 - \xi) \quad (9-59)$$

$$\xi = [(\varepsilon - \varepsilon_{lim}) / (1 - \varepsilon_{lim})]^{\sqrt{\beta_1 / 10}} \quad (9-60)$$

Figure 9-8 shows results obtained from this empirical model for a specific blade inlet angle and assuming no splitter blades are present. Loss coefficients to account for blade loading and hub-to-shroud loading effects are adapted from the impeller performance analysis for centrifugal compressors of Aungier [1]. They are defined as

$$Y_{BL} = \frac{1}{24} \left[\frac{\Delta W}{W_3} \right]^2 \quad (9-61)$$

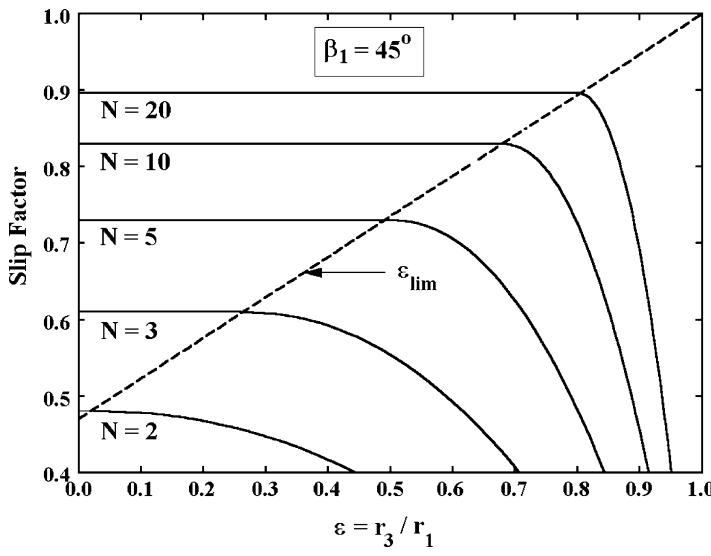


FIGURE 9-8. The Slip Factor Model

$$Y_{HS} = \frac{1}{6} \left[\frac{\kappa_m b_3 W_2}{W_3 \sin \alpha_3} \right]^2 \quad (9-62)$$

The hub-to-shroud loading loss differs from the corresponding centrifugal compressor model by the dependence on the exit absolute flow angle, α_3 . This term is included to account for the increased exit flow profile distortion expected for turbine impellers. Eq. (3-24) shows that swirling flow at the axial-exit of turbine impellers is expected to produce greater distortion than for the radial-exit compressor impellers. The blade clearance loss is also adapted from Aungier [1]. The average pressure difference across the blade clearance gap, ΔP , is estimated from the change in angular momentum in the impeller.

$$\Delta P [\rho_{ave} (rb)_{ave} L (N + N_{SB} F_{SB})] = \dot{m} |r_1 C_{\theta 1} - r_3 C_{\theta 3}| \quad (9-63)$$

The average density is given by Eq. (9-3). The average value of rb is calculated by a similar expression. The velocity of the leakage flow across the clearance gap is estimated by

$$u_{CL} = \sqrt{2 \Delta P / \rho_{ave}} \quad (9-64)$$

The clearance gap leakage mass flow is calculated assuming a gap contraction ratio of 0.816.

$$\dot{m}_{CL} = 0.816 \rho_{ave} u_{CL} L (N + N_{SB} F_{SB}) \delta_c \quad (9-65)$$

The clearance loss is given by

$$Y_{CL} = \dot{m}_{CL} \Delta P / [\dot{m}(P'_{t3} - P_3)] \quad (9-66)$$

Moisture loss is treated similar to the axial-flow turbine models in chapter 4. Basically, it is assumed that the liquid phase is ineffective in transferring work to the rotor since it cannot follow the vapor phase streamlines. Viewed as an equivalent enthalpy loss and corrected to the discharge entropy using Eq. (2-8), this can be expressed as

$$\Delta H_Q = [1 - (Q_1 + Q_3) / 2] |U_1 C_{\theta 1} - U_2 C_{\theta 2}| + T_{t1} (s_3 - s_1) \quad (9-67)$$

Expressed as a total pressure loss using Eq. (2-8), this yields

$$Y_Q = \Delta H_Q \rho'_{t1} / (P'_{t3} - P_3) \quad (9-68)$$

For this rotating component, rothalpy is conserved through the rotor. From Eq. (3-10),

$$I = H_1 + \Delta H_{DF} - \omega r_1 C_{\theta 1} \quad (9-69)$$

Eq. (9-69) corrects the inlet total enthalpy for the additional work due to disk friction on the rotating disk. The disk friction is calculated in the same fashion as for axial-flow turbines described previously in chapter 4. Since only one side of the disk contributes to this parasitic work, ΔH_{DF} is given by one-half of the result given in Eq. (4-109). From Eq. (3-13), the exit relative total enthalpy is given by

$$H'_3 = I + \frac{1}{2} (\omega r_3)^2 \quad (9-70)$$

The ideal exit relative total pressure, $P_{3,id}$, is calculated from the exit relative total enthalpy and the inlet entropy, using the appropriate equation of state from chapter 2. The actual exit relative total pressure is given by

$$P'_{t3} = (P'_{t3,id} + Y P_3) / (1 + Y) \quad (9-71)$$

$$Y = Y_p + Y_{inc} + Y_{BL} + Y_{HS} + Y_{CL} + Y_Q \quad (9-72)$$

The impeller exit mass balance is governed by

$$\dot{m} = (1 - \Delta) 2\pi r_3 b_3 \rho_3 W_3 \sin \alpha'_3 \quad (9-73)$$

Similar to the nozzle row, the boundary layer blockage, Δ in Eq. (9-73) includes the end-wall boundary layer blockage only. The discharge exit static enthalpy is given by

$$h_3 = H'_3 - \frac{1}{2} W_3^2 \quad (9-74)$$

Since the static entropy and total entropy are equal, the equation of state provides all other static conditions as a function of h_3 and s_3 . Hence, Eq. (9-73) can be solved to balance mass in an iterative manner. It is easily seen that the boundary layer analysis and the losses are functions of the impeller exit flow conditions, necessitating an iterative solution at station 3 to converge on Y .

The subsonic impeller analysis must also check for choked flow. Given the impeller discharge relative total thermodynamic conditions, an iterative solution is performed to determine the sonic relative velocity and density. The mass flow must be limited to not exceed the choking mass flow given by

$$\dot{m}_* = N b_{th} o (1 - \Delta) \rho_* W_* \quad (9-75)$$

For cases where the impeller is choked, the above procedure yields the choking mass flow and the choked impeller performance. As will be seen subsequently in this chapter, a choked component requires supplemental calculations to converge on an assigned discharge static pressure that is less than the choked impeller value. This is accomplished by imposing an isentropic expansion from the choked impeller solution. This yields all static thermodynamic conditions at the impeller exit. Then the discharge relative velocity and flow angle are given by

$$W_3 = \sqrt{2(H'_3 - h_3)} \quad (9-76)$$

$$\sin \alpha'_3 = \dot{m} / [(1 - \Delta) 2\pi r_3 b_3 \rho_3 W_3] \quad (9-77)$$

When imposing the isentropic expansion at the impeller discharge, it is important to check for certain physical limits in case the overall stage performance iteration procedure seeks a choked impeller discharge pressure that is not achievable. Similar to the nozzle row, an isentropic expansion may be limited by an annulus choke downstream of the impeller. This limit can be identified by the condition that the meridional velocity component is equal to the local sound speed. The minimum pressure that yields an annular passage choke can be determined from an iterative solution to determine the value of W_3 that matches the known relative total thermodynamic conditions, satisfies the equation of state and Eq. (9-74) and yields

$$C_{m3} = \dot{m} / [(1 - \Delta) 2\pi r_3 b_3 \rho_3] = a_3 \quad (9-78)$$

The corresponding value of P_3 is the minimum impeller exit static pressure that can be matched by an isentropic expansion and also balance mass. When this limit precludes matching the specified exit pressure, the limiting value is used. When this limit restricts the isentropic expansion, corrective action is needed by the overall stage performance iteration. That process will be described subsequently in this chapter.

When the impeller discharge relative flow is known from either the subsonic or supersonic solution, the absolute discharge tangential velocity is given by Eq. (3-1).

$$C_{\theta 3} = W_{\theta 3} + U_3 \quad (9-79)$$

Eq. (3-13) yields the absolute discharge total enthalpy.

$$H_3 = H'_3 + U_3 C_{\theta 3} - \frac{1}{2} U_3^2 \quad (9-80)$$

Since discharge entropy, s_3 , is identical for absolute and relative total conditions, the other absolute total thermodynamic conditions are provided by the equation of state as a function of H_3 and s_3 .

9.7 Vaneless Annular Passage Analysis

As illustrated in figure 9-1, there are typically one or more vaneless annular passages between the primary components in the stage. Consistent with other components, the vaneless passage geometry is specified for the inlet, midpassage and exit stations, as shown in figure 9-9. The data specified are z , r and b , designated by subscripts 1 through 3. The meridional coordinates measured from station 1 are obtained by numerical integration of Eq. (9-29). The passage areas for the three stations are given by Eq. (9-20). The mass flow, total thermodynamic conditions and swirl velocity at the inlet are known from the analysis of the upstream component. However, provision should be made for cases where r_1 , b_1 and A_1 differ from the upstream station where the inlet flow data are known. This situation is not uncommon in a practical stage configuration. Designating known parameters at the upstream station by the subscript u , the swirl velocity of the inviscid core flow at all stations is given by conservation of angular momentum.

$$C_\theta = C_{\theta u} r_u / r \quad (9-81)$$

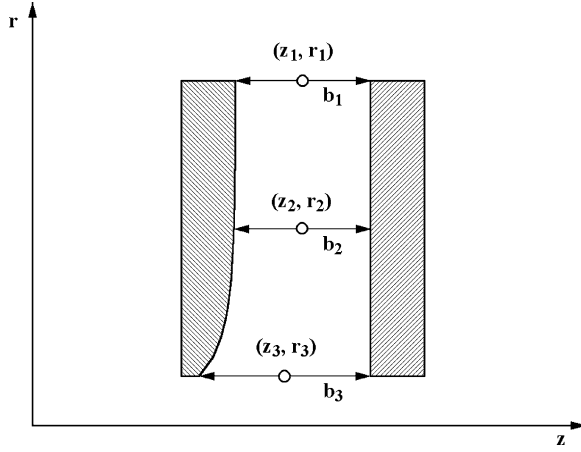


FIGURE 9-9. Vaneless Passage Geometry

An entrance loss coefficient is defined as

$$Y_{in} = [(A_1 / A_u - 1) \sin \alpha_1]^2 (P_{t1} - P_1) / (P_{t3} - P_3) \quad (9-82)$$

This loss coefficient is basically the well-known abrupt area expansion loss applied to the meridional component of the velocity head. Results from Benedict et al. [50] show that this is also a reasonable approximation for abrupt area contraction losses so long as the contraction is not too extreme. Other flow parameters at all stations are obtained from a mass balance using the inlet mass flow and the assigned tangential velocity components from Eq. (9-81). The analysis at station 3 must include the total pressure loss given by

$$Y = Y_p + Y_{in} = (P_{tu} - P_{t3}) / (P_{t3} - P_3) \quad (9-83)$$

$$P_{t3} = (P_{tu} + Y P_3) / (1 + Y) \quad (9-84)$$

The boundary layer analysis and losses depend on the flow data at station 3, necessitating an iterative solution at station 3 to converge on Y . Although choked flow in a vaneless annular passage is rare, it is not impossible. Hence, the mass balance at all stations must check for choke. As previously noted for other components, the condition for an annular passage choke at any station is

$$C_m = \dot{m} / [2\pi r b \rho] = a \quad (9-85)$$

Hence, the vaneless passage analysis must require $C_m \leq a$ at all stations. If that limit yields a mass flow rate less than the inlet mass flow rate the passage is choked. Then, the stage mass flow rate requires adjustment to the lower choked flow value in the overall stage performance iteration. That process will be described subsequently in this chapter.

9.8 Exhaust Diffuser Analysis

The exhaust diffuser geometry is specified at inlet and exit, designated by subscripts 1 and 2. The geometric data specified at these stations are z , r and ϕ , as illustrated in figure 9-10. The linear distance between the two stations is

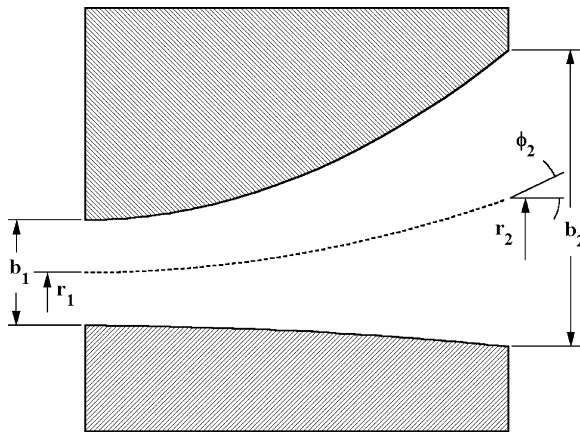
$$d = \sqrt{(z_2 - z_1)^2 + (r_2 - r_1)^2} \quad (9-86)$$

The curvature of the mean stream surface is proportional to the change in the slope angles, i.e.,

$$\Delta\phi = |\phi_2 - \phi_1| \quad (9-87)$$

If $\Delta\phi > 0$, the flow path length is assumed to be a circular-arc segment, i.e.,

$$L = d\Delta\phi / [2 \sin(\Delta\phi / 2)] \quad (9-88)$$

**FIGURE 9-10. Exhaust Diffuser Geometry**

Otherwise, $L = d$ is used. The performance analysis employs an empirical model for diffuser static pressure recovery by Aungier [1, 90, 91]. The empirical model is a correlation of the discharge blockage, Δ_2 , as defined in Eq. (9-15). The discharge flow is calculated using the reduced area due to viscous blockage and assuming isentropic flow. This determines the actual discharge static pressure for the diffuser. The blockage correlation is based on the effective diffuser divergence angle given by

$$2\theta_C = 2 \tan^{-1} [b_1 (A_2 / A_1 - 1) / (2L)] \quad (9-89)$$

It also depends on the ideal (no loss) ratio of the diffuser velocity-pressure ratio, P_{vr} .

$$P_{vr} = (P_{t1} - P_1) / (P_{t1} - P_{2,id}) \quad (9-90)$$

The diffuser discharge fractional blockage is given by

$$\Delta_2 = [K_1 + K_2(D - 1)]LA_1 / (A_2b_1) \quad (9-91)$$

D is a diffusion factor defined as

$$D = (\sqrt{P_{vr}} + 1)^2 / 4 \quad (9-92)$$

From Reneau et al. [92] it is known that diffuser static pressure recovery shows an abrupt deterioration when $2\theta_C$ exceeds about eleven degrees. To include those cases in the empirical model, a parameter K_θ was defined as

$$1 \leq K_\theta \geq 2\theta_C / 11^\circ \quad (9-93)$$

$$K_1 = 0.005 + [K_\theta - 1] / 5 \quad (9-94)$$

$$K_2 = 2\theta_c [1 - 2\theta_c / (22K_\theta)] / (125K_\theta) \quad (9-95)$$

These models for the empirical constants were found to yield static pressure recovery values that correlate well with vaned diffuser experimental performance data. Exhaust diffusers operate over a wider range of area ratios and passage lengths than vaned diffusers. Hence, K_1 is modified relative to the original model to extend the range of validity. Also, a limit of $D \leq 3.6$ is imposed when solving Eq. (9-91). These adjustments do not compromise the model's accuracy for the original vaned diffuser data, but they extrapolate that model consistent with the data of Reneau et al. [92]. They are explained in greater detail with exhaust diffuser design and analysis in chapter 12.

The basic analysis is quite simple. Conservation of angular momentum yields the exit tangential velocity, $C_{\theta 2}$, from the known inlet tangential velocity. The flow data at both stations are computed from a mass balance with the known tangential velocities and the inlet total thermodynamic conditions. This yields the ideal discharge static pressure. The discharge blockage is calculated and the mass balance at station 2 is repeated with the discharge blockage imposed to determine the actual exit static pressure, P_2 . Then the actual discharge total pressure required to produce this discharge static pressure using the actual (unblocked) discharge area is calculated to determine the total pressure loss. This requires an iterative procedure to conserve mass while matching P_2 and $C_{\theta 2}$. Since the total enthalpy is constant through the diffuser, the exit static enthalpy is given by

$$h_2 = H - \frac{1}{2} C_2^2 \quad (9-96)$$

The discharge static entropy, s_2 , and density, ρ_2 , are computed from the equation of state as a function of h_2 and P_2 . Then conservation of mass yields a new estimate of C_{m2} .

$$C_{m2} = \dot{m} / (\rho_2 A_2) \quad (9-97)$$

The process is repeated until successive estimates of C_{m2} converge within an acceptable tolerance. Then P_{t2} and other exit total conditions are calculated as a function of s_2 and H .

A more sophisticated performance analysis for the exhaust diffuser is described in chapter 12. That analysis can be used to predict an exhaust loss coefficient to be used in place of the diffuser analysis described in this section. However, a direct diffuser analysis is often more convenient, particularly when analyzing choked stages where total-to-static pressure

ratio must be specified rather than mass flow rate. It is not always possible to define a single exhaust loss coefficient that is representative for all operating conditions.

9.9 Imposed Total Pressure Loss

For additional generality, it is useful to include provision for one or more fictitious components that impose a general total pressure loss. This can be used to model nonstandard components such as inlet or interstage piping. It also provides a means to specify the alternate diffuser loss discussed in the previous section. A useful form for this imposed total pressure loss is

$$\Delta P_t = \Delta P_{t0} + [LC_m(C_m / C)^2 + LC_\theta(C_\theta / C)^2](P_t - P) \quad (9-98)$$

ΔP_{t0} is an assigned total pressure loss, while LC_m and LC_θ are loss coefficient based independently on the meridional and tangential components of the local velocity pressure. The other parameters in Eq. (9-98) are flow parameters calculated at the discharge of the upstream component. This form includes several alternative loss specifications. The specific loss forms to be imposed can be specified, while the other loss specifications are entered as zero. This fictitious component simply imposes the total pressure loss and recalculates total and static thermodynamic parameters assuming that the total enthalpy is unchanged.

9.10 Inlet Station Analysis

For generality, it is useful to provide for starting the stage performance analysis at a general inlet station. This simply involves entering the mean radius, passage area and inlet tangential velocity or flow angle to start the analysis. A simple mass balance yields all other inlet flow parameters. This permits starting the analysis at points within the stage rather than at the entrance to the inlet volute. For example, a performance analysis of a single component can be accomplished. It is also useful for specifying an appropriate inlet or interstage piping loss using the imposed loss described in the previous section of this chapter.

9.11 The Performance Analysis Strategy

The performance analysis can be performed for either an assigned mass flow rate or an assigned discharge static pressure, P_{dis} , (or, alternatively, the total-to-static pressure ratio). When the mass flow rate is assigned, the solution is limited to P_{dis} greater than or equal to the value corresponding to the onset of choke. When the turbine is choked, mass flow rate cannot uniquely define P_{dis} . If the specified mass flow rate exceeds the choke value, the analysis should adjust it to the choke value automatically. When P_{dis} is specified, an iterative process is required to determine the actual mass flow. In that case, it is necessary to make an initial guess for the mass flow rate. A "safe" initial guess is much more

important than an accurate initial guess to avoid initial calculations that result in numerical failure before the major iteration process gets started.

An effective method to initialize the mass flow rate is to locate the last component upstream of the first rotor that yields a reasonable estimate of the component's discharge area and flow angle. This includes an inlet station, an inlet volute or a nozzle row. For an inlet station, the flow angle is directly specified. For an inlet volute, an exit flow angle can be estimated by assuming gas density is constant and that angular momentum is conserved between the inlet and exit flow. This yields

$$\tan \alpha_3 = r_1 A_3 / (r_3 A_1) \quad (9-99)$$

For a nozzle row, the usual sine rule yields a reasonable estimate.

$$\sin \alpha_3 = o / s_3 \quad (9-100)$$

Then, the equation of state is used to compute the sound speed corresponding to sonic flow conditions, a_* , from the specified turbine inlet total thermodynamic conditions. If the last upstream component is a nozzle row, assume that $C_3 = 0.5a_*$. Otherwise, assume that $C_3 = 0.2a_*$. This permits calculation of a rather safe estimate of the mass flow rate using the component exit area and assuming isentropic flow from the turbine inlet, i.e.,

$$\dot{m} = \rho_3 C_3 A_3 \sin \alpha_3 \quad (9-101)$$

The component discharge density is obtained from the equation of state and Eq. (9-42).

If a rotor is present, the rotation speed, N , can be specified directly. If P_{dis} is specified, it is useful to also permit specification of the total-to-static velocity ratio, v , based on the rotor tip speed, U_{tip} , and spouting velocity, C_0 .

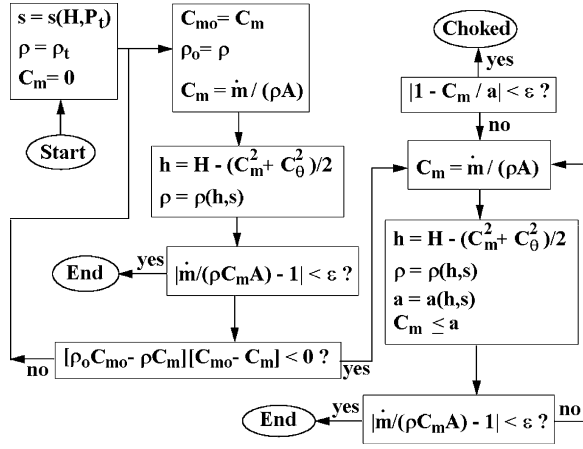
$$v = U_{tip} / C_0 \quad (9-102)$$

$$C_0 = \sqrt{2(H - h_{dis,id})} \quad (9-103)$$

The equation of state provides the ideal discharge static enthalpy as a function of P_{dis} and the turbine inlet entropy.

9.12 Mass Balance Procedures

From the previous descriptions of the component analyses, it should be obvious that a fairly general mass balance capability is required. The mass balance may be a true one-dimensional calculation with assigned passage area (e.g., the first two stations in the volute). A general mass balance with assigned C_θ or α and specified annulus area is also required. Figure 9-11 shows a flow chart for the assigned C_θ mass balance. The same logic can be employed for a simple one-dimensional mass balance by simply setting $C_\theta=0$. In this case, the value of C_m calculated is actually C . Similarly the assigned α case can be addressed by setting the passage area to $A \sin \alpha$ and $C_\theta=0$. Again, the value of C_m calculated is actually C . Then, α can be used to

**FIGURE 9-11. Mass Balance Flow Chart**

calculate C_m and C_θ . Hence, a single module of the type illustrated in figure 9-11 can be used for all mass balance calculations. The parameter ϵ represents any desired convergence tolerance. The mass balance logic first attempts to accomplish a subsonic or unchoked solution. This simply performs an iterative calculation estimating C_m from the previous estimate of ρ . This is commonly referred to as lagging the density and is known to provide stable and reliable convergence so long as C_m is subsonic. If the flow is choked, the subsonic iteration will produce a case where

$$\frac{\partial \rho}{\partial C_m} < 0 \quad (9-104)$$

The subsonic iteration checks for this situation using the current and previous estimates of ρ and C_m . If that occurs, the process switches to a choked solution iteration procedure. The lagged density approach continues to be used since it is not certain that the flow is truly choked (i.e., the choke indication could be due to numerical error). In this case, $C_m \leq a$ is imposed as an additional constraint. Note that C_m may actually be C in some cases as noted in the previous discussion. If $C_m = a$ within an acceptable tolerance while the calculated mass flow is less than the specified value, the flow is choked. In this case, the mass balance module should return the choked flow solution and flag the case as choked so the performance analysis logic can take corrective action. Note that the choke limit for nozzle rows and rotors is actually set by sonic flow conditions at the throat as described previously.

9.13 Subcritical Performance Analysis

The turbine critical total-to-static pressure ratio corresponds to the onset of choke in some component in the turbine. A performance analysis for a

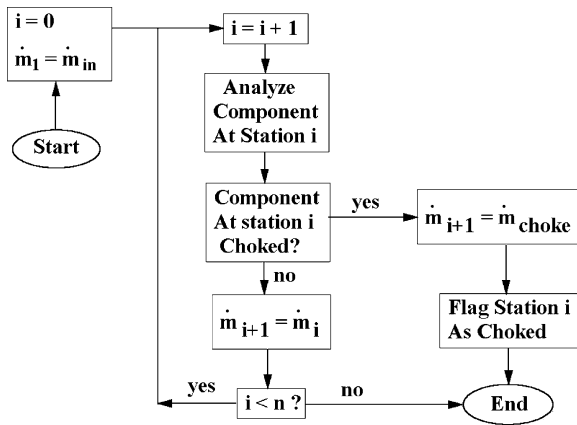
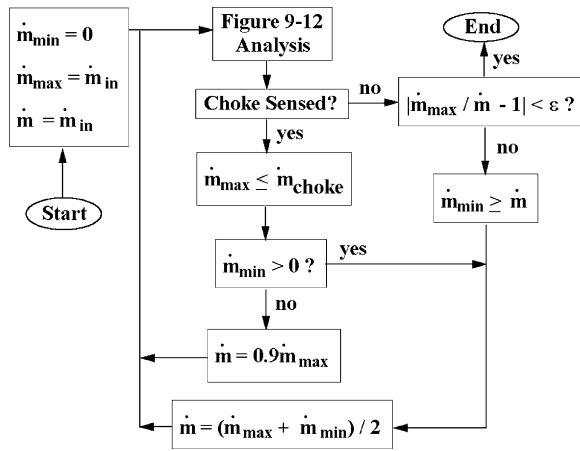


FIGURE 9-12. Basic Subcritical Analysis Flow Chart

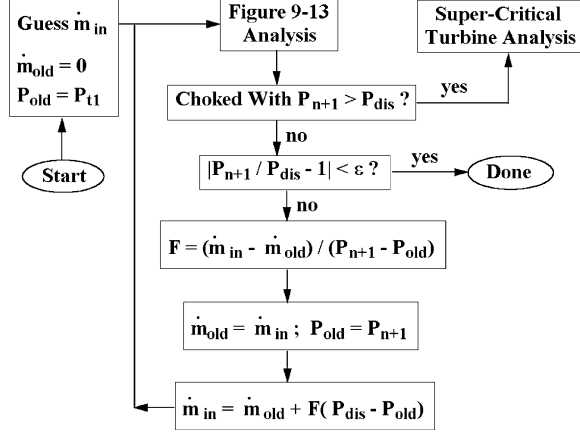
turbine total-to-static pressure ratio less than or equal to the critical value will be referred to as a subcritical solution. Any subcritical solution is uniquely defined by the turbine mass flow rate. Hence, the most direct specification for a subcritical solution is the mass flow rate, although a specified total-to-static pressure ratio or discharge static pressure can also yield a subcritical solution. In either case, the subcritical analysis is conducted for a specific mass flow rate, which may be a direct specification or an estimated value when seeking to converge on a specified discharge static pressure. Figure 9-12 is a flow chart of the basic subcritical turbine performance analysis. The analysis starts by setting the mass flow rate at the inlet to the first component equal to the assigned value. Designating the number of components in the turbine by n , the analysis proceeds through the components using the basic analysis procedures described previously in this chapter and supported by the mass balance procedure of figure 9-11. If the component analysis converges, the mass flow rate at the component discharge (or inlet to the next component) is set to the inlet (assigned) value. If all components are successfully analyzed, this analysis is complete. However, if any component chokes, it is flagged as choked and the component discharge mass flow rate is set to the mass flow rate corresponding to the onset of choke. This terminates the solution for this assigned or estimated mass flow rate. It identifies the component that is choked and supplies an estimate of the choked mass flow rate. The corrective action needed to continue the solution depends on the type of analysis being conducted.

The simplest case is when the turbine mass flow rate is the basic specification. Figure 9-13 shows a flow chart for this option. The maximum mass flow rate is set equal to the assigned value, while the minimum mass flow rate is set to zero. Note that if the analysis of figure 9-12 is successful on the first attempt, this satisfies the convergence check and ends the analysis with the desired mass flow rate solution. But if choke is sensed, the mass flow rate and its limiting

**FIGURE 9-13. Assigned Mass Flow Rate Flow Chart**

values are updated and an iterative procedure is used to converge on the choked flow solution within a suitable tolerance, ϵ . This corresponds to the onset of choke and the critical discharge static pressure, which is the limiting case for an assigned mass flow rate solution.

Figure 9-14 shows a flow chart for the case where turbine discharge static pressure, P_{dis} , is the specified parameter. With n components, there are $n+1$ stations where flow data are calculated. Hence, the objective is to achieve convergence between the predicted discharge pressure, P_{n+1} , and P_{dis} within an acceptable tolerance, ϵ . An initial guess is made for the mass flow rate as described previously in this chapter. The process used is to extrapolate for

**FIGURE 9-14. Assigned Discharge Pressure Flow Chart**

a corrected mass flow rate based on two successive solutions. To start the process, a fictitious previous solution is defined by a mass flow rate of zero for a discharge pressure equal to the turbine inlet total pressure. Then the analysis of figure 9-13 is conducted for the estimated mass flow rate. If that analysis results in a choked flow prediction, then the predicted discharge pressure will be the critical pressure for the turbine. Hence, a choked solution with the critical pressure greater than P_{dis} shows that the turbine total-to-static pressure ratio is supercritical. In that case, the supercritical analysis discussed subsequently in this chapter will be required. Otherwise, the estimate for mass flow rate is improved by extrapolation from the last two solutions and the process is repeated until convergence is obtained.

9.14 Supercritical Performance Analysis

The assigned discharge static pressure analysis of figure 9-14 may result in choked flow at a discharge pressure greater than the assigned discharge pressure. In that case, a supercritical performance analysis is required with the mass flow rate constant, as determined by the final (critical pressure ratio) solution from the analysis of figure 9-14. Designating the component number where choke occurs as i_c , figure 9-15 shows a flow chart of the setup for a supercritical analysis. In any well-designed turbine, choke will always occur in a nozzle row or rotor. Choke in other components is certainly possible, if the component is incorrectly sized so as to produce an annular passage choke. That case is of little practical interest and not really solvable by any practical physical model. It does need to be addressed in case it occurs during the design process. Hence, the flow chart shows that the solution will be aborted if that occurs. That will provide the solution for the critical pressure ratio and an appropriate error message so the designer can correct the problem.

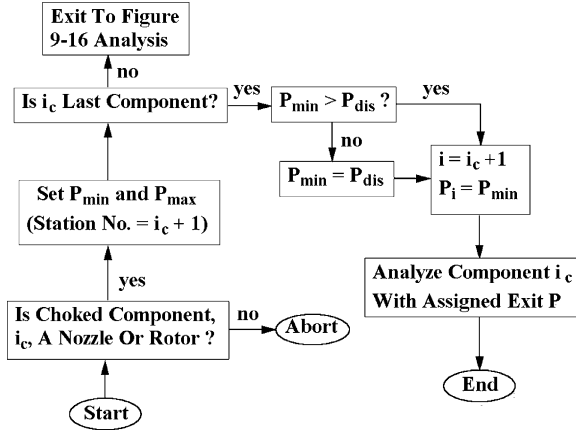


FIGURE 9-15. Flow Chart of Setup for Choked Flow

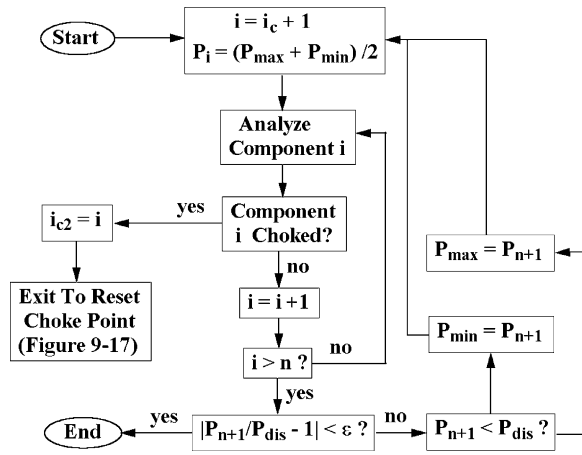


FIGURE 9-16. Supercritical Analysis Flow Chart

The final solution from the analysis of figure 9-14 is valid for all components upstream of the choked component. The remaining task is to solve for the choked component and any downstream components to match the assigned turbine discharge pressure. Procedures for analyzing choked nozzle rows and rotors using an assigned component exit discharge static pressure have been described previously in this chapter, including the practical limits on the exit static pressures that can be used. The component exit pressure from the solution for the critical pressure ratio is clearly an upper limit and is used as an initial estimate of P_{\max} . Similarly, a solution corresponding to an annular passage choke immediately downstream of the choked component is the lowest exit pressure that can be used and is used as an initial estimate of P_{\min} . If the choked component also happens to be the last component in the turbine, the supercritical analysis is trivial. As shown in figure 9-15, it is only necessary to solve for the performance of the last component with the desired turbine discharge static pressure. But if P_{\min} is greater than P_{dis} , then P_{\min} is the lowest turbine exit pressure that can be treated by the analysis. If the choked component is not the last component, the analysis follows the flow chart shown in figure 9-16. This systematically reduces the range between P_{\max} and P_{\min} based on comparison of the predicted and assigned turbine discharge pressure to convergence within an acceptable tolerance ϵ . This yields the desired turbine discharge pressure within the tolerance. It is possible that another downstream component may choke before the assigned turbine discharge pressure can be achieved. Designating the component number where this downstream choke occurs as i_{c2} , figure 9-17 shows a flow chart of the logic used to reset the choke point to this new choked component so the analysis can be continued. This just solves for the value of the exit pressure from the first choked component that corresponds to the onset of choke in the downstream component. That completes the solution for all components upstream of the second choked component. Then, i_c is

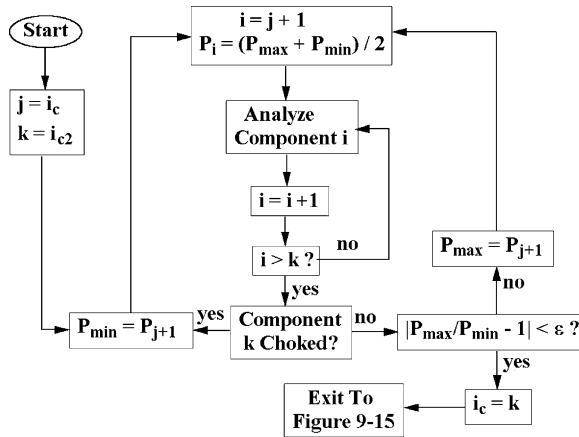


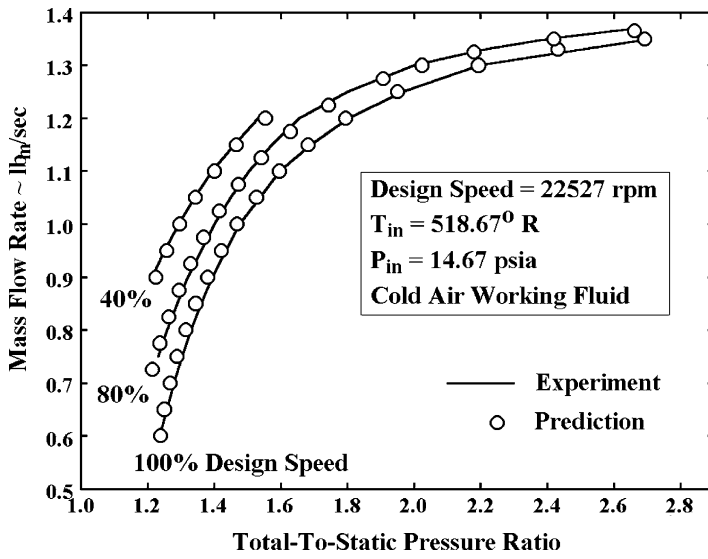
FIGURE 9-17. Flow Chart to Reset the Choke Point

reset to i_{c2} and the analysis returns to the flow chart of figure 9-15 to resume the supercritical analysis using the new choke location. Hence, the performance analysis is capable of addressing supercritical pressure ratios that result in more than one choked component.

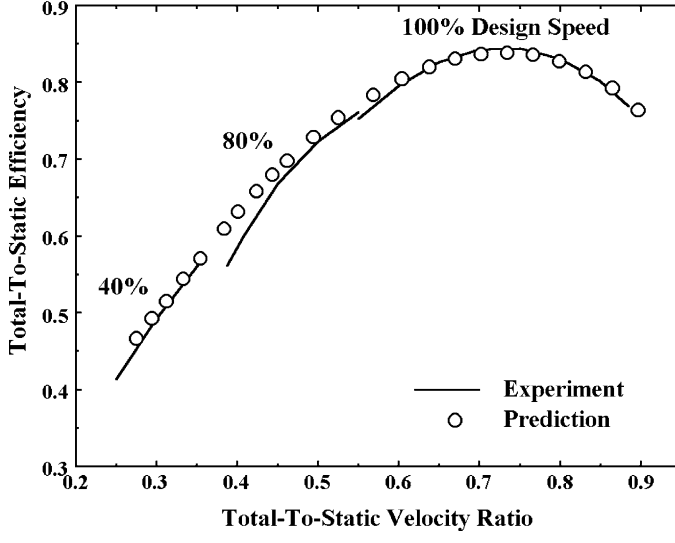
9.15 Typical Performance Analysis Results

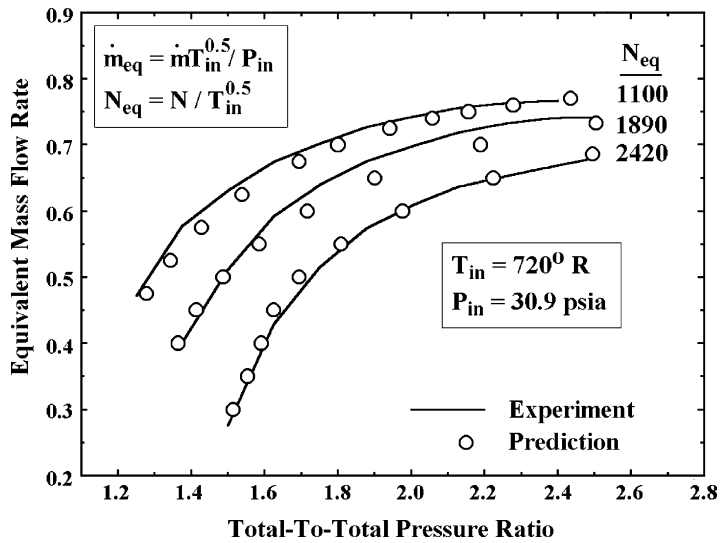
Kofskey and Holeski [4] report an extensive experimental performance evaluation of a radial-inflow turbine designed for a proposed application in a 10-kilowatt space power generation system based on the Brayton cycle. The performance evaluation was conducted at the NASA Lewis Research Center using both cold air and argon as working fluids. One accomplishment from this performance evaluation was to confirm the use of similitude for these two quite different working fluids as was previously discussed in chapter 1. The stage consisted of an inlet volute, a nozzle row with fourteen blades and a 6.02-inch-diameter impeller with eleven full-length blades and eleven splitter blades. The splitter blades extended over the first one-third of the impeller flow path. The impeller discharged axially into a simple annular passage, such that there was no exhaust diffuser present in the experiments. All experimental data are based on a total-to-static performance evaluation. All experimental data are corrected to air inlet conditions based on U.S. standard sea level conditions.

This radial-inflow turbine stage was modeled in the present performance analysis for comparison of predicted performance with the experiments using air as the working fluid. Figures 9-18 and 9-19 show comparisons of experimental data with predicted performance for several speed lines. Clearly the present performance analysis predicts the performance of this stage quite accurately over the wide range of operating conditions shown on the figures.

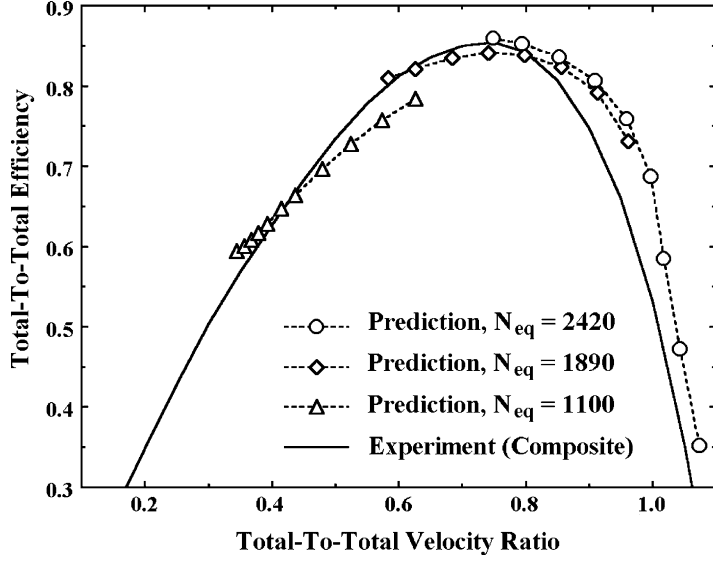
**FIGURE 9-18. NASA Turbine Mass Flow Rate Map**

Hiett and Johnston [93] report experimental performance results for radial-inflow turbines designed and tested at Ricardo & Co. under the sponsorship of the Ministry of Aviation. Their report includes sufficient information to apply the present performance analysis to the stage that they designate as the turbine

**FIGURE 9-19. NASA Turbine Efficiency Map**

**FIGURE 9-20. Ricardo Turbine Mass Flow Rate Map**

B configuration. That stage consisted of an inlet volute, a nozzle row with seventeen blades and a 5-inch diameter impeller with twelve full-length blades and no splitter blades. The nozzle blades are simple airfoils with no camber and an exit blade angle of 20°. The impeller discharges into an axial pipe

**FIGURE 9-21. Ricardo Turbine Efficiency Map**

rather than an exhaust diffuser. Experimental results are presented in terms of total-to-total performance. Figures 9-20 and 9-21 show comparisons of the experimental and predicted performance for this stage. The predicted mass flow rate map shows rather good agreement with the experimental data. The reference approximates the experimental efficiency map as a single composite curve of results for all speeds. The authors indicate that curve is accurate to within ± 1 percent for pressure ratios between 1.5 and 2.5, but they provide supporting evidence for that conclusion only for velocity ratios between 0.6 and 0.8. Clearly the predictions do not yield a single universal total-to-total efficiency curve, although that might be a reasonably approximation in the velocity ratio range that is validated in the reference. Overall agreement between the experimental and predicted efficiencies is considered acceptable, although obviously not as good as was achieved for the NASA turbine.

Chapter 10

PRELIMINARY AERODYNAMIC DESIGN OF RADIAL-INFLOW TURBINE STAGES

An effective preliminary aerodynamic design system provides substantial benefits in terms of quality and productivity for all types of turbomachinery stages. This was demonstrated in chapter 6 for axial-flow turbine stages. Similar benefits have been demonstrated for centrifugal compressors [1, 94] and axial-flow compressors [2]. The definition of a set of stage components that are well matched to each other for the stage design conditions is a very time-consuming process if done manually. Practical time constraints usually terminate such manual efforts with something acceptable rather than optimum. The computer can accomplish nearly all of the most of the time-consuming steps in this process once a logical preliminary design strategy is established. This permits the designer to explore a wide range of alternatives in a very brief period of time. When properly interfaced to an aerodynamic performance analysis, this also establishes well-qualified preliminary geometry to initiate the detailed aerodynamic design of the various components in the stage.

NOMENCLATURE

A = passage area; also ellipse axial semiaxis

AR = ellipse radial-to-axial aspect ratio = B/A

a = sound speed; also location of maximum camber along the chord

B = ellipse radial semiaxis

b = passage width; also maximum camber

C = absolute velocity

C₀ = spouting velocity

c = chord

d = location of maximum thickness along the chord

H = total enthalpy

h = static enthalpy

I = rothalpy

K_B = blade metal blockage factor

M = Mach number

m = meridional coordinate

\dot{m} = mass flow rate
 N = number of blades; also, rotation speed (rpm)
 n = the number of components in the turbine
 n_s = specific speed (total-to-static)
 o = blade passage throat width
 P = pressure
 Q = volume flow
 R = reaction
 R_c = radius of curvature
 r = radius
 s = blade pitch = $2\pi r/N$; also entropy
 T = temperature
 t = blade thickness
 U = local blade speed = $r\omega$
 W = relative velocity
 z = axial coordinate
 α = flow angle with respect to tangent
 β = blade angle with respect to tangent
 ΔH = stage heat (total enthalpy) drop
 γ = airfoil setting angle with respect to tangent
 η = efficiency
 θ = polar angle; also, airfoil camber angle
 $2\theta_C$ = diffuser divergence angle
 v = velocity ratio = U_4/C_0
 ρ = gas density
 σ = slip factor
 χ = camberline slope angle with the chord
 ω = rotation speed

Subscripts

h = hub parameter
 id = ideal (no loss) parameter
 m = meridional component; also, a mean value
 max = maximum value
 N = nozzle parameter
 R = rotor parameter
 s = total-to-static condition; also a shroud condition
 t = total thermodynamic condition
 1 = volute inlet parameter
 2 = volute exit and nozzle inlet parameter
 3 = nozzle exit parameter
 4 = rotor inlet parameter
 5 = rotor exit parameter
 6 = diffuser exit parameter
 θ = tangential component
 $*$ = parameter corresponding to sonic flow

Superscripts

- ' = a relative value in the rotating coordinate system
 * = an optimum (minimum loss) blade inlet condition

10.1 Preliminary Aerodynamic Design Strategy

The preliminary design procedure will address the basic stage components including the inlet volute, nozzle row, rotor and exhaust diffuser. Vaneless annular passages will automatically be inserted before and after the nozzle row. Component sizing calculations require specific aerodynamic and geometric calculations at stations located at the inlet and exit of all components. Parameters at those locations will be designated by subscripts 1 through 6 following the station nomenclature illustrated in figures 10-1 and 10-2. No distinction is made between the volute exit and the nozzle inlet stations since the vaneless passage inserted there is rather insignificant. It is really inserted only as a practical matter to provide the user with an easy access point for refining the preliminary design. This writer's preliminary design system handles the adjustment of station 2 data between the nozzle row inlet and volute exit automatically without any user intervention.

The stage performance is conveniently specified as total-to-static performance referenced to the rotor exit (station 5). The stage total-to-total performance and the influence of an exhaust diffuser can be forecast as part of the preliminary design to guide the designer in adjusting the performance specifications

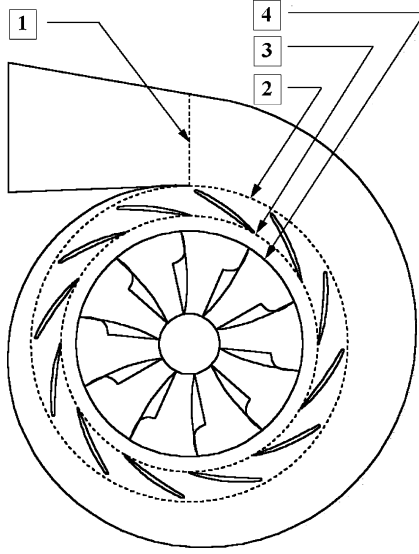
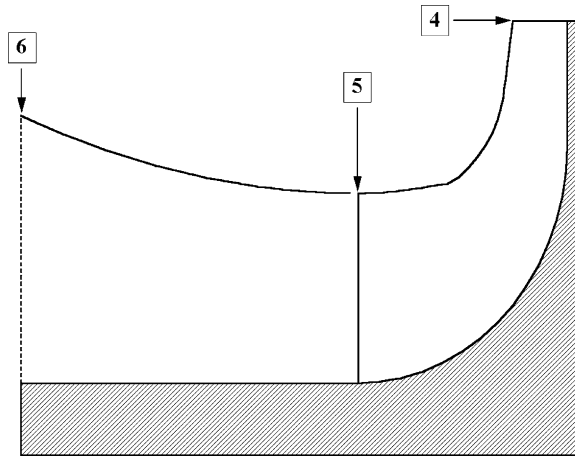


FIGURE 10-1. Stage Sizing Stations

**FIGURE 10-2. Rotor and Diffuser Sizing Stations**

if appropriate. Hence, the basic stage design specifications to be supplied by the designer are

- Stage inlet total temperature, T_{t1} .
- Stage inlet total pressure, P_{t1} .
- Stage mass flow rate.
- Total-to-static pressure ratio, P_{t1}/P_5 .
- Specific speed, n_s .
- Total-to-static efficiency, η_s .
- Total-to-static velocity ratio, v_s .
- Equation of state for the working fluid.

Following Balje [68], the specific speed is defined in dimensionless form as

$$n_s = \frac{\omega \sqrt{Q_5}}{(\Delta H_{id})^{0.75}} \quad (10-1)$$

The ideal heat drop, ΔH_{id} , corresponds to an isentropic expansion from the stage inlet total conditions to the rotor exit static pressure, P_5 . The volume flow, Q_5 , is defined from the mass flow and the rotor exit total density, i.e.,

$$Q_5 = \dot{m} / \rho_{t5} \quad (10-2)$$

Most of the basic stage design specifications are easily selected based on the proposed application. The values selected for n_s , v_s and η_s are exceptions. The choices for n_s and v_s really determine the quality of the design while η_s is a consequence of those choices. Initial choices for these parameters are usually selected based on generalized performance correlations. Many generalized correlations

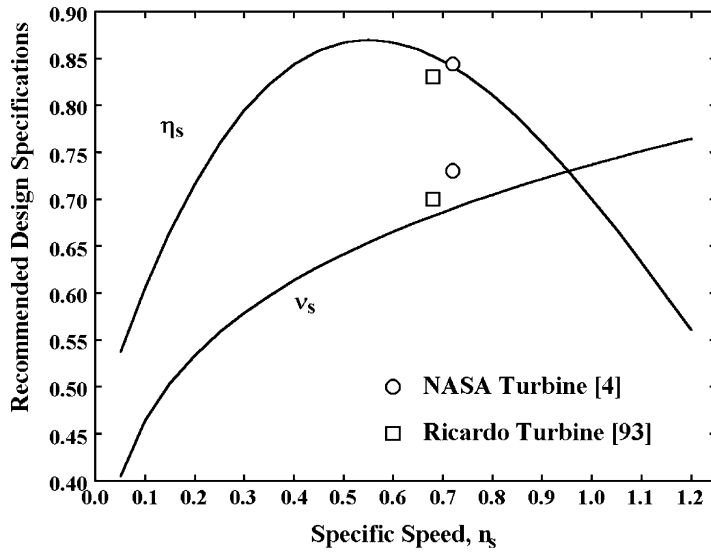


FIGURE 10-3. A Generalized Stage Performance Chart

of radial-inflow turbine performance potential are available from the literature, e.g., Wood [95], Linhardt [96], Rohlik [97] and Balje [68]. These typically provide estimates of the expected efficiency and recommended values of velocity ratio as a function of specific speed. Those correlations are based on various definitions of specific speed and differ with regard to whether total-to-total or total-to-static performance is estimated.

Figure 10-3 shows a generalized stage performance chart used for the present preliminary design system. This chart is based on a composite of the correlations cited in the previous paragraph, adjusted to total-to-static performance and to the present definition of specific speed where required. Due to significant differences in the various correlations, some preliminary designs were accomplished and analyzed with the performance analysis of chapter 9 for additional guidance in selecting the curves shown. Figure 10-3 also includes approximate experimental values corresponding to the design speed and optimum efficiency for the two radial-inflow turbines discussed in chapter 9. As a general rule, the preferred range of values for specific speed is 0.45 to 0.75. However, the specific speed is not really an arbitrary parameter, since size, speed, Mach number levels, mechanical integrity, etc. may impose definite constraints that preclude choices in the preferred range. Hence, the generalized chart extends well beyond the preferred range of specific speed to include those cases.

The best approach is for the preliminary design system to display figure 10-3 on demand to guide the designer in selecting the design specifications. It is also useful to provide the option to use these correlations to define default values of η_s and v_s as a function of the specified specific speed so that the designer can either use them directly or supply alternate values. Both of these features are easily incorporated using the following analytical equations, which correspond to the curves shown in figure 10-3.

$$v_s = 0.737 n_s^{0.2} \quad (10-3)$$

$$\eta_s = 0.87 - 1.07(n_s - 0.55)^2 - 0.5(n_s - 0.55)^3 \quad (10-4)$$

Once a preliminary design has been accomplished, it can be analyzed with the performance analysis of chapter 9 to improve the estimate for η_s . But n_s and v_s are more basic design specifications. Refining those specifications from performance analysis results requires a parametric evaluation of alternate choices.

The preliminary design of the complete stage requires many additional specifications to select well-matched and optimized stage components. If the designer must specify all of these component design parameters to obtain a design, the preliminary design system will be rather ineffective. A better approach used is to supply default values for all component design specifications such that the preliminary design system can generate a candidate stage design from the basic stage design specifications. The designer can optimize the design by adjusting any of the default specifications for the components. It is always more efficient to optimize component specifications from a reasonable set of existing values than to select a complete set of specifications. Much of the design optimization process can be accomplished within the preliminary design system. The component geometry and the flow data at inlet and exit to each component computed as part of the design process provide useful guidance for that purpose. But it is also important to provide the capability to export an input file for the performance analysis of chapter 9. This provides a direct evaluation of the actual performance to be expected from the design based on the more fundamental performance analysis rather than generalized correlations.

Another very useful feature is to provide for automatic processing of all design calculations. The error trapping capability of modern programming software makes it practical to safely process the stage preliminary design calculations as far as possible with the resident design specifications. When this leads to an error or convergence failure, the design process is terminated with a message as to the specific component where the problem occurred. In this way, the designer receives immediate feedback each time any design specifications are changed.

10.2 Rotor Tip Sizing

Once the basic stage design specifications are available, the important rotor tip sizing can be accomplished. The stage inlet total pressure and the pressure ratio specifications immediately determine the rotor exit static pressure, P_5 . The equation of state determines the stage inlet total enthalpy, H_1 , and entropy, s_1 . The equation of state yields the ideal heat drop as a function of H_1 , P_5 and s_1 . The discharge spouting velocity and the rotor tip blade speed are given by

$$C_{0s} = \sqrt{2\Delta H_{id}} \quad (10-5)$$

$$U_4 = v_s C_{0s} \quad (10-6)$$

From the specified efficiency,

$$H_5 = H_1 - \Delta H_{id}\eta_s \quad (10-7)$$

Since the rotor exit velocity is currently unknown, the discharge total density is approximated from the equation of state as a function of H_5 and P_5 . This is a reasonable approximation since a relatively low value of the rotor exit absolute Mach number at the design point operating conditions is an important design objective. Hence, the difference between total and static density is expected to be small in a well-designed stage. Then Eq. (10-1) can be solved for the rotation speed, ω , and Eq. (10-6) yields the rotor tip radius.

$$r_4 = U_4 / \omega \quad (10-8)$$

The portion of the stage losses that occur upstream of the rotor influences the rotor tip sizing. Using Eq. (2-8) and the isentropic enthalpy loss, an estimate of the rotor inlet total pressure found to be effective is given by

$$P_{t4} = P_{t1} - \rho_{t1} \Delta H_{id} (1 - \eta_s) / 4 \quad (10-9)$$

Since the turbine is being sized for optimum performance, it is assumed that $C_{\theta5} = 0$ to minimize the rotor leaving loss. Since $H_4 = H_1$, Eq. (3-9) and the definitions of v_s and η_s supply the rotor inlet tangential velocity.

$$C_{\theta4} = U_4 \eta_s / (2v_s^2) \quad (10-10)$$

10.3 Rotor Design Specifications

The following rotor design specifications have been found effective and are sufficient to complete the rotor design.

- The inlet flow angle, α_4
- The inlet blade thickness, t_{b4}
- The exit blade thickness, t_{b5}
- The exit hub radius, r_{h5}
- The exit shroud radius, r_{s5}
- The axial length, Δz_R
- The number of blades (including splitter blades, if used), N_R
- The inlet blade angle, β_4
- The impeller blade type
- Splitter blade option

The impeller blade types considered in this chapter are the straight-line element (three-dimensional, ruled surface) or radial element blades. For the latter type, the inlet blade angle is constrained to be 90°. As discussed previously

in this chapter, default values considered to be reasonable estimates for these parameters are provided. They may be used as initial estimates and subsequently revised as appropriate based on an evaluation of the results. Rohlik [97] recommends setting the nozzle exit or rotor inlet absolute flow angle as a function of specific speed. His graphical correlation can be approximated in the nomenclature of this book by

$$\alpha_4 = 10.8 + 14.2n_s^2 \quad (10-11)$$

Blade thicknesses and the exit hub radius are influenced by both aerodynamic and mechanical considerations. Suitable default values will depend on the application and the organization's normal design practice. This writer's preliminary design system uses the following default values.

$$t_{b4} = 0.04r_4 \quad (10-12)$$

$$t_{b5} = 0.02r_4 \quad (10-13)$$

$$r_{h5} = 0.185r_4 \quad (10-14)$$

The exit shroud radius and axial length are selected based on maintaining a reasonable ratio of passage width-to-the flow path radius of curvature. The following procedure has been found effective in estimating values for these parameters that achieve that goal.

$$C_{m5}/C_{m4} = 1 + 5(b_4/r_4)^2 \quad (10-15)$$

Since the inlet total thermodynamic conditions and the mass flow rate are known, Eqs. (10-10) and (10-4) are sufficient to compute C_{m4} and b_4 from a mass balance. Since $C_{\theta5}=0$ is assumed and r_{h5} is assigned, a similar process yields r_{s5} , b_5 and C_{m5} . Then, the rotor axial length is estimated by

$$\Delta z_R = 1.5(r_{s5} - r_{h5}) \quad (10-16)$$

Rohlik [97] developed an empirical equation for the optimum number of blades from a graphical correlation by Jamieson [98]. Expressed in the nomenclature of this book and corrected for an obvious misprint in [97], this equation is

$$N_R = 12 + 0.03(33 - \alpha_4)^2 \quad (10-17)$$

Jamieson's correlation is an estimate of the number of rotor blades required to avoid reverse flow on the blade surfaces. Eq. (10-17) must be rounded to an integer value and adjusted to an even number if splitter blades are used. The default estimate for the inlet blade angle is based on operation at the optimum rotor

incidence angle based on the slip factor model previously described in chapter 9. The precise process used for preliminary design is described in the next section of this chapter. Here it is simply noted that the slip factor depends on the inlet blade angle. Hence, a simple predictor-corrector iteration procedure is required to converge on the correct blade angle.

It can be seen that some of the default specifications depend on other rotor design specifications. Hence, the calculation of the default parameters must be performed in the appropriate order. They must also be recalculated when the designer modifies any of the rotor design specifications.

10.4 Rotor Sizing

The slip factor model of chapter 9 is simplified by ignoring the limiting radius ratio effect. This assumes that any modern design will avoid blades too short to be effective. If that assumption proves to be unjustified, it will be apparent when the design is evaluated by the performance analysis. Hence, the slip factor is given by

$$\sigma = 1 - \sqrt{\sin \beta_4 / N_R^{0.7}} \quad (10-18)$$

The impeller inlet blockage factor is given by

$$K_{B4} = 1 - N_R t_{b4} / [2\pi r_4 \sin \beta_4] \quad (10-19)$$

This parameter defines the fraction of the flow passage available for through-flow inside the blades after correction for the blade metal blockage. Since the slip factor is defined based on flow inside the blades and C_{m4} is defined outside the blades, the ideal tangential velocity inside the blades is approximated by assuming the gas density is equal to its value outside the blades, i.e.,

$$C_{\theta4}^* = \sigma [U_4 - C_{m4} \cot \beta_4 / K_{B4}] \quad (10-20)$$

The ideal and actual inlet incidence angles defined inside the blades are given by

$$i_4^* = \beta_4 - 90^\circ + \tan^{-1} [(U_4 - C_{\theta4}^*) K_{B4} / C_{m4}] \quad (10-21)$$

$$i_4 = \beta_4 - 90^\circ + \tan^{-1} [(U_4 - C_{\theta4}) K_{B4} / C_{m4}] \quad (10-22)$$

Note that when the default inlet blade angle specification is being used, these two incidence angles will be equal. Since the total enthalpy at the rotor inlet is known from its value at the stage inlet, the inlet static enthalpy is given by

$$h_4 = H_4 - \frac{1}{2} (C_{m4}^2 + C_{\theta4}^2) \quad (10-23)$$

The rotor inlet total pressure is given by Eq. (10-9). Hence the equation of state supplies the rotor inlet entropy from the known total enthalpy and total pressure. Then all other static conditions are given by the equation of state as a function of h_4 and s_4 . Conservation of mass then supplies the impeller tip width.

$$b_4 = \dot{m} / [2\pi r_4 \rho_4 C_{m4}] \quad (10-24)$$

The rotor exit radius and passage width are given by

$$r_5 = (r_{h5} + r_{s5}) / 2 \quad (10-25)$$

$$b_5 = r_{s5} - r_{h5} \quad (10-26)$$

The rotor exit total enthalpy is given by Eq. (10-7) and $C_{\theta5} = 0$ is assumed. Hence a mass balance can be performed at the rotor exit by an iterative solution of

$$C_{m5} = \dot{m} / (2\pi r_5 b_5 \rho_5) \quad (10-27)$$

$$h_5 = H_5 - \frac{1}{2} C_{m5}^2 \quad (10-28)$$

Improved estimates of static thermodynamic conditions, including ρ_5 , are given by the equation of state as a function of h_5 and P_5 on all iterations. When converged, this yields all absolute flow parameters at the rotor exit. The rotor exit relative velocity is given by

$$W_5 = \sqrt{C_{m5}^2 + (r_5 \omega)^2} \quad (10-29)$$

Since static conditions are invariant for relative and absolute flow the relative Mach number, M_5^* , is also known. The mean blade pitch at the rotor exit is given by

$$s_5 = 2\pi r_5 / N_R \quad (10-30)$$

Note that if splitter blades are being used, the pitch is twice the value given by Eq. (10-30). If $M_5^* \leq 1$, the rotor mean throat width is given by

$$o_5 = s_5 C_{m5} / W_5 \quad (10-31)$$

Otherwise, the equation of state is used to compute the relative sonic velocity and the throat width is given by

$$o_5 / s_5 = \rho_5 C_{m5} / (\rho_* W_*) \quad (10-32)$$

If the right-hand side of Eq. (10-32) yields a value greater than unity, the design is terminated since an annular passage choke precludes achieving the design specifications. A suitable error message is given so the designer knows that corrective action is needed.

A few other useful checks can be made to permit termination of the impeller design with an appropriate error message. It is better to inform the designer of any obvious problem with the current design specifications rather than simply have the rotor sizing process fail. The blade metal blockage at the inlet and exit should be required to be less than 50% of the unblocked area. It is also recommended that $\Delta z_R \geq 1.5b_4$ and $r_{s5} < 0.9r_4$ be required.

10.5 Evaluating the Rotor Design

The literature provides some useful guidelines for evaluating the rotor sizing results. Balje [68] recommends the following limits on the exit meridional velocity and shroud radius.

$$0.2 \leq C_{m5}/U_4 \leq 0.4 \quad (10-33)$$

$$r_{s5}/r_4 \leq 0.78 \quad (10-34)$$

Rohlik's [97] recommendation relative to the exit shroud radius is more general and more conservative.

$$r_{s5}/r_4 = 1.29n_s \quad (10-35)$$

$$r_{s5}/r_4 \leq 0.7 \quad (10-36)$$

Wood [95] recommends limiting the ratio of meridional velocities by

$$1 \leq C_{m5}/C_{m4} \leq 1.5 \quad (10-37)$$

Stage reaction is also known to influence performance. Reaction is defined as

$$R = (h_4 - h_5)/(H_1 - H_5) \quad (10-38)$$

Balje [68], Linhardt [96] and Watanabe et al. [99] all offer fairly different recommendations relative to reaction. While subject to some uncertainty, it appears reasonable to assign a preferred range for reaction as

$$0.45 \leq R \leq 0.65 \quad (10-39)$$

Also, the difference between the optimum and actual incidence angles given by Eqs. (10-21) and (10-22) should be as small as practical to minimize rotor losses near the design operating condition.

Once the preliminary design of the complete stage is available, a more comprehensive evaluation of the rotor design will be obtained by accomplishing an aerodynamic performance analysis as described in chapter 9. The rotor sizing described in sections 10.2 and 10.4 of this chapter is sufficiently complete to provide the basic dimensions required for a performance analysis of the rotor. However, neither the sizing procedure nor a performance analysis provides confirmation that a practical rotor passage can be designed to connect the rotor inlet and exit stations selected. An effective preliminary design system will address this issue to ensure that the detailed rotor design process has a high probability of success. Hence, a realistic preliminary design of the rotor end-wall contours and blades should be included. Simple graphical displays of the end-wall contours and key geometrical parameters can quickly alert the designer to impractical configurations so that corrective action can be taken before attempting the more time-consuming detailed rotor passage design.

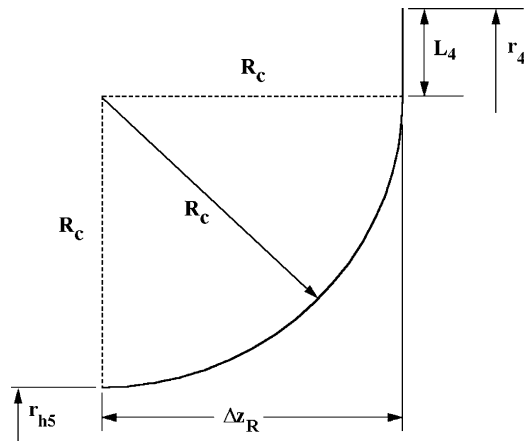
A more pragmatic justification for a preliminary rotor passage design will become apparent when detailed aerodynamic design process is described in chapter 11. The preliminary design can be exported to the general gas path design system as a starting point. It is far more efficient to refine a reasonable preliminary design than to accomplish a completely new detailed design. Hence, improved engineering productivity is another good justification for a preliminary rotor passage design.

10.6 Rotor End-Wall Contours

The preliminary design of the rotor end-wall contours seeks to confirm that the inlet and exit stations can be connected with smooth end-wall contours that yield a reasonable passage area distribution and avoid excessive flow profile distortion due to passage curvature effects. The rotor hub contour is constructed to minimize passage curvature effects by using the largest circular-arc that is compatible with the rotor dimensions obtained from the rotor sizing. Hence, the circular-arc radius of curvature, R_c , will be the smaller of either $(r_4 - r_{h5})$ or Δz_R . The remainder of the hub contour is constructed with a linear segment at the appropriate end of the circular-arc. Figure 10-4 illustrates the construction when $R_c = \Delta z_R$, where a linear segment, L_4 , at the inlet is required to complete the contour. It is easily seen that if $R_c = (r_4 - r_{h5})$ a linear segment, L_5 , at the exit would be required. The shroud contour is constructed to obtain a reasonable passage area distribution using a power-law relation.

$$r = r_{s5} + (r_4 - r_{s5})\xi^n \quad (10-40)$$

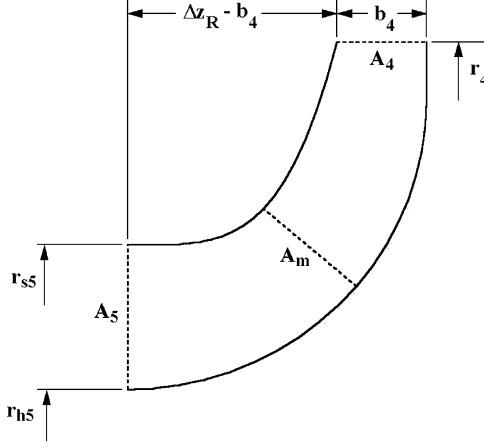
$$\xi = (z - z_5)/(\Delta z_R - b_4) \quad (10-41)$$

**FIGURE 10-4. Circular-Arc Hub Construction**

When the two end-wall contours are defined, the meridional distance along the contours can be calculated by numerical integration of

$$dm = \sqrt{(dz)^2 + (dr)^2} \quad (10-42)$$

Then, the coordinates for each contour at a mean value of m can be obtained by numerical interpolation. These are used to construct a mean quasi-normal as illustrated in figure 10-5. A reasonable basis for the shroud contour design is to achieve an area on this mean quasi-normal, A_m , that is approximately

**FIGURE 10-5. Power-Law Shroud Contour**

equal to the average of the known inlet and exit areas, A_4 and A_5 . This is easily accomplished by constructing alternate shroud contours using values of n from 2 through 9 and selecting the value of n that best achieves the desired mean passage area. Passage curvature effects are best evaluated with respect to a mean surface between the two end-wall contours. A series of quasi-normals across the passage are constructed by connecting equal-spaced points along the two end-wall contours. The points along the mean surface are defined by the midpoints of the quasi-normals. Then the radius of curvature of the mean surface can be calculated by numerical differentiation. Regarding the quasi-normal length as the passage width, the ratio, b/R_c , is computed for each point on the mean surface. This parameter is a qualitative measure of the hub-to-shroud flow profile distortion to be expected, as indicated by Eq. (3-24) or (3-30). It should be as small as practical, and values exceeding unity should be avoided if possible.

The value of the preliminary end-wall contours is best illustrated by results from a typical stage preliminary design. Figures 10-6 and 10-7 show graphical results provided as monitor screen displays by this writer's preliminary design system. Clearly the construction of smooth end-wall contours is possible for this case. The normalized passage width and area distributions are also reasonably smooth. The distribution of b/R_c is also reasonable and within acceptable limits. All of the distributions shown in figure 10-7 are expected to be further refined in the detailed design phase. While these end-wall contours are not sufficiently refined to be used to manufacture the rotor, the designer can be very confident that the detailed design phase will be successful.

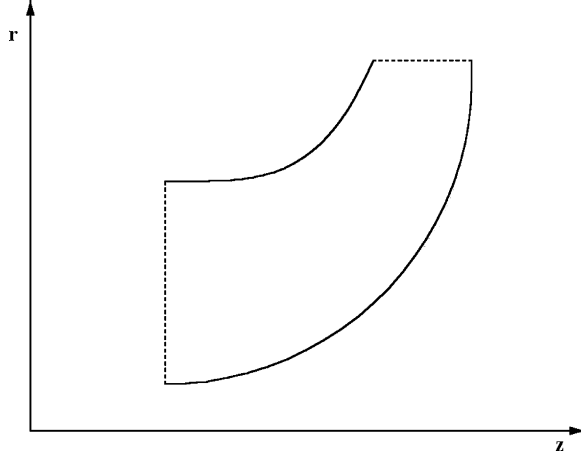


FIGURE 10-6. Typical Rotor End-Wall Contours

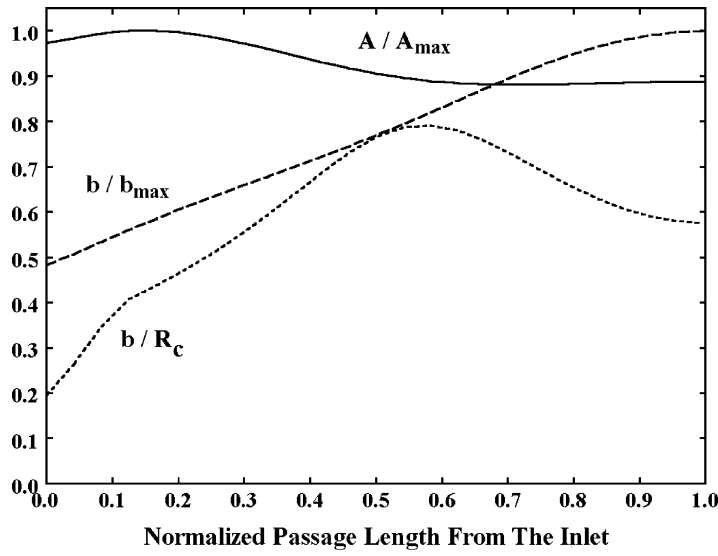


FIGURE 10-7. Typical Rotor Geometry Distributions

10.7 Straight-Line Element Rotor Blade Camberlines

Straight-line element blades are constructed by defining the blade geometry on the end-wall contours and connecting corresponding blade camberline and surface defining points with straight-line elements. This provides a fairly general three-dimensional blade geometry that is relatively easy to design, analyze and manufacture. The preliminary blade design is based on the same quasi-normals defined for the end-wall contours. For convenience, Eq. (10-42) will be integrated from station 5 to station 4 such that $m_5 = 0$ and m_4 is the total meridional length of the contour. The blade camberline along the shroud contour is defined by

$$\theta(m) = Am + Bm^3 + Cm^4 \quad (10-43)$$

The coefficients on the right-hand side of Eq. (10-43) are defined to match the blade angles at the end points and to require the first and second derivatives of Eq. (10-43) to be zero at the end points. This requires the blade angles on the end-wall contours to be related to the known blade angles at the midpassage position. It is assumed that the blade angle at the inlet station is constant from the hub to the shroud. At the rotor exit, it is assumed that $C_\theta = 0$ and C_m is constant from hub to shroud. Hence,

$$r_{s5} \tan \beta_{s5} = r_{h5} \tan \beta_{h5} = r_5 \tan \beta_5 \quad (10-44)$$

After some tedious algebra, it is easily shown that

$$A = \frac{\cot \beta_{5s}}{r_{5s}} \quad (10-45)$$

$$B = \frac{1}{m_4^2} \left[\frac{\cot \beta_4}{r_4} - \frac{\cot \beta_{5s}}{r_{52}} \right] \quad (10-46)$$

$$C = -\frac{B}{2m_4} \quad (10-47)$$

The camberline on the hub contour is defined by

$$\theta(m) = Dm + Em^2 + Fm^3 \quad (10-48)$$

The coefficients on the right-hand side of Eq. (10-48) are determined by matching the blade angles at the end points and requiring that θ_4 at the rotor inlet be constant from the hub to the shroud. It is easily shown that the shroud camberline definition yields

$$\theta_4 = \frac{m_4}{2} \left[\frac{\cot \beta_4}{r_4} + \frac{\cot \beta_{5s}}{r_{52}} \right] \quad (10-49)$$

After some tedious algebra, it is easily shown that the constants for the hub camberline are

$$D = \frac{\cot \beta_{5h}}{r_{5h}} \quad (10-50)$$

$$E = \frac{3\theta_4}{m_4^2} - \frac{1}{m_4} \left[2 \frac{\cot \beta_{5h}}{r_{5h}} + \frac{\cot \beta_4}{r_4} \right] \quad (10-51)$$

$$F = \frac{1}{m_4^2} \left[\frac{\cot \beta_{5h}}{r_{5h}} + \frac{\cot \beta_4}{r_4} \right] - \frac{2\theta_4}{m_4^3} \quad (10-52)$$

The corresponding blade angle distribution for either contour is given by

$$\cot \beta = r \frac{\partial \theta}{\partial m} \quad (10-53)$$

Figure 10-8 shows end-wall blade angle distributions generated with this camberline construction for the same stage preliminary design used to illustrate the end-wall contour design. This graphical presentation is also provided as a monitor screen display by this writer's preliminary design system for the designer's

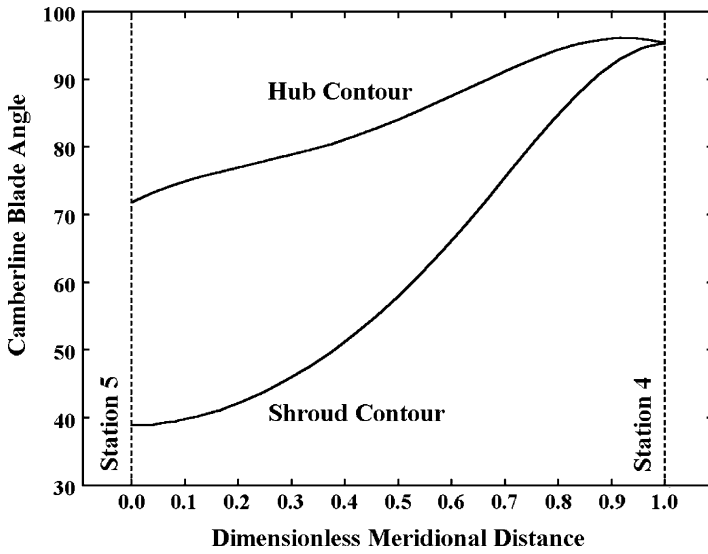


FIGURE 10-8. Straight-Line Element Blade Angles

guidance. The blade thickness is set equal to the blade inlet thickness except for the last 10% of the blade length where it is tapered linearly to the discharge blade thickness.

10.8 Radial Element Rotor Blade Camberlines

Rotor blade camberlines constructed with radial line elements are often used for turbines operating at high rotation speed. This eliminates bending stresses in the blades due to the centrifugal forces. While usually not the optimum choice from the perspective of aerodynamic performance, the radial-element blade type may be necessary to achieve adequate mechanical integrity. The radial element blade camberline is defined by

$$\frac{\partial \theta}{\partial r} = 0 \quad (10-54)$$

Hence, the camberline θ distribution can be assigned on only one end-wall contour. In addition, θ must be constant for all values of z from z_{s4} to z_{h4} , so the shroud camberline is the obvious choice. The shroud camberline defined by Eqs. (10-43) through (10-47) is used for the radial-element blade camberline also. The coefficients are somewhat simplified by the requirement that $\beta_4 = 90^\circ$. This defines the distribution of θ as a function of z . Hence, the hub camberline can be constructed by numerical interpolation of θ as a function of z .

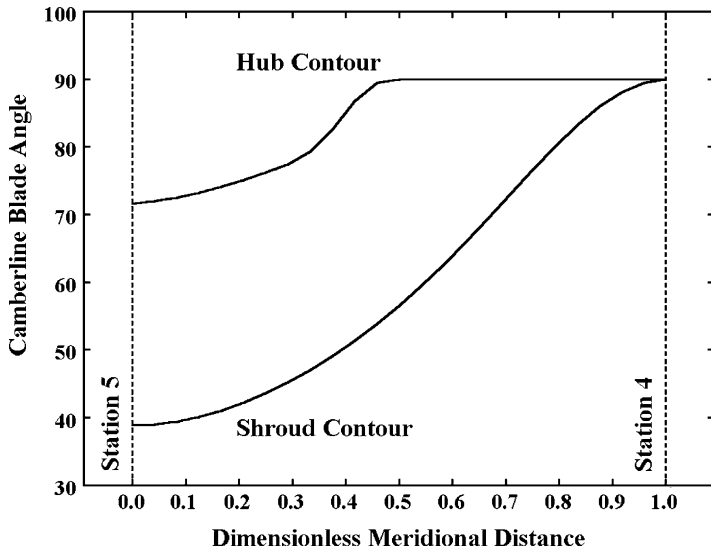
**FIGURE 10-9. Radial-Element Blade Angles**

Figure 10-9 shows the blade angle distributions obtained from Eq. (10-53) for the same stage preliminary design as figure 10-8, but with a radial-element camberline specified. The blade thickness distribution is handled in the same manner as for the straight-line element blade camberline.

10.9 Nozzle Blade Geometry

Nozzle blades are designed by imposing a general blade thickness distribution on a parabolic-arc camberline. This results in a very general airfoil geometry that should be adequate for any application. Aungier [2] shows that the governing equation for the parabolic-arc camberline is

$$x^2 + \frac{c-2a}{b}xy + \frac{(c-2a)^2}{4b^2}y^2 - cx - \frac{c^2-4ac}{4b}y = 0 \quad (10-55)$$

Figure 10-10 shows the simple (x, y) coordinate system and the defining constants used in this equation. The chord length, c , maximum camber, b , and its location, a , are the design specifications. For any value of x , Eq. (10-55) can be solved for y as a standard quadratic equation. This approach will be singular for $a/c = 0.5$, since two of the terms drop out. But that special case is a simple and direct solution. Aungier [2] notes that both cases can be treated by a numerical recursion equation of the form

$$y = x(c-x)/\left[\frac{(c-2a)^2}{4b^2}y + \frac{c-2a}{b}x - \frac{c^2-4ac}{4b}\right] \quad (10-56)$$

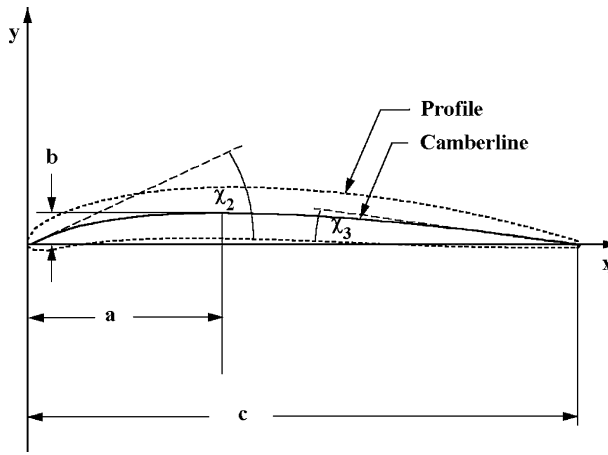


FIGURE 10-10. The Parabolic-Arc Camberline

Simply start with $y = 0$ and repeatedly solve this equation to converge on the correct value of y . The leading and trailing edge blade angles with respect to the chord line are obtained by differentiating Eq. (10-55) and evaluating the derivatives at $x = 0$ and $x = c$. It is easily shown that

$$\tan \chi_2 = 4b/(4a - c) \quad (10-57)$$

$$\tan \chi_3 = 4b/(3c - 4a) \quad (10-58)$$

The definition of the blade camber angle is

$$\theta = \chi_2 + \chi_3 \quad (10-59)$$

Eqs. (10-55) and (10-57) through (10-59) can be combined to yield.

$$b/c = [\sqrt{1 + (4 \tan \theta)^2 [a/c - (a/c)^2 - 3/16]} - 1]/(4 \tan \theta) \quad (10-60)$$

This defines the parabolic-arc camberline in terms of camber angle and the ratio, a/c . These are more useful design specifications for this application. Obviously, the leading and trailing edge angles should be restricted to be less than 90° , i.e.,

$$0.25 < a/c < 0.75 \quad (10-61)$$

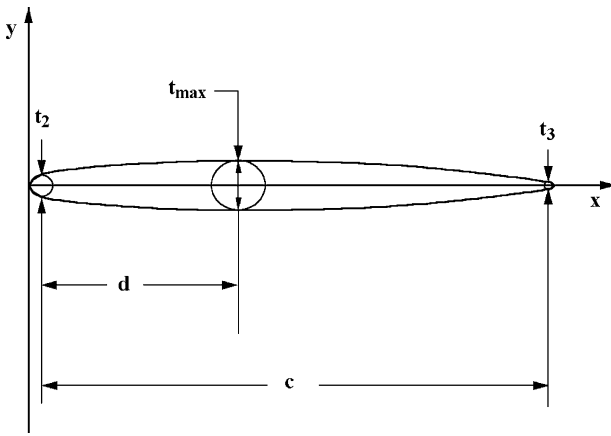


FIGURE 10-11. The Nozzle Blade Thickness Profile

The blade thickness distribution is adapted from a distribution used by Aungier [1] for return channel vanes. As shown on figure 10-11, the maximum blade thickness, t_{\max} , and its location, d , are specified along with the leading and trailing edge blade thicknesses. A “nose-radius” is imposed at each end of the camberline. The blade thickness at any location along the camberline is given by

$$t = t_{ref} + [t_{\max} - t_{ref}] \xi^e \quad (10-62)$$

$$t_{ref} = t_2 + [t_3 - t_2](x/d) \quad (10-63)$$

$$\xi = x/d; \quad x \leq d \quad (10-64)$$

$$\xi = (c - x)/(c - d); \quad x > d \quad (10-65)$$

$$e = \sqrt{0.4d/c}[0.95(1 - x/c)(1 - \xi) + 0.05] \quad (10-66)$$

This allows the airfoil geometry to be generated in dimensionless form by normalizing all parameters by the chord length. Hence, design specifications for a/c , d/c , θ , t_{\max}/c , t_2/c and t_3/c completely define the airfoil camberline and surface coordinates normalized by chord length. The camberline coordinates are given by Eq. (10-55) and the local blade thickness by Eq. (10-62). Designating the camberline coordinates by the subscript c , the surface coordinates are given by

$$x = x_c \pm \frac{1}{2} t \sin \chi \quad (10-67)$$

$$y = y_c \mp \frac{1}{2} t \cos \chi \quad (10-68)$$

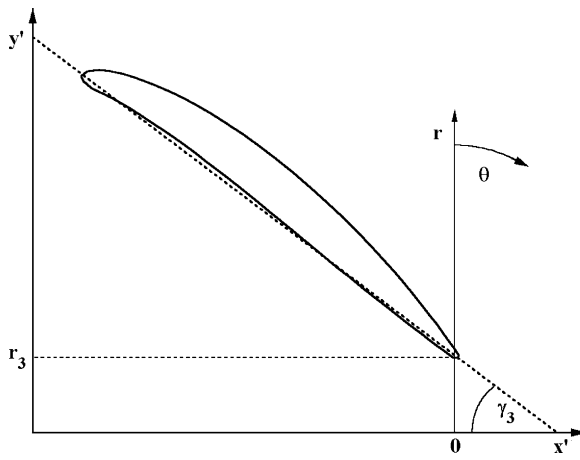


FIGURE 10-12. The Airfoil Setting Angle

$$\tan \chi = \frac{\partial y_c}{\partial x_c} \quad (10-69)$$

Since the chord length is yet to be determined, camberline and surface coordinates are normalized by chord so that the airfoil construction can be completed before sizing the nozzle. The normalized airfoil geometry can be used to define the nozzle blade by determining the chord and the nozzle setting angle, γ_3 , illustrated in figure 10-12. The camberline trailing edge is located at radius r_3 and polar angle, θ_3 , is arbitrarily set to zero. The basic airfoil coordinates that define the actual nozzle blade are obtained by a simple rotation of coordinates.

$$x' = (x - c) \sin \gamma_3 + y \cos \gamma_3 \quad (10-70)$$

$$y' = r_3 - (x - c) \cos \gamma_3 + y \sin \gamma_3 \quad (10-71)$$

The corresponding polar coordinates are given by

$$r = \sqrt{x'^2 + y'^2} \quad (10-72)$$

$$\tan \theta = x' / y' \quad (10-73)$$

Matching the nozzle row to the rotor inlet flow angle requires determining the nozzle throat width. For any specified number of blades, a second blade is constructed by changing all blade polar angles from Eq. (10-73) by an angle $\Delta \theta = 2\pi/N_N$. Then the minimum distance between the two blades can be determined numerically.

10.10 Nozzle Row Sizing

The nozzle row sizing strategy requires that the nozzle passage width is constant and is identical to the rotor inlet passage width determined from the rotor sizing. If the nozzle exit radius is known, the tangential velocity at the nozzle exit is given by conservation of angular momentum.

$$C_{\theta 3} = C_{\theta 4} r_4 / r_3 \quad (10-74)$$

Then a mass balance at the nozzle row exit yields all other flow data. The nozzle exit flow angle is estimated by the sine rule, neglecting the radius ratio correction described in chapter 9, i.e.,

$$o/s_3 = \sin \alpha_3 \quad (10-75)$$

If the nozzle exit velocity is supersonic, the nozzle throat width is given by conservation of mass between the choked throat passage and the discharge station.

$$o/s_3 = \rho_3 C_{m3} / (\rho_* a_*) \quad (10-76)$$

Hence, the nozzle throat width can be calculated from the nozzle exit radius and the number of blades. The nozzle inlet flow angle is somewhat arbitrary, but it will directly influence the volute sizing described subsequently in this chapter. It is convenient to determine this parameter indirectly by specifying the blade camber angle. The nozzle camber angle is always quite small. Hence, it has minimal effect on the nozzle sizing process. Indeed, the camber angle is really used to fine-tune the volute sizing. The following design specifications for the nozzle row have been found effective for implementing this nozzle sizing strategy.

- The ratio of the nozzle exit radius-to rotor inlet radius r_3/r_4
- The nozzle camber angle, θ
- The normalized location of the point of maximum camber, a/c
- The inlet blade thickness-to-chord ratio, t_2/c
- The exit blade thickness-to-chord ratio, t_3/c
- The maximum blade thickness-to-chord ratio, t_{\max}/c
- The normalized location of the point of maximum thickness, d/c
- The exit pitch-to-chord ratio, s_3/c
- The number of nozzle blades, N_N

The nozzle row sizing requires determining the setting angle, γ_3 , which yields the throat width required by Eq. (10-75) or (10-76). Starting with an initial guess for the setting angle, the two-blade cascade is constructed to determine its throat width, o_c . An iterative process is used to achieve convergence with the required throat width within an acceptable tolerance. Prior to convergence, the result obtained supplies either a maximum or a minimum value of γ_3 to limit the range

of valid future choices. These limits are saved as soon as they are available. An improved estimate of the setting angle for the next iteration is obtained from

$$\sin \gamma_3 \rightarrow \sin \gamma_3(o/o_c) \quad (10-77)$$

If either of the relevant limiting value of γ_3 exists, the new value is restricted to be between the current value and the average of the current and limiting values. The iteration process is required to satisfy the following constraints.

$$\gamma_3 \geq 5^\circ \quad (10-78)$$

$$1.1 \leq r_2/r_3 \leq 1.7 \quad (10-79)$$

Eqs. (10-70) through (10-72) with $x = y = 0$ yield r_2 for the current value of γ_3 . Clearly, some choices of the nozzle row design specifications will preclude satisfying all of these constraints. Also, some choices of the N_N will not produce an interior throat, such that $o_c = s_3$ will be obtained. When a valid cascade yielding the desired throat width cannot be obtained, the process terminates with an appropriate error message. The designer must then modify the nozzle design specifications until an acceptable result is obtained.

When an acceptable cascade matching the downstream rotor is achieved, the nozzle inlet conditions can be computed. The blade setting angle and blade camberline angle at station 2 are given by

$$r_2 \cos \gamma_2 = r_3 \cos \gamma_3 \quad (10-80)$$

$$\beta_2 = \gamma_2 - \chi_2 \quad (10-81)$$

It is prudent to check for unacceptable blade inlet angles and excessive blade metal blockage at the nozzle row inlet and exit at this point. A reasonable limit for the blade inlet angle is $\beta_2 \geq 5^\circ$. Blockage factors can be calculated analogous with Eq. (10-19) for rotors. Unacceptable values of these parameters should cause termination of the design process with an appropriate error message to prompt corrective action by the designer. Otherwise, the nozzle inlet flow angle is selected to achieve the optimum inlet angle given by Eqs. (9-35) and (9-36). The total thermodynamic conditions at the nozzle inlet are assumed to be identical to the stage inlet values, i.e., volute losses are neglected. Then, a mass balance at station 2 yields all other inlet flow parameters to complete the nozzle row design.

10.11 Evaluating the Nozzle Design

Evaluation of the preliminary design of the nozzle row is primarily a matter of assessing the flow parameters and blade geometry. Mach numbers, blade angles and flow angles require particular attention, both from the point of

view of performance expectations and practicality of manufacturing. Excessive blade metal blockage at the inlet and exit should be avoided. The location of the point of maximum camber for cambered airfoils should be selected to produce a smooth variation of the camberline angle from inlet to discharge. In most cases, this will require that $a/c \geq 0.5$ be used. Polar angle overlap of adjacent blades should always be required. The fractional polar angle overlap is given by

$$R_{OL} = N_N(\gamma_2 - \gamma_3)/360 \quad (10-82)$$

A sufficient number of blades should be used to maintain reasonable blade loading. The simple blade-loading diagram of figure 9-5 can be used for this purpose. Adjusting Eq. (9-38) to estimate of the maximum blade-to-blade velocity difference yields

$$(\Delta C)_{\max} = 4\pi(r_3 C_{\theta 3} - r_2 C_{\theta 2})/(cN_N) \quad (10-83)$$

A reasonable blade-loading limit for the nozzle row can be expressed as

$$2(\Delta C)_{\max}/(C_2 + C_3) \leq 1 \quad (10-84)$$

The vaneless passage between the nozzle row and rotor inlet is known to influence aerodynamic performance. Watanabe et al. [99] recommend a minimum vaneless passage radius ratio given by

$$r_3/r_4 = 1 + 2b_4 \sin \alpha_4 / r_4 \quad (10-85)$$

Mechanical integrity also can affect this choice due to interference of nozzle blade wakes with the downstream rotor.

10.12 Initial Estimates of the Nozzle Design Specifications

Similar to the rotor sizing procedure, initial or default values are supplied for all design specifications. This allows a candidate nozzle row design to be attempted as soon as successful rotor design exists. The designer can revise these default values as necessary to optimize the nozzle row design. Eq. (10-85) is used to estimate the default exit radius specification. Following typical axial-flow turbine design practice, a default value of $s_3/c = 0.75$ is used. Other default values used by this writer are $\theta = 0$, $a/c = 0.5$, $t_2/c = 0.025$, $t_3/c = 0.012$, $t_{\max}/c = 0.06$, and $d/c = 0.4$. The default estimate for the number of blades is based on maintaining a reasonable level of blade loading as expressed by Eq. (10-84). Since the nozzle inlet conditions are unknown at this point, the inlet flow angle is assumed to be equal to the inlet blade angle and the following approximation is used.

$$r_2 C_{m2} \approx r_3 C_{m3} \quad (10-86)$$

These approximations and standard trigonometric identities reduce Eq. (10-84) to

$$\frac{4s_3 \sin(\beta_2 - \alpha_3)}{c \sin \beta_2 [1 + r_3 \sin \alpha_3 / (r_2 \sin \alpha_2)]} \leq 1 \quad (10-87)$$

The lowest number of blades that satisfies the limit of Eq. (10-87) is used as the default value. This requires partial completion of the sizing calculations described previously in this section to the point where β_2 and r_2 are determined. Values that do not yield a valid nozzle sizing are rejected. Also, a practical upper limit of thirty blades is imposed. Similar to the rotor default specifications, these default specifications must be imposed in the proper order, and they must be recomputed when the designer manually modifies any of the nozzle row design specifications.

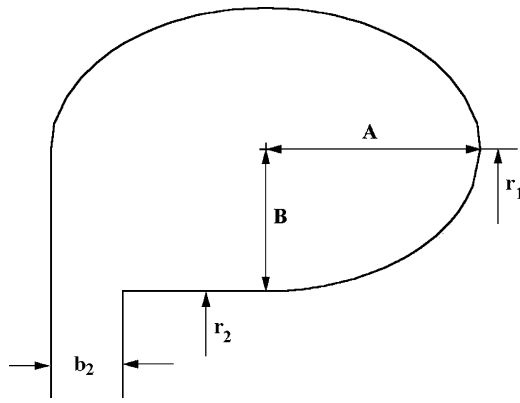
10.13 Volute Preliminary Design

The primary purpose of the volute preliminary design is to obtain estimates of the overall size of the stage in terms of maximum axial and radial dimensions. It is also useful to permit exporting a fairly complete input file for the performance analysis of chapter 9. Volute sizing is a fairly simple process that results in calculating the primary volute passage area, A_1 , and mean radius, r_1 , as previously illustrated in figure 9-3. These parameters are computed to conserve mass and match the angular momentum at the nozzle row inlet, i.e.,

$$\rho_1 C_1 A_1 = \dot{m} \quad (10-88)$$

$$r_1 C_1 = r_2 C_{\theta 2} \quad (10-89)$$

Although no distinction has been made between the volute exit and the nozzle inlet stations, as a practical matter, a vaneless passage will normally exist between them. Since angular momentum is conserved in a vaneless passage, the sizing equations are not affected by this vaneless passage. Hence, this writer's preliminary design program arbitrarily inserts a constant-width vaneless passage with an inlet-to-discharge radius ratio of 1.05. The only real significance of this vaneless passage is to obtain a more realistic estimate of the maximum stage radius required. The maximum stage radius is also affected by the style of cross-sectional area that is used. Figures 10-13 and 10-14 illustrate two volute types using an elliptical cross section. The external volute lies completely above the exit radius of the volute, whereas the internal volute is designed to yield volute inlet and exit radii that are identical. The external volute would be preferred since the change in radius will accelerate the flow to a higher discharge

**FIGURE 10-13. An External Elliptical Volute**

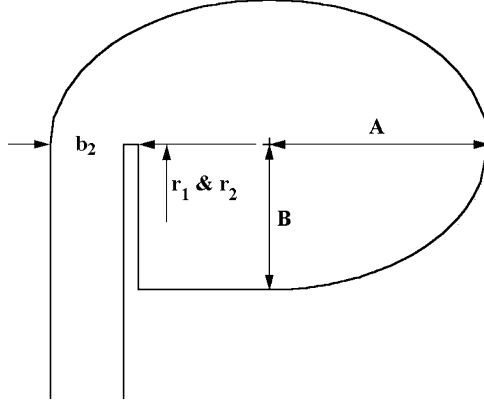
tangential velocity for the same inlet velocity. But the internal volute may offer the advantage of a lower maximum stage radius. The passage area and the mean radius of the external elliptical volute are

$$A_i = \left(\frac{3}{4} \pi + 1 \right) AB \quad (10-90)$$

$$r_1 = r_2 + B \quad (10-91)$$

The external volute is sized by an iterative procedure. Initially, assume $r_1 = r_2$. Then, Eq. (10-89) yields

$$C_1 = C_{\theta 2} r_2 / r_1 \quad (10-92)$$

**FIGURE 10-14. An Internal Elliptical Volute**

The static enthalpy is given by

$$h_1 = H_1 - \frac{1}{2} C_1^2 \quad (10-93)$$

The equation of state yields the static density as a function of h_1 and s_1 . Hence, Eq. (10-88) can be solved for A_1 . If the volute aspect ratio, $AR = A/B$ is specified, Eq. (10-90) can be solved for A and B . Then Eq. (10-91) yields a new estimate for r_1 . This process is repeated until values of r_1 on successive iterations agree within an acceptable tolerance. The sizing procedure for the internal volute is simpler since $r_1 = r_2$. Neglecting the wall thickness within the volute, the passage area for the internal volute is

$$A_1 = \left(\frac{3}{4} \pi + 1 \right) AB - B b_2 \quad (10-94)$$

The internal volute sizing follows the same process as for the external volute, except no iteration procedure is required. This writer's preliminary design system also offers the options of internal and external volutes with rectangular cross section. Volute sizing is handled in a similar fashion except that alternate expressions for the volute area as a function of A and B are required.

Hence, the design specifications used for the volute sizing are

Specify an internal or external volute.

Specify elliptical or rectangular cross section.

Specify the aspect ratio (limits of $0.75 \leq AR \leq 1.5$ are recommended).

The initial default specifications used are an external elliptical volute with $AR = 1$ (i.e., a circular cross section). As noted previously, the nozzle row inlet flow angle is somewhat arbitrary through the specification of the nozzle blade camber angle. That also provides a mechanism to modify the volute sizing by changing the nozzle inlet tangential velocity.

When the volute sizing is completed, the stage maximum radius and the stage axial length measured from the rotor inlet are given by

$$r_{\max} = r_1 + B \quad (10-95)$$

$$\Delta z = \Delta z_R - b_3 + 2A \quad (10-96)$$

If an exhaust diffuser is also included, the stage axial length will increase by the diffuser axial length. Diffuser sizing is discussed in the next section of this chapter.

10.14 Exhaust Diffuser Sizing

An exhaust diffuser can be included in the stage preliminary design as a performance enhancement. The preliminary design strategy is substantially more complicated if the influence of the diffuser is included in the basic stage

performance specifications. That is an unnecessary complication since the diffuser performance analysis described in chapter 9 can be used directly to forecast the performance improvement to be expected from the diffuser.

The diffuser divergence angle, $2\theta_c$, of Eq. (9-89) is the most significant parameter governing diffuser performance. As noted in chapter 9, the diffuser static pressure recovery coefficient deteriorates rapidly when $2\theta_c > 11^\circ$. It is also true that diffusers are most effective when operating close to this diffusion limit. Hence, a reasonable preliminary design strategy is to design for $2\theta_c = 11^\circ$. Eq. (9-89) can be written in terms of the present nomenclature to yield

$$2\theta_c = 2 \tan^{-1} [b_5 (A_6 / A_5 - 1) / (2L)] \quad (10-97)$$

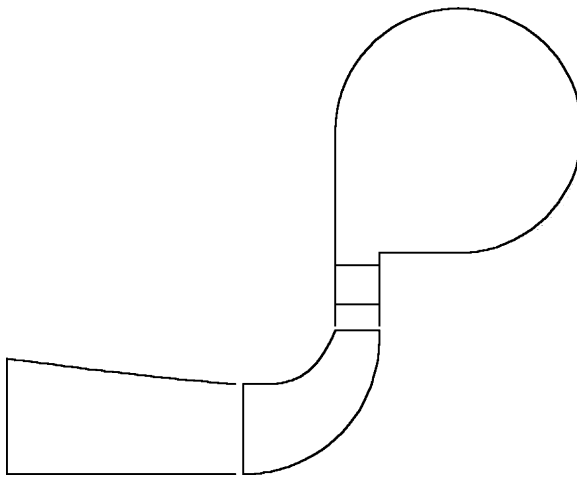
The precise definition of the diffuser flow path length, L , is given by Eq. (9-88). For the purpose of preliminary design it is sufficient to consider L to be the diffuser axial length. It is convenient to allow for two alternate design specifications for the diffuser, either the area ratio, A_6/A_5 , or the dimensionless diffuser length, L/b_5 . Either specification can be used to solve for the unspecified parameter using Eq. (10-97) with $2\theta_c = 11^\circ$. Then the diffuser performance analysis of chapter 9 can be applied directly to predict the diffuser static pressure recovery coefficient. This will result in an increase in the total-to-static pressure ratio and efficiency and a reduction in the corresponding total-to-total parameters. These adjusted performance parameters can be listed for the designer's review. The designer can choose to revise the stage design specifications to adjust for the influence of the diffuser. However, that is usually not really necessary for the purpose of a preliminary stage design. After the diffuser has been sized, the estimate of the overall stage axial length can be revised to include the diffuser axial length.

10.15 A Typical Preliminary Design Example

The preliminary design system is best illustrated by a typical example. The basic stage performance specifications used for this example are given in Table 10-1. The default design specifications were used for the rotor, nozzle row and volute

Table 10-1. Stage Design Specifications

Parameter	Specification
Fluid	Air
Specific speed	0.7
Efficiency	0.8476 (default)
Velocity ratio	0.6863 (default)
Pressure ratio	1.52
Mass flow rate	1.05 lb _m /sec
Inlet total pressure	14.68 psia
Inlet total temperature	518.7° R

**FIGURE 10-15. Stage Cross Section**

except for the nozzle blade camber angle, which was specified as 18° . An exhaust diffuser with an area ratio of 1.5 was included.

Figure 10-15 shows the stage cross-section that was obtained from the preliminary design procedure. This figure duplicates the monitor screen plot supplied by this writer's preliminary design system during the design process. Results from the rotor design for this example were shown previously in this chapter in figures 10-6 through 10-9. An input file for this preliminary stage design was exported to conduct an aerodynamic performance analysis as described in chapter 9. Table 10-2 compares the design and predicted total-to-static (T-S) and total-to-total (T-T) performance. The design values differ from those shown in Table 10-1 due to the influence of the exhaust diffuser. The performance analysis indicates that the actual performance of the stage preliminary design is quite close to the intended performance.

The stage operating conditions specified for this design example were selected from the peak efficiency point of the NASA turbine at design speed as reported by Whitney et al. [74]. Experimental performance of that turbine is shown in figures 9-18 and 9-19. This provides the opportunity to compare the basic stage preliminary design to an actual design for which the experimental performance is known. The NASA turbine is slightly different since it did not have an exhaust diffuser. But the present preliminary design procedure does

Table 10-2. Evaluation of the Preliminary Design

Parameter	Design	Prediction
T-S Pressure ratio	1.4970	1.5237
T-S Efficiency	0.8772	0.8682
T-T Pressure ratio	1.4790	1.5040
T-T Efficiency	0.9039	0.8943

Table 10-3. Comparison with the NASA Turbine

Parameter	Design	NASA
Rotor inlet radius	2.97 in.	3.01 in.
Rotor inlet passage width	0.733 in.	0.720 in.
Rotor inlet flow angle	17.8°	17.8°

not account for the diffuser performance in the basic component sizing. Hence it is meaningful to compare this design example with the successful turbine stage which it seeks to simulate. Table 10-3 shows that the key parameters from the rotor tip sizing are quite close to those actually used for the NASA turbine. That provides some confirmation that the procedures outlined in this chapter do represent good design practice. It is significant to note that this was accomplished using the recommended default values for nearly all of the design specifications.

10.16 A Computerized Preliminary Design System

The procedures described in this chapter are easily implemented in an interactive computerized design system. There are several useful features that can easily be incorporated to significantly improve the effectiveness of the system. Some of these features have been mentioned previously in this chapter but are probably worth repeating in the context of a complete computerized preliminary design system. Recommended features include the following.

- The capability to export an input file for the performance analysis of chapter 9 is really essential. The performance analysis should be used regularly during the design process to evaluate the preliminary designs with regard to actual performance potential. With proper interfacing, that evaluation is a rather trivial step.
- Use of error trapping procedures to permit automatic processing of available design specifications provides substantial productivity benefits. It is convenient to provide component sizing results as they are obtained. If the sizing of a component terminates due to an error, the designer can view the appropriate output block to determine what design specifications caused the termination.
- Similarly, provision to start the process of sizing components using the default initial specifications suggested previously in this chapter also benefits productivity. It is always faster to improve a candidate design than to supply all of the component design specifications for each application.
- Tabular and graphical presentations of results should be generated as part of the design process for each stage component. The designer should be able to conveniently view these results on the monitor screen for rapid evaluation. Some or all of these results can subsequently be combined to supply printed output, if the designer requests them.

- The capability to export input files for the detailed aerodynamic design systems described in chapter 11 also benefits productivity. The component preliminary design procedures of this chapter provide a good basis for supplying an initial configuration to be refined by the detailed design procedures.
- Provision to export input files for internal flow analysis is also useful. Sometimes a blade-to-blade flow analysis or a quasi-three-dimensional flow analysis is needed to evaluate the component designs during the detailed design phase. The preliminary design system can export complete input files, including operating conditions and equation of state data not available in the detailed design applications. These same input files can subsequently be updated by the component detailed design applications to support the detailed design process as well.

Chapter 11

DETAILED AERODYNAMIC DESIGN OF RADIAL-INFLOW TURBINE COMPONENTS

The nozzle-blade preliminary aerodynamic design procedure described in chapter 10 is easily modified to provide a sound basis for the detailed aerodynamic design also. That approach is almost always sufficient to achieve design objectives for both aerodynamic performance and mechanical integrity. Impeller detailed design is conveniently accomplished using procedures essentially identical to those commonly used for centrifugal compressors. Indeed, this writer uses the detailed design system described in Aungier [1] for both types of impellers. The only modification required to extend the centrifugal compressor impeller detailed design procedure to radial-inflow turbines was to include provision to reverse the geometry exported to aerodynamic analysis, applications such that the flow direction is reversed. Hence, the inlet becomes the discharge, and inversely, when the detailed geometry is reversed. This was simply a matter of convenience due to the fact that a sophisticated impeller gaspath design system already existed. Investigators developing this system specifically for radial-inflow turbines would normally avoid the need to reverse the geometry. Hence, the descriptions provided in this chapter address this problem in the turbine orientation. But it is appropriate to acknowledge the fact that the present description is really no different than the impeller gaspath design system described in [1].

The detailed design process really addresses design details that are largely ignored by the performance analysis of chapter 9 and the preliminary design system of chapter 10. Indeed, a fundamental assumption of the performance analysis is that the components have been designed consistent with good design practice. The limited geometry specified for the performance analysis can be produced by a wide variety of detailed component designs. Those specifications are by no means sufficient to ensure that the components will perform as predicted. That issue is addressed in the detailed design process by evaluating the internal flow produced by the design. This requires use of internal flow analysis procedures describe in subsequent chapters of this book. These include blade-to-blade flow analysis (chapter 13), quasi-three-dimensional flow analysis (chapter 14) and boundary layer analysis (chapters 13 and 14). In the present context, it is not necessary to be familiar with the theory behind the internal flow analyses of chapters 13 and 14. The objective of the detailed design process is to avoid excessive diffusion and flow separation along the blade surfaces and

end-wall contours of the components. This objective is less challenging for the accelerating flow in turbines as compared to the diffusing flow in compressors.

AQ: Au.
Please check
the sentence.

But it does remain a necessary step to achieving good aerodynamic performance.

NOMENCLATURE

- A = passage area
- a = location of point of maximum camber along the chord
- B = Bezier polynomial coefficient
- b = passage width
- c = blade chord length
- h = distance between points on adjacent blade surfaces
- i = point number
- L = length of a line segment
- m = meridional coordinate
- N = number of points on a curve
- n = distance along a quasi-normal
- \vec{P} = vector locating Bezier reference points
- R_c = radius of curvature
- r = radius
- \vec{S} = a vector tangent to blade camberline in a meridional surface
- \vec{T} = a vector normal to blade mean surface
- t_b = blade thickness
- U = dimensionless parameter for curve generation
- X = general Cartesian coordinate for curve definition
- x = Cartesian coordinate = $r\sin\theta$
- Y = general Cartesian coordinate for curve definition
- y = Cartesian coordinate = $r\cos\theta$
- z = axial coordinate
- β = blade camberline angle with respect to tangent
- δ = angle of rotation of coordinates
- η = rotated Cartesian coordinate
- θ = polar angle; also blade camber angle
- ξ = dimensionless distance
- ϕ = meridional surface slope angle with respect to z
- χ = rotated Cartesian coordinate
- τ = quasi-normal angle with radial direction

Subscripts

- B = a blade parameter
- c = parameter on the blade camberline
- h = parameter on the hub contour
- s = parameter on the shroud contour
- t = a throat parameter

1 = component inlet parameter
 2 = component discharge parameter

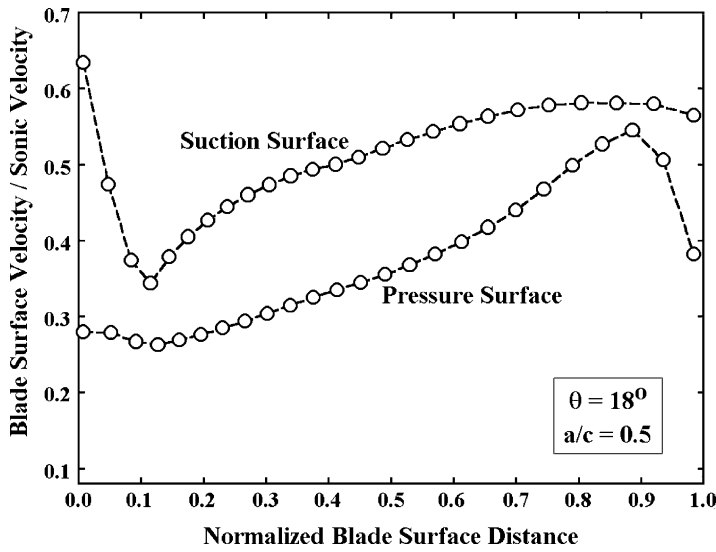
Superscript

' = first derivative

11.1 Nozzle Blade Detailed Design

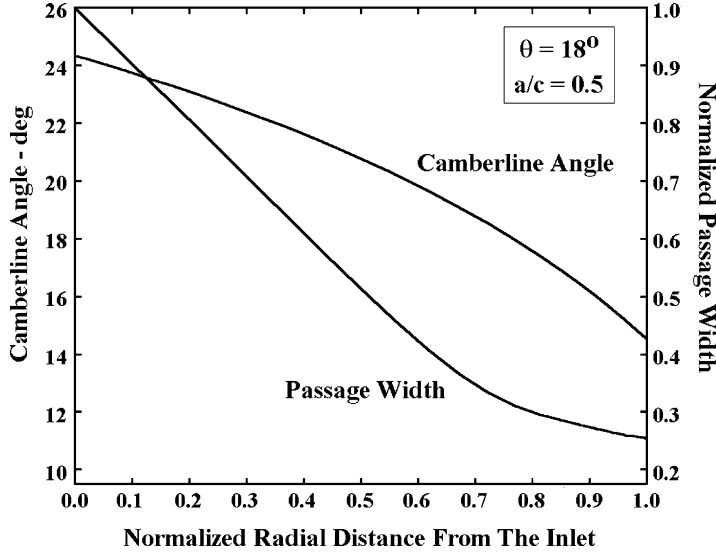
The nozzle row construction used for the preliminary design is easily adapted to the detailed design process also. The methodology is identical to that previously described in chapter 10, but all design specifications are supplied directly rather than evaluated indirectly from the stage design specifications. Specifically, the detailed design is required to match to a known inlet flow angle and must produce a known gauging angle at a known discharge radius. All other design specifications for the nozzle row are identical to those used in chapter 10. The nozzle inlet radius may also be known at this point. That case can easily be handled by adjusting the blade discharge pitch-to-chord ratio for any specified number of blades. For added generality, it is useful to leave the inlet radius unspecified unless design constraints require a specific value. By reviewing the process used in chapter 10, it is easily seen that the same procedures can be applied to this alternate set of design specifications. Indeed, the preliminary design system could be used for this purpose. But that would usually require generating a fictitious stage design that yields the proper inlet and discharge specifications. When the preliminary design system exists, it is a trivial process to adapt it to handle the detailed aerodynamic design problem directly. That also provides the opportunity to add interfacing capabilities for internal flow analysis and for supplying geometry for mechanical analysis, drafting and manufacturing. The simplest way to start the process is to export an input file for the nozzle detailed design application from the preliminary design system to provide an initial design.

The nozzle preliminary design from the stage preliminary design example of chapter 10 will be used to illustrate the process. Figure 11-1 shows a blade-loading diagram for the preliminary nozzle design predicted by the two-dimensional blade-to-blade potential-flow flow analysis described in chapter 13. Clearly, the nozzle incidence angle is not an optimum as was intended. This is evidenced by the significant difference in the suction and pressure surface velocities near the leading edge. In chapter 13 it will be shown that the accuracy of the blade loading at the leading and trailing edges is always suspect, particularly for blades having large differences in blade surface slopes on the two sides of the blade such as these airfoil shapes. The abrupt drop in the pressure surface velocity near the trailing edge can be ignored. It simply indicates that the trailing edge separation occurs on the pressure side of the blade. The blade-to-blade analysis closes the loading diagram immediately outside of the blade passage as a means of estimating the discharge flow angle. In this case the predicted discharge flow angle agreed with the intended value (the gauging angle) within 0.8°. When evaluating the design, the suction surface

**FIGURE 11-1. The Preliminary Design Blade Loading**

velocity distribution is the most critical concern. Clearly that distribution is quite reasonable and free of any undesirable diffusion.

Blade loading is primarily a function of the blade camberline angle and passage area distributions and the flow incidence angle. Figure 11-2 shows the

**FIGURE 11-2. The Preliminary Design Distributions**

relevant distributions for the preliminary nozzle design. Variations of both parameters are smooth and well behaved. The gradient of the blade camberline angle distribution near the trailing edge is rather high. A low gradient would be preferred to provide better flow guidance near the trailing edge. The large difference in the leading edge surface velocities is indicative of a poor incidence match. Despite the uncertainty of the blade loading prediction at the leading edge, it is clear that a smooth entry of the flow into the blade passage is not achieved. This indicates that the incidence angle is higher than would be preferred for the design operating condition. For a typical stage consisting of an inlet volute followed by a nozzle row, the nozzle blade will operate at nearly the same incidence angle for off-design operating conditions also. Hence it is usually good practice to design for good nozzle incidence angle matching. Incidence angle matching can be adjusted by modifying either the design flow angle or the inlet blade angle.

For the purpose of illustration, the preliminary nozzle design was modified to reduce the incidence angle and to reduce the gradient in the blade angle distribution near the trailing edge. A reduction in the blade camber angle was used to reduce the incidence angle. Simply shifting the point of maximum camber closer to the trailing edge reduced the blade angle gradient at the trailing edge. Figure 11-3 shows the modified blade angle and passage width distributions obtained by these two simple revisions. Figure 11-4 shows the blade loading for the modified design. The revised incidence angle match clearly results in a smoother entry of the flow into the blade passage. The adjustment to the gradient of camberline angle has resulted in higher suction surface velocity levels and some deceleration on the suction surface near the trailing edge.

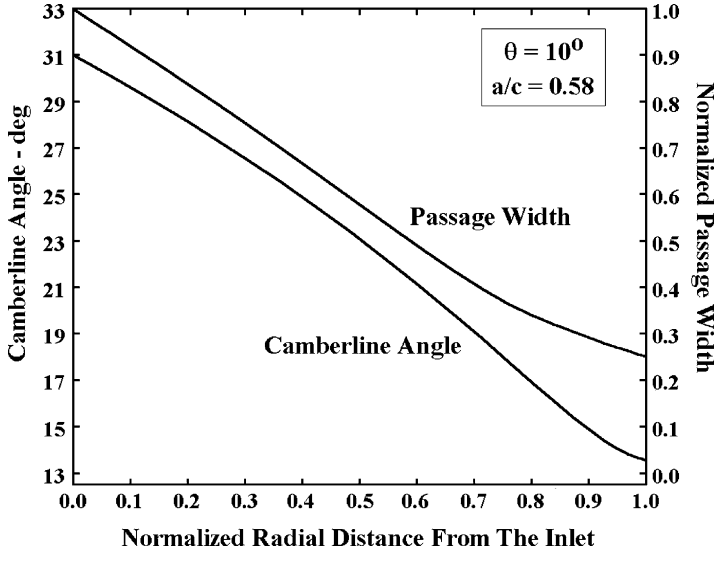
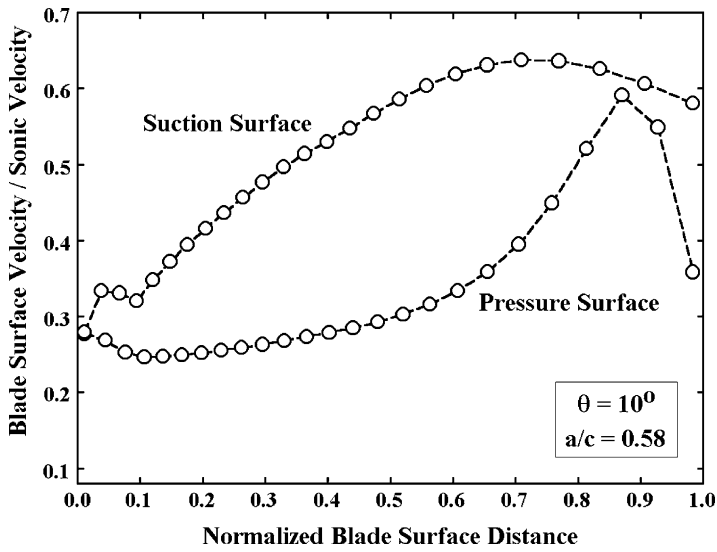


FIGURE 11-3. The Modified Design Distributions

**FIGURE 11-4. The Modified Design Blade Loading**

Hence, that is probably not a beneficial modification. But it does show that the general nozzle blade airfoil developed in chapter 10 offers considerable flexibility for modifying the internal flow in the nozzle row. If greater flexibility is needed, the general gaspath design system described subsequently in this chapter can be used. While that system is primarily intended for impeller design, it has also been successfully applied to nozzle blade design. However, the standard airfoil family is usually quite adequate and is a much easier approach for detailed nozzle row design.

Designers familiar with this style of airfoil from axial-flow turbomachinery should note that the influence of design modifications is often quite different for radial-inflow applications. For example, a reduction in the gradient of the camberline angle near the trailing edge for an axial-flow blade is achieved by shifting the point of maximum camber closer to the leading edge. In the previous example, the opposite trend is observed. The reason for the difference in behavior is the fact that the blade chord setting angle varies with the radius in the radial-inflow application. This airfoil family is convenient for the flexibility it offers, but design practices appropriate for axial-flow turbomachinery do not carry over to this application.

11.2 A General Approach to Gaspath Detailed Design

The general gaspath design system presented in Aungier [1] is well suited to radial-inflow turbine detailed aerodynamic design. That system develops the end-wall contours and blades using a variety of curve forms well suited to this application. Blades are defined by distributions of the polar angle, θ

(or blade angle, β) and the blade thickness, t_b , along the camberline. Three basic types of blade geometry can be considered.

- Two-dimensional, axial element blades: $\theta_c = \theta_c(r)$, $t_b = t_b(r)$
- Two-dimensional radial element blades: $\theta_c = \theta_c(z)$, $t_b = t_b(z)$
- Three-dimensional straight-line element blades: $\theta_c = \theta_c(\xi)$, $t_b = t_b(\xi)$ for both the hub and shroud contours, where $\xi = (m - m_2)/(m - m_1)$, is the dimensionless meridional distance along the contours from the trailing edge to the leading edge. These blades are constructed by connecting the blade surfaces on the two end-wall contours with straight-line elements.

Axial element blades are appropriate for nozzle blade design. Impellers often employ radial element blades to eliminate centrifugal blade bending stresses. The more general straight-line element blades generally offer superior impeller aerodynamic performance potential when acceptable mechanical integrity can be achieved.

Considering the blade camberline blade angle distributions on the appropriate defining surface provides a convenient camberline definition for the different blade types. For the axial-element blade, the defining surface is a surface of constant z . The camberline angle in that surface is defined by

$$\cot \beta_c = \frac{r \partial \theta}{\partial r} \quad (11-1)$$

Hence, the camberline can be defined by $\beta_c = \beta_c(r)$. It is often easier to develop a curve defining this distribution rather than one for $\theta_c = \theta_c(r)$. Similarly, for the radial-element blade, the defining surface is a surface of constant r . The camberline angle in that surface is defined by

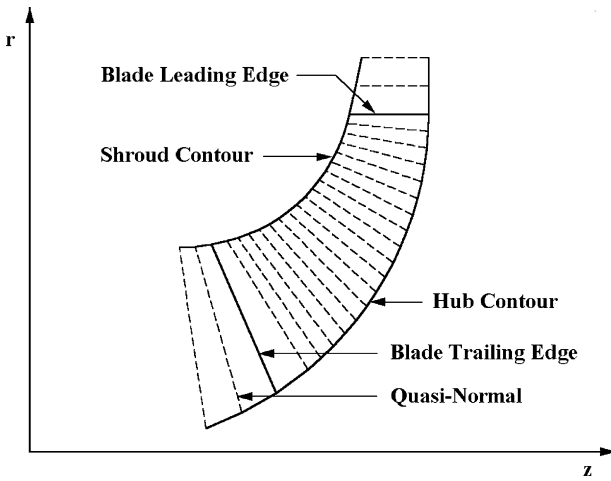
$$\cot \beta_c = \frac{r \partial \theta}{\partial z} \quad (11-2)$$

Hence, the camberline can be defined by $\beta_c = \beta_c(z)$ for a specified value of r . For the straight-line element blade, the defining surface is one of the end-wall contours rotated to form an axisymmetric surface. The camberline angle in that surface is defined by

$$\cot \beta_c = \frac{r \partial \theta}{\partial m} \quad (11-3)$$

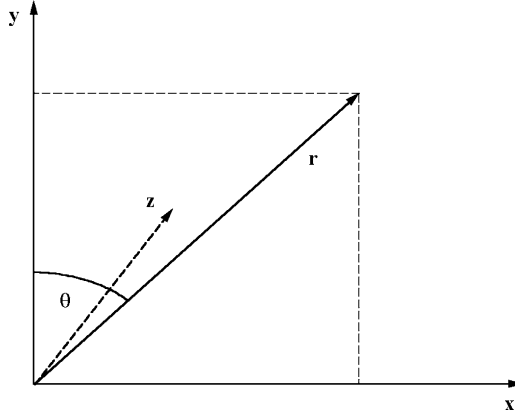
Hence, the camberline can be defined by $\beta_c = \beta_c(\xi)$.

Figure 11-5 illustrates a meridional view of the gaspath design problem for a radial-inflow turbine impeller. The hub and shroud contours are defined by specific curves defining $r = r(z)$. Then a series of quasi-normals connecting the two contours are defined. Quasi-normals are straight lines constructed to be approximately normal to the two end-wall contours. The blade leading and trailing edges are defined by two specific quasi-normals. When straight-line element blades are used, these quasi-normals define the corresponding points on the two end-wall contour camberlines that are connected by straight lines to

**FIGURE 11-5. General Gaspath Design**

form the complete blade camberline. Figure 11-6 shows the basic Cartesian and cylindrical coordinate systems used in the gaspath design process. The z -axis is common to both coordinate systems and corresponds to the axial direction. The meridional coordinate, m , is also used, where m is the distance along an end-wall contour. The origin is arbitrary and can be chosen for convenience, typically at the blade leading or trailing edge location.

The basic gaspath design strategy reduces the process to defining the end-wall contours, camberline angle distributions and blade thickness distributions. The designer's task is to develop a series of curves to define these contours and distributions. These are used to construct the complete gaspath. This involves

**FIGURE 11-6. Basic Coordinate Systems**

some very complex geometrical calculations, but computers can easily accomplish them, leaving the designer free to concentrate on the important issues of aerodynamic performance, mechanical integrity and manufacturing constraints. Before describing the gaspath construction process, a number of curve forms particularly useful for gaspath design will be described.

11.3 Useful Curve Forms

The Bezier polynomial curve [100, 101] is a very general method for generating smooth curves that are well suited to the gaspath design process. This curve form is generated from a series of reference points. If $n + 1$ is the number of reference points numbered 0 to n , the vector location of the k th reference point in a general Cartesian coordinate system (X, Y) is given by

$$\vec{P}_k = X_k \vec{i} + Y_k \vec{j} \quad (11-4)$$

The Bezier polynomial curve is generated as a function of a parameter, U , which varies from 0 to 1 along the length of the curve. The vector location of any point on the curve is given by

$$\vec{R}(U) = \sum_{k=0}^n \vec{P}_k B_k^n(U) \quad (11-5)$$

The Bezier polynomial is defined by

$$B_k^n = \binom{n}{k} U^k (1-U)^{(n-k)} \quad (11-6)$$

$$\binom{n}{k} = \frac{n(n-1) \dots (n-k+1)}{k!} \quad (11-7)$$

Figure 11-7 illustrates a typical Bezier polynomial curve and the reference points used to generate it. The slope and radius of curvature of the curve can be computed by differentiating the X and Y components of Eq. (11-5).

$$\frac{dY}{dX} = \frac{dY/dU}{dX/dU} \quad (11-8)$$

$$\frac{1}{R_c} = \frac{\frac{dX}{dU} \frac{d^2Y}{dU^2} - \frac{dY}{dU} \frac{d^2X}{dU^2}}{\left[\left(\frac{dX}{dU} \right)^2 + \left(\frac{dY}{dU} \right)^2 \right]^{1.5}} \quad (11-9)$$

Special definitions for the derivatives of the Bezier polynomials are required.

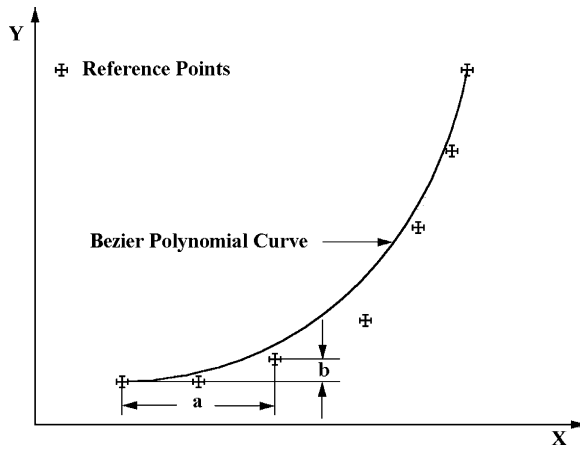


FIGURE 11-7. The Bezier Polynomial Curve

They are

$$\frac{dB_k^n}{dU} = n \left[B_{k-1}^{n-1}(U) - B_k^{n-1}(U) \right] \quad (11-10)$$

$$\frac{d^2 B_k^n(U)}{dU^2} = n(n-1) \left[B_{k-2}^{n-2}(U) - 2B_{k-1}^{n-2}(U) + B_k^{n-2}(U) \right] \quad (11-11)$$

For any value of k , the following special relations apply.

$$B_0^k(U) = B_{-1}^k(U) = B_{k-2}^k(U) = B_{k-3}^k(U) = 0 \quad (11-12)$$

Forest [101] provides a procedure for setting the radius of curvature at the end points on the curve using the parameters, a and b , illustrated in figure 11-7.

$$R_c = \frac{n}{n-1} \frac{a^2}{b} \quad (11-13)$$

Several features of the Bezier polynomial curve make it particularly useful for the gas path design application.

- The curve passes through the end reference points (but usually not through any other reference points).
- The end-point slope is identical to the slope of lines connecting the end reference point and the adjacent reference point.
- The end-point curvature depends only on the end reference point and the two adjacent reference points.
- The interior points influence the curve shape. In general, moving a reference point will cause the curve to move in the same direction, but only by about one-third as much.
- The curve is always smooth and continuous.

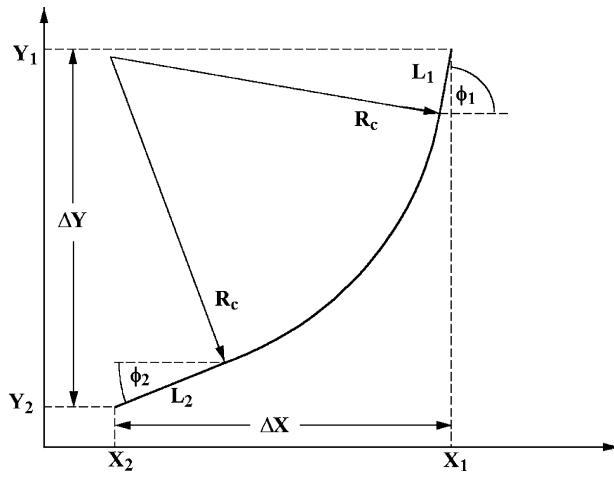
- Points can be distributed along the curve by selecting a distribution of discrete values of U . This allows defining the quasi-normal end points for the end-wall contours and a distribution of points to be used for interpolation for blade angle or blade thickness curves.

The major disadvantage of the Bezier polynomial curve is the need for a fairly sophisticated interactive graphics procedure to use it effectively. This writer's design system displays the reference points on the monitor screen along with the curve defined by them (similar to the display shown in figure 11-7). The designer can add, delete or reposition reference points by keyboard entry or a drag-and-drop technique to fine-tune the curve shape. End-point slopes and curvatures can also be set, assuming a sufficient number of reference points are used. At least seven reference points should be used so that at least one reference point is free to shape the curve without affecting the end-point slopes and curvatures. By providing automatic resetting of end-point slopes and curvatures as an option, all of the reference points can be used to shape the curve while maintaining the desired end-point constraints. Another disadvantage of the Bezier polynomial curve is that it is not easily initialized by the preliminary design system. In chapter 10, initial impeller end-wall contours and blade camberline were developed as initial estimates for export to the detailed design system. This writer's gaspath design system provides the capability to approximate any initial curve with a Bezier polynomial curve. This is accomplished by distributing $(n + 1)$ points along the curve (equal to the number of reference points to be used). Then Eq. (11-5) is used to generate a series of $(n + 1)$ equations with $(n + 1)$ unknowns for both X_k and Y_k . These equations can be solved by simple matrix inversion to define the reference points that approximate the initial curve. Then the Bezier polynomial curve can be used for detailed design while still taking advantage of the initial estimates from the preliminary design system.

Another useful curve form for end-wall contour design is to employ a circular-arc with the largest radius of curvature allowed by the impeller axial and radial dimensions. Linear extensions are added to one or both ends of the circular-arc to complete the contour. This curve form was used in chapter 10 to define the impeller hub contour. Figure 11-8 illustrates the construction of this curve. The coordinates, (X, Y) , and the angle of the contour slope, ϕ , are defined for each end-point. It is useful to include specification of a minimum linear segment length, L , to be used at each end of the contour. Normally these lengths will be zero unless required by manufacturing constraints. Modern computer-aided manufacturing techniques usually no longer require these linear segments. But provision to include them adds no complication to the construction, so it is worth including it for generality. Then, the maximum circular-arc radius of curvature, R_c , that can be used and the length and location of any linear segment required must be computed. It is easily shown that

$$\Delta X = R_c(\sin \phi_1 - \sin \phi_2) + L_1 \cos \phi_1 + L_2 \cos \phi_2 \quad (11-14)$$

$$\Delta Y = R_c(\cos \phi_2 - \cos \phi_1) + L_1 \sin \phi_1 + L_2 \sin \phi_2 \quad (11-15)$$

**FIGURE 11-8. The Circular-Arc Curve**

Simple elimination of R_c using Eqs. (11-14) and (11-15) yields a necessary and sufficient condition to construct the circular-arc curve form.

$$L_1 - L_2 = \frac{\Delta Y(\sin \phi_1 - \sin \phi_2) - \Delta X(\cos \phi_2 - \cos \phi_1)}{1 - \sin \phi_1 \sin \phi_2 - \cos \phi_1 \cos \phi_2} \quad (11-16)$$

This may require that one end-point linear segment length be increased to satisfy Eq. (11-16). Then R_c is calculated from either Eq. (11-14) or (11-15). The coordinates of the center of the circular-arc are given by

$$X_0 = X_2 + L_2 \cos \phi_2 - R_c \sin \phi_2 \quad (11-17)$$

$$Y_0 = Y_2 + L_2 \sin \phi_2 + R_c \cos \phi_2 \quad (11-18)$$

Then the circular-arc and any end-point linear segments defining the contour are easily constructed.

Figure 11-9 shows a useful curve form based on the cubic spline fit [102]. The coordinates, (X, Y) , and the slopes, Y' , of the curve end points, along with optional linear segments to be imposed at each end point are specified. The linear segment lengths and slopes are used to compute the end-point coordinates of the spline-fit curve, (X_{i-1}, Y_{i-1}) and (X_{i+1}, Y_{i+1}) . A third point is used to define the spline-fit curve. The coordinates of this point, (X_i, Y_i) , are chosen by the designer to shape the curve. The spline-fit curve passes through the three points and matches the slopes at the two end points. Cubic polynomial curves are used to define the curve between each pair of adjacent points. The two cubic polynomial curves are constrained to achieve matching first and second derivatives at the common point. Walsh et al. [102] develop expressions for the three coefficients that are required to define the spline connected cubic curves.

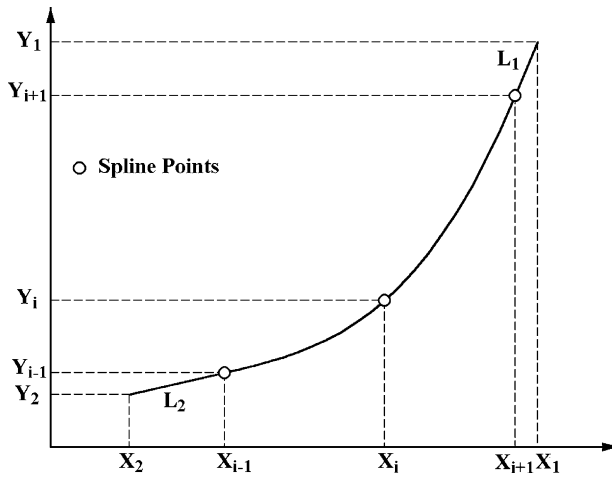


FIGURE 11-9. The Three-Point Cubic Spline Curve

$$M_i = \frac{6(Y_{i+1} - Y_i)}{(X_{i+1} - X_i)(X_{i+1} - X_{i-1})} - \frac{6(Y_i - Y_{i-1})}{(X_i - X_{i-1})(X_{i+1} - X_{i-1})} + \frac{2(Y'_{i-1} - Y'_{i+1})}{X_{i+1} - X_{i-1}} \quad (11-19)$$

$$M_{i-1} = \frac{3(Y_i - Y_{i-1})}{(X_i - X_{i-1})^2} - \frac{3Y'_{i-1}}{X_i - X_{i-1}} - \frac{M_i}{2} \quad (11-20)$$

$$M_{i+1} = \frac{3Y'_{i+1}}{X_{i+1} - X_i} - \frac{3(Y_{i+1} - Y_i)}{(X_{i+1} - X_i)^2} - \frac{M_i}{2} \quad (11-21)$$

These coefficients can be used to compute Y as a function of X by selecting the proper coefficients. If $X_{k-1} \leq X \leq X_k$,

$$Y = \frac{M_{k-1}(X_k - X)^3}{6(X_k - X_{k-1})} + \frac{M_k(X - X_{k-1})^3}{6(X_k - X_{k-1})} + \left[\frac{Y_k}{X_k - X_{k-1}} - \frac{M_k(X_k - X_{k-1})}{6} \right] (X - X_{k-1}) \\ + \left[\frac{Y_{k-1}}{X_k - X_{k-1}} - \frac{M_{k-1}(X_k - X_{k-1})}{6} \right] (X_k - X) \quad (11-22)$$

The three-point cubic spline curve can be useful for end-wall contour definition when attempting to control the passage area at some intermediate location for specified inlet and discharge passage areas. The contour is always smooth and continuous, although not necessarily useful. Indeed, poor choices of the optional spline definition point inevitably yield wild sinusoidal oscillations. Like the Bezier polynomial curve, effective use of this curve form requires an

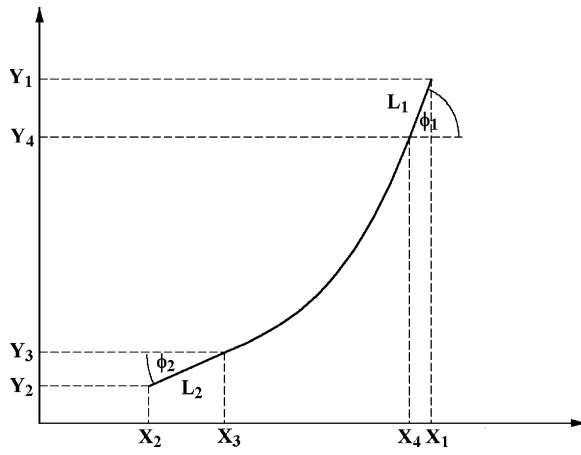


FIGURE 11-10. The Third-Order Polynomial Curve

interactive graphics approach. This writer's gaspath design system displays the three defining points and the curve they produce on the monitor screen (similar to the display in figure 11-9). The arbitrary point is moved by a drag-and-drop procedure and the curve is regenerated, until the designer is satisfied with the results.

Another useful curve form is a simple third-order polynomial curve. This curve can be defined by specifying the coordinates, (X, Y) , and the slope angles, ϕ , of the curve end points, along with option linear segments to be imposed at each end point. The linear segment lengths and slopes are used to compute the end-point coordinates of the polynomial curve, (X_3, Y_3) and (X_4, Y_4) as illustrated in figure 11-10. The third-order polynomial supplies the curve from X_3 to X_4 . It is convenient to employ the dimensionless coordinate, ξ , to define the polynomial curve.

$$\xi = (X - X_3)/(X_4 - X_3) \quad (11-23)$$

Then the curve is defined by

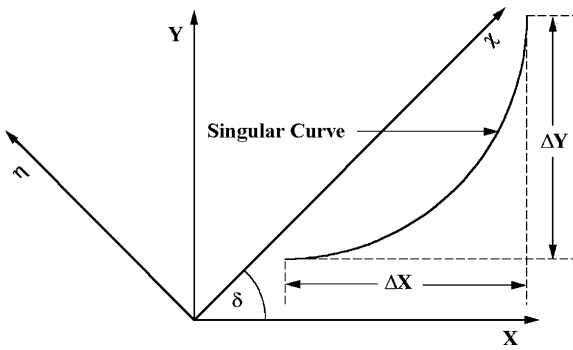
$$Y = A + B\xi + C\xi^2 + D\xi^3 \quad (11-24)$$

The coefficients are defined to match the coordinates and slopes at the end points of the curve. It is easily shown that this yields

$$A = Y_3 \quad (11-25)$$

$$B = (X_4 - X_3)Y'_3 \quad (11-26)$$

$$C = -(X_4 - X_3)(2Y'_3 + Y'_4) \quad (11-27)$$

**FIGURE 11-11. Rotation of Coordinates**

$$D = (X_4 - X_3)(Y'_3 + Y'_4) \quad (11-28)$$

The design of end-wall contours for radial-inflow turbine impellers often involves cases where $\phi=90^\circ$. Hence, the end-point slopes may be undefined, and some of the equations presented for the circular-arc, cubic spline and third-order polynomial curve forms are also undefined. That problem is easily avoided by accomplishing a simple rotation of coordinates before generating the curves. Figure 11-11 illustrates the rotated coordinate system (χ, η) obtained by rotating the (X, Y) coordinate system by the angle, δ , given by

$$\sin \delta = \frac{\Delta Y}{\sqrt{(\Delta X)^2 + (\Delta Y)^2}} \quad (11-29)$$

$$\cos \delta = \frac{\Delta X}{\sqrt{(\Delta X)^2 + (\Delta Y)^2}} \quad (11-30)$$

The curve coordinates and slopes for the two coordinate systems are related by

$$\chi = X \cos \delta + Y \sin \delta \quad (11-31)$$

$$\eta = Y \cos \delta - X \sin \delta \quad (11-32)$$

$$\eta' = \tan(\phi - \delta) \quad (11-33)$$

It can be seen that the curve that is singular in the (X, Y) coordinate system in figure 11-11 has no singularity in the rotated coordinate system. After the curves are generated in the (χ, η) coordinate system, the (X, Y) coordinates of the curve are recovered by

$$X = \chi \cos \delta - \eta \sin \delta \quad (11-34)$$

$$Y = \eta \cos \delta + \chi \sin \delta \quad (11-35)$$

11.4 Constructing the Annulus and Quasi-Normals

The annulus geometry is constructed by selecting suitable curves to define the end-wall contours. It is also necessary to develop appropriate straight-line quasi-normals as previously illustrated in figure 11-5. Then meridional surfaces are added to form a meridional plane grid structure similar to that shown in figure 11-12. This will be needed to construct blades within the passage, compute the throat area and the passage area distribution, etc. The meridional surfaces are defined to include a constant fraction of the total annulus area between each surface and the hub contour. The meridional coordinate, m , along each meridional surface is defined as the distance along the surface measured from the discharge, i.e.,

$$m_i = \int_{z_2}^{z_i} \sqrt{1 + \left(\frac{\partial r}{\partial z}\right)^2} dz \quad (11-36)$$

Eq. (11-36) requires numerical integration, which can be complicated by the possibility of an infinite slope. The rotation of coordinates discussed previously can avoid this, but it is simpler to perform the integration parametrically using the quasi-normal number, i , as the parameter.

$$m_i = \int_1^i \sqrt{\left(\frac{\partial z}{\partial i}\right)^2 + \left(\frac{\partial r}{\partial i}\right)^2} di \quad (11-37)$$

In this case, the quasi-normal number provides a parameter consisting of equal-spaced values. This permits very accurate finite-difference approximations to

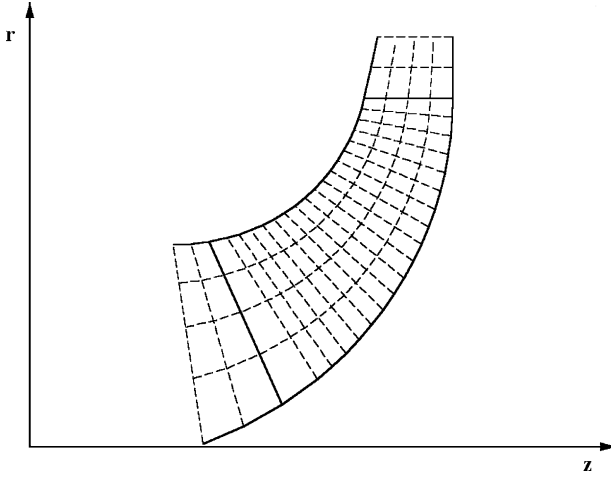


FIGURE 11-12. The Meridional Grid Structure

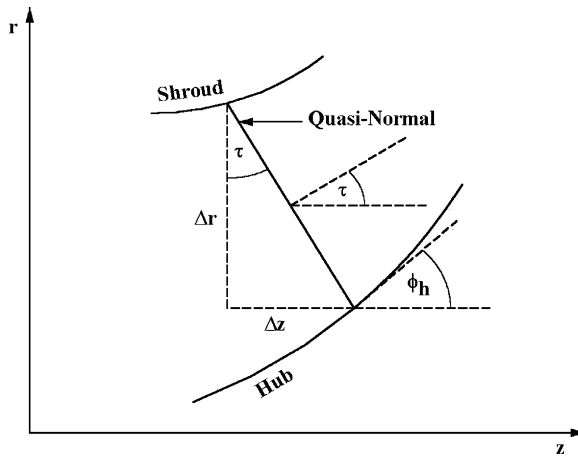


FIGURE 11-13. The Quasi-Normal Construction

be used for the derivatives with no chance of singularities. For any grid point, the meridional surface angle with the axial direction is given by

$$\sin \phi = \frac{\partial r}{\partial m} \quad (11-38)$$

The construction of the quasi-normals is somewhat arbitrary, but they should be approximately normal to the meridional surfaces to minimize corrections required for internal flow analysis and passage area calculations. Figure 11-13 illustrates the important geometrical parameters. The angle, τ , between the quasi-normal and the radial direction is defined as

$$\tan \tau = \frac{\Delta z}{\Delta r} \quad (11-39)$$

The deviation angle between the meridional surface angle and a normal to the quasi-normal, ϵ , is given by

$$\epsilon = \tau - \phi \quad (11-40)$$

All gaspath and internal flow calculations should account for the fact that ϵ is usually not zero, but it is good practice to minimize those corrections by maintaining reasonably small values of ϵ when possible. The meridional surfaces are reasonable approximations to the stream surfaces expected from an internal flow analysis. Hence, ϵ is an approximate measure of the deviation of a quasi-normal from a true normal to the stream surfaces. Some care is necessary when applying the various equations defining the quasi-normal geometry. Coordinate systems must be carefully defined and applied consistently. Also, an angle convention for ϕ and τ must be established to include cases where these angles lie

in various quadrants. Clearly the desired result for a quasi-normal is that $\varepsilon_h = -\varepsilon_s$. This can be used as the basis of an automated quasi-normal construction, but that approach is not very reliable. This writer's gaspath design system relies on an interactive graphics approach. The hub and shroud contours are displayed on the monitor screen along with the quasi-normal structure. Initially the quasi-normals are equal-spaced along the two contours. The designer can interactively move quasi-normal end points to obtain a reasonable structure. Usually this involves adjusting two or three key quasi-normals while equal-spacing intermediate ones. Once again, the computer performs some complex interpolations and calculations during this process, but the designer's task is quite simple.

11.5 Constructing the Blade Camberline

The blade camberline construction is accomplished using predefined curves for camberline angle distributions integrated to provide distributions of the polar angle. For two-dimensional blades, this results in $\theta_c(z)$ or $\theta_c(r)$ distributions. For three-dimensional straight-line element blades, $\theta_c(\xi)$ distributions for the hub and shroud contours are obtained, where ξ is the normalized meridional distance (0 to 1) along the contour. Local camberline data can be calculated from the local values of θ_c obtained from these distributions and the local values of z_c and r_c on the meridional surface.

$$x_c = r_c \sin \theta_c \quad (11-41)$$

$$y_c = r_c \cos \theta_c \quad (11-42)$$

$$\cot \beta_c = r_c \frac{\partial \theta_c}{\partial m} \quad (11-43)$$

For two-dimensional blades, this process yields the blade camberline data on all meridional surfaces. For the three-dimensional straight-line element blades, this process defines the blade camberline on the hub and shroud contours. If the normalized distance (0 to 1) from the hub contour along the line element connecting the hub and shroud camberline points is designated as ξ , the camberline data on intermediate meridional surfaces are obtained by

$$x_c = x_{ch} + (x_{cs} - x_{ch})\xi \quad (11-44)$$

$$y_c = y_{ch} + (y_{cs} - y_{ch})\xi \quad (11-45)$$

$$z_c = z_{ch} + (z_{cs} - z_{ch})\xi \quad (11-46)$$

$$r_c = \sqrt{x_c^2 + y_c^2} \quad (11-47)$$

$$\tan \theta_c = x_c / y_c \quad (11-48)$$

Hence, if ξ is known on the intermediate stream surface, the camberline data can be determined. This requires determining the intercept of the line element and the meridional surface. The rotation of coordinates defined by Eqs. (11-29) through (11-31) is applied to the meridional surface avoid singularities. In this case, only the χ -coordinate is needed to provide a correlation of the radius on the meridional surface in the form $r = r(\chi)$. The line-element coordinates can also be defined as a function of χ . After some tedious algebra, it can be shown that

$$r_c = \sqrt{r_{ch}^2 + A\xi + B\xi^2} \quad (11-49)$$

$$\chi = E + F\xi + G\xi^2 \quad (11-50)$$

The constants in Eqs. (11-49) and (11-50) are

$$A = 2[x_{ch}(x_{cs} - x_{ch}) + y_{ch}(y_{cs} - y_{ch})] \quad (11-51)$$

$$B = (x_{cs} - x_{ch})^2 + (y_{cs} - y_{ch})^2 \quad (11-52)$$

$$C = z_{cs} - z_{ch} \quad (11-53)$$

$$E = z_{ch} \cos \delta + r_{ch} \sin \delta \quad (11-54)$$

$$F = C \cos \delta + A \sin \delta \quad (11-55)$$

$$G = B \sin \delta \quad (11-56)$$

The local camberline coordinates can be computed numerically by an iterative process to reduce the difference between $r(\chi)$ and $r_c(\chi)$ to zero within an acceptable tolerance using ξ as a parameter. Once ξ is known Eqs. (11-44) through (11-48) provide all local camberline data for the straight-line element blade and Eq. (11-43) yields the local camberline angle.

11.6 Constructing the Blade Surfaces

The predefined curves representing the blade thickness distribution are imposed on the camberline to define the blade surfaces. For two-dimensional blades, this results in $t_b(z)$ or $t_b(r)$ distributions. For three-dimensional straight-line element blades, $t_b(\xi)$ distributions for the hub and shroud contours are obtained, where ξ is the normalized meridional distance (0 to 1) along the contour. It is often useful to provide some additional generality for two-dimensional blades. The designer will often want to taper the blades near the discharge to provide a thinner trailing edge to reduce the size of the wakes leaving the blades. Hence, it is

useful to provide the option to impose a taper over a specified distance near the trailing edge as a modification to the base thickness distribution obtained from the predefined curve.

The blade thickness must be imposed in a direction normal to the surface define by the camberline construction. To determine the local normal direction, define a unit vector \vec{S} tangent to blade camberline in the meridional surface and a unit vector \vec{B} directed along the defining line element for the specific blade type. The cross-product of these two unit vectors yields a unit vector \vec{T} normal to the camberline surface. Using standard vector notation for unit vectors in a Cartesian coordinate system, this process can be expressed as

$$\vec{S} = S_x \vec{i} + S_y \vec{j} + S_z \vec{k} \quad (11-57)$$

$$\vec{B} = B_x \vec{i} + B_y \vec{j} + B_z \vec{k} \quad (11-58)$$

$$\vec{T} = \vec{S} \times \vec{B} = T_x \vec{i} + T_y \vec{j} + T_z \vec{k} \quad (11-59)$$

After some tedious algebra, it can be shown that vector tangent to blade camberline is given by

$$S_x \sin \theta_c \sin \phi \sin \beta_c + \cos \theta_c \cos \beta_c \quad (11-60)$$

$$S_y = \cos \theta_c \cos \phi \sin \beta_c - \sin \theta_c \cos \beta_c \quad (11-61)$$

$$S_z = \cos \phi \sin \beta_c \quad (11-62)$$

The vector along the defining line element depends on the specific blade type being designed. For the three-dimensional straight-line element blade with the camberline surface line element of length L , it is given by

$$B_x = (x_{cs} - x_{ch}) / L \quad (11-63)$$

$$B_y = (y_{cs} - y_{ch}) / L \quad (11-64)$$

$$B_z = (z_{cs} - z_{ch}) / L \quad (11-65)$$

For the two-dimensional axial-element blade, it is given by

$$B_x = B_y = 0 \quad (11-66)$$

$$B_z = -1 \quad (11-67)$$

For the two-dimensional radial-element blade, it is given by

$$B_x = \sin \theta_c \quad (11-68)$$

$$B_y = \cos\theta_c \quad (11-69)$$

$$B_z = 0 \quad (11-70)$$

From the definition of the cross-product, the unit vector normal to the blade camberline surface is given by

$$T_x = S_z B_y - S_y B_z \quad (11-71)$$

$$T_y = S_x B_z - S_z B_x \quad (11-72)$$

$$T_z = S_y B_x - S_x B_y \quad (11-73)$$

Hence, the local blade surface coordinates are given by

$$x = x_c \pm \frac{1}{2} t_b T_x \quad (11-74)$$

$$y = y_c \pm \frac{1}{2} t_b T_y \quad (11-75)$$

$$z = z_c \pm \frac{1}{2} t_b T_z \quad (11-76)$$

For two-dimensional blades, this defines the blade surface coordinates over the entire grid structure. For three-dimensional straight-line element blades this defines the blade surface coordinates for the hub and shroud contours. Intermediate stream surfaces are defined by connecting hub and shroud surface points with straight-line elements. This is accomplished using the same procedure as previously applied for the camberline.

It is fairly common practice to maintain a constant impeller tip radius on all meridional surfaces to simplify the final machining process. This can be accomplished by a special adjustment at that location. A unit vector in the θ direction is defined by

$$\vec{e}_\theta = \cos\theta_c \vec{i} - \sin\theta_c \vec{j} \quad (11-77)$$

Then, the blade thickness in the θ direction is given by

$$t_\theta = t_b / [T_x \cos\theta_c - T_y \sin\theta_c] \quad (11-78)$$

The blade surface polar coordinates at a constant radius are given by

$$\theta = \theta_c \pm \tan^{-1}[t_\theta / (2r_c)] \quad (11-79)$$

The other blade surface coordinates can be calculated with Eqs. (11-41) and (11-42).

11.7 The Blade Passage Throat Geometry

Accurate calculation of the blade passage throat widths and total throat area are essential to the aerodynamic design process to determine the component's choke flow limit and the discharge flow angles. Calculation of the throat passage width, o , on the meridional surfaces is the most difficult step in this process. The throat width lies on a three-dimensional surface with both r and θ varying along the width. The throat width calculation can be accomplished using a conformal mapping transformation to map the (m, θ) surface into a simple (X, Y) Cartesian plane. A path-independent conformal transformation that accomplishes this is given by

$$X = \int_{m_2}^m \frac{dm}{r} \quad (11-80)$$

$$Y = \theta \quad (11-81)$$

Figure 11-14 illustrates the use of this transformation. Note that the throat is a straight line in the transformed space. Since angles are preserved by conformal transformations, this shows that the throat width has a constant angle along its length, i.e.,

$$\frac{\partial Y}{\partial X} = r \frac{\partial \theta}{\partial m} = \text{constant} \quad (11-82)$$

Since this angle is constant, the throat width can be calculated by

$$o = \int_{m_2}^m \sqrt{1 + \left(\frac{r \partial \theta}{\partial m} \right)^2} dm = \sqrt{1 + \left(\frac{\Delta \theta}{X} \right)^2} \Delta m \quad (11-83)$$

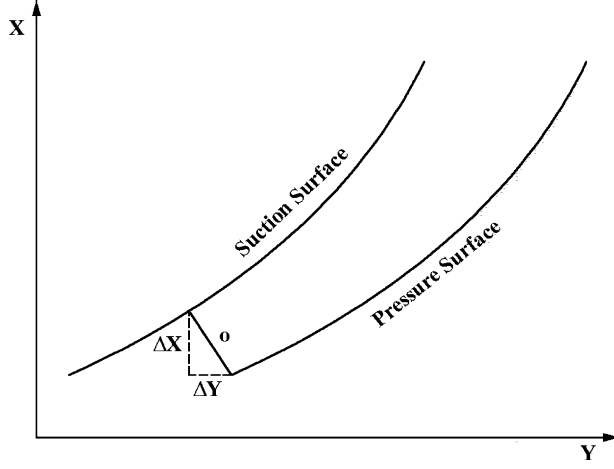


FIGURE 11-14. Conformal Map of the Throat Width

The parameters $\Delta\theta$ and Δm are computed as differences from values on the two blade surfaces and X is calculated on the left blade surface in figure 11-14. Eq. (11-83) can be applied between any two points on opposing surfaces to compute the distances between them. Hence it is applied to all points along the suction surface using the fixed pressure surface point. This allows the minimum distance to be located numerically to define the throat width. If n is the distance along the quasi-normal, the throat area contained between two adjacent meridional surfaces is given by

$$\Delta A = \overline{o \cos \varepsilon} \Delta n \quad (11-84)$$

This equation uses the average throat width on the two meridional surfaces corrected to account for the fact that the quasi-normal may not be normal to the meridional surface. The total throat area is obtained by a summation of the values of ΔA between all adjacent meridional surfaces. The accuracy of this calculation is improved by including more meridional surfaces.

11.8 An Effective Gaspath Design System

The procedures described in this chapter can be used to formulate an efficient computerized gaspath design system. This writer's gaspath design system evolved over several years based on experience gained from impeller design for centrifugal compressors. Although the basic design strategy is unchanged from the original concept, the implementation of that strategy was revised many times to arrive at the effective version used today. Most of the revisions were too subtle to be anticipated until their benefits became obvious through practical design experience. It is considered worthwhile to provide some discussion of some beneficial features learned from experience.

There are significant benefits from implementing the design system in two separate applications. One application generates the basic curves used to define the end-wall contours and the blade geometry. The other application selects the curves to be used and generates the gaspath design. When implemented as a single application, the user interface proved to be too confusing. Even experienced users found it difficult to navigate through the massive number of choices available. After several attempts to restructure the user interface failed to fully resolve that issue, separation into two applications proved to be the best solution. Simple interfacing between the two applications proved to be the most effective approach. Simply requiring the same base input file name with different file name extenders accomplishes that goal. Modern programming languages offer many ways to fully integrate two different applications. It has become fashionable to take that approach largely for image enhancement. It offers minimal benefit and increased risk for complex applications intended for many different users with varying levels of skill and experience. It is almost impossible to anticipate all of the ways users can find to create conflicts when the computer implements modifications without a conscious decision by the user.

The curve generation application develops the curves and distributes points along the curves to define quasi-normal end points or to provide data for

interpolation in the case of blade geometry distributions. Some useful features recommended for this application are:

- Each curve should be designated as either a geometric contour or a blade data distribution. Interactive graphics procedures need to display the two types differently. Geometric contours should be displayed to proper scale or aspect ratio. Distribution curves are displayed to make full use of the monitor screen size.
- The curve definition function should provide for input of the defining data for the specific curve form and subsequent editing of that data. As previously discussed, the Bezier polynomial and cubic spline curve forms require interactive graphics support to effectively define the curve shape.
- The distribution of points along the curve is best accomplished through an interactive graphics procedure. Multiple options for positioning the points should be included. Moving points interactively, direct editing of point coordinates, equal spacing of points between specified points, etc. can greatly speed up the process.
- All interactive graphics procedures should include the option to show a second curve as background for additional guidance. Typically, a curve for the hub is displayed while designing a curve at the shroud, and inversely. In the case of geometric contours, the second curve can also supply additional useful data (e.g., the passage area distribution). It is also essential to the final process of locating appropriate quasi-normal end points. Visual display of contours and quasi-normals is the most effective way to accomplish this. Also include provision to switch the curves, i.e., the background curve becomes the edited curve and inversely.
- In addition to the curve forms described previously, curves defined by a series of points and curves formulated as a composite of two or more existing curves are useful curve types. The composite curve is a particularly good way to add vaneless passage extensions before and after the blade passage, (which are needed for an internal flow analysis).
- The curves should be stored in a curve file with appropriate labels to simplify their selection in the gaspath design application. Multiple curves should be allowed so that alternative curves can be investigated without deleting previous attempts. Provision to copy an existing curve is a useful feature to retain the existing curve before editing the copy.
- The initial curves should be supplied by the preliminary design system as describe in chapter 10. These may be edited directly, copied and edited or converted to Bezier polynomial curves as described previously in this chapter.

The gaspath design application selects curves from the curve file developed by the curve generation application to construct the end-wall contours and blades. It performs all of the tedious calculations required for that construction, establishes the grid structure, calculates the throat area, etc. It should also be capable of exporting input files for the performance analysis of chapter 9 and the internal flow analysis of chapter 14. These analyses are needed to evaluate the detailed design. Provision to export geometry data for stress analysis,

computer aided drafting and manufacturing can also yield substantial productivity benefits. Other useful features are:

- The preliminary design system of chapter 10 should create the initial input file for this application as well as the curve generation application.
- Extensive monitor screen displays of graphical and tabular results should be provided, including front and side views of the gaspath and key distributions such as β , ϕ , t_b , curvature, passage areas, etc.
- The application must recognize the impact of changes made and maintain only valid geometrical results. Hence, all resident gaspath geometry dependent on a revised curve or parameter should automatically be eliminated until it is recalculated. The design system must not be capable of providing incorrect geometry.
- The number of meridional surfaces used should be arbitrary. Provision to scale the geometry or reverse the direction of rotation can be useful.
- Provision to specify the difference between hub and shroud polar angles at the blade leading or trailing edge for three-dimensional straight-line element blades is needed to permit adjusting the "rake" angles between the defining line elements and the meridional plane. This may be required to achieve mechanical integrity. One useful option that often works well is to balance the rake angles at the leading and trailing edges (i.e., set them equal with opposite signs).
- When exporting input files for aerodynamic analysis, use an update approach if the input file already exists. The gaspath design system lacks aerodynamic data or other component data that may be needed for these input files. Usually these data will already exist in the old input file and should be retained.
- Provision to export geometry in simple text format for subsequent import into other applications has proven to be extremely valuable. It is not possible to anticipate all of the needs that may arise for mechanical evaluation, drafting, manufacturing, publishing, etc. But it is not difficult to identify the major contours, distributions, etc. that might be useful and make provision to export them in line or column format. The user can then select the data to be exported and the format desired. This writer developed a general export utility for this purpose that is used by many computer applications. Indeed, most of the figures in this book were created using that type of exported data.

Many of the procedures described in this chapter can also be applied to an application suitable for treating existing designs. Most of the blade and gaspath construction logic and data export procedures developed for detailed design can be used directly. The major difference is that the contours and blades are specified by a series of points rather than curves. This provides a logical way to introduce existing designs into a general aerodynamic design and analysis system to make full use of its capabilities. This type of application can also provide additional capability not specific to detailed gaspath design. Imposing new shroud contours to change flow capacity, trimming or extending impeller tips to alter the work, scaling geometry, etc. are typical examples. This capability is included

in this writer's design and analysis systems for both compressors and turbines. It has unquestionably been the most used application in the compressor design and analysis system, even exceeding use of the performance analysis.

11.9 Application to Impeller Design

The gaspath detailed design procedure is applicable to most turbomachinery components. But its most common application is to impeller design for radial-inflow turbines and centrifugal compressors. The design example used in chapter 10 will be used to illustrate this application. The impeller design results obtained from the preliminary design system are presented in figures 10-6 through 10-8. Figure 11-15 shows the hub and shroud blade loading predicted for this preliminary impeller design with the quasi-three-dimensional flow field analysis of chapter 14. The shroud blade loading is clearly unacceptable due to substantial flow deceleration on the suction surface. The blade also overturns the flow such that the blade force reverses in direction near the trailing edge. The hub blade loading is hardly ideal either, but the experienced aerodynamic designer will recognize that the ability to control that aspect of the design is quite limited due to the low blade speeds and the relatively high blade angles. Figure 11-16 shows a similar blade-loading plot after applying the gaspath design system to modify the geometry obtained from the preliminary design system. The process used is to revise the geometry in the gaspath design system and export that geometry to the quasi-three-dimensional flow analysis for evaluation. Hence, the detailed impeller design is primarily an iterative process between the gaspath design system and the quasi-three-dimensional flow field analysis. For this design example, this is a simple and somewhat academic exercise, since the

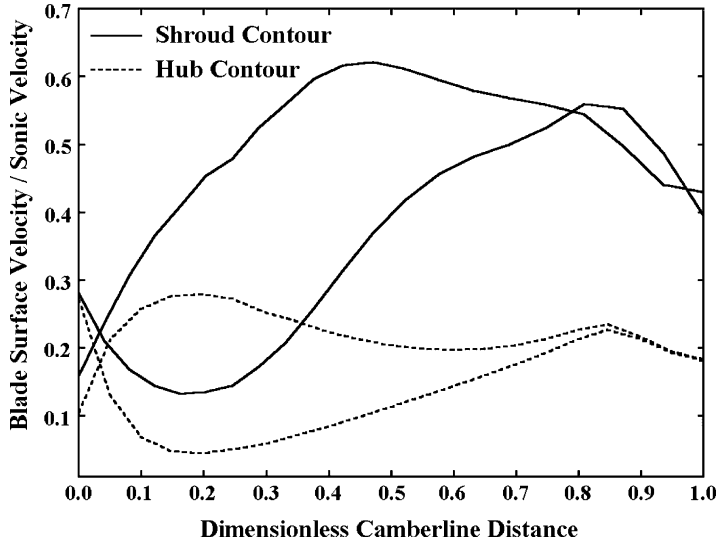
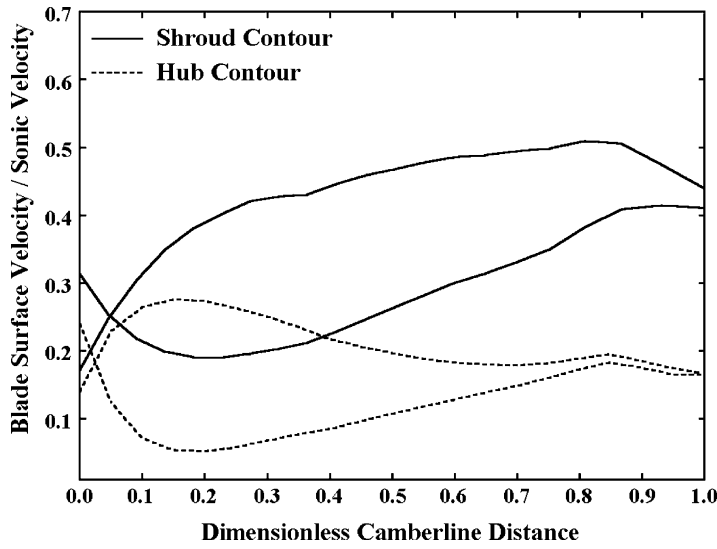
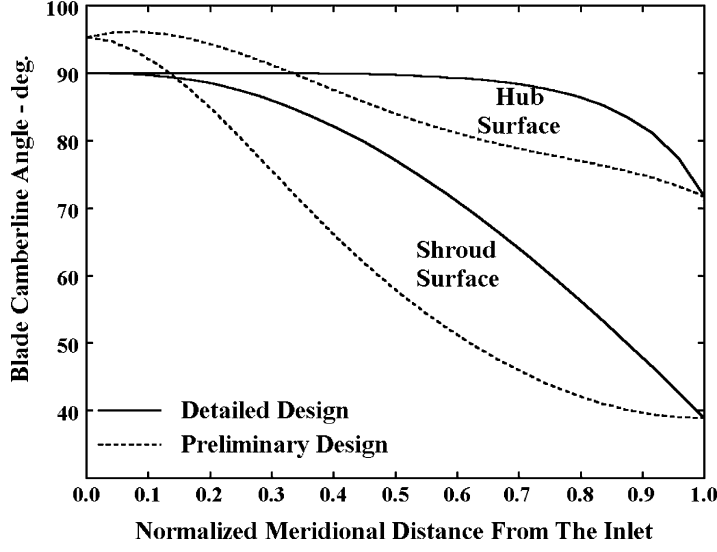


FIGURE 11-15. Preliminary Design Blade Loading

**FIGURE 11-16. Detailed Design Blade Loading**

large number of aerodynamic and mechanical constraints the designer usually must address are not defined. The results shown in figure 11-16 were obtained after six iterations. Although this detailed impeller design is by no means optimized, it demonstrates the dramatic improvements that are possible with a minimal effort. Figure 11-17 compares blade camberline angle distributions

**FIGURE 11-17. Blade Camberline Angle Distributions**

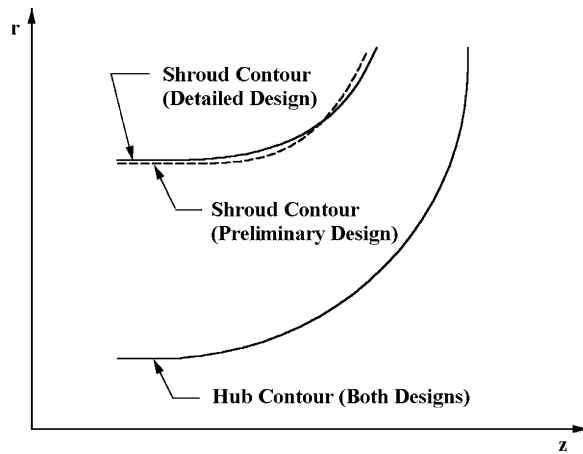
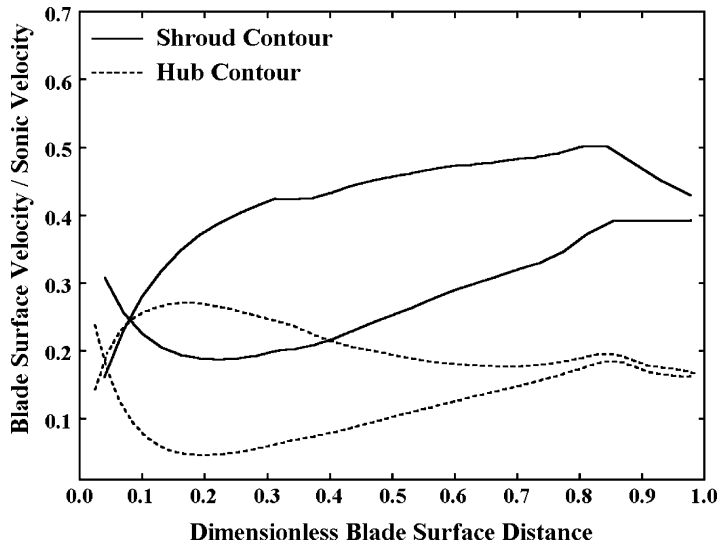


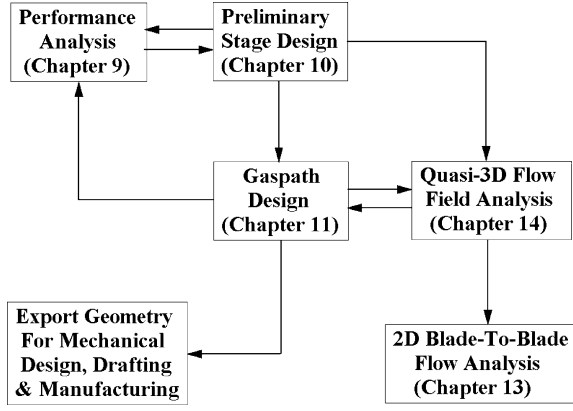
FIGURE 11-18. Impeller End-Wall Contours

for the preliminary and detailed designs on the hub and shroud contours. The modified shroud surface blade camberline angle distribution produced nearly all of the blade-loading improvement. The hub blade camberline angle distribution was also revised to attempt to shift the blade loading more toward the discharge, but with minimal effect. A modest modification to the shroud contour was also accomplished to reduce the flow deceleration over the aft portion of the impeller passage. Figure 11-18 shows the end-wall contours for both designs. The blade angle distributions and the shroud contour form the preliminary design were all converted to Bezier polynomial curve fits. The revisions were all accomplished using those more general curve forms. In chapter 14, it will be seen that an approximate linearized blade-to-blade flow model is used in the quasi-three-dimensional flow analysis. That model is generally very accurate for thin blades such as are commonly used for impellers. But it is always recommended that a more accurate two-dimensional blade-to-blade flow analysis be conducted on key stream surfaces as a final evaluation of the blade loading. When a quasi-three-dimensional flow analysis is accomplished, all required geometry for the more accurate two-dimensional blade-to-blade flow analysis is available. This is used to export an input file such that accomplishing the more accurate analyses is a fairly trivial process. Figure 11-19 shows results for the detailed design from the more accurate two-dimensional, potential flow blade-to-blade analysis of chapter 13 for the hub and shroud surfaces. In this case, these results simply confirm that the linearized blade-to-blade flow model is quite accurate for this case. Indeed, nearly all of the difference seen is due to the difference in the abscissa used for the two figures. The two-dimensional analysis can identify blade surface distance explicitly, whereas the linearized model must rely on camberline distance.

Figure 11-20 shows an impeller detailed design flow chart to clarify the process. In this writer's aerodynamic design and analysis system, the interfacing between analyses is automated through the exporting of the input files required.

**FIGURE 11-19. Blade-to-Blade Flow Results**

The preliminary design system initializes most of those input files, since it has all input/output units, operating conditions and the equation of state needed by the internal flow analyses, whereas the gaspath detailed design system does not. Preliminary design relies on an iterative process with the performance analysis as previously described in chapter 10. Similarly, an iterative process between the detailed gaspath design and the quasi-three-dimensional flow analysis is used to arrive at acceptable internal flow characteristics. The gaspath detailed design system can also update the impeller geometry for the performance analysis so that acceptable performance can be confirmed for the detailed impeller design.

**FIGURE 11-20. Impeller Detailed Design Flow Chart**

The quasi-three-dimensional flow analysis supplies a complete input file for the two-dimensional blade-to-blade flow analysis for any of stream surfaces that it has analyzed. The final step in the process is export of the geometry from the gaspath design system for use by mechanical designers, drafting, manufacturing, or for a final internal flow analysis using a viscous flow computational fluid dynamics code.

Chapter 12

AERODYNAMIC DESIGN AND PERFORMANCE ANALYSIS OF EXHAUST DIFFUSERS

Both axial-flow and radial-inflow turbines often employ annular exhaust diffusers to improve the turbine efficiency. The flow typically enters the diffuser in the axial direction for both turbine types. The inlet flow usually has a significant tangential component, particularly when the last stage operates at off-design conditions. The diffuser may also discharge primarily in the axial direction, or it may turn the flow from the axial direction to the radial direction. There are a number of excellent experimental investigations relative to diffuser performance reported in the literature, including two-dimensional, conical and annular diffusers (e.g., Reneau et al. [92], Sovran and Klomp [103], Dolan and Runstadler [104]). These include experimental performance maps that provide useful design guidance but lack the generality required to address the complex flow conditions and various exhaust diffuser configurations encountered in turbines. An approximate diffuser performance analysis model was previously described in chapter 9. That model is based on a vaned diffuser empirical model from Aungier [1, 90]. Although more general than the published performance maps, that model does not account for the influence of the passage shape between the inlet and the discharge. Also, it does not account for the complex interaction of swirling flow on diffuser performance. This chapter describes a more general performance analysis that can address swirling flow in typical exhaust diffuser configurations. Aungier [1, 105] used it to treat the various annular passages encountered in centrifugal compressors, including extensive qualification with experimental data. Aungier [2] generalized it to axial-flow compressor exhaust diffusers and qualified it with data obtained from classical diffuser experiments.

NOMENCLATURE

- A = passage area
- A_m = maximum, stall-free passage area
- A_R = diffuser area ratio
- B = fractional area blockage
- B_{BL} = boundary layer fractional area blockage

- B_{SEP} = minimum fractional area blockage due to flow separation
 b = passage width
 C = absolute velocity
 C_p = static pressure recovery coefficient
 c_f = skin friction coefficient
 $D = 2 \tan \theta_c$
 D_m = limiting value of D for low diffusion losses
 d = characteristic diameter for Reynolds number definition
 E = diffusion efficiency parameter
 e = peak-to-valley surface roughness
 e_{rms} = root-mean-square surface roughness
 H = total enthalpy
 h = static enthalpy
 I_C = passage curvature loss term
 I_D = passage diffusion loss term
 K_1 = parameter defined in Eq. (12-11)
 K_2 = parameter defined in Eq. (12-8)
 K_θ = parameter defined in Eq. (12-9)
 L = diffuser meridional length
 m = meridional coordinate
 \dot{m} = mass flow rate
 P = pressure
 Re = Reynolds number
 r = radius
 δ = boundary layer thickness
 δ^* = boundary layer displacement thickness
 ε = diffuser effectiveness
 θ = polar angle
 θ_C = diffuser divergence angle
 κ_m = stream surface curvature
 Λ = a diffusion parameter defined in Eq. (12-10)
 μ = gas viscosity
 ρ = gas density
 τ_w = wall shear stress
 ϕ = angle of the streamline slope with the axial direction
 $\psi = (P_{t1} - P_1)/(P_{t1} - P_{2i})$
 $\bar{\omega}$ = total pressure loss coefficient

Subscripts

- 1 = parameter at the diffuser inlet
 2 = parameter at the diffuser exit
 $2i$ = ideal (no loss) discharge condition
 L = laminar condition
 m = meridional component
 t = total thermodynamic condition
 θ = tangential component

12.1 Basic Diffuser Technology

The nomenclature normally employed for diffusers is derived from the classical two-dimensional diffuser illustrated in figure 12-1. The performance of the diffuser is generally expressed in terms of the static pressure recovery coefficient.

$$C_p = (P_2 - P_1) / (P_{in} - P_1) \quad (12-1)$$

Many investigators have shown that C_p is a function of the dimensionless length, L/b_1 , the divergence angle, $2\theta_c$, the area ratio, A_R , and the inlet boundary layer blockage, B_1 , where

$$A_R = b_2 / b_1 \quad (12-2)$$

$$B_1 = 2\delta^* / b_1 \quad (12-3)$$

The definition of the boundary layer displacement thickness, δ^* , is given in Eq. (3-34).

Turbine exhaust diffusers are not two-dimensional diffusers. Usually they are annular diffusers or possibly conical diffusers. Fortunately, the performance of conical and annular diffusers is quite similar to two-dimensional diffusers when b is defined as the passage height and an equivalent divergence angle is defined as

$$2\theta_c = 2 \tan^{-1} [(A_R - 1)b_1 / (2L)] \quad (12-4)$$

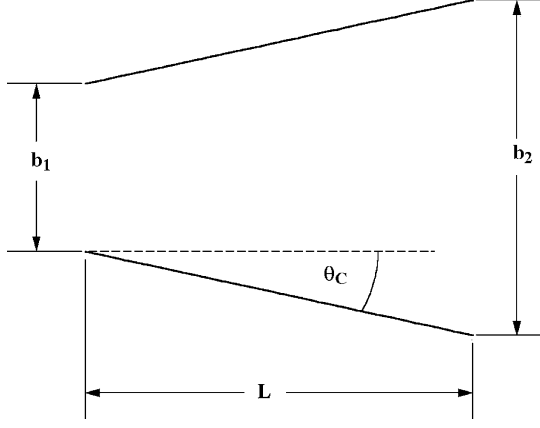


FIGURE 12-1. Two-Dimensional Diffuser Geometry

Note that this definition of the equivalent divergence angle yields an actual wall divergence angle only for the two-dimensional diffuser. This can result in some confusion when interpreting experimental performance maps for other diffuser types. It is not uncommon to encounter experimental diffuser performance maps based on an actual wall divergence angle, which may be quite different from the equivalent divergence angle. In those cases, similarity with two-dimensional diffuser performance with respect to divergence angle will not be observed.

Another difference between exhaust diffusers and classical diffuser experimental data is the Mach number level. Most classical experiments were conducted for incompressible flows. Turbine exhaust diffusers do not normally involve high Mach numbers, but neither are they incompressible flows. Aungier [1, 90] addressed this problem by introducing the parameter, ψ , defined as

$$\psi^2 = (P_{t1} - P_1) / (P_{t1} - P_{2i}) \quad (12-5)$$

Here, P_{2i} is the ideal discharge static pressure assuming isentropic flow in the diffuser. Note that for simple incompressible diffuser flow, $\psi = C_1/C_2 = A_R$. Hence, ψ is a more general measure of the level of diffusion than A_R .

12.2 An Approximate Performance Analysis

Aungier [1, 90] presents an approximate diffuser performance model developed as an empirical model based on experimental performance data for vaned diffusers in centrifugal compressors. That performance model includes a correction for excessive blade-to-blade loading. That correction is not applicable to the exhaust diffuser problem. Neglecting the blade-loading correction, the empirical model is given by

$$B_2 = [K_1 + K_2(\Lambda - 1)]L/b_2 \quad (12-6)$$

$$K_1 = 0.005 + (1 - 1/K_\theta)/5 \quad (12-7)$$

$$K_2 = 2\theta_C [1 - 2\theta_C/(22K_\theta)]/(125K_\theta) \quad (12-8)$$

$$1 \leq K_\theta \geq 2\theta_C/11 \quad (12-9)$$

$$\Lambda = (\psi + 1)^2 / 4 \quad (12-10)$$

The static pressure recovery coefficient is calculated by simple mass balances at the inlet and discharge, assuming isentropic flow with the discharge area reduced by the discharge blockage. This is the basis for the exhaust diffuser model given in chapter 9. However, two modifications were included to extend the model to include cases where geometrical parameters outside of

the range correlated for vaned diffusers are encountered. That is virtually impossible for a vaned diffuser and very unlikely for a well-designed exhaust diffuser, but failure to consider that possibility might mislead designers to select a poor exhaust diffuser design. One concern is that excessively large equivalent divergence angles might be attempted. Consequently, Eq. (12-7) is modified to

$$K_1 = 0.005 + (K_\theta - 1)/5 \quad (12-11)$$

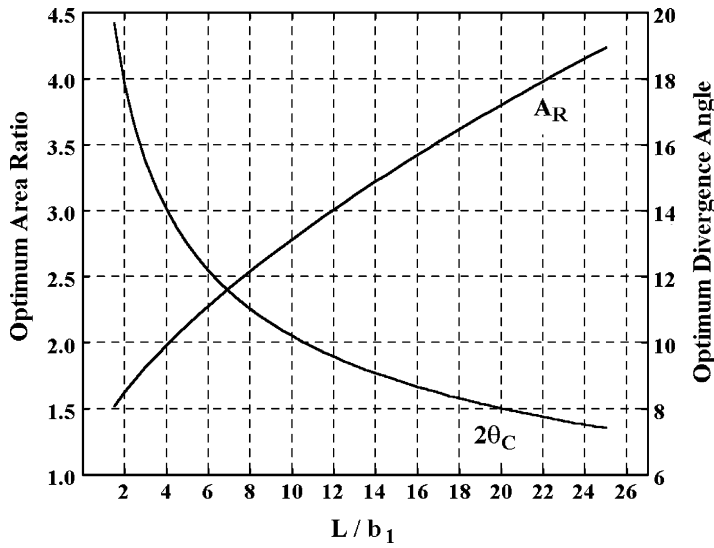
This substitution has negligible effect on the correlation accuracy for the vaned diffuser problem, but avoids an inaccuracy when excessively large values of $2\theta_c$ are employed. This extension to include larger values of $2\theta_c$ is based on the two-dimensional diffuser data of Reneau et al. [92]. The second area of concern relates to high diffusion levels. Figure 4(d) of [92] shows that for an inlet boundary layer blockage level of $B_1 = 0.05$, values of $\psi > 2.5$ yield a reduction in C_p , followed by a near constant pressure recovery as ψ continues to increase. Again, it is virtually impossible to encounter this situation in the vaned diffuser application, but it could encourage poor design decisions when designing an exhaust diffuser. The present empirical model shows good agreement with the data of [92] if a limit of $\Lambda \leq 3.6$ is imposed when solving Eq. (12-6). It is likely that inlet boundary layer blockage levels in exhaust diffusers will be at least 0.05 and quite possibly higher. Hence, this is considered to be a prudent adjustment to this approximate performance analysis. It should be noted that some type of limit is needed if the empirical model is to be applied to diffusion levels well in excess of the data originally correlated. Otherwise, Eq. (12-6) will eventually yield values of $B_2 > 1$, which is impossible. In the vaned diffuser application, an upper limit on B_2 was imposed simply as a precaution, even though it is unlikely to ever be needed.

12.3 Sizing the Exhaust Diffuser

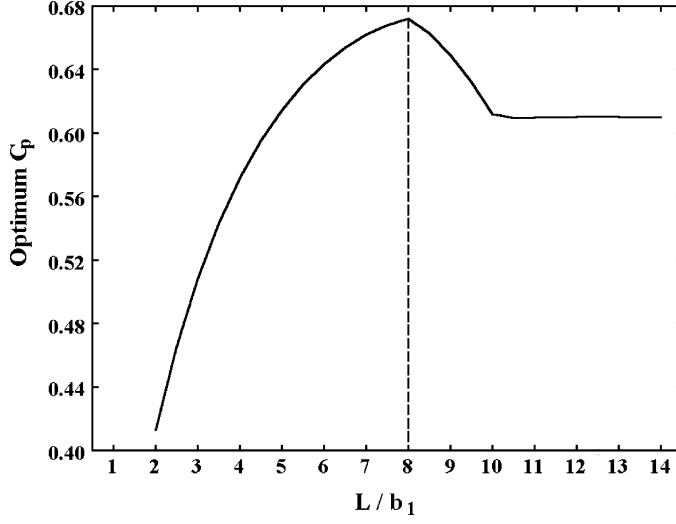
The logical design objective for exhaust diffusers is to achieve the highest value of C_p possible within space and cost restrictions. Figure 8(b) of Reneau et al. [92] provides a graphical correlation of the area ratio that yields the peak C_p as a function of L/b_1 . Aungier [2] developed an analytical correlation of this result in the form

$$A_R = 1 + 0.4(L/b_1)^{0.65} \quad (12-12)$$

Figure 12-2 presents Eq. (12-12) graphically along with the corresponding equivalent divergence angle from Eq. (12-4). Figure 12-2 provides an estimate of the area ratio and effective divergence angle expected to yield the optimum static pressure recovery coefficient for the available axial length. For industrial turbines, the additional cost of including an exhaust diffuser is also an important design constraint. In that context, design guidelines from figure 12-2 are rather abstract, since they do not quantify the value added by an exhaust diffuser. That requires an estimate of the achievable static pressure recovery to

**FIGURE 12-2. Optimum Design Parameters**

determine the total-to-static efficiency improvement provided by an exhaust diffuser. The available axial length for an exhaust diffuser is usually the primary design constraint. Outer casing size constraints may also limit the area ratio that can be accommodated. Figures 12-3 and 12-4 show the optimum static pressure recovery coefficient as a function of dimensionless axial length and area ratio, respectively. These figures were generated with the approximate

**FIGURE 12-3. Optimum C_p versus L/b_1**

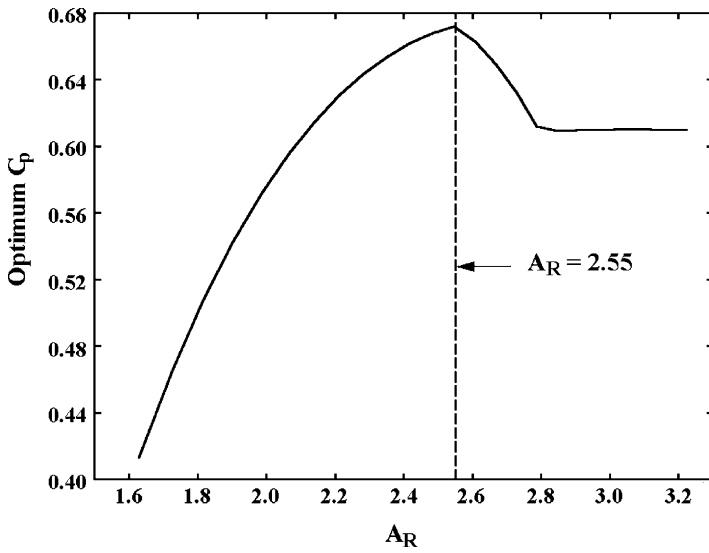


FIGURE 12-4. Optimum C_p versus A_R

performance analysis assuming incompressible flow and using the optimum area ratio given by Eq. (12-12) in all cases. These figures provide estimates of the static pressure recovery potential offered by including an exhaust diffuser, subject to constraints on axial length or area ratio. Figures 12-2 through 12-4 show that the best achievable static pressure recovery is expected from a design with $A_R \approx 2.55$, $2\theta_C \approx 11^\circ$ and $L/b_1 \approx 8$.

Figures 12-3 and 12-4 provide a qualitative evaluation of the benefit expected from an exhaust diffuser. But they are not recommended for use as diffuser design charts. The optimum area-ratio correlation of Reneau et al. [92] and the performance analysis used to estimate C_p are both too approximate to justify using them in that role. The principal conclusion to be drawn from these figures is that designing for an area ratio greater than about 2.5 is unlikely to be productive and may even be detrimental. This diffusion limit is based on performance estimates and experimental data for incompressible flow. Mach number levels encountered in exhaust diffusers are normally sufficiently low that compressible flow corrections are rather modest. But to generalize this diffusion limit to compressible flow, it should be expressed as a limit on ψ rather than A_R .

Subject to this diffusion limit, the most effective design parameter for exhaust diffusers is the equivalent divergence angle. This is illustrated in figure 12-5, which shows the performance predicted for two diffusers with quite different diffusion levels as a function of the equivalent divergence angle. These constant ψ predictions are for the constant area ratio corresponding to ψ rather than the optimum area ratio of Eq. (12-12). It is seen that the predicted optimum performance occurs at $2\theta_C \approx 11^\circ$, independent of the area ratio. Since that is also a condition where an abrupt breakdown in performance is expected, the designer may prefer some margin of safety. Hence, the recommended exhaust diffuser sizing criteria are

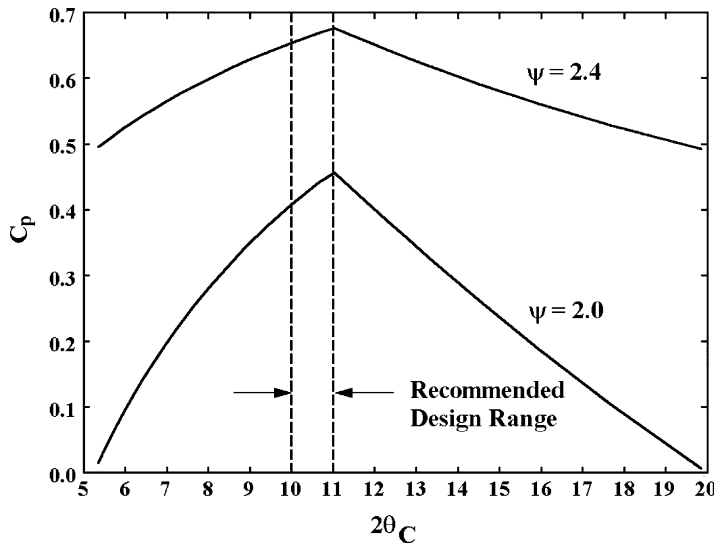


FIGURE 12-5. Recommended Range for $2\theta_c$

$$10^\circ \leq 2\theta_c \leq 11^\circ \quad (12-13)$$

$$\psi \leq 2.5 \quad (12-14)$$

These criteria can be used to size the exhaust diffuser to make best use of the available axial length.

The performance estimates obtained from the approximate performance analysis during the diffuser sizing process are only preliminary estimates. The internal flow and performance of an exhaust diffuser are influenced by many parameters not established by the diffuser sizing. These include the passage area distribution, the passage mean-radius distribution, passage curvature effects, Reynolds number and the inlet swirl velocity. The final performance estimate and the detailed aerodynamic design of the diffuser both require a more fundamental aerodynamic performance analysis capable of considering these effects. An exhaust diffuser aerodynamic performance analysis suitable for that purpose is presented in the next section of this chapter.

12.4 A Detailed Aerodynamic Performance Analysis

Many exhaust diffuser configurations are used for turbomachinery. The most common type is the axial diffuser illustrated in figure 12-6. This type diffuses the meridional velocity component through the passage area increase but provides minimal diffusion of any tangential velocity component present at the inlet. Occasionally the exhaust diffuser turns the flow from the axial direction to the radial direction similar to the configuration illustrated in

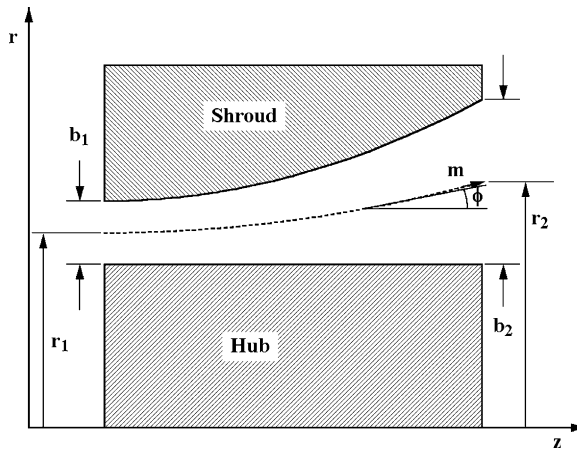
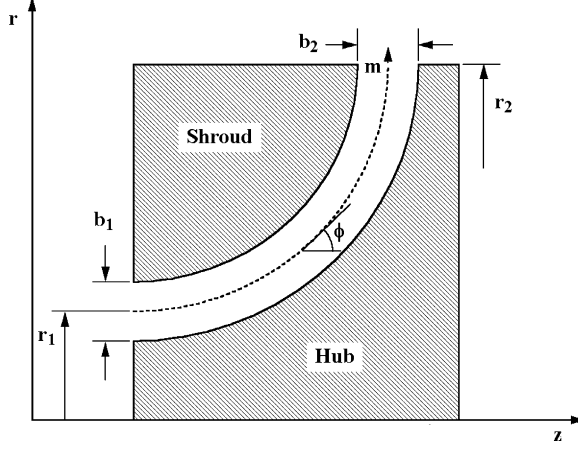
**FIGURE 12-6. An Axial Exhaust Diffuser**

figure 12-7. The flow is then collected in a plenum to exit through a radial discharge pipe. This type also diffuses the meridional velocity component through the passage area increase. But the radius increase also results in significant diffusion of the tangential velocity component through conservation of angular momentum.

A very general performance analysis is required to consider the many configurations that may be encountered. A performance analysis developed by Aungier [1, 105] is sufficiently general for this purpose. That analysis was developed to predict the performance of the many types of annular passages encountered in centrifugal compressors. These range from simple radial vaneless diffusers to 90° and 180° annular bends. The accuracy of this method has been well established by comparison of its predictions with experimental data.

**FIGURE 12-7. An Axial-to-Radial Exhaust Diffuser**

Aungier [2] extended this performance analysis to exhaust diffusers for axial-flow compressors by including additional capabilities not required for the centrifugal compressor application. These include extending the analysis to nonswirling flows and to cases with very thin boundary layers. That modified form of the analysis is directly applicable to turbine exhaust diffusers as well. While its description in this chapter is adapted specifically to the turbine exhaust diffuser application, the analysis is virtually identical to one previously described in Aungier [2].

The performance analysis is a mean-streamline or one-dimensional method with wall friction and empirical corrections for diffusion and curvature effects. Figures 12-6 and 12-7 illustrate the mean streamline and the nomenclature used in the analysis. The governing equations for one-dimensional flow with wall friction are

$$2\pi rb\rho C_m(1-B) = \dot{m} \quad (12-15)$$

$$bC_m \frac{d(rC_\theta)}{dm} = -rCC_\theta c_f \quad (12-16)$$

$$\frac{1}{\rho} \frac{dP}{dm} = \frac{C_\theta^2 \sin \phi}{r} - C_m \frac{dC_m}{dm} - \frac{CC_m c_f}{b} - \frac{dI_D}{dm} - I_C \quad (12-17)$$

$$H = h + \frac{1}{2} C^2 \quad (12-18)$$

The blockage, B , specifies the fraction of the passage area unavailable for the inviscid through flow, due to viscous effects. The skin friction coefficient, c_f , supplies a correction for the effect of the wall shear stress τ_w .

$$c_f = \frac{\tau_w}{\frac{1}{2} \rho C^2} \quad (12-19)$$

The terms I_D and I_C are introduced to account for losses due to diffusion and passage curvature, respectively. In other respects, this set of equations follows directly from the governing equations for inviscid flow presented in chapter 3, when simplified to time-steady, axisymmetric, one-dimensional flow in a stationary coordinate system.

The effective divergence angle for an annular diffuser is given by Eq. (12-4) if the passage area is $A = 2\pi rb$ and $L = m_2$, is the length of the mean streamline. Defining a divergence parameter, D , as

$$D = 2 \tan \theta_C = b_1 (A_2 / A_1 - 1) / m_2 \quad (12-20)$$

From Eq. (12-12), diffusion losses are expected to be low if $D < D_m$, where

$$D_m = 0.4(b_1 / m_2)^{0.35} \quad (12-21)$$

Aungier [105] used an analogy with these classical diffuser parameters, defined as local diffusion parameters, i.e.,

$$D = -\frac{b}{C} \frac{dC}{dm} \quad (12-22)$$

$$D_m = 0.4 \sin \alpha (b_1 / m_2)^{0.35} \quad (12-23)$$

Based on detailed comparisons with predicted and measured losses in a substantial number of centrifugal compressor vaneless diffusers, an empirical model was developed for a diffusion efficiency parameter, E .

$$E = 1; \quad D \leq 0 \quad (12-24)$$

$$E = 1 - 0.2(D/D_m)^2; \quad 0 < D < D_m \quad (12-25)$$

$$E = 0.8\sqrt{D_m/D}; \quad D \geq D_m \quad (12-26)$$

Then the streamwise diffusion term in Eq. (12-17) is given by

$$\frac{dI_D}{dm} = -2(P_t - P)(1 - E) \frac{1}{\rho C} \frac{dC}{dm} \quad (12-27)$$

It was also found to be necessary to check for excessive diffusion in the meridional direction as well as the streamwise direction, again using an analogy with classical diffuser technology. The maximum stall-free local passage area, A_m , is estimated from

$$A_m = A_l[1 + 0.1925m/b_l] \quad (12-28)$$

This corresponds to a local divergence angle limit of $2\theta_C \approx 11^\circ$. A minimum value of I_D is estimated when $A > A_m$

$$I_D \geq 0.65(P_t - P)[1 - A_m/A]/\rho \quad (12-29)$$

This value is imposed as a lower local limit on I_D obtained by integrating Eq. (12-27) from the inlet. The local passage curvature, κ_m , is used to estimate I_C as

$$I_C = |\kappa_m|(P_t - P)C_m/(13\rho C) \quad (12-30)$$

$$\kappa_m = -\frac{d\phi}{dm} \quad (12-31)$$

A simple one-seventh-power-law velocity profile is used as the boundary layer approximation, since a one-dimensional flow analysis really does not provide an adequate basis for modeling boundary layer shape factors in any reasonable fashion. The original centrifugal compressor version relies on the wall friction effects on the tangential momentum balance as a basis for estimating boundary layer growth. This is not suitable for the exhaust diffuser, since cases where there is no tangential velocity component must be expected. Aungier [2] replaced that part of the analysis by using the meridional velocity profile with a simple flat-plate estimate of the boundary layer growth, including adjustment for variations in radius and the boundary layer edge meridional momentum. Pai [49] shows that turbulent boundary layer growth along a flat plate can be estimated from

$$\frac{d\delta}{dm} \approx 5c_f \quad (12-32)$$

This is generalized to the annular passage with two end-wall boundary layers in the form

$$\frac{d[r b \rho C_m^2 (2\delta/b)]}{dm} = 10c_f \rho r C C_m \quad (12-33)$$

The radius and the boundary layer edge meridional momentum corrections in this equation are similar to momentum thickness corrections of Eq. (3-43). This follows from the approximation that the boundary layer shape factor is constant, which requires that the ratio of the boundary layer thickness to the momentum thickness be constant. The boundary layer thicknesses estimated from Eq. (12-33) must be limited by the fully developed viscous flow profile condition, i.e., $2\delta \leq b$.

The fractional area blockage due to the two end-wall boundary layers will be designated as B_{BL} . The boundary layer blockage for one-seventh power law profiles can be shown to be

$$B_{BL} = (2\delta/b)/8 \quad (12-34)$$

For the exhaust diffuser, it must also be recognized that viscous blockage may increase substantially if the rate of diffusion becomes excessive, i.e., if the maximum stall-free local passage area, A_m , is exceeded. If that occurs, it is assumed that further diffusion of C_m is suppressed by a minimum blockage, B_{SEP} , where

$$B_{SEP} = 0 ; \quad A \leq A_m \quad (12-35)$$

$$B_{SEP} = 1 - A_m/A ; \quad A > A_m \quad (12-36)$$

B_{SEP} can be imposed as a lower limit on the blockage estimated from Eq. (12-34), but it has been found that a smooth transition between these two values is obtained from the following empirical equation.

$$B = 1 - (1 - B_{SEP})(1 - B_{BL} + B_{SEP}^2) \quad (12-37)$$

Solution of the governing equations also requires an empirical model for the skin friction coefficient. For fully developed viscous flow, Eqs. (9-6) through (9-12), as illustrated in figure 9-2, provide an appropriate model. The fully developed flow model can also be applied to boundary layer flows simply by replacing the hydraulic diameter, d , with 2δ . That is the approach used in this analysis.

The mean-line performance analysis divides the diffuser passage into a series of equal-spaced grid points along the mean-line meridional coordinate, m , illustrated in figures 12-6 and 12-7. The governing equations and empirical models are cast in finite-difference form and integrated along m to obtain the distribution of all mean-line flow parameters through the diffuser. The flow data at the diffuser exit defines the overall diffuser performance.

The extensive qualification of the original formulation for the various components of centrifugal compressors does not provide confirmation of the prediction accuracy for the zero-swirl, thin boundary layer modifications incorporated to extend the analysis to the exhaust diffuser application. Some confirmation can be obtained by comparing experimental data from two-dimensional diffusers with predictions for equivalent annular diffusers. Figures 12-8 and 12-9 show that type of comparison with the experimental data

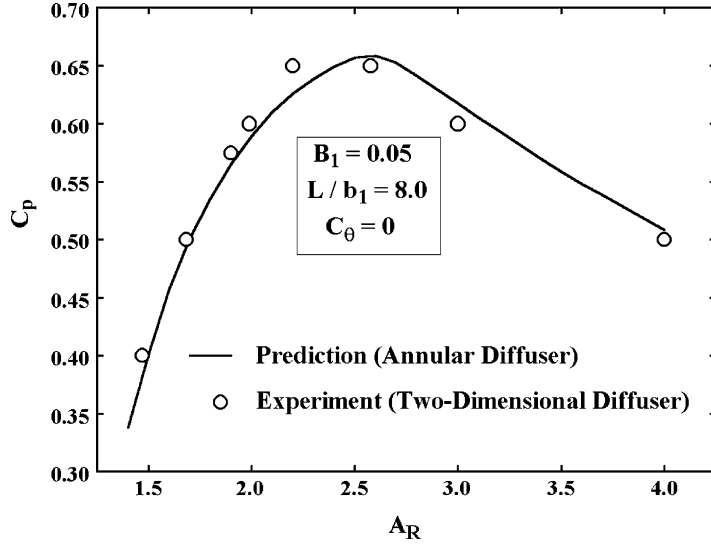


FIGURE 12-8. Qualification with Constant Length

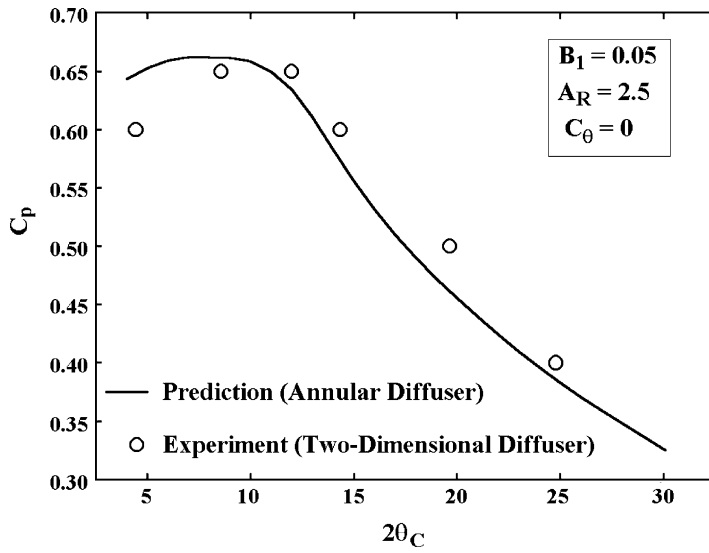


FIGURE 12-9. Qualification with Constant A_R

from figure 4(d) of Reneau et al. [92]. Predictions were generated for constant area ratio and for constant dimensionless diffuser length. The annular diffusers had a constant hub radius with a conical shroud wall. The inlet conditions were selected to match the Reynolds number and Mach number levels of the experiments. The values of the constant parameters used were selected to intersect at the peak static pressure recovery condition defined by the experiments. It is seen that the performance predictions are in rather good agreement with the experiments. Hence, the performance analysis appears to be rather effective for use on this application. It provides a method to investigate the influence of the detailed passage geometry and swirl velocity for a very broad range of diffuser configurations. These effects cannot be evaluated from published diffuser maps or by the approximate performance analysis used to size the diffuser.

Chapter 13

TWO-DIMENSIONAL ANALYSIS OF THE FLOW IN THE BLADE-TO-BLADE PLANE

Prediction of the flow through cascades of blades is fundamental to all aspects of turbomachinery aerodynamic design and analysis. The flow through the annular cascades of blades in any turbomachine is really a three-dimensional flow problem. But the simpler two-dimensional blade-to-blade flow problem offers many advantages. It provides a natural view of cascade fluid dynamics to help designers develop an understanding of the basic flow processes involved. Indeed, very simple two-dimensional cascade flow models were used in this educational role long before computational methods and computers had evolved enough to produce useful design results.

Today, blade-to-blade flow analysis is a practical design and analysis tool that provides useful approximations to many problems of interest. Inviscid blade-to-blade flow analysis addresses the general problem of two-dimensional flow on a stream surface in an annular cascade as discussed in chapter 3. Two-dimensional boundary layer analysis can be included to provide an approximate evaluation of viscous effects. That approach ignores the secondary flows that develop due to the migration of low momentum boundary layer fluid across the stream surfaces. Its accuracy becomes highly questionable when significant flow separation is present. These limitations require particular care when analyzing the diffusing flow in compressor cascades. They are less significant for analysis of the accelerating flow in turbine cascades, but designers still must recognize the approximations and limitations involved.

Previous chapters of this book have emphasized the influence of the blade surface velocity distributions on nozzle row and rotor performance. A graph of the blade surface velocity distributions as a function of distance along the blade surface is often referred to as the blade-loading diagram. The simple blade-loading diagram shown in figure 9-5 was used as the basis for the profile loss models for the nozzle rows and rotors of radial-inflow turbines in chapter 9. The fundamental role of blade loading diagrams for the evaluation of blade detailed aerodynamic designs was discussed in chapters 7 and 11. Blade-to-blade flow analysis provides a practical method to calculate these blade-loading diagrams. Indeed, blade-to-blade flow analysis is an essential part of a modern aerodynamic design system. This chapter reviews useful theoretical methods to model the two-dimensional blade-to-blade flow.

The methods reviewed here are essentially the same as those previously presented in Aungier [1, 2], but the descriptions have been adapted specifically to the turbine application. Aungier [1] provides more detailed guidance relative to efficient numerical analysis techniques to implement these methods. Readers interested implementing these procedures in a numerical analysis may find that original reference helpful.

NOMENCLATURE

- A = area; also a function defined by Eq. (13-20)
- a = sound speed; also a parameter in Eq. (13-51)
- B = function defined by Eq. (13-21)
- b = stream sheet thickness
- C = absolute velocity and a function defined by Eq. (13-22)
- c_f = skin friction coefficient
- C_p = specific heat at constant pressure
- D = function defined by Eq. (13-23)
- E = function defined by Eq. (13-24) and the entrainment function
- \vec{e} = a unit vector
- H = total enthalpy and a boundary layer shape factor
- H_k = boundary layer kinematic shape factor
- H_l = a boundary layer shape factor
- h = enthalpy
- I = rothalpy
- K = shape factor of Eq. (13-125)
- M = Mach number = C/a
- m = meridional coordinate
- \dot{m} = mass flow rate
- \vec{n} = unit vector normal to an area element
- P = pressure
- Q = velocity component of Eq. (13-76)
- Re_θ = momentum thickness Reynolds number
- r = radius
- S = blade pitch = $r(\theta_1 - \theta_0)$
- T = temperature
- t = time
- u = general function
- V = volume
- v = general function
- W = relative velocity
- x = distance along a wall
- Y = total pressure loss coefficient
- y = distance normal to a wall
- z = axial coordinate
- α = flow angle
- β = coordinate angle

γ = blade stagger angle
 δ = boundary layer thickness
 δ' = density thickness
 δ^* = displacement thickness
 δ_E = energy thickness
 δ_h = enthalpy thickness
 δ_u = velocity thickness
 η = dimensionless tangential coordinate (figure 13-3)
 θ = polar angle and momentum thickness
 Λ = shape factor of Eq. (13-113)
 μ = stabilizing term and viscosity
 ξ = streamwise coordinate (figure 13-3)
 ρ = density
 Φ = stabilizing term
 ϕ = stream surface slope angle with axial direction
 ψ = stream function
 τ_w = wall shear stress
 ω = rotation speed

Subscripts

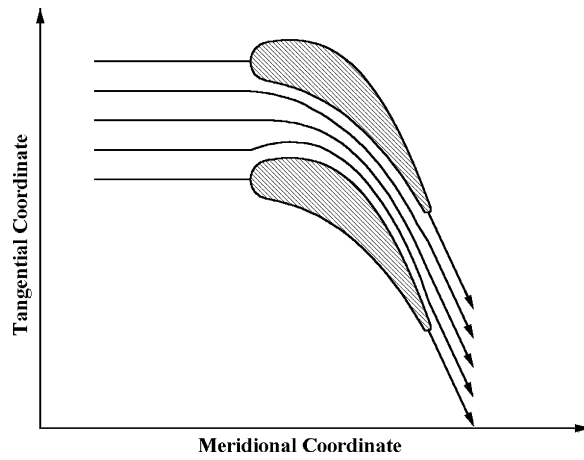
in = cascade inlet condition
 m = meridional component
 out = cascade discharge condition
 q = component normal to ξ coordinate
 t = total thermodynamic condition
 θ = tangential component
 ξ = component tangent to ξ coordinate
 0 = parameter on blade surface θ_0 (figure 13-3)
 1 = parameter on blade surface θ_1 (figure 13-3)

Superscripts

(η) = relative to the η direction
 (ξ) = relative to the ξ direction
 $'$ = relative condition and first derivative
 $''$ = second derivative

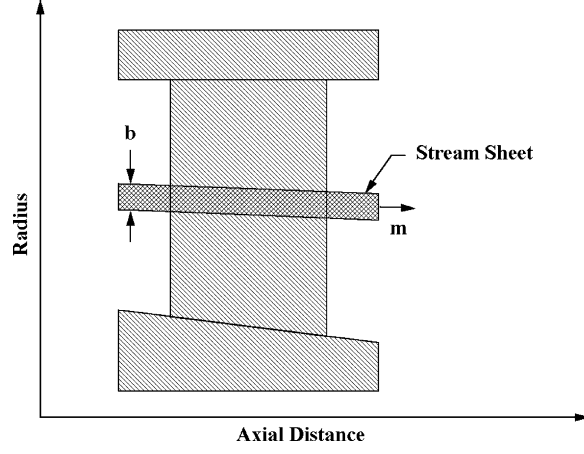
13.1 The Blade-to-Blade Flow Problem

The two-dimensional blade-to-blade flow analysis is conducted on a thin stream sheet between adjacent blades. Figure 13-1 illustrates the streamline pattern on the solution domain to be considered. The solution is accomplished for a single

**FIGURE 13-1. Blade-to-Blade Stream Surface**

blade passage. This is sufficient since the flow is considered to be identical in all blade passages. In the case of radial-inflow turbine impellers with splitter blades, a single blade passage refers to the passage between adjacent full-length blades. Splitter blades must be included in the analysis of the flow in the single full-blade passage.

Figure 13-2 illustrates the stream sheet on a side view of a blade row. A stream sheet is a thin annular passage bounded by two stream surfaces. By definition, a stream surface has no velocity component normal to it and no mass flow across it. Hence, the mass flow rate is constant in the stream sheet. The stream sheet will be assumed to be axisymmetric. That is not a

**FIGURE 13-2. Stream Sheet Geometry**

necessary assumption, but it greatly simplifies the problem. The distributions of the stream sheet thickness, b , and the mean radius, r , are assumed to be known. This reduces the problem to a two-dimensional flow problem. In practice, the stream sheet geometry may be assigned by a suitable approximation, such as a linear variation between known inlet and discharge flow distributions from a performance analysis or a hub-to-shroud flow analysis. That is typically sufficient for axial-flow turbine blades. In chapter 14, a more rigorous method known as a quasi-three-dimensional flow analysis will be described. That approach is typically used for more complex blade passages such as radial-inflow turbine impellers.

The blade-to-blade flow analysis will solve the governing equations for time-steady inviscid flow followed by a blade surface boundary layer analysis to approximate viscous effects. It is assumed that the rothalpy and entropy are both constant at the upstream boundary. From the time-steady form of Eqs. (3-25), (3-28) and (3-29) it can be seen that these assumptions require rothalpy and entropy to be constant over the entire stream sheet. The time-steady form of Eqs. (3-28) and (3-29) govern the conservation of momentum in the stream sheet. Since rothalpy and entropy are constant, it is easily shown that these two equations are identical for the present problem. Indeed, from Eqs. (3-1), (3-29) and (3-63) it can be shown that the component of the absolute vorticity normal to the stream sheet must be zero. This defines a classical potential flow problem governed by conservation of mass, Eq. (3-21), and the irrotational flow condition, Eq. (3-29).

The mathematical character of the governing equations of motion for time-steady inviscid flow introduces a major complication. When the flow is everywhere subsonic ($W < a$), the governing equations are elliptic in form. This presents a classical boundary value problem where the solution is completely determined by conditions imposed on the boundaries of the solution domain. When the flow is supersonic ($W > a$), the governing equations are hyperbolic in form. This type of problem requires some type of marching solution, such as the method of characteristics. When supersonic flow is present, subsonic flow is usually also present in the solution domain. This mixed subsonic-supersonic flow problem requires two solution techniques that must be matched in some fashion. It is now common practice to consider time-unsteady flow in these cases. The governing equations for unsteady inviscid flow are hyperbolic for both subsonic and supersonic flow. This solution technique is commonly called the time-marching or time-dependent technique. The solution is simply advanced in time until it has reached essentially a steady flow prediction. When the time-marching approach is used, the simplifications leading to a potential flow model are no longer valid. For example, Eq. (3-25) must be solved, since rothalpy can no longer be treated as a constant on the stream sheet. Nor are the two momentum equations for the flow in the stream sheet identical for the time-unsteady case. A potential flow analysis can be used for subsonic flow, but a more general method is required for the mixed subsonic-supersonic flow case. These more general methods are often referred to as Euler methods, which includes the time-marching method. A Euler method solves the conservation equations for mass, momentum and energy without simplifying assumptions such as isentropic flow.

13.2 Coordinate System and Velocity Components

Figure 13-3 shows the solution domain for the blade-to-blade flow analysis. The blade surfaces are specified in functional form as $\theta_0(m)$ and $\theta_1(m)$, including suitable upstream and downstream extensions. The coordinate system (ξ, η) is introduced such that blade surfaces correspond to lines of constant η . Note that this is a general (nonorthogonal) coordinate system. The new coordinates are given by

$$\xi = \int_0^m \frac{dm}{\sin \beta} \quad (13-1)$$

$$\eta = \frac{\theta - \theta_0}{\theta_1 - \theta_0} \quad (13-2)$$

This transforms the solution domain into a rectangular domain, where η varies from 0 to 1 as θ varies from θ_0 to θ_1 . The angle, β , between lines of constant η and the tangential direction is given by

$$\cot \beta = \left[\frac{r \partial \theta}{\partial m} \right]_\eta \quad (13-3)$$

From Eq. (13-2) and Eq. (13-3), β at any point in the solution domain can be expressed in terms of the known values on the side boundaries defined by $\theta_0(m)$ and $\theta_1(m)$, i.e.,

$$\cot \beta = \cot \beta_0 + \eta [\cot \beta_1 - \cot \beta_0] \quad (13-4)$$

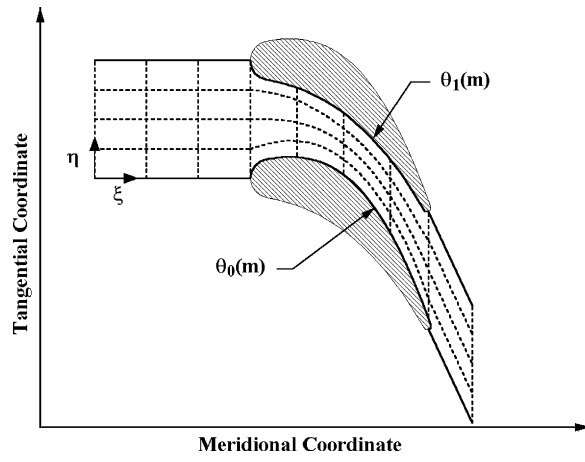


FIGURE 13-3. The Solution Domain

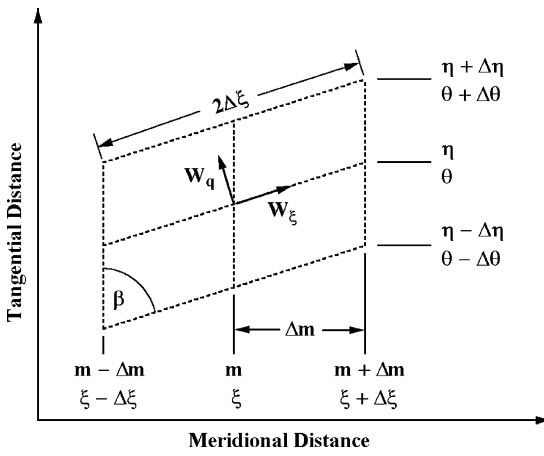
**FIGURE 13-4. A Control Volume**

Figure 13-4 shows a control volume within the solution domain. It also illustrates two special velocity components that are useful for developing the governing equations in the transformed coordinate system. W_ξ and W_q are the velocity components parallel and normal to lines of constant η , respectively. These velocity components are related directly to W_m and W_θ by

$$W_\xi = W_m \sin \beta + W_\theta \cos \beta \quad (13-5)$$

$$W_q = W_\theta \sin \beta - W_m \cos \beta \quad (13-6)$$

$$W_m = W_\xi \sin \beta - W_q \cos \beta \quad (13-7)$$

$$W_\theta = W_q \sin \beta + W_\xi \cos \beta \quad (13-8)$$

13.3 The Potential Flow Solution Procedure

As discussed previously, potential flow analysis on a blade-to-blade stream surface assumes that the absolute flow is time-steady, inviscid and adiabatic, with rothalpy and entropy both constant on this surface. This does not preclude variation of rothalpy and entropy normal to the stream surface. Rothalpy and entropy generally do vary from stream surface to stream surface, which is quite compatible with the present analysis. The governing equations are conservation of mass, Eq. (3-21), and the irrotationality condition, Eq. (3-29). The steady form of these equations could be transformed directly into the (ξ, η) space by developing transformations for the

derivatives from Eqs. (13-1) and (13-2). But a more accurate numerical analysis is obtained by a more fundamental development using the basic control volume shown in figure 13-4. Conservation of mass for this control volume can be stated as

$$2\Delta m \left[\left(\frac{\rho b W_q}{\sin \beta} \right)_{m,\eta-\Delta\eta} - \left(\frac{\rho b W_q}{\sin \beta} \right)_{m,\eta+\Delta\eta} \right] + 2\Delta\eta \left[(S\rho b W_m)_{m-\Delta m,\eta} - (S\rho b W_m)_{m+\Delta m,\eta} \right] = 0 \quad (13-9)$$

The subscripts in Eq. (13-9) identify specific grid points on the control volume of figure 13-4, and the tangential spacing, $S(m)$, is defined by

$$S = r(\theta_1 - \theta_0) \quad (13-10)$$

Taking the limit as Δm and $\Delta\eta$ approach zero, Eq. (13-9) reduces to the following continuity equation.

$$\frac{\partial}{\partial\eta} \left[\frac{\rho b W_q}{\sin \beta} \right] + \frac{\partial(S\rho b W_m)}{\partial m} = 0 \quad (13-11)$$

It can be noted that the continuity equation contains coordinates m and η and velocity components W_q and W_m from two different coordinate systems. While perhaps a little unconventional, this results in a more precise statement of conservation of mass for use in the numerical analysis. Numerical approximations to the governing equations are applied to a finite control volume. More accurate numerical approximations result from using this control volume approach to develop the equations rather than a mathematical transformation of the derivatives in Eq. (3-21). The condition for irrotational absolute flow in the stream surface requires that the component of the absolute vorticity normal to the stream sheet be zero, i.e.,

$$\vec{e}_n \cdot (\vec{\nabla} \times \vec{C}) = \vec{e}_n \cdot [\vec{\nabla} \times (\vec{W} + r\omega \vec{e}_\theta)] = 0 \quad (13-12)$$

Stokes theorem is a convenient method to impose this condition on the control volume. Stokes theorem relates the line integral of the velocity about any closed path to the integral of the normal component of vorticity over the area enclosed by the path. In the rotating coordinate system, Stokes theorem can be applied as

$$\oint_C \vec{W} \cdot d\vec{r} = \int_A \vec{e}_n \cdot (\vec{\nabla} \times \vec{W}) da = - \int_A \vec{e}_n \cdot (\vec{\nabla} \times r\omega \vec{e}_\theta) da \quad (13-13)$$

When applied to the control volume, this yields

$$2\Delta m \left[\left(\frac{W_{\xi}}{\sin \beta} \right)_{m,\eta-\Delta\eta} - \left(\frac{W_{\xi}}{\sin \beta} \right)_{m,\eta+\Delta\eta} \right] + 2\Delta\eta \left[(SW_{\theta})_{m-\Delta m,\eta} - (SW_{\theta})_{m+\Delta m,\eta} \right] = 4\Delta\eta \Delta m \frac{S}{r} \frac{\partial r^2 \omega}{\partial r} \quad (13-14)$$

Taking the limit as Δm and $\Delta\eta$ approach zero, Eq. (13-14) reduces to

$$\frac{\partial}{\partial \eta} \left[\frac{W_{\xi}}{\sin \beta} \right] = \frac{\partial (SW_{\theta})}{\partial m} + 2S\omega \sin \phi \quad (13-15)$$

The angle, ϕ , between a tangent to the stream sheet and the axial direction is given by

$$\sin \phi = \frac{\partial r}{\partial m} \quad (13-16)$$

It is easily shown that the continuity equation can be identically satisfied by defining a stream function, ψ , by

$$\dot{m} \frac{\partial \psi}{\partial m} = -\rho b (W_{\theta} - W_m \cot \beta) \quad (13-17)$$

$$\dot{m} \frac{\partial \psi}{\partial \eta} = S\rho b W_m \quad (13-18)$$

Inside the blade passage, ψ varies from 0 to 1 as θ varies from θ_0 to θ_1 or as η varies from 0 to 1. Since rothalpy is constant on the stream sheet, both conservation of mass and energy are satisfied. The inviscid flow field analysis is reduced to solving the irrotationality condition given by Eq. (13-15). Introducing the stream function, this equation can be written as

$$\begin{aligned} \frac{\partial}{\partial \eta} \left[\frac{\dot{m}(1 + \cot^2 \beta)}{Sb\rho} \frac{\partial \psi}{\partial \eta} - \frac{\dot{m} \cot \beta}{b\rho} \frac{\partial \psi}{\partial m} \right] \\ = \frac{\partial}{\partial m} \left[\frac{\dot{m} \cot \beta}{b\rho} \frac{\partial \psi}{\partial \eta} - \frac{\dot{m} S}{b\rho} \frac{\partial \psi}{\partial m} \right] + 2S\omega \sin \phi \end{aligned} \quad (13-19)$$

This equation can be simplified by introducing the following functions.

$$A(m, \eta) = \dot{m} / (Sb\rho \sin^2 \beta) \quad (13-20)$$

$$B(m, \eta) = \dot{m} \cot \beta / (b \rho) \quad (13-21)$$

$$C(m, \eta) = \dot{m} S / (b \rho) \quad (13-22)$$

$$D(m, \eta) = \frac{\partial A}{\partial \eta} - \frac{\partial B}{\partial m} \quad (13-23)$$

$$E(m, \eta) = \frac{\partial C}{\partial m} - \frac{\partial B}{\partial \eta} \quad (13-24)$$

Substitution of these functions into Eq. (13-19) yields

$$A \frac{\partial^2 \psi}{\partial \eta^2} - 2B \frac{\partial^2 \psi}{\partial \eta \partial m} + C \frac{\partial^2 \psi}{\partial m^2} + D \frac{\partial \psi}{\partial \eta} + E \frac{\partial \psi}{\partial m} = 2S\omega \sin \phi \quad (13-25)$$

Potential flow is a boundary value problem, such that the solution is completely determined by conditions imposed on the boundaries of the solution domain. The boundary conditions are conveniently expressed in terms of ξ and η . On the blade surfaces,

$$\psi(\xi, 0) = 0 \quad (13-26)$$

$$\psi(\xi, 1) = 1 \quad (13-27)$$

For the side boundaries upstream and downstream of the blade passage, the periodicity condition is used. Since the flow is identical in all blade passages, the flow field must repeat in the tangential direction with a period of $\Delta\eta = 1$. This periodic nature of the flow can be used to extend the solution into adjacent passages such that points on these side boundaries can be treated exactly the same as points interior to the solution domain.

$$\psi(\xi, \eta + 1) = \psi(\xi, \eta) + 1 \quad (13-28)$$

$$\rho(\xi, \eta + 1) = \rho(\xi, \eta) \quad (13-29)$$

$$W_m(\xi, \eta + 1) = W_m(\xi, \eta) \quad (13-30)$$

$$W_\theta(\xi, \eta + 1) = W_\theta(\xi, \eta) \quad (13-31)$$

On the upstream and downstream boundaries, the flow angle is required to be constant. The geometry of the side boundaries is defined such that β equals the

local flow angle on these boundaries. From Eqs. (13-1) and (13-17), it is easily shown that the appropriate upstream and downstream boundary condition is

$$\frac{\partial \psi}{\partial \xi} = \sin \beta \frac{\partial \psi}{\partial m} = 0 \quad (13-32)$$

To simplify specification of this boundary condition β is assigned to vary uniformly along the side boundary from the upstream boundary flow angle to the blade leading edge blade camberline angle, and analogously for the downstream boundary. Simple integration of Eq. (13-3) yields $\theta_0(m)$ and $\theta_1(m)$ from these assigned distributions of β , noting that $\beta_0 = \beta_1$ outside the blade passage. A potential flow analysis can be accomplished for virtually any specified flow angles at the upstream and downstream boundaries. But, in reality, these two flow angles are not independent. A prediction of the downstream flow angle for any upstream flow conditions is to be preferred. To accomplish this, some additional constraint is required. Typically, the well-known Kutta condition is applied at the trailing edge. This requires that the velocities on the two sides of the blades must be equal at the trailing edge. Some adjustment is required since the trailing edge nodes are inside the blades. Aungier [1] found that an average of the velocities inside and outside the blades, W_{out} , is appropriate for the Kutta condition, where

$$W_{out} = \frac{1}{2} W + W_m / (\sin \beta_0 + \sin \beta_1) \quad (13-33)$$

An iterative solution is required to determine the downstream flow angle that yields equal values of W_{out} on the two surfaces at the trailing edge. In practice, this can be accomplished as part of the normal solution procedure since an iterative solution is also required to converge on the gas density. The trailing-edge condition simply adds another convergence criterion to an iterative solution that is required anyway.

Eq. (13-25) is solved subject to the boundary conditions while treating the gas density field throughout the solution domain as known, starting with an initial guess for the density field. After the stream function is predicted Eqs. (13-17) and (13-18) are used to compute the velocity field. Then the density field is updated using an appropriate equation of state from chapter 2. The stream function is then recalculated, and the process continued until convergence is achieved. A grid structure is developed over the solution domain, as illustrated in figure 13-3. The spacing between nodes in each direction (Δm and $\Delta \eta$) is constant. Unequal spacing can be used, but this writer's experience has shown that the benefits of unequal spacing do not justify the added complexity and reduced computational speed. Eq. (13-25) is reduced to linear form using standard finite-difference approximations for the derivatives. Designating the meridional and tangential node numbers by

subscripts i and j , respectively, the relevant finite-difference approximations for interior points are

$$\frac{\partial \psi}{\partial m} = \frac{\psi_{i+1,j} - \psi_{i-1,j}}{2\Delta m} \quad (13-34)$$

$$\frac{\partial \psi}{\partial \eta} = \frac{\psi_{i,j+1} - \psi_{i,j-1}}{2\Delta \eta} \quad (13-35)$$

$$\frac{\partial^2 \psi}{\partial m^2} = \frac{\psi_{i+1,j} - 2\psi_{i,j} + \psi_{i-1,j}}{(\Delta m)^2} \quad (13-36)$$

$$\frac{\partial^2 \psi}{\partial \eta^2} = \frac{\psi_{i,j+1} - 2\psi_{i,j} + \psi_{i,j-1}}{(\Delta \eta)^2} \quad (13-37)$$

$$\frac{\partial^2 \psi}{\partial m \partial \eta} = \frac{\psi_{i+1,j+1} - \psi_{i-1,j+1} - \psi_{i+1,j-1} + \psi_{i-1,j-1}}{4\Delta m \Delta \eta} \quad (13-38)$$

Eqs. (5-34) through (5-38) are easily derived using truncated Taylor series expansions of ψ as functions of m and η . The terms D and E in Eqs. (13-23) and (13-24) require approximations for the first derivatives at nodes on the boundary. These can be developed in the same way as the difference equations for interior points. They are

$$\frac{\partial \psi}{\partial m} = \frac{4\psi_{i+1,j} - 3\psi_{i,j} - \psi_{i+2,j}}{2\Delta m} \quad (13-39)$$

$$\frac{\partial \psi}{\partial \eta} = \frac{4\psi_{i,j+1} - 3\psi_{i,j} - \psi_{i,j+2}}{2\Delta \eta} \quad (13-40)$$

$$\frac{\partial \psi}{\partial m} = \frac{3\psi_{i,j} - 4\psi_{i-1,j} + \psi_{i-2,j}}{2\Delta m} \quad (13-41)$$

$$\frac{\partial \psi}{\partial \eta} = \frac{3\psi_{i,j} - 4\psi_{i,j-1} + \psi_{i,j-2}}{2\Delta \eta} \quad (13-42)$$

Substitution of the finite-difference approximations into Eq. (13-25) for any interior node (i, j) yields a simple linear equation for ψ

$$\begin{aligned} \psi_{i,j} + \tilde{A}_{i,j}\psi_{i-1,j} + \tilde{B}_{i,j}\psi_{i+1,j} + \tilde{C}_{i,j}\psi_{i,j-1} + \tilde{D}_{i,j}\psi_{i,j+1} \\ + \tilde{E}_{i,j}[\psi_{i+1,j+1} - \psi_{i+1,j-1} - \psi_{i-1,j+1} + \psi_{i-1,j-1}] = \tilde{Q}_{i,j} \end{aligned} \quad (13-43)$$

The coefficients in Eq. (13-43) are given by

$$\tilde{A}_{i,j} = -\left[\frac{C_{i,j}}{(\Delta m)^2} - \frac{E_{i,j}}{2\Delta m} \right] / \left[\frac{2A_{i,j}}{(\Delta \eta)^2} + \frac{2C_{i,j}}{(\Delta m)^2} \right] \quad (13-44)$$

$$\tilde{B}_{i,j} = -\left[\frac{C_{i,j}}{(\Delta m)^2} + \frac{E_{i,j}}{2\Delta m} \right] / \left[\frac{2A_{i,j}}{(\Delta \eta)^2} + \frac{2C_{i,j}}{(\Delta m)^2} \right] \quad (13-45)$$

$$\tilde{C}_{i,j} = -\left[\frac{A_{i,j}}{(\Delta \eta)^2} - \frac{D_{i,j}}{2\Delta \eta} \right] / \left[\frac{2A_{i,j}}{(\Delta \eta)^2} + \frac{2C_{i,j}}{(\Delta m)^2} \right] \quad (13-46)$$

$$\tilde{D}_{i,j} = -\left[\frac{A_{i,j}}{(\Delta \eta)^2} + \frac{D_{i,j}}{2\Delta \eta} \right] / \left[\frac{2A_{i,j}}{(\Delta \eta)^2} + \frac{2C_{i,j}}{(\Delta m)^2} \right] \quad (13-47)$$

$$\tilde{E}_{i,j} = \left[\frac{B_{i,j}}{2\Delta m \Delta \eta} \right] / \left[\frac{2A_{i,j}}{(\Delta \eta)^2} + \frac{2C_{i,j}}{(\Delta m)^2} \right] \quad (13-48)$$

$$\tilde{Q}_{i,j} = -[2S\omega \sin \phi] / \left[\frac{2A_{i,j}}{(\Delta \eta)^2} + \frac{2C_{i,j}}{(\Delta m)^2} \right] \quad (13-49)$$

Numerical solution of the linearized stream function equation can be accomplished with a relaxation technique, e.g., Katsanis [106, 107] or a matrix method, e.g., Smith and Frost [108] and Aungier [1]. This writer has used both methods and found the matrix method to be superior in both computational speed and reliability. In the matrix method, Eq. (13-43) is used to develop equations for all nodes, resulting in a matrix equation, where the major matrix is a square matrix with the number of rows and columns equal to the number of nodes. It is a very sparse matrix, having nonzero values only in a band about its diagonal, so that a rather small number of values actually need to be stored in the computer's memory. Aungier [1] provides a rather detailed description of a very efficient matrix solution for this problem.

After each solution for the stream function, the density field must be updated using a new velocity field estimate from Eqs. (13-17) and (13-18). Since rothalpy is constant on the stream sheet, Eqs. (3-11) and (3-13) require

$$h = H' - \frac{1}{2}W^2 = I + \frac{1}{2}(r\omega)^2 - \frac{1}{2}W^2 \quad (13-50)$$

Since entropy is constant on the stream sheet, all thermodynamic properties can be calculated as a function of (h, s) using an appropriate equation of state from chapter 2. While conducting iterations to converge on the density field, convergence on a discharge flow angle to satisfy the trailing edge Kutta condition is also accomplished. As long as the flow is subsonic, this procedure of lagging the density solution one iteration behind the stream function

solution offers excellent numerical stability and rapid convergence. But when supersonic velocities are encountered, the solution becomes unstable and will almost always diverge. Blade-to-blade flow problems involving local patches of supersonic flow are often encountered in turbomachinery. The usefulness of a potential flow analysis is greatly increased if it is extended to be capable of addressing these transonic flow cases. This can be accomplished by readjusting the mass flow rate and speed or the inlet total sound speed such that the inlet velocity triangle is the same as for the actual problem but all velocities are subsonic. After solving the subsonic flow problem, the streamline pattern is assumed to be correct, and some type of streamline curvature numerical technique can be used to calculate the flow for the actual inlet conditions. Katsanis [107] is a good example of this type of extension of a potential flow solution. The weakness in that approach is that the resulting flow field no longer satisfies the irrotationality condition. Aungier [1] presents a better technique that can predict an irrotational flow field that also conserves mass when local patches of supersonic flow are present. The inlet total sound speed is adjusted to reduce all velocities to subsonic values. At the same time, the stream sheet thickness distribution is adjusted such that conservation of mass for the subsonic problem yields a velocity field that also conserves mass for the actual transonic flow problem when the actual inlet conditions and stream sheet thickness distribution are used. Thus, when the subsonic flow solution is obtained, it is only necessary to accomplish a final update of all thermodynamic data with the predicted velocity field to satisfy all governing equations for the transonic flow case. Implementation of this extension to the analysis is straightforward, but depends to some degree on the equation of state used in the analysis. Aungier [1] provides an illustration of its implementation for the special case of a calorically and thermally perfect gas.

The grid structure near the leading and trailing edges of the blades has a significant influence on the numerical stability of the solution procedure. Figure 13-5 illustrates two methods of locating the grid near the leading edge.

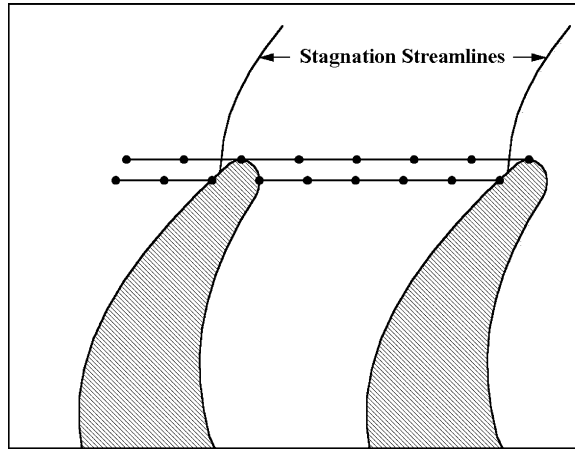
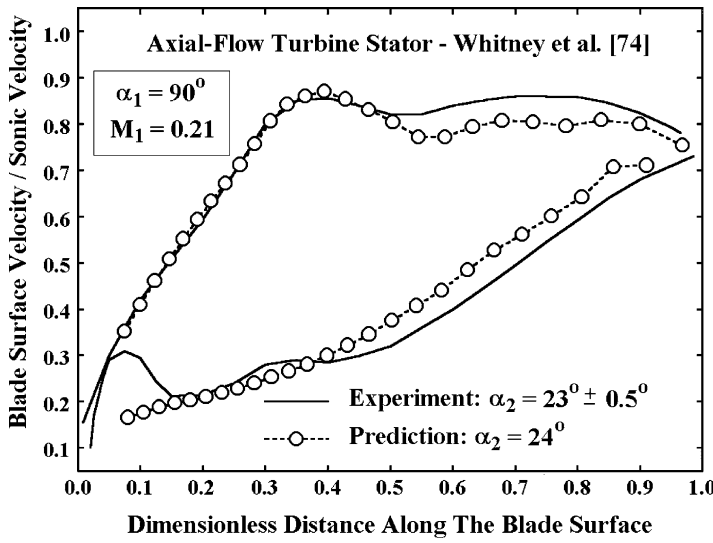
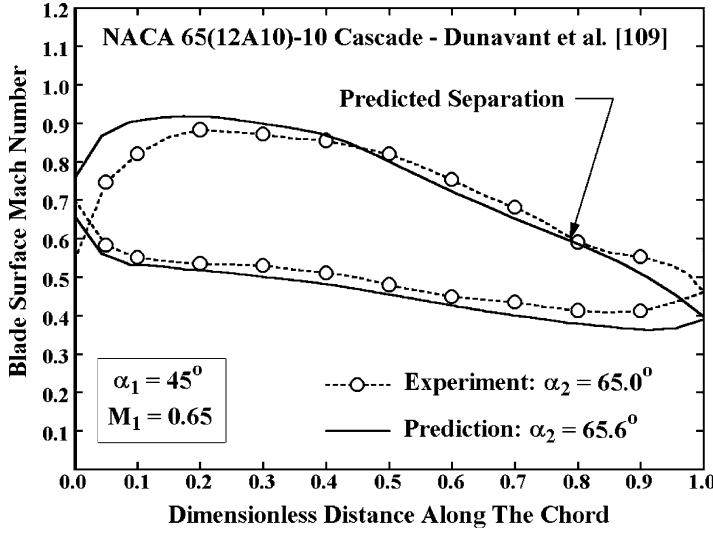


FIGURE 13-5. Leading Edge Grid Structure

In one case, the first nodes on the blade surface are outside the passage, touching the blade at a single point. The other case locates the first nodes on the blade surfaces inside the passage with a node on each blade surface. Experience has shown that the first method can result in local numerical instability, while when the second method is used that problem is almost never experienced. The cause of instability has been traced to the behavior of the stagnation streamline, coupled with the finite-difference approximations for derivatives with respect to η used at blade surface points. In the illustration in figure 13-5, it is seen that the stagnation streamline passes between the blade surface and the node next to the surface when the leading edge nodes are outside the passage. Since ψ has the same value on the stagnation streamline and the blade surface, a difference approximation to the tangential derivative will provide a poor estimate. Furthermore, special logic must be included to decide which tangential difference approximation should be used for the node on the blade, i.e., Eq. (13-40) or (13-42). In the case illustrated, nodes to the right of the leading edge node should be used, i.e., Eq. (13-40). Even when the proper difference approximation is selected, minor changes in gas density at the leading edge can induce the stagnation streamline to move, possibly even making it shift to the opposite blade surface. It is not uncommon for this to result in an oscillation on successive iterations, all occurring very local to this region, such that a converged solution is never realized. This problem can be alleviated by numerical damping or by using a finer grid point spacing near the leading edge. A simpler and more effective approach is to move the leading edge nodes inside the blade passage as illustrated in figure 13-5. This removes the ambiguity regarding the direction to be used for the surface derivatives. When that is done the local oscillation problem almost never occurs. It is a very simple method to avoid a tendency toward local numerical instability near the leading and trailing edges.

Many of the illustrations shown in the previous figures show axial-flow turbine blades for convenience. But it should be noted that this potential flow analysis is applicable to radial-flow and mixed-flow blades as well. Indeed, this blade-to-blade flow analysis was originally developed for application to centrifugal compressors. It has been used for many years in that role as has been demonstrated in Aungier [1]. Its role in radial-inflow turbine design should be evident from the discussions in chapter 11.

Figure 13-6 shows a comparison of a blade loading prediction with experimental data for an axial-flow turbine stator row reported by Whitney et al. [74]. The analysis is unable to fully resolve the flow behavior near the thick leading edge, but otherwise shows rather good agreement with the experiment. The blade row discharge flow angle prediction is also in good agreement with the experiment. The trailing edge Kutta condition used by the potential flow analysis yields good results for this case. Figure 13-7 shows a similar comparison for an axial-flow compressor cascade test reported by Dunavant et al. [109]. Good agreement between predictions and experiment is evident, both for the blade loading and the discharge flow angle. Some deviation in the blade-loading diagram is seen near the trailing edge. In this case, the boundary layer analysis described subsequently in this chapter predicts boundary layer separation is expected at almost exactly the point where the prediction starts to deviate from

**FIGURE 13-6. Turbine Cascade Results****FIGURE 13-7. Compressor Cascade Results**

the experimental data. The expected consequence of boundary layer separation is to suppress the blade's capability for further diffusion. The experimental data appear to be consistent with that premise. Figure 13-8 shows a comparison of predictions with experiment for the same compressor cascade with a higher inlet Mach number. In this case, the flow field contains a significant patch of supersonic flow on the blade suction surface. This case illustrates the value of

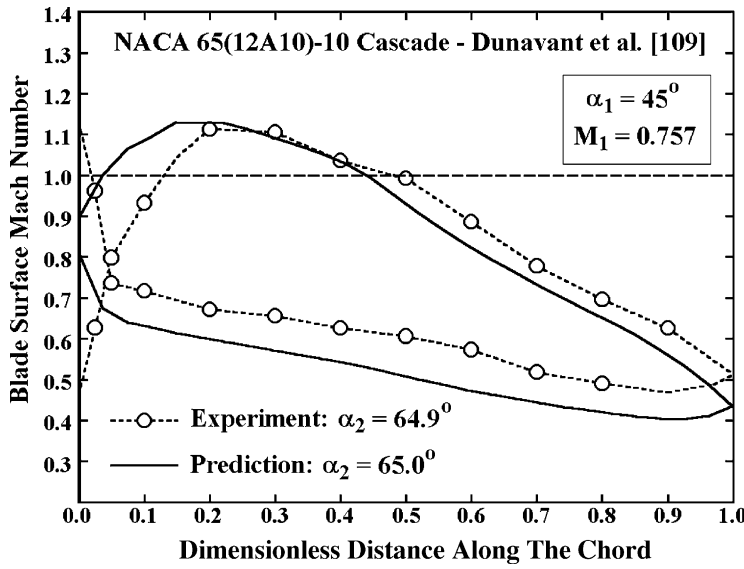


FIGURE 13-8. Transonic Compressor Cascade Results

the transonic extension to the potential flow analysis. It yields a rather accurate estimate of the blade loading for a problem that could not be solved by a potential flow analysis without that extension.

For Mach number levels through the low transonic, this potential flow analysis is an excellent method for blade loading evaluation. It is computationally very fast, highly reliable and very easy to use. This writer considers it to be the method of choice whenever the Mach number level is not too high for it to converge. As a general rule, blade-loading predictions close to the leading edge should always be viewed with some skepticism. In part, this is related to the problem of resolving the location of the stagnation streamline discussed previously in this chapter. But in other respects, this blade-to-blade flow analysis provides excellent support for the detailed aerodynamic design of turbine or compressor blades.

13.4 A Linearized Potential Flow Procedure

Aungier [1, 2, 90] developed a simplified blade-to-blade flow analysis based on a linearized version of the general potential flow analysis described in the previous section. This analysis is exceptionally fast and has consistently achieved surprising accuracy for the thin blades typically used in compressors. It is generally equally effective for radial-inflow turbine impellers, which also employ relatively thin blades. Its accuracy is far more suspect for the relatively thick airfoils common to other turbine applications. The major advantage that is offered by this linearized method is its computational speed. Its primary purpose is to support the exceptionally efficient quasi-three-dimensional flow

analysis described subsequently in chapter 14. It is widely used in this writer's compressor design and analysis system. But its role in turbine aerodynamic design and analysis is largely limited to radial-inflow turbine impeller design as previously described in chapter 11. It is convenient to describe the linearized analysis in this chapter since it is nearly identical to the general potential flow analysis described in the previous section.

The linearized potential flow analysis uses the following approximation for the stream function.

$$\psi(m, \eta) = a(m)[\eta - \eta^2] + \eta^2 \quad (13-51)$$

Substituting Eq. (13-51) into Eq. (13-18) yields

$$\rho W_m = \dot{m}[a + 2(1-a)\eta]/b \quad (13-52)$$

Hence, Eq. (13-51) assumes a linear variation of ρW_m with η . Eq. (13-15) is solved in integral form. Since $W = W_\xi$ on the blade surfaces, this requires

$$\frac{W_1}{\sin \beta_1} - \frac{W_0}{\sin \beta_0} = \int_0^1 \frac{\partial SW_\theta}{\partial m} d\eta + 2S\omega \sin \phi \quad (13-53)$$

On the blade surfaces, the velocity normal to the surface must be zero. Hence, blade surface velocities must satisfy the following constraint.

$$W = \frac{W_m}{\sin \beta} = \frac{1}{\sin \beta} \frac{\dot{m}}{Sb\rho} \frac{\partial \psi}{\partial \eta} \quad (13-54)$$

Combining Eqs. (13-51), (13-53) and (13-54) supplies the terms on the left-hand side of Eq. (13-53).

$$\frac{W_1}{\sin \beta_1} = \frac{\dot{m}(2-a)}{Sb\rho \sin^2 \beta_1} \quad (13-55)$$

$$\frac{W_0}{\sin \beta_0} = \frac{\dot{m}a}{Sb\rho \sin^2 \beta_0} \quad (13-56)$$

From Eqs. (13-17), (13-18) and (13-51)

$$SW_\theta = \dot{m}[\cot \beta(a - 2a\eta + 2\eta) - a'S(\eta - \eta^2)]/(b\rho) \quad (13-57)$$

The prime notation denotes the total derivative with respect to m . Similar to the two-dimensional potential flow analysis, the stream function solution is accomplished assuming that the density field is known. It is convenient to define the following functions.

$$u(m, \eta) = \dot{m} \cot \beta / (b \rho) \quad (13-58)$$

$$v(m, \eta) = \dot{m} S / (b \rho) \quad (13-59)$$

Differentiating Eq. (13-57) and introducing the functions u and v yields

$$\frac{\partial SW_\theta}{\partial m} = \frac{\partial u}{\partial m} (a - 2a\eta + 2\eta) + (1 - 2\eta)ua' - (va'' + \frac{\partial v}{\partial m}a')(\eta - \eta^2) \quad (13-60)$$

A three-point difference approximation to the integral of any function $F(\eta)$ is easily obtained from a truncated Taylor series expansion as a function of values of F at $\eta = 0, 0.5$ and 1 . Using an overbar to designate parameters at $\eta = 0.5$, the difference approximation is

$$\int_0^1 F(\eta) d\eta = (F_0 + 4\bar{F} + F_1)/6 \quad (13-61)$$

After some tedious algebra, the integral term in Eq. (13-53) is given by

$$\int_0^1 \frac{\partial SW_\theta}{\partial m} d\eta = [au'_0 + u_0a' + 4\bar{u}' - \bar{v}a'' - \bar{v}'a' + u'_1(2-a) - u_1a']/6 \quad (13-62)$$

Combining Eqs. (13-53), (13-55), (13-56) and (13-62) yields a simple linear differential equation.

$$a'' + Ad' + Ba = C \quad (13-63)$$

The parameters A , B and C are functions of m , only, given by

$$A(m) = [\bar{v}' - u_0 + u_1]/\bar{v} \quad (13-64)$$

$$B(m) = \frac{u'_1 - u'_0}{\bar{v}} - \frac{6}{\bar{v}S^2} \left[\frac{v_1}{\sin^2 \beta_1} + \frac{v_0}{\sin^2 \beta_0} \right] \quad (13-65)$$

$$C(m) = \frac{2u'_1 + 4\bar{u}' + 12\omega \sin \phi}{\bar{v}} - \frac{12v_1}{\bar{v}S^2 \sin^2 \beta_1} \quad (13-66)$$

The solution of Eq. (13-63) requires boundary conditions at the blade leading and trailing edges. The leading edge boundary condition follows from the known inlet angular momentum supplied by the upstream flow, $W_{\theta,in}$.

Integrating W_θ across the passage at the leading edge using Eq. (13-61) yields the following leading edge boundary condition.

$$a' + a[u_1 - u_0]/\bar{v} = [4\bar{u} + 2u_1 - 6SW_{\theta,in}]/\bar{v} \quad (13-67)$$

The Kutta condition is again used as the trailing edge boundary condition, i.e., $W_0 = W_1$ at the trailing edge. From Eqs. (13-55) and (13-56), the trailing edge boundary condition is

$$a = 2 \sin \beta_0 / [\sin \beta_1 + \sin \beta_0] \quad (13-68)$$

Using the finite-difference approximations previously introduced, Eq. (13-63) is cast in finite-difference form to develop a matrix equation for solution. This results in a simple tri-diagonal matrix, except for the equation at the leading edge point, which contains one extra term. Inversion of a tri-diagonal matrix is a rather trivial numerical analysis problem. This results in an exceptionally efficient blade-to-blade flow analysis. The iteration process to update the gas density field follows the same process as that for the two-dimensional potential flow, and the same transonic flow extension is incorporated. Aungier [1] provides a more detailed description of the numerical analysis used to implement this model.

Figure 13-9 shows a comparison of blade-loading diagrams predicted by the linearized and general potential flow analyses for the nozzle blade design evaluated previously in figure 11-1. The linearized method provides a reasonable approximation but generally should not be relied on for blade loading

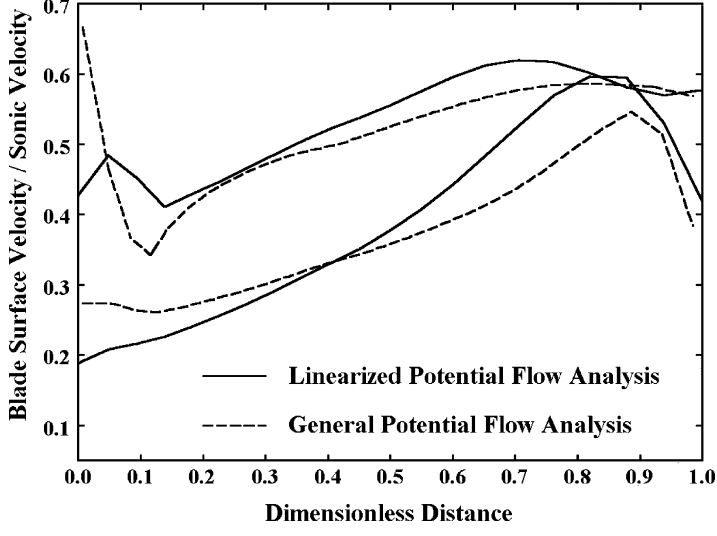


FIGURE 13-9. Blade-Loading Diagram Comparison

evaluation of the relatively thick airfoil shapes commonly used for turbines. For the relatively thin blades used in radial-inflow turbine impellers, the accuracy of the linearized method is usually excellent as was illustrated in figures 11-16 and 11-19. The primary role of this linearized potential flow analysis in the quasi-three-dimensional flow analysis of chapter 14 is to define the streamwise variation of the average angular momentum of the fluid. Even for the airfoil blades, its accuracy is sufficient to accomplish that quite well. Typical practice is to provide a direct and automated interface from the quasi-three-dimensional flow analysis to the two-dimensional blade-to-blade analysis to obtain more accurate blade loading predictions for any stream surfaces of special interest to the designer. When the quasi-three-dimensional flow analysis has been completed, the stream sheet geometry and flow conditions are well defined for input to the more accurate two-dimensional method. This process is illustrated in the flow chart in figure 11-20.

13.5 The Time-Marching Solution Procedure

The potential flow method can be applied to a very wide range of blade-to-blade flow problems, particularly with the transonic flow extension. But when Mach numbers become too high, a more general analysis technique is needed. That is often true for turbine blade rows, which may operate choked with complex imbedded shock and expansion wave patterns at the discharge. The time-marching method provides a more general solution capability that is suitable for subsonic, supersonic or mixed subsonic-supersonic flow problems. Von Neumann and Richtmyer [110] suggested this method in 1950 for treating flows with imbedded shock waves. Lax [111] and Lax and Wendroff [112] developed the technique further, but its practical use had to wait for computers with sufficient speed and capacity to evolve. By the late 1960s, practical use of the method to predict the flow field about hypersonic reentry vehicles became feasible. This writer had the good fortune to be in the right place at the right time to participate in that development, e.g., Aungier [113–116]. Following its successful application to the reentry problem, investigators recognized its advantages for the blade-to-blade flow problem. Gopolakrishnan and Bozzola [117] contributed an important investigation relative to proper specification of boundary conditions for time-dependent blade-to-blade flow analysis in 1973. Denton [118] published a time-dependent blade-to-blade flow analysis in 1982, which has been widely used for this application.

The time-marching technique of Aungier [114–116] has also been adapted to this application. Since many of the original references would be difficult to obtain today, Aungier [1] provides a detailed description of fundamental fluid mechanics used to develop the technique. An abbreviated description of the technique is provided in this chapter. This includes sufficient detail to understand the method or even to implement it. Readers interested in a more detailed background on the development of the method should refer to Aungier [1].

The time-marching solution will be accomplished using the same solution domain, velocity components and coordinate system as previously used for the potential flow analysis, i.e., figure 13-3 and Eqs. (13-1) through (13-8).

The governing equations are Eqs. (3-21), (3-22), (3-23) and (3-25). In this case, the governing equations are solved over the stream sheet in their full time-unsteady form. The solution will be advanced in time until the flow becomes approximately steady with time. This actually results in an asymptotic approach to the steady-state solution. Consequently, a true steady-state solution cannot actually be achieved. Rather, the solution is advanced in time until variations with time are considered negligible. Common practice is to simply transform the derivatives in the governing equations so they can be solved them in the (ξ, η) coordinate system. As previously discussed for the potential flow analysis, more accurate numerical approximations are obtained when the governing equations are developing specifically for the control volume to be used in the solution. This is accomplished by applying the integral form of the equations of motion to the control volume in figure 13-4. The integral form of the continuity, momentum and energy equations for inviscid, time-unsteady flow are

$$\int_V \frac{\partial \rho}{\partial t} dV + \int_A \rho (\vec{W} \cdot \vec{n}) dA = 0 \quad (13-69)$$

$$\int_V \frac{\partial \rho \vec{W}}{\partial t} dV + \int_A \rho \vec{W} (\vec{W} \cdot \vec{n}) dA + \int_A P \vec{e} (\vec{e} \cdot \vec{n}) dA = \int_V \vec{f} dV \quad (13-70)$$

$$\int_V \left[\rho \frac{\partial H'}{\partial t} - \frac{\partial P}{\partial t} \right] dV + \int_A \rho H' (\vec{W} \cdot \vec{n}) dA = \int_V \rho (\vec{f} \cdot \vec{W}) dV \quad (13-71)$$

V and A denote volume and area integrals, respectively, \vec{n} is a unit vector normal to the area and directed out of the control volume, \vec{e} is a unit vector along \vec{W} and \vec{f} is a body force. The body force is used to account for the Coriolis and centrifugal acceleration terms in the rotating curvilinear coordinate system. After some tedious algebra, application of these integral equations to the control volume yield

$$Sb \frac{\partial \rho}{\partial t} + \frac{\partial}{\partial m} [Sb \rho W_m] + \frac{\partial}{\partial \eta} [b \rho Q] = 0 \quad (13-72)$$

$$\begin{aligned} Sb \frac{\partial \rho W_m}{\partial t} + \frac{\partial}{\partial m} [Sb(\rho W_m^2 + P)] - \cot \beta \frac{\partial bP}{\partial \eta} + \frac{\partial}{\partial \eta} [b \rho Q W_m] \\ = \frac{1}{r} SB \rho \sin \phi (W_\theta + r \omega)^2 + P \frac{\partial Sb}{\partial m} \end{aligned} \quad (13-73)$$

$$\begin{aligned} Sb \frac{\partial \rho W_\theta}{\partial t} + \frac{1}{r} \frac{\partial}{\partial m} [r Sb \rho W_m (W_\theta + r \omega)] + \frac{\partial}{\partial \eta} [b(\rho Q W_\theta + P)] \\ = r \omega \frac{\partial}{\partial m} [Sb \rho W_m] \end{aligned} \quad (13-74)$$

$$Sb \frac{\partial(\rho I - P)}{\partial t} + \frac{\partial}{\partial m}[Sb\rho W_m I] + \frac{\partial}{\partial \eta}[b\rho QI] = 0 \quad (13-75)$$

Following a suggestion by Lax [111], these equations are written in conservation form so that they will be valid when applied across a shock wave. The parameter, Q , is a special velocity component defined to conserve properties at the constant η boundaries of the control cell.

$$Q = W_q / \sin \beta = W_\theta - W_m \cot \beta \quad (13-76)$$

Points on the blade surfaces require special handling since $W=W_\xi$ and $Q=W_q=0$. Applying the integral momentum equation in the ξ direction yields a special momentum equation for points on the blade surfaces.

$$\begin{aligned} Sb \frac{\partial \rho W_\xi}{\partial t} + \frac{\partial}{\partial m}[Sb(\rho W_m W_\xi + P \sin \beta)] + \frac{\partial}{\partial \eta}[b\rho QW_\xi] \\ = P \frac{\partial}{\partial m}[Sb \sin \beta] + Sb\rho \sin \phi \sin \beta r \omega^2 \end{aligned} \quad (13-77)$$

$$W_m = W_\xi \sin \beta \quad (13-78)$$

$$W_\theta = W_\xi \cos \beta \quad (13-79)$$

Eqs. (13-77) through (13-79) replace Eqs. (13-73) and (13-74) for points on the blade surfaces.

The boundary condition on the blade surface is that the velocity normal to the blade surface is zero. This boundary condition is satisfied by Eqs. (13-78) and (13-79). On the side boundaries upstream and downstream of the blade passage, the periodicity condition applies, similar to the potential flow problem. Hence, the solution is extended into adjacent passages so that those points can be treated in the same fashion as any interior point. Boundary conditions for the upstream and downstream boundaries require special care. The number and type of boundary conditions that are applicable depend on how the flow inside the solution domain influences these boundaries. A fundamental property of hyperbolic differential equations is that there are certain characteristic directions along which derivatives of the dependent variables normal to these "characteristics" can be discontinuous. For each characteristic direction, certain dependent variables can be determined by integration along them. Aungier [1] shows that the characteristic directions for the upstream and downstream boundaries are

$$\frac{dm}{dt} = W_m + a \quad (13-80)$$

$$\frac{dm}{dt} = W_m - a \quad (13-81)$$

$$\frac{dm}{dt} = W_m \quad (13-82)$$

A physical interpretation of these characteristics is that information can be transmitted within the flow field by waves traveling at the fluid velocity and waves where the fluid velocity is augmented or opposed by the local acoustic velocity. Aungier [1] shows that the characteristics defined by Eqs. (13-80) and (13-81) determine W_m and P , while the characteristic defined by Eq. (13-82) determines W_θ and I . These characteristics determine the number and type of boundary conditions needed for the upstream and downstream boundaries.

Figure 13-10 illustrates the characteristics at an upstream or downstream boundary when the local value of the meridional velocity component is subsonic. In this case, two of the three characteristics that determine the flow at time $t + \Delta t$ from the flow at the flow at time t lie upstream of the boundary and one lies downstream of the boundary. Hence, if this is an upstream boundary, one parameter on the boundary is determined by the flow in the solution domain and the other three conditions must be assigned as boundary conditions. Since the characteristic for W_θ and I lies outside of the solution domain, both of them must be assigned. A logical choice for the computed dependent variable is density. Then, P and W_m follow directly from the equation of state and the definition of rothalpy if entropy is known. The most logical upstream boundary conditions for this case are W_θ , P_t , and T_t . They are usually known conditions for a blade-to-blade flow analysis and they specify rothalpy and entropy through the equation of state and Eq. (3-10). So, for an upstream boundary with $W_m < a$, the continuity equation will be solved for density. All other dependent

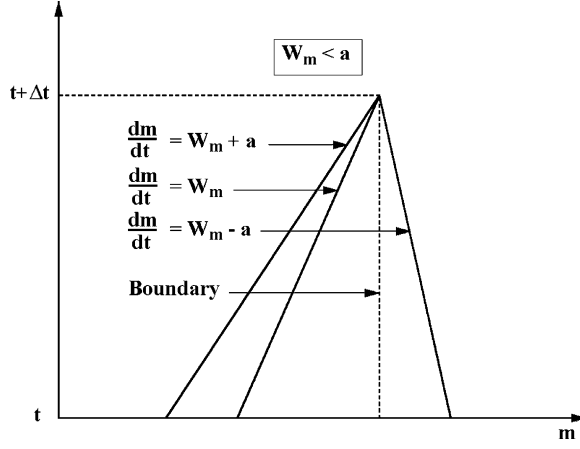


FIGURE 13-10. A Subsonic Characteristic

variables must be computed from the boundary conditions. By contrast, if this is the downstream boundary, only one boundary condition can be imposed and the other three dependent variables must be computed as part of the solution procedure. The usual practice is to specify the discharge static pressure as the boundary condition. It can be convenient to specify the mass flow rate instead, but then the solution procedure must compute the discharge pressure needed to produce the assigned mass flow rate.

Figure 13-11 illustrates the characteristics at an upstream or downstream boundary when the local value of the meridional velocity component is supersonic. In this case, all of characteristics that determine the flow at time $t + \Delta t$ lie upstream of the boundary. Hence, if this is an upstream boundary, all dependent variables must be assigned as boundary conditions. If this is a downstream boundary, all of the characteristics that determine the flow at $t + \Delta t$ lie inside the solution domain. This means that all dependent variables can be computed from the solution so no boundary conditions are required. But

AQ: Au.
Please
check the
sentence.
it usually it is not possible to state that W_m is supersonic at the downstream boundary. That is a very unique case for each set of upstream boundary conditions. Rather, the discharge static pressure is normally specified in all cases. If the solution requires $W_m > a$ to achieve that pressure, the solution procedure must ignore the boundary condition and compute all discharge conditions. Unlike the potential flow analysis no empirical Kutta condition is needed. Indeed, there would be no way to actually impose it. Since the characteristic that determines W_θ always lies upstream of the downstream boundary, W_θ must always be computed as part of the solution. But the Kutta condition is applied indirectly by virtue of the periodicity condition for all solution points downstream of the trailing edge. It is important to note that these boundary condition requirements are not optional. Failure to specify the right number and type of boundary conditions will not produce a valid solution and usually will cause the solution to diverge.

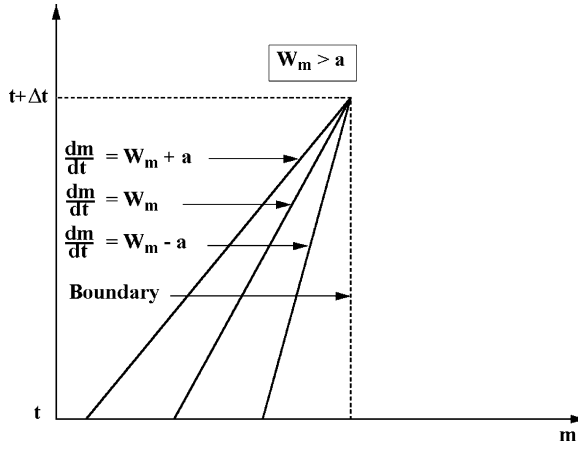


FIGURE 13-11. A Supersonic Characteristic

It is well known that a finite-difference solution of the governing equations that is explicit in time is unconditionally unstable. An explicit numerical solution of the governing equations predicts the flow at time $t + \Delta t$ from the flow at time t . By contrast, implicit numerical solutions seek to use conditions at both t and $t + \Delta t$ for this purpose. Implicit solutions also have critical numerical stability issues, but this book will deal with only the explicit solution procedures. The method used to achieve numerical stability has a critical influence on the accuracy and reliability of a time-marching numerical solution.

Von Neumann and Richtmyer [110] developed a stability analysis specifically for this problem. They used it to develop a stable numerical solution by including additional stabilizing terms in the governing equations similar in form to viscous terms. This approach is often referred to as including artificial viscosity terms. Lax [111] used an averaging scheme for parameters at time t to project data at $t + \Delta t$, which is equivalent to introducing artificial viscosity terms. Lax and Wendroff [112] applied a Taylor series expansion in time to the governing equations to extend them to second-order accuracy in time. Some investigators have extended that approach to higher-order accuracy Taylor series expansions. Regardless of the approach used, stabilizing terms must always be added to the governing equations to achieve a stable explicit finite-difference solution. Unless extreme care is taken, these stabilizing terms can significantly influence the accuracy of the solution. Aungier [114–116] developed a method that has a definite advantage in that regard. It always permits the user of the analysis to reduce the influence of the stabilizing terms as much as necessary to achieve an accurate solution. Reduction of the influence of the stabilizing terms is accomplished at the cost of requiring longer computation times for a steady-state solution. This method was developed by conducting a Von Neumann stability analysis on a simplified one-dimensional momentum equation to determine the minimum allowable magnitude of the stabilizing terms for a specified time step. Aungier [1] describes that stability analysis in considerable detail. Here, only the results will be reviewed. It is convenient to represent any of the governing equations in the general form

$$u_t = v(\xi, \eta, t) + \mu^{(\xi)} u_{\xi\xi} + \mu^{(\eta)} u_{\eta\eta} \quad (13-83)$$

The subscript notation designates the first and second partial derivatives. The last two terms on the right hand side are fictitious terms that are added to the governing equation to achieve numerical stability. To achieve a stable solution for any time step, Δt , the stability analysis shows that the coefficients of the stabilizing terms must satisfy the following conditions.

$$\mu^{(\xi)} \geq \frac{1}{2} (|W_m| + a)^2 \Delta t \quad (13-84)$$

$$\mu^{(\eta)} \geq \frac{1}{2} (|W_\theta| + a)^2 \Delta t \quad (13-85)$$

$$\mu^{(\xi)} \geq \frac{1}{2} [(|W_\xi| + a) \sin \beta]^2 \Delta t \quad (13-86)$$

$$\mu^{(\eta)} \geq \frac{1}{2} [(|W_q| + a) / \sin \beta]^2 \Delta t \quad (13-87)$$

These results yield stable solutions for nearly any blade-to-blade flow problem. But occasional exceptions have been encountered when the grid structure is highly skewed and the node spacing is much smaller in the tangential direction than in the meridional direction. An empirical correction has been developed to extend the validity of the stability analysis to include those cases. After the meridional stabilizing term is established from Eqs. (13-84) and (13-86), the following empirical correction is imposed.

$$\mu^{(\xi)} \rightarrow \mu^{(\xi)} + \frac{1}{2} [(|W_\theta| + a) \cos^2 \beta (\Delta m) / (S \Delta \eta)]^2 \Delta t \quad (13-88)$$

The stabilizing terms have been defined for an arbitrary time step. An upper limit on time step that can be used is imposed by the well-known Courant-Friedricks-Lowy (CFL) stability criterion of Courant et al. [119]. Indeed, the stability analysis confirms that the CFL limit applies. The CFL criterion limits Δt to the time it takes for the fastest relevant characteristic wave to travel between adjacent nodes in the solution field. Once waves from adjacent nodes intersect, the information based the flow at time t ceases to be valid for time $t + \Delta t$. Thus, the maximum value of the time step allowed by this CFL limit is given by

$$\Delta t_{\max} \leq \frac{\Delta m}{|W_m| + a} \quad (13-89)$$

$$\Delta t_{\max} \leq \frac{S \Delta \eta}{|W_\theta| + a} \quad (13-90)$$

The maximum allowable time step is computed on all time iterations by applying Eqs. (13-89) and (13-90) at all nodes in the solution field. The actual time step to be used is specified as some fraction, μ_0 , of the maximum time step.

$$\Delta t = \mu_0 \Delta t_{\max} \quad (13-91)$$

Experience has shown that the following limits should be observed to avoid numerical instability problems.

$$0.1 \leq \mu_0 \leq 0.9 \quad (13-92)$$

If the time derivative in Eq. (13-83) is approximated by a forward finite-difference approximation, the general governing equation is

$$u(\xi, \eta, t + \Delta t) = u(\xi, \eta, t) + [v(\xi, \eta, t) + \mu^{(\xi)} u_{\xi\xi} + \mu^{(\eta)} u_{\eta\eta}] \Delta t \quad (13-93)$$

Eqs. (13-84) through (13-88) show that the coefficients of the stabilizing terms are proportional to Δt . Hence the influence of the stabilizing terms in Eq. (13-93) is second order with respect to Δt . But the influence of the dynamic terms (represented by the general function v) in Eq. (13-93) is first order with respect to Δt . Hence, simply using smaller values of Δt will reduce the influence of the stabilizing terms relative to the dynamic terms. Of course, that will require more time iterations for the solution to approach a steady state. An effective approach is to start the analysis with a fairly large value of μ_0 (typically, 0.75) and steadily reduce it to some smaller value (typically, 0.25) as the solution approaches a steady state. This allows fairly large time steps to be used in the early iterations to accelerate the approach to a steady state, but relatively small time steps when the solution is close to a steady state to reduce the effect of the stabilizing terms.

The stability analysis provides other useful results. It shows that for points on the blade surfaces, no stabilizing term normal to the surface is required, i.e., the last term in Eq. (13-83) is omitted for nodes on the blade surface. Another useful result is obtained when a backward difference approximation is used for the meridional partial derivatives, i.e.,

$$\frac{\partial u}{\partial m} = [u_{i,j} - u_{i-1,j}] / \Delta m \quad (13-94)$$

In that case, the stability analysis shows that when $W_m > a$, no stabilizing term in the ξ direction is required, i.e., the second term on the right-hand side of Eq. (13-83) can be omitted. A similar result is obtained for negative W_m , except a forward difference approximation is used, i.e.,

$$\frac{\partial u}{\partial m} = [u_{i+1,j} - u_{i,j}] / \Delta m \quad (13-95)$$

Hence, supersonic W_m with “upwind” differences requires no stabilizing term in the ξ direction. This permits special procedures to be used on partial derivatives with respect to m to improve the accuracy for very high Mach number flows. This improvement can be very significant for the high Mach numbers often encountered in turbine blades. Experience has shown that these results can be generalized to include any meridional Mach number level by using a weighted-average of forward and backward differences as follows:

$$u_m = F[u_{i+1,j} - u_{i,j}] / \Delta m + (1 - F)[u_{i,j} - u_{i-1,j}] / \Delta m \quad (13-96)$$

$$F = \left[\frac{1}{2} - \frac{2\bar{W}_m |\bar{W}_n|}{(|\bar{W}_m| + \bar{a}) + (|\bar{W}_m| + \bar{a})^2} \right] \quad (13-97)$$

$$\bar{W}_m = \frac{1}{4} [W_m(m + \Delta m, \eta) + 2W_m(m, \eta) + W_m(m - \Delta m, \eta)] \quad (13-98)$$

$$\bar{a} = \frac{1}{4} [a(m + \Delta m, \eta) + 2a(m, \eta) + a(m - \Delta m, \eta)] \quad (13-99)$$

$$\mu^{(\xi)} \rightarrow 4\mu^{(\xi)}F(1-F) \quad (13-100)$$

This procedure uses basic central-difference approximations and the basic stabilizing term form outlined previously when $W_m = 0$. As $|W_m| \rightarrow a$, $F \rightarrow 0$. Hence, for $|W_m| \geq a$, the solution will use an upwind difference approximation for the partial derivative, and the ξ stabilizing term will be zero. As a result, the minimum magnitude of the stabilizing terms allowed for stability is always used. It also results in faster convergence and sharper “shock capturing” when imbedded shock waves form in the flow field. For a period of time, a similar procedure was used relative to partial derivatives and stabilizing terms relative to the η direction. It was found that no significant benefit resulted for high Mach number turbine blade problems, and the procedure occasionally slowed convergence and sometimes produced mild numerical instability. Interaction with the side boundaries and the higher probability that W_θ at a given node may change sign during the solution are believed to be the source of the problem. Presently, this writer uses standard central difference approximations and the basic stabilizing terms relative to the η direction.

The stabilizing terms should be formulated such that their magnitude is expected to be small when the flow approaches a steady state. This has no adverse effect on numerical stability but reduces the stabilizing term influence on the solution. The recommended stabilizing terms to be added to the right-hand side of Eqs. (13-72) through (13-75) and Eq. (13-77), in that order, are

$$\Phi_\rho = Sb[\mu^{(\xi)}\rho_{mm} + \mu^{(\eta)}\rho_{\eta\eta}] \quad (13-101)$$

$$\Phi_m = \mu^{(\xi)}(Sb\rho W_m)_{mm} + \mu^{(\eta)}(Sb\rho W_m)_{\eta\eta} + \Phi_\rho W_m \quad (13-102)$$

$$\Phi_\eta = Sb\rho[\mu^{(\xi)}(rC_\theta)_{mm} + \mu^{(\eta)}(rC_\theta)_{\eta\eta}] / r + \Phi_\rho W_\theta \quad (13-103)$$

$$\Phi_l = Sb\rho[\mu^{(\xi)}I_{mm} + \mu^{(\eta)}I_{\eta\eta}] + \Phi_I I \quad (13-104)$$

$$\Phi_\xi = \mu^{(\xi)}(Sb\rho W_\xi)_{mm} + \Phi_\rho W_\xi \quad (13-105)$$

The terms involving Φ_ρ in Eqs. (13-102) through (13-105) can be shown to be direct corrections for the known error in mass conservation caused by Φ_ρ when solving Eq. (13-72).

The numerical analysis used is a fairly straightforward finite-difference analysis applied to the grid structure illustrated in figure 13-3. The only subtle feature required relates to defining the side boundaries outside of the blade

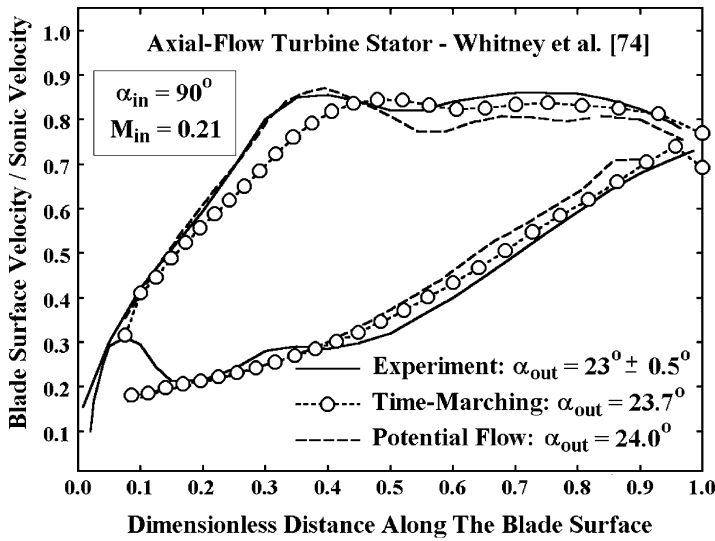


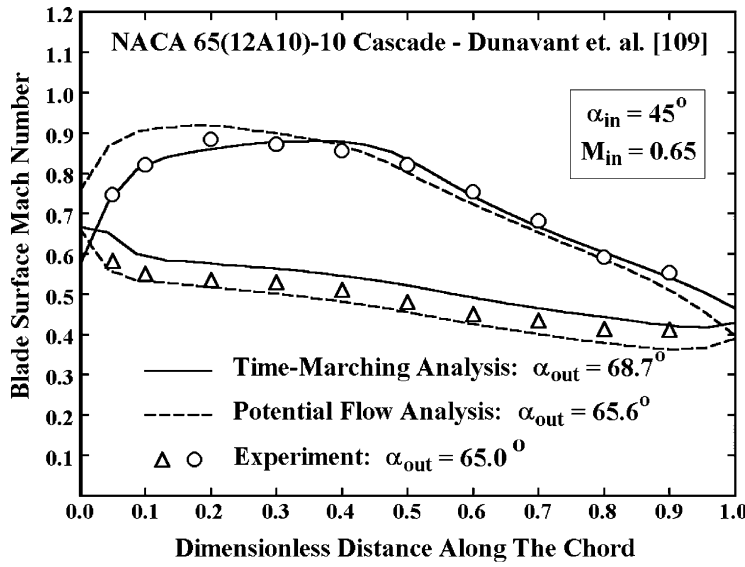
FIGURE 13-12. Turbine Stator Time-Marching Results

passages. When Eq. (13-77) is solved at the blade leading and trailing edges, the finite-difference approximation for the ξ derivative involve parameters at the closest node outside the blade passage. Eq. (13-77) was derived for nodes where $W_q = 0$. As the solution proceeds, the side boundaries outside the blade are continually readjusted such that β is equal to the local flow angle at the closest node outside the blade passage. That ensures that W_q will be zero at this node so that the difference approximation used in Eq. (13-77) will be valid. Aungier [1] provides additional details on the numerical analysis that may be of useful to readers considering implementing this method in a numerical analysis.

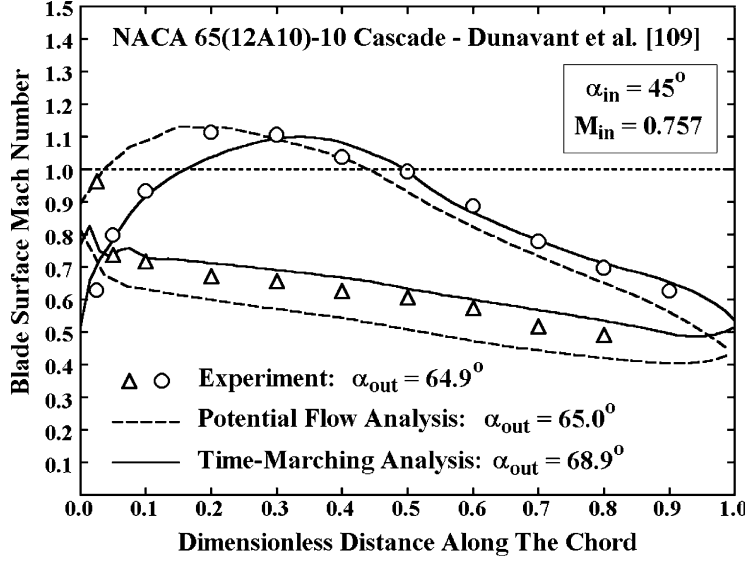
Figure 13-12 compares the blade-loading diagram predicted by the time-marching blade-to-blade flow analysis with experimental results for the turbine stator of Whitney et al. [74]. Results for the potential flow analysis from figure 13-6 are shown as background for comparison. The two analyses yield similar results as would be expected. Each method shows slightly better agreement with experiment in certain regions, but the differences are minor. The discharge flow angle predictions from the two methods are also nearly identical. Hence, for practical purposes, there is little reason to favor either analysis for this case. The principal difference is that the computation time required for the potential flow analysis is significantly less than for the time-marching analysis.

Figure 13-13 shows results for the subsonic compressor cascade previously considered including the potential flow analysis results from figure 13-7. The time-marching analysis blade-loading diagram is in better agreement with the experimental data than the potential flow analysis results. But the discharge flow angles predicted by the potential flow analysis is in better agreement with the experimental value than the time-marching analysis prediction.

Figure 13-14 shows results for the transonic compressor cascade previously considered including the potential flow analysis results from figure 13-8. This

**FIGURE 13-13. The Subsonic Compressor Cascade**

comparison is a little ambiguous due to the fact that this case operates very close to the cascade choke limit. Indeed, the time-marching analysis predicts the cascade choke limit is about 0.5% lower than the mass flow rate reported for the experiment and estimated by the potential flow analysis. This could

**FIGURE 13-14. The Transonic Compressor Cascade**

easily be due to experimental error, but it is more likely due to the influence of the stabilizing terms. Hence, the time-marching analysis results are for the lowest discharge static pressure that could be analyzed without predicting choke. Similar to the subsonic case, the time-marching analysis appears to better estimate the blade-loading diagram, but potential flow analysis provides the more accurate estimate of the discharge flow angle.

The potential flow and time-marching blade-to-blade flow analyses provide the designer with the capability to evaluate the blade-loading distribution for guidance in the detailed aerodynamic design of turbine blades. The potential flow analysis is the simplest and fastest method if the Mach number levels encountered are not too high. In the case of higher Mach number cases, the time-marching method provides an alternative that can be used for nearly any case.

13.6 Blade Surface Boundary Layer Analysis

The blade-loading diagrams predicted by an inviscid blade-to-blade flow analysis provide valuable guidance to the designer. But the primary objective of the detailed blade design process is to avoid adverse viscous flow effects. In particular, the designer seeks to avoid excessive losses and flow separation. The blade-to-blade flow problem is well suited to an approximate evaluation of viscous effects using a blade surface boundary layer analysis. The basic assumption of boundary layer theory is that viscous effects are confined to a thin layer close to the walls. This is usually a valid assumption for the flow in a blade-to-blade stream sheet, particularly for the accelerating flow in turbine blade rows. It is relatively simple to include an efficient two-dimensional boundary layer analysis for this purpose. This provides a qualitative evaluation of viscous effects to supplement the designer's judgment while establishing appropriate blade-loading diagrams. This provides an approximate evaluation, but it ignores the influence of the end-wall boundary layers and pressure gradients normal to the stream sheet. Unlike the inviscid flow, the low momentum boundary layer fluid is unable to balance these normal pressure gradients, causing the boundary layer fluid to migrate across stream sheets. Boundary layer analysis provides a practical and useful method to evaluate boundary layer growth and to identify likely boundary layer separation problems. These phenomena are very important since they govern the level of total pressure loss that will occur as the flow passes through the blade row.

Boundary layer analysis in turbomachinery is most conveniently accomplished by applying the boundary layer equations in integral form. The basic governing equation is the momentum-integral equation derived in chapter 3 as Eq. (3-42). In the context of the present problem, this equation can be written

$$\frac{1}{b} \frac{\partial b \rho_e W_e^2 \theta}{\partial x} + \delta^* \rho_e W_e \frac{\partial W_e}{\partial x} = \tau_w \quad (13-106)$$

The subscript, e , designates the inviscid boundary layer edge parameters, x is the distance along the blade surfaces and τ_w is the wall shear stress. The momentum and displacement thicknesses are defined as

$$\rho_e W_e^2 \theta = \int_0^\delta \rho W (W_e - W) dy \quad (13-107)$$

$$\rho_e W_e \delta^* = \int_0^\delta (\rho_e W_e - \rho W) dy \quad (13-108)$$

The coordinate, y , is measured normal to the wall and δ is the boundary layer thickness. The wall shear stress is usually expressed in terms of the skin friction coefficient, c_f , where

$$c_f = \frac{\tau_w}{\frac{1}{2} \rho_e W_e^2} \quad (13-109)$$

When the boundary layer initially forms on the blade, the flow will be laminar. After sufficient boundary layer growth has occurred, transition to turbulent flow will occur. This is usually the case in turbomachinery, so both laminar and turbulent boundary layer analyses are needed for this application.

The compressible laminar boundary layer analysis of Gruschwitz [120] as reviewed by Schlichting [27] is well suited to this application. This is a generalization of the classical incompressible Karmen-Pohlhausen solution of Pohlhausen [121]. When paired with a turbulent boundary layer entrainment solution, the Gruschwitz method allows a very direct treatment of transition from laminar to turbulent flow by direct application of conservation of mass and momentum. This avoids some rather arbitrary assumptions normally required. The method is based on a universal laminar boundary layer velocity profile in the form

$$\frac{W}{W_e} = C_1 \eta + C_2 \eta^2 + C_3 \eta^3 + C_4 \eta^4 \quad (13-110)$$

$$\eta = \frac{1}{\delta'} \int_0^y \frac{\rho}{\rho_e} dy \quad (13-111)$$

$$\delta' = \int_0^\delta \frac{\rho}{\rho_e} dy \quad (13-112)$$

The boundary layer thickness, δ' , is referred to as the density thickness. Denoting the fluid viscosity by μ , a boundary layer shape factor, Λ , is defined as

$$\Lambda = \frac{\rho_e^2}{\rho_w} \frac{(\delta')^2}{\mu} \frac{dW_e}{dx} \quad (13-113)$$

The coefficients in Eq. (13-110) are calculated to matching the boundary layer edge conditions, i.e.,

$$C_1 = 2 + \Lambda / 6 \quad (13-114)$$

$$C_2 = -\Lambda / 2 \quad (13-115)$$

$$C_3 = \Lambda / 2 - 2 \quad (13-116)$$

$$C_4 = 1 - \Lambda / 6 \quad (13-117)$$

The boundary layer momentum thickness, θ , energy thickness, δ_E , and velocity thickness, δ_W , are given by

$$\frac{\theta}{\delta'} = \frac{37}{315} - \frac{\Lambda}{945} - \frac{\Lambda^2}{9072} \quad (13-118)$$

$$\frac{\delta_E}{\delta'} = \int_0^\delta \frac{\rho W}{\rho_e W_e} \left[1 - \frac{W^2}{W_e^2} \right] dy = \frac{798048 - 4656\Lambda - 758\Lambda^2 - 7\Lambda^3}{4324320} \quad (13-119)$$

$$\frac{\delta_W}{\delta'} = \int_0^\delta \left[1 - \frac{W}{W_e} \right] dy = \frac{3}{10} - \frac{\Lambda}{120} + \frac{FW_e^2}{2c_p T_e} \quad (13-120)$$

The function F in Eq. (13-120) is given by

$$F = 0.232912 - 0.831483 \frac{\Lambda}{100} + 0.650584 \left[\frac{\Lambda}{100} \right]^2 + 17.8063 \left[\frac{\Lambda}{100} \right]^3 \quad (13-121)$$

For the case of adiabatic walls with the Prandtl number equal unity, the boundary layer enthalpy thickness, δ_h , and the displacement thickness, δ^* , are given by

$$\frac{\delta_h}{\delta'} = \int_0^\delta \frac{\rho W}{\rho_e W_e} \left[\frac{h}{h_e} - 1 \right] dy = \frac{W_e^2 \delta_E}{2c_p T_e \delta'} \quad (13-122)$$

$$\delta^* = \delta_h + \delta_W \quad (13-123)$$

Again considering adiabatic walls with the Prandtl number equal unity, the following parameters are introduced for convenience:

$$b_0 = \frac{\rho_e}{\rho_w} = \frac{T'_e}{T_e} \quad (13-124)$$

$$K = \Lambda \left[\frac{\theta}{\delta'} \right]^2 = b_0 \frac{\rho_e \theta^2}{\mu} \frac{dW_e}{dx} \quad (13-125)$$

Gruschwitz [120] shows that

$$\frac{1}{2} c_f = \frac{\mu}{\rho_e W_e \delta'} \left[1 + \frac{\Lambda}{6} \right] \quad (13-126)$$

$$K = \left[\frac{37}{315} - \frac{\Lambda}{945} - \frac{\Lambda^2}{9072} \right]^2 \Lambda \quad (13-127)$$

The above equations are sufficient to permit numerical integration of Eq. (13-106) along x , starting at the leading edge, where $\theta = 0$, to predict θ , δ^* and δ at all other stations. Gruschwitz imposes the following limits on the shape factor Λ .

$$-12 \leq \Lambda \leq 12 \quad (13-128)$$

The most important limit is $\Lambda = -12$, which corresponds to boundary layer separation. Boundary layers on blade surfaces of turbomachines often undergo transition to turbulent flow. Many criteria for boundary layer transition have been proposed none of which can be considered more than an approximation. This writer prefers a transition criterion based on the momentum thickness Reynolds number.

$$Re_\theta = \frac{\rho_e W_e \theta}{\mu} > 250 \quad (13-129)$$

Once the boundary layer undergoes transition to turbulent flow, different empirical relations are required to integrate Eq. (13-106). The entrainment method of Head [35, 36] as adapted by Green [122] to compressible flows is well suited to this application. This requires integration of the entrainment equation, presented previously as Eq. (3-44). In context of the present application, this is written as

$$\frac{\partial b \rho_e W_e (\delta - \delta^*)}{\partial x} = b \rho_e W_e E \quad (13-130)$$

The entrainment function, E , specifies the rate at which mass is entrained into the boundary layer at the boundary layer edge. To integrate Eqs. (13-106) and (13-130), empirical relations are required for E , c_f and the various boundary layer thicknesses as a function of θ and $(\delta - \delta^*)$. Head's entrainment method was developed for incompressible boundary layers based on the following shape factors.

$$H_1 \equiv (\delta - \delta^*) / \theta \quad (13-131)$$

$$H = \delta^* / \theta \quad (13-132)$$

Green [122] recommends using a kinematic shape factor H_k in place of H to generalizing the incompressible boundary layer model to compressible flow.

$$H_k = \frac{1}{\theta} \int_0^\delta \frac{\rho}{\rho_e} \left(1 - \frac{W}{W_e} \right) dy \quad (13-133)$$

For adiabatic walls with the Prandtl number equal unity, Green shows that H_k can be related to H by

$$H = (H_k + 1)T'_t/T_e - 1 \quad (13-134)$$

Solution of the governing equations requires empirical models for E and c_f and to relate H_k and H_l . Many alternate empirical models have been suggested for this purpose. This writer has found the following relations suitable for the present application:

$$H_k = 1 + [0.9/(H_l - 3.3)]^{0.75} \quad (13-135)$$

$$E = 0.025(H_k - 1) \quad (13-136)$$

The skin friction coefficient correlation of Ludwieg and Tillmann [123] is commonly used for incompressible turbulent boundary layer analysis.

$$c_{f,inc} = 0.246 \exp(-1.561H_k) \text{Re}_\theta^{-0.268} \quad (13-137)$$

Green [122] recommends correcting this incompressible flow correlation to compressible flow by

$$c_f = c_{f,inc} H_k (H_k + 1) / [2H_k + H(H_k - 1)] \quad (13-138)$$

These empirical relations are sufficient to integrate Eqs. (13-106) and (13-130), starting at the transition point. At the transition point, the mass and momentum flow in the turbulent boundary layer must match the values computed for the laminar boundary layer. From Eqs. (3-35) and (3-38), this requires

$$(\delta - \delta^*)_{turb} = (\delta - \delta^*)_{lam} \quad (13-139)$$

$$\theta_{turb} = \theta_{lam} \quad (13-140)$$

From the Gruschwitz [120] boundary layer profiles, it can easily be shown that

$$\delta - \delta^* = \delta' \left[\frac{7}{10} + \frac{\Lambda}{120} \right] \quad (13-141)$$

Eq. (13-140) is normally applied at the transition point, along with some assumption on how H changes during transition from laminar to turbulent flow. The Gruschwitz laminar boundary layer model permits a more

fundamental method based on conservation of mass and momentum. This writer uses $H_k \geq 2.4$ as a separation criterion for turbulent boundary layers. During the analysis, the kinematic shape factor is limited to this value to avoid solution divergence and permit the analysis to continue through a separation zone. This is necessary, since it is not uncommon for the boundary layer to reattach, particularly on the pressure surface of the blade.

When boundary layers on the blade surfaces have been computed, it is useful to estimate the total pressure loss coefficient for the cascade from the boundary layer data at the trailing edge. Following Lieblein and Roudebush [87], the total pressure loss coefficient based on the cascade exit velocity pressure can be approximated by

$$Y = \frac{\Delta P_t}{(P_t - P)_{out}} = \frac{2\Theta + (\Delta^*)^2}{(1 - \Delta^*)^2} \quad (13-142)$$

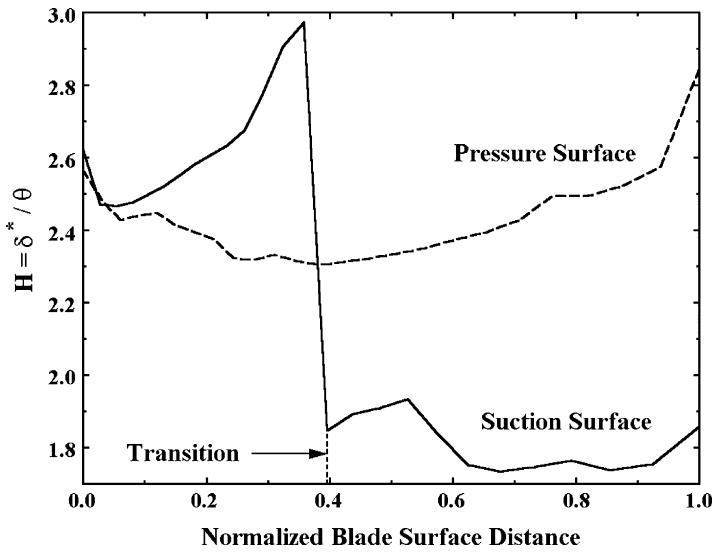
$$\Theta = \frac{\sum \theta}{S \sin \alpha_{out}} \quad (13-143)$$

$$\Delta^* = \frac{\sum \delta^*}{S \sin \alpha_{out}} \quad (13-144)$$

The summations in Eqs. (13-143) and (13-144) are carried out for the boundary layers on both blade surfaces at the blade trailing edge. In the case of rotor blade rows, this total pressure loss coefficient can also be used to estimate the rotor efficiency via the methods described in chapter 2. Eq. (13-142) is derived directly from conservation of mass and momentum at the blade trailing edge, while assuming that the low momentum boundary layer fluid instantly mixes with the inviscid free stream fluid and that the static pressure is unaffected by the mixing process.

Loss coefficients estimated from two-dimensional boundary layer predictions are only approximations. These loss estimates neglect a number of phenomena that can significantly affect the losses in annular cascades. These include secondary flows associated with boundary layer migration normal to the stream sheets, boundary layer interaction with the inviscid core flow and the influence of the end-wall boundary layers. Also, the boundary layers may be predicted to separate at some point along the blade surface. The basic assumptions of boundary layer theory are not valid in separation zones, causing the predictions to be of doubtful accuracy. It can be expected that the loss coefficient in an annular cascade of a turbomachine will be significantly higher than estimates from Eq. (13-142). Loss coefficients calculated in this fashion should be used only for qualitative guidance based on the relative differences in the loss for alternative cascade designs.

Figure 13-15 shows predicted boundary layer shape factors from the axial-flow turbine stator analysis shown in figure 13-6. This analysis is a simulation of a low-pressure, cold-air cascade test. Reynolds numbers are sufficiently low that the pressure surface boundary layer remains laminar throughout. The suction

**FIGURE 13-15. Boundary Layer Analysis**

surface boundary layer transitions to turbulent flow near the point of maximum velocity. Both boundary layers remained attached throughout.

The numerical analysis of the two-dimensional boundary layer equations is straightforward. The governing equations are parabolic in mathematical form. This means that the solution at each streamwise station depends only on the upstream boundary layer parameters. Hence, a simple marching-type numerical solution is needed. The streamwise derivatives in the governing equations are replaced with backward-difference approximations of the form of Eq. (13-94). An iterative solution procedure is used to complete the integration of the governing equations at each streamwise station before proceeding to the next station. This process is so fast and simple that the boundary layer analysis has virtually no impact on the computation time required for the complete blade-to-blade flow analysis.

13.7 Summary

The analysis methods described in this chapter are representative of available theoretical methods for two-dimensional blade-to-blade flow analysis. There are many alternate solution techniques in use, both for the inviscid flow and the boundary layer. But the precise technique used is less significant than the approximations that are inherent in the two-dimensional flow model. It has been seen that reasonable estimates of the blade loading and fluid turning can be achieved for blade rows operating close to their design condition. But the inviscid flow and the boundary layer analyses suffer a dramatic loss of

accuracy when applied under far off-design conditions, where severe flow separation usually exists. Indeed, there is very little merit in even applying them to such cases. The primary role of these methods is for the detailed aerodynamic design of blades, where the blades can be expected to operate at moderate incidence angles. In that role they offer reasonable accuracy and computational speed appropriate to the large number of analyses required to arrive at an optimum design.

The designer requiring a more general analysis will use a viscous flow computational fluid dynamics (CFD) code. Designers typically employ one of several commercially available CFD codes that are well suited to turbomachinery applications. Viscous CFD offers considerable promise for removing most of the limitations of the methods described in this chapter. Indeed, it has already greatly alleviated many of them, although much remains to be done in the areas of turbulence modeling, numerical methods and computational speed before these methods can be considered exact. Viscous CFD is occasionally applied to the two-dimensional blade-to-blade flow problem, but its real merit lies in treating the fully three-dimensional flow problem, where the important secondary flow patterns are also modeled. At present, the primary role of viscous CFD is for final evaluation and fine-tuning of complete blade row or stage designs where its more fundamental fluid dynamics models can be used to advantage for reducing losses and increasing the operating range within practical computer running times.

Chapter 14

QUASI-THREE-DIMENSIONAL BLADE PASSAGE FLOW FIELD ANALYSIS

A quasi-three-dimension flow analysis employs two-dimensional flow analyses in the hub-to-shroud and blade-to-blade surfaces to approximate the three-dimensional flow in a blade passage. The fundamental concept is generally credited to Wu [26] and was introduced previously in chapter 3, section 3.3. The specific analysis described in this chapter is widely used for centrifugal compressor design and analysis [1]. It is also employed for axial-flow compressor design and analysis [2], but in a more limited role. Its primary role for turbine design and analysis is to support the detailed aerodynamic design of radial-inflow turbine impellers as described in chapter 11, section 11.9. It has also been used effectively to design nozzle blades for radial-inflow turbines. But the detailed nozzle blade design procedure presented in chapter 11 has largely replaced it for that application.

The present analysis achieves exceptional computational speed and reliability largely due to its use of the linearized blade-to-blade flow analysis described in chapter 13, section 13.4. But that also imposes some limitations on the method that are particularly significant for turbines. Its limitation to subsonic or low transonic Mach number levels excludes a number of turbine applications. As noted in chapter 13, its accuracy is compromised when it is applied to the rather thick airfoils often used for turbines. It certainly could be extended for more general use on turbines by substituting a more general blade-to-blade flow analysis such as the time-marching method of chapter 13. But that would substantially increase the computation time required and significantly reduce its reliability. It is very doubtful that this quasi-three-dimensional flow analysis would remain an attractive design tool if that were done. Indeed, it would lose most of its advantages over commercially available viscous computational fluid dynamic (CFD) codes while offering a less general solution.

NOMENCLATURE

B^* = stream surface repositioning damping factor

b = stream sheet thickness

C = absolute velocity

D = stream surface curvature damping factor

- E = entrainment function
 f = blade force
 $g = 2\rho r \sin \alpha / N$
 H = total enthalpy
 H_1 = meridional shape factor = δ_1^*/θ_{11}
 H_2 = boundary layer tangential shape factor = δ_2^*/θ_{22}
 h = static enthalpy
 I = rothalpy
 K_B = blade or boundary layer blockage factor
 M = Mach number
 m = meridional coordinate
 \dot{m} = mass flow rate
 N = number of blades
 n = normal coordinate
 P = pressure
 q = inlet dynamic head
 r = radius
 s = entropy
 T = temperature
 t_b = blade thickness
 V = velocity relative to the wall
 W = velocity relative to the blade row
 y = distance along quasi-normal or normal to the wall
 z = axial coordinate
 α = flow angle
 β = camberline angle
 ΔA = stream sheet area
 Δv = increment in v due to blade guidance
 δ = boundary layer thickness
 δ_c = blade clearance
 δ_1^* = boundary layer meridional displacement thickness
 δ_2^* = boundary layer tangential displacement thickness
 ϵ = angle between quasi-normal and true normal
 η = dimensionless tangential coordinate
 θ = tangential coordinate and streamwise momentum thickness
 θ_{11} = meridional momentum thickness
 θ_{12} = tangential momentum flux thickness
 θ_{22} = tangential momentum thickness
 κ_n = stream surface curvature
 λ = quasi-normal angle (figure 14-4)
 v = blade force defect thickness
 ρ = fluid density
 ϕ = stream surface angle with the axial direction
 ω = rotation speed, radians/sec

Subscripts

- h = parameter at the hub contour
 m = meridional component

s = parameter at the shroud contour

w = parameter at the wall

θ = tangential component

Superscripts

' = parameter in rotating coordinates

– = mass-averaged value

14.1 Quasi-Three-Dimensional Flow

Figure 14-1 shows a meridional plane view of a blade row to be analyzed. The annular passage is divided into a series of stream sheets, separated by stream surfaces. By definition, a stream sheet has no velocity component normal to it and no mass flow across it. The stream surfaces are spaced to yield equal mass flow in all stream sheets. For simplicity, it is assumed that all stream surfaces are axisymmetric, i.e., stream sheet twisting will be ignored. The meridional coordinate, m , is measured along the stream surfaces, the stream sheet thickness is designated as b and ϕ is the stream surface slope angle. The hub-to-shroud flow analysis must supply the geometry of the stream surfaces and the distributions of b for all stream surfaces. Then a complete two-dimensional blade-to-blade flow analysis can be conducted on all stream surfaces using one of the methods described in chapter 13. Figure 14-2 shows a typical blade-to-blade surface view to illustrate the solution domain for a blade-to-blade flow analysis over one of the stream sheets. The linearized potential flow analysis of section 13.4 is used for this purpose, including the extension to transonic flow. Hence, the solution domain lies entirely within the blade passage. That method

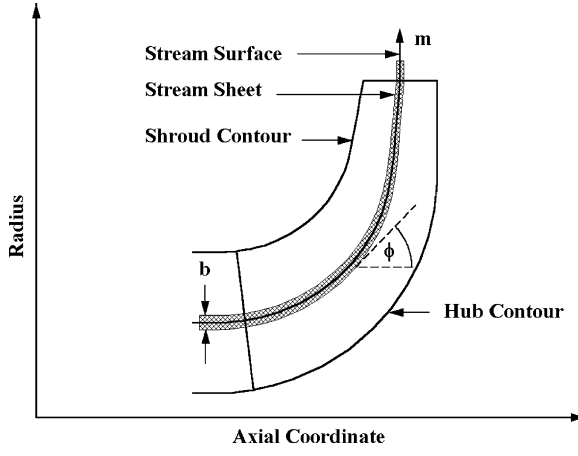


FIGURE 14-1. Hub-to-Shroud Flow Geometry

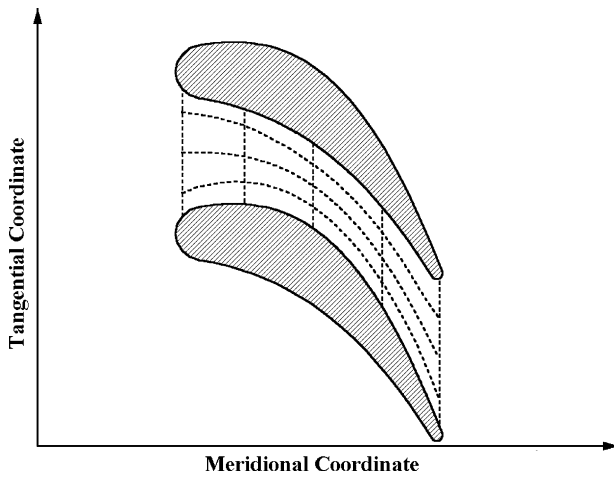


FIGURE 14-2. Blade-to-Blade Flow Geometry

limits the range of Mach numbers that can be considered but offers exceptional computation speed and reliability. In its primary role of radial-inflow turbine impeller detailed design, this is usually an acceptable limitation. It may be necessary to accomplish the detailed impeller design at operating conditions different from those of primary interest. Basically the impeller will be designed for a mass flow less than the choke limit. This will be acceptable for typical radial-inflow turbine impellers. When a radial-inflow turbine stage is designed to operate choked, the nozzle row is almost always the choked component.

The detailed design process can still take advantage of the more accurate two-dimensional blade-to-blade flow analyses of chapter 13. The accuracy of the linearized method is sufficient to support the hub-to-shroud flow analysis, such that accurate stream surface locations and stream sheet thicknesses are obtained. Once the quasi-three-dimensional flow analysis is complete, all input data needed for the two-dimensional blade-to-blade flow analyses are available. It is quite simple to include provision to generate input files for those more exact methods for any or all stream surfaces. That is a more efficient approach than incorporating one of the more exact methods directly into the quasi-three-dimensional flow analysis. Indeed, it is not uncommon for a complete quasi-three-dimensional flow analysis to require significantly less computer time than a two-dimensional blade-to-blade flow analysis on a single stream sheet for the same problem.

The hub-to-shroud flow analysis usually predicts the average meridional through-flow in the passage. Alternatively, the meridional flow field on a mean hub-to-shroud stream surface is sometimes predicted. The prediction of the average through flow will be used in this chapter, since it is more consistent with the assumption of axisymmetric blade-to-blade stream surfaces. This approach predicts an axisymmetric flow field corresponding to the hub-to-shroud flow averaged across the blade passage width. The governing equations for this

hub-to-shroud flow analysis were previously presented as Eqs. (3-21), (3-25) and (3-30). After simplifying them to their axisymmetric time-steady form, the governing equations are.

$$\frac{\partial r \rho W_m}{\partial m} + \kappa_n r \rho W_m = 0 \quad (14-1)$$

$$\frac{\partial I}{\partial m} = \frac{\partial s}{\partial m} = 0 \quad (14-2)$$

$$\kappa_m W_m^2 + \frac{W_\theta}{r} \frac{\partial(rW_\theta + \omega r^2)}{\partial n} + W_m \frac{\partial W_m}{\partial n} = \frac{\partial I}{\partial n} - T \frac{\partial s}{\partial n} \quad (14-3)$$

The curvature terms in these equations are defined in Eqs. (3-26) and (3-27). Hence, the analysis will consider flows with rothalpy and entropy gradients normal to the stream surfaces, but those parameters are assumed to be constant on all stream surfaces. Solution of this set of equations requires that W_θ or the relative flow angle, α' , must be specified by some external means. Within the blade passage, this will be accomplished using results from the blade-to-blade flow analyses. Upstream and downstream of the blade passage, conservation of angular momentum supplies the required data, i.e.,

$$\frac{\partial(rW_\theta + \omega r^2)}{\partial m} = \frac{\partial r C_\theta}{\partial m} = 0 \quad (14-4)$$

This equation follows directly from the axisymmetric time-steady form of Eq. (3-28) and Eq. (14-2).

14.2 The Quasi-Normal Coordinate System

The hub-to-shroud flow analysis will be conducted using the quasi-normal coordinate system introduced in chapter 11. Quasi-normals are straight lines constructed to be approximately normal to the two end-wall contours. Figure 14-3 illustrates a quasi-normal coordinate system for a typical impeller. The coordinate along a quasi-normal, y , is measured from the hub. The other two coordinates are the meridional distance along stream sheets, m , and the polar angle, θ . The flow analysis should include a few quasi-normals upstream and downstream of the blade passage to provide better definition of the stream surface curvature near the blade leading and trailing edges. The governing equations can be solved in the quasi-normal coordinate system by expressing the derivatives with respect to n in terms of derivatives with respect to m and y . This process is summarized by the following equations using the nomenclature of figure 14-4.

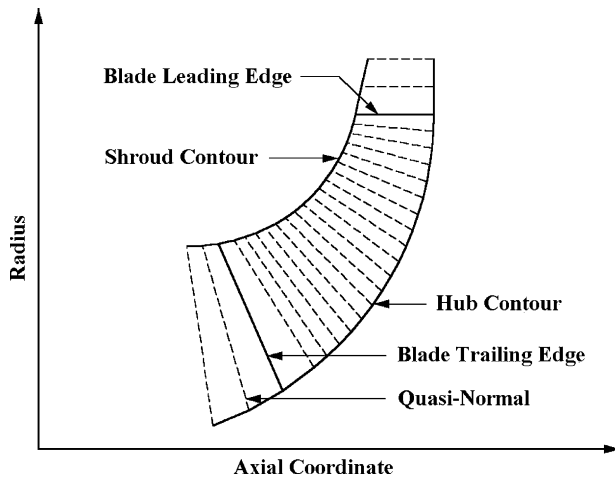


FIGURE 14-3. The Quasi-Normal Coordinate System

$$\tan \lambda = \frac{\Delta z}{\Delta r} = \frac{z_h - z_s}{r_s - r_h} \quad (14-5)$$

$$\sin \phi = \frac{\partial r}{\partial m} \quad (14-6)$$

$$\varepsilon = \phi - \lambda \quad (14-7)$$

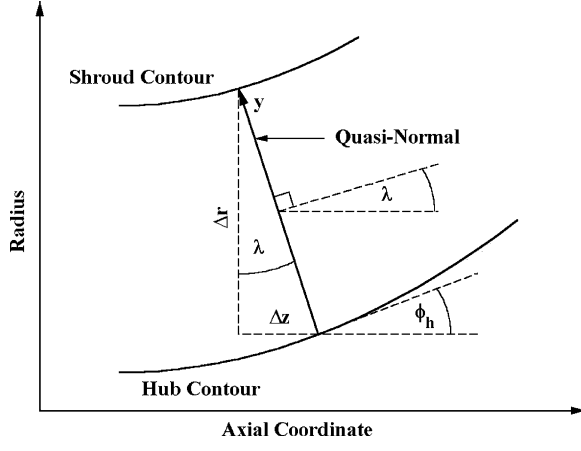


FIGURE 14-4. Quasi-Normal Geometry

$$\frac{\partial}{\partial n} = \frac{1}{\cos \varepsilon} \left[\frac{\partial}{\partial y} - \sin \varepsilon \frac{\partial}{\partial m} \right] \quad (14-8)$$

$$\kappa_m = -\frac{\partial \phi}{\partial m} \quad (14-9)$$

The angle, ϕ , is the angle of the slope of a stream surface with the axial direction as illustrated in figure 14-1. Note that the angle, ε , is the local deviation between a quasi-normal and a true stream surface normal. Quasi-normals are constructed with the intent of keeping ε as small as practical to improve the numerical accuracy.

It will be convenient to satisfy the continuity equation in integral form rather than using Eq. (14-1). Conservation of mass along a quasi-normal can be expressed in the form

$$\dot{m} = 2\pi \int_0^{y_s} K_B r \rho W_m \cos \varepsilon dy \quad (14-10)$$

K_B is the blade blockage factor, which corrects the stream sheet area available for through-flow to account for blade metal blockage. If β is the angle formed by a tangent to the blade camberline with respect to the tangential direction, t_b is the blade thickness and N is the number of blades, K_B is given by

$$K_B = 1 - t_b N / (2\pi r \sin \beta) \quad (14-11)$$

Conservation of the normal momentum is expressed by Eq. (14-3). It can be solved for W_m if W_θ , rothalpy and entropy are known on all stream surfaces. Since rothalpy and entropy are constant on all stream surfaces, they can be supplied through assigned upstream boundary conditions. Eq. (14-2) provides values at all other points in the flow field. The distribution of W_θ on the stream surfaces must be obtained from the blade-to-blade flow analysis. The time-steady form of Eq. (3-29) for constant rothalpy and entropy was used as the primary momentum equation for the blade-to-blade flow analysis in chapter 13, i.e.,

$$\frac{\partial(rW_\theta + \omega r^2)}{\partial m} = \frac{\partial W_m}{\partial \theta} \quad (14-12)$$

Clearly, a hub-to-shroud flow analysis restricted to axisymmetric stream surfaces can match only a single distribution of W_θ in the meridional plane. The most logical choice is to use the meridional distribution of the mass-averaged W_θ obtained from the blade-to-blade flow analyses on the various stream surfaces. In effect, the hub-to-shroud flow analysis will generate an axisymmetric flow field that is consistent with the mass-averaged angular momentum distribution predicted by the blade-to-blade flow analyses. This approximate hub-to-shroud analysis basically ignores Eq. (14-12) for all points within a blade passage. As noted previously, Eq. (14-12) reduces to

Eq. (14-4) for points outside of the blade passage, where the conservation of the mass-averaged angular momentum is required. Substitution of Eqs. (3-1), (14-2) and (14-8) into Eq. (14-3) yields

$$\begin{aligned} \frac{\partial W_m}{\partial y} + \left[\kappa_m \cos \epsilon - \frac{\sin \epsilon}{W_m} \frac{\partial W_m}{\partial m} \right] W_m + \frac{W_\theta}{r W_m} \left[\frac{\partial r C_\theta}{\partial y} - \sin \epsilon \frac{\partial r C_\theta}{\partial m} \right] \\ = \frac{1}{W_m} \left[\frac{\partial I}{\partial y} - T \frac{\partial s}{\partial y} \right] \end{aligned} \quad (14-13)$$

For points within the blade passage it will be more convenient to express the angular momentum in terms of the relative flow angle, noting that $W_\theta = W_m \cot \alpha'$. This yields

$$\begin{aligned} \left[\kappa_m \cos \epsilon - \frac{\sin \epsilon}{W_m \sin^2 \alpha'} \frac{\partial W_m}{\partial m} + \frac{\cot \alpha'}{r} \left(\frac{\partial r \cot \alpha'}{\partial y} - \sin \epsilon \frac{\partial r \cot \alpha'}{\partial m} \right) \right] W_m \\ + \frac{1}{\sin^2 \alpha'} \frac{\partial W_m}{\partial y} + 2\omega \cot \alpha' (\cos \lambda - \sin \phi \sin \epsilon) = \frac{1}{W_m} \left[\frac{\partial I}{\partial y} - T \frac{\partial s}{\partial y} \right] \end{aligned} \quad (14-14)$$

Eq. (14-14) can be simplified for points outside the blade passage by using Eq. (14-4). Introducing $W_\theta = W_m \cot \alpha'$ into Eq. (14-4), it is easily shown that

$$\frac{W_m \cot \alpha'}{r} \frac{\partial r \cot \alpha'}{\partial m} = -\cot^2 \alpha' \frac{\partial W_m}{\partial m} - 2\omega \sin \phi \cot \alpha' \quad (14-15)$$

Substituting Eq. (14-15) into (14-14) yields

$$\begin{aligned} \frac{W_m}{\sin^2 \alpha'} \frac{\partial W_m}{\partial y} + \kappa_m W_m^2 \cos \epsilon - C_m \sin \epsilon \frac{\partial W_m}{\partial m} + \frac{W_m^2 \cot \alpha'}{r} \frac{\partial (r \cot \alpha')}{\partial y} \\ + 2W_m \omega \cot \alpha' \cos \lambda = \frac{\partial I}{\partial y} - T \frac{\partial s}{\partial y} \end{aligned} \quad (14-16)$$

Eq. (14-16) is identical to Eq. (5-13) used in the axisymmetric through-flow analysis in chapter 5 as would be expected. Similarly, Eq. (5-11) is easily shown to be equivalent to Eq. (14-13) outside of the blade passages, i.e.,

$$W_m \frac{\partial W_m}{\partial y} + \kappa_m W_m^2 \cos \epsilon - W_m \sin \epsilon \frac{\partial W_m}{\partial m} + \frac{W_\theta}{r} \frac{\partial r C_\theta}{\partial y} = \frac{\partial I}{\partial y} - T \frac{\partial s}{\partial y} \quad (14-17)$$

While the alternate forms of these equations are mathematically equivalent for points outside of the blade passage, some care is recommended when formulating a numerical analysis. Use of Eqs (14-13) and (14-14) is necessary when the angular momentum distribution is supplied externally by the blade-to-blade flow analyses. But outside of the blade passage where angular momentum is conserved on stream surfaces, use of Eqs. (14-16) and (14-17) is likely to result in a more accurate numerical solution.

14.3 Numerical Integration of the Governing Equations

The governing equations for conservation of mass and momentum can be numerically integrated for a specified stream surface geometry and flow angle distribution through the blade passage. The numerical analysis used is basically identical to the method used in chapter 5. The momentum equation is written in the form

$$\frac{\partial W_m}{\partial y} = f_1(y)W_m + f_2(y) + \frac{f_3(y)}{W_m} \quad (14-18)$$

The functions f_1 , f_2 and f_3 are known functions of y . For quasi-normals inside the blade passage,

$$f_1(y) = \sin^2 \alpha' \left[-\kappa_m \cos \varepsilon - \frac{\cot \alpha'}{r} \left(\frac{\partial r \cot \alpha'}{\partial y} - \sin \varepsilon \frac{\partial r \cot \alpha'}{\partial m} \right) \right] + \frac{\sin \varepsilon}{W_m} \frac{\partial W_m}{\partial m} \quad (14-19)$$

$$f_2(y) = -2 \omega \sin \alpha' \cos \alpha' [\cos \lambda - \sin \phi \sin \varepsilon] \quad (14-20)$$

$$f_3(y) = \sin^2 \alpha' \left[\frac{\partial I}{\partial y} - T \frac{\partial s}{\partial y} \right] \quad (14-21)$$

For quasi-normals upstream and downstream of the blade passage,

$$f_1(y) = -\kappa_m \cos \varepsilon + \frac{\sin \varepsilon}{W_m} \frac{\partial W_m}{\partial m} \quad (14-22)$$

$$f_2(y) = 0 \quad (14-23)$$

$$f_3(y) = \frac{\partial I}{\partial y} - T \frac{\partial s}{\partial y} - \frac{W_\theta}{r} \frac{\partial (r C_\theta)}{\partial y} \quad (14-24)$$

At the upstream boundary, it is usually more convenient to supply boundary conditions in the stationary frame of reference, in terms of distributions of H , s and either C_θ or α . The first case is easily modeled by substituting C_θ for W_θ and H for I in Eq. (14-24). Eqs. (14-19) through (14-21) expressed in the stationary frame of reference are

$$f_1(y) = \sin^2 \alpha \left[-\kappa_m \cos \varepsilon - \frac{\cot \alpha}{r} \frac{\partial (r \cot \alpha)}{\partial y} + \frac{\sin \varepsilon}{W_m} \frac{\partial W_m}{\partial m} \right] \quad (14-25)$$

$$f_2(y) = 0 \quad (14-26)$$

$$f_3(y) = \sin^2 \alpha \left[\frac{\partial H}{\partial y} - T \frac{\partial s}{\partial y} \right] \quad (14-27)$$

The normal momentum equation is solved for the resident stream surface geometry and flow angle distributions through the blade passage. Hence, f_1 , f_2 and f_3 are evaluated at all grid points before integrating the momentum equation. This process is straightforward with the exception of the meridional gradient of W_m in f_1 , which depends on the solution. Usual practice is to use values of W_m from the previous iteration to evaluate this gradient. That approach can result in numerical stability problems in cases where W_m is changing rapidly between iterations. Since W_m appears in the denominator, it can also produce singular results if W_m approaches zero. Aungier [1] developed a better approach based on simple conservation of mass in all stream sheets. If the local through-flow area of a stream sheet is designated by ΔA , conservation of mass in the stream sheet requires

$$\Delta \dot{m} = \rho W_m \Delta A \quad (14-28)$$

Hence, the meridional gradient in f_1 can be replaced by

$$\frac{1}{W_m} \frac{\partial W_m}{\partial m} = - \frac{1}{\rho \Delta A} \frac{\partial \rho \Delta A}{\partial m} \quad (14-29)$$

This expresses the gradient in terms of the stream sheet geometry and gas density. The streamsheet geometry is constant during the process of integrating the mass and momentum conservation equations. It is still necessary to rely on values of gas density from the previous iteration, but density normally does not vary greatly between successive iterations. Since the mass flow rate in all stream sheets is constant, the risk of singular results is also eliminated. Aungier [1] applied the same approach to remove the singularity in Eq. (14-18) when W_m approaches zero by defining a new function, f_4 , as

$$f_4(y) = f_2(y) + f_3(y) \frac{\rho \Delta A}{\Delta \dot{m}} \quad (14-30)$$

Then Eq. (14-18) can be replaced by

$$\frac{\partial W_m}{\partial y} = f_1(y) W_m + f_4(y) \quad (14-31)$$

The solution of this linear differential equation has already been given in chapter 5 as

$$W_m(y) = W_m(0)F(y) + F(y) \int_0^y \frac{f_4(y)}{F(y)} dy \quad (14-32)$$

$$F(y) = \exp \left[\int_0^y f_1(y) dy \right] \quad (14-33)$$

The meridional velocity on the hub contour, $W_m(0)$, is the constant of integration. It is determined from conservation of mass through Eq. (14-10). Eqs. (14-31) and (14-10) are solved in an iterative numerical scheme, successively improving the estimate of $W_m(0)$ until mass is conserved and the momentum equation is satisfied. This requires calculation of thermodynamic properties such as ρ , using an appropriate equation of state from chapter 2. At any point in the flow field, the relative total enthalpy is given by Eq. (3-13), i.e.,

$$H' = I + \frac{1}{2}(r\omega)^2 \quad (14-34)$$

The local static enthalpy is given by

$$h = H' - \frac{1}{2}W^2 \quad (14-35)$$

The assigned upstream boundary conditions determine the rothalpy, entropy and the angular momentum, rC_θ , upstream of the blade passage on all stream surfaces. The relative total thermodynamic conditions are calculated as a function of H' and s and the static thermodynamic conditions as functions of h and s . The angular momentum downstream of the blade passage on each stream surface is obtained from the solution at the blade trailing edge quasi-normal. The absolute total enthalpy, H , is determined from Eqs. (3-1) and (3-10).

$$H = I + r\omega(W_\theta + r\omega) \quad (14-36)$$

Then the absolute total thermodynamic conditions are calculated as a function of H and s . When the iterative solution of the mass and momentum conservation equations is converged, the flow field is known for the resident stream sheet geometry. But that stream sheet geometry may not be consistent with the predicted flow field. Eq. (14-10) provides the calculated mass flow distribution as

$$\dot{m}_c(y) = 2\pi \int_0^y K_B r \rho W_m \cos \varepsilon dy \quad (14-37)$$

This calculated mass flow function can be used to calculate new stream sheet coordinates on all quasi-normals by numerical interpolation, such that each stream sheet contains the same fraction of the total mass flow. Since the solution of Eq. (14-10) may differ from the actual mass flow rate as permitted by the convergence tolerance, the interpolation process should seek the proper fraction of the calculated mass flow at y_s from Eq. (14-37) rather than of the specified mass flow rate. An outer iteration loop is required to progressively reposition the stream surfaces and repeat the mass and momentum conservation iteration until the stream surface positions have converged within an acceptable tolerance. In chapter 5, this outer iteration loop was avoided by using an approximate normal equilibrium equation. While quite adequate for the axial-flow turbine performance analysis, that simplified model is not adequate for more complex passages such as found in radial-inflow turbine impellers.

14.4 Repositioning the Stream Surfaces

The process of repositioning the stream surfaces requires fairly sophisticated numerical damping procedures to avoid numerical instability problems. Novak [59] suggests a numerical damping procedure that has been found to be quite effective for this purpose. The stream surfaces are repositioned by a fraction, F , of the difference between the resident positions and the new positions calculated from the flow field prediction. For quasi-normals outside of the blade passages Novak recommends

$$\frac{1}{F} = 1 + \frac{(1 - M_m^2)(\Delta y)^2}{B^*(\Delta m)^2} \quad (14-38)$$

B^* is an empirical constant, Δy is the hub-to-shroud quasi-normal length, Δm is the minimum meridional spacing with adjacent quasi-normals and M_m is the meridional Mach number. For quasi-normals inside the blade passage, Novak suggests

$$\frac{1}{F} = 1 + \frac{(1 - M'^2)(\sin \alpha' \Delta y)^2}{B^*(\Delta m)^2} \quad (14-39)$$

This damping procedure has been found to be quite effective as long as M_m and M' are limited to be no greater than 0.9. B^* values used are typically in the range of 8 to 16, but the numerical procedure should adjust B^* automatically based on whether the stream surface position errors are increasing or decreasing on successive iterations.

14.5 The Hub-to-Shroud Flow Analysis

To start the solution, an initial guess must be supplied for the stream sheet geometry and the flow field data used in the hub-to-shroud solution. Since no

blade-to-blade flow analysis results are available at that point, the initial guess must include an approximate blade-to-blade flow definition. The following procedure has been found to be effective for initializing the data required:

- Stream surfaces are positioned such that all stream sheets contain the equal through-flow area on each quasi-normal.
- Entropy and rothalpy are computed for all stream surfaces from the upstream boundary conditions.
- The meridional velocity is computed from local conservation of mass assuming the local gas density is equal to the relative total density.
- C_θ upstream of the blade is obtained from conservation of angular momentum, Eq. (14-4), using the upstream boundary conditions. This includes the blade leading edge quasi-normal.
- The blade is assumed to provide perfect guidance to the flow over the last 85% of the blade passage length based on the blade camberline angle, β .
- C_θ downstream of the blade is obtained from conservation of angular momentum using the value at the trailing edge quasi-normal.
- An “inlet slip” condition is applied over the first 15% of the blade passage length based on the relative flow angle computed at leading edge quasi-normal and the blade camberline angle, β , i.e.,

$$\cot \alpha' = \cot \alpha'_{LE} + (\cot \beta - \cot \alpha'_{LE})[(m - m_{LE})/(m_{TE} - m_{LE})/0.15]^2 \quad (14-40)$$

This initialization procedure is so conservative that it is virtually certain to successfully start the analysis. But Eq. (14-40) is a rather crude approximation for the blade-to-blade flow. Consequently, convergence of the hub-to-shroud flow analysis is often slow for the initial data. Once the first blade-to-blade flow analysis results are obtained, convergence of the hub-to-shroud analysis consistently improves dramatically. A much more efficient overall analysis is obtained by simply not requiring convergence on the first attempt at the hub-to-shroud flow analysis. This writer simply limits the number of iterations on the hub-to-shroud flow governing equations on this first attempt to, say, ten to twelve regardless of whether convergence is achieved. That is a sufficient number of iterations to obtain a reasonable stream sheet pattern to run the first blade-to-blade flow analysis.

The general procedure used for the hub-to-shroud flow analysis is a direct application of the well-known streamline curvature technique. The basic conservation equations are solved at each quasi-normal using the procedures described in section 14.3. Then the stream surfaces are repositioned as described in section 14.4. The process is repeated until the stream surface positions and flow field data have converged within acceptable tolerances. This procedure is adequate for most problems, but Aungier [1] suggested two simple extensions that can greatly improve the reliability of the analysis to the point that a converged solution is almost always obtained. First, the hub-to-shroud flow analysis should check for choked flow, and limit the overall mass flow rate to the choke value when it occurs. In the nomenclature of

section 14.3, the flow on any quasi-normal is locally beyond the choke limit when

$$\frac{\partial \dot{m}_c}{\partial W_m(0)} \leq 0 \quad (14-41)$$

When this condition is encountered, the solution procedure should determine the mass flow rate for which this gradient term is zero, which is the choke value. The choked flow condition of Eq. (14-41) does not always indicate a true choke. Often it is caused by numerical errors during the early iterations. The solution should always proceed using the largest acceptable mass flow rate, but not exceeding the specified mass flow rate. In the case of a false choke due to numerical error, the mass flow rate will gradually increase to the specified value as the solution converges. This simple procedure avoids the most common cause of solution divergence. Another common cause of solution divergence is numerical errors in the stream surface curvature terms. The numerical damping of the stream surface repositioning given in section 14.4 avoids most of these problems. But that damping procedure is indirect with respect to the curvature terms. This writer also imposes a direct damping procedure on κ_m based on the new estimate from the repositioned stream surfaces, $\kappa_{m,new}$, and the value used for the current iteration, $\kappa_{m,old}$.

$$\kappa_m \rightarrow (\kappa_{m,new} + D\kappa_{m,old})/(1+D) \quad (14-42)$$

D is a curvature-damping factor. Typically, $D = 1$ is used, but D is increased if successive iterations show a significant increase in convergence errors.

14.6 Coupling the Two Basic Flow Analyses

The quasi-three-dimensional flow analysis is obtained by coupling the hub-to-shroud flow analysis described in this chapter with the linearized blade-to-blade flow analysis described in chapter 13. The hub-to-shroud flow analysis defines the stream sheet geometry and corresponding blade geometry for the blade-to-blade flow analysis. The stream sheet thickness distribution is also required. This is computed from the hub-to-shroud flow data and the specified stream sheet mass flow by simple conservation of mass.

$$b = \Delta m / (2\pi r K_B \rho W_m) \quad (14-43)$$

When the blade-to-blade flow analyses have been completed, the results are mass-averaged across the blade passage to provide the relative flow angle distribution for the next hub-to-shroud flow analysis. Since the tangential coordinate,

η , used in the blade-to-blade flow analysis varies from 0 to 1, the required data are given by

$$\bar{W}_m = \frac{\int_0^1 \rho b W_m^2 d\eta}{\int_0^1 \rho b W_m d\eta} \quad (14-44)$$

$$\bar{W}_\theta = \frac{\int_0^1 \rho b W_m W_\theta d\eta}{\int_0^1 \rho b W_m d\eta} \quad (14-45)$$

$$\cot \alpha' = \bar{W}_\theta / \bar{W}_m \quad (14-46)$$

In addition to requiring convergence of the two-component analyses, a convergence criterion is needed for the overall quasi-three-dimensional flow analysis. All relative flow angles predicted by Eq. (14-46) on successive blade-to-blade flow analyses should be required to converge within an acceptable tolerance.

Figure 14-5 shows a basic flow chart for the quasi-three-dimensional flow analysis. The combination of the present hub-to-shroud analysis with the linearized blade-to-blade flow analysis of chapter 13 provides a very reliable and efficient quasi-three-dimensional flow analysis for a wide range of turbomachinery blade passage problems of interest. The major limitation is with regard to Mach number levels as discussed previously in this chapter. The other

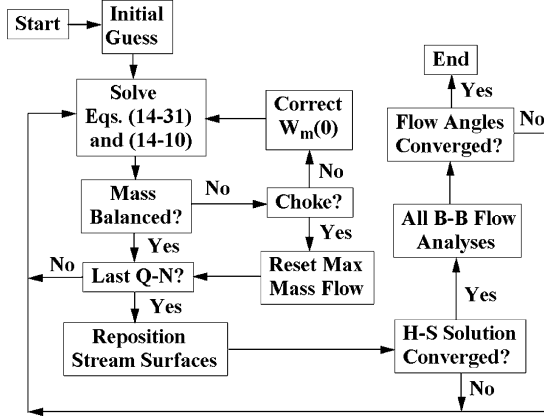


FIGURE 14-5. Flow Chart of the Analysis

major restriction follows from the basic assumption of inviscid flow. This is a reasonable assumption for turbine blade rows as long as the incidence angles are reasonable. Extreme incidence angles results in excessive local diffusion and substantial flow separation. That situation simply cannot be adequately modeled by an inviscid flow analysis. To obtain meaningful results, those cases require a more fundamental viscous computational fluid dynamics code.

The quasi-three-dimensional flow analysis requires a very large number of equation of state calculations. The pseudoperfect gas equation of state model described in chapter 2 can greatly reduce the computational time relative to real gas models, or even ideal gas models with temperature-dependent specific heats. This model is usually adequate for blade passage flow analyses. Obvious exceptions are cases with liquid present in the flow and extreme blade-row pressure ratios that produce significant variation in the gas compressibility factor. The Mach number limit normally requires blade passage pressure ratios low enough to justify the pseudoperfect gas model. Similarly, two-phase flows are not common for design conditions.

14.7 Boundary Layer Analysis

Boundary layer analysis provides a useful extension to an inviscid internal flow analysis. It can provide an approximate evaluation of viscous effects with no significant increase in computation time. Chapter 13 describes a two-dimensional blade surface boundary layer analysis and loss coefficient model that can be incorporated into the quasi-three-dimensional flow field analysis directly. The limitations of those models have also been discussed in chapter 13.

Unlike the case of blade surface boundary layers, there is little merit in considering two-dimensional models for the highly three-dimensional end-wall boundary layers. For application to the accelerating flow in turbine blade rows, end-wall boundary layers are not a major concern. That is far from true when dealing with the diffusing flow in compressor blade rows, where they can have a substantial influence on performance. End-wall boundary layer analysis really provides limited benefit to a quasi-three-dimensional flow analysis intended only for turbine applications. But if a more general analysis appropriate to compressor applications also is intended, an end-wall boundary layer analysis is well worth the effort required to include it.

Aungier [1] introduced an end-wall boundary layer analysis for this purpose for application to centrifugal compressors. Aungier [2] improved on that model based on a more refined model for the blade force defects that was developed for axial-flow compressors. That refined version is described in this chapter for the benefit of readers seeking a fairly general quasi-three-dimensional flow analysis. The axisymmetric, three-dimensional boundary layer analysis described in chapter 3 is employed for this purpose. Boundary layers inside of the blade passages certainly are not axisymmetric. There the model seeks to predict the gap-averaged boundary layer behavior as discussed in chapter 3. This approach is about the only method that can provide meaningful results and still offer the computation speed and reliability suitable for this application. The end-wall boundary layers are assumed to be turbulent in all cases. This is expected to be true for most blade passage analyses in turbomachinery.

Axisymmetric, three-dimensional boundary layer analysis yields excellent results when applied to vaneless annular passages, e.g., Aungier [29], Davis [30] and Senoo [31]. It has also been used effectively to predict end-wall boundary layers in axial-flow compressors, which is an essential part of an aerodynamic performance analysis, e.g., Balsa and Mellor [32] and Aungier [2]. Its use to approximate the gap-averaged end-wall boundary layers within blade passages was suggested by Horlock [33]. Aungier [2] applied this model to the internal flow analysis of an axial-flow compressor blade row and showed that the predicted boundary layer growth through the blade row was in qualitative agreement with trends observed in experiments.

The governing equations for axisymmetric, three-dimensional boundary layers were previously developed in chapter 3, section 3.6, in a general rotating coordinate system. It is convenient to express these equations in terms of velocity components relative to the wall, rather than relative to the blades to avoid confusion. The rotation speed of the wall and the blades will be designated as ω_w and ω , respectively. The velocity relative to the wall is designated as V . Hence, the velocity components relative to the wall and relative to the blades are related to the absolute velocity components by

$$C_m = W_m = V_m \quad (14-47)$$

$$C_\theta = W_\theta + r\omega = V_\theta + r\omega_w \quad (14-48)$$

The governing equations in terms of V follow directly from those in developed in chapter 3 simply by replacing W with V , i.e.,

$$\frac{\partial}{\partial m} [r\rho_e V_{me} (\delta - \delta_1^*)] = r\rho_e V_e E \quad (14-49)$$

$$\begin{aligned} \frac{\partial}{\partial m} [r\rho_e V_{me}^2 \theta_{11}] + \delta_1^* r\rho_e V_{me} \frac{\partial V_{me}}{\partial m} - \rho_e V_{\theta e} \sin \phi [V_{\theta e} (\delta_2^* + \theta_{22}) + 2\omega_w r\delta_2^*] \\ = r[\tau_{mw} + f_{me} v_m] \end{aligned} \quad (14-50)$$

$$\begin{aligned} \frac{\partial}{\partial m} [r^2 \rho_e V_{me} V_{\theta e} \theta_{12}] + r\delta_1^* \rho_e V_{me} \left[r \frac{\partial V_{\theta e}}{\partial m} + \sin \phi (V_{\theta e} + 2r\omega_w) \right] \\ = r^2 [\tau_{\theta w} + f_{\theta e} v_\theta] \end{aligned} \quad (14-51)$$

The blade forces at the boundary layer edge are known from conservation of momentum, i.e.,

$$f_{me} = \rho_e V_{me} \frac{\partial V_{me}}{\partial m} + \frac{\partial P_e}{\partial m} - \frac{\sin \phi}{r} \rho_e (V_{\theta e} + \omega_w r)^2 \quad (14-52)$$

$$f_{\theta e} = \frac{\rho_e V_{me}}{r} \left[r \frac{\partial V_{\theta e}}{\partial m} + \sin \phi (V_{\theta e} + 2r\omega_w) \right] = \frac{\rho_e V_{me}}{r} \frac{\partial r C_{\theta e}}{\partial m} \quad (14-53)$$

Eqs. (14-51) and (14-53) can be combined to yield

$$\frac{\partial}{\partial m} [r^2 \rho_e V_{me} V_{\theta e} \theta_{12}] + r^2 \delta_1^* f_{\theta e} = r^2 [\tau_{\theta w} + f_{\theta e} v_{\theta}] \quad (14-54)$$

If y is the distance normal to the wall and δ is the boundary layer thickness, the various defect thicknesses in the boundary layer equations defined in chapter 3 can also be expressed in terms of V .

$$\rho_e V_{me} \delta_1^* = \int_0^\delta (\rho_e V_{me} - \rho V_m) dy \quad (14-55)$$

$$\rho_e V_{me}^2 \theta_{11} = \int_0^\delta \rho V_m (V_{me} - V_m) dy \quad (14-56)$$

$$\rho_e V_{me} V_{\theta e} \theta_{12} = \int_0^\delta \rho V_m (V_{\theta e} - V_{\theta}) dy \quad (14-57)$$

$$\rho_e V_{\theta e} \delta_2^* = \int_0^\delta (\rho_e V_{\theta e} - \rho V_{\theta}) dy \quad (14-58)$$

$$\rho_e V_{\theta e}^2 \theta_{22} = \int_0^\delta \rho V_{\theta} (V_{\theta e} - V_{\theta}) dy \quad (14-59)$$

$$v_m f_{me} = \int_0^\delta (f_{me} - f_m) dy \quad (14-60)$$

$$v_{\theta} f_{\theta e} = \int_0^\delta (f_{\theta e} - f_{\theta}) dy \quad (14-61)$$

Solution of the governing equations requires empirical correlations for the entrainment function, E , the wall shear stresses, τ_{wm} and $\tau_{w\theta}$, and the force defect thicknesses, v_m and v_{θ} . It also requires empirical relationships between the mass and momentum defect thicknesses. The boundary layer analysis assumes that the boundary layer velocity profiles can be represented by power-law profiles of the form

$$\frac{V_m}{V_{me}} = \left(\frac{y}{\delta} \right)^n \quad (14-62)$$

$$\frac{V_\theta}{V_{\theta e}} = \left(\frac{y}{\delta} \right)^m \quad (14-63)$$

Substitution of these velocity profile assumptions into the definitions of the various mass and momentum defect thicknesses, assuming that density can be regarded as essentially constant, yields the following relationships.

$$n = \theta_{11}/(\delta - \delta_1^* - 2\theta_{11}) \quad (14-64)$$

$$m = \theta_{12}(n+1)^2 / [\delta - \theta_{12}(n+1)] \quad (14-65)$$

$$H_1 = \delta_1^*/\theta_{11} = 2n + 1 \quad (14-66)$$

$$\delta - \delta_1^* = 2H_1\theta_{11}/(H_1 - 1) \quad (14-67)$$

$$\delta_1^*/\delta = n/(n+1) \quad (14-68)$$

$$H_2 = \delta_2^*/\theta_{22} = 2m + 1 \quad (14-69)$$

$$\delta_2^*/\delta = m/(m+1) \quad (14-70)$$

The boundary layer analysis may have to be conducted on an end-wall that is rotating in some regions and stationary in others. An obvious example is the hub wall of an impeller, which is stationary upstream of the blades but rotating in the blade passage. From Eqs. (14-48) and (14-57) a jump condition at a point where V abruptly changes from C to W , is given by

$$C_{\theta e}\theta_{12} = W_{\theta e}\theta'_{12} \quad (14-71)$$

The prime designates the tangential momentum defect thickness viewed in the rotating coordinate system. Since $C_{\theta e}$ and $W_{\theta e}$ will generally have opposite signs, the tangential defect thickness may change sign when the wall changes from rotating to stationary and inversely. Indeed, all tangential defect thicknesses may be negative with $H_2 < 1$ and $m < 0$. Hence, a deficit in tangential momentum in the rotating coordinate system may correspond to excess tangential momentum in the stationary coordinate system and inversely. Aungier [1] extends the tangential velocity profile assumption by restricting Eq. (14-63) to cases where $m \geq 0.05$. For values of $m < 0.05$ the following profile assumption is used.

$$\frac{V_\theta}{V_{\theta e}} = \left(\frac{y}{\delta} \right)^{0.05} + 0.1705(1-20m) \left(1 - \frac{y}{\delta} \right)^2 \left(\frac{y}{\delta} \right)^{0.1} \quad (14-72)$$

Equation (14-72) simply extends the power-law profiles in a plausible fashion to include cases where the integrated tangential momentum in the boundary layer exceeds the boundary layer edge value. From Eqs. (14-62) and (14-72) it is easily shown that

$$m = 0.05 + \left[\frac{\theta_{12}}{\delta} - \frac{0.05}{(n+1)(n+1.05)} \right] \frac{(n+1.1)(n+2.1)(n+3.1)}{6.82} \quad (14-73)$$

$$H_2 = \frac{\delta_2^*}{\theta_{22}} = \frac{20}{21(0.95 - 1.684m)} \quad (14-74)$$

$$\frac{\delta_2^*}{\delta} = \frac{20m}{21} \quad (14-75)$$

$$\frac{\theta_{22}}{\delta} = 0.95m - 1.684m^2 \quad (14-76)$$

Figures 14-6 and 14-7 illustrate this extended tangential velocity profile and shape factor assumption.

The well-known skin friction coefficient model of Ludwig and Tillmann [123] is used to approximate the wall shear stresses.

$$c_f = 0.246 \exp(-1.561H) (\rho_e V_e \theta / \mu)^{-0.268} \quad (14-77)$$

The momentum thickness and shape factor in Eq. (14-77) are defined in the free stream direction, and μ is the fluid viscosity. Designating the free stream

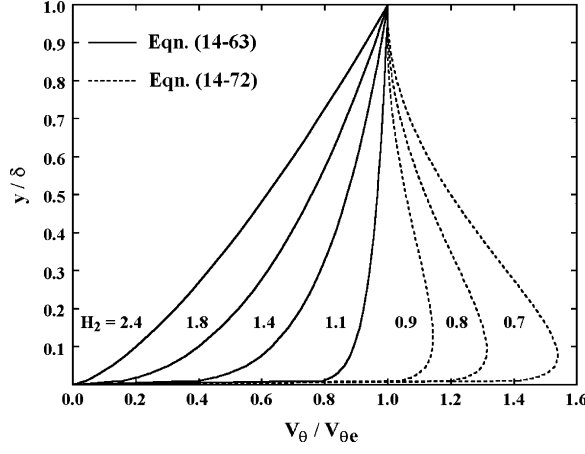
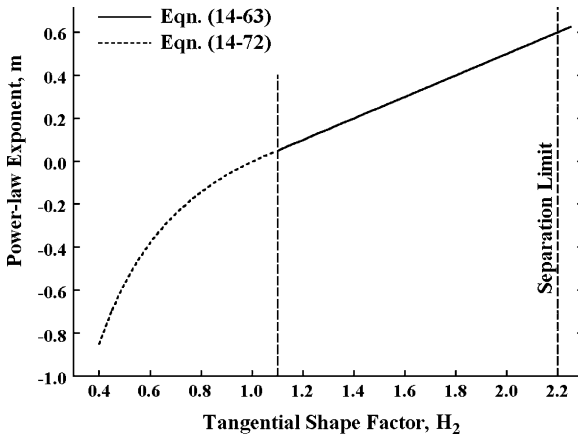


FIGURE 14-6. Extended Tangential Velocity Profiles

**FIGURE 14-7. Boundary Layer Shape Factor**

component of the fluid velocity within the boundary layer by V_s , it is easily shown that

$$V_s = V_m \cos \beta_e + V_\theta \sin \beta_e \quad (14-78)$$

$$\delta^* = \delta_1^* \cos^2 \beta_e + \delta_2^* \sin^2 \beta_e \quad (14-79)$$

$$\begin{aligned} \theta = & (\theta_{11} + \delta_1^*) \cos^4 \beta_e + (\theta_{22} + \delta_2^*) \sin^4 \beta_e \\ & + 2(\theta_{12} + \delta_1^*) \sin^2 \beta_e \cos^2 \beta_e - \delta^* \end{aligned} \quad (14-80)$$

$$H = \delta^* / \theta \quad (14-81)$$

It is assumed that the wall shear stress is directed along the boundary layer edge streamline. Hence,

$$\tau_{mw} = \frac{1}{2} c_f \rho_e V_e V_{me} \quad (14-82)$$

$$\tau_{\theta w} = \frac{1}{2} c_f \rho_e V_e V_{\theta e} \quad (14-83)$$

Following Aungier [1, 2] the boundary layer entrainment function in blade free passages is approximated by

$$E = 0.025(H_1 - 1) \quad (14-84)$$

Within a blade passage, where the flow is guided by the blades, the free stream shape factor, H , is more relevant, much like the case in classical two-dimensional boundary layer theory, i.e.,

$$E = 0.025(H - 1) \quad (14-85)$$

End-wall boundary layer analysis within blade passages is complicated by the existence of the blade force defect terms defined in Eqs. (14-60) and (14-61). Mellor and Wood [37] suggested that blade force defects are the most logical explanation for observed axial-flow compressor performance trends. Smith [38], Koch and Smith [39] and Hunter and Cumpsty [40] provide experimental confirmation that significant tangential blade force defects do exist. Correlations of the experimental data reported in the literature are generally almost useless due to the extreme data scatter. Aungier [2] developed a more useful empirical correlation of the experimental data of Koch and Smith [39] that is shown in figure 14-8. While significant experimental data scatter is present here also, it is sufficiently reduced to suggest a usable empirical model for boundary layer analysis. The experimental data provides boundary layer data at the inlet and exit to the blade row. Since a correlation applicable to points within the blade passage is needed, figure 14-8 employs parameters that are averages of the inlet and discharge values. The meridional displacement thickness used is defined in Eq. (14-55), δ_c is the clearance gap between the blade and the end-wall and the local staggered spacing, g , is defined by

$$g = 2\pi r \sin \alpha'_e / N \quad (14-86)$$

The experimental tangential force defect thickness data relate to the blade discharge location where the flow is well guided by the blades. Hence, the flow angles within the boundary layer are expected to be essentially the same as the boundary layer edge values. This condition is commonly referred to as collateral

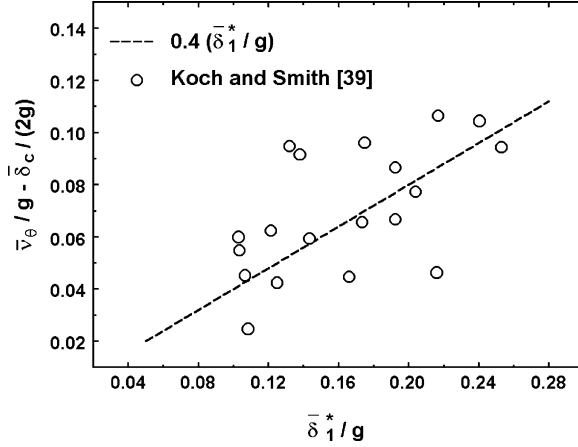


FIGURE 14-8. Tangential Force Defect Thickness

flow. Within the blade passage, the blade guidance may be far from ideal. Hence, a basic blade force defect thickness applicable to collateral flow is defined as

$$v_0 = 0.4\delta_1^* + \delta_c / 2 \quad (14-87)$$

The actual blade force defect thickness is defined as

$$v = v_0 + \Delta v \quad (14-88)$$

The term, Δv , accounts for the influence of the local deviation of the boundary layer flow from collateral flow. The condition for collateral flow can be expressed in terms of the momentum thicknesses defined in Eqs. (14-56) and (14-57) as

$$V_{\theta e} \theta_{12} = W_{\theta e} \theta_{11} \quad (14-89)$$

Following Balsa and Mellor [32], the blade force is assumed to be normal to the free-stream velocity throughout the boundary layer, i.e.,

$$f_m = -W_{\theta e} f_\theta / W_{me} \quad (14-90)$$

$$v_\theta = v_m = v \quad (14-91)$$

If the boundary layers are integrated between successive stations separated by the distance, Δm , with $\Delta v = 0$, Aungier [2] shows that the value of $\Delta v \bar{w} \sigma$ that must be imposed to achieve the collateral flow condition at the downstream station is

$$\xi \Delta v = \theta_{11} - \theta_{12} \quad (14-92)$$

$$\xi = \left[\frac{\bar{r}}{r} + \frac{\bar{W}_{\theta e} W_{\theta e}}{\bar{W}_{me} W_{me}} \right] \frac{\bar{r} f_{\theta e} \Delta m}{r \rho_e W_{me}} \quad (14-93)$$

The overbar in Eq. (14-93) denotes an average of the values at the local and upstream stations. In practice, it would require an infinite number of blades to provide perfect guidance to the flow, so the actual value imposed is a fraction, F , of the value given by Eq. (14-92).

$$\Delta v = (W_{\theta e} \theta_{11} - V_{\theta e} \theta_{12}) F / \xi \quad (14-94)$$

$$F = [1 - \delta_c / \delta] m / [m + g] / 2; \quad \delta_c \leq \delta \quad (14-95)$$

$$F = 0; \quad \delta_c > \delta \quad (14-96)$$

The meridional distance, m , is measured from the blade leading edge, and δ is the local boundary layer thickness. This form of the function F is based on the following assumptions.

- The blades guide the flow toward collateral flow primarily close to the blade surfaces. It is assumed that the gap-averaged deviation from collateral flow imposed by integrating the boundary layer equations, using only v_0 , will be reduced by about 50% due to the blade guidance.
- The influence of blade guidance and clearance gap on the blade force defect is negligible when the blade clearance gap is greater than the boundary layer thickness.
- The influence of blade guidance and clearance gap on the blade force defect is negligible at the blade row leading edge. Their influence is assumed to increase proportional to the ratio of the meridional distance to the blade spacing.

The second assumption simply recognizes the special case where the boundary layer and blades are not really interacting. Although this situation is probably very rare in turbomachinery, it can easily occur in the present analysis if the entrance boundary layer thickness is specified small enough. Experience has shown that this can lead to erratic and highly questionable results unless Eq. (14-96) is required. The third assumption recognizes that the influence of the blades will not extend across the entire blade passage spacing until the flow penetrates well into the guided passage.

Eq. (14-94) is to be solved using boundary layer data obtained with $\Delta v = 0$. In practice, it is preferable to correct the blade force defect thickness continually as part of the iterative solution of the governing equations. That can be done as long as the correction process accounts for any nonzero value of Δv used in the previous iteration. Aungier [2] shows that Δv on any iteration can be imposed as an update of the value used on the previous iteration in the form

$$\Delta v \rightarrow [\Delta v - (V_{\theta e} \theta_{12} - W_{\theta e} \theta_{11})/\xi]F \quad (14-97)$$

The boundary layer analysis has been developed in terms of the fluid velocity relative to the wall, where the wall may be stationary or rotating. It is necessary to consider jump conditions for cases where the boundary layer moves from a stationary wall to a rotating wall, or inversely. For clarity, designate the velocity relative to the wall rotating at rotation speed ω as W and C to be the velocity relative to the stationary wall. Boundary layer parameters relative to the rotating wall will be designated with a prime. Hence,

$$W_\theta = C_\theta - \omega r \quad (14-98)$$

Substituting Eq. (14-98) into the definitions of the various boundary layer defect thicknesses yields

$$C_{\theta e} \theta_{12} = W_{\theta e} \theta'_{12} \quad (14-99)$$

$$C_{\theta e} \delta_2^* = W_{\theta e} \delta'^*_2 \quad (14-100)$$

$$C_{\theta e}^2 \theta_{22} = W_{\theta e}^2 \theta'_{22} + \omega r W_{\theta e} \delta_2'^* \quad (14-101)$$

$$C_{\theta e}^2 \theta_{22} (1 + H_2) = W_{\theta e}^2 \theta'_{22} (1 + H'_2) + 2 \omega r W_{\theta e} \delta_2'^* \quad (14-102)$$

Eqs. (14-99) and (14-102) contain basic terms in the momentum-integral equations. Since they are identical in form for stationary and rotating walls, no special logic is required to integrate these equations across transitions between rotating and stationary walls.

Since this end-wall boundary layer analysis considers only turbulent boundary layers, boundary layer data must be specified at the compressor inlet. The data needed are θ_{11} , θ_{12} , H_1 and H_2 . It is reasonable to start the analysis with $H_1 = 1.4$, which is a typical value for simple flat-plate boundary layer flow. The classical one-seventh power-law profile is a reasonable choice for the tangential velocity profile, i.e., $m = 1/7$ or $H_2 = 1.286$. A convenient specification is the boundary layer blockage factor, K_B , at the inlet. This specifies the portion of the inlet passage area available for through flow after correcting for the end-wall boundary layer mass defect thicknesses. Assuming that the blockage is equally split between the two boundary layers,

$$2\pi r \rho_e V_{me} \delta_1^* = \frac{1}{2} (1 - K_B) \dot{m} \quad (14-103)$$

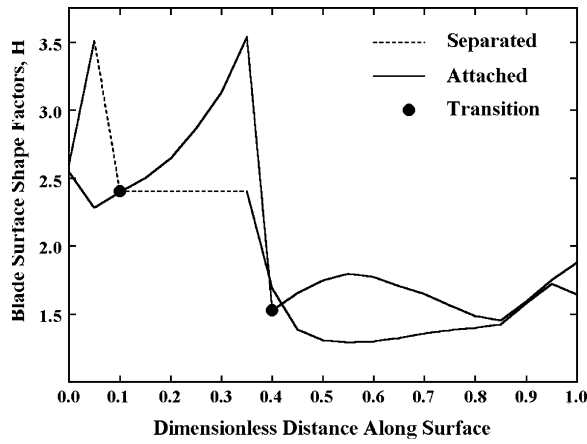
The assumed shape factors and Eqs. (14-66) through (14-70) provide all other initial boundary layer data. The analysis on each end-wall can be accomplished by a simple marching solution, starting at the second meridional station, and completing the solution at each station before proceeding to the next. There are two precautions recommended to prevent numerical divergence. First, the boundary layers must be turbulent, so impose a minimum momentum thickness, θ_{11} , based on the following transition condition.

$$Re_\theta = \rho_e V_e \theta_{11} / \mu \geq 250 \quad (14-104)$$

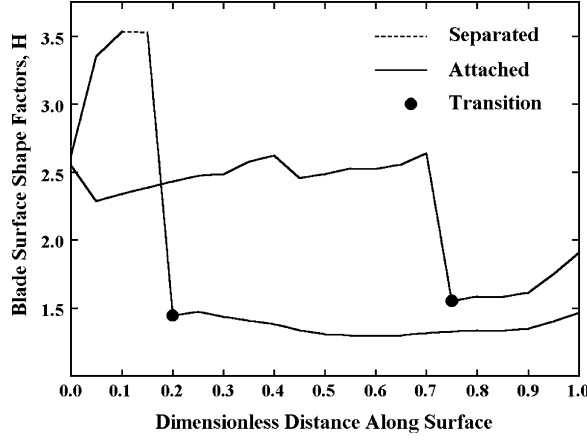
Second, large values of θ_{12} can cause Eq. (14-65) to become singular. Hence, the following limit should be imposed.

$$\theta_{12} \leq 0.99 \delta / (n - 1) \quad (14-105)$$

Figures 14-9 and 14-10 show blade surface boundary layer shape factor predictions for the sample radial-inflow turbine impeller detailed aerodynamic design of figure 11-16. There is a fairly significant laminar separation zone on the hub pressure surface and a rather minor one at the

**FIGURE 14-9. Hub Blade Surface Shape Factors**

shroud. As previously noted in chapter 11, this detailed impeller design is by no means optimized. The blade surface boundary layer analyses clearly show some of the weaknesses in the design. Figure 14-11 shows the meridional shape factor predictions for the end-wall boundary layers. As noted previously in this chapter, end-wall boundary layers in radial-inflow turbine impellers are usually very thin and well behaved. By contrast,

**FIGURE 14-10. Shroud Blade Surface Shape Factors**

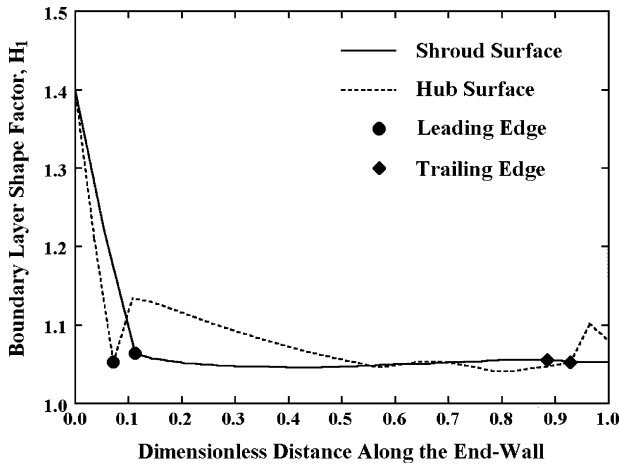


FIGURE 14-11. End-Wall Shape Factors

Aungier [2] shows that end-wall boundary layers in compressor blade rows can have a significant influence on the internal flow and losses. Hence, the end-wall boundary layer analysis is not too significant for the present application but may be worth including for greater generality.

REFERENCES

- [1] Aungier, R. H., 2000, *Centrifugal Compressors: A Strategy for Aerodynamic Design and Analysis*, ASME Press, New York.
- [2] Aungier, R. H., 2003, *Axial-Flow Compressors: A Strategy for Aerodynamic Design and Analysis*, ASME Press, New York.
- [3] Sheppard, D. G., 1956, *Principles of Turbomachinery*, Macmillan, New York.
- [4] Kofskey, M. G. and Holeski, D. E., 1966, "Cold Performance Evaluation of a 6.02-Inch Radial Inflow Turbine Designated for a 10-Kilowatt Shaft Output Brayton Cycle Space Power Generation System," NASA Technical Note TN D-2987, National Aeronautics and Space Administration, Washington, DC.
- [5] Whitney, W. J. and Stewart, W. L., 1962, "Analytical Investigation of Performance of Two-Stage Turbine Over a Range of Ratios of Specific Heats from 1.2 to $1\frac{2}{3}$," Technical Note TN D-1288, NASA, Washington, DC.
- [6] Aungier, R. H., 1998, "Thermodynamic State Relations," in *The Handbook Of Fluid Dynamics* (Johnson, R. W., editor), CRC Press, Boca Raton, FL, pp. 4-29–4-34.
- [7] Aungier, R. H., 1995, "A Fast, Accurate Real Gas Equation of State for Fluid Dynamic Analysis Applications," *Trans. ASME Journal of Fluids Engineering*, June, pp. 277–281.
- [8] Schultz, J. M., 1962, "The Polytropic Analysis of Centrifugal Compressors," *Trans. ASME, Journal of Engineering for Power*, Jan., pp. 69–82.
- [9] Mallen, M. and Saville, G., 1977, "Polytropic Processes in the Performance Prediction of Centrifugal Compressors," Institution of Mechanical Engineers, Paper No. C183/77, pp. 89–96.
- [10] Huntington, R. A., 1985, "Evaluation of Polytropic Calculation Methods for Turbomachinery Performance," ASME Paper No. 85-GT-13, ASME, New York.
- [11] Ried, R. C., Prausnitz, J. M. and Sherwood, T. K., 1977, *The Properties of Gases and Liquids*, McGraw-Hill, New York.
- [12] Ried, R. C., Prausnitz, J. M. and Poling, B. E., 1987, *The Properties of Gases and Liquids*, 4th edition, McGraw-Hill, New York.
- [13] Yaws, C. L., 1999, *Chemical Properties Handbook*, McGraw-Hill, New York.

- [14] Nelson, L. C. and Obert, E. F., 1954, "Generalized pVT Properties of Gases," *Trans. ASME*, **76**, pp. 1057–1066.
- [15] Pitzer, K. S., Lippmann, D. Z., Curl, R. F., Huggins, C. M. and Peterson, D. E., 1955, "The Volumetric and Thermodynamic Properties of Fluids. II. Compressibility Factor, Vapor Pressure and Entropy of Vaporization," *American Chemical Society*, **77**, pp. 3427–3440.
- [16] Redlich, O. and Kwong, J., 1949, "On the Thermodynamics Solution. V. An Equation of State. Fugacities of Gaseous Solutions," *Chemical Review*, **44**, pp. 233–244.
- [17] Barnes, F. J., 1973, Ph.D. thesis, Department of Chemical Engineering, University of California, Berkeley.
- [18] Soave, G., 1972, "Equilibrium Constants from a Modified Redlich-Kwong Equation of State," *Chemical Eng. Science*, **27**, 1197–1203.
- [19] Wilson, G. M., 1966, "Calculation of Enthalpy Data from a Modified Redlich-Kwong Equation of State," *Adv. Cryogenic Eng.*, **11**, p. 392.
- [20] Ried, R. C. and Sherwood, T. K., 1966, *The Properties of Gases and Liquids*, McGraw-Hill, New York.
- [21] Chen, N. H., 1965, "Generalized Correlation for Latent Heat of Vaporization," *J. Chemical Eng. Data*, American Chemical Society, Washington, DC, pp. 207–210.
- [22] Gunn, R. D. and Yamada, T., 1971, *AICHE Journal*, **17**, p. 1341.
- [23] Dean, D. E. and Stiel, L. I., 1965, *AICHE Journal*, **11**, p. 526.
- [24] Novak, R. A., 1967, "Streamline Curvature Computing Procedures for Fluid-Flow Problems," *Trans. ASME, Journal of Engineering for Power*, Oct., pp. 478–490.
- [25] Vavra, M. H., 1960, *Aero-Thermodynamics and Flow in Turbomachines*, Wiley, New York.
- [26] Wu, C. H., 1952, "A General Theory of Three-Dimensional Flow in Subsonic and Supersonic Turbomachines of Axial-, Radial- and Mixed-Flow Types," Technical Note TN 2604, National Advisory Committee for Aeronautics (NACA), Washington, DC.
- [27] Schlichting, H., 1968, *Boundary-Layer Theory*, 6th Ed., McGraw-Hill, New York.
- [28] Schlichting, H., 1979, *Boundary-Layer Theory*, McGraw-Hill, New York.
- [29] Aungier, R. H., 1988, "A Performance Analysis for the Vaneless Components of Centrifugal Compressors," *Flows in Non-Rotating Turbomachinery Components, FED*, Vol. 69, ASME, New York, pp. 35–43.
- [30] Davis, W. R., 1976, "Three-Dimensional Boundary-Layer Computation on the Stationary End-Walls of Centrifugal Turbomachinery," *Trans. ASME, Journal of Fluids Engineering*, Sept., pp. 431–442.
- [31] Senoo, Y., Kinoshita, Y. and Ishida, M., 1977, "Axisymmetric Flow in Vaneless Diffusers of Centrifugal Blowers," *Trans. ASME, Journal of Fluids Engineering*, March, pp. 104–114.

- [32] Balsa, T. F. and Mellor, G. L., 1975, "The Simulation of Axial Compressor Performance Using an Annulus Wall Boundary Layer Theory," *Trans. ASME, Journal of Engineering for Power*, July, pp. 305–317.
- [33] Horlock, J. H., 1970, "Boundary Layer Problems in Axial Turbomachines," in *Flow Research on Blading* (L. S. Dring, editor), Elsevier Publishing, Amsterdam, pp. 322–371.
- [34] Rotta, J. C., 1966, "Recent Developments in Calculation Methods for Turbulent Boundary Layers with Pressure Gradients and Heat Transfer," *Trans. ASME, Journal of Applied Mechanics*, p. 429.
- [35] Head, M. R., 1958, "Entrainment in the Turbulent Boundary Layer," R&M 3152, Aeronautical Research Council, London.
- [36] Head, M. R., 1968, "Cambridge Work on Entrainment," in *Proceedings of Computation of Turbulent Boundary Layers*, Thermosciences Division, Stanford University, CA, pp. 188–194.
- [37] Mellor, G. L. and Wood, G. M., 1971, "An Axial Compressor End-Wall Boundary Layer Theory," *Trans. ASME, Journal of Basic Engineering*, pp. 300–316.
- [38] Smith, L. H. Jr., 1970, "Casing Boundary Layers in Multi-Stage Axial-Flow Compressors," in *Flow Research on Blading* (Dring, L. S., editor), Elsevier, Amsterdam, pp. 275–304.
- [39] Koch, C. C. and Smith, L. H. Jr., 1976, "Loss Sources and Magnitudes in Axial-Flow Compressors," *Trans. ASME, Journal of Engineering for Power*, pp. 411–424.
- [40] Hunter, I. H. and Cumpsty, N. A., 1982, "Casing Wall Boundary-Layer Development Through an Isolated Compressor Rotor," *Trans. ASME, Journal of Engineering for Power*, Oct., pp. 805–818.
- [41] Ainley, D. G. and Mathieson, G. C. R., 1951, "A Method of Performance Estimation for Axial-Flow Turbines," R&M 2974, Aeronautical Research Council, London.
- [42] Dunham, J. and Came, P. M., 1970, "Improvements to the Ainley-Mathieson Method of Turbine Performance Prediction," *Trans. ASME, Journal of Engineering for Power*, July, pp. 252–256.
- [43] Kacker, S. C. and Okapuu, U., 1981, "A Mean Line Prediction Method for Axial Flow Turbine Efficiency," Paper No. 81-GT-58, ASME, New York.
- [44] Craig, H. R. M. and Cox, H. J. A., 1971, "Performance Estimation of Axial Flow Turbines," *Proceedings of the Institution of Mechanical Engineers, London*, **185**, pp. 407–424.
- [45] Traupel, W., 1966, *Thermische Turbomaschinen*, Springer-Verlag, Berlin.
- [46] Stewart, W. L., 1961, "A Study of Axial Flow Turbine Efficiency Characteristics in Terms of Velocity Diagram Parameters," Paper No. 61-WA-37, ASME, New York.
- [47] Lee, J. F., 1954, *Theory and Design of Steam and Gas Turbines*, McGraw-Hill, New York.

- [48] Pai, S., 1956, *Viscous Flow Theory, I—Laminar Flow*, Van Nostrand, Princeton, NJ.
- [49] Pai, S., 1957, *Viscous Flow Theory, II—Turbulent Flow*, Van Nostrand, Princeton, NJ.
- [50] Benedict, R. P., Carlucci, N. A. and Swetz, S. D., 1966, "Flow Losses in Abrupt Enlargements and Contractions," *Trans. ASME, Journal of Engineering for Power*, Jan., pp. 73–81.
- [51] Kreith, F., 1966, *Principles of Heat Transfer*, International Book Company, Scranton, PA.
- [52] Egli, A., 1935, "The Leakage of Steam Through Labyrinth Glands," *Trans. ASME*, **57**, pp. 115–122.
- [53] Suter, P. and Traupel, W., 1959, "Untersuchungen über den Ventilationsverlust von Turbinenradern," *Mittl. Inst. Therm. Turbomasch.*, ETH, Zurich, **4**.
- [54] Horlock, J. H., 1966, *Axial-Flow Turbines*, Butterworths, London.
- [55] Daily, J. W. and Nece, R. E., 1960, "Chamber Dimension Effects on Induced Flow and Frictional Resistance of Enclosed Rotating Disks," *Trans. ASME, Journal of Basic Engineering*, Mar., pp. 217–232.
- [56] Daily, J. W. and Nece, R. E., 1960, "Roughness Effects on Frictional Resistance of Enclosed Rotating Disks," *Trans. ASME, Journal of Basic Engineering*, Sept., pp. 553–562.
- [57] Baumann, K., 1921, "Some Recent Developments in Large Steam Turbine Practice," *Journal of the Institution of Electrical Engineers*, **59**, p. 565.
- [58] Katsanis, T., 1964, "Use of Arbitrary Quasi-Orthogonals for Calculating Flow Distribution in the Meridional Plane of a Turbomachine," Technical Note TN D-2546, NASA, Washington, DC.
- [59] Novak, R. A., 1973, "Axisymmetric Computing Systems for Axial Flow Turbomachinery," Lecture Notes from the ASME Turbomachinery Institute Fluid Dynamics of Turbomachinery, Iowa State University, Ames, Lecture 25.
- [60] Perera, J. V., 1990, "Steam Turbine Performance Gains from Improved Blade Designs," 1990 Joint Power Generation Conference, Boston, MA.
- [61] Perera, J. V., 1992, "Redesigned Turbine Blading and Steam Path Optimization for Higher Efficiency," 1992 EPRI Steam and Combustion Turbine Blading Conference, Orlando, FL.
- [62] Hirsch, C. and Denton, J. D. (editors), 1982, "Through Flow Calculations in Axial Turbomachines," in *AGARD Advisory Report No. 175*, North Atlantic Treaty Organization.
- [63] Groschup, G., 1977, *Stromungstechnische Untersuchung einer Axialturbinenstufe im Vergleich zum Verhalten der ebenen Gitter ihrer Beschaufelung*, Doktor Ingenieur dissertation, Technical University of Hannover, Germany.

- [64] Lueders, H. G., 1967, "Experimental Investigation of Advanced Concepts to Increase Turbine Blade Loading—I. Analysis and Design," NASA CR-735, NASA, Washington, DC.
- [65] Lueders, H. G., 1968, "Experimental Investigation of Advanced Concepts to Increase Turbine Blade Loading—II. Performance Evaluation of Plain Rotor Blade," NASA CR-1172, NASA, Washington, DC.
- [66] Welna, H. and Dahlberg, D. E., 1971, "Investigation of a Highly Loaded Two-Stage Fan-Drive Turbine," Technical Report AFAPL-TR-69-92, Vol. VI, Air Force Aero Propulsion Laboratory, Wright-Patterson AFB, OH.
- [67] Carmichael, A., 1972, "The Aerodynamic Design of Axial-Flow and Radial-Inflow Turbines," in *Sawyer's Gas Turbine Engineering Handbook* (Sawyer, J. W., editor), Gas Turbine Publications, Stamford, CT, Chapter 4.
- [68] Balje, O. E., 1981, *Turbomachines, A Guide to Design, Selection and Theory*, Wiley, New York.
- [69] Fielding, L., 2000, *Turbine Design, The Effect on Axial Turbine Performance of Parameter Variation*, ASME Press, New York.
- [70] Smith, S. F., 1965, "A Simple Correlation of Turbine Efficiency," *Journal of the Royal Aeronautical Society*, **69**, pp. 467–470.
- [71] Zweifel, O., 1945, "The Spacing of Turbo-Machine Blading Especially with Large Angular Deflection," *Brown-Boveri Review*, Dec., pp. 436–444.
- [72] Ye, Z.-Q., 1984, "A Systematic Computational Design System for Turbine Cascades, Airfoil Geometry and Blade-to-Blade Analysis," *Trans. ASME, Journal of Engineering for Gas Turbines and Power*, July, pp. 598–605.
- [73] Pritchard, L. J., 1985, "An Eleven Parameter Axial Turbine Airfoil Geometry Model," Paper No. 85-GT-219, ASME, New York.
- [74] Whitney, W. J., Szanca, E. M., Moffitt, T. P. and Monroe, D. E., 1967, "Cold-Air Investigation of a Turbine for High-Temperature-Engine Application," Technical Note TN D-3751, NASA, Washington, DC.
- [75] Khalil, I. M., Tabakoff, W. and Hamed, A., 1976, "Losses in Radial-Inflow Turbines," Paper No. 76-FE-9, ASME, New York.
- [76] Wallace, F. J., Bains, N. C. and Whitfield, A., 1976, "A Unified Approach to the One-Dimensional Analysis and Design of Radial and Mixed Flow Turbines," Paper No. 76-GT-100, ASME, New York.
- [77] Benson, R. S., 1971, "Prediction of Performance of Radial Gas Turbines in Automotive Turbochargers," Paper No. 71-GT-66, ASME, New York.
- [78] Rohlik, H. E., 1968, "Analytical Determination of Radial-Inflow Turbine Design Geometry for Maximum Efficiency," Technical Note TN D-4384, NASA, Washington, DC.
- [79] Jansen, W. and Qvale, E. B., 1967, "A Rapid Method of Predicting the Off-Design Performance of Radial-Inflow Turbines," Paper No. 67-WA/GT-3, ASME, New York.

- [80] Rogers, C., 1966, "Efficiency and Performance Characteristics of Radial Turbines," Paper No. 660754, Society of Automotive Engineers (SAE), New York.
- [81] Futral, S. M., 1965, "Off-Design Performance Prediction with Experimental Verification for a Radial-Inflow Turbine," Technical Note TN D-2621, NASA, Washington, DC.
- [82] Jamieson, A. W. H., 1955, "The Radial Turbine", in *Gas Turbine Principles and Practice* (Cox, H. R., editor), Van Nostrand, Princeton, NJ, Chapter 9.
- [83] Balje, O. E., 1952, "A Contribution to the Problem of Designing Radial Turbomachines," *Trans. ASME*, **74**, pp. 451–472.
- [84] Thwaites, B., 1949, "Approximate Calculation of the laminar Boundary Layer," *Aeronautical Quarterly*, **1**, pp. 245–280.
- [85] Buri, A., 1931, "A Method of Calculation for the Turbulent Boundary Layer with Accelerated or Retarded Flow," Thesis No. 652, Federal Tech. College, Zurich, Switzerland.
- [86] Nikuradse, J., 1930, "Laws of Resistance and Velocity Distributions for Turbulent Flow of Water in Smooth and Rough Pipes," Proceedings 3rd International Congress for Applied Mechanics, Stockholm, Sweden, pp. 239–248.
- [87] Lieblein, S. and Roudebush, W. H., 1956, "Theoretical Loss Relations For Low-Speed Two-Dimensional-Cascade Flow," Technical Note TN 3662, National Advisory Committee For Aeronautics (NACA), Washington, DC.
- [88] Herrig, L. J., Emery, J. C., and Erwin, J. R., 1957, "Systematic Two-Dimensional Cascade Tests of NACA 65-Series Compressor Blades at Low Speeds," Technical Note TN 3916, NACA, Washington, DC.
- [89] Wiesner, F. J., 1967, "A Review of Slip Factors for Centrifugal Impellers," *Trans. ASME, Journal of Engineering for Power*, Oct., pp. 558–572.
- [90] Aungier, R. H., 1988, "A Systematic Procedure for the Aerodynamic Design of Vaned Diffusers," in *Flows in Non-Rotating Turbomachinery Components*, Vol. 69, ASME, New York, NY, pp. 27–34.
- [91] Aungier, R. H., 1990, "Aerodynamic Performance Analysis of Vaned Diffusers," in *Fluid Machinery Components*, Vol. 101, ASME, New York, pp. 27–44.
- [92] Reneau, L., Johnston, J. and Kline, S., 1967, "Performance and Design of Straight Two-Dimensional Diffusers," *Trans. ASME, Journal of Basic Engineering*, pp. 141–150.
- [93] Hiett, G. F. and Johnston, I. H., 1964, "Experiments Concerning the Aerodynamic Performance of Inward Flow Radial Turbines," *Proceedings of the Institution of Mechanical Engineers, London*, **178**, pp. 30–63.

- [94] Aungier, R. H., 1995, "Centrifugal Compressor Preliminary Aerodynamic Design and Component Sizing," Paper No. 95-GT-78, ASME, New York.
- [95] Wood, H. J., 1963, "Current Technology of Radial-Inflow Turbines for Compressible Fluids," *Trans. ASME, Journal of Engineering for Power*, pp. 72–83.
- [96] Linhardt, H. D., 1973, "Cryogenic Turboexpanders," *LNG/Cryogenics*, Feb./Mar., pp. 7–15.
- [97] Rohlik, H. E., 1968, "Analytical Determination of Radial Inflow Turbine Design Geometry for Maximum Efficiency," Technical Note TN D-4384, NASA, Washington, DC.
- [98] Jamieson, A. W. H., 1955, "The Radial Turbine," in *Gas Turbine Principles and Practice* (Roxbee-Cox, Sir H., editor), George Newnes, London, Chapter 9.
- [99] Watanabe, I., Ariga, I. and Mashimo, T., 1970, "Effect of Dimensional Parameters of Impellers on Performance Characteristics of a Radial-Inflow Turbine," Paper No. 70-GT-90, ASME, New York.
- [100] Casey, M. V., 1983, "A Computational Geometry for the Blades and Internal Flow Channels of Centrifugal Compressors," *Trans. ASME, Journal of Engineering for Power*, **105**, pp. 288–295.
- [101] Forest, A. R., 1972, "Interactive Interpolation and Approximation by Bezier Polynomials," *Computer Journal*, **15**, pp. 71–79.
- [102] Walsh, J. L., Ahlberg, J. H. and Nilson, E. N., 1962, "Best Approximation Properties of the Spline Fit," *Journal of Mathematics and Mechanics*, **11**, pp. 225–234.
- [103] Sovran, G. and Klomp, E. D., 1967, "Experimentally Determined Optimum Geometries for Rectilinear Diffusers with Rectangular, Conical or Annular Cross-Section," *Fluid Mechanics of Internal Flows* (Soveran, G., editor), Elsevier, Amsterdam.
- [104] Dolan, F. X. and Runstadler, P. W., 1973, "Pressure-Recovery Performance of Conical Diffusers at High Subsonic Mach Numbers, Report CR-2299, NASA, Washington, DC.
- [105] Aungier, R. H., 1993, "Aerodynamic Design and Analysis of Vaneless Diffusers and Return Channels," Paper No. 93-GT-101, ASME, New York.
- [106] Katsanis, T., 1968, "Computer Program for Calculating Velocities and Streamlines on a Blade-To-Blade Stream Surface of a Turbomachine," Technical Note TN D-4525, NASA, Washington, DC.
- [107] Katsanis, T., 1969, "Fortran Program for Calculating Transonic Velocities on a Blade-To-Blade Stream Surface of a Turbomachine," Technical Note TN D-5427, NACA, Washington, DC.
- [108] Smith, D. J. L. and Frost, D. H., 1969, "Calculation of the Flow Past Turbomachine Blades," *Proceedings of the Institute of Mechanical Engineers*, **184**, Paper 27.

- [109] Dunavant, J. C., Emery, J. C., Walch, H. C. and Westphal, W. R., 1955, "High-Speed Cascade Tests of the NACA 65-(12A₁₀)-10 and NACA 65-(12A₂I_{8b})-10 Compressor Blade Sections," Research Memorandum RM-L55I08, NACA, Washington, DC.
- [110] Von Neumann, J. and Richtmyer, R. D., 1950, "A Method for the Numerical Calculation of Hydrodynamic Shocks," *Journal of Applied Physics*, **21**, pp. 232–237.
- [111] Lax, P. D., 1954, "Weak Solutions of Nonlinear Hyperbolic Equations and Their Numerical Computation," *Commun. Pure Appl. Math.*, **7**, pp. 159–193.
- [112] Lax, P. D. and Wendroff, B., 1964, "Differencing Schemes for Hyperbolic Equations with High Order of Accuracy," *Commun. Pure Appl. Math.*, Vol. **17**, pp. 381–398.
- [113] Aungier, R. H., 1968, "A Time-Dependent Numerical Method for Calculating the Flow about Blunt Bodies," Technical Report AFWL-TR-68-52, Air Force Weapons Laboratory, Kirtland AFB, NM.
- [114] Aungier, R. H., 1970, "A Computational Method for Exact, Direct and Unified Solutions For Axisymmetric Flow over Blunt Bodies of Arbitrary Shape (Program BLUNT)," Technical Report AFWL-TR-70-16, Air Force Weapons Laboratory, Kirtland AFB, NM.
- [115] Aungier, R. H., 1971, "A Computational Method for Unified Solutions to the Inviscid Flow Field about Blunt Bodies," in *The Entry Plasma Sheath and Its Effects on Space Vehicle Electromagnetic Systems (Proceedings of the Fourth Plasma Sheath Symposium)*, Special Publication SP-252, NASA, Washington, DC, pp. 241–260.
- [116] Aungier, R. H., 1971, "A Computational Method for Two-Dimensional, Axisymmetric and Three-Dimensional Blunt Body Flows (Program ATTACK)," Technical Report AFWL-TR-70-124, Air Force Weapons Laboratory, Kirtland AFB, NM.
- [117] Gopalakrishnan, S. and Bozzola, R., 1973, "Numerical Representation of Inlet and Exit Boundary Conditions in Transient Cascade Flow," Paper No. 73-GT-55, ASME, New York.
- [118] Denton, J. D., 1982, "An Improved Time-Marching Method for Turbomachinery Flow Calculation," Paper No., 82-GT-239, ASME, New York.
- [119] Courant, R., Friedrichs, K. O. and Lewy, H., 1928, "Über die Partiellen Differenzengleichungen der Mathematischen Physik," *Math. Ann.*, **100**, p. 32.
- [120] Gruschwitz, E., 1950, "Calcul Approché de la Couche Limité Laminaire en Ecoulement compressible Sur Une Paroi Non-conductrice de la Chaleur," Office National d'Etudes et de Recherche Aeronautiques (ONERA), Paris, Publication No. 47.
- [121] Pohlhausen, K., 1921, "Zur Naherungsweisen Integration der Differential-Gleichung der Laminare Reibungsschicht," *ZAMM*, **1**, p. 235.

- [122] Green, J. E., 1968, "The Prediction of Turbulent Boundary Layer Development in Compressible Flow," *Journal of Fluid Mechanics*, **31**, p. 753.
- [123] Ludwieg, H. and Tillmann, W., 1950, "Investigations of the Wall-Shearing Stress in Turbulent Boundary Layers," Technical Memorandum TM 1285, NACA, Washington, DC.

ABOUT THE AUTHOR

Since retiring in 2004, Mr. Aungier has been an independent consultant in turbomachinery aerodynamics, working from his home in Greensburg, Pennsylvania. He has been active in fluid mechanics research and development for thirty-nine years, including thirty-five years specializing in the aerodynamic design and analysis of centrifugal compressors, axial-flow compressors, radial-inflow turbines and axial-flow turbines. He has numerous publications in this field, primarily through the American Society of Mechanical Engineers. He is a graduate of Cornell University, where he received a masters degree in Aerospace Engineering and a bachelors degree in Engineering Physics. Mr. Aungier is a Fellow of the ASME.

Mr. Aungier started his career in 1966 as an officer in the U.S. Air Force, conducting research in hypersonic reentry vehicle aerodynamics at the Air Force Weapons Laboratory in Albuquerque, New Mexico. He is the author of numerous Air Force and NASA publications, some of which are the basis for one of the analysis techniques described in this book. Mr. Aungier joined the Research Division of Carrier Corporation in Syracuse, New York in 1970, where he spent eleven years managing and conducting applied research on the fluid dynamics of turbomachinery and air handling equipment. His individual research at Carrier focused on turbomachinery aerodynamics, including the development of aerodynamic performance analysis techniques for axial-flow compressors, centrifugal compressors and radial-inflow turbines.

In 1981 Mr. Aungier transferred to the Elliott Company (then a division of Carrier Corporation) in Jeannette, Pennsylvania as the manager of Compressor Development. There his interests expanded to include the development of systematic and efficient techniques for the aerodynamic design of turbomachinery. His responsibilities were extended to include turbine aerodynamic development in 1983 and mechanical design and analysis in 1987. He held several positions of increasing responsibility with the Elliott Company the last of which was the manager of Advanced Technology. Throughout his career, he has been an active contributor to turbomachinery aerodynamic technology, specializing in comprehensive aerodynamic design and analysis systems. ASME Press published his first book, describing his centrifugal compressor aerodynamic design and analysis system, in 2000 followed by a similar book on axial-flow compressors in 2003. The present book provides a similar description of his axial-flow turbine and radial-inflow turbine aerodynamic design and analysis systems.

